University of Plymouth

PEARL **https://pearl.plymouth.ac.uk**

04 University of Plymouth Research Theses 01 Research Theses Main Collection

1995

Computer Models of Corrosion in Passivating Systems

Phillips, Simon Sebastian

http://hdl.handle.net/10026.1/1278

http://dx.doi.org/10.24382/4774
University of Plymouth

All content in PEARL is protected by copyright law. Author manuscripts are made available in accordance with publisher policies. Please cite only the published version using the details provided on the item record or document. In the absence of an open licence (e.g. Creative Commons), permissions for further reuse of content should be sought from the publisher or author.

COMPUTER MODELS OF CORROSION IN PASSIVATING SYSTEMS

by

SIMON SEBASTIAN PHILLIPS

A thesis submitted to the University of Plymouth

in partial fulfilment for the degree of

DOCTOR OF PHILOSOPHY

Engineering Materials Section

Department of Materials Technology

Faculty of Technology

Royal Naval Engineering College

Manadon

Plymouth

In collaboration with

School of Manufacturing, Materials and Mechanical Engineering

University of Plymouth

July 1995

Abstract

Computer Models of Corrosion in Passivating Systems by Simon Sebastian Phillips

Analysis of corrosion in marine and acid environments is a complicated task, involving the interaction of thermodynamic, kinetic and geometrical factors. Two mathematical models which predict corrosion behaviour have been implemented for personal computers.

The first program uses an assumption of unidirectional current flow to simplify the prediction of potential distributions for systems of essentially cylindrical geometry containing natural seawater-based electrolytes of differing strength. Using experimentally determined electrochemical and flow rig data, experimental and theoretical results were compared. The correlation between the two was shown to be poor, and this is attributed to the unrepresentative nature of the electrochemical data input to the model.

The second model involves the synthesis of polarization curves. Several algorithms to model passivating behaviour have been studied, and one was selected and incorporated into the calculation routine. A number of kinetic and thermodynamic parameters are used in algorithms describing such behaviour, along with activation, concentration and solution polarization effects, for a number of redox reactions, which are then combined to produce an overall potential-log current density curve.

Experimentally determined data for pure iron and different stainless steels in marine and acid environments of differing dissolved oxygen content and temperature were obtained. Theoretical models were constructed for each system, and compared to experimental data.

Excellent correlation between experimental and theoretical data was obtained for potential ranges in excess of 2 V.

Trends in parameter values were discussed, and compared to published data. The transition between stable and unstable passivity of stainless steels was shown to be dependent on the oxygen reduction diffusion limited current density and the iron dissolution reaction free corrosion current density, which in turn was linked to the dissolved oxygen content and temperature of the electrolyte. A new model for the behaviour of stainless steels in the transpassive region was proposed.

Table of Contents

Abstract i

Table of Contents iii

List of Figures xiv

List of Tables xxvi

Chapter 1 The GC Galvanic Corrosion Computer Model 1

1.1 INTRODUCTION 1

1.1.1 Definitions of Corrosion 1

1.1.2 The Behaviour of Metals in Electrolytes 2

1.1.3 Electrode Potentials 3

1.1.4 Polarization Curves 4

1.1.4.1 Activation Polarization 5

1.1.4.2 Diffusion-Limited Polarization 6

1.1.4.3 Resistance Polarization 7

1.1.5 Galvanic Corrosion Theory 7

1.1.5.1 Evans Diagrams 7

1.1.5.2 Factors Affecting Galvanic Corrosion 7

1.1.6 Seawater Composition and Properties 11

1.2 MODELLING OF GALVANIC CORROSION 13

1.2.1 Complex and Analytical Solutions 14

1.2.2 Simple Solutions - Unidirectional Current Flow 14

1.2.3 Limitations of Unidirectional Current Flow 16

1.3 THE GC COMPUTER MODEL 18

1.3.1 Description of Algorithm 18

1.3.2 Model Predictions 20

1.3.2.1 Effect of Electrolyte Resistivity on Potential Distribution 20

1.3.2.2 Variation of Junction Potential with Slope of Cathodic Polarization Curve 20

1.3.2.3 Variation of Junction Potential with Slope of Anodic Polarization Curve 22

1.3.2.4 Variation of Junction Potential with Number of Cathodic Tubes 23

1.3.2.5 Relationship Between Anode Length and Junction Potential 23

1.3.2.6 Variation of Junction Potential with Length of Cathode 24

1.3.2.7 Variation of Junction Potential with Cathodic Tube Radius. 25

1.4 EXPERIMENTAL 26

1.4.1 Materials and Methods 26

1.4.2 Material Analysis 27

1.4.3 Equipment Design and Manufacture 28

1.4.4 Electrolyte 29

1.4.6 Flow Loop and Static Studies 30

1.4.7 Potentiodynamic Studies 31

1.5 RESULTS AND INITIAL DISCUSSION 32

1.5.1 Material Composition 32

1.5.2 Potentiodynamic Testing 33

1.5.3 Potential Distributions for Static Flow 35

1.5.3.1 The Effect of Electrolyte Resistivity 36

1.5.3.2 The Effect of Differing Anode Length 38

1.5.3.3 The Effect of Differing Cathode Diameter 43

1.5.3.4 The Effect of Altering Number of Cathodic Tubes . . 45

1.5.4 Potential Distributions for Flow Conditions 48

1.5.4.1 The Effect of Different Flow Rates 49

1.5.4.2 The Effect of Different Electrolyte Resistivity 51

1.5.4.3 Different Number of Cathodic Tubes 54

1.6 DISCUSSION 56

1.6.1 Correlation Between Experimental and Predicted Results 56

Chapter 2 Theory of Passivation 58

2.1 PROTECTION AND PASSIVATION 58

2.2 ANODIC PROTECTION 58

2.3 CHEMICAL PASSIVATION 60

2.4 CHARACTERISTICS OF PASSIVATION 64

2.5 THE SOLID STATE THEORY OF PASSIVATION 68

2.6 ALTERNATIVE MODEL FOR PASSIVATION - THE ELECTRODIC MODEL 69

2.7 PERCOLATION THEORY OF PASSIVATION 71

2.8 THE MARCUS PASSIVITY PROMOTER ARGUMENT 72

2.9 THE NATURE OF THE PASSIVE FILM ON STAINLESS STEELS . . 75

Chapter 3 A Polarization Curve Model For Passivating Materials 80

3.1 INTRODUCTION 80

3.2 POLARIZATION CURVE MODELS 81

3.2.1 Equations Used to Model Non-Passivating Behaviour 81

3.2.2 The SIMPLER™ Algorithm 83

3.2.3 Passivation Algorithms 86

3.2.3.1 Devereux and Yeum 86

3.2.3.2 Bernhardsson 87

3.2.3.3 Mueller 92

3.2.3.4 Trethewey and Wilson 97

3.2.3.5 Hines 98

3.2.4 Rationale Behind Algorithms Used 99

3.2.5 Equations Used for Transitions 100

3.3 INCORPORATION OF PASSIVATING BEHAVIOUR ROUTINES INTO THE SIMPLER™ SOFTWARE 102

3.3.1 The Buffer Equation 102

3.3.1.1 Alterations to Published Form of Buffer Equation . . . 104

3.3.1.2 Incorporation of the Buffer Equation into the Modelling Software 105

3.3.1.3 Floating Point Errors within The SBUF Module 106

3.3.1.4 The Current Density Supported by the Unfilmed Metal During the Active-to-Passive Transition 107

3.3.1.5 Effect of Altering the Potential at the Midpoint of the S Function 110

3.3.1.6 Effect of Altering the Power p 111

3.3.1.7 The Effect of Altering the Passive Current Density . . 113

3.3.1.8 Effect of Altering the Constant A 114

3.3.1.9 Observations Made Regarding the Buffer Equation . . 116

3.3.2 The Raindrop Equation 116

3.3.2.1 Effect of Altering Active-to-Passive Transition Potential 116

3.3.2.2 Effect of Altering Power Used In Raindrop Equation 118

3.3.2.3 Effect of Altering i_{pass} 119

3.3.2.4 Effects of Altering A in Raindrop Equation 120

3.3.2.5 Observations Regarding the Raindrop Equation 121

3.4 THE EFFECTS OF ADDING HYDROGEN AND OXYGEN REACTIONS 122

Chapter 4 Section 1 Modelling the Electrochemical Behaviour of Iron in Aqueous Sulphuric Acid 125

4.1.1 INTRODUCTION 125

4.1.2 EXPERIMENTAL PROCEDURE 128

4.1.3 RESULTS 129

4.1.3.1 Electrochemical Reaction Scheme for Iron in Sulphuric Acid 129

4.1.3.2 Modelling the Cathodic and Anodic Activation-Controlled Reactions 130

4.1.3.3 Modelling the Active-to-Passive Transition 132

4.1.3.4 Addition of the Fe(II) Oxidation Process and Addition of the Oxygen Evolution Reaction 134

4.1.4 DISCUSSION OF RESULTS 138

4.1.4.1 Effects of Scan Rate and Electrode Rotation 138

4.1.4.2 Possible Explanations for Deviations in Behaviour of Active-to-Passive Transition 139

4.1.4.3 Comparison of Parameters Used with Published Data 144

4.1.4.4 Passive Current Density 144

4.1.5 CONCLUDING REMARKS 145

Chapter 4 Section 2 Modelling the Polarisation Curve Behaviour of Type 304 Stainless Steel in Aerated and Deaerated Sulphuric Acid Solution 146

4.2.1 INTRODUCTION 146

4.2.2 EXPERIMENTAL 147

4.2.3 MODELLING PROCEDURE 147

4.2.3.1 304 Stainless Steel in Deaerated 5% H_2SO_4 148

4.2.3.2 Dissolution Model Proposed for 304 Stainless Steel 150

4.2.3.3 The Devereux and Yeum Model 150

4.2.3.4 Chromium Oxide Influence 154

4.2.3.5 Effect of Coefficients in Nernst Equation and Symmetry Factor on Tafel Slopes for the Oxygen Evolution Reaction . . 156

4.2.3.6 Role of the Dichromate and Acid Chromate Ions 160

4.2.3.7 The Form of the Cr_2O_3 Film 164

4.2.3.8 Final Set of Parameters Used To Model 304 Stainless Steel in Deaerated Sulphuric Acid 165

4.2.3.9 Modelling the Behaviour of 304 in Aerated 5% Sulphuric Acid 167

4.2.3.10 Modelling the Behaviour of 304 in 5% Sulphuric Acid with Restricted Oxygen Access 174

4.2.4 DISCUSSION 180

4.2.4.1 The Oxygen Reduction Reaction and Overpotential 180

4.2.4.2 Modelling in Aerated and Deaerated Sulphuric Acid 182

4.2.4.3 Passive Current Density 183

2.4.4 Current Density Limits in Oxidation Reactions 184

4.2.5 CONCLUDING REMARKS 186

Chapter 4 Section 3 Polarization Curve Behaviour of 304 Stainless Steel in 5% H_2SO_4 with Three Different Levels of Dissolved Oxygen at Different Temperatures 188

4.3.1 INTRODUCTION 188

4.3.2 EXPERIMENTAL 188

4.3.3 RESULTS AND INITIAL DISCUSSION 189

4.3.3.1 Experimental Results 189

4.3.3.2 304 Stainless Steel in Deaerated 5% H_2SO_4 193

4.3.3.3 Reactions Used in Model 195

4.3.3.4 Change of Tafel Slope for Reaction 3 195

4.3.3.5 Introduction of Concept of Multistep Electron Transfer Reactions 196

4.3.3.6 Calculation of Transfer Coefficients for A Multistep Reaction 197

4.3.3.7 Reaction Paths for Reaction 3 201

4.3.3.8 Incorporation of Different Reaction Mechanisms and $\alpha^{\rightarrow}$ into the Tafel Constant Calculation 207

4.3.3.9 Dissolved Oxygen Measurements 212

4.3.3.10 Models of 304 Stainless Steel in Deaerated 5% H_2SO_4 213

4.3.3.11 Models of 304 Stainless Steel in Aerated 5% H_2SO_4 218

4.3.3.12 Models of 304 Stainless Steel in Stagnant 5% H_2SO_4 222

4.3.4 ANALYSIS OF MODELLING TRENDS 226

4.3.4.1 Change in Behaviour Between Stable and Unstable Passivity in 5% H_2SO_4 with Different Oxygen Contents 226

4.3.4.2 Variation of Transition Potential E_t with Temperature. 232

4.3.4.3 Variation of Reaction 7 α with Temperature 233

4.3.4.4 Solution Resistance 236

4.3.5 CONCLUDING REMARKS 237

Chapter 4 Section 4 The Corrosion of Duplex Stainless Steel in Natural Seawater 240

4.4.1 INTRODUCTION 240

4.4.2 EXPERIMENTAL 241

4.4.3 RESULTS 242

4.4.3.1 Potentiodynamic scans 242

4.4.3.2 Cyclic Polarization Scans 245

4.4.4.3 24°C Model 250

4.4.3.4 30°C Model 253

4.4.3.5 35°C Model 255

4.4.3.6 45°C Model 257

4.4.4 DISCUSSION 259

4.4.4.1 Alloy Composition 259

4.4.4.2 PRE_N Calculations 259

4.4.4.3 Comparison of Ferralium with Other Stainless Steels 260

4.4.4.4 Dependence of Breakdown Potential on Temperature 262

4.4.4.5 Modelling the Dependence of Breakdown Potential on Temperature 265

4.4.4.6 Modelling of Active Dissolution of Iron 267

4.4.4.7 The Oxygen Reduction Reaction 268

4.4.4.8 Other Efforts at Modelling Breakdown Potential 269

4.4.4 CONCLUDING REMARKS 269

Chapter 4 Section 5 The Corrosion of 316 Stainless Steel in 5% H_2SO_4 and Natural Seawater 271

4.5.1 INTRODUCTION 271

4.5.2 EXPERIMENTAL 272

4.5.3 RESULTS 273

4.5.3.1 Potentiodynamic Scans 273

4.5.3.2 Models for 316 Stainless Steel in Deaerated 5% H_2SO_4. 275

4.5.3.3 Models for 316 Stainless Steel in Aerated 5% H_2SO_4 279

4.5.3.4 Model for 316 Stainless Steel in Stagnant 5% H_2SO_4 283

4.5.3.5 Models for 316 Stainless Steel in Natural Seawater 287

4.5.4 ANALYSIS OF MODELLING TRENDS 291

4.5.4.1 Modelling the Behaviour of 316 Stainless Steel in 5% H_2SO_4 - Variation of Reaction 7 i_{lim} and α 291

4.5.4.2 Modelling the Behaviour of 316 Stainless Steel in 5% H_2SO_4 variation of Reaction 1 i_o with Temperature and Oxygen Concentration 295

4.5.4.3 Modelling the Iron Dissolution Reaction Behaviour for 316 Stainless Steel and Ferralium in Natural Seawater 296

4.5.4.4 Modelling Reaction 7 for 316 Stainless Steel and Ferralium in Seawater 299

4.5.4.5 Modelling the Variation of E_b with Temperature for 316

Stainless Steel in Natural Seawater 303

4.5.5 CONCLUDING REMARKS 305

4.2.6 Conclusions 307

Appendices 308

APPENDIX A CALCULATIONS FOR CRYOGENIC FITTING OF NAB INSERT 308

APPENDIX B POTENTIODYNAMIC CURVES FOR NAB AND TITANIUM IN 5, 50 AND 100 % CONDUCTIVITY SEAWATER AT DIFFERING FLOW RATES 309

APPENDIX C FORTRAN MODULE FOR BUFFER EQUATION 327

APPENDIX D FORTRAN MODULE FOR RAINDROP EQUATION 328

APPENDIX E PARAMETERS USED FOR 304 STAINLESS STEEL IN DEAERATED 5% H_2SO_4. 330

APPENDIX F PARAMETERS USED FOR 304 STAINLESS STEEL IN AERATED 5% H_2SO_4. 334

APPENDIX G PARAMETERS USED FOR 304 STAINLESS STEEL IN STAGNANT 5% H_2SO_4. 338

APPENDIX H PARAMETERS USED FOR 316 STAINLESS STEEL IN DEAERATED 5% H_2SO_4. 342

APPENDIX I PARAMETERS USED FOR 316 STAINLESS STEEL IN AERATED 5% H_2SO_4. 346

APPENDIX J PARAMETERS USED FOR 316 STAINLESS STEEL IN STAGNANT 5% H_2SO_4 350

APPENDIX K PARAMETERS USED FOR 316 STAINLESS STEEL IN

NATURAL SEAWATER 354

References 358

List of Figures

Chapter 1

Figure 1.1 Typical polarization curve for a metal in seawater.

Figure 1.2 Evans diagram for titanium and nickel aluminium bronze.

Figure 1.3 Effect of solution resistance on distribution of potential and corrosion rate of anode.

Figure 1.4 Variation of potential distribution with electrolyte resistivity predicted by model.

Figure 1.5 Dependence of junction potential on slope of cathodic polarization curve for a given anode component.

Figure 1.6 Dependence of junction potential on slope of anodic polarization curve for a given cathodic component.

Figure 1.7 Variation of junction potential with number of cathodic tubes.

Figure 1.8 Relationship between anode length and junction potential.

Figure 1.9 Cathode length-junction potential relationship.

Figure 1.10 Cathode tube radius relationship with junction potential.

Figure 1.11 Schematic of recirculating flow rig.

Figure 1.12 SSC Electrode placement on NAB anode.

Figure 1.13 Microstructure of NAB (x 250).

Figure 1.14 Variation in potential over 72 hour period. 4 x 1.25 cm ϕTi tubes, 608 cm NAB, 5% SW, static flow.

Figure 1.15 Potential distribution for 2 Ti tubes, 12.5 cm diameter, 45.0 cm length, NAB 60.8 cm, 5- 100% SW, static flow.

Figure 1.16 Potential distribution for 2 Ti tubes, 12.5 cm diameter, 45.0 cm length, NAB 60.8 cm, 100% SW, static flow.

Figure 1.17 Potential distribution for 2 Ti tubes, 12.5 cm diameter, 45.0 cm length, NAB

60.8 cm, 50% SW, static flow.

Figure 1.18 Potential distribution for 2 Ti tubes, 12.5 cm diameter, 45.0 cm length, NAB 60.8 cm, 5% SW, static flow.

Figure 1.19 Potential distributions for 4 Ti tubes, 19.0 cm diameter, 53.2 cm length, NAB 31.3 and 60.8 cm, 100% SW, static flow.

Figure 1.20 Potential distribution for 4 Ti tubes, 19.0 cm diameter, 53.2 cm length, NAB 60.8 cm, 100% SW, static flow.

Figure 1.21 Potential distribution for 4 Ti tubes, 19.0 cm diameter, 53.2 cm length, NAB 31.3 cm, 100% SW, static flow.

Figure 1.22 Potential distribution for 4 Ti tubes, 19.0 cm diameter, 53.2 cm length, NAB 31.3 and 60.8 cm, 50% SW, static flow.

Figure 1.23 Potential distribution for 4 Ti tubes, 19.0 cm diameter, 53.2 cm length, NAB 60.8 cm, 50% SW, static flow.

Figure 1.24 Potential distribution for 4 Ti tubes, 19.0 cm diameter, 53.2 cm length, NAB 31.3 cm, 50% SW, static flow.

Figure 1.25 Potential distribution for 4 Ti tubes, 19.0 cm diameter, 53.2 cm length, NAB 60.8 cm, 500 and 100% SW, static flow.

Figure 1.26 Potential distribution for 2 Ti tubes, 19.0 and 25.4 cm diameter, NAB 60.8 cm, 50% SW, static flow.

Figure 1.27 Potential distribution for 2 Ti tubes, 25.4 cm diameter, 136.0 cm length, NAB 60.8 cm, 50% SW, static flow.

Figure 1.28 Potential distribution for 2 Ti tubes, 25.4 cm diameter, 136.0 cm length, NAB 60.8 cm, 50% SW, static flow.

Figure 1.29 Potential distribution for 2 and 4 Ti tubes, 12.5 cm diameter, 45.0 cm length, NAB 31.3 cm, 50% SW, static flow.

Figure 1.30 Potential distribution for 2 Ti tubes, 12.5 cm diameter, 45.0 cm length, NAB

31.3 cm, 50% SW, static flow.

Figure 1.31 Potential distribution for 4 Ti tubes, 19.0 cm diameter, 53.2 cm length, NAB 31.3 cm, 50% SW, static flow.

Figure 1.32 Potential distribution for electrically uncoupled NAB and titanium, 50% static SW.

Figure 1.33 Variation of potential distribution with time for 4 titanium tubes (19 cm diameter and length 53.2 cm), 60.8 cm NAB, 5% flowing SW (1 ms^{-1}).

Figure 1.34 Potential distributions for 2 titanium tubes (19 cm diameter, 106.0 cm length), NAB length 60.8 cm, flowing 50% SW (1 and 2 m s^{-1})

Figure 1.35 Potential distributions for 2 titanium tubes (19 cm diameter, 106.0 cm length), NAB length 60.8 cm, flowing 50% SW (1 m s^{-1})

Figure 1.36 Potential distributions for 2 titanium tubes (19 cm diameter, 106.0 cm length), NAB length 60.8 cm, flowing 50% SW (2 m s^{-1}).

Figure 1.37 Potential distributions for 2 titanium tubes (19 cm diameter, 106.0 cm length), NAB length 60.8 cm, flowing 50% SW (2 m s^{-1}).

Figure 1.38 Potential distribution for 4 titanium pipes of 19 cm diameter, length 53.2 cm., NAB of length 60.8 cm, in flowing 5, 50 and 100% SW, 1 ms^{-1}.

Figure 1.39 Potential distributions for 4 titanium tubes of diameter 19 cm and length 53.2 cm, NAB length 60.8 cm, in flowing seawater, 1 ms^{-1}.

Figure 1.40 Potential distribution for 4 titanium pipes of 19 cm diameter, length 53.2 cm., coupled to NAB of length 60.8 cm, in flowing 50% SW, 1 ms^{-1}.

Figure 1.41 Potential distribution for 4 titanium pipes of 19 cm diameter, length 53.2 cm., coupled to NAB of length 60.8 cm, in flowing 5% SW, 1 ms^{-1}.

Figure 1.42 Potential distributions for 2 and 4 titanium tubes of diameter 12.5 cm and length 45.0 cm, NAB 60.8 cm, flowing 100% SW, 1 ms^{-1}.

Figure 1.43 Potential Distribution for 2 titanium tubes of diameter 12.5 cm and length

45.0 cm, NAB 60.8 cm, flowing 100% SW, 1 ms^{-1}.

Figure 1.44 Potential Distribution for 4 titanium tubes of diameter 12.5 cm and length 45.0 cm, NAB 60.8 cm, flowing 100% SW, 1 ms^{-1}.

Chapter 2

Figure 2.1 Corrosion and passivation of a passivating material.

Figure 2.2 Schematic polarization curve for a passivating material showing effects of adding hydrogen evolution and oxygen reduction reactions.

Figure 2.3 Passivation - activation curves.

Figure 2.4 Schematic polarization curve when magma is formed as a precursor to passivation.

Figure 2.5 Schematic potential-time curves for a series of different current densities.

Figure 2.6 Time-current density curve for a passivating material.

Figure 2.7 'Synergy' Diagram, showing elements considered as passivity promoters and dissolution moderators.

Figure 2.8 Schematic of passive film on a stainless steel.

Figure 2.9 Schematic representation of bipolar passive film (after Brooks[81]).

Chapter 3

Figure 3.1 Schematic of Devereux and Yeum Model.

Figure 3.2 Desired form of S function plotted against potential.

Figure 3.3 S Curve generated by original form of the 'buffer' equation.

Figure 3.4 S Curves for non-integer values of p.

Figure 3.5 Curve generated using value of i at E_t as i_{anodic} in Equation 3.44.

Figure 3.6 Curve generated by using Equation 3.4 for i_{active} in Equation 3.44.

Figure 3.7 Modelled curve generated using 'buffer' equation with limiting value of log X = ± 23.

Figure 3.8 Effect of altering E_t, the potential at the midpoint of the S function on the

anodic polarization curve of a passivating material using the 'buffer' equation.

Figure 3.9 Effect of altering the power p in the 'buffer' equation on the anodic polarization curve of a passivating material.

Figure 3.10 S Function used to generate Figure 3.9.

Figure 3.11 Effect of altering the passive current density supported by the unfilmed surface on the anodic polarization curve of a passivating material using the 'buffer' equation.

Figure 3.12 Effect of altering the constant A in the 'buffer' equation on the anodic polarization curve of a passivating material.

Figure 3.13 Effect of altering the active-to-passive transition potential on the anodic polarization curve of a passivating material using the 'raindrop' equation.

Figure 3.14 Effect of altering the power p in the 'raindrop' equation on the anodic polarization curve of a passivating system.

Figure 3.15 Effect of altering the passive current density on the anodic polarization curve of a passivating system using the 'raindrop' equation.

Figure 3.16 Effect of altering the constant A in the 'raindrop' equation on the anodic polarization curve of a passivating system.

Figure 3.17 Modelled curve for a passivating material with the hydrogen and oxygen reduction processes, $i_{lim}O_2 > i_{crit}, > i_{pass}$.

Figure 3.18 Modelled polarization curve for a passivating material, $i_{lim}O_2 < i_{crit}$.

Figure 3.19 Modelled polarization curve, $i_{lim}O_2 > i_{crit}, i_{pass} > i_{lim}O_2$.

Chapter 4 Section 1

Figure 4.1.1 Ideal S Curve for a passivating metal (from Uhlig[110]).

Figure 4.1.2 Ideal S Curve with Secondary Passivation (from ASTM Vol 13[111]).

Figure 4.1.3 Experimental Curve for Iron in H_2SO_4 (from Steigerwald and Greene[160]).

Figure 4.1.4 Experimental Curve for Iron in 5% Deaerated H_2SO_4, 0.1 mV s^{-1} scan rate, 24 °C.

Figure 4.1.5 Experimental Curve for Iron in Aerated 5% H_2SO_4, 0.1 mV s^{-1} scan rate, 24 °C.

Figure 4.1.6 Model showing both Reaction 1 and 3 under activation control.

Figure 4.1.7 More Detailed View of Figure 4.1.6.

Figure 4.1.8 Introduction of 'Raindrop' Passivation Algorithm to Reaction 1.

Figure 4.1.9 Model of iron in deaerated 5% H_2SO_4, introducing Reaction 8.

Figure 4.1.10 Model showing addition of passivation routine to Reaction 8.

Figure 4.1.11 Final Model for Iron in Deaerated 5% H_2SO_4.

Figure 4.1.12 Effects of different scan rates on polarization curve of pure iron in deaerated 5% H_2SO_4.

Figure 4.1.13 Effect of rotation speed on the polarization curve for pure iron in deaerated 5% H_2SO_4

Chapter 4 Section 2

Figure 4.2.1 Link between composition of 304 stainless steels and other alloy systems.

Figure 4.2.2 Experimental polarization curve for 304 stainless steel in deaerated 5% H_2SO_4.

Figure 4.2.3 Experimental polarization curves for pure iron and type 304 stainless steel in deaerated 5% H_2SO_4.

Figure 4.2.4 Modelling the behaviour of 304 stainless steel in deaerated 5% H_2SO_4 using the same reactions as Devereux and Yeum.

Figure 4.2.5 More Detailed View of the Curve Modelled in Figure 4.2.4.

Figure 4.2.6 Model of behaviour of 304 Stainless Steel in deaerated 5% H_2SO_4, using reactions 1,2,3 and 4.

Figure 4.2.7 Model showing effect of Reaction 2 with $\alpha = 0.25$, $z = 4$ and $i_o = 0.1$ nA cm^{-2}

Figure 4.2.8 Model showing effect of Reaction 2 with $\alpha = 0.23$, $z = 4$ and $i_o = 10^{-5}$ nA cm^{-2}

Figure 4.2.9 Model showing effect of Reaction 2 with $\alpha = 0.5$, $z = 1$ and $i_o = 3$ nA cm^{-2}

Figure 4.2.10 Stability diagram showing relative predominance of hexavalent chromium ions.

Figure 4.2.11 Acid chromate and dichromate reactions shown together.

Figure 4.2.12 Modelled curve showing effect of considering Cr_2O_3 to have two forms, from which $HCrO_4^-$ ions are formed.

Figure 4.2.13 Modelled curve for 304 stainless steel in deaerated 5% H_2SO_4.

Figure 4.2.14 Experimental polarization for 304 stainless steel in aerated and deaerated 5% H_2SO_4.

Figure 4.2.15 Modelled polarization curve for 304 stainless steel in aerated 5% H_2SO_4, using Reactions 1, 2, 3, 5 and 7.

Figure 4.2.16 Modelled polarization curve for 304 stainless steel in aerated 5% H_2SO_4.

Figure 4.2.17 Model of 304 stainless steel in aerated 5% H_2SO_4 using alternative kinetic parameters for Reaction 7.

Figure 4.2.18 Experimental polarization curve for 304 stainless steel in 5% H_2SO_4 with intermediate dissolved oxygen concentration.

Figure 4.2.19 Schematic polarization curve showing effect of different levels of dissolved oxygen[1].

Figure 4.2.20 Modelled polarization curve for 304 stainless steel in 5% H_2SO_4 with intermediate level of dissolved oxygen.

Figure 4.2.21 Model of 304 stainless steel in 5% H_2SO_4 with alternative kinetic parameters

for Reaction 7.

Chapter 4 Section 3

Figure 4.3.1 Polarization curves of 304 stainless steel in deaerated 5% H_2SO_4 at 4 temperatures.

Figure 4.3.2 Polarization curves of 304 stainless steel in aerated 5% H_2SO_4 at 4 temperatures.

Figure 4.3.3 Polarization curves of 304 stainless steel in stagnant 5% H_2SO_4 at 4 temperatures.

Figure 4.3.4 Polarization curves of 304 stainless steel in 5% H_2SO_4 at 24°C with three different dissolved oxygen contents.

Figure 4.3.5 Polarization curves of 304 stainless steel in 5% H_2SO_4 at 30°C with three different dissolved oxygen contents.

Figure 4.3.6 Polarization curves of 304 stainless steel in 5% H_2SO_4 at 35°C with three different dissolved oxygen contents.

Figure 4.3.7 Polarization curves of 304 stainless steel in 5% H_2SO_4 at 45°C with three different dissolved oxygen contents.

Figure 4.3.8 Experimental curves for 304 stainless steel in deaerated 5% H_2SO_4.

Figure 4.3.8a Cathodic and active-to-passive transition portions of the Figure 4.3.8 in greater detail.

Figure 4.3.9 Schematic showing effect of transfer coefficient on form of polarization curves.

Figure 4.3.10 Model of conditioned 304 stainless steel in deaerated 5% H_2SO_4 - Reaction 3 modelling region B'B.

Figure 4.3.11 Model of conditioned 304 stainless steel in deaerated 5% H_2SO_4 - Reaction 3 modelling region AB'.

Figure 4.3.12 Dissolved oxygen *vs* temperature for 5% H_2SO_4 for three different aeration regimes.

Figure 4.3.13 SEM micrograph showing surface of sample polarized in deaerated 5% H_2SO_4 at 24°C

Figure 4.3.14 Model of 304 stainless steel in deaerated 5% H_2SO_4 at 24°C

Figure 4.3.15 Model of 304 stainless steel in deaerated 5% H_2SO_4 at 30°C

Figure 4.3.16 Model of 304 stainless steel in deaerated 5% H_2SO_4 at 35°C

Figure 4.3.17 Model of 304 stainless steel in deaerated 5% H_2SO_4 at 45°C

Figure 4.3.18 Model of 304 stainless steel in aerated 5% H_2SO_4 at 24°C

Figure 4.3.19 Model of 304 stainless steel in aerated 5% H_2SO_4 at 30°C

Figure 4.3.20 Model of 304 stainless steel in aerated 5% H_2SO_4 at 35°C

Figure 4.3.21 Model of 304 stainless steel in aerated 5% H_2SO_4 at 45°C

Figure 4.3.22 Model of 304 stainless steel in stagnant 5% H_2SO_4 at 24°C

Figure 4.3.23 Model of 304 stainless steel in stagnant 5% H_2SO_4 at 30°C

Figure 4.3.24 Model of 304 stainless steel in stagnant 5% H_2SO_4 at 35°C

Figure 4.3.25 Model of 304 stainless steel in stagnant 5% H_2SO_4 at 45°C

Figure 4.3.26 Diffusion-limited current density for Reaction 7 *vs* temperature

Figure 4.3.27 i_o values used for Reaction 1 *vs* temperature for 304 stainless steel in 5% H_2SO_4.

Figure 4.3.28 Theoretical curve showing effect of using i_{lim} and α values such that i_{cath} does not exceed i_{crit}.

Figure 4.3.29 Experimental polarization curve for 304 stainless steel in aerated 5% H_2SO_4 starting at 45°C, and decreasing.

Figure 4.3.30 E_t *vs* temperature for 304 stainless steel in 5% H_2SO_4.

Figure 4.3.31 Variation of Reaction 7 α with temperature in 5% H_2SO_4.

Figure 4.3.32 Variation of resistance with temperature for 304 stainless steel in 5% H_2SO_4.

Chapter 4 Section 4

Figure 4.4.1 Potentiodynamic curves for duplex stainless steel in seawater at 24, 30, 35

and 45 °C.

Figure 4.4.2 Relationship between log i_{pass} and 1/T for duplex stainless steel in seawater.

Figure 4.4.3 Cyclic polarization curves for duplex stainless steel at 24, 30, 35 and 45 °C in seawater.

Figure 4.4.4 Ferralium duplex stainless steel sample polarized at 24 °C.

Figure 4.4.5 Ferralium duplex stainless steel sample polarized at 45 °C.

Figure 4.4.6 SEM micrograph of Ferralium duplex stainless steel after polarization at 45 °C (x 64).

Figure 4.4.7 SEM micrograph of Ferralium duplex stainless steel after polarization at 45 °C (x 600).

Figure 4.4.8 SEM micrograph of Ferralium duplex stainless steel after polarization at 24 °C (x 100).

Figure 4.4.9 SEM micrograph of Ferralium duplex stainless steel after polarization at 24 °C (x 1000).

Figure 4.4.10 Model for duplex stainless steel in natural seawater at 24 °C.

Figure 4.4.11 Model for duplex stainless steel in natural seawater at 30 °C.

Figure 4.4.12 Model for duplex stainless steel in natural seawater at 35 °C.

Figure 4.4.13 Model for duplex stainless steel in natural seawater at 45 °C.

Figure 4.4.14 Polarization curves for four stainless steels in natural seawater at 24 °C.

Figure 4.4.15 E_b *vs* temperature curve for 316 stainless steel in NaCl solution.

Figure 4.4.16 E_b *vs* temperature curve for duplex stainless steel in natural seawater.

Figure 4.4.17 i_o values used to model Reaction 9 *vs* Temperature

Figure 4.4.18 SRET images for Ferralium duplex stainless steel in natural seawater at 35 °C; rotation speed 150 rpm.

Figure 4.4.19 Model of Ferralium in seawater, 24 °C, using 5.2 x 10^{-5} nA cm^{-2} as Reaction 7 i_o.

Chapter 4 Section 5

Figure 4.5.1 Potentiodynamic polarization curves for 316 stainless steel in 5% deaerated H_2SO_4.

Figure 4.5.2 Potentiodynamic polarization curves for 316 stainless steel in 5% aerated H_2SO_4.

Figure 4.5.3 Potentiodynamic polarization curves for 316 stainless steel in 5% stagnant H_2SO_4.

Figure 4.5.4 Potentiodynamic polarization curves for 316 stainless steel in natural seawater.

Figure 4.5.5 Model of 316 stainless steel in deaerated H_2SO_4 at 24°C.

Figure 4.5.6 Model of 316 stainless steel in deaerated H_2SO_4 at 30°C.

Figure 4.5.7 Model of 316 stainless steel in deaerated H_2SO_4 at 35°C.

Figure 4.5.8 Model of 316 stainless steel in deaerated H_2SO_4 at 45°C.

Figure 4.5.9 Model of 316 stainless steel in aerated H_2SO_4 at 24°C.

Figure 4.5.10 Model of 316 stainless steel in aerated H_2SO_4 at 30°C.

Figure 4.5.11 Model of 316 stainless steel in aerated H_2SO_4 at 35°C.

Figure 4.5.12 Model of 316 stainless steel in aerated H_2SO_4 at 45°C.

Figure 4.5.13 Model of 316 stainless steel in stagnant H_2SO_4 at 24°C.

Figure 4.5.14 Model of 316 stainless steel in stagnant 5% H_2SO_4 at 30°C.

Figure 4.5.15 Model of 316 stainless steel in stagnant H_2SO_4 at 35°C.

Figure 4.5.16 Model of 316 stainless steel in stagnant H_2SO_4 at 45°C.

Figure 4.5.17 Model of 316 stainless steel in natural seawater at 24°C.

Figure 4.5.18 Model of 316 stainless steel in natural seawater at 30°C.

Figure 4.5.19 Model of 316 stainless steel in natural seawater at 35°C.

Figure 4.5.20 Model of 316 stainless steel in natural seawater at 45°C.

Figure 4.5.21 Variation of Reaction 7 i_{lim} with temperature for 316 stainless steel in 5%

H_2SO_4.

Figure 4.5.22 Variation of Reaction 7 i_{lim} for 304 and 316 stainless steels in aerated 5% H_2SO_4.

Figure 4.5.23 Variation of Reaction 7 i_{lim} for 304 and 316 stainless steels in stagnant 5% H_2SO_4.

Figure 4.5.24 Variation of Reaction 7 α for 316 stainless steel in 5% H_2SO_4.

Figure 4.5.25 Variation of Reaction 1 α for 316 stainless steel with temperature for 316 stainless steel in 5% H_2SO_4.

Figure 4.5.26 Variation of Reaction 1 i_o with temperature for 316 stainless steel and Ferralium in natural seawater.

Figure 4.5.27 Variation of E_t with temperature for 316 stainless steel and Ferralium in natural seawater.

Figure 4.5.28 Variation of Reaction 7 i_{lim} with temperature for 316 stainless steel and Ferralium in natural seawater.

Figure 4.5.29 Variation of Reaction 7 i_{lim} with temperature for 316 stainless steel and Ferralium in natural seawater.

Figure 4.5.30 Variation of dissolved oxygen concentration with temperature in natural seawater.

Figure 4.5.31 Variation of Reaction 9 (hydrated) i_o with temperature for 316 and Ferralium in natural seawater.

Figure 4.5.32 Variation of Reaction 9 (anhydrous) i_o with temperature for 316 and Ferralium in natural seawater.

List of Tables

Chapter 1

Table 1.1 Concentrations of major chemical compounds in seawater.

Table 1.2 EDAX analysis of titanium

Table 1.3 Comparison of EDAX analysis and NES 747 alloy specification.

Table 1.4 Properties of seawater at various dilutions at 20°C.

Table 1.5 Experimental Matrix

Table 1.6 Analysis of NAB Phases by AMTE and UMIST.

Table 1.7 Summary of electrochemical data for static conditions.

Table 1.8 Summary of electrochemical data for 1 m s^{-1} flow conditions.

Table 1.9 Summary of electrochemical data for 2 m s^{-1} flow conditions.

Chapter 2

Table 2.1 Some common metals and their Flade potentials at pH 0.

Table 2.2 i_{crit}, E_f and charge required to passivate Fe-Cr alloys in 10% H_2SO_4.

Chapter 3

Table 3.1 Parameters input to the 'buffer' equation to obtain Figure 3.3.

Table 3.2 Passivation parameters used in Figures 3.4 and 3.5.

Table 3.3 Parameters used to generate Figure 3.8.

Table 3.4 Parameters used to generate Figure 3.9.

Table 3.5 Parameters used by passivation algorithm to generate Figure 3.11.

Table 3.6 Parameters used by passivation algorithm to generate Figure 3.12.

Table 3.7 Parameters used in Figure 3.13.

Table 3.8 Parameters used in Figures 3.14.

Table 3.9 Parameters used in Figure 3.15.

Chapter 4 Section 1

Table 4.1.1 Parameters for Reactions 1 and 2 used in Figure 4.1.6.

Table 4.1.2 Parameters Used in Raindrop Passivation Algorithm for Reaction 1 in Figure 4.1.8.

Table 4.1.3 Parameters for Reaction 8 used in Figure 4.1.9.

Table 4.1.4 Kinetic Parameters for Reactions 2 and 8 used in Figures 4.1.10 and 4.1.11.

Table 4.1.5 Parameters Used in Raindrop Passivation Algorithm for Reaction 8.

Chapter 4 Section 2

Table 4.2.1 Parameters used in Figure 4.2.4.

Table 4.2.2 Parameters used in passivation routine for reaction 1.

Table 4.2.3 Modified parameters for Reactions 1,2, 3 and 4.

Table 4.2.4 Parameters used in Figures 4.2.7 to 4.2.9

Table 4.2.5 E° (V SHE) values for reactions 4 and 5 for Cr_2O_3 in differing forms.

Table 4.2.6 Parameters used for Reactions 4 and 5 in Figure 4.2.11.

Table 4.2.7 Kinetic parameters for the two acid chromate reactions considered.

Table 4.2.8 List of parameters used to model 304 stainless steel in deaerated 5% sulphuric acid.

Table 4.2.9 List of parameters used to model 304 stainless steel in aerated 5% sulphuric acid.

Table 4.2.10 List of parameters used to model 304 stainless steel in aerated 5% sulphuric acid using alternative kinetic parameters for Reaction 7.

Table 4.2.11 Parameters used to model behaviour of 304 stainless steel in 5% sulphuric acid with restricted oxygen access.

Table 4.2.12 Parameters used to model behaviour of 304 stainless steel in 5% sulphuric acid with restricted oxygen access.

Chapter 4 Section 3

Table 4.3.1 Parameters required for calculation of cathodic transfer coefficient for Reaction 3.

Table 4.3.2 Transfer coefficients for 6 mechanisms for Reaction 3.

Table 4.3.3 Exchange current density for Reaction 3 in 1M H_2SO_4.

Table 4.3.4 Kinetic parameters used in Figure 4.3.10

Table 4.3.5 Kinetic parameters used in Figure 4.3.11.

Table 4.3.6 Range of kinetic parameters used in Figures 4.3.14 to 4.3.17

Table 4.3.7 Range of parameters used in passivation routine for Reaction 1 in Figures 4.3.14 to 4.3.17

Table 4.3.8 Range of kinetic parameters used to model behaviour of 304 stainless steel in aerated 5% H_2SO_4

Table 4.3.9 Range of parameters used in passivation routine for Reaction 1 to model behaviour of 304 stainless steel in aerated 5% H_2SO_4.

Table 4.3.10 Kinetic parameters used to model the behaviour of 304 stainless steel in stagnant 5% H_2SO_4

Table 4.3.11 Range of parameters used in passivation routine for Reaction 1 to model the behaviour of 304 stainless steel in stagnant 5% H_2SO_4

Table 4.3.12 Reaction 7 i_{lim} (in nA cm^{-2}) values for aerated and stagnant 5% H_2SO_4 .

Table 4.3.13 Values of i_o (in nA cm^{-2}) used to model Reaction 1.

Table 4.3.14 Values of E_t used to model passivating behaviour of 304 stainless steel in 5% H_2SO_4.

Table 4.3.15 Values of α used to model passivating behaviour of 304 stainless steel in 5% H_2SO_4.

Table 4.3.16 Values of Ω used to model passivating behaviour of 304 stainless steel in 5% H_2SO_4.

Chapter 4 Section 4

Table 4.4.1 Composition of alloy studied and manufacturer's specification.

Table 4.4.2 Summary of electrochemical data obtained from potentiodynamic scans

Table 4.4.3 Parameters for the model of duplex stainless steel in natural seawater at 24°C.

Table 4.4.4 Parameters used in passivation routine for the Reaction 1 for duplex stainless steel in natural seawater at 24°C.

Table 4.4.5 Parameters for the model of duplex stainless steel in natural seawater at 30°C.

Table 4.4.6 Parameters used in passivation routine for the Reaction 1 for duplex stainless steel in natural seawater at 30°C.

Table 4.4.7 Parameters for the model of duplex stainless steel in natural seawater at 35°C.

Table 4.4.8 Parameters used in passivation routine for the Reaction 1 for duplex stainless steel in natural seawater at 35°C.

Table 4.4.9 Kinetic parameters for model of duplex stainless steel in natural seawater at 45°C .

Table 4.4.10 Parameters used in passivation routine for the Reaction 1 for duplex stainless steel in natural seawater at 45°C.

Table 4.4.11 Table showing E_b, % Cr and % Mo for four stainless steels in natural seawater at 24°C

Chapter 4 Section 5

Table 4.5.1 Chemical composition of 316 alloy used (* from residual carbon/sulphur analyzer).

Table 4.5.2 Range of parameters used to model 316 stainless steel in deaerated 5% H_2SO_4.

Table 4.5.3 Range of passivation parameters used to model 316 stainless steel in deaerated 5% H_2SO_4.

Table 4.5.4 Range of passivation parameters used to model 316 stainless steel in aerated

5% H_2SO_4.

Table 4.5.5 Passivation parameters for model of 316 stainless steel in aerated 5% H_2SO_4.

Table 4.5.6 Range of parameters used to model 316 stainless steel in stagnant 5% H_2SO_4.

Table 4.5.7 Range of passivation parameters for model of 316 stainless steel in stagnant 5% H_2SO_4.

Table 4.5.8 Range of parameters used to model 316 stainless steel in natural seawater.

Table 4.5.9 Range of passivation parameters for model of 316 stainless steel in natural seawater.

Table 4.5.10 Reaction 7 i_{lim} values for 316 stainless steel in 5% H_2SO_4.

Table 4.5.11 Variation of Reaction 7 α with temperature for 316 stainless steel in 5% H_2SO_4.

Table 4.5.12 Variation of Reaction 1 i_o for 316 stainless steel in 5% H_2SO_4.

Table 4.5.13 Reaction 1 i_o values for 316 stainless steel and Ferralium in natural seawater.

A C K N O W L E D G E M E N T

This study was financed with the aid of grants from EPSRC/MTD Ltd and the MOD. The author would particularly like to thank the supervisor Dr Ken Trethewey and Dr David Marsh, for all their help and guidance throughout the period of study.

Other thanks go to Mr Derek Sargeant, Commander (now Captain) Bob Ditchfield RN and Commander Peter Hadden RN, all Heads of Materials Technology, RNEC Manadon in the period 1992 -1995.

Mr Chris Clark (Engineering Materials Section Laboratory Manager) is thanked for his help with the technical equipment used in this study. Dr Cheryl Pitt and Miss Judith Nash are thanked for their assistance with the SEM microscopy. Lieutenant Commander John Keenan is thanked for help in computing matters.

Mr 'Dusty' Miller, Mr Arthur Miller and Mr Brian Williams are thanked for all their help in the design and manufacture of equipment and specimens throughout the last three years.

Miss Anthea Dolman is thanked for her patience.

AUTHOR'S DECLARATION

At no time during the registration for the Degree of Doctor of Philosophy has the author been registered for any other University award.

This study was financed with the aid of grants from EPSRC/MTD Ltd and the MOD.

A programme of advanced study was undertaken, which included learning Fortran and Visual Basic programming languages, gathering of potentiodynamic, potential profile and scanning reference electrode technique data as well as optical and scanning electron microscopy.

Relevant scientific seminars and conferences were attended, at which work was presented. External institutions were visited for consultative purposes, and papers prepared for publication.

PUBLICATIONS

(i) Trethewey, K R; S S Phillips and P R Roberge
"Development of a Knowledge-Base Elicition Shell for Materials Performance Evaluation in Seawater Systems"
National Association of Corrosion Engineer's Conference, Baltimore, February 1994.

(ii) Trethewey, K R, S S Phillips, D A Sargeant and D J Marsh
Electrochemical Impedance Analysis of Ceramic Coated Nickel Aluminium Bronze in Seawater.
45th Meeting of the International Society of Electrochemistry, Oporto, August 1994

(iii) Phillips S S, K R Trethewey and D J Marsh

The Corrosion of Duplex Stainless Steel in Natural Seawater

UK Institute of Corrosion Conference, Bournemouth, Oct 1994

(iv) Sargeant D A, S S Phillips and G R Ronaldson

Investigation of the Corrosion of 316 Stainless Steel using the Scanning Reference Electrode Technique

Journal of Microscopy, to be published in Jan 1996

Seminars, Conferences and External Institutions Visited or Attended

DRA Haslar, Portsmouth, May 1992.

John Brown Engineering Company, London, July 1993.

Naval Surface Warfare Center (formerly the David Taylor Research Center), Annapolis, Maryland, USA, August 1993.

National Association of Corrosion Engineer's Conference, Baltimore, February 1994.

DRA Holton Heath, June 1994

45th Meeting of the International Society of Electrochemistry, Oporto, August 1994

35th Corrosion Science Seminar, Manchester, September 1994

UK Institute of Corrosion Conference, Bournemouth, Oct 1994

University of Birmingham Library, Jan 1995.

Engineering Materials Department, University of Southampton, Oct, Jan, May 1995.

External Contacts :

Mr Ian Perryman, Vosper Thorneycroft Ltd.

Dr Brian Hall, NA 132, MOD Procurement Executive, Bath (retired).

Mr Brian Angell, DRA Holton Heath (retired).

Dr John Murray, Naval Surface Warfare Center, Annapolis, MD, USA.

Signed.....

Date.....11 October 1995.....

Chapter 1 The GC Galvanic Corrosion Computer Model

1.1 INTRODUCTION

This chapter details the construction and use of a computer model which attempts to predict the electrical potential distribution of essentially cylindrical geometry carrying seawater electrolyte, together with the methods used to obtain experimental results against which the model is compared. Relevant aqueous and galvanic corrosion theory is introduced, along with a description of the nature of the electrolyte. The rationale behind the model is examined, along with some of the limitations of the model. Experimental and theoretical results are compared, followed by a discussion of the trends discovered.

1.1.1 Definitions of Corrosion

Corrosion may be defined as the degradation of a material by an electrochemical reaction with its environment[1], electrochemistry being concerned with the phenomena occurring when a current is passed through a solution of an electrolyte[2]. Galvanic corrosion occurs when a metal or alloy is electrically coupled to another metal or conducting nonmetal in the same electrolyte. Corrosion of the less resistant metal increases, while corrosion of the more corrosion-resistant metal decreases. The driving force for corrosion (current flow) is the potential developed between the dissimilar metals[3].

Due to the constraints of both cost and design, seawater systems can rarely be manufactured from a single material. Therefore, care must be exercised with respect to the galvanic interactions between the different materials that the constituent items of the equipment in question are manufactured from.

1.1.2 The Behaviour of Metals in Electrolytes

If the behaviour of a metal M, immersed in a conducting electrolyte and connected to a voltmeter with high internal resistance is studied, a potential (difference) is set up between the metal and the electrolyte. This occurs by the dissolution of the metal to form positively aqueous charged ions by the following anodic (oxidation) reaction:

$$M \rightarrow M^{z+} + ze^- \qquad 1.1$$

The metal now has a net negative charge of ze^-, since electrons cannot move through electrolyte and thus remain in the metal. It is these electrons and positive ions that create the potential difference, and they exist in a non-homogenous distribution of ions between the metal and the bulk electrolyte. This is called the double layer. When a certain concentration of dissolved species is reached, the reaction comes to equilibrium and assumes a steady potential. The greater the degree of dissolution, the greater the potential difference. If the high resistance (of the voltmeter) is removed, electron-accepting species in the electrolyte may move towards the surface of the metal, and a cathodic (reduction) reaction may occur in which these excess electrons are consumed. Thus electron-producing and electron-consuming processes are occurring on the same surface. Flow of positive ions though the electrolyte will complete an electrical circuit, and thus a current may flow. This will cause the metal to be disturbed from its equilibrium potential (becoming more electropositive), and thus more dissolution will occur in order to restore the equilibrium. The most common reduction reactions are hydrogen evolution (1.2), reduction of dissolved oxygen (1.3 and 1.4), metal ion reduction (1.5) and metal deposition (1.6):

$$2H^+ + 2e^- \rightarrow H_2 \qquad 1.2$$

$$O_2 + 4H^+ + 4e^- \rightarrow 2H_2O \qquad \text{(Acid media)} \qquad 1.3$$

$$O_2 + 2H_2O + 4e^- \rightarrow 4OH^- \qquad \text{(Basic media)} \qquad 1.4$$

$$M^{z+} + e^- \rightarrow M^{(z-1)+} \quad 1.5$$

$$M^{z+} + ze^- \rightarrow M \quad 1.6$$

Currents produced by cathodic processes are considered to be negative, while those produced by anodic reactions are considered to be positive in nature. Thus, when metal ions are being produced and the resultant free electrons are consumed by the reduction of oxygen, the equilibrium potential is achieved when the rate of the reduction and oxidation reactions are equal ie the net current is zero. This potential is termed the free corrosion potential (E_{corr}). The value of these two equal but opposite currents at this potential is called the exchange current I_o (or exchange current density, i_o, if the current is divided by sample area).

If a potential is externally imposed upon the metal such that it is disturbed from E_{corr}, the metal is said to be polarized. For anodic polarization (η_a), a more electropositive potential is imposed and the oxidation process is favoured (at the expense of the reduction process), whereas for cathodic polarization (η_c), a potential more electronegative than E_{corr} is imposed and the reduction reaction is favoured.

1.1.3 Electrode Potentials

Since absolute potentials of metals acting as electrodes cannot be measured, an arbitrary redox reaction (the hydrogen evolution reaction) is chosen as a reference, and assigned a potential of 0.000 V. Such an electrode (usually using a platinum as an inert reaction substrate) is called a standard hydrogen electrode (SHE). Each material has its own standard electrode potential (E°) value, which is a specifically measured potential relative to a SHE at 25°C, where all the ion concentrations are 1 molar, gases are at 1 atmosphere

pressure and solid phases are pure. The electrode potential changes with concentration, temperature, pH and partial pressure of gases. The Nernst equation links the standard electrode potential E° to the actual electrode potential (E_1):

$$E_1 = E_0 \pm (\frac{c}{d})\frac{RT}{zF}pH \pm (\frac{a}{b})\frac{RT}{zF}[ion] \qquad 1.7$$

where a,b,c,d are constants dependent upon the number of species in each redox reaction

R is the gas constant (8.314 J mol^{-1} K^{-1})

T is the temperature (K)

F is Faraday's constant (96494 C)

z is the number of electrons transferred

⊏ion⊐ is the concentration of the aqueous species

1.1.4 Polarization Curves

The current response of a material may be determined by using a potentiostat to externally impose a potential upon a metal in an electrolyte, and measuring the current response at each increment of potential. The current measured is the net current flowing at that particular potential, and is made up of the partial currents from all the oxidation and reduction (redox) processes that occur. Current density may be plotted instead of current, in order to make the resultant curve independent of specimen size. A polarization curve consists of the resultant addition of the separate reduction and oxidation components of two or more electrode processes. In seawater, where the pH > 7 and the levels of dissolved oxygen are high, the dominant cathodic reaction is the reduction of dissolved oxygen. Figure 1.1 shows a typical polarization curve for a metal in seawater, plotting potential (E) against log current density (log *i*). The solid line is the resultant curve generated from the

partial currents shown in the dotted lines. C is the free corrosion potential (E_{corr}), ABC is the portion of the curve where cathodic currents predominate, CD that where anodic currents predominate.

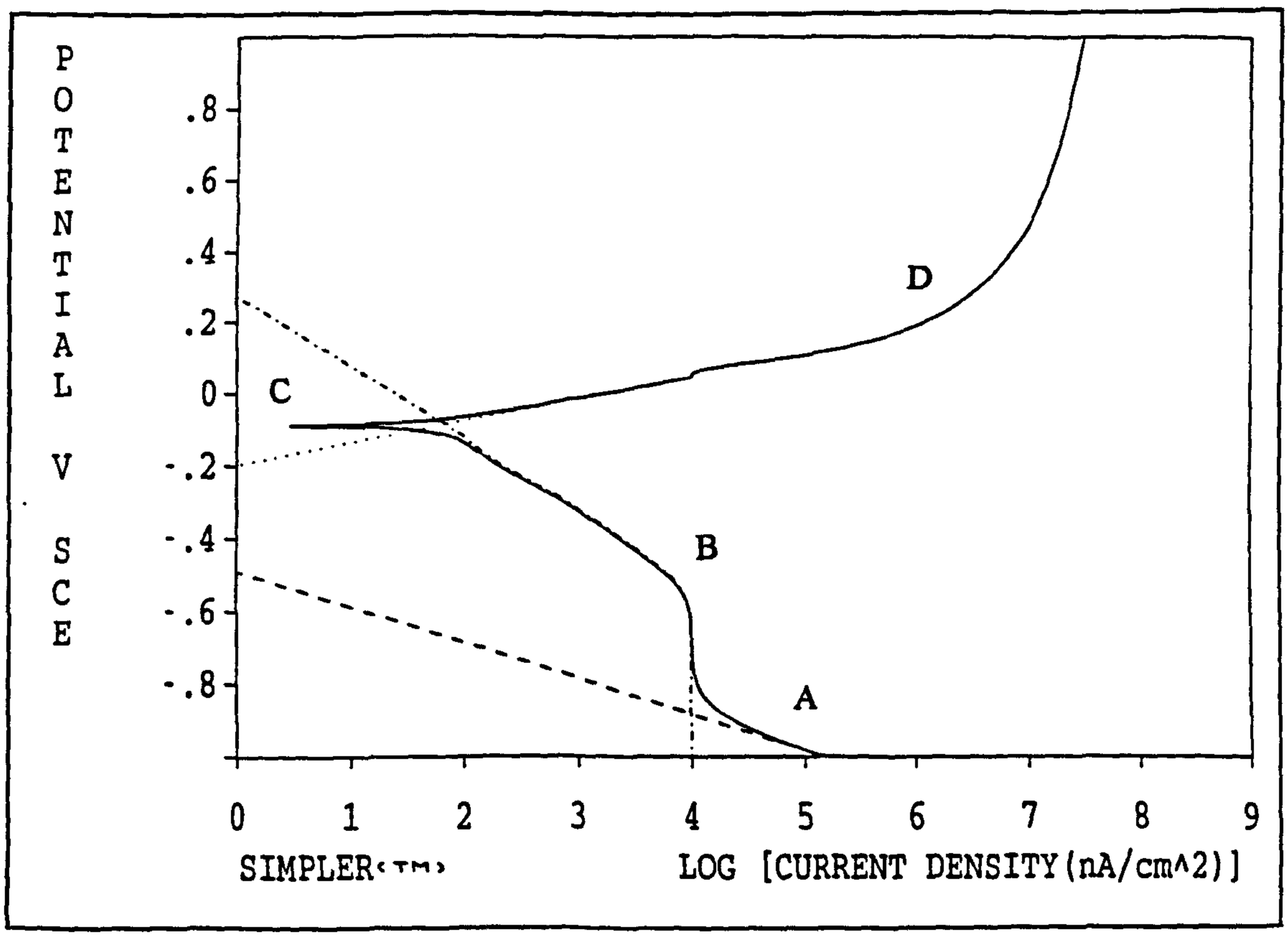

Figure 1.1 Typical polarization curve for a metal in seawater.

1.1.4.1 Activation Polarization

For electrochemical reactions which proceed at such a rate that they are unaffected by the supply of reactants or products to and from the surface, a relationship between current and polarization has been found:

$$\eta = b_x \log(\frac{i}{i_0}) \qquad 1.8$$

where i_o is the exchange current density

b_x is the anodic or cathodic Tafel constant

$$b_a = \frac{2.303RT}{\beta zF} \qquad 1.9$$

$$b_c = \frac{2.303RT}{(1-\beta)zF} \qquad 1.10$$

where β is the symmetry coefficient

b is the slope of a current - polarization curve, with i_0 being the intercept. This slope will be a straight line (in the regions close to E_{corr}) if current (or current density) is plotted on a logarithmic axis. Since the redox reactions are controlled by the transfer of electrons, this straight line behaviour (in semi-logarithmic space) is termed activation (or charge transfer) polarization. Regions BC and CD are due to cathodic and anodic activation-controlled polarization of the oxygen reduction and metal dissolution reactions respectively.

1.1.4.2 Diffusion-Limited Polarization

The curved region BC is not controlled by the reduction of oxygen - rather the limiting factor is the rate at which oxygen can diffuse to the surface in order to be reduced, since the activation-controlled reaction has reached such a rate that the concentration of dissolved oxygen close to the electrode is less than that of the bulk solution. In the limit, the surface concentration will fall to zero, the process will be completely under diffusion (mass transport) control and the current will be independent of potential.

1.1.4.3 Resistance Polarization

The resistance to charge transfer polarization in the body of the metal is negligible, but the resistance of the electrolyte (R_{sol}) and the metal surface ($R_{surface}$) may be appreciable, and act as a barrier to the passage of current. The resistance polarization will then be the product of the current and the total resistance ($R_{sol} + R_{surface}$). Its effect upon a polarization curve is to add curvature to the current density lines.

1.1.5 Galvanic Corrosion Theory

1.1.5.1 Evans Diagrams

The essential components for galvanic corrosion to occur are materials with different surface potentials, a common electrolyte and a common electrical path. If these are all present, the junction of the two materials will assume a potential between the potentials of the uncoupled materials. Thus, the more reactive (base) material will be anodically polarized at the junction, while the more noble (less reactive) material will be cathodically polarized. The base and noble materials are now acting as sites for the individual anode and cathode respectively, rather than having both anodic and cathodic processes occurring on their respective surfaces. This may be shown using an Evans Diagram (Figure 1.2) . If the electrolyte is seawater, the two intersecting reactions are now dissolution of the metal and oxygen reduction on the cathode.

1.1.5.2 Factors Affecting Galvanic Corrosion

The corrosion rate will be heavily, but not solely, dependent upon the differences

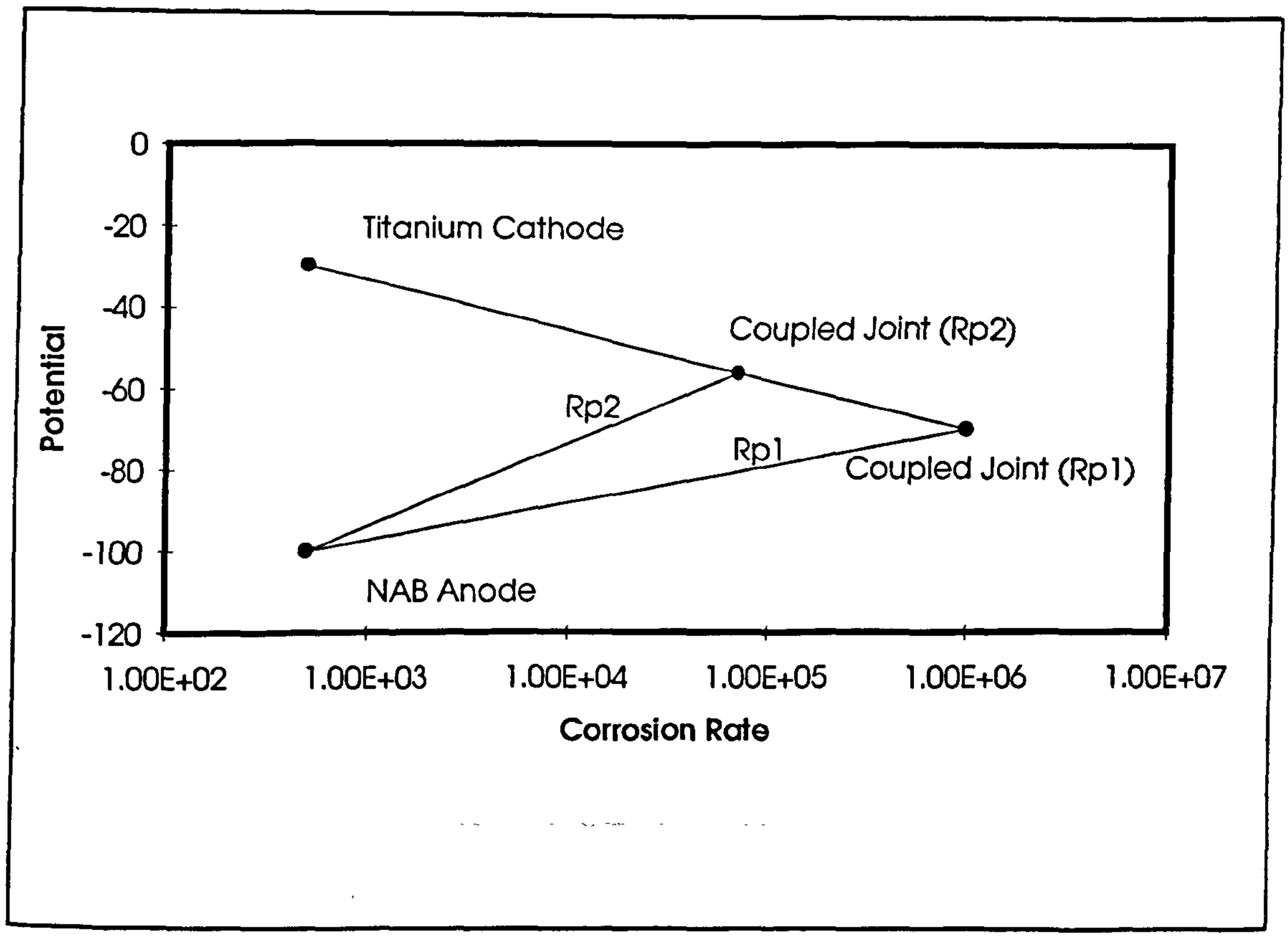

Figure 1.2 Evans diagram for titanium and nickel aluminium bronze.

in potential. Factors such as the ratio of anodic and cathodic areas, distance between electrically connected materials, geometric configuration, electrolyte resistance and the polarization resistances, R_p, (the slope of the E-*i* plot) of the anodic and cathodic components, will all have an effect on the magnitude of galvanic attack. Figure 1.2 shows the effect of an anode having the same E_{corr} , but with different R_p values. The potential at which the current densities are equal differ, and the resultant rates of galvanic corrosion (related to i_{corr}) also differ.

The relative areas of anode and cathode are also important. A large cathode presents a greater surface area on which oxygen reduction can occur, thus greater dissolution of the anode will occur. The opposite case of a large anode-cathode ratio will produce only a small increase in galvanic activity as a result of the predominant polarization of the more noble material.

If the areas of the two metals are comparatively small, and the solution conductivity is high, the effect of the transfer of electrons will be to make the whole surface equipotential[4]. If this is not the case, there will be a potential distribution over the structure with the greatest polarization closest to the junction of anode and cathode, decreasing with increasing distance from the junction. This arises from the resistance to current flow in the electrolyte. The actual value of the potential at the junction of anode and cathode is little affected by electrolyte resistance, since it is controlled by polarization effects[4,5], but the distribution of potential is markedly affected. As the electrolyte resistivity is increased, the distribution of potential becomes less uniform over the structure, and instead becomes primarily distributed around the junction (see Figure 1.3).

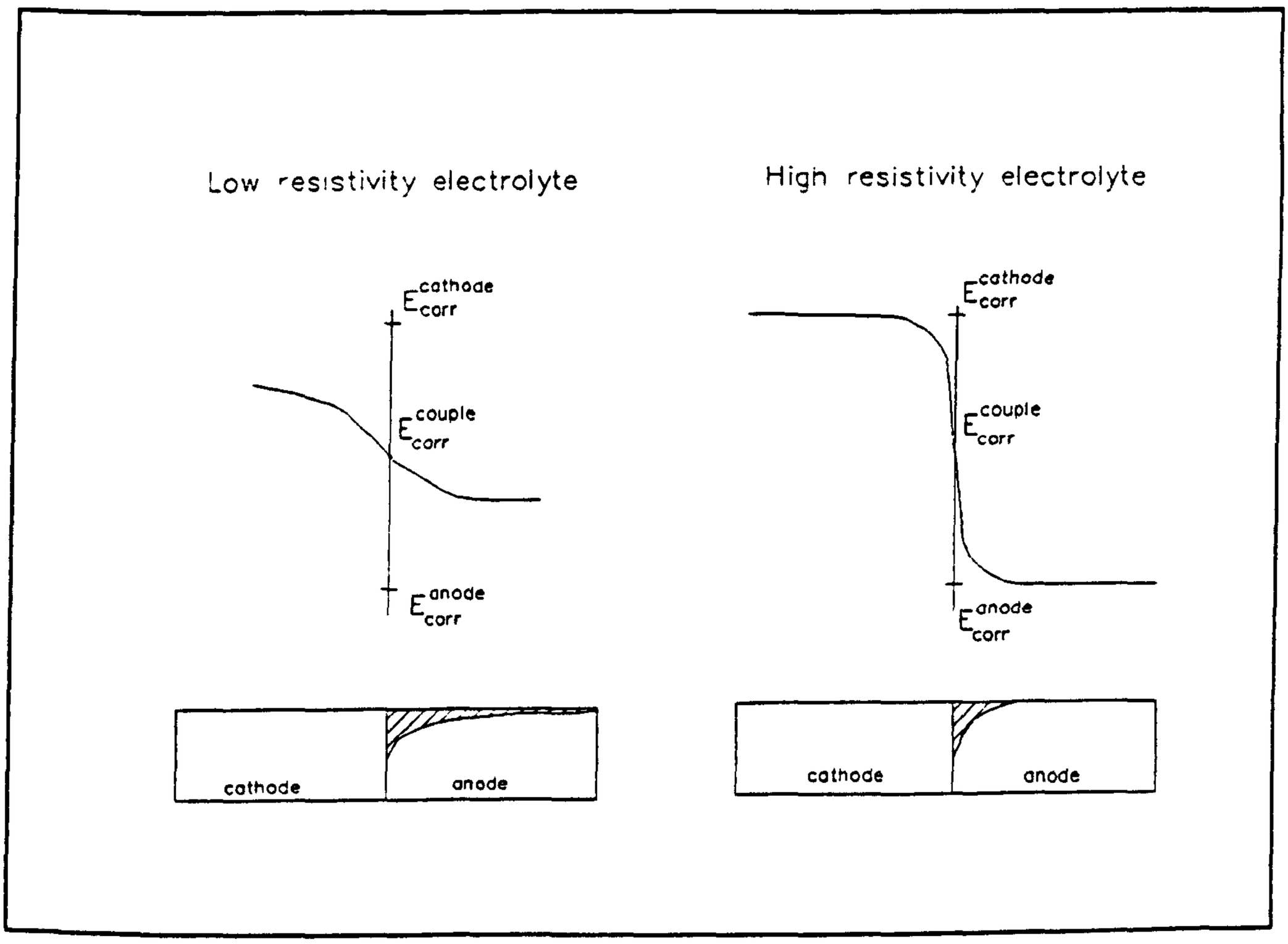

Figure 1.3 Effect of solution resistance on distribution of potential and corrosion rate of anode.

If the electrolyte resistivity is high, the geometrical area ratio may differ from the

effective area ratio, since there will be parts of the two components that do not 'see' each other *ie* are effectively electrically isolated from one another. The geometry of the structure is also important, in that current will always take the path of least resistance, and thus does not flow round corners easily.

The extent of galvanic activity is dependent upon the rate at which electrons can be produced and consumed. Anodic reactions can attain very high rates, thus galvanic corrosion in seawater is generally controlled by the rate at which the electrons are consumed by the oxygen reduction reaction. The maximum rate of oxygen reduction is controlled by the diffusion of oxygen to the surface, and thus the rate of galvanic attack is under cathodic diffusion control. Whitman[6] and Mansfeld[7] showed that under these conditions, the rate of galvanic attack is proportional to the area of cathodic component, and independent of the area of the anodic metal. This is called the catchment principle.

The cathodic diffusion-limited current density is given by :

$$i_{lim} = \frac{zFD_{M^{z+}}(h_{M^{z+}}^{electrode} - h_{M^{z+}}^{solution})}{\delta} \qquad 1.11$$

where D is the diffusion coefficient of the species in question

h is the concentration of species in question at position denoted by superscript

δ is the thickness of the double layer

z is the number of electrons transferred

F is Faraday's constant

Increasing the flow rate or convection of the electrolyte will increase the

concentration of oxygen in the solution and decrease the thickness of the double layer, thereby increasing the value of i_{lim}. An example of this is the greater current demand on a ship's ICCP* system (where the hull is cathodically polarized into the oxygen reduction region in order to prevent iron dissolution) for under-way conditions then for static flow[8]. As a result, galvanic activity in systems where oxygen reduction is the major cathodic reaction is enhanced by flow.

1.1.6 Seawater Composition and Properties

Seawater is the most abundant corrosive electrolyte, covering over two-thirds of the earth's surface[9]. Seawater from the open seas may be considered as a dynamic aqueous system[10] containing dissolved salts, gases and organic compounds, undissolved material and living organisms. The concentration of salts in seawater is expressed in terms of the chloride content, either as chlorinity or salinity, where salinity may be defined as[11]:

$$Salinity = 0.03 + (1.805 \; x \; Chlorinity) \qquad 1.12$$

where both are expressed in parts per thousand (‰).

* ICCP Impressed Cathodic Current Protection

Ion or molecule	concentration (g kg^{-1}) (Rowlands[11])	concentration (g kg^{-1}) (Riley[14])
Salinity	34‰	35‰
Chloride (Cl^{-1})	18.9799	19.3540
Sulphate (SO_4^{2-})	2.6486	2.7120
Bicarbonate (HCO_3^-)	0.1397	0.1400
Bromide (Br^-)	0.0646	0.0670
Fluoride (F^-)	0.0013	0.0013
Boric acid (H_3BO_3)	0.0260	0.0257
Sodium (Na^+)	10.5561	10.7700
Magnesium (Mg^{2+})	1.2720	1.2900
Calcium (Ca^{2+})	0.4001	0.4120
Potassium (K^+)	0.3800	0.3990
Strontium (Sr^{2+})	0.0133	0.0080

Table 1.1 Concentrations of major chemical compounds in seawater.

In the majority of oceans, the salinity of seawater does not vary widely, generally lying in the range 34 - 37‰. A figure of 35‰ (19.4‰ chlorinity) is often taken as the average for 'open sea' water[12]. Semi-enclosed seas have higher salinities, 39‰ in the Mediterranean and 41‰ in the Red Sea. The North Sea has generally found to have salinities in the range 34 to 35‰[13]. Table 1.1 shows the major constituents of seawater in

waters of 34 and 35‰ (parts per thousand) salinity.

The pH of seawater is normally about 8.1 with variations from 8.0 to 8.3[15]. The pH falls with increasing depth, with values ranging from 7.6 to 7.9[16]. The primary effect of seawater composition is on the level of dissolved oxygen and the resistivity. The saturated oxygen concentration falls with both increasing temperature and salinity, while resistivity falls with increased salinity and temperature. Values of seawater resistivity range from 27 to 33 Ω cm in the North Sea[17], while seawater taken from sheltered areas will have increased salt content, thereby decreasing the resistivity.

Seawater obtained from Plymouth Marine Laboratories used in this study was found to have conductivities in the range 4.7 to 5.3 S m^{-1}. The conductivity of the seawater is easier to measure; the resistivity can be obtained from the reciprocal relationship between conductivity and resistivity. Thus, the seawater used in this study was found to have resistivities in the range 18.8 to 21.3 Ω cm.

The corrosive nature of seawater is due to the high dissolved salt content, which has two main actions. The first is the presence of chloride ions, which generate metal dissolution via complexation reactions, and also penetrate passive films in localised areas, leading to breakdown and subsequent pitting, crevice or intergranular corrosion. The second is the high electrical conductivity (50 to 200 times that of freshwater[18]), which leads to larger galvanic currents for a given dissimilar metal/electrolyte/geometry system.

1.2 MODELLING OF GALVANIC CORROSION

The corrosion rate of a system is related to the electrode potential, and thus to

determine the corrosion rate within a system, the potential distribution must be known.

1.2.1 Complex and Analytical Solutions

Various methods are available for such a task, such as boundary and finite element analysis, finite difference analysis[19,20,21,22,23,24] and analytical solutions. An exact prediction within a cylindrical system requires the solution of Laplace's Equation for the electrostatic potential P at a position defined by the longitudinal and radial co-ordinates x and r :

$$\frac{\partial^2 P}{\partial x^2} + \frac{\partial P^2}{\partial r^2} + \frac{1}{r}\frac{\partial P}{\partial r} = 0 \qquad 1.13$$

The use of this equation is, in effect, an assumption that there are no significant concentration variations in the electrolyte and that mass transfer occurs solely by ionic migration. This condition is satisfied by moving seawater[25,16]. The solutions to this equation are non-trivial, and analytical solutions are often not possible even for simple geometries.

1.2.2 Simple Solutions - Unidirectional Current Flow

When studying systems with cylindrical geometry, if an assumption is made that the electrostatic potential in the electrolyte varies only in the axial direction (*ie* not in the radial direction), then analytical solutions can be made using linear electrode kinetics, leading to a prediction for the electrode potential distribution over the geometry. Such an approach is in effect an assumption of unidirectional current flow.

Using such an assumption for a tube filled with flowing electrolyte polarised at one end, the electrode potential gradient parallel to the tube walls must be related to the

uniform density of current (i_L) flowing parallel to the tube walls by Ohm's law :

$$-\frac{dP}{dx} = \frac{dE}{dx} = \pm\rho i_L \qquad 1.14$$

where ρ is the electrolyte resistivity

E is the electrode potential with respect to a standard reference electrode

x is measured in the direction of decreasing electrode potential.

The equality between (-dP/dx) and (dE/dx) follows from the fact that[26]:

$$-\frac{dP}{dx} = \frac{dE}{dx} + a\ constant \qquad 1.15$$

A convention of assigning negative values of (dE/dx) to oxidation reactions and positive to reduction reactions is adopted.

Applying Kirchoff's law for the change in i_L over a very small distance and the corresponding current supply over the same distance from the tubewalls due to their polarised condition:

$$d\frac{i_L\ \pi\ r^2}{dx} = -2\pi i_s \qquad 1.16$$

where r is the tube radius

i_s the net current density on the tube surface at distance x.

Combination of the above equations leads to :

$$\frac{d^2E}{dx^2} = \pm\frac{2\rho i_s}{r} \qquad 1.17$$

The second order differential equation thus produced may be solved for the dependence of the electrode potential and current upon distance x if the relationship between i_s and the electrode potential is known. Astley[26,27,5] solved this equation for a number of commonly occurring geometries.

1.2.3 Limitations of Unidirectional Current Flow

The assumption of unidirectional current flow was first considered by Frumkin[28], who showed that the validity of the assumption decreased as the diameter of the system increased. He showed that by inserting the value obtained for $(\partial^2P/\partial x^2)$ by using the assumption of unidirectional current flow into the Laplace equation shown above, the radial potential drop may be derived, and thus the limit to be placed upon system diameter before the ratio of radial to axial potential drops becomes appreciable. In this way, for the instance when the rate of oxygen reduction and metal dissolution reactions at the surface of a metal were linearly dependent upon potential, the assumption of unidirectional flow resulted in negligible error when :

$$r < (\frac{2}{\rho}).(\frac{dE}{di}) \qquad 1.18$$

The quantity $((dE/di)/\rho)$ is termed the Wagner polarization parameter. It is effectively the ratio of interfacial polarization resistance to the resistance to ionic conduction in the electrolyte, and thus may be considered as :

$$W = \frac{kinetic\ resistance}{ohmic\ resistance} \qquad 1.19$$

It may be used to determine the uniformity of current distribution; a large Wagner polarisation parameter leads to a uniform distribution over the system in question, while a low value of W to a non-uniform distribution. It has the units of length; thus, if a characteristic length L is introduced into the denominator, it becomes a dimensionless number. It is this number that is kept constant in scale modelling of electrochemical systems *ie* if a system is scaled by a model *n* times smaller in scale, the electrolyte resistivity must be increased *n* times in order to achieve the same potential distribution. This technique, known as Dimension and Conductivity Scaling (DACS) has been used to model ship ICCP systems[29,30,31,32]. It suffers from the problem that altering the resistivity of the electrolyte alters the electrochemical behaviour of the material(s) in question, namely the polarization resistance and the free corrosion potentials. The pH of the electrolyte may also alter with dilution.

In a subsequent study based upon systems exhibiting linear electrode kinetics, de Levie[33] set an upper limit of $(1/8\rho)(dE/di)$, although Astley[26] considers that a value of $(1/2\rho)(dE/di)$ is a more reasonable value to place as a limiting factor using de Levie's calculations. This less stringent condition leads to the assumption of unidirectional current flow being valid for diameters of 500 cm for freshly exposed copper alloy in seawater under conditions for rapid flow.

Typical values of the Wagner polarisation parameter in static seawater are 5000 cm for titanium and copper-based alloys commonly used in seawater systems, while for a freshly corroded copper-based alloy surface in flowing seawater environment, the value falls

to about 500 cm. The value of the Wagner polarisation parameter falls by an even greater amount when the electrolyte falls in conductivity, in which case its value may fall to tens of millimetres.

Astley[26] has shown through a combination of experimentation and modelling that even the de Levie limit is too stringent, and quotes a figure of 'about 800 cm' as the upper limit of diameter that may modelled without appreciable error.

1.3 THE GC COMPUTER MODEL

1.3.1 Description of Algorithm

The GC model was written in Fortran, and can be used to analyze the following geometries :

(i) tube to tube

(ii) tube to tubeplate

(iii) tubebundle/tubeplate to large diameter pipe

(iv) condensor arrangement (tubebundle/tubeplate - header-pipe)

The experimental work detailed in this chapter has used the geometry described in option (iii). The following parameters are required by the model :

Geometrical

anode and cathode radius

anode and cathode length

number of cathodic tubes

Electrochemical

wagner number

or polarization curve slope and resistivity

free corrosion potential for both anodic and cathodic components

These parameters are input to the model, which then uses the solution (appropriate for the geometrical configuration) to Equation 1.17 to calculate the potential at the junction of anode and cathode (E_{beg}). The polarization ($E - E_{corr}$) over the length of the anode and cathode at distance x from the junction is then calculated in the following manner:

$$E - E_{corr} = (E_{beg} - E_{corr}) \frac{\cosh \frac{(x_{end} - x)}{K^{0.5}}}{\cosh \left(\frac{x_{end}}{K^{0.5}}\right)} \qquad 1.20$$

where E_{corr} is the free corrosion potential

E_{beg} is the junction potential

x_{end} is the total length of the component in question

and

$$K = \frac{rRT}{2\rho i_c kF} \qquad 1.21$$

where r is the radius of anode or cathode (as appropriate)

R is the gas constant (8.314 J mol^{-1} K^{-1})

T is the absolute temperature (K)

ρ is the resistivity of the electrolyte

i_c is corrosion current density (current at E_{corr})

F is Faraday's constant (96494 C)

k number of electrons transferred

The resultant potential-distance relationship is then plotted.

1.3.2 Model Predictions

1.3.2.1 Effect of Electrolyte Resistivity on Potential Distribution

Figure 1.4 shows the potential distributions predicted by the model for a system consisting of an anode of length 50 cm and radius 3.2 cm and 4 cathodic tubes of radii 1.22 cm, length 100 cm. The free corrosion potential and R_p values of anode and cathode are -100 mV, 1 x 10^4 Ω and 0 mV, 5 x 10^4 Ω respectively. The resistivity ranges from 1 to 500 Ω cm. It may be seen that the value of the potential at the junction of anode and cathode does not vary markedly with resistivities above 1 Ω cm, but that the variation of potential along the anode and cathode is markedly dependent upon its value.

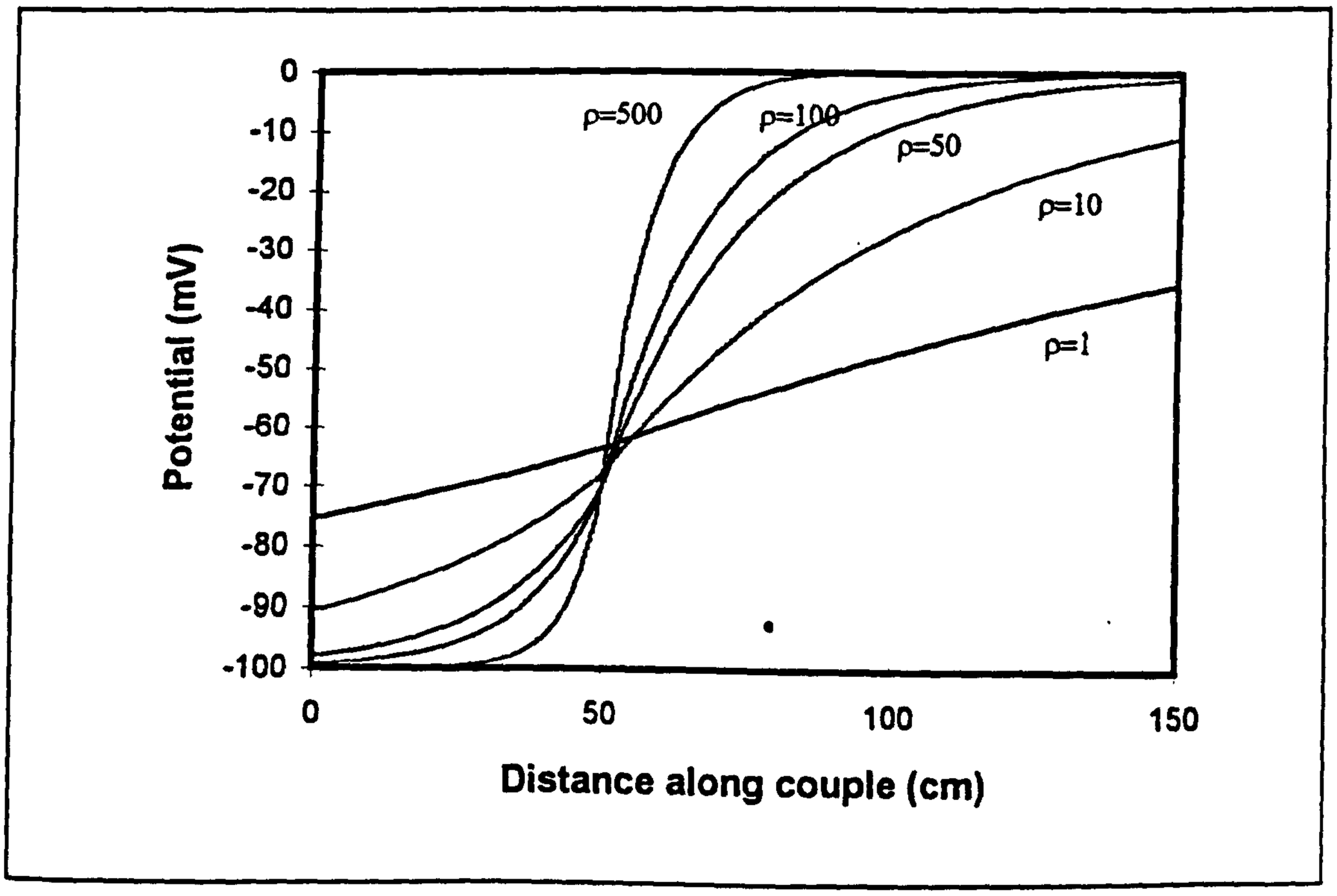

Figure 1.4 Variation of potential distribution with electrolyte resistivity predicted by model.

1.3.2.2 Variation of Junction Potential with Slope of Cathodic Polarization Curve

The dependence of $E_{junction}$, the potential at the junction of anode and cathode for

the system described above (save that resistivity is kept constant at 100 Ω cm, cathodic slope varies between 1 x 10^3 to 1 x 10^6 Ω) is shown in Figure 1.5. The total current flowing into (or from) each tube is given by[26]:

$$I = \frac{\pi r^2}{\rho K^{0.5}}(E_{junction} - E_{corr})\tanh\frac{x_{end}}{K^{0.5}} \qquad 1.22$$

The algorithm assumes a current balance between anodic and cathodic components of the couple. The junction potential (which determines the polarization of each component) is in effect the common factor between the current expressions for the two components. For a given anodic component system (*ie* length, radius, E_{corr} and R_p), the lower the polarization resistance of the cathode, the less the polarization of the cathode required to accept (and use in the reduction process which occurs on the inside surface of the tubes) a given amount of current.

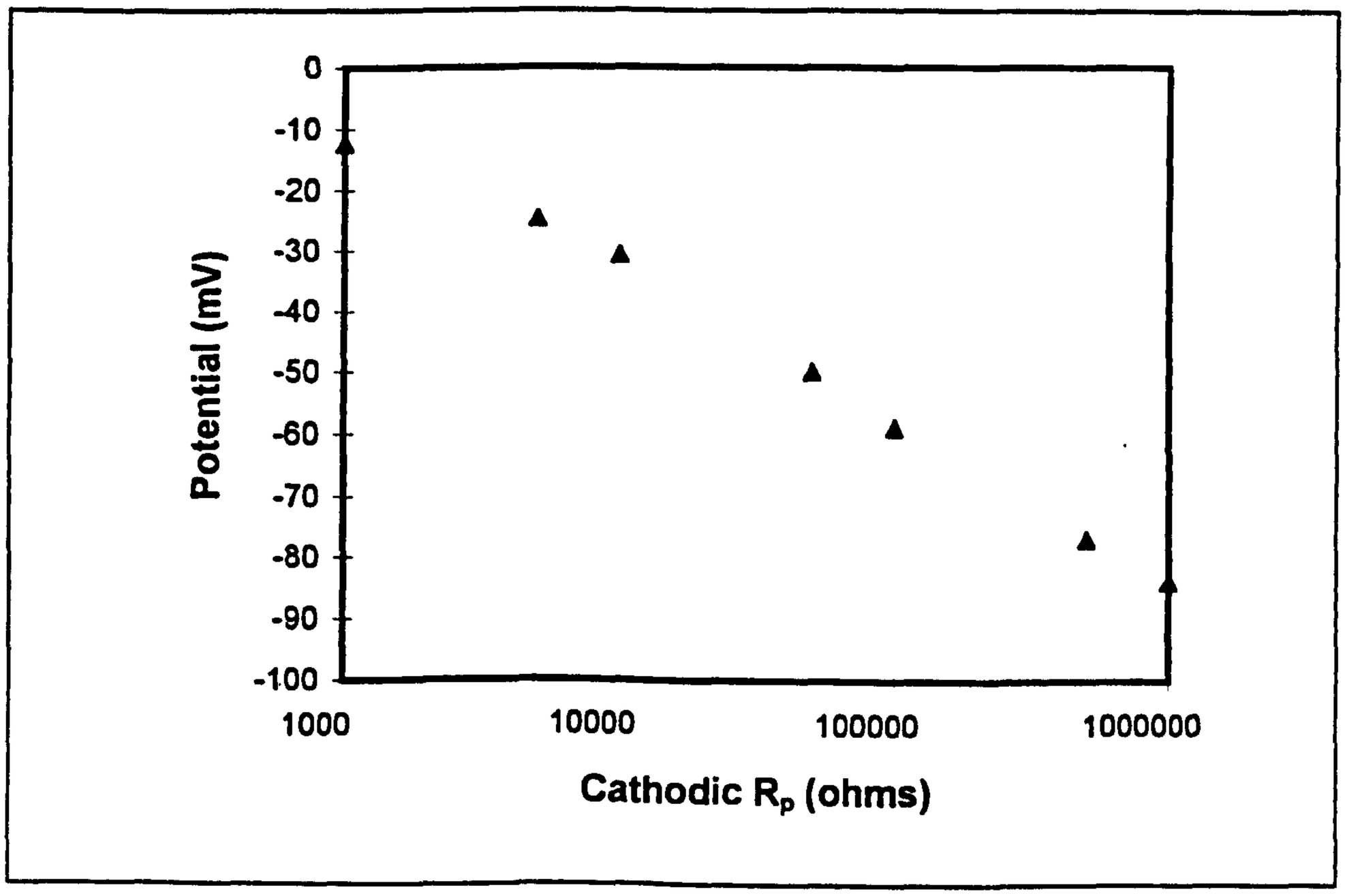

Figure 1.5 Dependence of junction potential on slope of cathodic polarization curve for a given anode component.

Thus, increasing the polarization resistance of the cathodic component increases the

difficulty of accepting a given current ie the magnitude of the polarization ($E_{junction}$ - E_{corr}) must increase, thus the junction potential therefore becomes more electronegative. This is shown in Figure 1.5.

1.3.2.3 Variation of Junction Potential with Slope of Anodic Polarization Curve

The variation of junction potential on the slope of the anodic polarization curve is shown in Figure 1.6, for a constant cathodic system of 4 tubes of diameter 1.22 cm and length 100 cm. The anode is 50 cm long and has a radius of 3.2 cm. The cathodic R_p is 5 x 10^4 Ω and the electrolyte resistivity is 100 Ω cm. As the R_p value increases, the junction potential becomes more electropositive, denoting the need for greater polarization to be able to supply the constant cathodic current being accepted by the cathodic component.

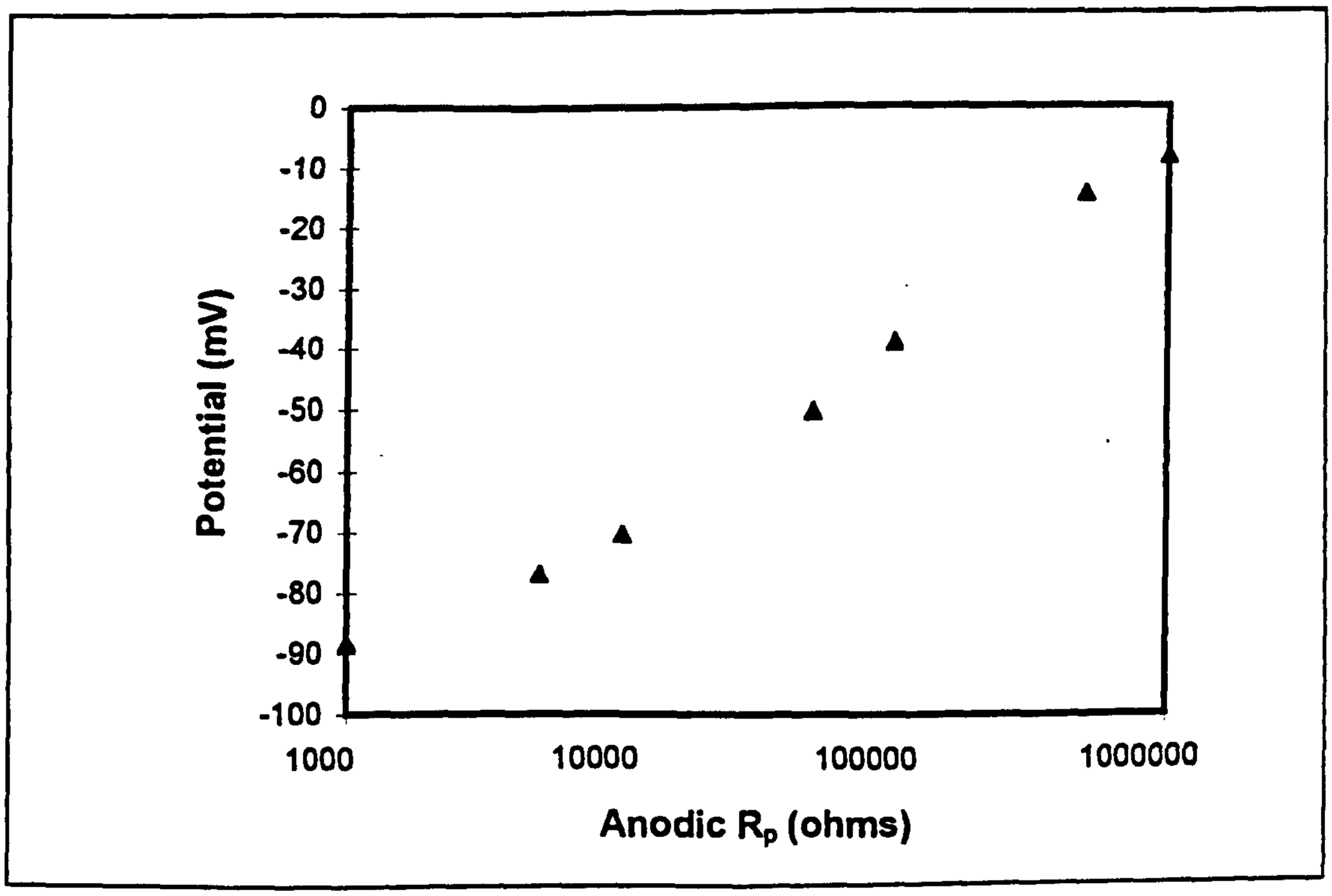

Figure 1.6 Dependence of junction potential on slope of anodic polarization curve for a given cathodic component.

1.3.2.4 Variation of Junction Potential with Number of Cathodic Tubes

The dependence of the potential at the junction of anode and cathode with the number of tubes is shown in Figure 1.7, for a system with cathodic tubes of length 100 cm, radius 1.22 cm, anode of length 50 cm and radius 3.2 cm

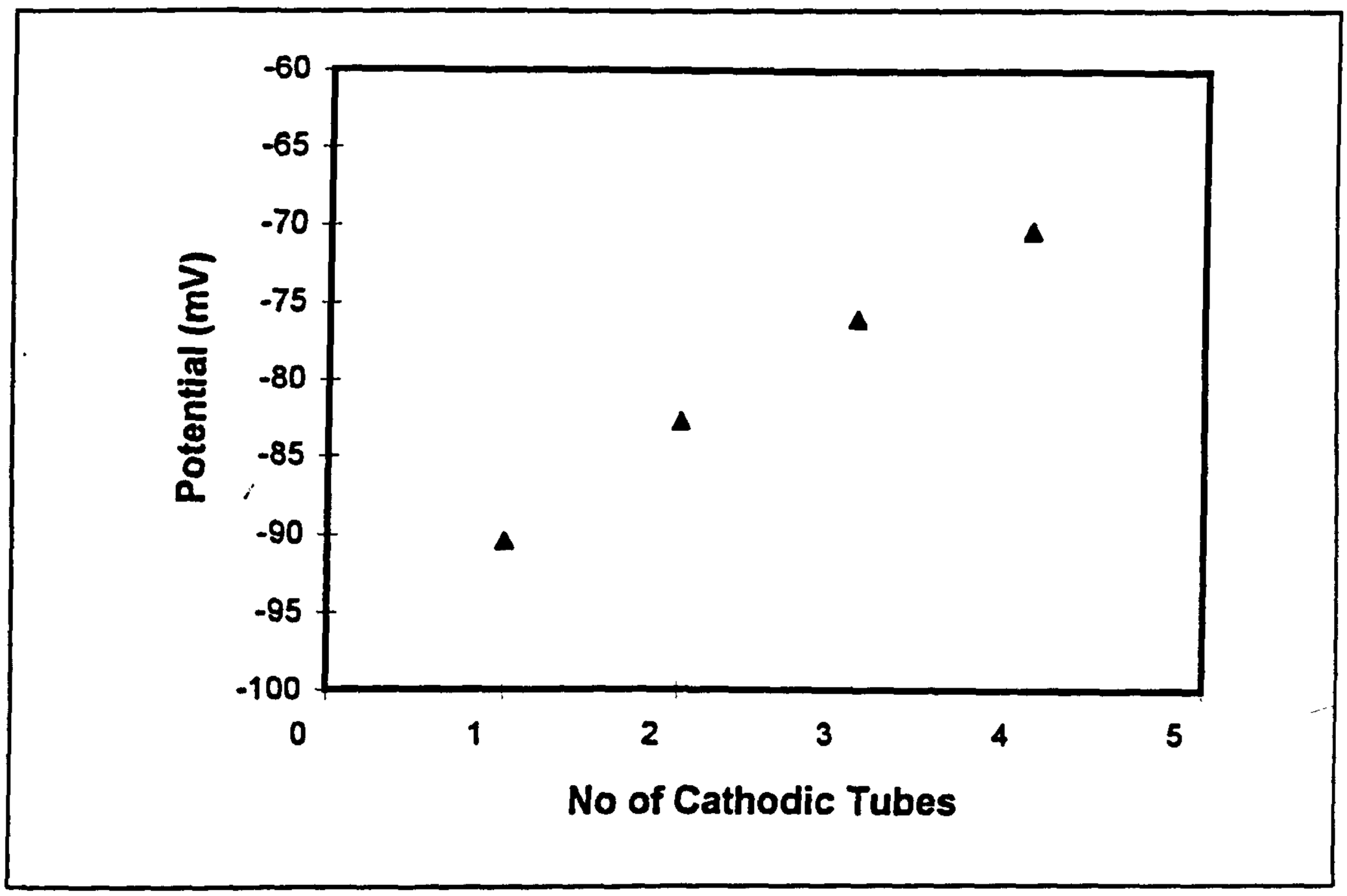

Figure 1.7 Variation of junction potential with number of cathodic tubes.

It may be seen that increasing the number of tubes increases the surface area on which reduction can occur, and thus polarization of the cathodic components required to provide a balance to the oxidation current will decrease. Thus the junction potential will become electropositive.

1.3.2.5 Relationship Between Anode Length and Junction Potential

Figure 1.8 shows that the model predicts a fall in junction potential with increasing anode length for a given cathodic system. This is because increasing the anode length

means there is more anodic area on which oxidation reactions can occur; thus for greater areas, the oxidation reaction requires less impetus, therefore the magnitude of anodic polarization falls *ie* the junction potential becomes more electronegative.

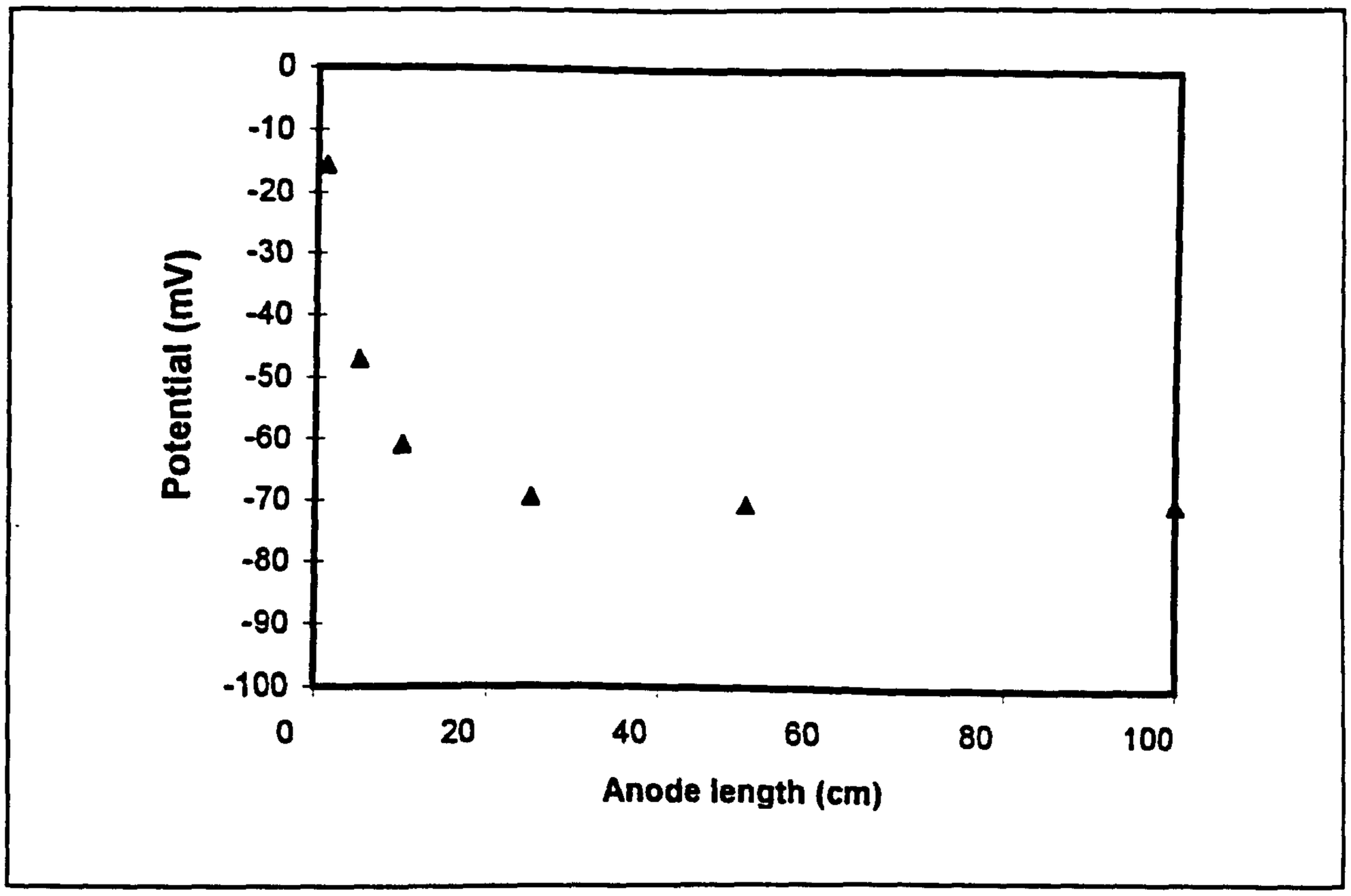

Figure 1.8 Relationship between anode length and junction potential.

The system considered had 4 cathodic tubes of 1.22 cm radius and length 100 cm, connected to an anode of varying length and containing electrolyte of 100 Ω cm resistivity. The anodic and cathodic R_p values were 1 and 5 x 10^4 Ω respectively. It can be seen that above a certain anode length (~27 cm in the system considered here), the junction potential does not vary. This length is a function of the R_p values and resistivity, and may be considered the length of anode that the cathode 'sees' ie the throwing power of the cathode onto the anode.

1.3.2.6 Variation of Junction Potential with Length of Cathode

For a given anode system, decreasing the length of the cathodic tubes means less

surface area on which reduction reactions can occur, thus these reactions must be driven at greater rate *ie* the cathodic polarization increases. This is manifested in more electronegative junction potentials, such that (E_{corr} - $E_{junction}$) increases. The predicted relationship is shown in Figure 1.9. The same system (save that the anode length was fixed at 50 cm and the cathode length varied) as used in the previous section was considered. Once again, there is a limiting length (of the cathode) above which the junction potential does not alter. This may be considered the 'throwing power' of the anode onto the cathode.

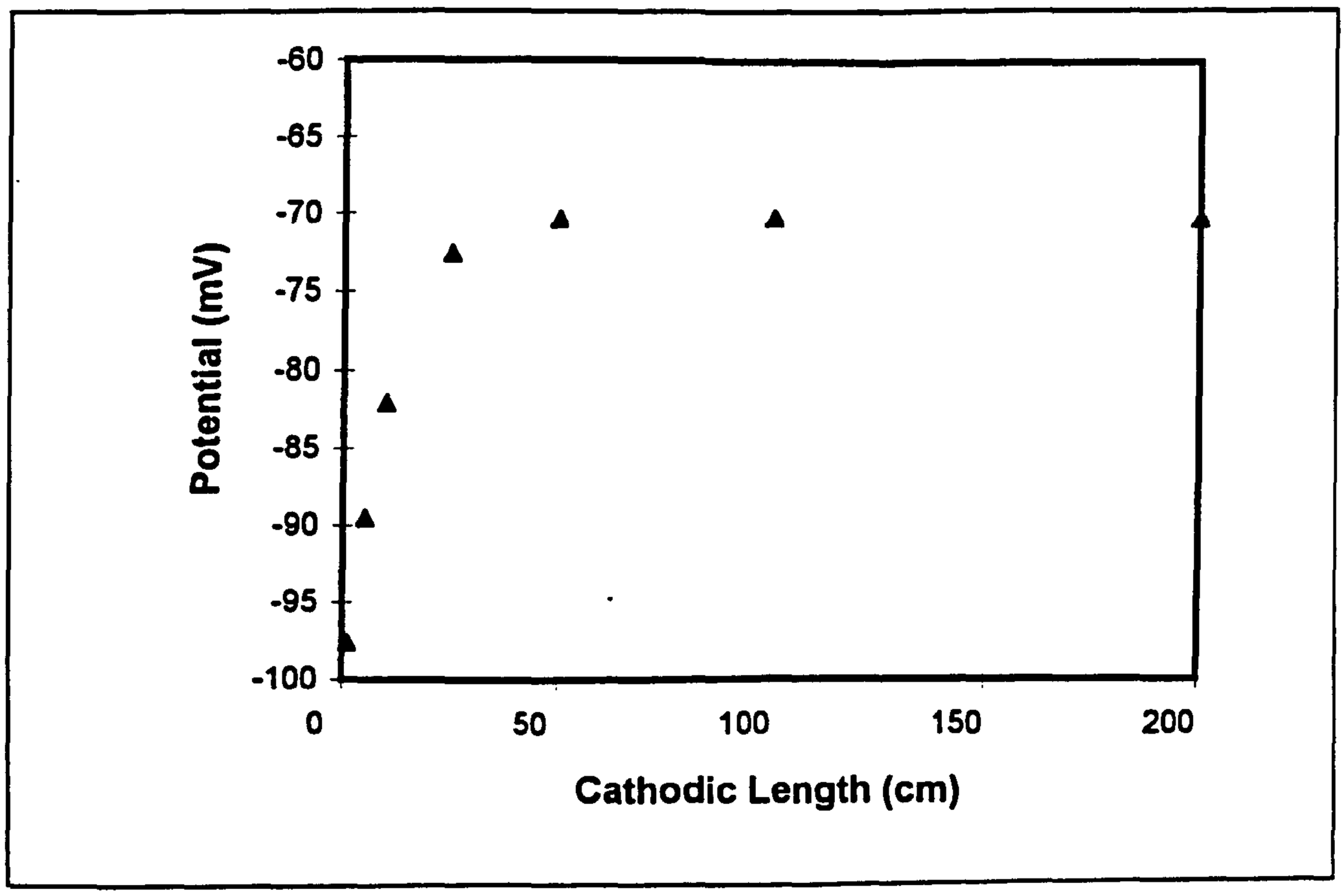

Figure 1.9 Cathode length-junction potential relationship.

1.3.2.7 Variation of Junction Potential with Cathodic Tube Radius.

As for increasing the cathodic length, increasing the radius of the cathodic tubes increases the area available for reduction reactions, thereby lowering the polarization required to provide a current balance for a given anode system. This effect is predicted by the model, and the dependence of the junction potential with tube radius is shown in Figure 1.10.

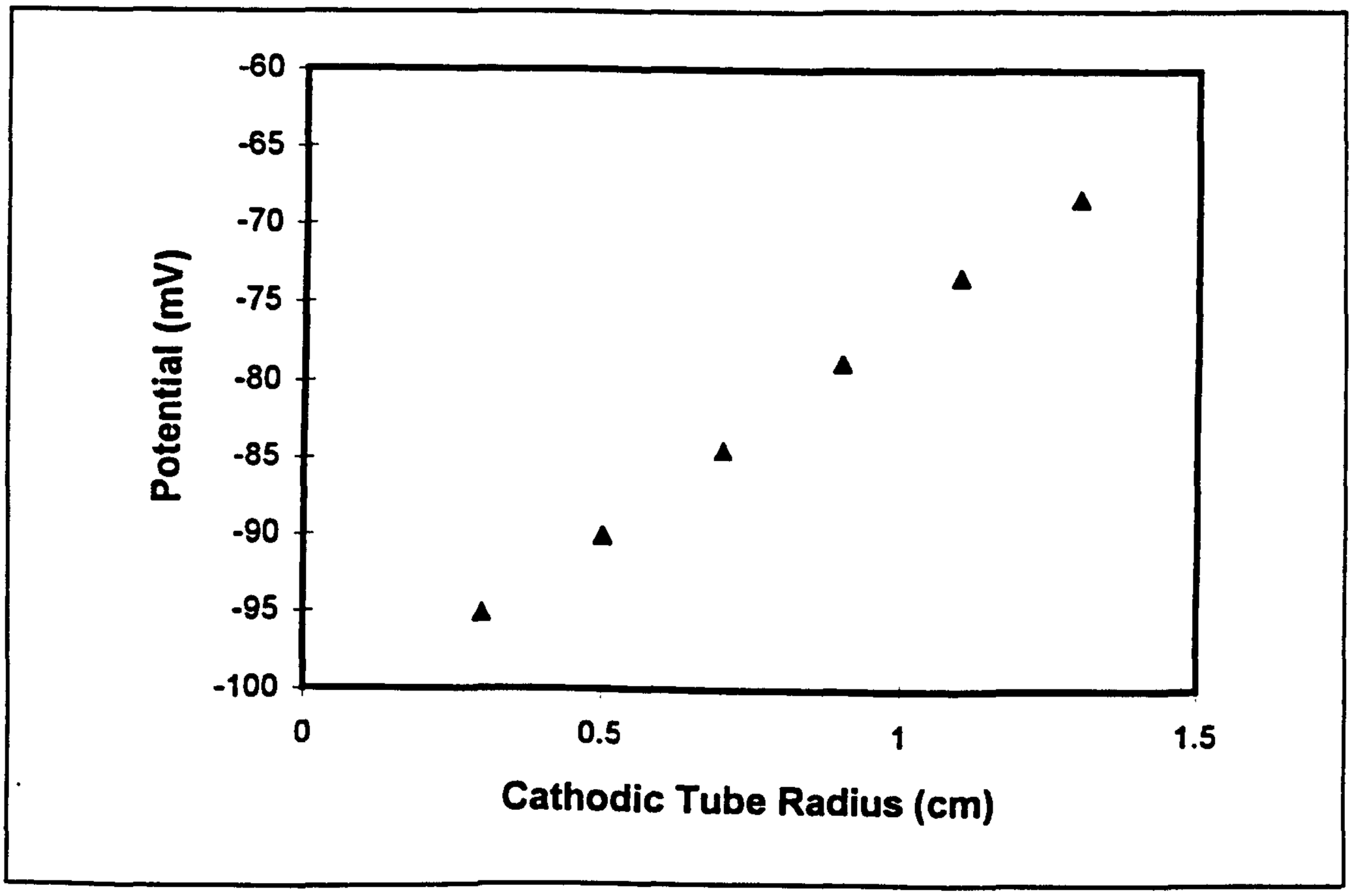

Figure 1.10 Cathode tube radius relationship with junction potential.

1.4 EXPERIMENTAL

1.4.1 Materials and Methods

In order to simulate a common combination of materials used in heat exchangers, the materials considered were titanium and nickel aluminium bronze (NAB) to naval engineering specification NES 747[34] supplied from Defence Research Agency (formerly Admiralty Marine Technology Establishment) Holton Heath. These were connected in a tubebundle/tubeplate/pipe arrangement in a recirculating flow rig[35] (Figure 1.11) with seawater of varying dilutions under both static and flowing conditions. Silver-silver chloride electrodes were used to measure the potentials at different positions along the couple.

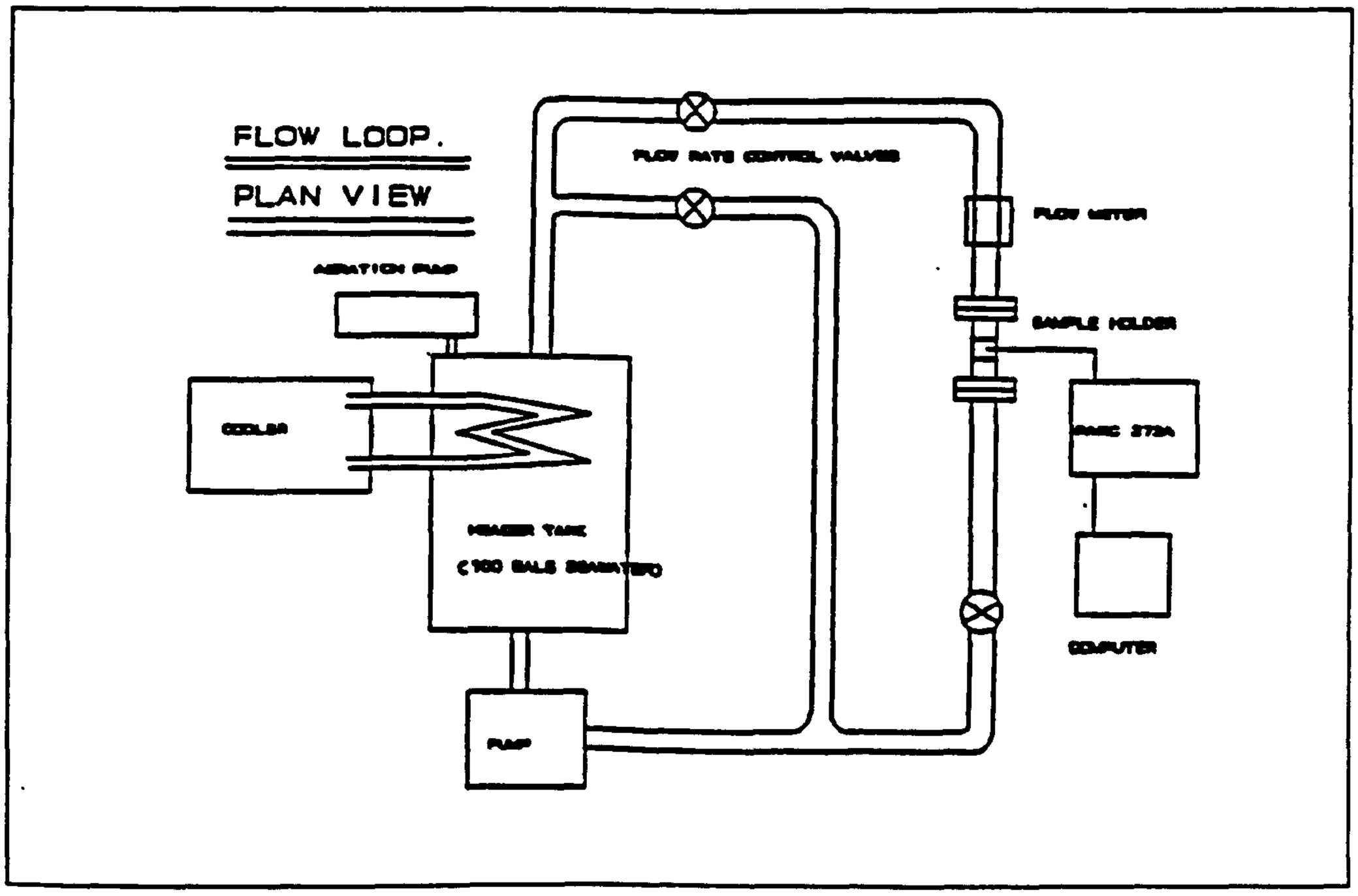

Figure 1.11 Schematic of recirculating flow rig.

1.4.2 Material Analysis

EDAX analysis was taken using an ISI-DS 130 scanning electron microscope with a PGT OM16 I010 X-ray microanalysis probe, and yielded the following results for titanium and NAB respectively:

Element	wt %
Aluminium	2.8
Silicon	0.7
Titanium	95.6

Table 1.2 EDAX analysis of titanium

Element	NES 747	EDAX
Nickel	4.5 - 5.5	4.77
Aluminium	8.9 - 9.6	11.19
Manganese	1.0 - 1.4	0.46
Iron	4.0 - 5.0	3.32
Copper	Remainder	80.26

Table 1.3 Comparison of EDAX analysis and NES 747 alloy specification.

1.4.3 Equipment Design and Manufacture

The NAB portion of the couple comprised a cylindrical hollow tube of 6.32 cm internal diameter (ϕ_{int}) and 8.89 cm external diameter (ϕ_{ext}) and original length 60.8 cm, later shortened to 31.3 cm. To simulate the tubesheet, a NAB plate was machined and then cryogenically shrunk into one end with liquid nitrogen, such that a watertight fit was obtained. The calculations made to shrink the NAB insert are shown in Appendix A. Previous attempts to attach the tubesheet to the NAB pipe using plastic bolts (into holes drilled and tapped into the tube wall thickness) were unsuccessful in achieving a watertight seal.

Holes of the appropriate size were drilled into the NAB tubesheet, and titanium pipes of varying length and diameter (1.25, 1.9 and 2.54 cm) were inserted. This combination constituted the galvanic couple. ABS (acrylonitrile butadiene styrene) flanges were attached to both ends of the couple in order to allow fitting into the flow rig without

a metal contact.

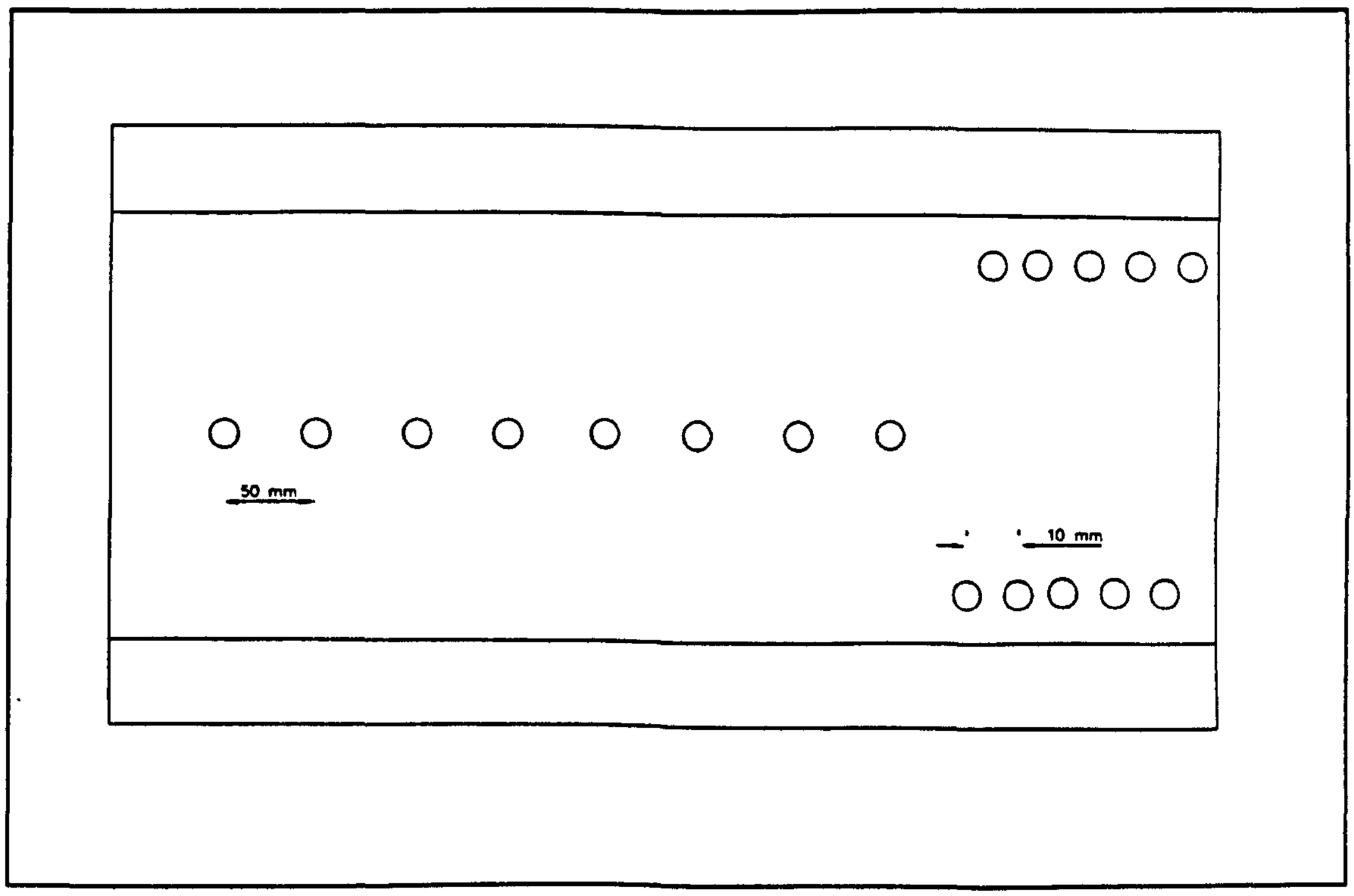

Figure 1.12 SSC Electrode placement on NAB anode.

Potential readings were taken by using silver-silver chloride (SSC) electrodes constructed using the methods described by Paris[36]. These were inserted into a PTFE dowel and secured using epoxy resin. Tapped BA holes were drilled every 5.0 cm along the NAB, with the gap falling to 1.0 cm close to the junction of NAB and titanium. The electrode positioning is shown in Figure 1.12. Electrodes were also placed at various positions along the titanium tubes.

1.4.4 Electrolyte

The electrolyte used was seawater obtained from Plymouth Marine Laboratory, the source of which was Plymouth Sound. The conductivity was measured with a BIBBY MC1 conductivity meter, and found to be in the range 4.7 to 5.3 S m^{-1}, which corresponds to resistivities of 18.8 to 21.3 Ω cm. This water was placed in the water reservoir of the flow

rig, where the temperature of which was kept at 20°C by a Emscope Trim 5 water cooler. Dilution of the seawater was made using distilled water, the results of which are shown in Table 1.4.

Dilution	Conductivity ($S\ m^{-1}$)	Resistivity (Ω cm)	DO_2 (ppm)	pH
100%	5.15	19.4	7.2	8.0
50%	2.55	39.2	8.6	7.5
5%	0.26	384.6	9.1	7.4

Table 1.4 Properties of seawater at various dilutions at 20°C.

1.4.6 Flow Loop and Static Studies

The following set of experiments was carried out.

No of Tubes	2 titanium tubes			4 titanium tubes		
Operation	Flowing		Static	Flowing		Static
Flow rate	1 ms^{-1}	2 ms^{-1}	0 ms^{-1}	1 ms^{-1}	2 ms^{-1}	0 ms^{-1}
100%						
50%						
5%						

Table 1.5 Experimental Matrix

Only two 2.5 cm diameter titanium tubes were used, as it was the NAB diameter was such that it was physically impossible to fit four. In addition, only a flow rate of 1 ms^{-1} was used, as the pump could not supply a 2 ms^{-1} flow rate with this experimental combination.

Experiments were run for up to 24 hours, with potential readings taken periodically through the duration of the test. Static tests were often left for 24 hours, while flow tests did not exceed 8 hours.

The flow rates were set by use of a bypass valve. Prior to each run, air was bubbled through the seawater in the reservoir by an aeration pump. Conductivity and DO_2 readings were taken before each run commenced.

1.4.7 Potentiodynamic Studies

In order to obtain the electrochemical data required for the model, the free corrosion potential and R_p values for each material-electrolyte combination were obtained. Titanium and NAB samples (of size 1.0 x 1.0 x 1.0 cm) were mounted in a hole cut into the wall of a perspex tube of wall thickness 1.0 cm, ϕ_{ext} = 2.5 cm. The edges of the sample were coated with epoxy resin in order to prevent crevice attack. Results from samples which suffered such attack were discarded. This tube was then placed in the recirculating flow rig. A platinum mesh was also attached to the inside of the tube to act as a counter electrode. No surface preparation was applied, in order that the material was in the same condition as during the experiments. Potentiodynamic polarization scans were obtained using an EG&G PAR model 273 potentiostat with 352 software™ control. The potential was stepped from -0.25 to 0.2 V SSCE using a scan rate of 0.1 mV s^{-1}.

1.5 RESULTS AND INITIAL DISCUSSION

1.5.1 Material Composition

From Table 1.3, it appears that the NAB is of incorrect specification. However, the alloy consists of an extremely complex microstructure, with up to seven separate phases having been reported[17]. Figure 1.13 shows the microstructure of a cross sectioned sample of NAB.

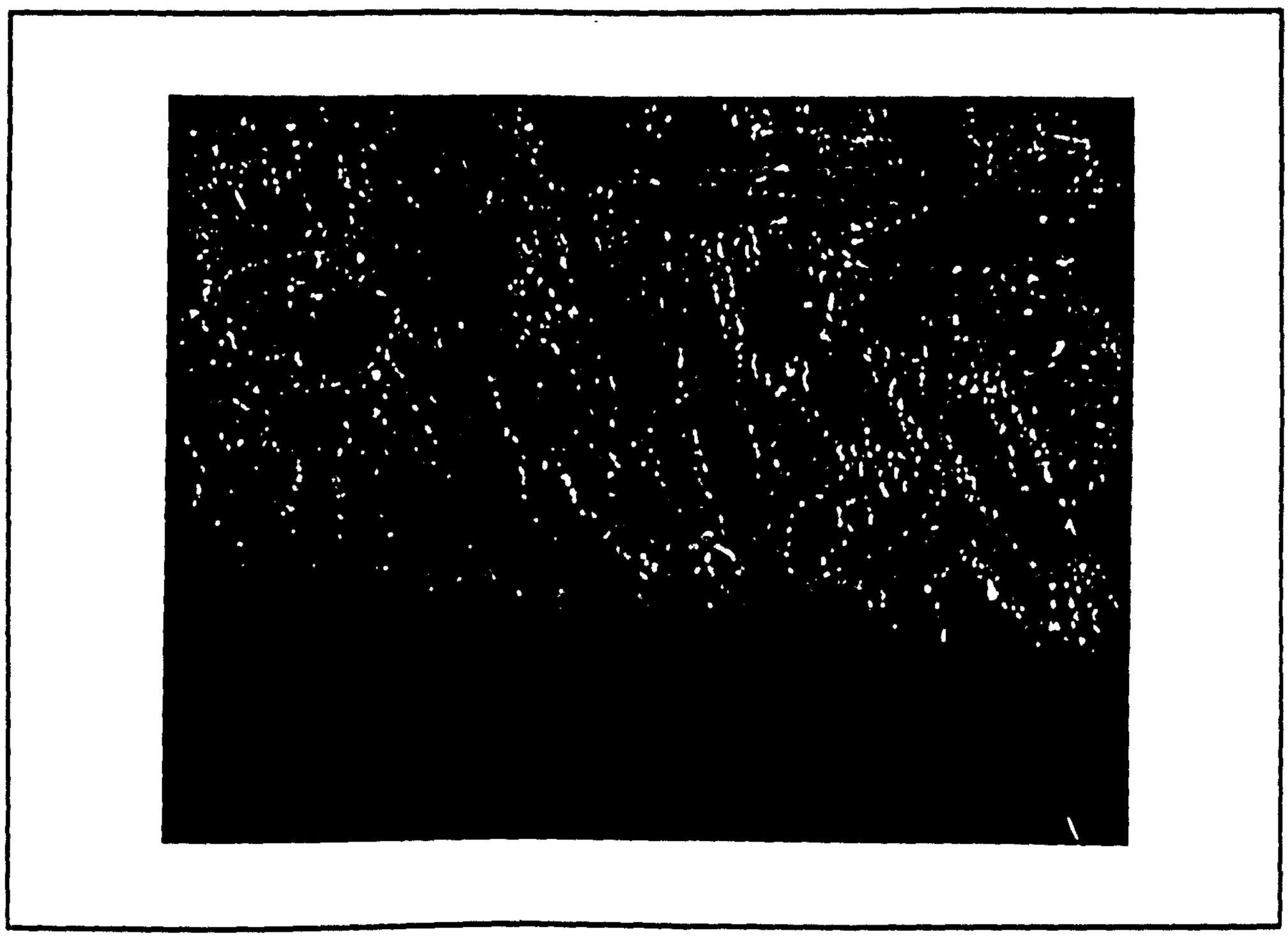

Figure 1.13 Microstructure of NAB (x 250).

The α matrix forms from the β phase (stable at temperatures above 900°C). On further cooling, several κ phases are precipitated from α and remaining β. There are several different compositions of κ. κ_{III} forms continuous 3-D networks around α, and being the most anodic phase, preferentially dissolves. This causes α grains to become detached from the body of the metal and to fall out. Heat treatment regimes have been developed to aid

the breakdown of this phase. The compositions reported[38,39] are detailed in Table 1.6.

Source	phase	Al	Mn	Fe	Ni	Cu
AMTE	κ_I	13	2	58	15	12
AMTE	κ_{II}	20	2	35	28	15
AMTE	κ_{III}	20	2	28	35	15
AMTE	Matrix	6.5	1.5	2	3	87
UMIST	κ_{III}	25	2	19	41	13
UMIST	κ_I and κ_{VI}	6	3	81	3	5

Table 1.6 Analysis of NAB Phases by AMTE[38] and UMIST[39].

Assurances were given from DRA Holton[40] that the bulk analysis for the alloy was in specification. With the number of phases present, it is assumed that the size and positioning of the sampling beam used in the EDAX analysis was such that a sample unrepresentative of the whole sample was taken.

1.5.2 Potentiodynamic Testing

The potentiodynamic curves obtained for titanium and NAB in 5, 50 and 100% conductivity seawater under static, 1 m s^{-1} and 2 m s^{-1} flow conditions are shown in Appendix B. The results are tabulated in Tables 1.7 to 1.9. It should be noted that the gradients are for E/*i* and not E/log *i*.

% Seawater	100%		50%		5%	
Material	NAB	Ti	NAB	Ti	NAB	Ti
R_p ($\Omega \times 10^3$)	169	8868	86.8	190	608.1	1832
E_{corr} (mV SCE)	-188	15	-118	25	-106	-22
ρ (Ω cm)	19.4		39.2		384.6	

Table 1.7 Summary of electrochemical data for static conditions.

% Seawater	100%		50%		5%	
Material	NAB	Ti	NAB	Ti	NAB	Ti
R_p ($\Omega \times 10^3$)	88.39	264.1	185.2	246	380.4	199.4
E_{corr} (mV SCE)	-177	-33	-185	-61	-70	2
ρ (Ω cm)	19.4		39.2		384.6	

Table 1.8 Summary of electrochemical data for 1 m s^{-1} flow conditions.

% Seawater	100%		50%		5%	
Material	NAB	Ti	NAB	Ti	NAB	Ti
R_p ($\Omega \times 10^3$)	9.6	403.8	8.64	270.1	522.4	60.8
E_{corr} (mV SCE)	-200	-38	-162	-3.5	-66	47
ρ (Ω cm)	19.4		39.2		384.6	

Table 1.9 Summary of electrochemical data for 2 m s^{-1} flow conditions.

For the following figures, the distance along the couple is plotted with the distance 0 to x (here x = 31.3 or 60.8 cm) being the distance along the NAB anode. The remaining distance represents length along the cathodic titanium tubes.

1.5.3 Potential Distributions for Static Flow

The first set of experiments carried out measured the potential distributions along titanium-NAB couples containing static electrolyte. Figure 1.14 shows the variation in potential distribution with time over a 72 hour period for a given couple (SW = seawater). It may been seen that there are only minor potential variations with time.

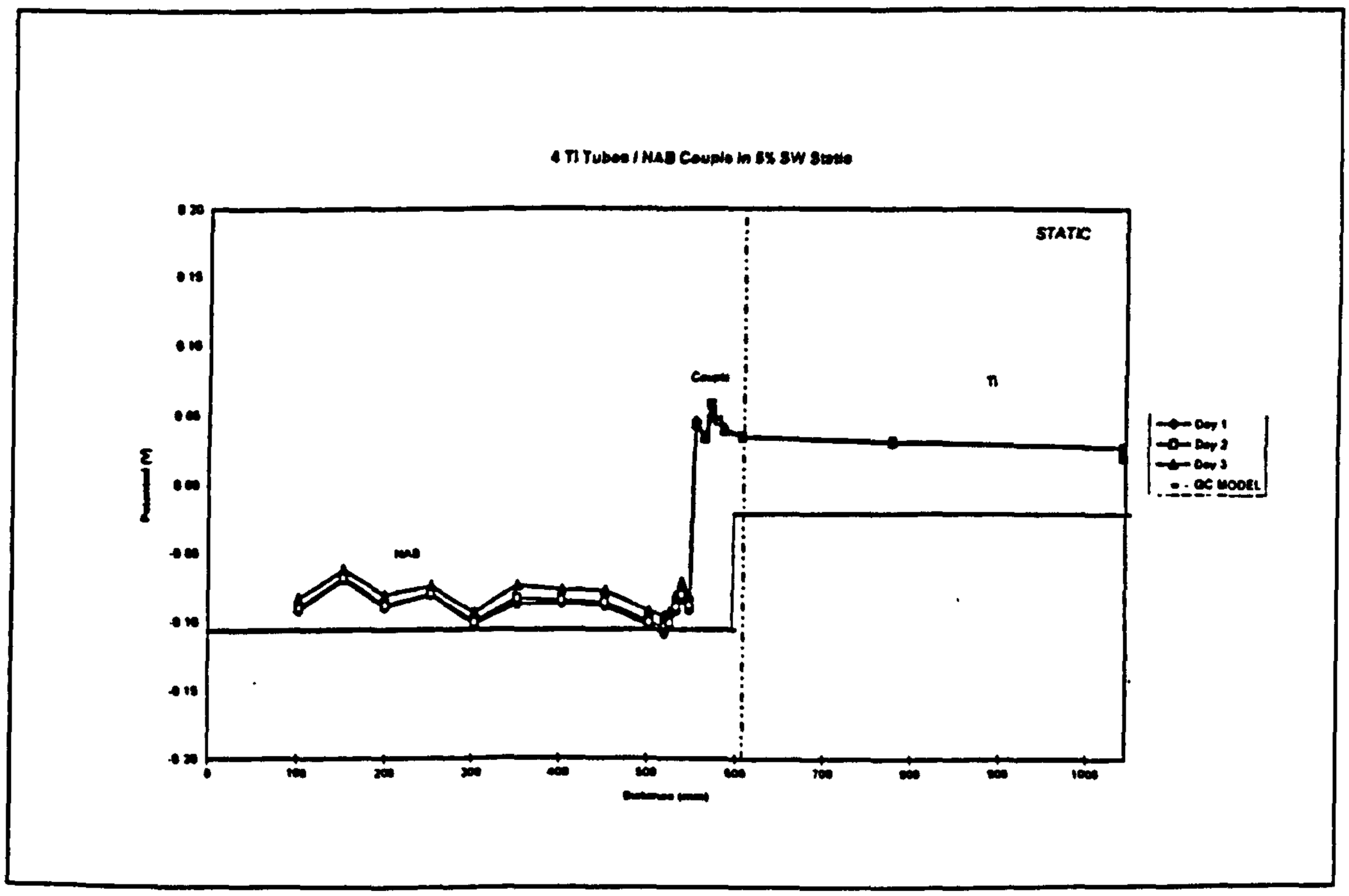

Figure 1.14 Variation in potential over 72 hour period. 4 x 1.25 cm ϕTi tubes, 608 cm NAB, 5% SW, static flow.

As mentioned in Section 1.4.6, experiments were of 24 hour duration. Thus, the last reading taken in this 24 hour period was taken as being representative of the couple in question.

1.5.3.1 The Effect of Electrolyte Resistivity

The effect of differing electrolyte resistivity was investigated using a couple consisting of 2 tubes (diameter = 1.25 cm, length 45 cm) and NAB of length 60.8 cm.

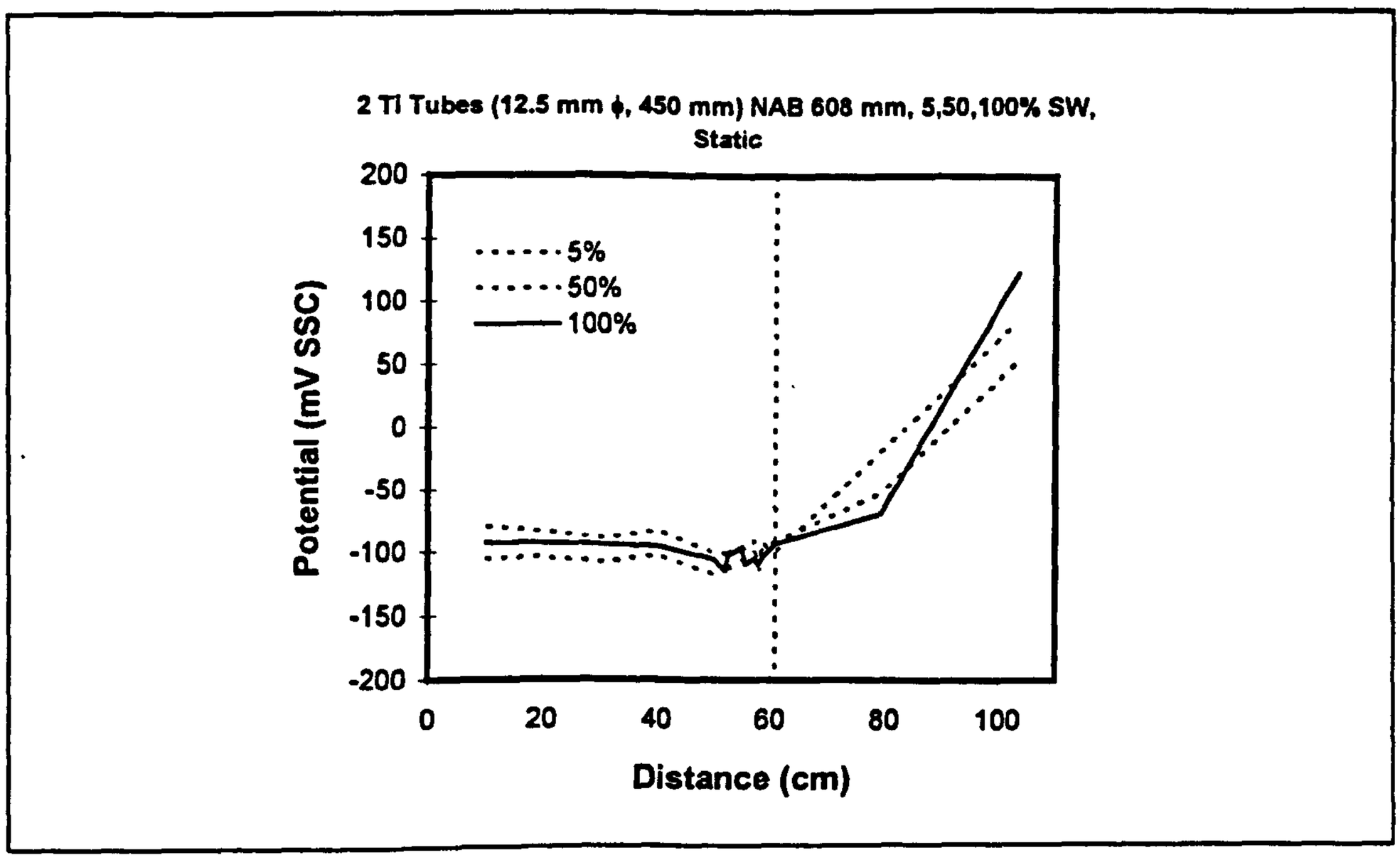

Figure 1.15 Potential distribution for 2 Ti tubes, 12.5 cm diameter, 45.0 cm length, NAB 60.8 cm, 5- 100% SW, static flow.

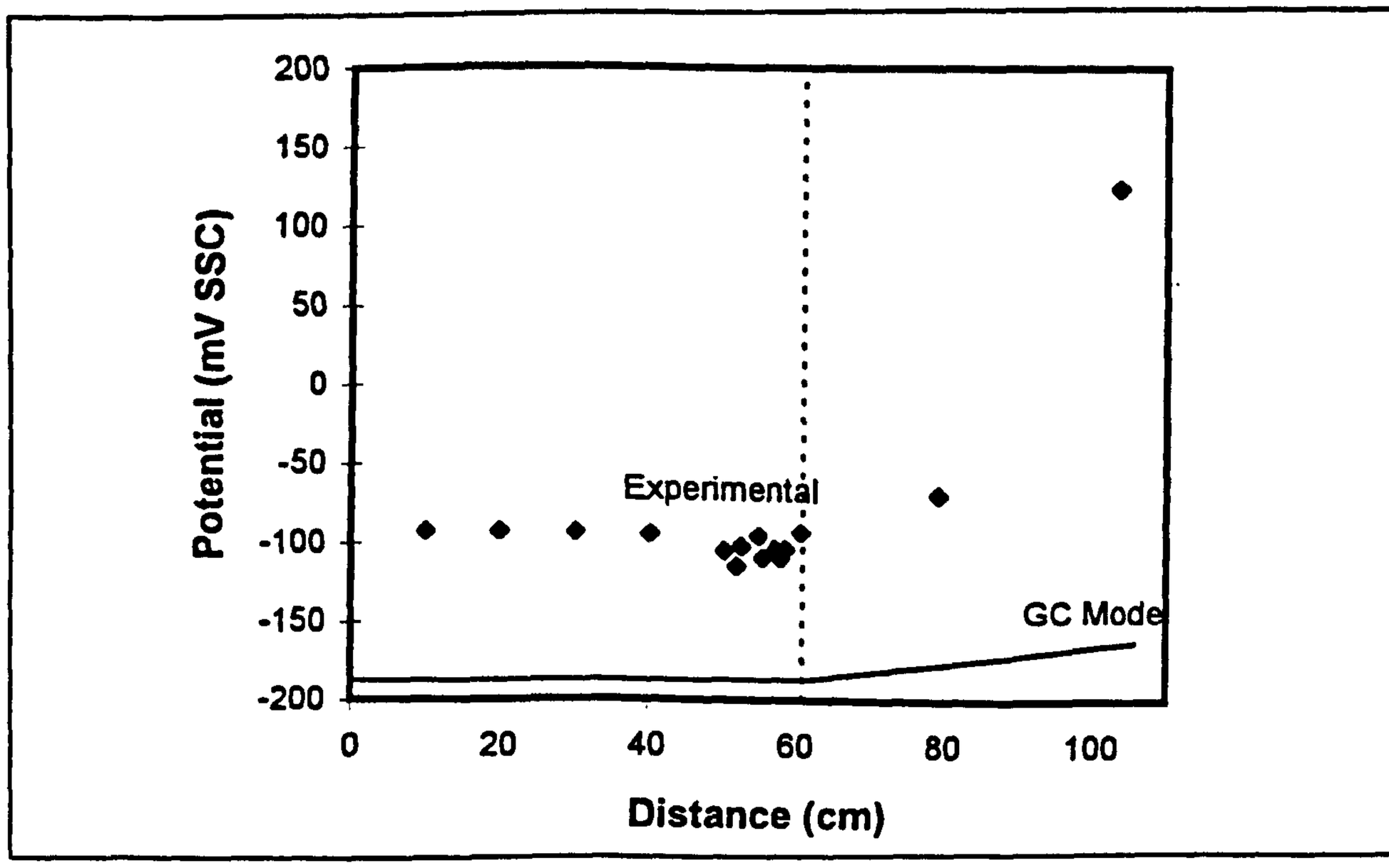

Figure 1.16 Potential distribution for 2 Ti tubes, 12.5 cm diameter, 45.0 cm length, NAB 60.8 cm, 100% SW, static flow.

Dilution of the electrolyte was made on the basis of 5, 50 and 100% of the conductivity of seawater. Figures 1.15 shows the experimental potential distributions for the three different conductivities, while Figures 1.16 to 1.18 show the experimental and theoretical potential distributions for these different couple/electrolyte combinations.

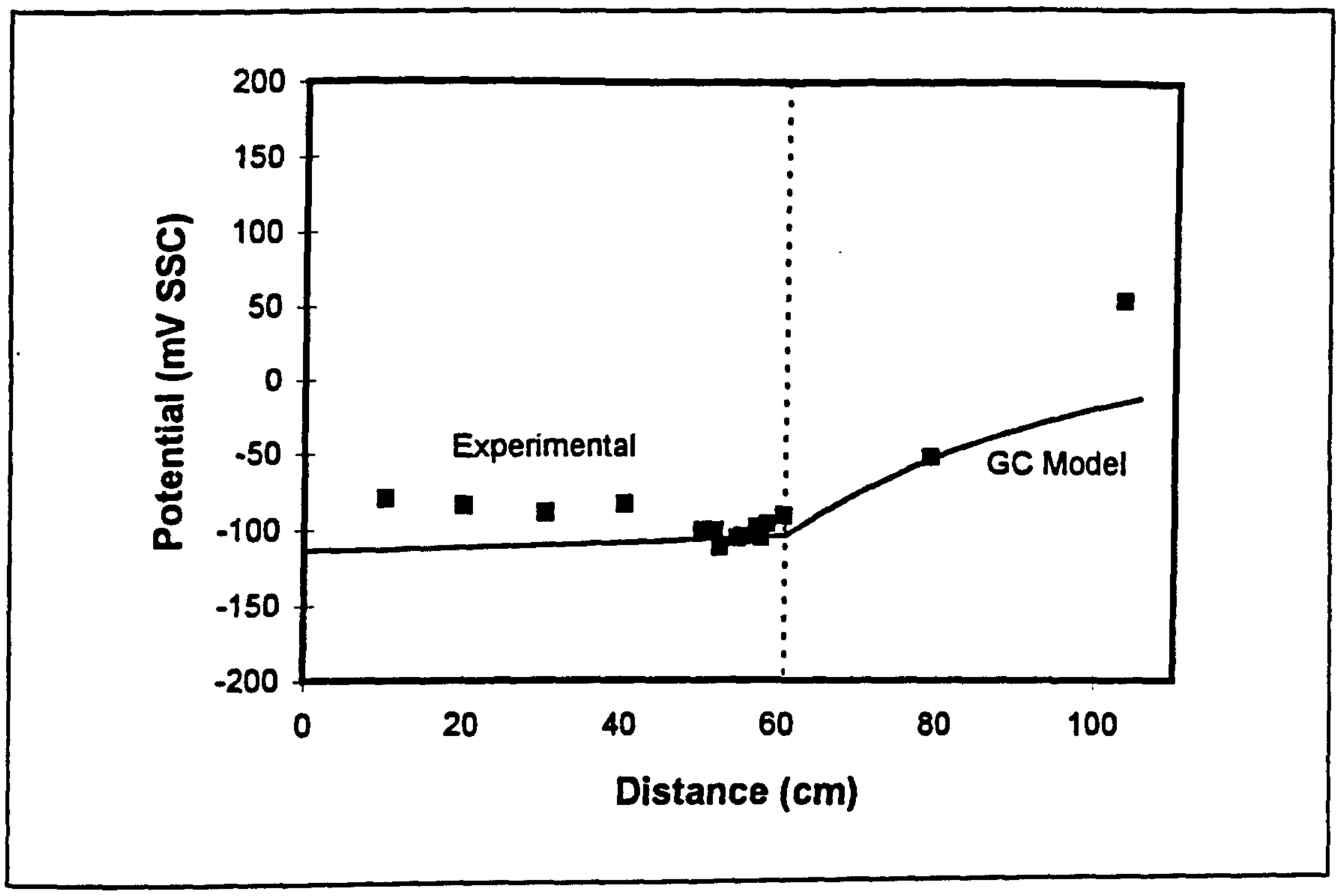

Figure 1.17 Potential distribution for 2 Ti tubes, 1-2.5 cm diameter, 45.0 cm length, NAB 60.8 cm, 50% SW, static flow.

The theoretical plots are generated using the relevant physical data listed above together with the electrochemical data in Table 1.7. The potentials along the NAB anode are fairly uniform, and become more electropositive at the junction of anode and cathode, as predicted by the model. However, the potential distribution predicted by the model is too electronegative for the entire length of the couple containing full strength seawater, but the correlation between theoretical and experimental results for the anode increases with increasing electrolyte resistivity.

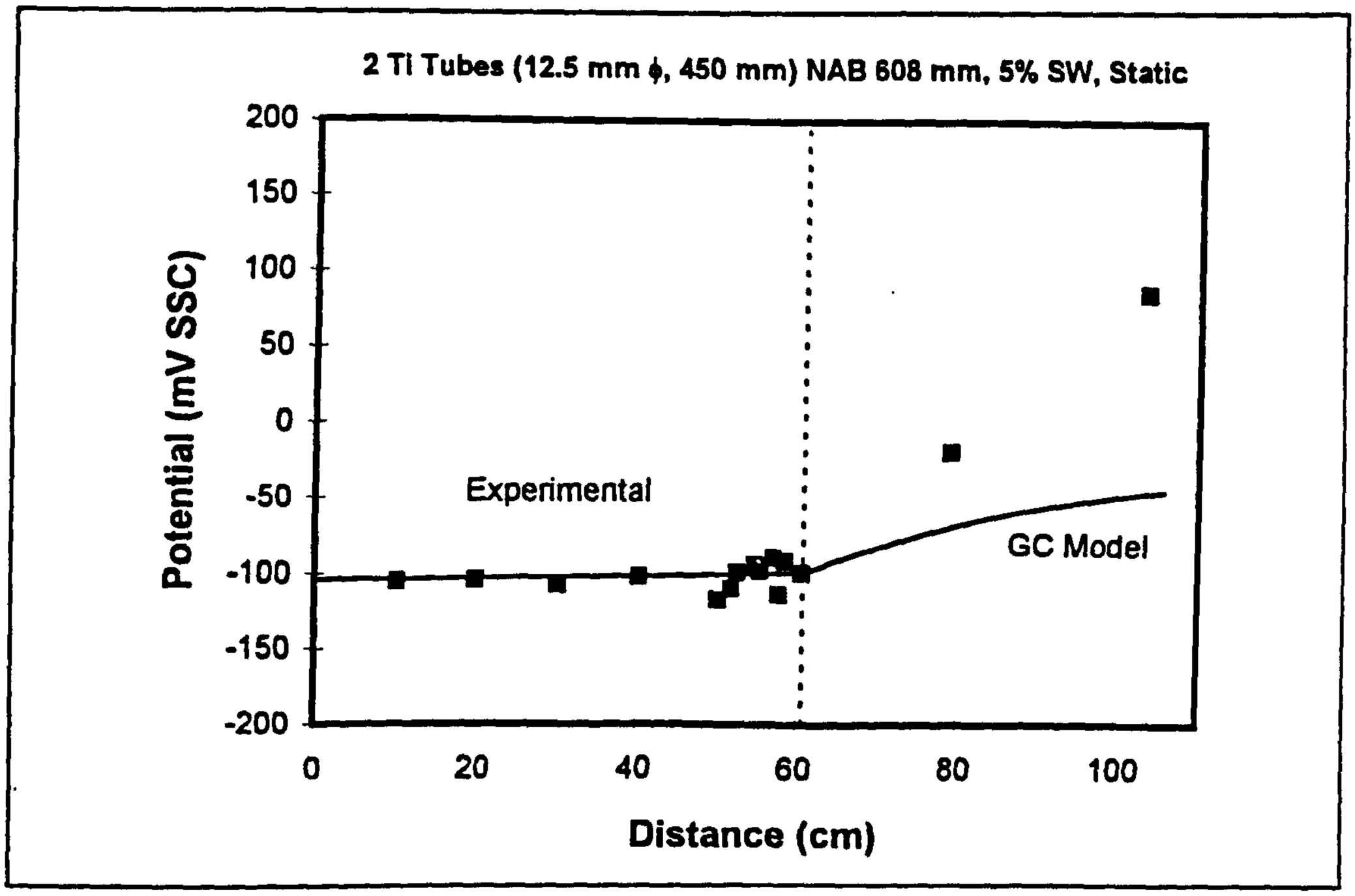

Figure 1.18 Potential distribution for 2 Ti tubes, 12.5 cm diameter, 45.0 cm length, NAB 60.8 cm, 5% SW, static flow.

1.5.3.2 The Effect of Differing Anode Length

To consider the effect of altering the length of the anode section, the tube bundles consisted of 4 titanium tubes of diameter 19 cm and length 53.2 cm, while the NAB lengths were 31.3 and 60.8 cm. The electrolyte was undiluted seawater. Figures 1.19 shows the two experimental results, while Figures 1.20 and 1.21 show the theoretical result overlaid with the appropriate experimental curve. The two plots are overlaid such that the anode-cathode junction is in the same place for both plots.

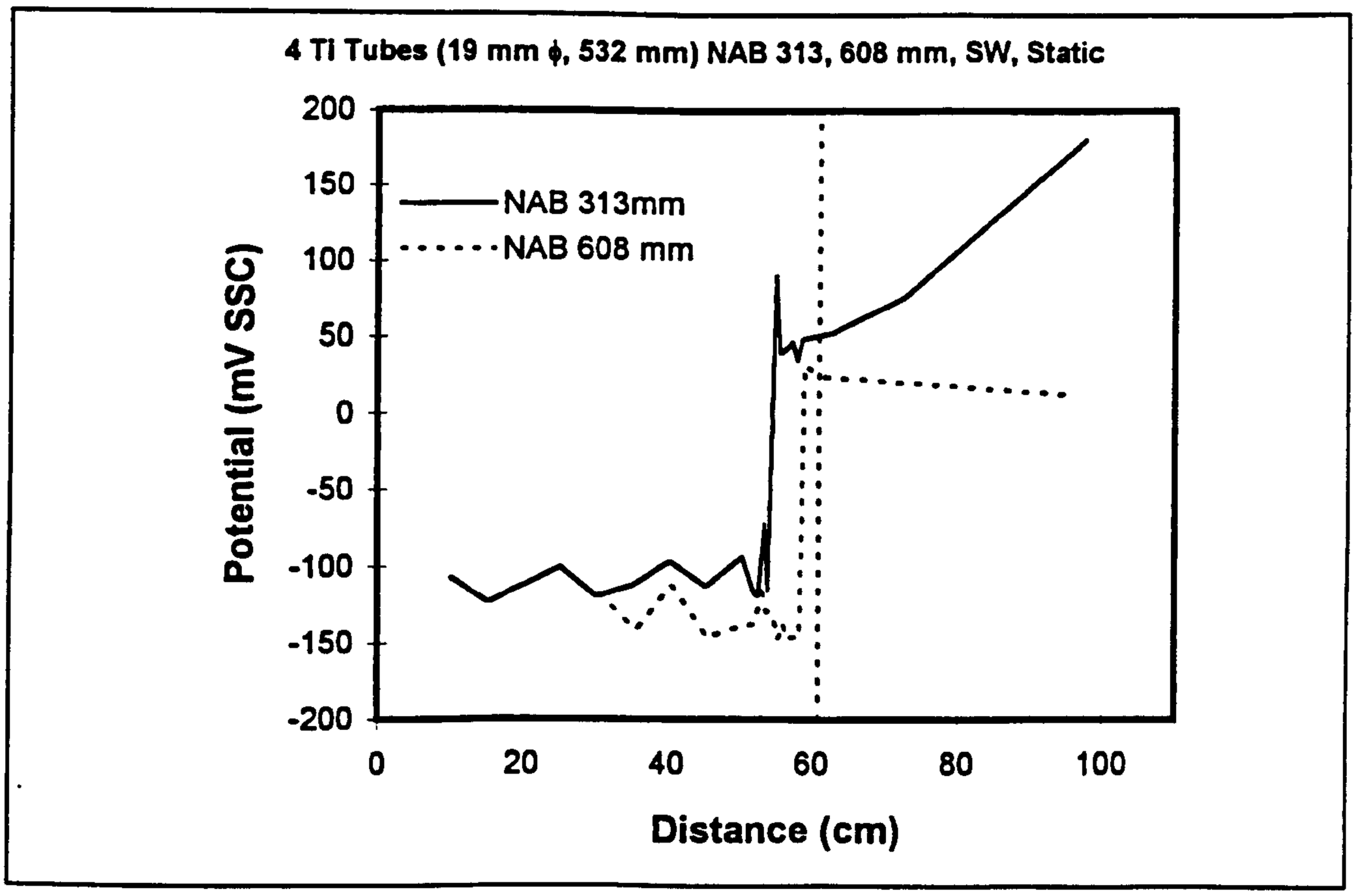

Figure 1.19 Potential distributions for 4 Ti tubes, 19.0 cm diameter, 53.2 cm length, NAB 31.3 and 60.8 cm, 100% SW, static flow.

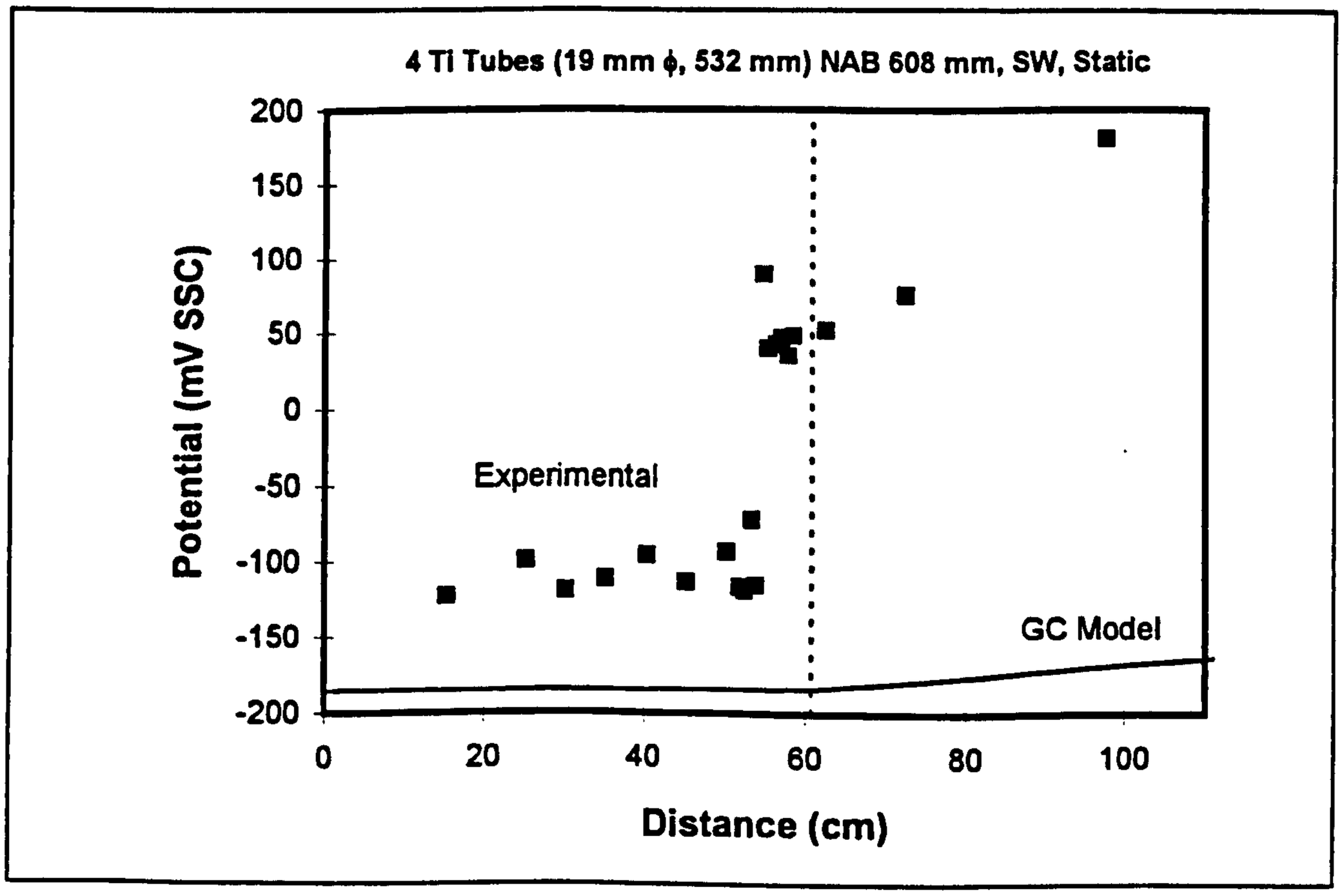

Figure 1.20 Potential distribution for 4 Ti tubes, 19.0 cm diameter, 53.2 cm length, NAB 60.8 cm, 100% SW, static flow.

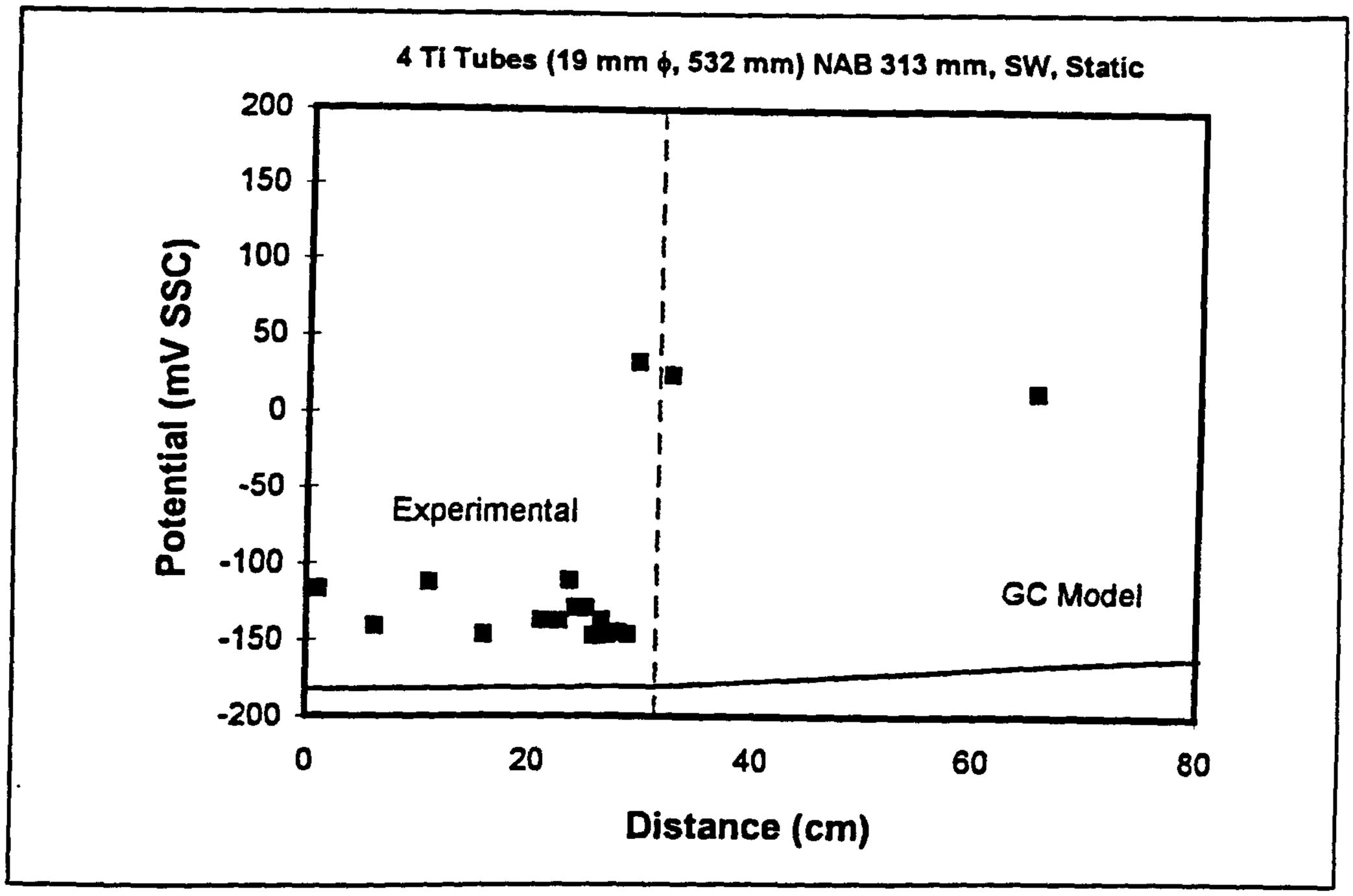

Figure 1.21 Potential distribution for 4 Ti tubes, 19.0 cm diameter, 53.2 cm length, NAB 31.3 cm, 100% SW, static flow.

For both anode lengths, the greatest change in potential does not occur at the anode-cathode interface, but rather at positions ~ 3 cm (for the shorter 31.3 cm anode) and ~ 8 cm (for the longer 60.8 cm anode) away from the interface on the anode side. This differs from the model, which assumes that the junction represents the point of greatest anodic and cathodic polarization. The reason for this is not clear.

Figures 1.22 shows the experimental potential distributions for the same system considered in Figure 1.19, but with 50% conductivity seawater instead of full strength. Once again, the greatest change of potential occurs on the NAB, rather than at the junction. The model predicts that the potentials along the couple are far more electronegative than the experimental results show. However, it does predict that the potentials along the NAB anode remain similar, while becoming more positive with increasing distance from the anode along the cathode. Figures 1.23 and 1.24 show the overlaid experimental and

theoretical distributions for the two couples.

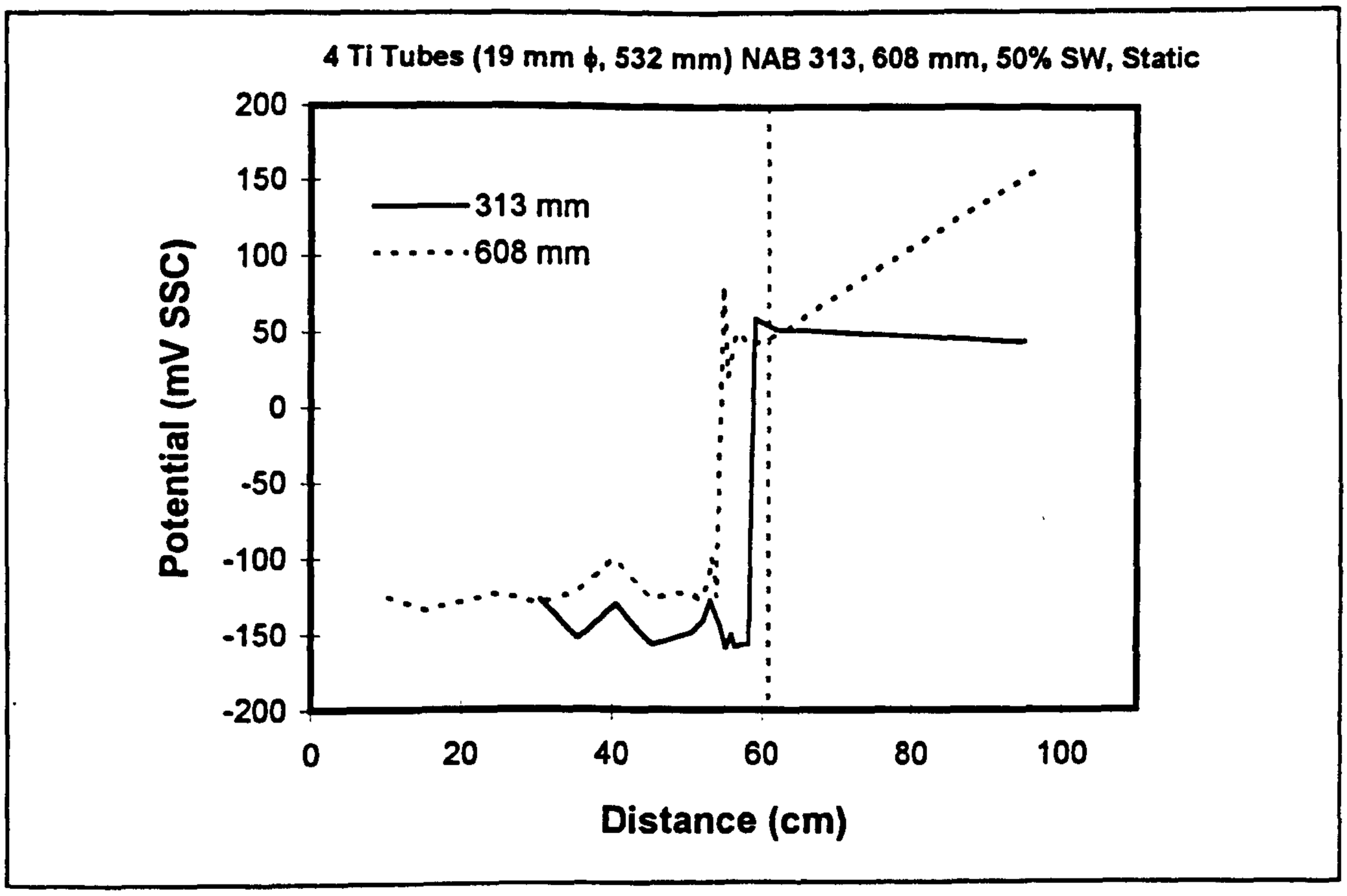

Figure 1.22 Potential distribution for 4 Ti tubes, 19.0 cm diameter, 53.2 cm length, NAB 31.3 and 60.8 cm, 50% SW, static flow.

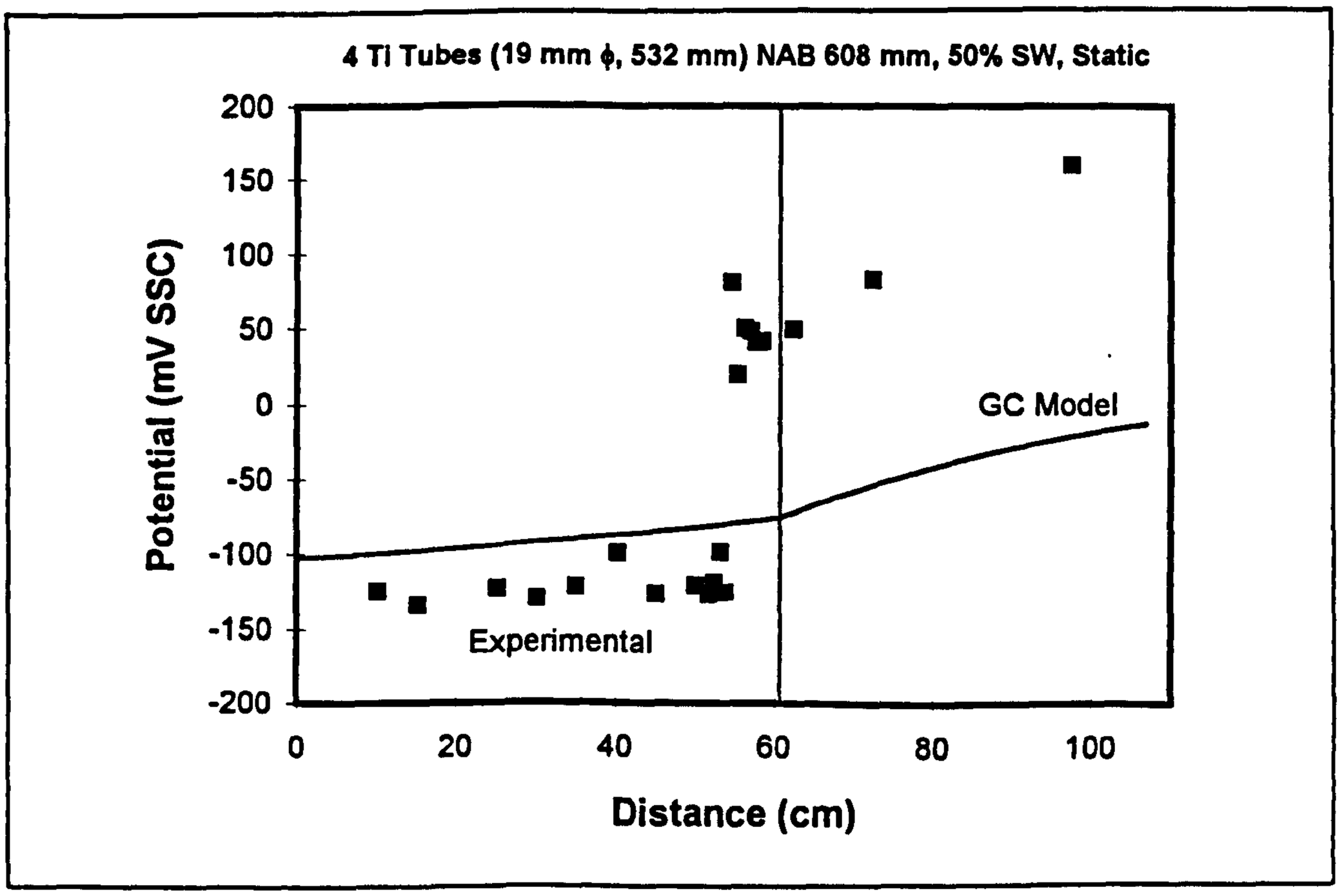

Figure 1.23 Potential distribution for 4 Ti tubes, 19.0 cm diameter, 53.2 cm length, NAB 60.8 cm, 50% SW, static flow.

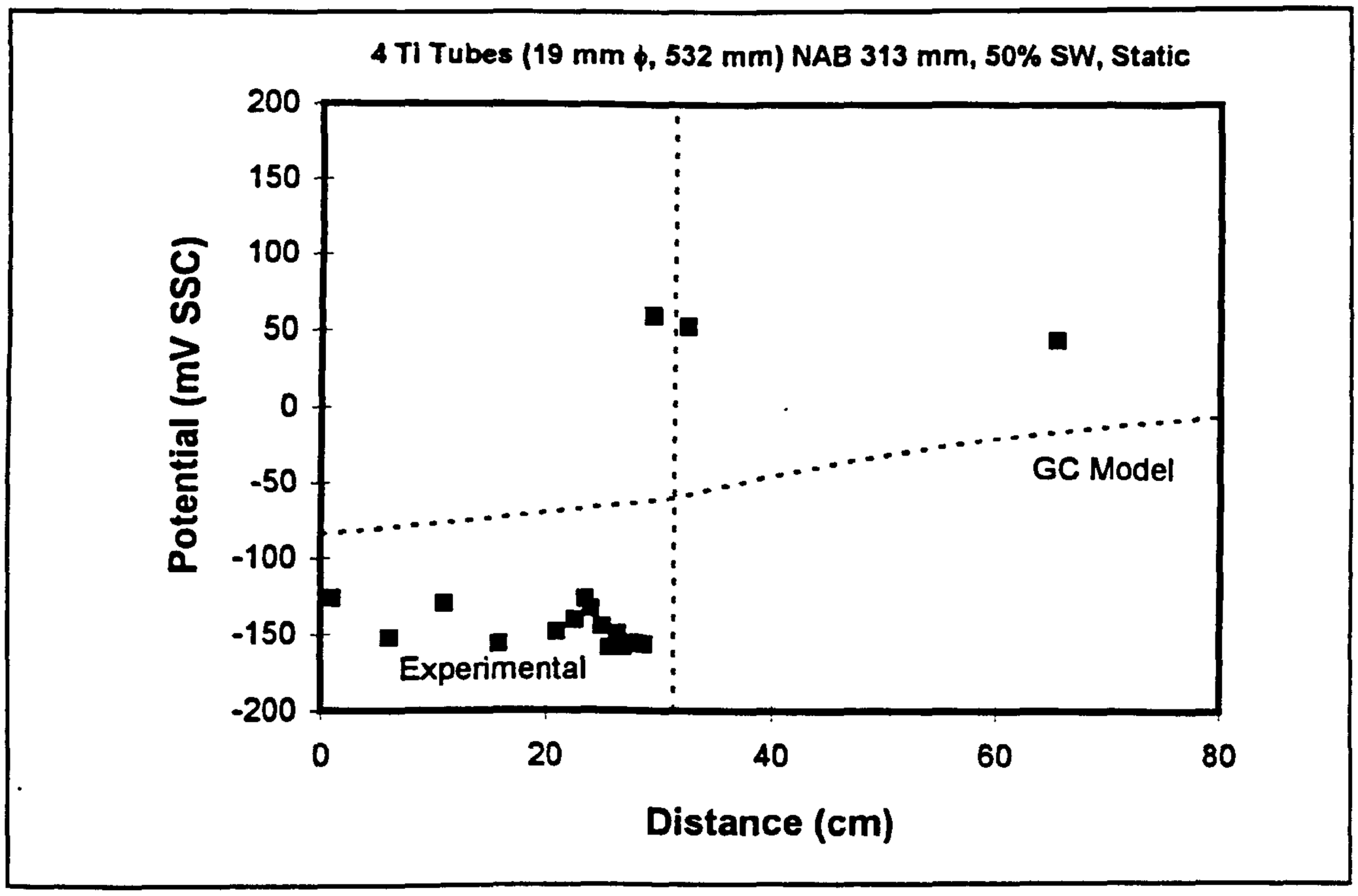

Figure 1.24 Potential distribution for 4 Ti tubes, 19.0 cm diameter, 53.2 cm length, NAB 31.3 cm, 50% SW, static flow.

Figure 1.25 shows the experimental curves for the larger anode with both electrolytes.

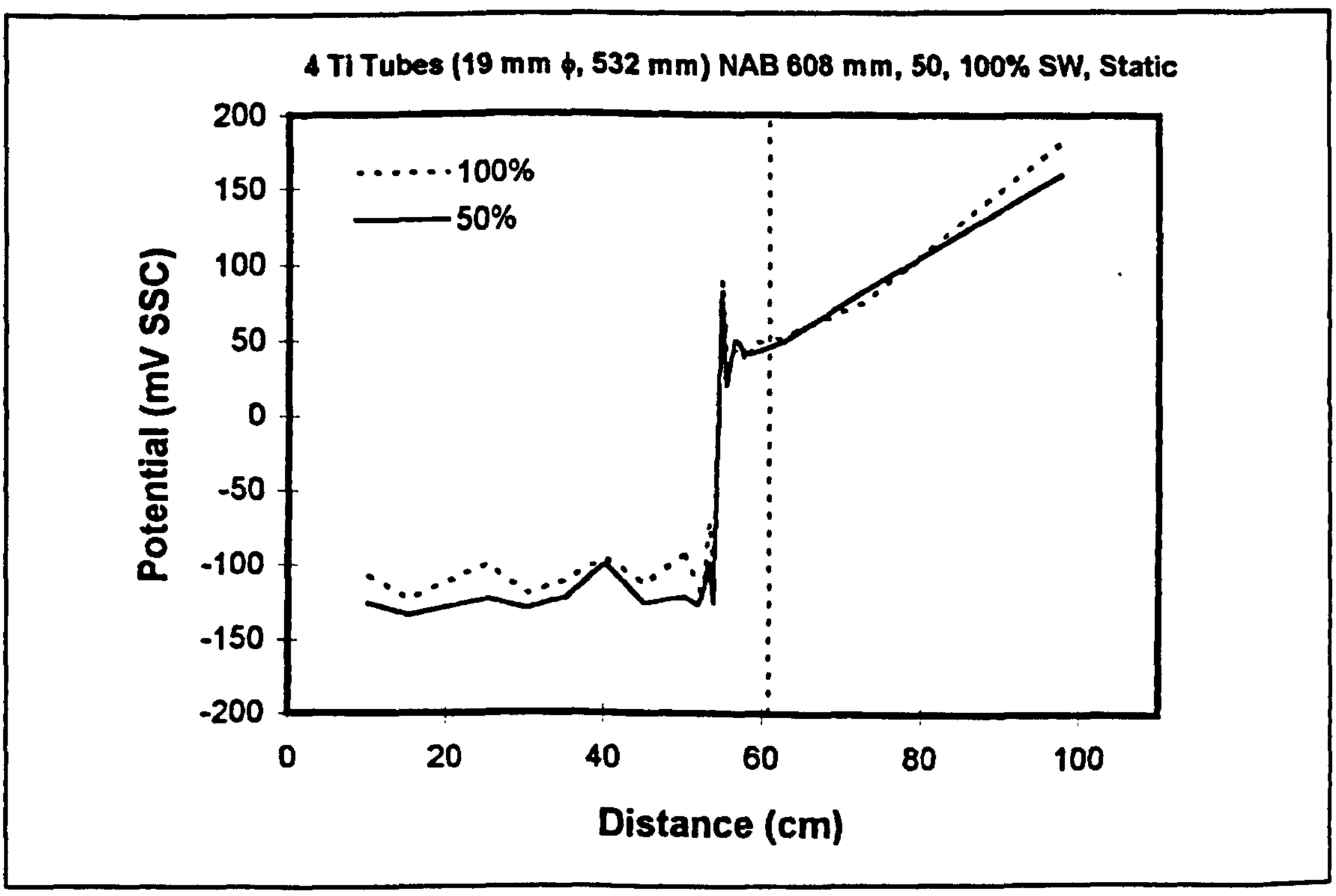

Figure 1.25 Potential distribution for 4 Ti tubes, 19.0 cm diameter, 53.2 cm length, NAB 60.8 cm, 500 and 100% SW, static flow.

The distances at which the large change in potential occurs are very similar for the two different conductivity electrolytes. The potential distributions on the cathodic tubes are similar for the longer NAB anode, both increasing in the electropositive direction with increasing direction, while for the shorter anode, the potentials remain similar along the length of the tubes.

1.5.3.3 The Effect of Differing Cathode Diameter

Figures 1.26 shows the experimental results found using a tube bundle (length in excess of 100 cm) containing 2 titanium tubes of diameter 19.0 and 25.4 cm respectively, connected to NAB length of length 60.8 cm, containing 50% conductivity seawater electrolyte.

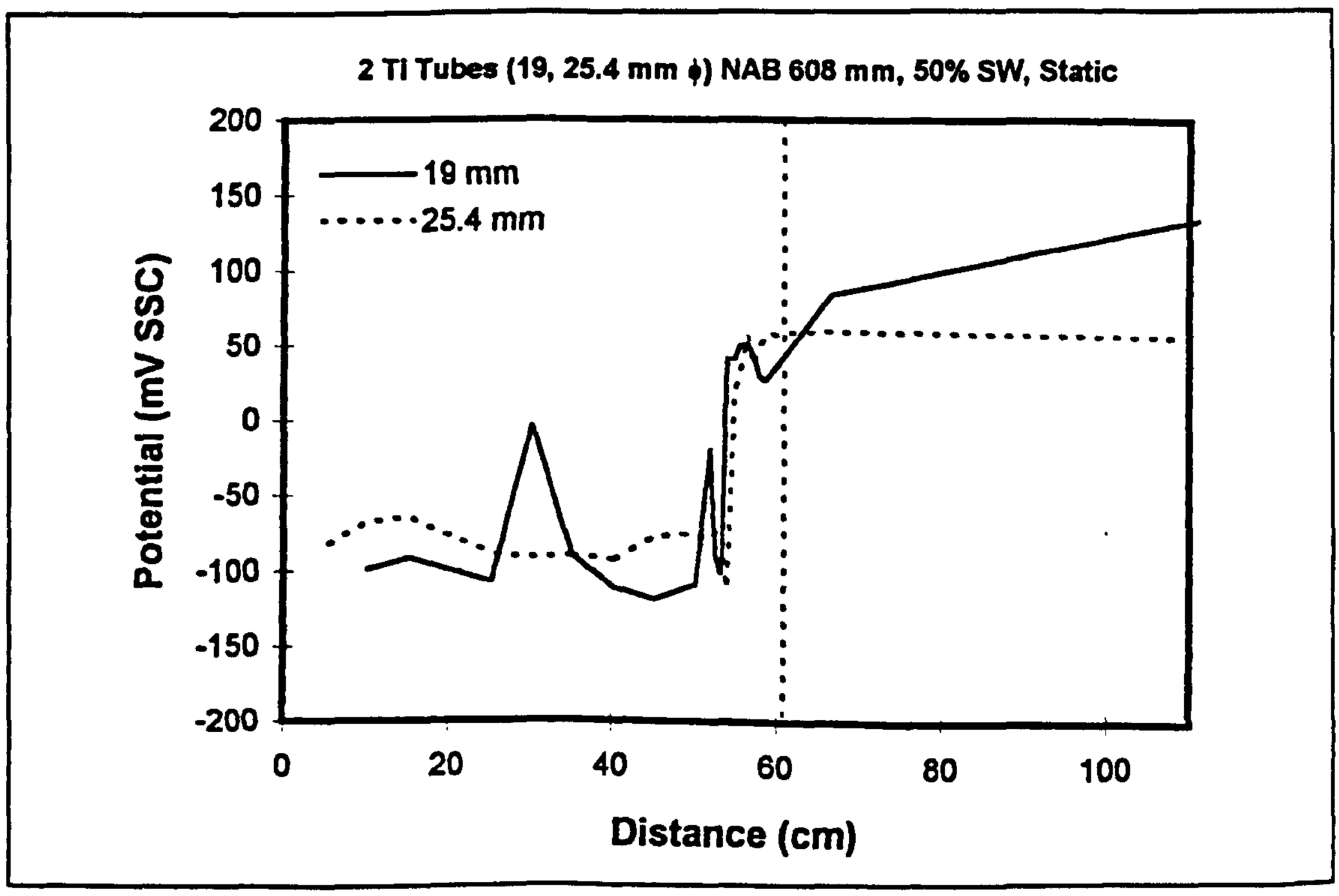

Figure 1.26 Potential distribution for 2 Ti tubes, 19.0 and 25.4 cm diameter, NAB 60.8 cm, 50% SW, static flow.

Again, the change of potential occurs on the NAB anode, with the distance being

similar for both diameter titanium tubes. Figures 1.27 and 1.28 show the poor correlation between experimental and theoretical curves.

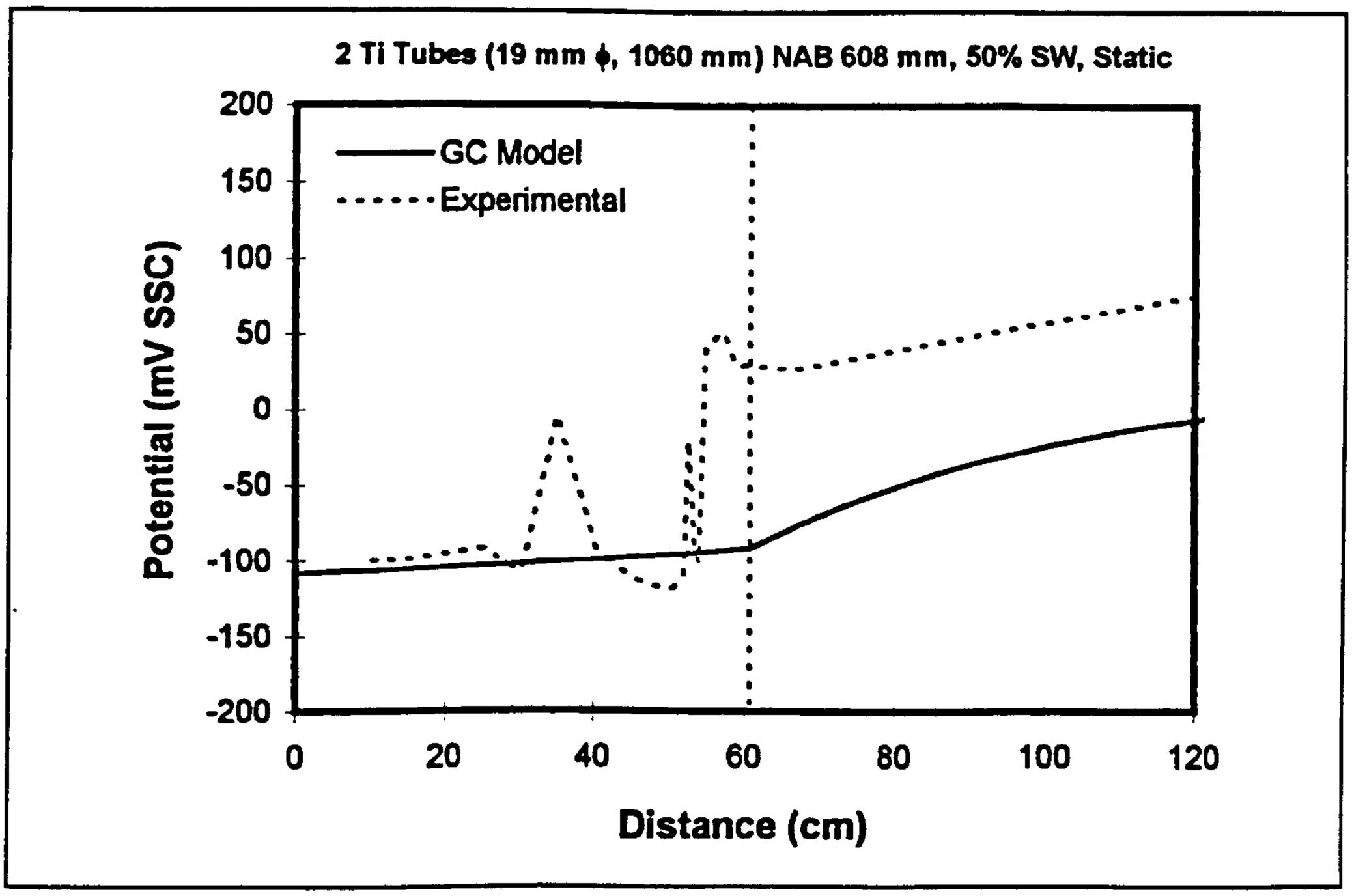

Figure 1.27 Potential distribution for 2 Ti tubes, 19.0 cm diameter, 106.0 cm length, NAB 60.8 cm, 50% SW, static flow.

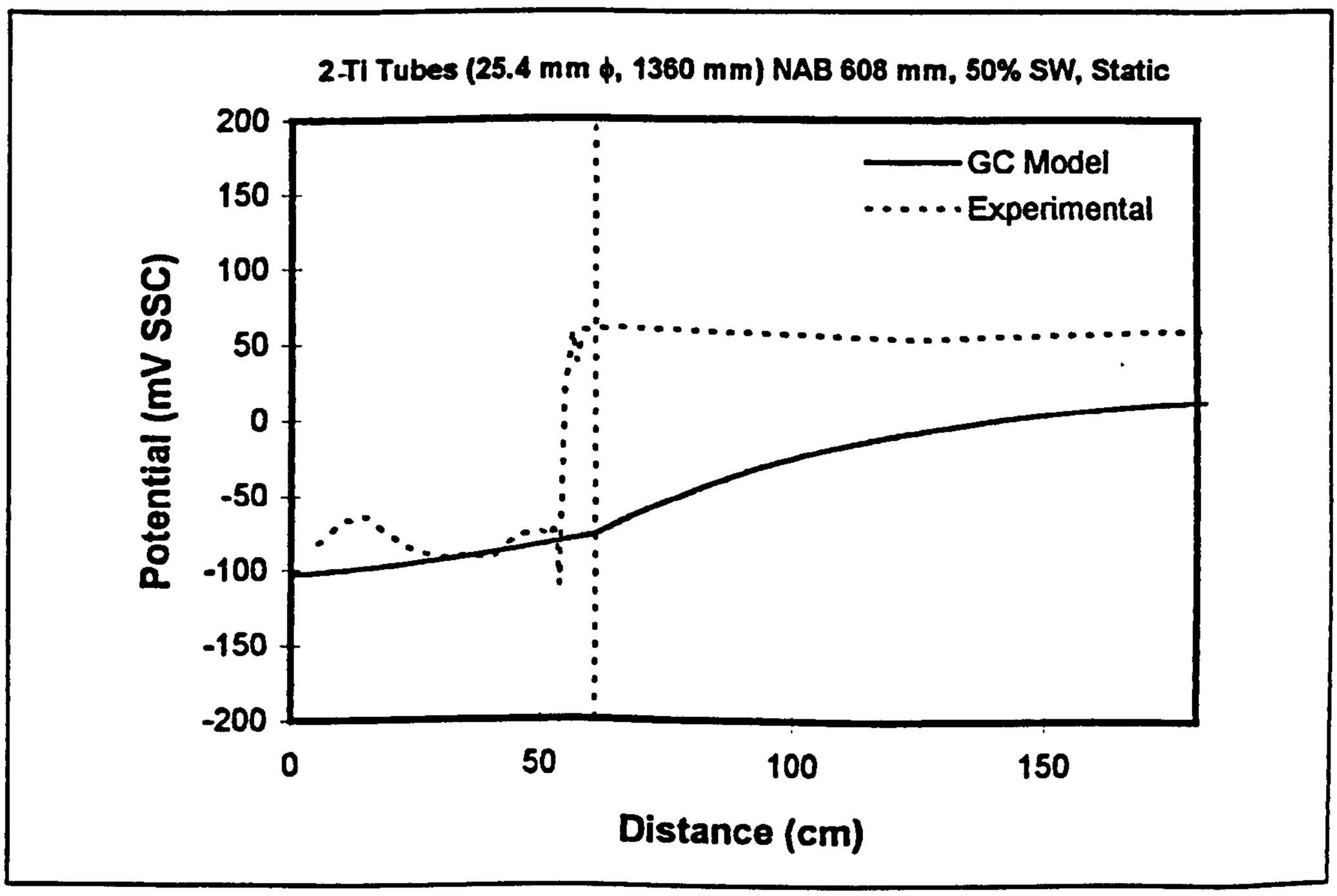

Figure 1.28 Potential distribution for 2 Ti tubes, 25.4 cm diameter, 136.0 cm length, NAB 60.8 cm, 50% SW, static flow.

1.5.3.4 The Effect of Altering Number of Cathodic Tubes

The next variable to be changed was the number of tubes in the bundle, and this was done for two combinations of NAB-titanium. Figures 1.29 shows the experimental results for 2 and 4 titanium tubes, 53.2 cm long and 19.0 cm in diameter, joined to NAB of length 31.3 cm. The predicted and actual distributions are shown together in Figures 1.30 and 1.31.

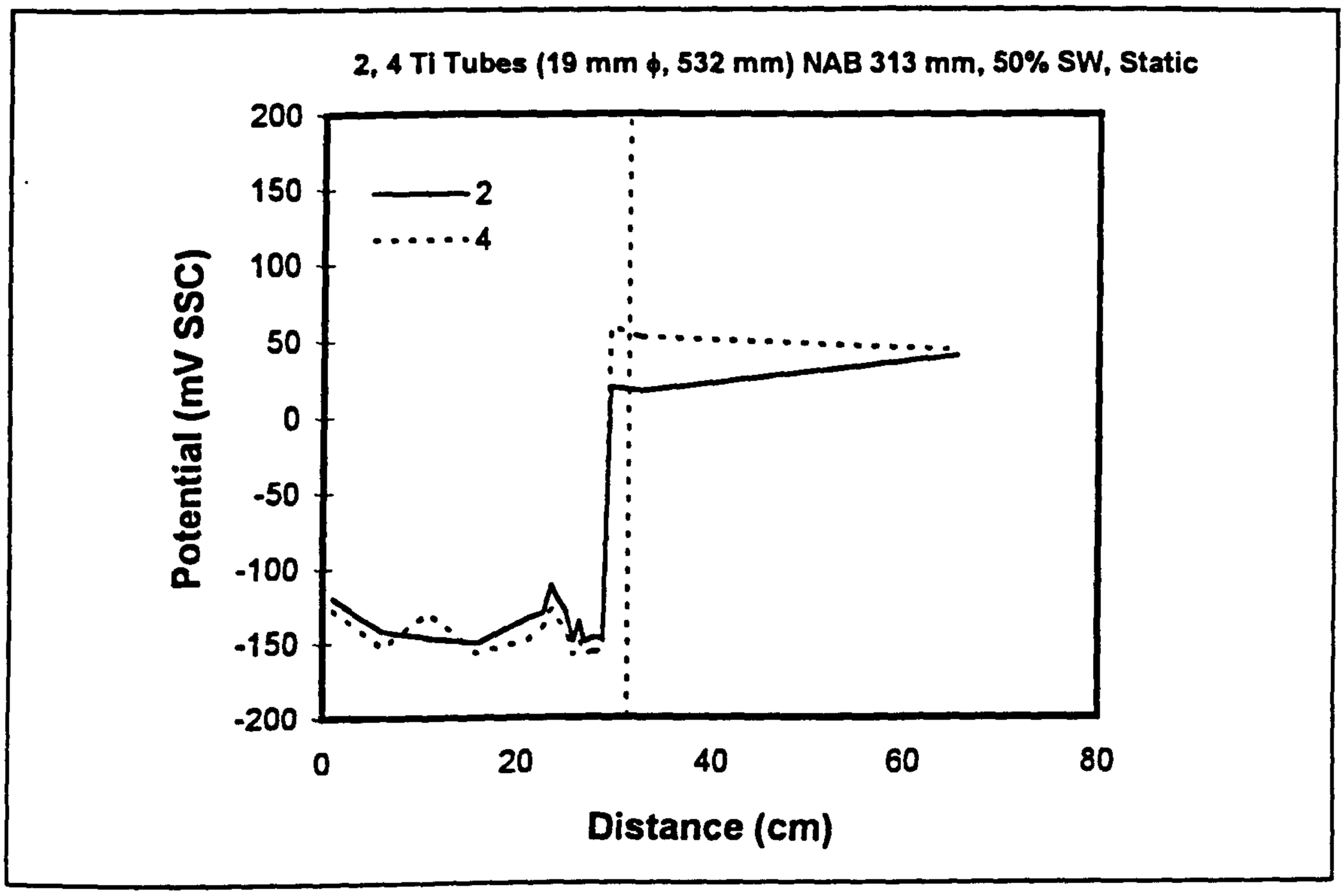

Figure 1.29 Potential distribution for 2 and 4 Ti tubes, 19.0 cm diameter, 53.2 cm length, NAB 31.3 cm, 50% SW, static flow.

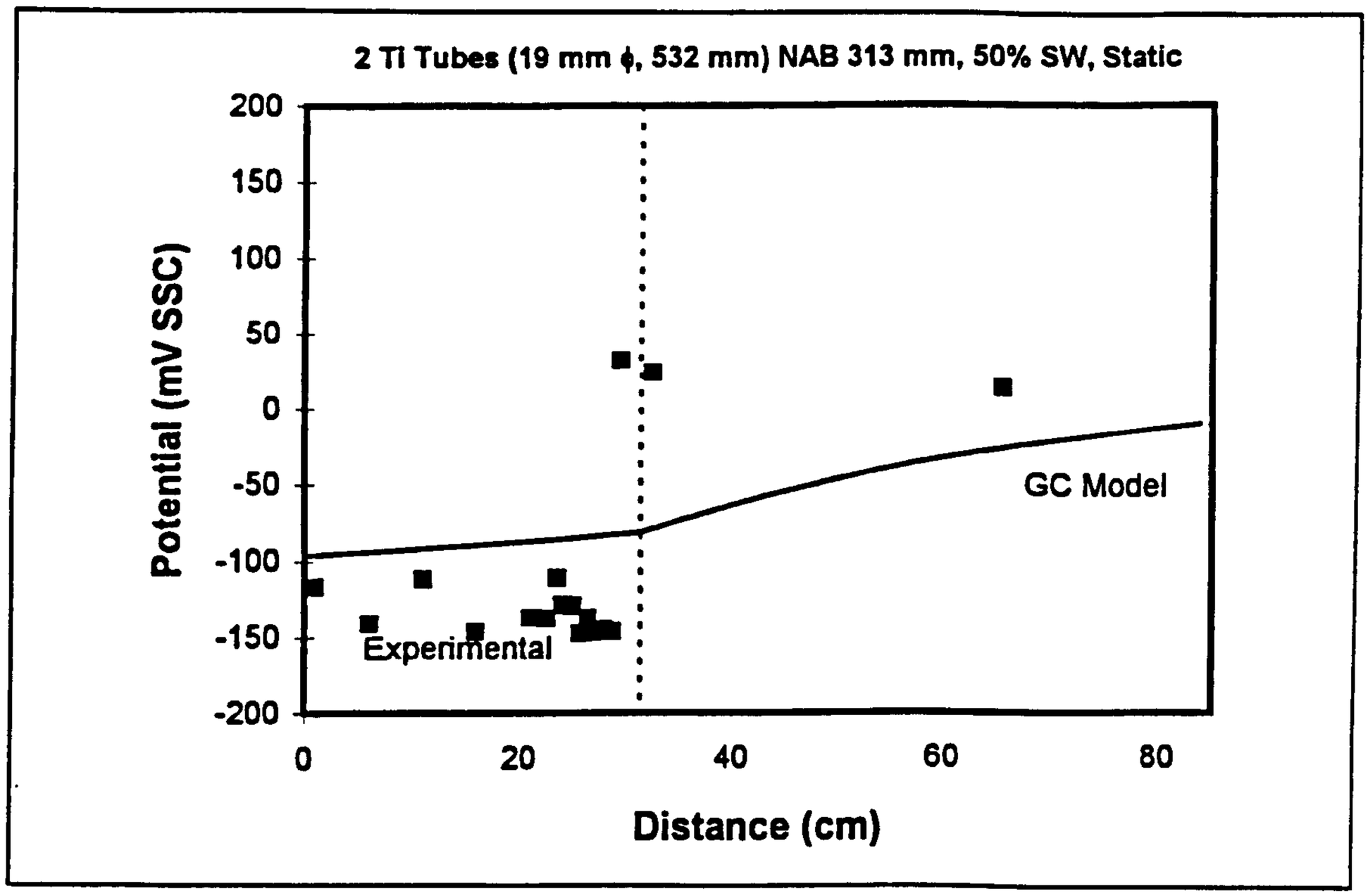

Figure 1.30 Potential distribution for 2 Ti tubes, 19.0 cm diameter, 53.2 cm length, NAB 31.3 cm, 50% SW, static flow.

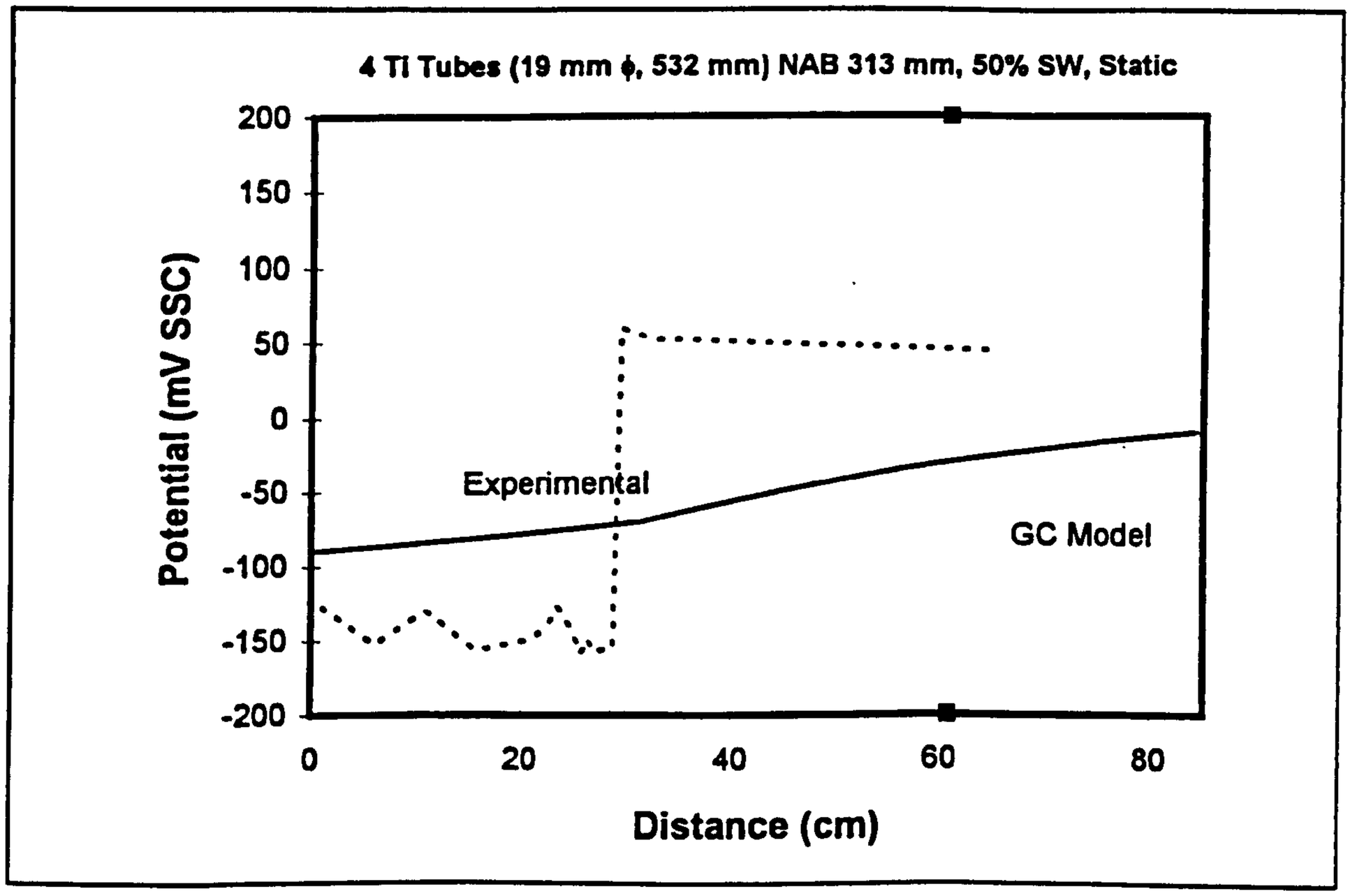

Figure 1.31 Potential distribution for 4 Ti tubes, 19.0 cm diameter, 53.2 cm length, NAB 31.3 cm, 50% SW, static flow.

The potential distribution along the anode is very similar for both tube bundles, with the step change in potential occurring at the same distance from the cathodic tubes. As expected, the greater cathodic polarization is exhibited by the 2 titanium tubes, since there is less area on which a given amount of electrons can take place in the reduction of oxygen.

1.5.3.5 Potential Distribution for Uncoupled Materials

The final experiment for static flow conditions examined the effect of electrically uncoupling the NAB and titanium tubes, such that the SSC electrodes recorded the free corrosion potentials of the materials. The result for static 50% conductivity seawater is shown in Figure 1.32. It may be seen that there is a small trend to more electronegative values on moving down the length of the NAB portion towards the couple.

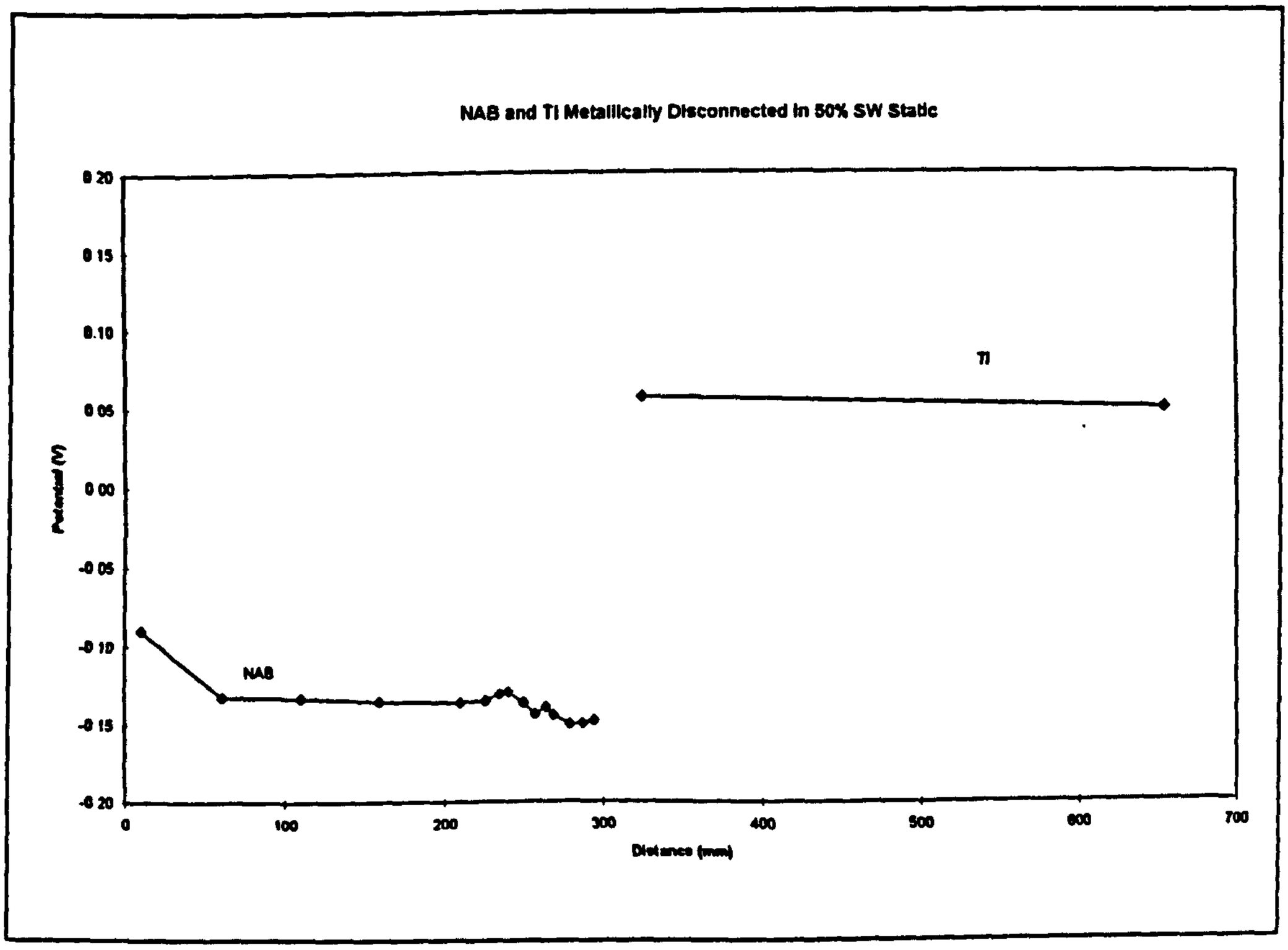

Figure 1.32 Potential distribution for electrically uncoupled NAB and titanium, 50% static SW.

1.5.4 Potential Distributions for Flow Conditions

Flow experiments were carried out using flow rates of 1 and 2 ms^{-1} , the latter value being used only for the 19 cm diameter pipes, since the flow rig pump could not supply a flow rate of 2 ms^{-1} for titanium pipes of diameter 25.4 cm. The maximum flow velocity allowed in Royal Navy heat exchangers is 3 ms^{-1} [41]. Figure 1.33 shows the variation in potential over a 8 hour period for a given couple/electrolyte, showing minor variations (max ~ 15 mV) with time. As mentioned in Section 1.4.6, the maximum duration of a flow test was 8 hours. Thus the last reading for each experiment was taken as being representative for each couple/electrolyte combination.

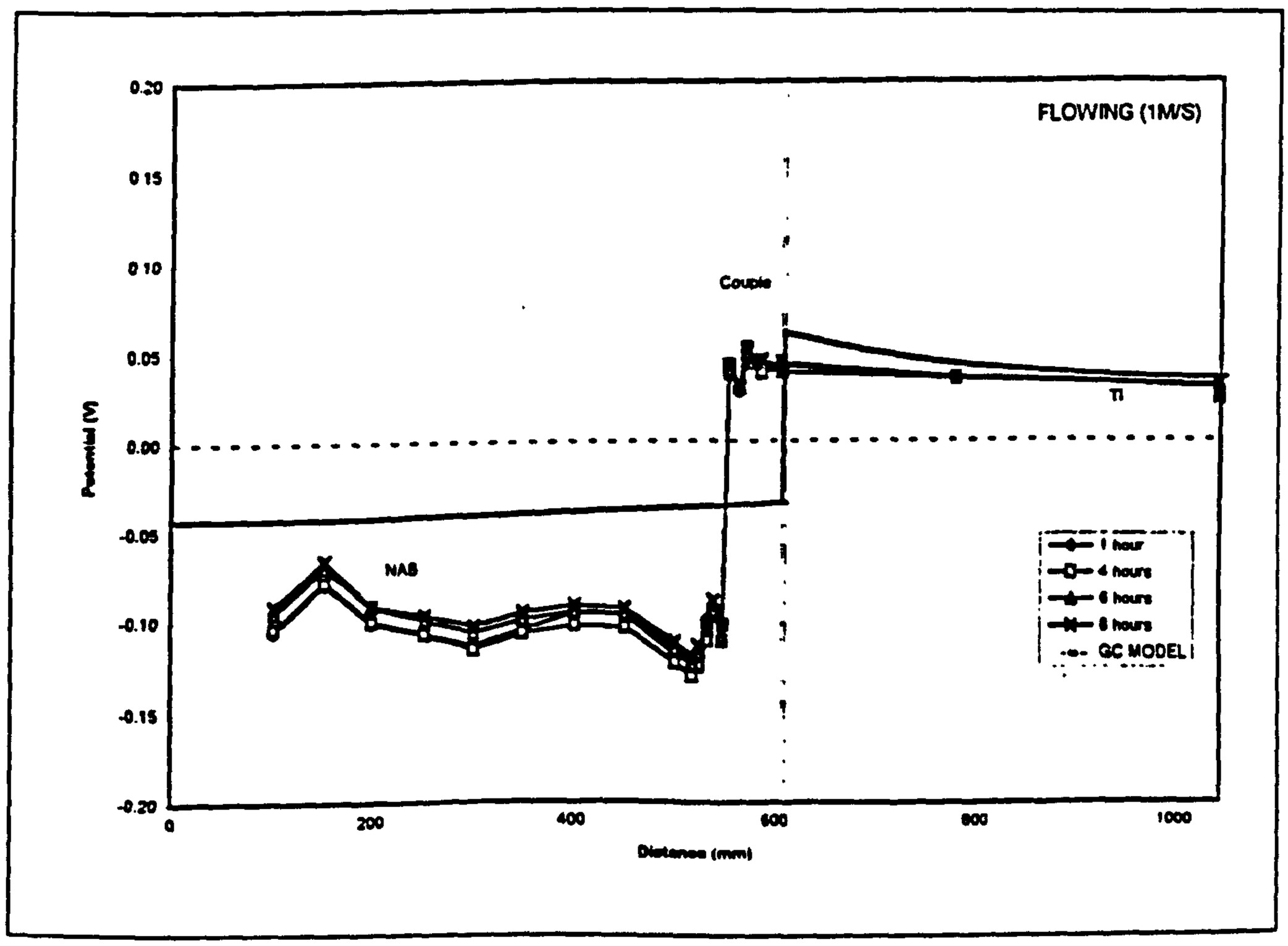

Figure 1.33 Variation of potential distribution with time for 4 titanium tubes (19 cm diameter and length 53.2 cm), 60.8 cm NAB, 5% flowing SW (1 ms^{-1}).

1.5.4.1 The Effect of Different Flow Rates

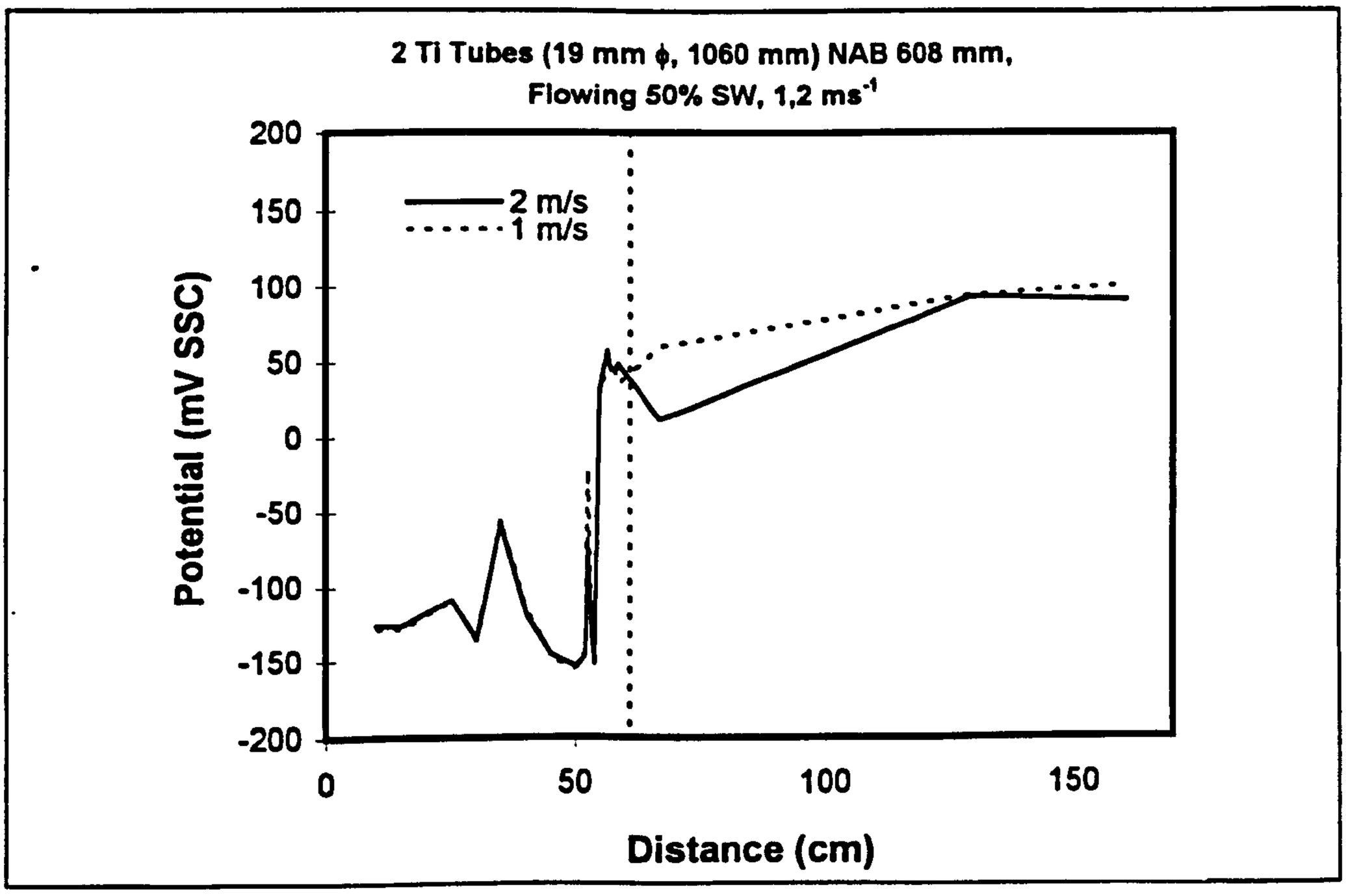

Figure 1.34 Potential distributions for 2 titanium tubes (19 cm diameter, 106.0 cm length), NAB length 60.8 cm, flowing 50% SW (1 and 2 m s^{-1})

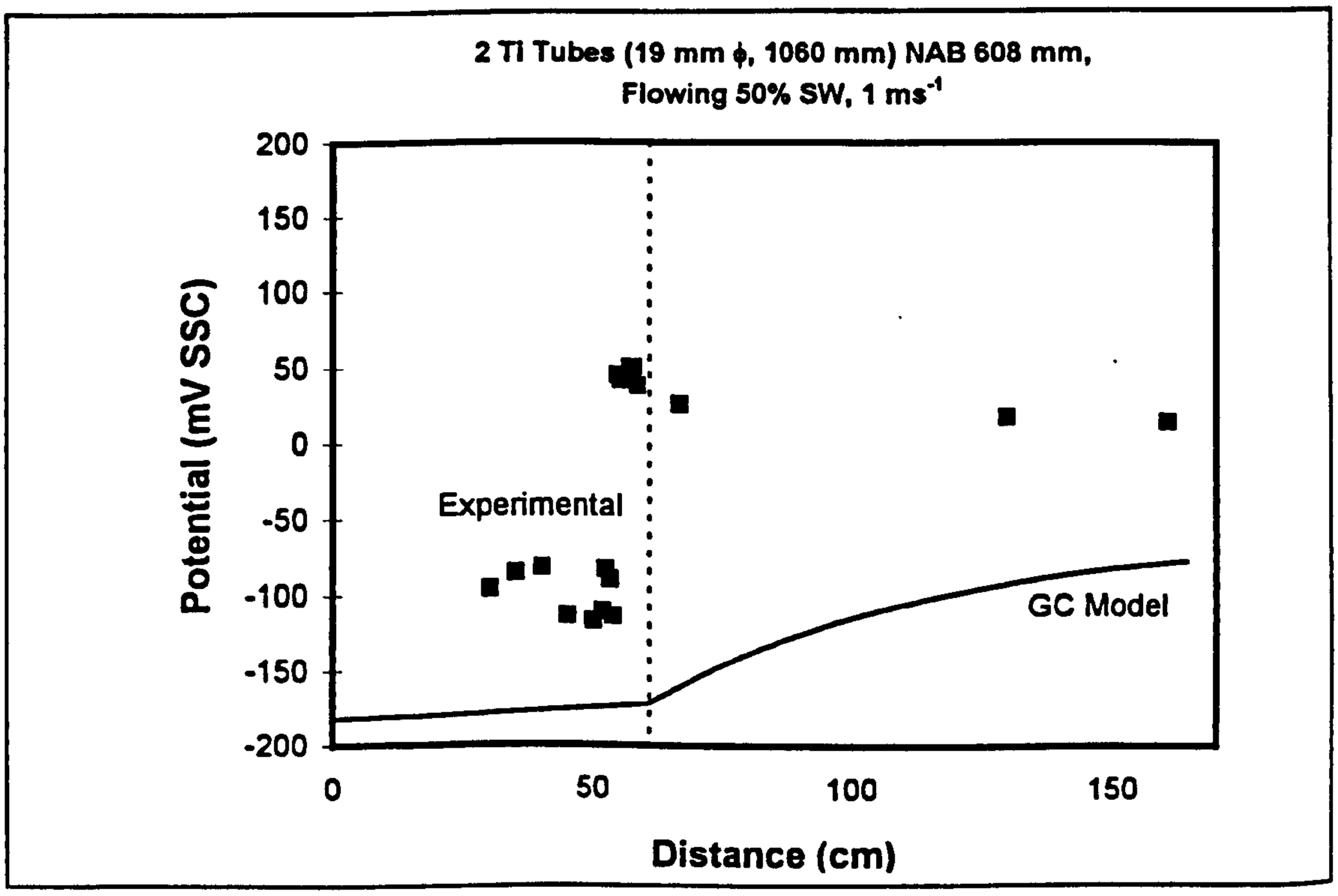

Figure 1.35 Potential distributions for 2 titanium tubes (19 cm diameter, 106.0 cm length), NAB length 60.8 cm, flowing 50% SW (1 m s^{-1})

Figure 1.34 shows the measured potential distributions for a system comprising 2 titanium tubes of diameter 19 cm and length 106.0 cm, connected to a NAB anode of length 60.8 cm. The electrolyte was 50 % conductivity seawater flowing at 1 and 2 ms^{-1}.

As for many of the static experiments, the ~ 5 cm of the NAB anode closest to the junction of anode and cathode assumed a potential close to that titanium tubes, while the distribution over the rest of the NAB was almost identical for the two flow rates. Figure 1.35 and 1.36 show the predicted and measured distributions.

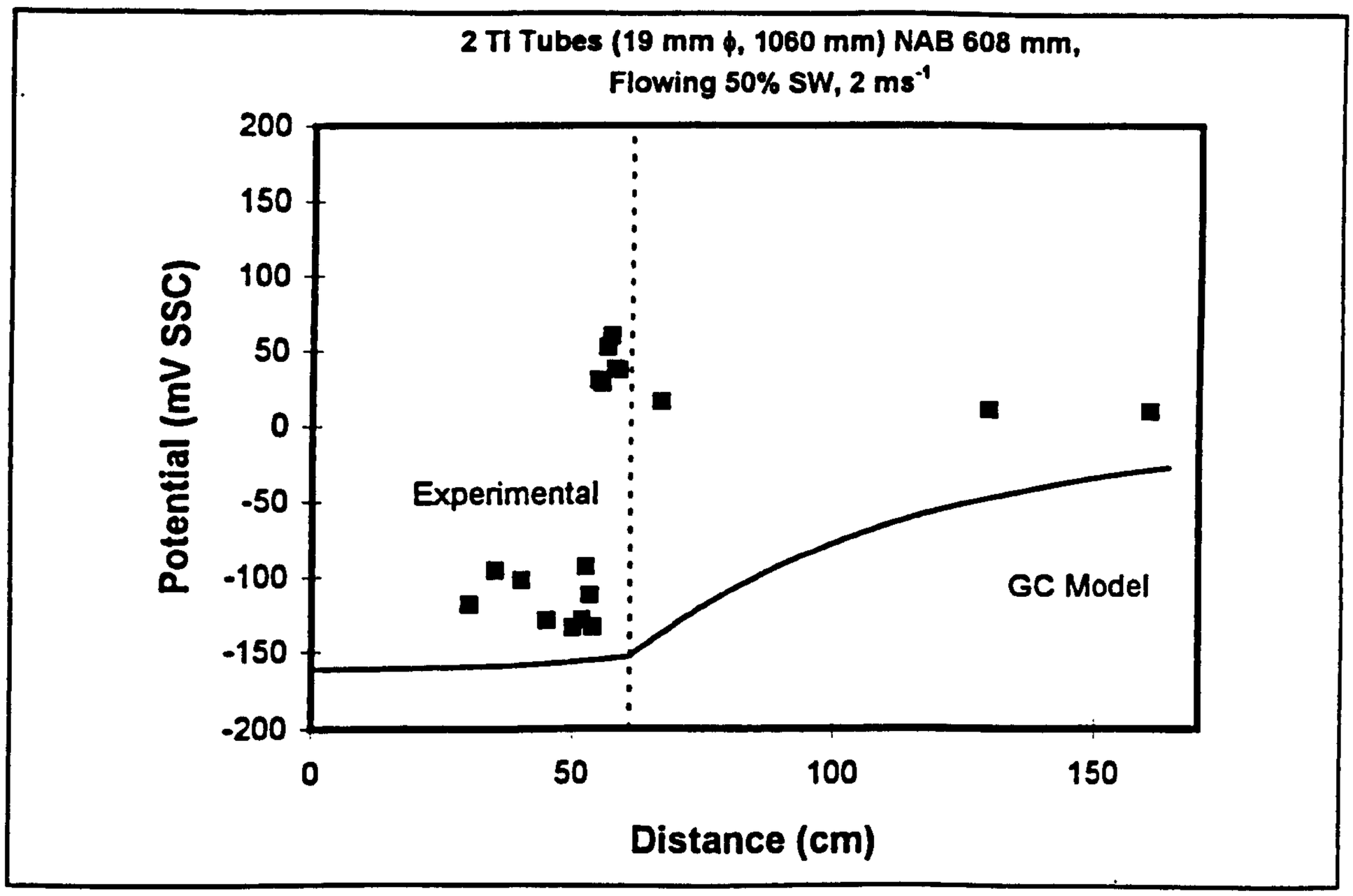

Figure 1.36 Potential distributions for 2 titanium tubes (19 cm diameter, 106.0 cm length), NAB length 60.8 cm, flowing 50% SW (2 m s^{-1}).

Figure 1.37 shows measured potential distributions for the same system with natural seawater. Once again, the potential distributions over the anode are almost identical.

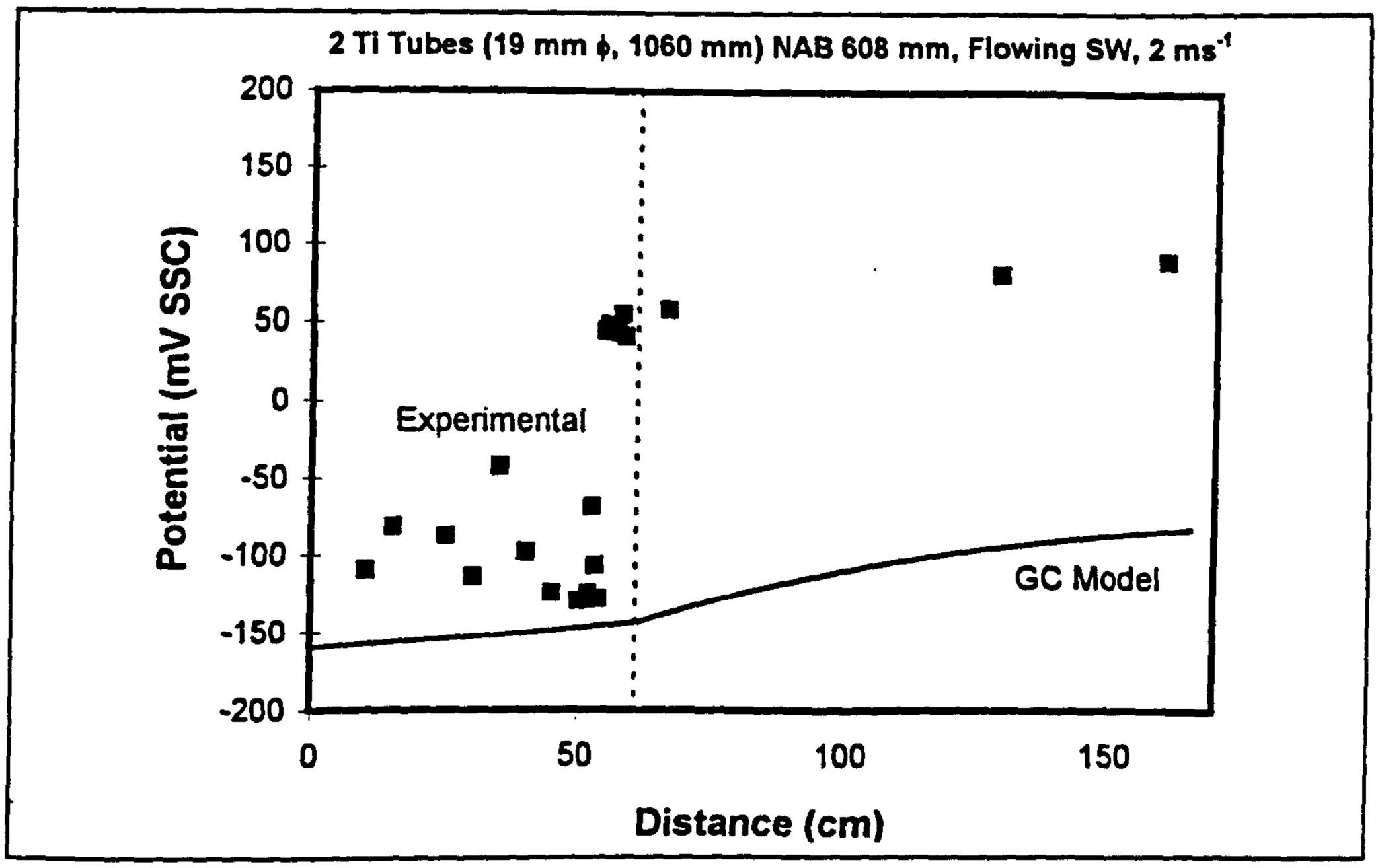

Figure 1.37 Potential distributions for 2 titanium tubes (19 cm diameter, 106.0 cm length), NAB length 60.8 cm, flowing 50% SW (2 m s^{-1}).

1.5.4.2 The Effect of Different Electrolyte Resistivity

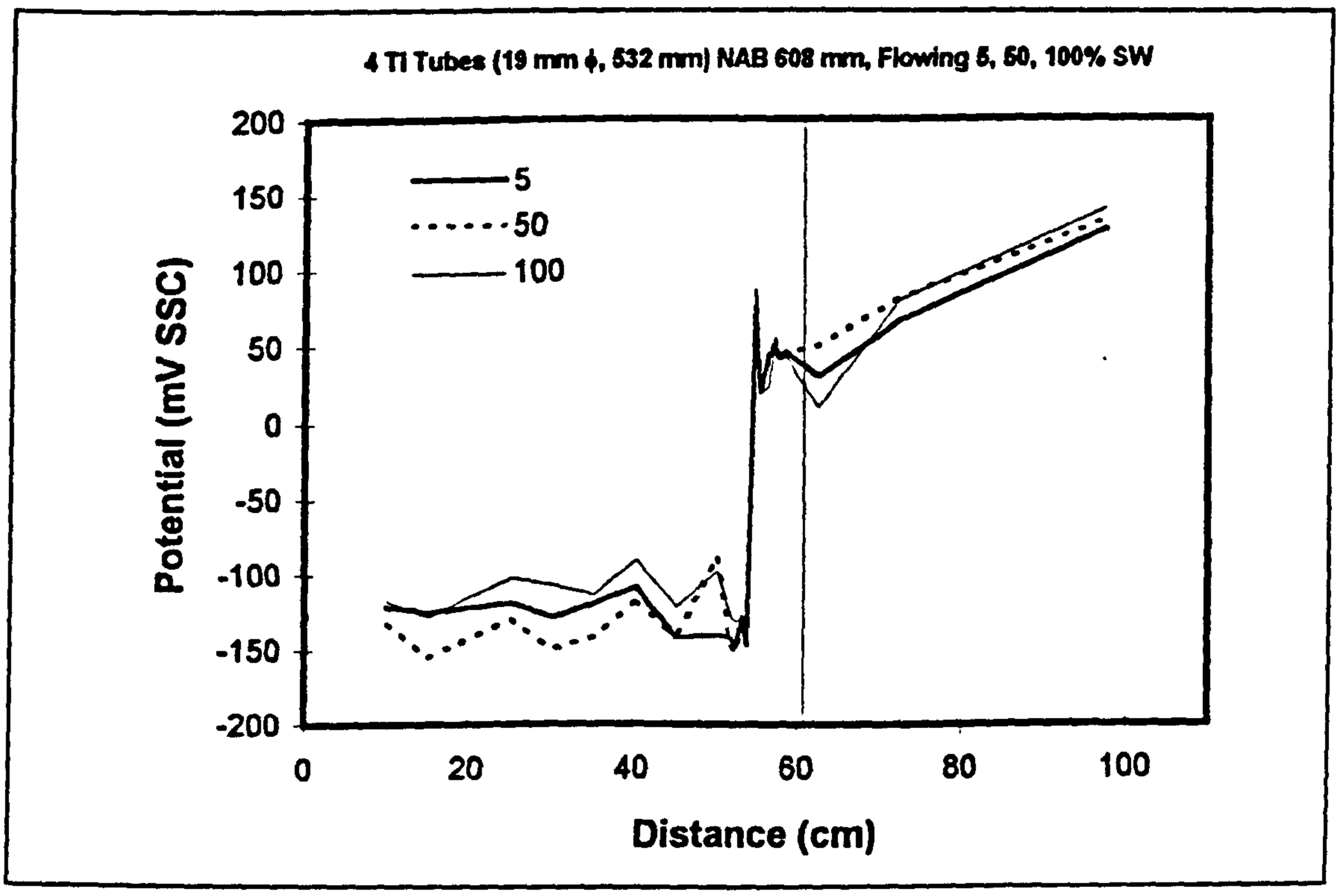

Figure 1.38 Potential distribution for 4 titanium pipes of 19 cm diameter, length 53.2 cm., NAB of length 60.8 cm, in flowing 5, 50 and 100% SW, 1 ms^{-1}.

Figures 1.38 shows the variations in experimental potential distributions for 4 titanium tubes of length 53.2 cm and diameter 19 cm, connected to NAB of length 60.8 cm containing 5, 50 and 100% conductivity seawater flowing at 1 ms^{-1}.

The greatest change in potential takes place on the anode ~ 3 cm from the tubesheet, and occurs at the same place, regardless of solution conductivity.

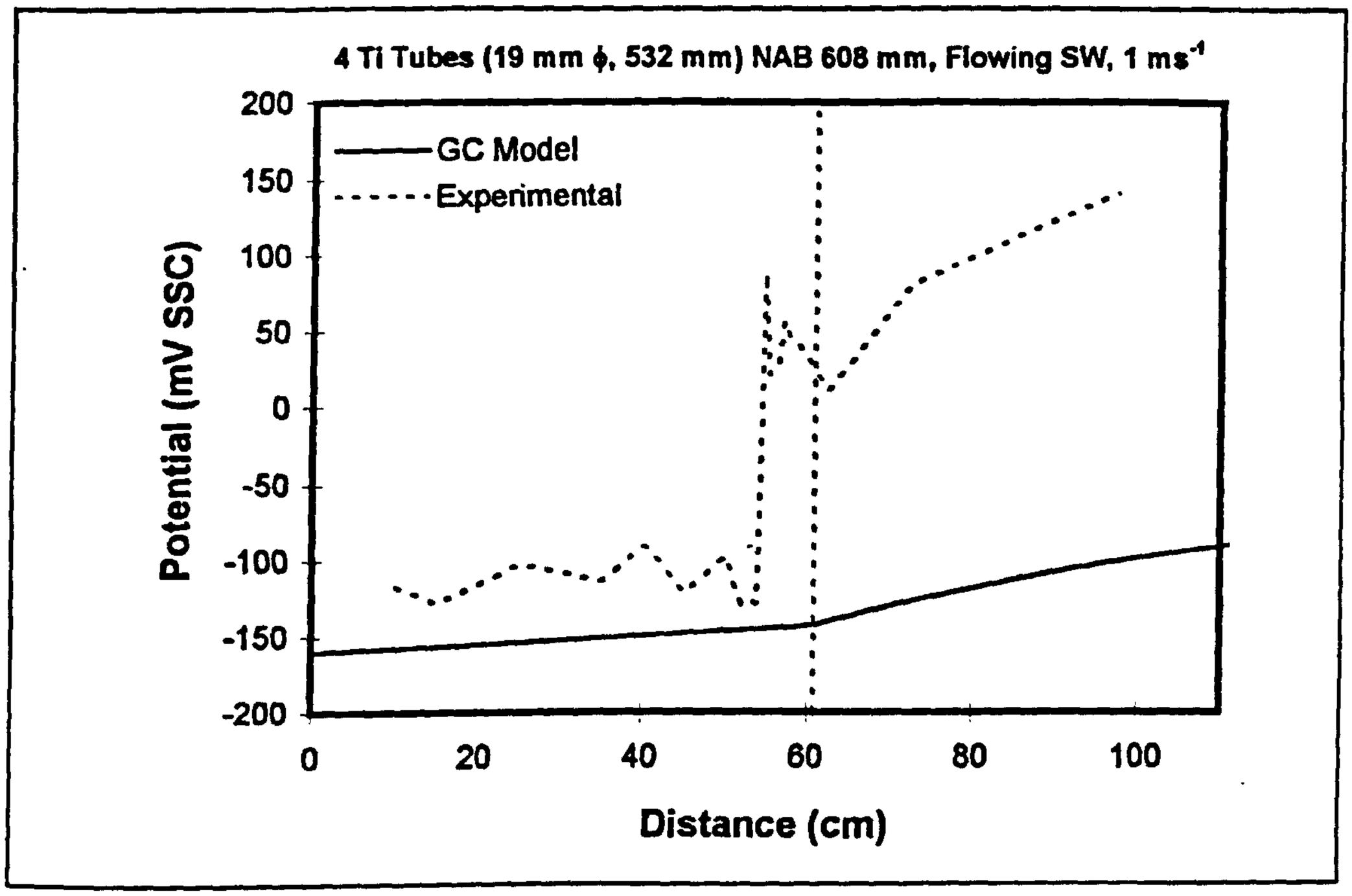

Figure 1.39 Potential distributions for 4 titanium tubes of diameter 19 cm and length 53.2 cm, NAB length 60.8 cm, in flowing seawater, 1 ms^{-1}.

The measured profiles differ little with conductivity. The correlation between predicted and experimental potentials (Figures 1.39 to 1.41) is poor.

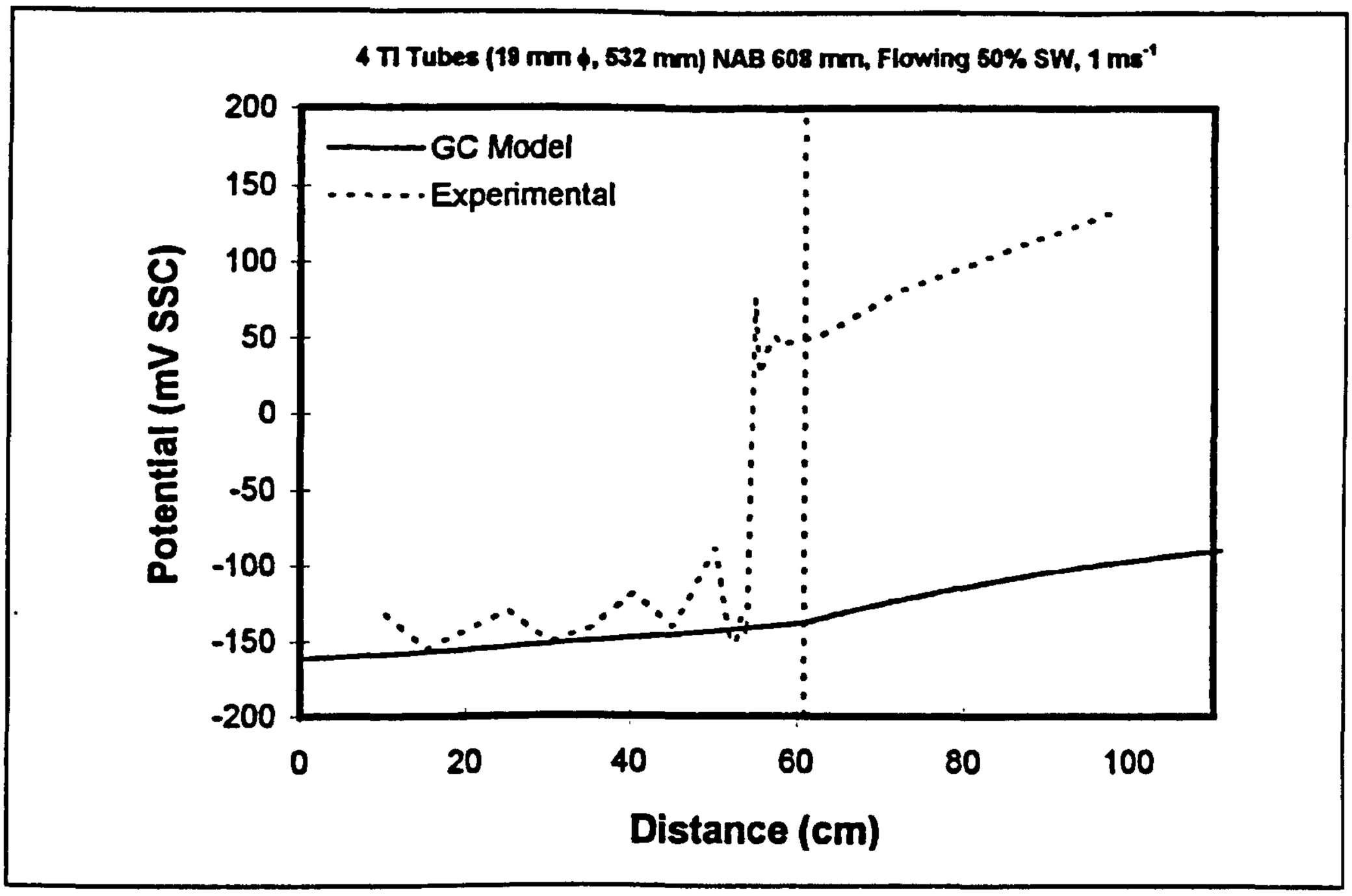

Figure 1.40 Potential distribution for 4 titanium pipes of 19 cm diameter, length 53.2 cm., coupled to NAB of length 60.8 cm, in flowing 50% SW, 1 ms^{-1}.

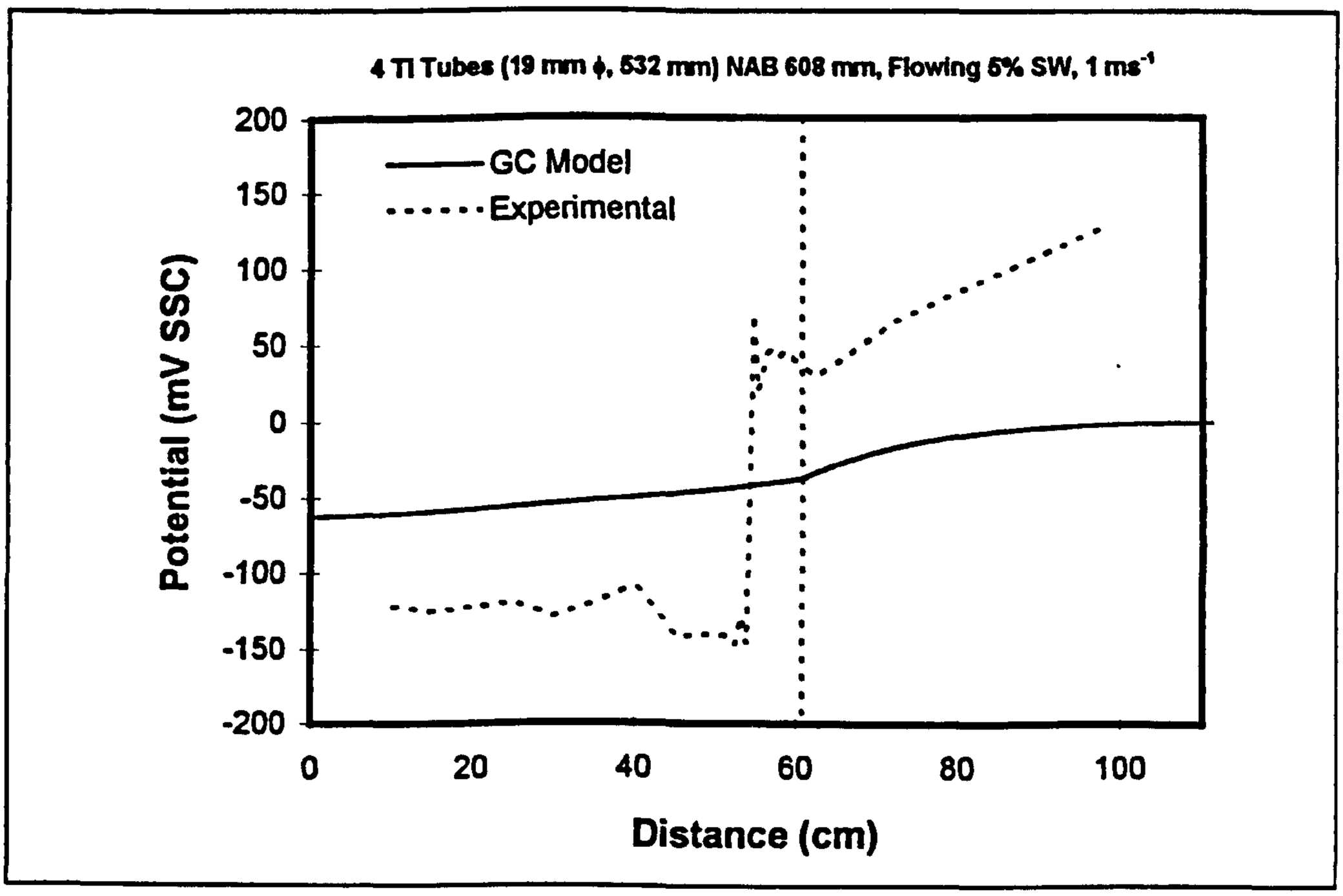

Figure 1.41 Potential distribution for 4 titanium pipes of 19 cm diameter, length 53.2 cm., coupled to NAB of length 60.8 cm, in flowing 5% SW, 1 ms^{-1}.

1.5.4.3 Different Number of Cathodic Tubes

Figure 1.42 shows the potential distributions for 2 and 4 titanium tubes of length 45.0 cm and diameter 12.5 cm connected to NAB of length 60.8 cm in flowing seawater at 1 ms^{-1}.

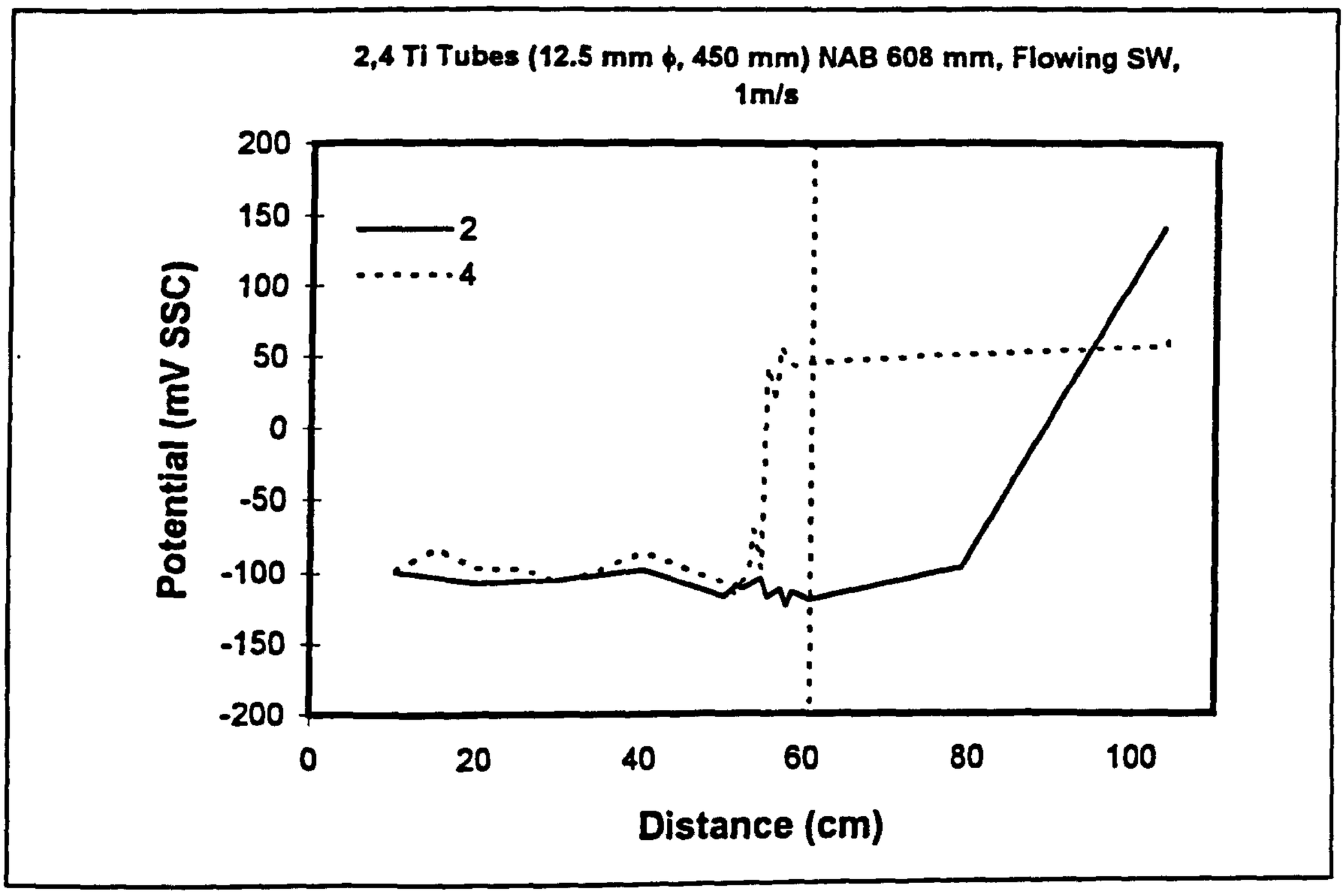

Figure 1.42 Potential distributions for 2 and 4 titanium tubes of diameter 12.5 cm and length 45.0 cm, NAB 60.8 cm, flowing 100% SW, 1 ms^{-1}.

Figures 1.43 and 1.44 show the measured and predicted distributions for the two systems. It may be seen that the couple with two tubes shows a change of potential at the junction, while that with 4 tubes has the ~ 3 cm of anode closest to the join polarized to ~ 50 mV SSC, with the remainder of the anode assuming a potential of ~ -100 mV SSC in both cases. The model predicts more electronegative potentials than those observed experimentally for the two couples.

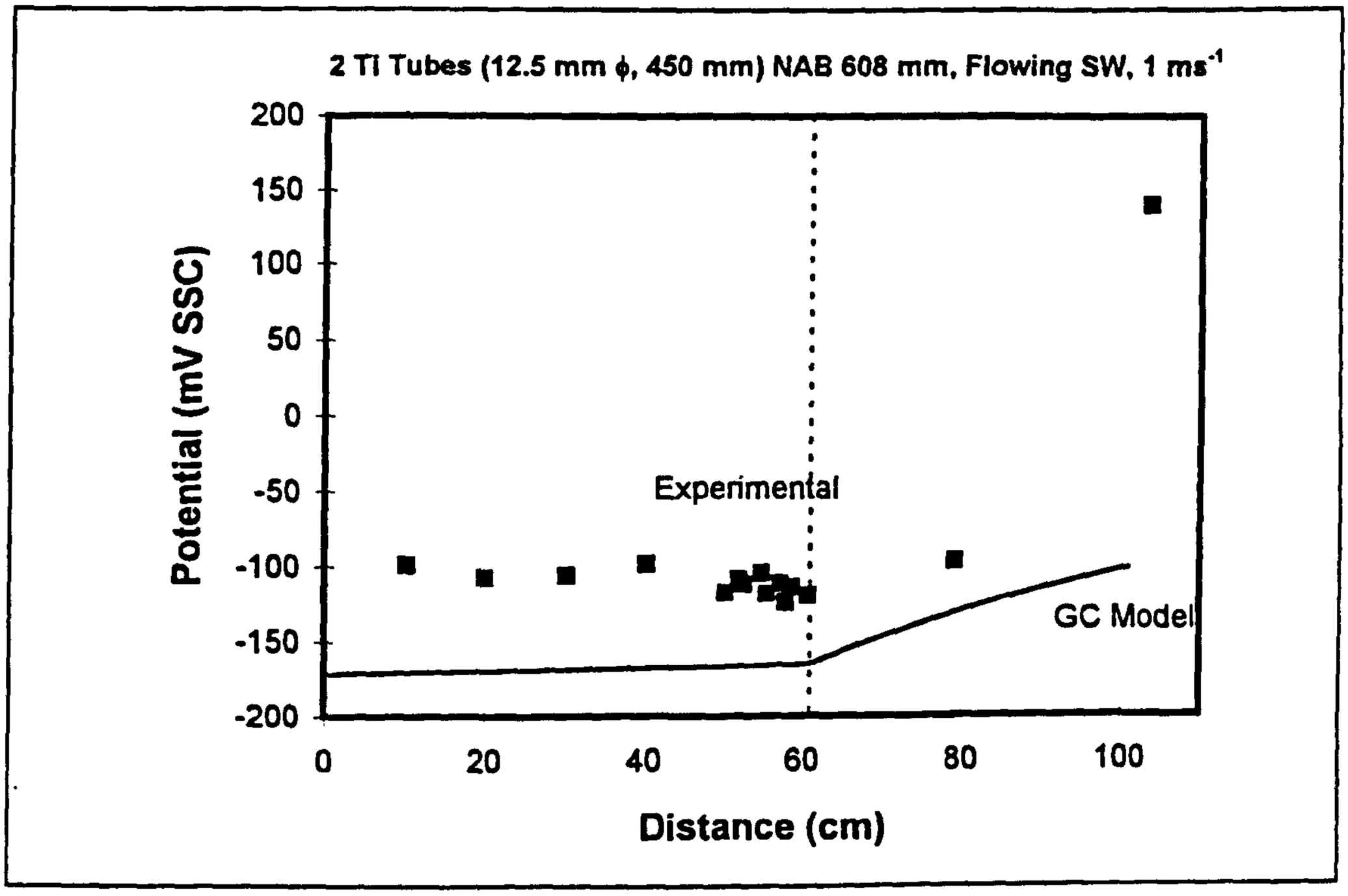

Figure 1.43 Potential Distribution for 2 titanium tubes of diameter 12.5 cm and length 45.0 cm, NAB 60.8 cm, flowing 100% SW, 1 ms^{-1}.

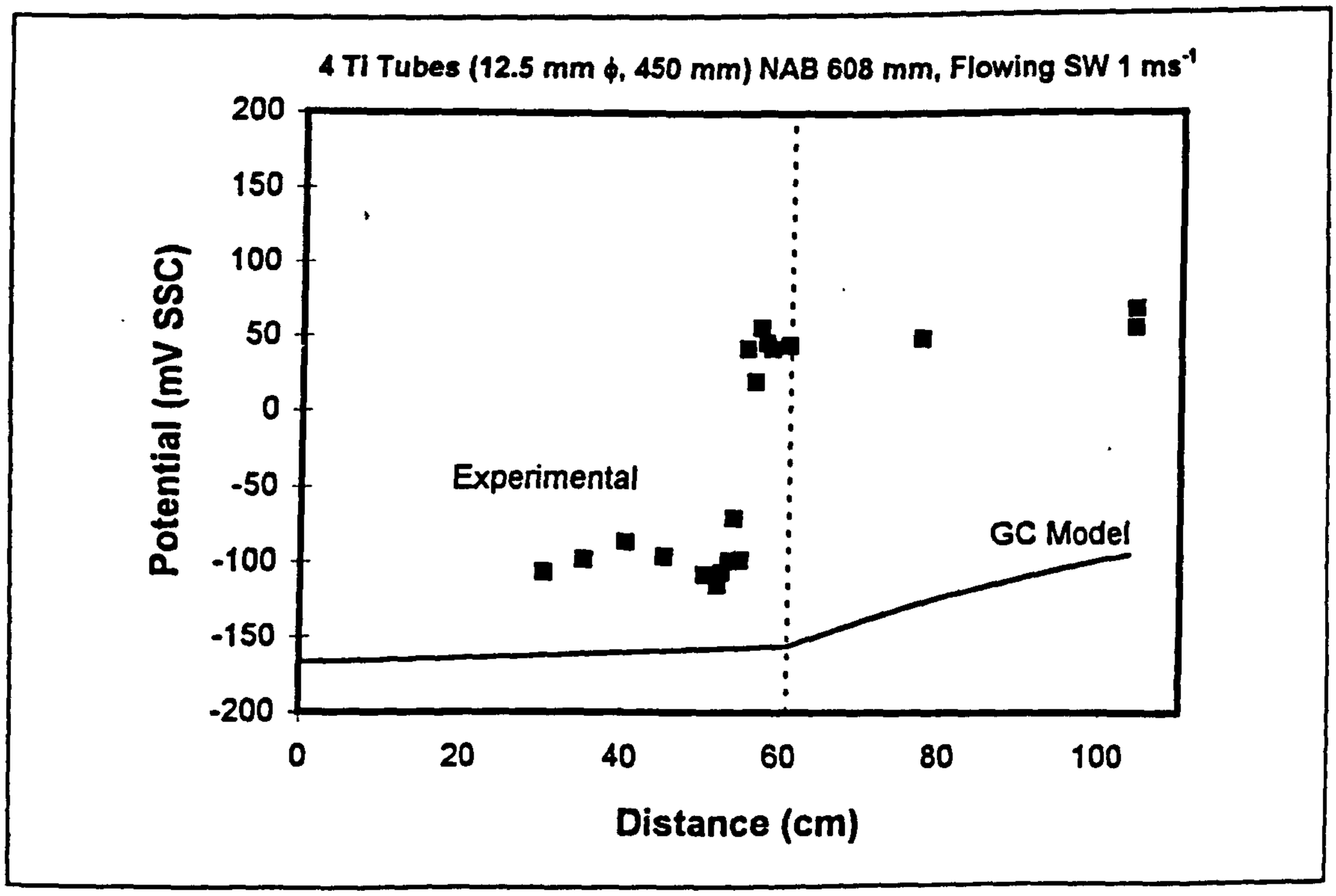

Figure 1.44 Potential Distribution for 4 titanium tubes of diameter 12.5 cm and length 45.0 cm, NAB 60.8 cm, flowing 100% SW, 1 ms^{-1}.

1.6 DISCUSSION

1.6.1 Correlation Between Experimental and Predicted Results

With a few exceptions, the correlation between experimental and predicted potential distributions has been shown to be poor. The greatest change in potential has been shown to occur on the anode at positions several cm from the anode-cathode interface, rather than at the interface, as assumed by the model.

The exceptions to this were those experiments carried out using 2 titanium tubes of 1.25 cm diameter and length 45 cm connected to NAB of length 60.8 cm (Figure 1.15), which were the first experiments to be carried out. Due to a shortage of material, the same piece of NAB was used throughout the duration of the investigation. The next test in chronological sequence used 4 tubes of the same geometry connected to the same length of NAB. Figure 1.42 shows a comparison between the experimental results for 2 and 4 tubes.. It can be seen that the step change in potential occurs on the anode for the 4 tube case, in contrast to the 2 tube case, where the potential profile for the anode is fairly uniform. It is suggested that the previous experiments had resulted in some dissolution of the NAB's protective oxide coating at regions close to the couple. This would initially make the exposed surface more reactive *ie* the free corrosion potential will become more electronegative and the corrosion rate increase. However, solid deposits of corrosion products soon build up, and were viewed on the region of NAB closest to the tubesheet. It has been shown[42] that such deposits substantially lower the corrosion rate during potentiostatic tests of NAB in aerated seawater, but more importantly, the polarization resistance of the materials will also increase. The model predicts that a higher value of anode R_p will increase the polarization of the anode and cathode (see Section 1.3.2.3), but

that the maximum polarization will still be at the junction.

The potentiodynamic tests were carried out on material in the same finish as at the start of the investigation *ie* without surface deposits, and in the short duration of the potentiodynamic tests, there will not be enough time for the deposits to build up. Hack *et al*[43,44] have also noted the effects of time on polarization curves and the difficulty this places on prediction of galvanic corrosion. The model is heavily dependent upon the quality of electrochemical data for both anode and cathode material, and unrepresentative data will result in incorrect predictions. Errors with the cathodic data may be associated with the low conductivity nature of the passive film on the surface of the titanium tubes, which can lead to large differences in R_p values and E_{corr} values, both of which will markedly affect the predicted potential distributions. Trethewey and Marsh[45] had great difficulty in obtaining current density readings for titanium in potentiostatic tests in similar environments to the testing of NAB previously mentioned[42], while several of the potentiodynamic tests conducted on titanium in 5% conductivity electrolyte in this study resulted in very unstable readings, which had to be discarded. The nature of the film on titanium may also mean that the effective resistance of the couple is not solely attributable to the electrolyte, but that the film resistance must also be accounted for. The model does not at present take this into consideration.

Chapter 2 Theory of Passivation

2.1 PROTECTION AND PASSIVATION

The supply of electrons from an external source to a metal structure immersed in a conducting electrolyte reduces the corrosion rate of the structure, since the potential difference between the metal and the electrolyte is reduced. Such an action is called cathodic protection and may be effected by electrically coupling more electronegative metals to the corroding metal (such as zinc to steel), or by impressing an external direct current. One of the earliest industrial examples was the cathodic protection of condenser tubes in a UK power station in the 1920's[46], using current supplied via iron anodes connected to a DC generator.

On a microstructural scale, the corroding metal becomes more stable by the imposition of a double layer field that retards the metal dissolution process. If a field is imposed such that this reaction is accelerated, it may be expected that the rate of corrosion will increase, and indeed this is the case for many metals.

2.2 ANODIC PROTECTION

However, for certain metals (under the right conditions), the imposition of a more electropositive potential difference (anodic polarization) of an actively corroding surface can result in the reduction of the corrosion rate by several orders of magnitude. This is caused by the formation of a stable, passive film, and may be termed anodic passivity[47]. A schematic anodic polarization (potential *vs* log current density) curve for a passivating metal is shown in Figure 2.1. The lower portion of the anodic curve shows the active

dissolution region, where the polarization is under activation control *ie* a charge transfer reaction resulting in the dissolution of the metal into aqueous ions, the rate of which increases with increasing potential. However, above a certain potential corresponding to a critical current density i_{crit}, there is a marked decrease in the net current density. This phenomenon is called passivation. The potential at which a metal passivates is called the passivation potential, E_{pp}, and the current density supported by the passivated surface, i_{pass}.

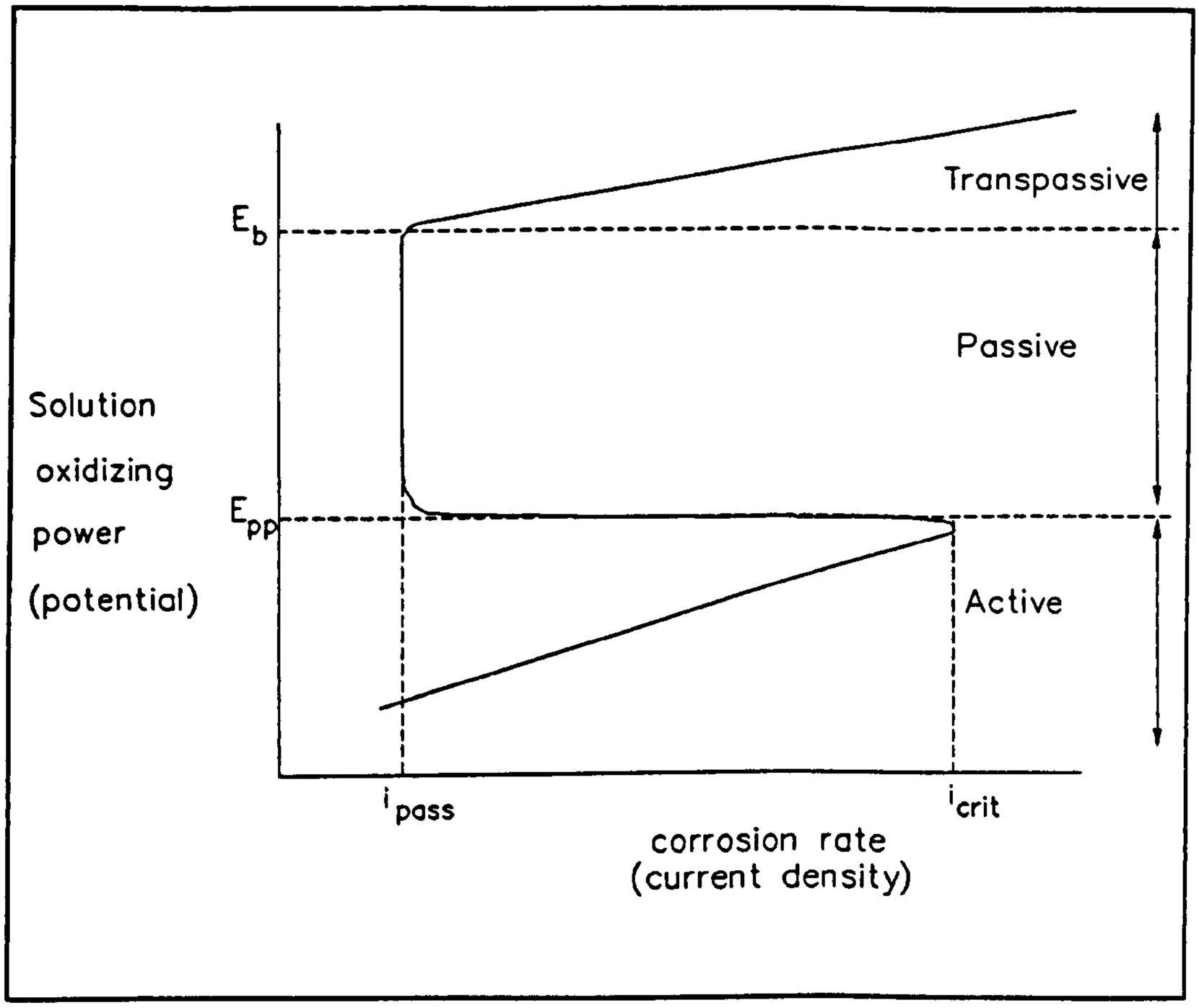

Figure 2.1 Corrosion and passivation of a passivating material.

E_{pp} is almost the same as the Flade Potential (E_f), which can be defined as the potential corresponding to the inflection point on the polarization curve more positive than the passivation potential. Once passivation has occurred, the current densities supported by the metal are often two to three orders of magnitude less than the current densities supported by the metal surface at potentials lower than the passivation potential. It must be stressed that this reduced current is still anodic and that corrosion still occurs, albeit at

a much reduced rate.

The phenomenon of externally-induced passivation used to protect chemical plant on a large scale is called anodic protection. The structure is protected by increasing the anodic polarization of the material, causing electrons to flow *from* the metal, in contrast to the supply of electrons *to* the metal, which causes the potential to be become more negative, as in the case of cathodic protection. It has been reported that the corrosion rate of titanium in sulphuric acid at 60 C is reduced by 33000 times by the use of anodic protection[48]. Passivation may also occur by direct reaction of a material with the electrolyte, without any external power; this is called chemical passivation.

2.3 CHEMICAL PASSIVATION

Chemical passivation occurs when an isolated metal surface remains substantially unattacked (*ie* passive) in a solution with which it has a thermodynamic tendency to react. This is normally due to anodic passivity, which arises from the cathodic processes which occur on the metal surface supplying sufficient electrons to exceed i_{crit}.

Both E_{pp} and i_{pass} are relevant to chemical passivation. As the values of E_f in Table 2.1 show, titanium and chromium may be spontaneously passivated by acidic solutions, since their $E_{pp} < 0.0$ V SHE, while other metals require solutions with higher redox potentials.

Metal	E_f (V SHE)
Au	1.36
Pt	0.87
Fe	0.58
Ag	0.40
Ni	0.36
Cr	-0.22
Ti	-0.24

Table 2.1 Some common metals and their Flade potentials at pH 0. (After Shreir)

For passivation, the following criteria must be met :

(i) the redox potential > E_{pp}

(ii) $i_{cath} > i_{crit}$

This is the basis of Faraday's experiments on iron. He found that, while iron will passivate in concentrated HNO_3 (an oxidizing medium), it will corrode vigorously in dilute HNO_3. This is because the redox potential of the latter solution is not sufficient to 'drag' the potential of the iron into the passive region. In a reducing acid, such as H_2SO_4, iron will passivate if an external potential is applied such that the potential of the metal exceeds E_{pp}.

Another way of improving the passive behaviour of iron is to alloy it with materials that have lower values of i_{crit} and E_{pp}

Composition (w % Cr)	i_{crit} (mA cm^{-2})	E_f (V SHE)	Charge (mC cm^{-2})
0	1000	0.58	1600
2.8	360	0.58	620
6.7	340	0.35	70
9.5	27	0.15	14
12	27	0.01	15
14	19	-0.03	9
16	12	-0.02	9
18	11	+0.10	8
18+8% Ni	2	-0.10	8

Table 2.2 i_{crit}, E_f and charge required to passivate Fe-Cr alloys in 10% H_2SO_4. (Data after Olivier[49]).

As Table 2.2 shows, i_{crit}, E_f and the amount of charge required to passivate Fe-Cr in H_2SO_4 all decrease with increasing alloy additions.

Figure 2.2 shows a schematic anodic polarization curve for a passivating system, such as an austenitic stainless steel (*ie* one whose atoms are packed in a face-centred cubic mode) in sulphuric acid. If the solution is oxygen-free, the cathodic current is supplied by the hydrogen evolution reaction (HER).

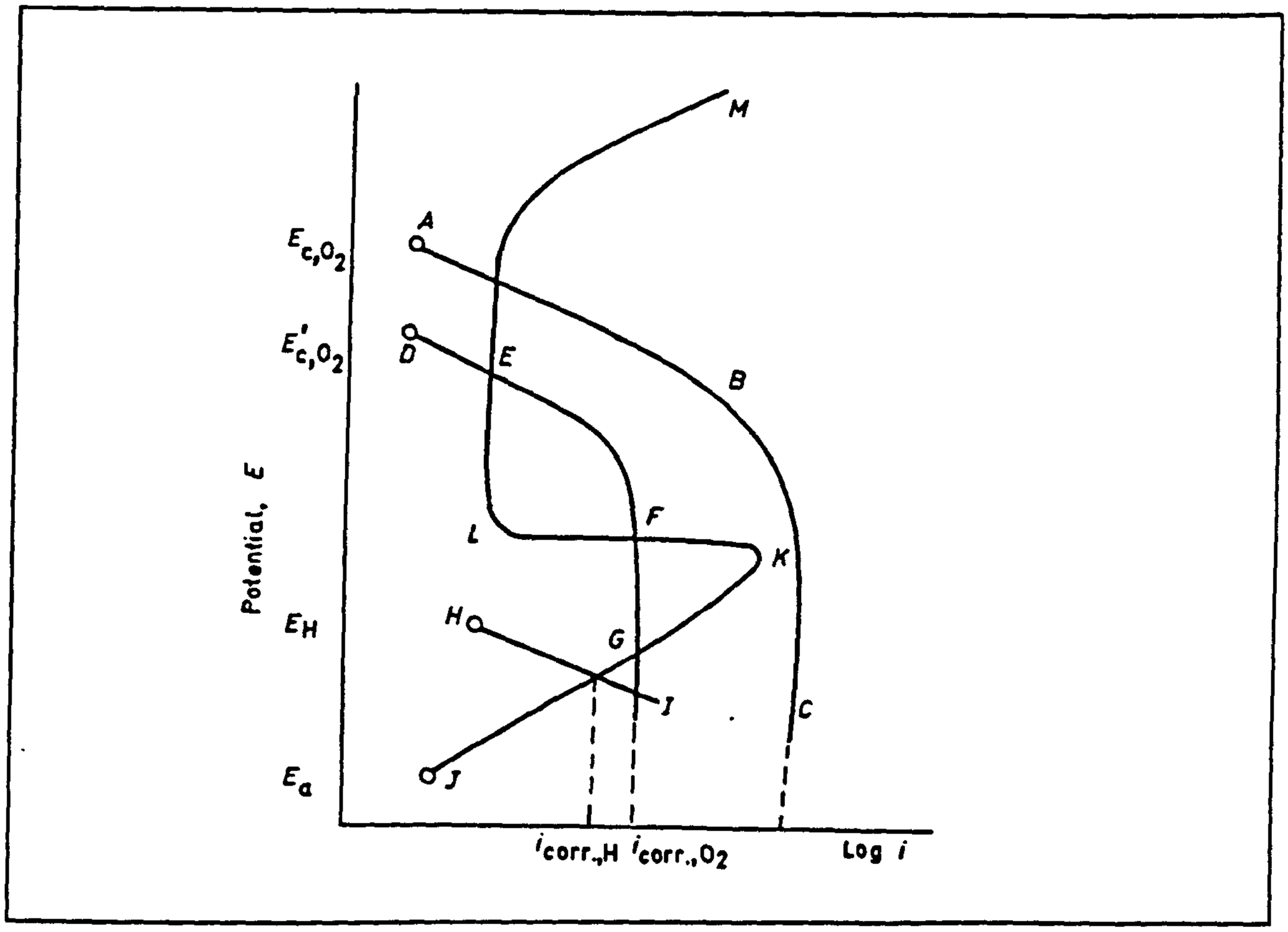

Figure 2.2 Schematic polarization curve for a passivating material showing effects of adding hydrogen evolution and oxygen reduction reactions.

The metal will corrode at a rate $i_{corr}H_2$, since neither of the criteria given above for passivation are satisfied. DEFG is the curve for a low concentration of dissolved oxygen, which worsens the situation since again both criteria are not obeyed, and thus the increased corrosion rate is given by $i_{corr}O_2$. If the concentration of oxygen is increased such that curve ABC is obtained, passivation occurs and the rate falls to i_{corr}pass.

Ferritic stainless steels (ie ones whose atoms display a body-centred cubic structure) have values of i_{crit} around 10^7 nA cm^{-2} [50]. Thus cannot be passivated by oxygen alone, since the limiting current density ($i_{lim}O_2$ is too small), but with additions of oxidizing agents such as HNO_3 or Cu^{2+}, passivation may occur as such species have large values of i_{lim}.

In the transpassive region, the current again begins to increase, and this may be due

to the evolution of gases such as chlorine or oxygen, a result of metal dissolution, or a combination of both. In the case of chromium in H_2SO_4 of = pH 0, tranpassivity occurs at about 1.1 V SCE, and thus is below the potential for oxygen evolution (1.23 V SHE at pH 0). Thus the transpassive region is associated with the formation of metal ions. In stainless steels, chromium (VI) ions (CrO_4^{2-} or $Cr_2O_7^{2-}$) are produced. Which ion is produced depends upon the pH and prior concentration of ions present in solution, as predicted by the E-pH diagram[51].

2.4 CHARACTERISTICS OF PASSIVATION

If a metal is anodically polarized in an aqueous solution containing anions with which it forms sparingly soluble salts, spontaneous passivation can occur, resulting in low (anodic) current flow. If the metal is treated similarly in aqueous solution, but this time with anions with which it forms soluble salts, the anodic product initially formed is often a hydroxide. The production of this hydroxide is accompanied by an equivalent amount of H^+ ions, and pH rapidly falls to such a value that the metal freely forms ions, since hydrated metal cations may now exist in high concentrations in the solution.

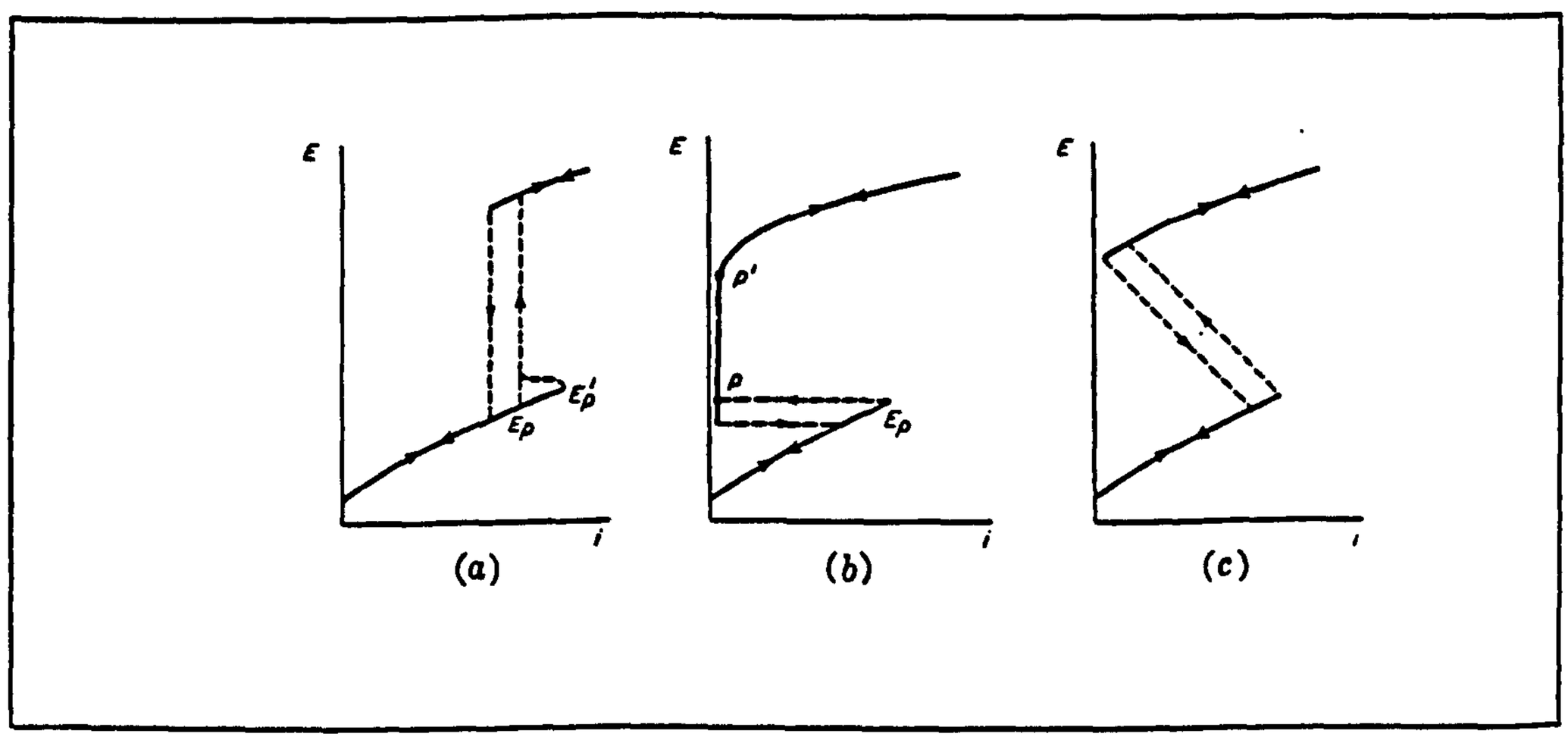

Figure 2.3 Passivation - activation curves.

As the degree of anodic polarization increases, the current density and concentration of hydrated metal ions also rise, until, at a threshold value of current density, passivation occurs.

The shape of the curve depends on whether it is generated galvanostatically or potentiostatically. If the former method is used, a constant current is supplied to the metal electrode and the resultant potential is measured. Figure 2.3a shows a galvanostatically-generated curve. At the current density required to passivate the material, the potential of the anode rises rapidly through the region of anodic passivity and into the region of transpassivity, where processes such as oxygen evolution may occur. In the potentiostatic case (where a constant potential is supplied and the resultant current recorded), a curve such as Figure 2.3b is generated, in which the fall in current from i_{crit} to i_{pass} is approximately two to three orders of magnitude, while Figure 2.3c shows the intermediate effect of circuitry of mixed nature. The 'hysteresis' between the forward and reverse curves is caused by the finite time required for the film to form and to disappear.

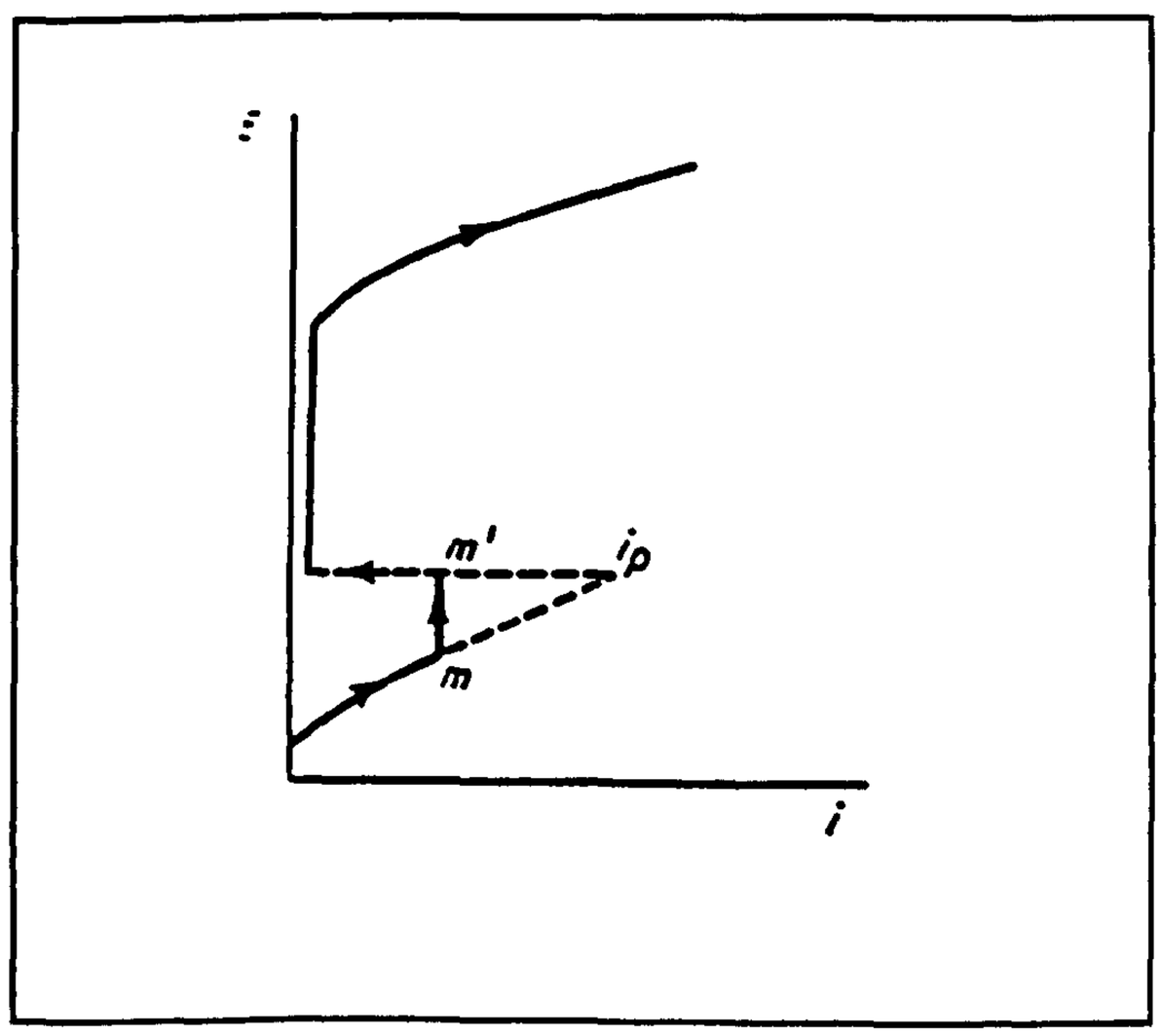

Figure 2.4 Schematic polarization curve when magma is formed as a precursor to passivation.

Such curves are 'ideal' and may only be obtained by the use of fast scan rates, since for slower scan rates curves of the form shown in Figure 2.4 are obtained, especially if the physical orientation of the anode is such that it allows anodic products to accumulate on its surface.

Such a change in behaviour may often be attributed to the presence of a precursor film. This is formed by a 'magma' of crystals precipitated from the soluble metal salts in the solution, once the solubility limit has been exceeded close to the electrode surface. This is shown occurring in the region *mm'* (Figure 2.4), and has the effect of decreasing the effective anodic area. This discontinuity decreases in magnitude as the scanning rate increases, since less time is given for the metal ions to reach the critical solubility limit required. Stephenson[52] observed the formation of such a magma in the case of iron in sulphuric acid. The real passivating current density i_{pass} is not measured because the magma forms over the range *mm'* and reduces the effective anode area. The effect becomes less marked if the curve is traced rapidly. The rate of formation of this magma is dependent upon the magnitude of current, and thus the concept of induction time may be introduced.

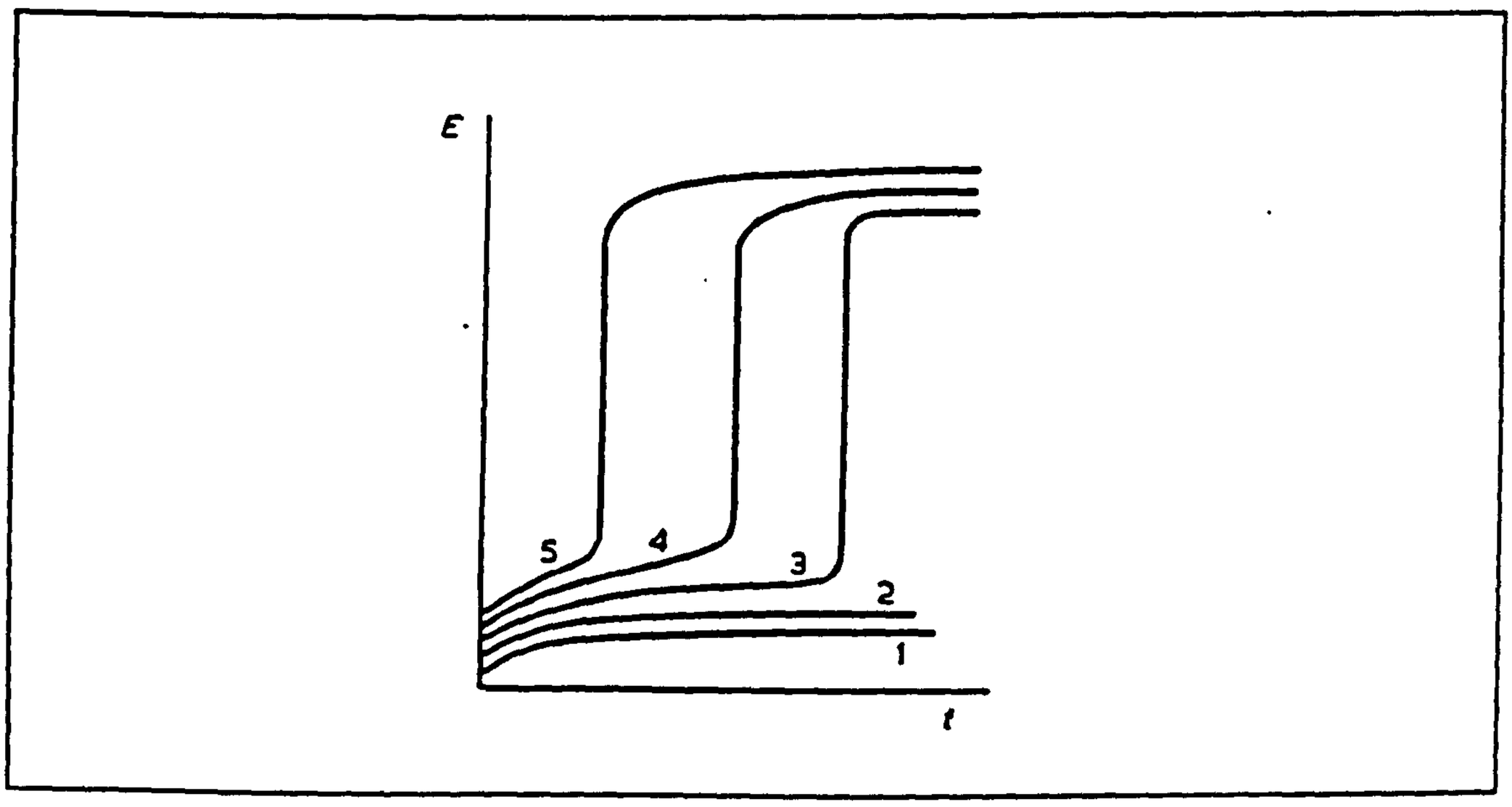

Figure 2.5 Schematic potential-time curves for a series of different current densities.

Figure 2.5 shows the potential *vs* time behaviour of a passivating material when five different currents ($i_1<i_2<i_3<i_4<i_5$) are applied to it.

These curves show the effect of increasing the current applied to the anode. Below i_3, i_{crit} is not exceeded, and thus passivation does not occur, hence no rapid increase of potential with constant current density is observed. Above this threshold of i_{crit}, passivation occurs, with consequent rapid rise in potential at i_{crit}. Higher values of i lead to passivation occurring more quickly, *ie* the induction time is reduced. This is as expected with regard to rates of diffusion, convection and migration of metal cations away from the anode, assuming this magma is a precursor to passivation. Figure 2.6 is an alternative method of showing that there is a minimum current density required to initiate passivation, and increasing current densities decrease the time for this passivation to occur. Below a certain minimum current density, the induction time is so high, passivation does not occur.

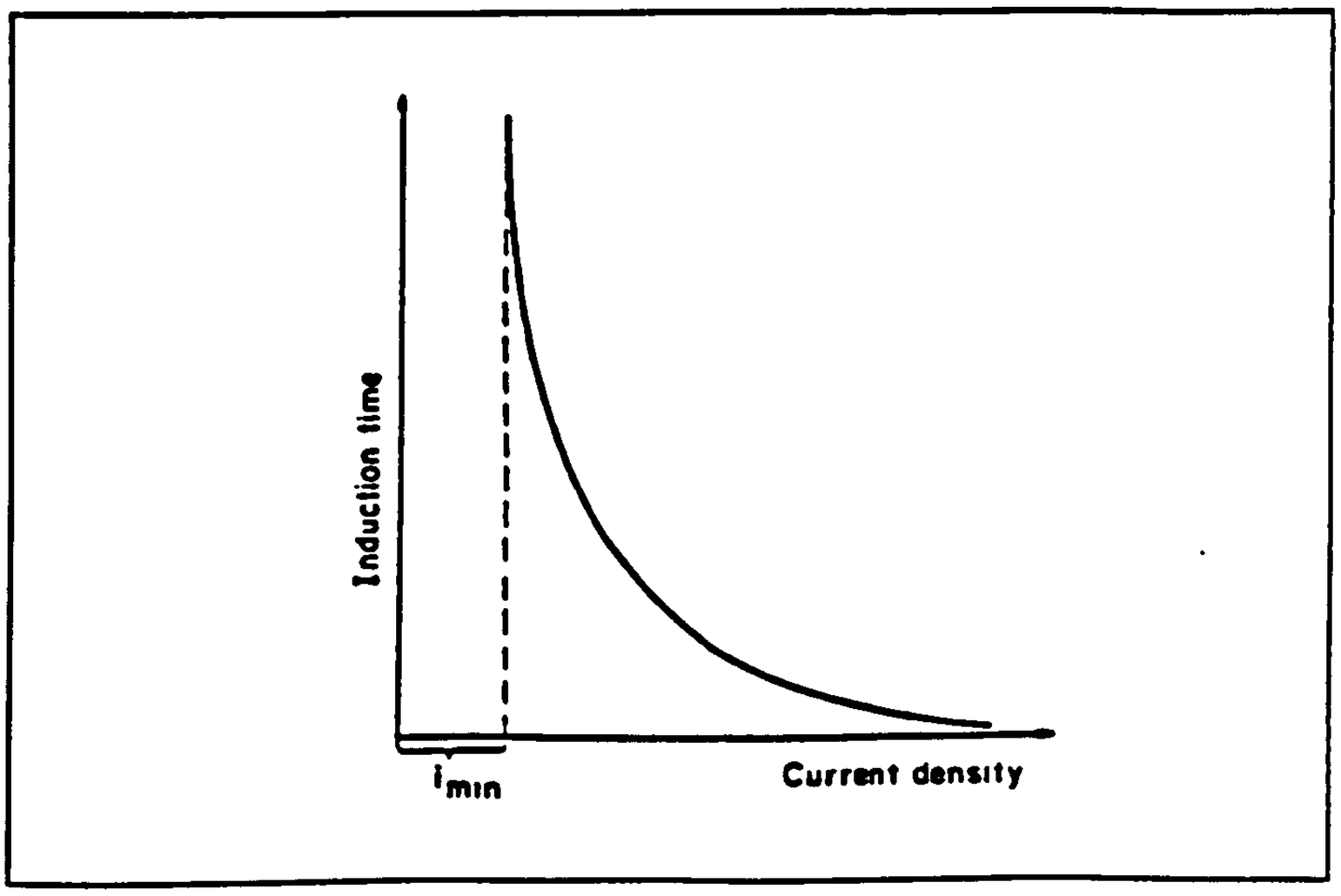

Figure 2.6 Time-current density curve for a passivating material.

However, curves generated by scan rates above a critical level are not of much practical use, since they do not correspond to in-service conditions. This critical rate is dependent upon the concentrations of diffusing species across the double layer and the

diffusion coefficient of the species in question and also the time taken by the system to reach a constant value of current[45].

2.5 THE SOLID STATE THEORY OF PASSIVATION

If the potentiostatic behaviour of nickel in acidic solution is studied, it is found[53] that, as the degree of anodic polarization increases, there is a potential at which a film of $Ni(OH)_2$ is formed. This is not the passivation potential, and thus the film is called a precursor or pre-passive film.

Experiments with light reflected from the polarized surface have shown that this film does not absorb light, but at potentials above the passivating potential, the new film does absorb light. This may be explained in the two following ways:

(i) There is a change in the physical properties of the film such that it is just now capable of absorbing light quanta of the particular wavelength used.

(ii) At the passivation potential, the film now has free electrons, which may absorb light quanta of any frequency, and thus may now function as a conductor, whereas below E_{pp}, the absence of free electrons lead to an insulating precursor film.

As the electrical conductivity develops in the oxide film during the change from precursor film to passive film in this second case, the resistance falls, and the potential difference across the film disappears. Thus, there is no driving force to transport ions from the metal surface into the solution, *ie* dissolution ceases and passivation occurs. It appears

that a precursive film that can acquire free electrons is a precondition for passivation[54] in such systems.

As noted in Section 2.4, there is an induction time associated with passivation, when differing magnitudes of current densities are applied (Figure 2.5). This supports the hypothesis of metal dissolution leading to local high concentrations of metal ions near the surface, and subsequent precipitation when the solubility limit is exceeded.

Further evidence for this mechanism is found on two counts. Firstly, there is an increase in the induction time on stirring the solution (or by using a rotating disk electrode[55,56]), since this produces a more uniform ion concentration throughout the solution. This homogeneity is achieved at the expense of reducing the metal ion concentration close to the electrode surface. Secondly, there is a value of i below which passivation does not occur, *ie* the induction time is infinite.

Such a model may be called a solid state model, since passivation is considered to occur as a result of changes in the properties of a film[57], formed when the solubility limit of the salt or hydroxide (formed by dissolution of the metal) is exceeded.

2.6 ALTERNATIVE MODEL FOR PASSIVATION - THE ELECTRODIC MODEL

An alternative model proposes that the fall in current is attributable to the formation of a very thin layer of an adsorbed species, such as O^{2-}, OH or other anion. This species can cause a fall in current even when less than a complete monolayer, since the anion may block an area of preferential dissolution, such as a kink site. Since passivation is dependent upon events occurring on the surface, rather than in the electrode, this is called the

electrodic theory of passivation.

The distinction between the two theories is in the thickness of the anodic film. The solid state theory predicts that a 'thick' film (*ie* greater than a monolayer) is formed, while the electrodic theory predicts that passivation can begin to occur at coverages less than or equal to a monolayer.

Advances in electrochemical techniques allowed the determination of the passive film thickness, which was shown to be 'thick', advancing the solid state theory. The electrodic theory was then modified to consider that the film was a coincidental effect of the process, rather than the cause of it. The cause was proposed[58] to be that the fraction of filmed surface increases at potentials below the current density peak, and that current density falls with increasing coverage of chemisorbed anion *ie* increasing potential in a potential-controlled system or increasing time, in a galvanostatic system. Thus, the potential at which the species begins to be adsorbed should be close to the potential at which the current density reaches its peak value.

Armstrong[55,56] used the rotating disk electrode (RDE) technique to determine which mechanism was responsible. Armstrong suggested that as the speed of rotation increased, if a dissolution-precipitation mechanism was responsible, the shape of the polarization curve would change due to increased mass transport of the metallic ions away from the electrode. The shape of the curve would be unaltered if a chemisorption mechanism was responsible. Armstrong[56] and Ekerbakh[59] found that chemisorption was responsible for passivation on nickel and chromium, in direct contradiction to the results found by Bockris[53]. Bernhardsson[60],[61] conducted RDE experiments and found that a chemisorption mechanism was responsible for passivity on Types 304 and 316 stainless steels.

2.7 PERCOLATION THEORY OF PASSIVATION

This model of passivation, based on the work of Newman[62,63,64] is a modified version of the electrodic theory. It assumes that the passivation process of a stainless steel occurs by a mechanism which involves the selective dissolution of iron atoms from the surface, and subsequent oxidation of those chromium atoms formerly bonded to these iron atoms by adsorbed O^{2-} or OH^{-} anions to form extended -O-Cr-O-Cr-O- chains. These chains then block further iron dissolution from ledge sites. This model still allows bulk Cr to enter solution during the active-to-passive transition, mainly by the dissolution of iron atoms and subsequent undermining of bulk material. Thus, the anomaly between mass loss and charge supplied may be explained.

Using the assumption that the active sites move in a descending spiral due to the emergence of screw dislocations (*ie* the process is an inherently 3D process), this model predicts threshold behaviour changes at 9.5 and 17.5 w % Cr. These lie in the region of transition from 'iron-like' to 'chromium-like' behaviour in acid solutions[65,66]. Such transitions were also predicted by Uhlig[67,68], based upon calculations of the filling of the iron *d* orbitals when chromium is added as an alloying addition.

Such a mechanism of enriching the Cr content near the surface of a Fe-Cr alloy has also been proposed by Davenport[69]. Griffin[70,71] also predicted a bridging network of anions between neighbouring cations in his cation monolayer theory.

The active region above the free corrosion potential thus corresponds to the dissolution of iron. The current supported by the filmed area is less than on the unfilmed areas (*ie* that supplied by iron going into solution), and thus, the total current from the

material will fall as a greater fraction of the surface becomes covered with -O-Cr-O-Cr-O- chains. This is manifested as an active-to-passive 'nose' in a polarization curve.

2.8 THE MARCUS PASSIVITY PROMOTER ARGUMENT

Marcus[72] uses a modified version of the electrodic theory of passivation *(ie* passivation occurs by the adsorption of oxygen or OH from water, and that an oxide film grows by a nucleation and growth mechanism) in order to predict those metals which will passivate, or act as suitable alloying additions in passivating alloys. Evidence for this nucleation and growth mechanisms of oxide growth has been obtained using scanning tunnelling microscopy techniques[73,74].

The two critical factors for passivity are considered to be the anion chemisorption bond strength and the ease with which the adsorbed species can be converted into a 3D oxide structure. An element with a high heat of adsorption of oxygen will promote passivity, since this is associated with a high heat of formation (ΔH_{ads}) and subsequent stability of the oxide. Less obvious is the fact that the formation of a passive film requires an activation energy barrier to be exceeded in order for the chemisorbed species to be converted into a 3D oxide. This process of oxide growth requires the breaking of metal-metal (M-M) bonds, and hence passivity is favoured by metals with low M-M bond strengths (ε_{M-M}). Low values of this M-M bond strength will also favour metal dissolution, and thus a balance between the two terms is essential for passivation. As an approximation, ε_{M-M} is defined as $2\Delta H_{sub}$ /Z, where ΔH_{sub} is the heat of sublimation and Z is the coordination number (the number of atoms immediately surrounding a particular atom) of the metal in question.

Metal	'Bond Strength' $\varepsilon_{M\text{-}M}$ (KJ mol-1)	Heat of adsorption of oxygen ΔH_{ads} (KJ mol-1)
Al	54.4	900
Ti	78.3	992
Cr	99.1	737
Fe	104.1	571
Ni	71.6	461
Cu	56.4	293
Zn	21.8	277
Nb	181.5	875
Mo	164.5	718
Ta	195.5	900
W	212.3	819
Pt	94.2	285

Table 2.3 Values used in Marcus' 'Synergy' Table for Passivity Promotion (after Marcus[72].

Using these criteria, it was suggested that metals with high ΔH_{ads} and low $\varepsilon_{M\text{-}M}$ will be beneficial to the growth of a passive film, and thus enhance passivity through a 'synergistic' action. Such materials may be defined as passivity promoters. Once the film has formed, minimizing the concentration of defects becomes more important for continued

passivity than the heat of formation.

Materials with a high M-M bond strength may be termed dissolution moderators. Due to their high heat of formation, they are not detrimental to passivation (*ie* their oxides are stable), and indeed, they may participate in the process and become incorporated into the passive film. Figure 2.7 shows the elements in Table 2.3 plotted on a 'synergy' diagram, with ΔH_{ads} and $\varepsilon_{M\text{-}M}$ as the axes.

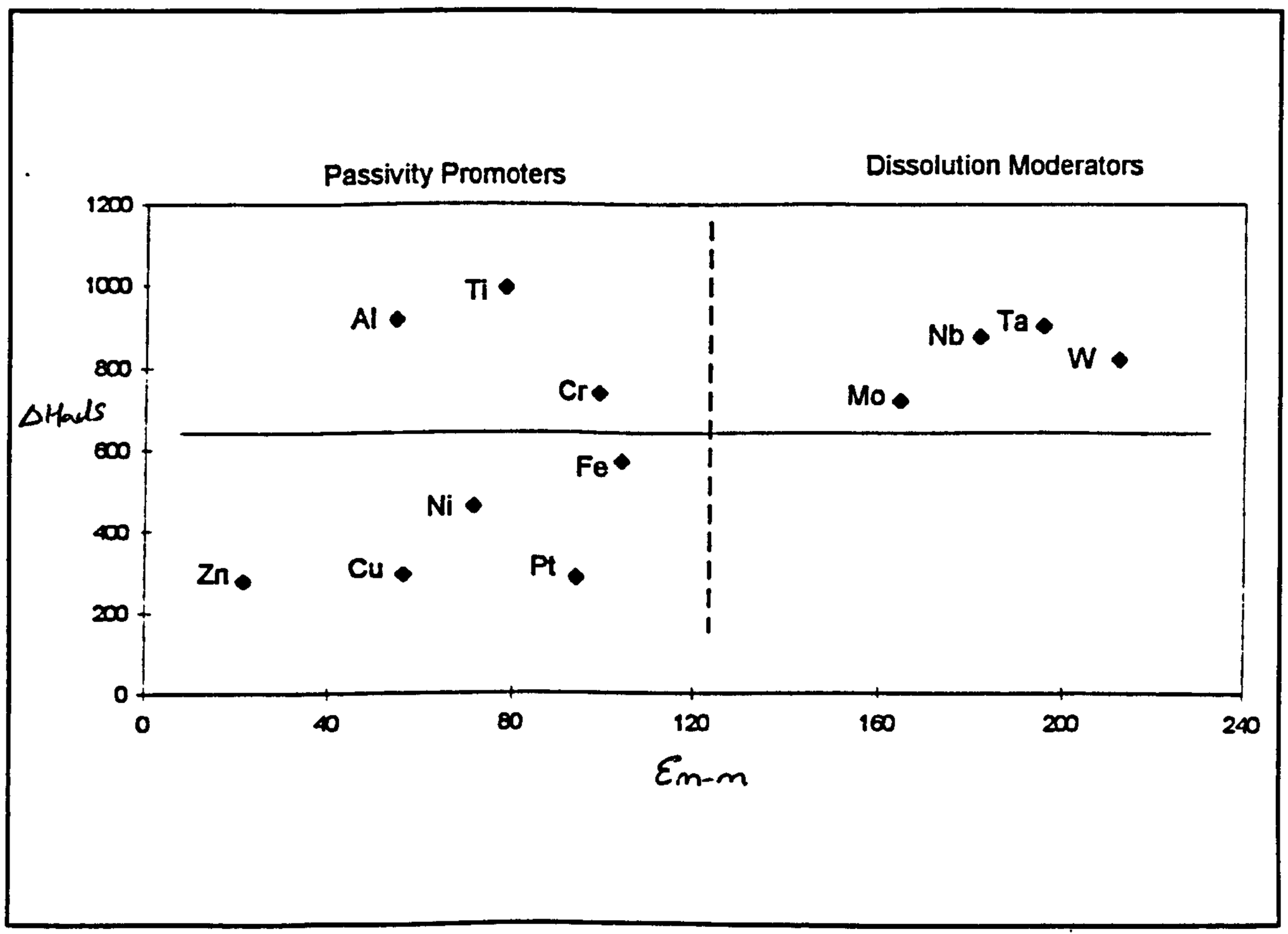

Figure 2.7 'Synergy' Diagram, showing elements considered as passivity promoters and dissolution moderators.

Chromium and molybdenum are both used as alloying additions in stainless steels. The heats of formation for the two alloys are similar, but molybdenum has a much higher M-M bond strength. The lower value of $\varepsilon_{Cr\text{-}Cr}$ means that the energy release on adsorption of oxygen disrupts Cr-Cr bonds, but not Mo-Mo. Thus, the oxide may be nucleated prior to complete coverage by the oxide monolayer. The high value for molybdenum lowers the

dissolution rate by increasing the activation energy barrier for the disruption of metal bonds on the surface.

Marcus states that this view of passivation differs from the percolation theory of passivation detailed in the previous section, which states that -O-Cr-O-Cr-O- chains are formed without breaking Cr-Cr chains. For pure chromium this may be the case, but Newman considers that the passivation of stainless steels occurs by the selective dissolution of iron. In this case, it is Cr-Fe bonds (rather than Cr-Cr bonds) that are broken, and subsequent formation of -O-Cr-O-Cr-O- chains in areas where chromium atoms have been thus exposed. This mechanism is favoured by the difference in heats of formation and bond strengths for iron and chromium.

2.9 THE NATURE OF THE PASSIVE FILM ON STAINLESS STEELS

Investigations into the nature of the passive film on different Fe-Cr based alloys by many investigators[75,76,77,78,79,80,81,82] have shown that it is not homogeneous in nature, and that it has at least two layers of different Cr (III) species. Most have found the inner layer to be Cr_2O_3, and the outer layer an amorphous, hydrated chromium hydroxide $Cr(OH)_3.nH_2O$. The Cr_2O_3 is considered to initially form[83] by direct reaction of water and chromium, and subsequent film development is by solid state oxidation following oxygen anion migration to the metal surface. Some authors[83,84] have found an intermediate hydroxyoxide species present, but it is generally agreed that the outer layer of hydrated $Cr(OH)_3$ forms at the oxide solution interface.

Oblongsky and Devine[79] used the in-situ SERS (Surface Enhanced Raman Spectroscopy) technique to investigate passive films on stainless steels, and postulated that

$Cr(OH)_3$ is accompanied by another hydrated form of chromium, and not Cr_2O_3. However, they used a more basic borate buffer media (pH = 8.4), and, as noted by Sunseri[85] the degree of hydration present in the passive layer increases with the basicity of media used.

Clayton and Lu[81] found that a clear separation between the inner and outer layers of the passive film existed, while Stypuka[84] found that the O/Cr ratio decreased on moving through the passive film from the electrolyte towards the metal. They found that the ratio was close to CrOOH, and that the Cr^{3+} layers were slightly hydrated in 1M H_2SO_4.

Such observations are in agreement with the bipolar passive film model proposed by Sakashita and Sato[86], which considers the nature of ion-selective corrosion products. Passivity is enhanced when the film consists of inner anion-selective and outer cation-selective layers.

If 304 stainless steel in 1M H_2SO_4 is considered, the Cr_2O_3 film previously described is initially formed at the metal-electrolyte interface. Some CrO_3 may also be found in the Cr_2O_3 film. This is to be expected, since the heats of formation of Cr_2O_3 and CrO_3 are similar[80]. This layer is not ion selective[86]. $Cr(OH)_3$ forms at the subsequent oxide-electrolyte interface, and at this stage, some CrO_4^{2-} may be formed by a solid state reaction:

$$Cr(OH)_3 + 5OH^- \rightarrow CrO_4^{2-} + 4H_2O + 3e^-$$

CrO_4^{2-} is not normally considered stable at pH values close to zero, but in the film, the presence of OH^- and bound water may alter the local pH and allow its formation. Such species are known to have an inhibitive effect when added to a solution. This may be due to such anions acting as electron acceptors, resulting in both an increase in M-O bond

strength and a decrease in electrical conductivity. Such anodic inhibitors are reported to work efficiently at 4% surface coverage[87]. An alternative explanation attributes this to a rectifying effect on the migration of ions through the film, which will now be explained.

The formation of CrO_4^{2-} depends on the presence of a hydrated layer within the $Cr(OH)_3$. Since this layer is normally closer to the electrolyte than the metal, it may be considered that there are now two parts to the $Cr(OH)_3$ layer; an inner CrO_4^{2-}-free portion, and an outer layer which contains CrO_4^{2-}. Hydrated chromium (III) oxides are found to be cation selective in the presence of MO_4^{n-} anions (where M is a metal), and anion selective in their absence[86]. Thus, the outermost portion of the passive film ($Cr(OH)_3$ with CrO_4^{2-}) is cation-selective, the middle portion ($Cr(OH)_3$) anion-selective, and the innermost part ($Cr_2O_3.CrO_3$) is not ion selective (Figure 2.8). Such a film resists the ingress of anions such as OH^- and Cl^-, as well as the egress of metal cations into solution.

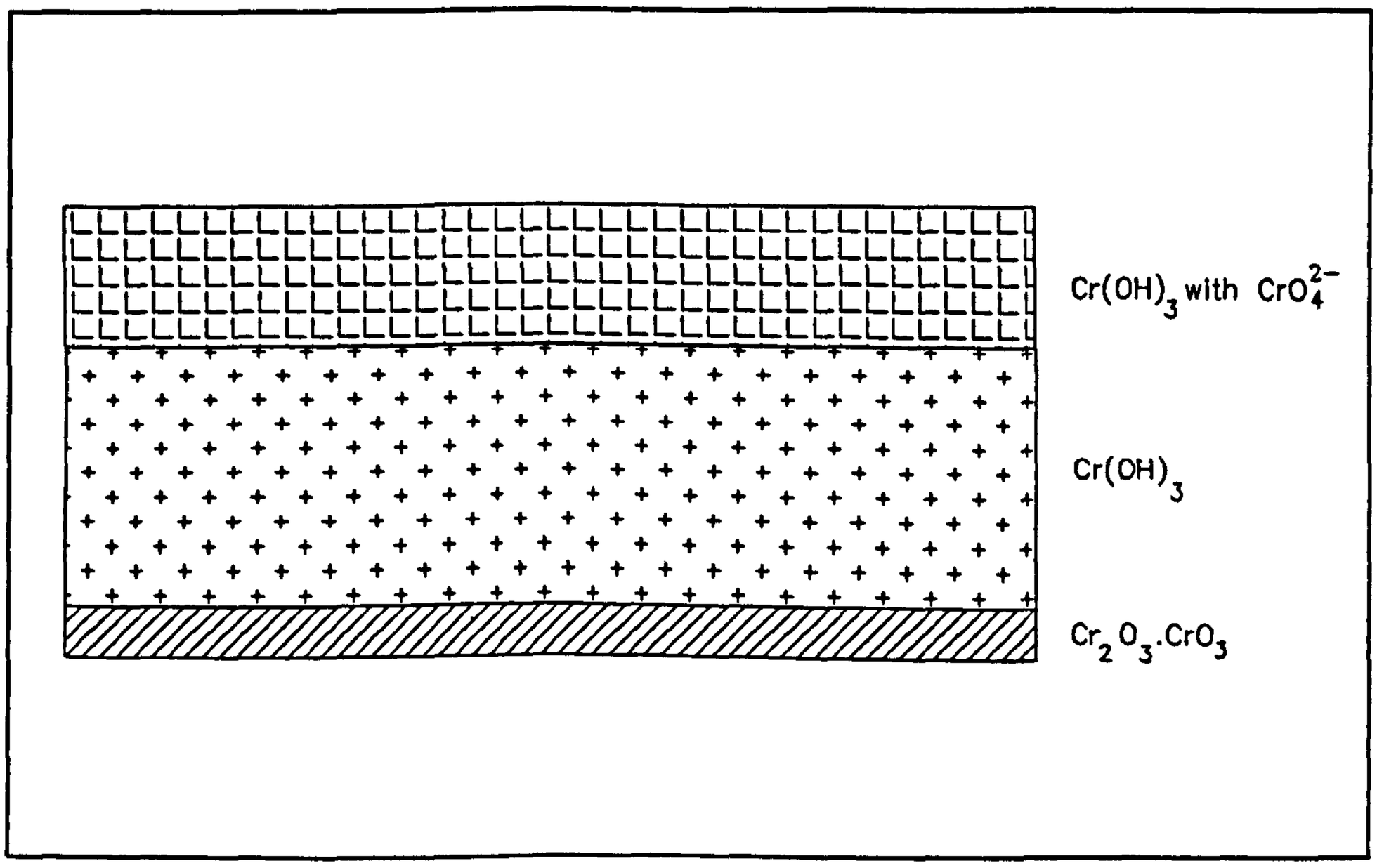

Figure 2.8 Schematic of passive film on a stainless steel.

An externally-imposed anodic potential will cause protons (from OH^- at the interface of the two layers) to move outwards towards the surface through the cation selective layer.

The movement of cations from the surface will be hindered by the anion-selective nature of the inner layer, a positive space charge will be set up, causing O^{2-} ions to move towards the metal surface, through this anion selective layer, where they will react with chromium at the surface, and thereby form an oxide, without any bound water. This is shown schematically in Figure 2.9.

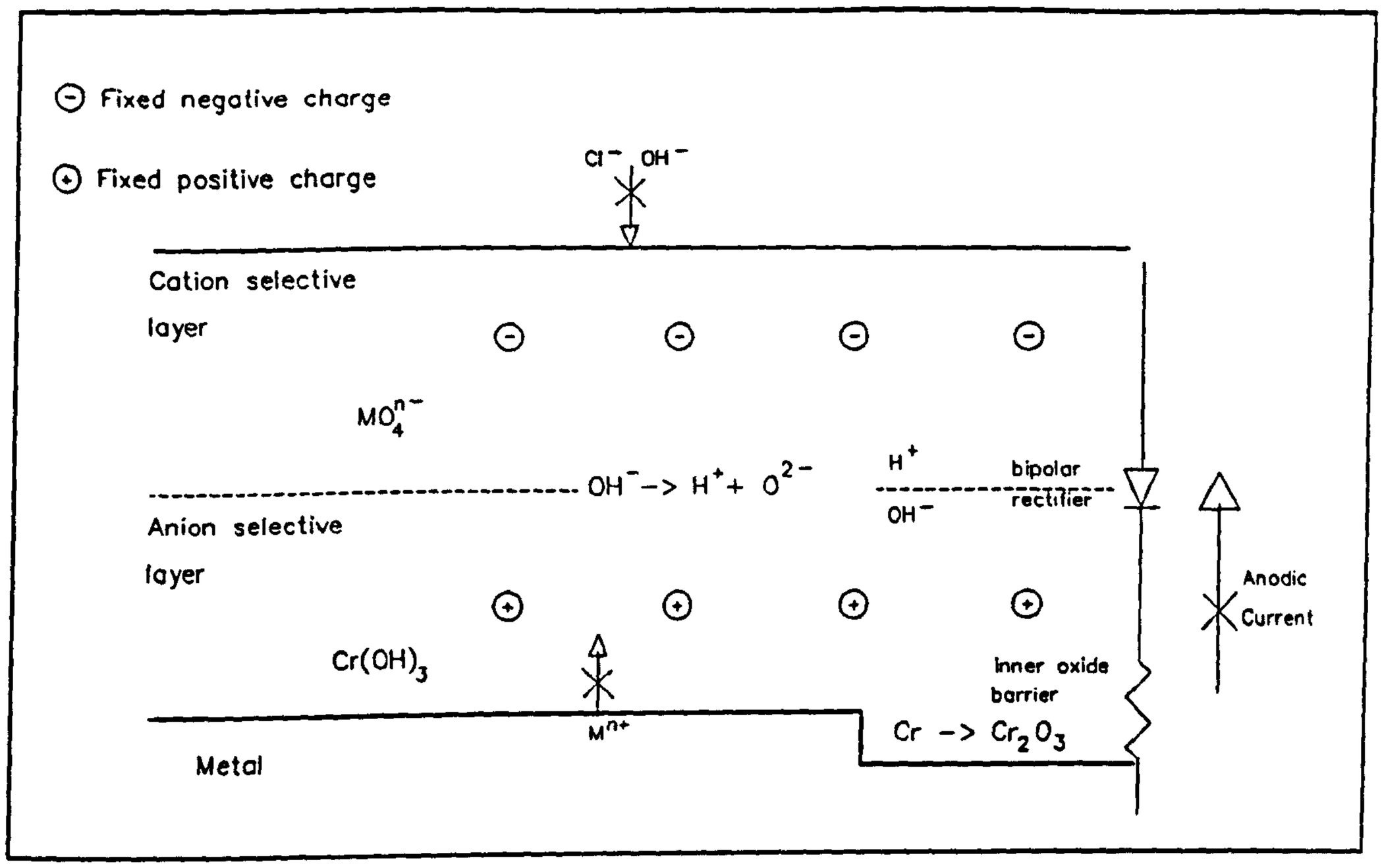

Figure 2.9 Schematic representation of bipolar passive film (after Brooks[81]).

These Cr-O bonds determine the strength of the passive film, and thus the extent of alloy passivity depends on the efficiency of the rate of proton escape *ie* the efficiency of the cation selective layer.

Mo additions, such as are made to 316 stainless steels, improve the passive behaviour of such alloys[88]. MoO_4^{2-} is thought to form by reaction of Mo^{4+} and lattice water[83,89,89,90] in the following manner:

$$MoO(OH)_2 + 4OH^- \rightarrow MoO_4^{2-} + 3H_2O + 3e^-$$

MoO_4^{2-} can act as a cation selective species[91]. In conjunction with CrO_4^{2-}, it increases the efficiency of the outer cation selective layer, thereby providing greater resistance to hostile species such as Cl^-.

At potentials approaching the transpassive region, CrO_4^{2-} is lost from the film by selective dissolution , and the film becomes enriched in Cr_2O_3. This is due to the CrO_4^{2-} species being formed at the metal-electrolyte interface and being lost by subsequent dissolution[81].

Chapter 3 A Polarization Curve Model For Passivating Materials

3.1 INTRODUCTION

The SIMPLER™ (SImulation and PLotting of Electrochemical Reactions) software model has been written at the Royal Naval Engineering College[92,93]. It models the polarization of an electrode as the result of the summation of the partial currents resulting from all the anodic and cathodic reactions occurring upon the surface of the electrode.

To correlate the results predicted by the model with experimental data, the SIMPLER™ software has two main parts. The first part is the model, which performs the calculations necessary to display a wide range and number of redox processes, such that the overall polarization curve may be found by summation of all relevant reactions. The second part is a library, which allows the retrieval of any curve, whether imported from experimental sources or previously calculated by the model.

The model calculates the redox potential for each of the electrode processes selected under chosen conditions of pH, species activity, solution resistance and temperature by using a generalised form of the Nernst equation. The currents due to activation, diffusion and resistance polarization are then calculated at each increment of potential. This is repeated for all the reactions under consideration, and then the sum of the respective anodic (positive) and cathodic (negative) currents is calculated. The final data file of net current and potential readings constitutes the resultant curve. The software then outputs all the individual curves, along with the overall curve to the screen. Graphics hardcopy is also

available.

Parameters that can be altered freely include pH, temperature, and oxygen concentration. The SIMPLER™ modelling software has successfully been used for the corrosion behaviour of iron in water, steel in flowing and diluted seawater, painted steel in seawater[92] and zinc in acidified sodium chloride solutions. Recent work has also been carried out to model the corrosion of surfaces flame-sprayed with ceramic coatings [94], and the behaviour of stainless steel in ferric chloride [95].

At present, the commercially available version of SIMPLER™ is not able to model strongly passivating behaviour, and this chapter describes the development of an algorithm for modelling and evaluating such behaviour.

3.2 POLARIZATION CURVE MODELS

3.2.1 Equations Used to Model Non-Passivating Behaviour

Various other attempts to model polarization curves[96,61,97,98,99,100,101,102,103,104] have been made. All have used equations which have current density (i) as their subject. They consider that the total anodic and cathodic currents can be represented by combinations of partial currents, each of which represent a single reaction, and can be defined by a single equation. These equations are either considered as independent (ie cathodic reactions) or competitive (anodic reactions, such as activation and passivation).

Hines and Edeleanu realised that although it is quite easy to rearrange equations with only a single component, such as a reaction solely under activation control, this is not

the case for a reaction under both activation and diffusion control. Instead, they neglected the effect of solution resistance, and considered the film resistance to be either negligible, or so large that it rendered all other components of polarization to be negligible[99]. This allows a less complicated expression with i as the subject. In order to avoid the use of "seriously ill-conditioned equations" [99], a further mathematical simplification is made.

In order to avoid the use of i_o and E_o, a *characteristic potential* (E^*) for each redox reaction is considered. E^* is defined as the potential at which the current density has unit value[96,99]. This is dependent upon which units of current density are being used, and often does not lie on the actual curve. It is instead considered as a mathematical quantity. The equation used to model the combined current density due to the activation-controlled and diffusion-limited current densities is shown below:

$$i = \frac{i_{lim}}{1 + i_{lim}\exp(\frac{E^* - E}{B_x})} \qquad 3.1$$

where

i_{lim} is the limiting current density

E^* is the characteristic potential

E is the potential

B_x is either the anodic (B_a) or cathodic (B_c) Tafel constant ($RT/\alpha zF$)

The polarization curve is generated by inserting relevant values of i_{lim} , E^* and B_x into the equation, and incrementing the value of E used in order to obtain a set of E-i values. These may then be plotted on a semi-logarithmic scale.

Such an equation yields acceptable curves, but the introduction of E^*, which often does not lie on the actual curve, is a simplification which the SIMPLER™ software does not use.

In order to model the combined effects of activation, diffusion and resistance polarization, the algorithm used by the SIMPLER™ software mimics a real experiment, which applies potentials and measures current. This is a true potentiodynamic system. Thus E is the independent variable, and *i* the dependent variable. Unfortunately, the expression for the total polarization is :

$$\eta_{total} = \eta_{act} + \eta_{diff} + \eta_{IR} \qquad 3.2$$

This is solvable for *i* in terms of E, and interpolation is used to overcome the problem.

3.2.2 The SIMPLER™ Algorithm

To model the activation-controlled polarization, the algorithm rearranges the Tafel equation

$$\eta = b_x \log(\frac{i}{i_0}) \qquad 3.3$$

to the form shown here :

$$i = 10^{\frac{\eta}{b_x}} + i_0 \qquad 3.4$$

where i is the activation controlled current density

i_o is the exchange current density

η is the polarization ($E - E_1$)

b_x is either the anodic (b_a) or cathodic (b_c) Tafel constant ($2.303RT/\alpha zF$)

R is the gas constant (8.314 J mol^{-1} K^{-1})

T is the absolute temperature (K)

It should be noted that the SIMPLER algorithm uses current densities expressed in base 10 logarithms, in contrast to Hines, who used natural logs. Thus the Tafel constants in the latter model are denoted by upper case symbols, while those used in the SIMPLER model are shown in lower case. The two are related by a conversion factor of 2.303.

E_1 is calculated from the Nernst equation in the following manner:

$$E_1 = E_0 \pm (\frac{c}{d})\frac{RT}{F}pH \pm (\frac{a}{b})\frac{RT}{F}[ion] \qquad 3.5$$

The SIMPLER™ model then calculates the Tafel constants (b_{anodic} and $b_{cathodic}$) in the following way:

$$b_x = \frac{2.303RT}{\alpha zF} \qquad 3.6$$

where

if a = 0, then z = (d/c)

otherwise

if $a \neq 0$, then $z = (b/a)$

The problems of rearranging complex equations to make *i* the subject are overcome by using an interpolation method for the solution of the equations. The software calculates the current density due to charge transfer for a given reaction using the Tafel relationship, using increments of potential over the range of potential to be studied. When the activation-controlled current density approaches 0.8 times the diffusion-limited current density (a user defined input parameter), the mathematical routine then applies a series of forty predefined constants (between 0 and 1) to this diffusion-limited current density. In the region of between 0.8 and 1.0 times the diffusion limited current density, the potential is calculated by adding the redox potential to the overall polarization due to the summing of the individual polarization components. These polarization components are calculated from the charge transfer, the diffusion limited and the solution currents. The equations used are given in equations 3.7 to 3.9.

$$\eta_{lim} = \frac{2.303RT}{zF}\log(1 - \frac{i}{i_{lim}}) \qquad 3.7$$

$$\eta_{sol} = ohm * i \qquad 3.8$$

$$\eta_{activation} = b_x \log\frac{i_0}{i} \qquad 3.9$$

ohm in equation 3.8 is the resistance associated with the electrolyte and the metal

surface.

This region now uses *i* as the dependent variable, as opposed to the potential region below 0.8 times the diffusion limit, which uses E. In order to generate a smooth curve, the series of equally spaced *i* and corresponding E values must be converted to equally spaced E values and corresponding *i* values. This is achieved by the use of a standard cubic-spline based mathematical interpolation routine.

Above the limiting current density, E is again used as the dependent variable, with the *i* value corresponding to the diffusion limit.

In this way, SIMPLER™ avoids the use of a characteristic potential E^*.

3.2.3 Passivation Algorithms

There have been several attempts to synthesise polarization curves which exhibit passivating behaviour.

3.2.3.1 Devereux and Yeum

Devereux and Yeum[96] studied the behaviour of 304 stainless steel in deaerated sulphuric acid. They modelled passivating behaviour by reversing the sign and direction of the Tafel slope of the preceding anodic charge transfer reaction, until the line intersected the passive current density represented by a vertical line (see Figure 3.1).

Such an approach yielded curves of the correct general form, but were not very successful in mapping the curvature of the active-to-passive transition closely. At potentials

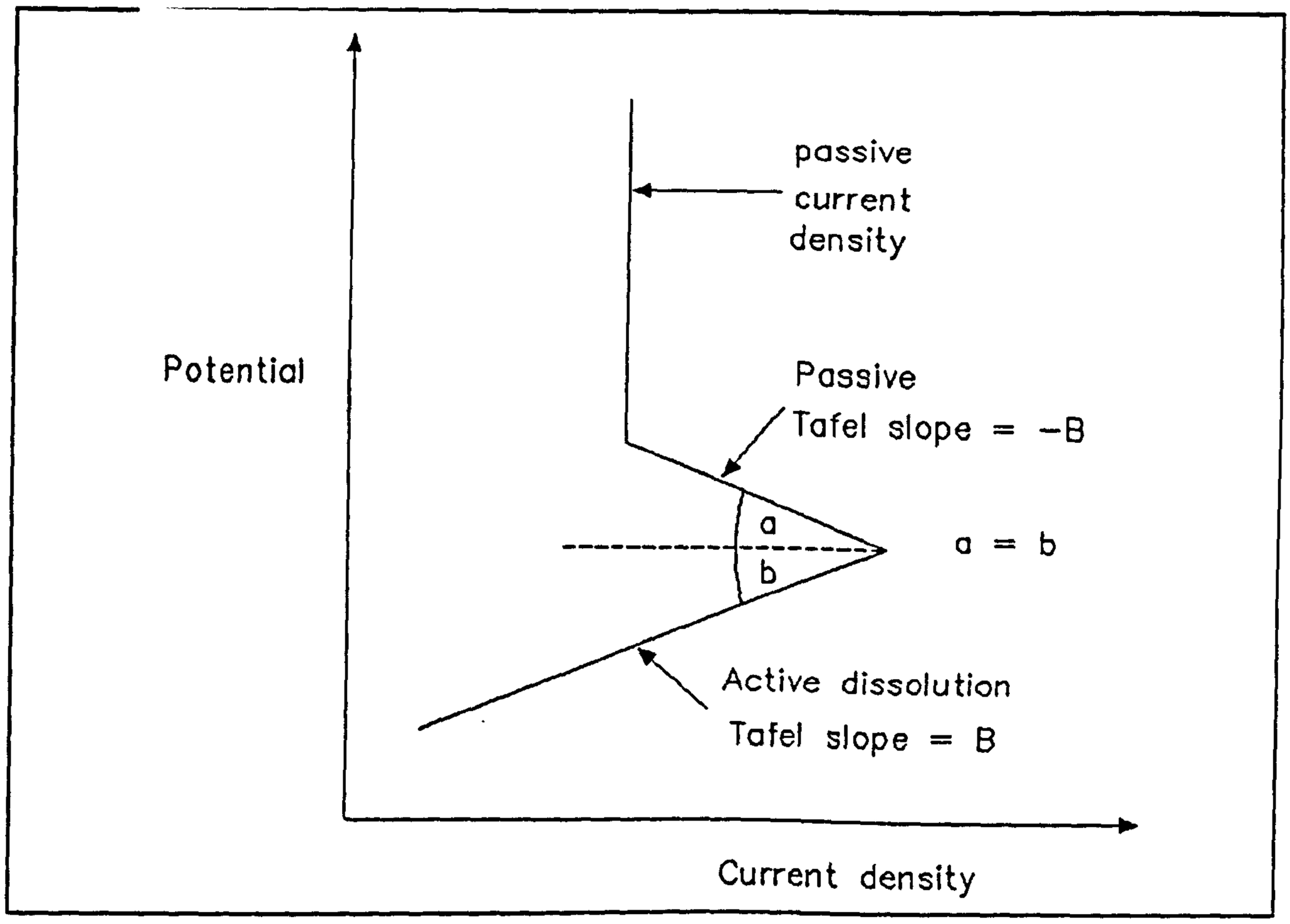

Figure 3.1 Schematic of Devereux and Yeum Model.

more electropositive than the passive region, their model appears to be incorrect. This is discussed in Section 4.2.3.3.

3.2.3.2 Bernhardsson

Bernhardsson[60,61] used an alternative algorithm based upon the Langmuir adsorption isotherm to model the behaviour of stainless steels. The Langmuir adsorption isotherm is an equation derived from the kinetic theory of gases, which relates the amount of gas adsorbed at a plane solid surface to the pressure of gas in equilibrium with the surface. In this derivation, it is assumed that the adsorption is restricted to a monolayer at the surface, which is considered to be energetically uniform. It is also assumed that there is no interaction between the adsorbed species. The equation shows that at a gas pressure, p, the fraction θ, of the surface covered by the adsorbate is given by :

$$\theta = \frac{gp}{1 + gp} \qquad 3.10$$

where g is a constant called the adsorption coefficient, which is the equilibrium constant for the adsorption process.

Bernhardsson used the rotating disc electrode test devised by Armstrong[55] to determine that chemisorption was the reaction mechanism responsible for anodic passivation, rather than dissolution-precipitation. Contradictory results have been obtained by Bockris[53]. The reaction mechanism used by Bernhardsson[61] (based upon the work of Lorenz *et al*[105]) for his model in this treatment is shown below:

$$\begin{array}{ccccccc} & +OH^- & & & & & \\ & -e^- & & -e^- & & -OH^- & \\ M & \rightleftharpoons & (MOH)_{ads} & \underset{RDS}{\rightleftharpoons} & MOH^+ & \rightleftharpoons & M^{2+}_{aq} \\ \updownarrow & +OH^- & & +OH^- & & & \\ & -e^- & & -e^- & & & \\ & [M(OH)_2]_{ads} & & \underset{RDS}{\rightleftharpoons} & [M(OH)_3]_{ads} & \rightleftharpoons & oxide \\ & & & & \theta & & \end{array} \qquad 3.11$$

The total anodic current density, i_t, for a stainless steel, may be expressed as :

$$i_t = (i_a + i_{ox}).(1 - \theta) \qquad 3.12$$

where

i_a = partial current density due to anodic dissolution

i_{ox}= partial current density due to anodic passivation

θ = degree of coverage of $M(OH)_3^{ads}$

The Langmuir isotherm may be expressed as :

$$C\frac{d\theta}{dt} = k_{ox}(1 - \theta) - k_d\theta \qquad 3.13$$

k_d is the dissolution rate of the passive film. k_{ox} is assumed to be dependent upon potential, while k_d is assumed to be potential-independent. C is a measure of species[61] adsorbed onto the surface. In the steady state:

$$C\frac{d\theta}{dt} = 0 \qquad 3.14$$

hence :

$$\theta = \frac{k_{ox}}{k_{ox} + k_d} \qquad 3.15$$

If the charge transfer valences for k_d and k_{ox} are assumed to be equal, multiplication by zF leads to :

$$\theta = \frac{i_{ox}}{i_{ox} + i_d} \qquad 3.16$$

i_d is taken as the passive current density supported by the metal surface (a constant), while i_{ox} is the current density supported by the film while undergoing the active-to-passive transition. Combining Equations 3.12 and 3.16 :

$$i_t = \frac{i_d(i_a + i_{ox})}{i_d + i_{ox}} \qquad 3.17$$

now :

$$i_a = A_a \exp(B_a E) \qquad 3.18$$

$$i_{ox} = A_{ox} \exp(B_{ox} E) \qquad 3.19$$

where E is the potential

$$A_i = i_i^o \exp(-B_i e_i^o)\ A\ cm^{-2}\ vs\ E_{ref} \qquad 3.20$$

and

$$B_i = \frac{2.303}{b_i}\ mV^{-1} \qquad 3.21$$

where b_i =Tafel slope

i_i^o= exchange current density

e_i^o=single equilibrium potential

A_i depends on the value of the reference electrode chosen.

Equation 3.17 may now be rewritten in the following form :

$$i_t = \frac{i_d[A_a\exp(B_aE)+A_{ox}\exp(B_{ox}E)]}{i_d + A_{ox}\exp(B_{ox}E)} \qquad 3.22$$

This is a function describing an anodic polarization curve with one maximum. For the region where current density decreases with increasing potential,

$$i_a > i_{ox} > i_d \qquad 3.23$$

Thus,

$$i_t = \frac{i_d\, A_a\exp(B_aE)}{A_{ox}\exp(B_{ox}E)} \qquad 3.24$$

ie

$$i_t = i_d\frac{A_a}{A_{ox}}\exp[E(B_a - B_{ox})] \qquad 3.25$$

The slope of the curve prior to the maximum current density is given by B_a, while the slope of the curve between the current maximum and the passive current density is given by $(B_a - B_{ox})$.

Bernhardsson used this equation to analyze the behaviour of a number of stainless steel alloys in sulphuric acid. He found that the addition of chromium increases the rate of

anodic dissolution and passivation, while nickel and molybdenum have the opposing effect. The algorithm used here does not consider any cathodic reactions. Unfortunately, the anodic polarization curve and the hydrogen evolution reaction (the dominant cathodic reaction in the deaerated acid solutions considered by Bernhardsson) overlap in the region of interest, complicating the determining of A_a and B_a. In such cases, he took B_a to have a constant value. It is shown later (Sections 4.2, 4.3 and 4.4) that the position of the hydrogen evolution reaction alters (with respect to the potential and current density axes of a polarization curve) with different stainless steels, as well as different solution oxygen concentrations and temperatures.

3.2.3.3 Mueller

Mueller[97] developed an algorithm to describe the passivating behaviour of materials based on the assumption that OH^- ions react with the metal surface and form a passivating film. During the conversion from the active to passive state, the rate of the anodic dissolution is assumed to be proportional to the ratio of film-free area to total area. The electrochemical reaction for the formation of the passivating film is :

$$M + n(OH)^- \rightarrow M(OH)_n + ne^- \qquad 3.26$$

The rate of this reaction depends on the OH^- concentration and the metal-electrolyte potential difference. If oxygen-free solutions are considered, the rate of formation of filmed surface r_f on a film-free surface at pH 0 is given by :

$$r_f = r_0[\ 2.3n_{OH}\ (pH) + \frac{\alpha_p n_p F}{RT}(E - E_0)] \qquad 3.27$$

where r_o is the rate of formation on a film-free surface at pH = 0

E_o is a characteristic potential at pH = 0

n_{OH} is the order of the process with respect to OH^-

α_p is the symmetry factor

n_p is the valency controlling the rate of oxide formation

At steady state, the rate of film formation is equal to the rate of film dissolution. Hence

$$a_c r_c = a_f r_f \qquad 3.28$$

where a_c is the film-covered area

a_f is the film-free area

r_c is the rate of film dissolution of metal oxide or hydroxide

r_c is assumed to be potential-independent, as no charge is exchanged on dissolution of the passive film. The ratio of film-free to total area is given by :

$$\frac{a_f}{a_t} = 1 + \frac{r_f}{r_c} \qquad 3.29$$

Combining Equations 3.27 and 3.29 leads to :

$$\frac{a_f}{a_t} = \frac{1}{1 + \frac{r_0}{r_c}\exp[2.3n_{OH}(pH) + \frac{\alpha_p n_p F}{RT}(E - E_0)]} \qquad 3.30$$

The anodic current density of a totally film-free area is given by :

$$i_a = i_0 f(pH) \exp \frac{\alpha_a n_a F}{RT}(E - E_0) \qquad 3.31$$

f(pH) is the dependence of the Tafel relationship on pH.

If it is assumed that only the film-free areas contribute to the anodic current, and that the partial coverage of the surface by an insoluble film reduces this current density to an amount that is proportional to the ratio of the film-free area to total area, then Equations 3.30 and 3.31 may be combined to calculate the anodic current density i_{af} during the transition :

$$i_{af} = i_o \frac{f(pH) \exp \frac{\alpha_a n_a F}{RT}(E - E_0)}{1 + \frac{r_0}{r_c} \exp[2.3 n_{OH} + \frac{\alpha_p n_p F}{RT}(E - E_0)]} \qquad 3.32$$

To use Equation 3.32, the ratio r_o/r_c must be known. There is a relationship between r_o/r_c and i_{po}/i_p ($i_{po} = i_p$ at pH = 0). When 50% of the surface is covered with the protective film, the current density $i_{0.5}$ becomes 50% of the value predicted for a film-free surface, and the potential becomes $E_{0.5}$. When $E = E_{0.5}$ in Equation 3.32, $i_o f(pH) = 2i_{0.5}$ and thus the denominator becomes 2. Thus :

$$\frac{r_o}{r_c} \exp[2.3 n_{OH} + \frac{\alpha_p n_p F}{RT}(E_{0.5} - E_0)] = 1 \qquad 3.33$$

Where $E_{0\text{-}0.5}$ for $E_{0.5}$ at pH = 0

$r_{0\text{-}0.5}$ for r_o at pH = 0 and E = 0.5

From Equation 3.33, $r_{0\text{-}0.5}$ equals r_c when E_o equals $E_{0\text{-}0.5}$. Thus :

$$\frac{r_{0\text{-}0.5}}{r_c}\exp[2.3n_{OH}(pH) + \frac{\alpha_p n_p F}{RT}(E_{0.5} - E_{0\text{-}0.5})] = 1 \qquad 3.34$$

$$\frac{r_{0\text{-}0.5}}{r_c} = \frac{i_{po}}{i_p} \qquad 3.35$$

Substituting Equation 3.35 into Equation 3.32 results in :

$$i_{af} = \frac{i_o f(pH)\exp\frac{\alpha_a n_a F}{RT}(E - E_o)}{1 + \frac{i_{po}}{i_o}\exp[2.3n_{OH}(pH) + \frac{\alpha_p n_p F}{RT}(E - E_{0.5})]} \qquad 3.36$$

The current density of the anodic dissolution current on a film-free surface may be described by using any pair of related i and E values to replace $i_o f(pH)$ and E_o, such as $2i_{0.5}$ and $E_{0.5}$. Thus the second term of the denominator of Equation 3.36 may be expressed as :

$$\frac{i_{po}}{i_p}\exp[2.3n_{OH}(pH) + \frac{\alpha_p n_p F}{RT}(E_{0.5} - E_{0\text{-}0.5})]\exp\frac{\alpha_p n_p F}{RT}(E - E_{0.5}) \qquad 3.37$$

Substituting Equation 3.35 into 3.32, and the result into 3.37, it is found that:

$$i_{af} = 2i_{0.5}\frac{\exp\frac{\alpha_a n_a F}{RT}(E - E_{0.5})}{1 + \exp\frac{\alpha_p n_n F}{RT}(E - E_{0.5})} \qquad 3.38$$

This expression does not include the current density attributable to the dissolution of the passive film at a completely filmed surface. This partial current density i_d is proportional to the ratio of the film-covered to total area. From Equations 3.30 and 3.33, this ratio is given by :

$$\frac{1}{1} + \exp\frac{\alpha_p n_p F}{RT}(E - E_{0.5}) \qquad 3.39$$

If the ratio of film-covered to total area is considered as a factor of i_p, then :

$$i_d = i_p\frac{\exp\frac{\alpha_p n_p F}{RT}(E - E_{0.5})}{1 + \exp\frac{\alpha_p n_p F}{RT}(E - E_{0.5})} \qquad 3.40$$

If i_d forms a substantial part of the total current density, then the combined current density i_c requires the addition of i_d to i_{af}:

$$i_c = \frac{2i_{0.5}\exp\frac{\alpha_a n_a F}{RT}(E - E_{0.5}) + i_p\frac{\alpha_p n_p F}{RT}(E - E_{0.5})}{1 + \exp\frac{\alpha_p n_p F}{RT}(E - E_{0.5})} \qquad 3.41$$

Equation 3.41 is an expression for the anodic current density as a function of potential including both the active and the passive states.

The form of the curve described by Equation 3.41 depends on the value of β, where :

$$\beta = \frac{\alpha_p n_p}{\alpha_a n_a} \qquad 3.42$$

A unity value of β leads to an S-shaped transition, while a value of 2 leads to a symmetrical transition . If the value of β exceeds 2, then the decrease in the current density in the active to passive transition exceeds the rate of increase of current density in the solely active state. No comparisons were made with experimental data.

3.2.3.4 Trethewey and Wilson

Trethewey and Wilson[98] adopted an empirical approach in which five separate modes of behaviour in a polarization curve were considered as having equations of the form:

$$i = C + Ae^{(BE)} \qquad 3.43$$

where i is the current density

E is the potential

A,B,C are positive or negative constants.

The modes considered were the cathodic region, the anodic region, the active-to-passive transition, the passive region and the transpassive region. The polarization curve was generated by summing the five curves. The curves generated by this model were of the general form required, but this approach was discontinued in favour of more theoretically based equations. This new approach[92,93] has been detailed in section 3.2.2, and the work detailed in sections 3.3 and onwards represents the addition of passivating behaviour to this model.

3.2.3.5 Hines

Hines and Edeleanu[99] assumed that the transition between active and passive regions could be modelled by dividing the surface into proportions of two independently behaving regions. These regions are assumed to support the competing active (charge transfer) and passive reactions, which occur in the same manner as outside the transition region. This may be represented as :

$$i_{anodic} = Si_{active} + (1-S)i_{passive} \qquad 3.44$$

where i_{active} and $i_{passive}$ are represented by equations used outside of the transition area, i_{anodic} is resultant current density, and S is a function which governs the proportion of the surface supporting the reaction in which metal ions are formed at the greatest rate. S ranges from 1 at the start of the transition loop to 0 at its end.

Thus their model made two major assumptions :

(i) The partial currents are independent;

(ii) The surface of the immersed metal may be regarded as supporting two independent processes during the transition between two corrosion processes.

3.2.4 Rationale Behind Algorithms Used

The Devereux and Yeum approach was considered to be an over-simplification, while Trethewey and Wilson's method was not used as it was wished to use equations representing solution, activation and diffusion polarization effects for non-passivating behaviour.

Bernhardsson's method, although it considered a chemisorption mechanism, was considered to be flawed in that it did not allow for any alteration in the kinetics of the hydrogen evolution reaction. This is shown later not to be the case (Sections 4.2 and 4.3) This would have caused greater problems in aerated solutions, where the oxygen reduction process would also overlap with the anodic curve close to the region of interest.

Mueller's model also considered chemisorption as the mechanism responsible for passivation. However, it required the determination of $E_{0.5}$ (the potential at the midpoint of the active-to-passive transition) prior to being able to calculate the form of the anodic polarization curve. This is not as easy as determining E_t (the potential at which the anodic polarization curve deviates from being solely under a single activation controlled process) required by the Hines model. As a result, the Hines algorithm was used as the basis for

modelling the behaviour of passivating systems.

The model proposed for the passivation algorithm therefore consists of the anodic reaction being that of iron being selectively dissolved (under activation control) from the surface. The current due to this process is i_{active} in Equation 3.44. At a potential of E_t (in this active dissolution region), there is a deviation from the behaviour predicted by solely activation-controlled kinetics. This is assumed to be the point at which the surface coverage by anions begins to be noticeable. The current density attributable to this now-passivated surface is $i_{passive}$ in Equation 3.44, while S is the fraction of the surface not covered by this film.

3.2.5 Equations Used for Transitions

In order to model the transition between (active and passive) states, an S-function can be used, as described in Section 3.2.2.5. The transition can then be thought of in two ways:

1 : The active-to-passive transition is deemed to be a nucleation and growth process, and S is the fraction of the surface not affected by the transition. The 'raindrop' equation was first used to consider ripples caused by a raindrop in a pond[106]. It is shown in a modified form below :

$$S = Exp(-A(E - E_t)^p) \qquad 3.45$$

where E_t is the potential at which nucleation begins.

A and p are determined empirically, and S-curves derived using such assumptions

are asymmetrical around the midpoint. The experimentally observed hysteresis on active-to-passive and passive-to-active transitions can be modelled by treating them separately[99].

2 : The model for the transition assumes the surface, whether metal or film, changing its composition via two redox reactions, which both contribute partial currents under activation control. The proportions of the species in question are determined by the redox reaction, thus :

$$S = \frac{X}{1 + X} \qquad 3.46$$

where $X = \exp(A(E - E_t)^p)$

E_t is the potential at the midpoint of the active-passive transition.

A, p are constants

The S-curve thus obtained is symmetrical around the midpoint, defined by the potential E_t. As the form of such S-curves resembles the strong acid/strong base buffer curve, the equation is referred to as the 'buffer' equation.

Equations 3.45 and 3.46 may be used to determine the S function used in Equation 3.44.

Other authors[104,107,100,103] have used the routines devised by Hines as the basis for modelling passivating behaviour. Bird *et al* modelled the breakdown of pure iron in deaerated solutions of pH 10 - 14 with chloride ion concentrations of between 0 and 1M. The scan rate used in these experiments was 1200 mV $hour^{-1}$ ie ~ 0.33 mV s^{-1}. Marsh has

shown that there is a critical scan rate, above which polarization curves do not correlate with steady state conditions. This scan rate corresponds to the rate at which reacting species can diffuse across the double layer. For mild steel in seawater, this critical scan rate was found to be 0.2 mV s^{-1} [108].

Otieno-Alego *et al*[103] observed the behaviour of low carbon steel in sodium benzoate solutions and A470 low alloy steel in a simulated low pressure steam turbine environment. They used scan rates of between 5 and 140 mV s^{-1}, and subsequently found variations in the polarization curves generated by different scan rates.

These investigating groups have both used the 'buffer' equation, rather than the 'raindrop' equation, to model the active-to-passive transition in the systems considered.

3.3 INCORPORATION OF PASSIVATING BEHAVIOUR ROUTINES INTO THE SIMPLER™ SOFTWARE

Both the 'raindrop' and the 'buffer' equations were incorporated in the modelling calculation software. The mechanics of this process and the results generated is detailed in the following sections.

3.3.1 The Buffer Equation

As noted in section 3.2.2.6, the basis behind the use of the 'buffer' equation is the assumption that the metal surface consists of two independently-behaving regions. One of these regions is covered with a film, the other is not. As the potential of the metal surface becomes more positive, the fraction of the filmed surface increases at the expense of the

unfilmed surface fraction. The quantity S then determines the fraction of the surface unfilmed. Figure 3.2 shows the desired form of the S function plotted against potential ie S = 1 at more negative potentials, and S = 0 at more positive potentials. The passivation parameters used in the 'buffer' equation to generate the curve are shown in Table 3.1.

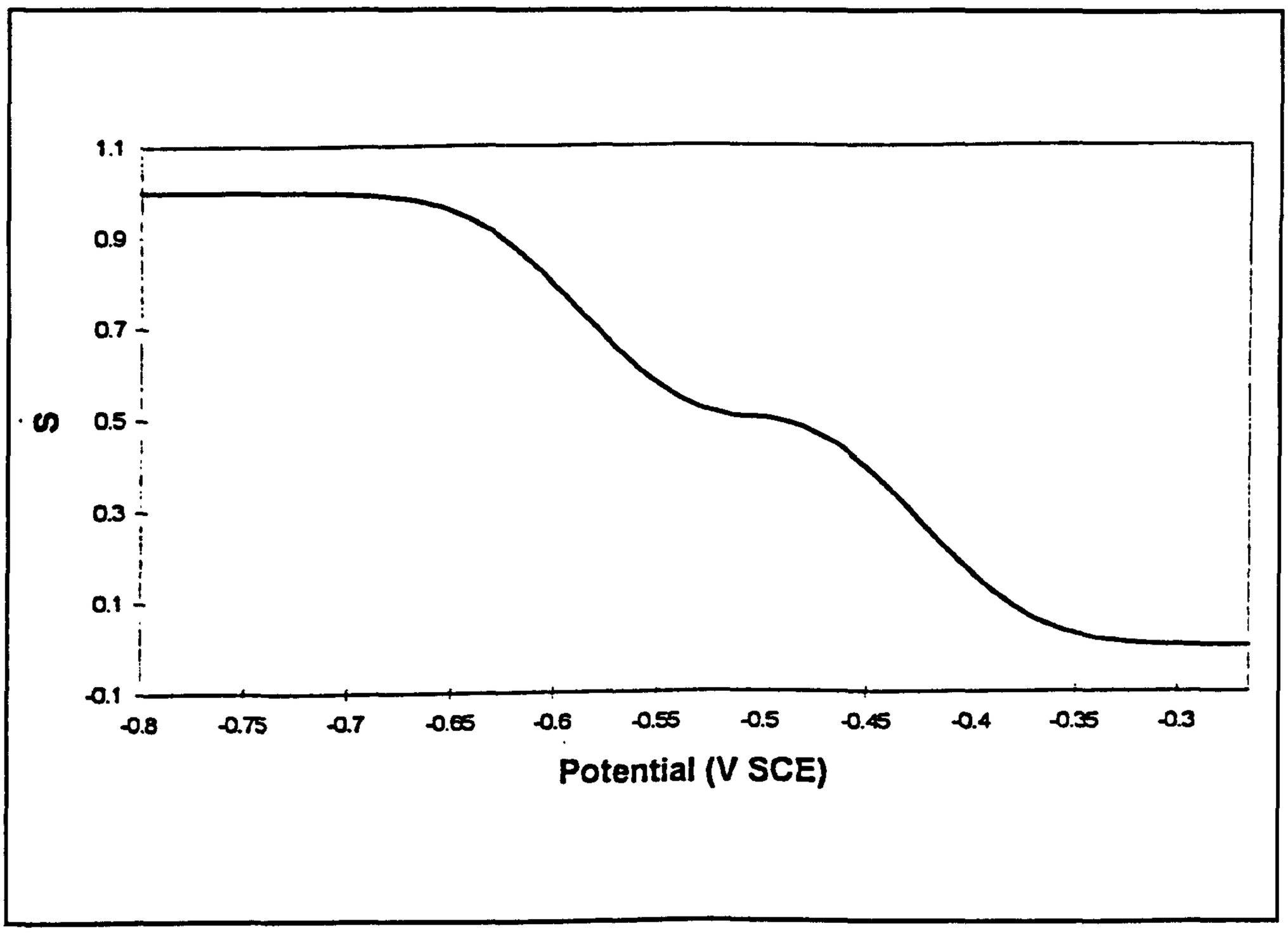

Figure 3.2 Desired form of S function plotted against potential.

The result of using the 'buffer' equation as shown in Equation 3.46 is shown in Figure 3.3. The curve of S against E (potential) was obtained by using the parameters shown in Table 3.1.

A (V^{-p})	p	E_t (V SCE)
2	2	-0.5

Table 3.1 Parameters input to the 'buffer' equation to obtain Figure 3.3.

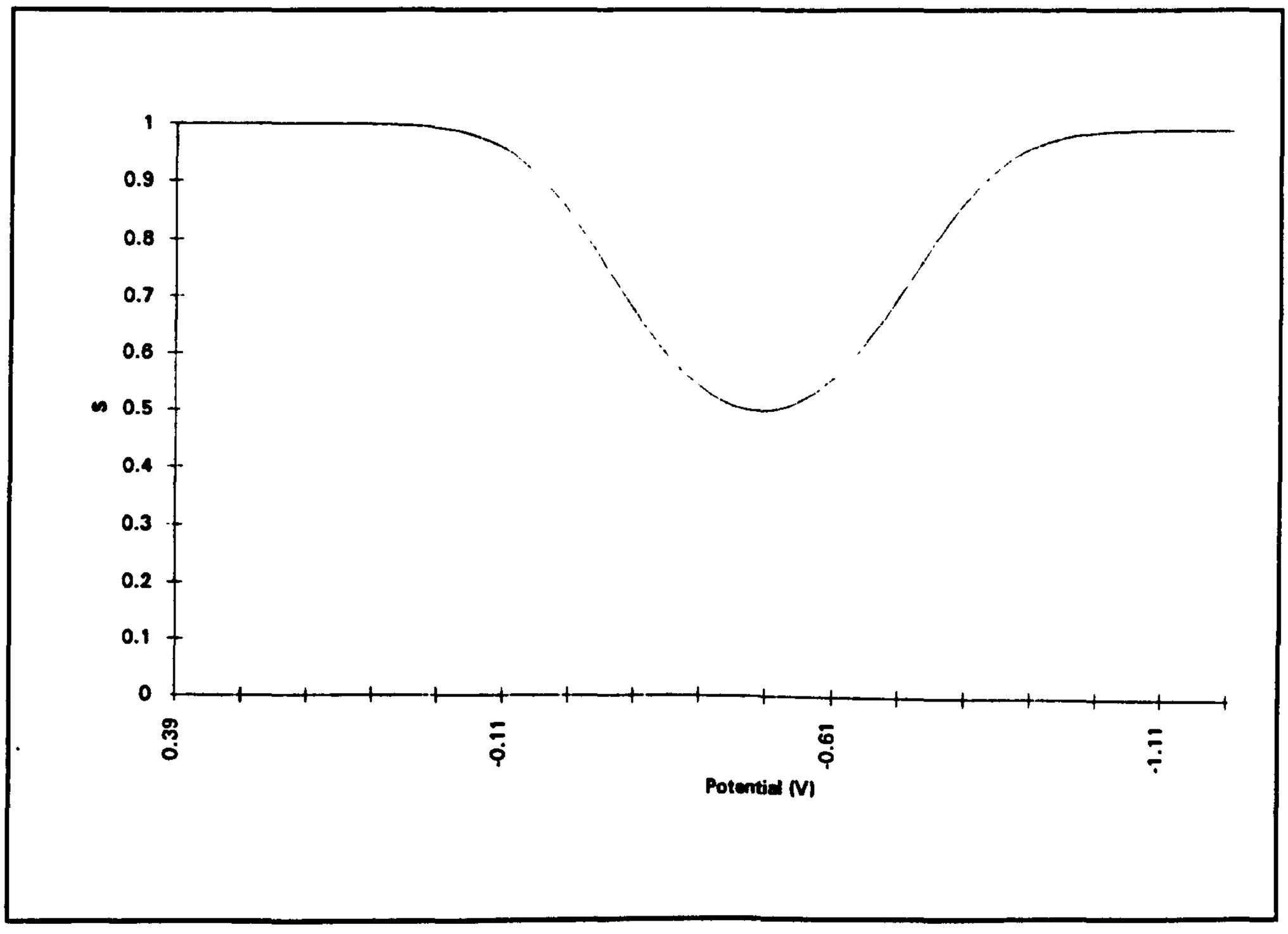

Figure 3.3 S Curve generated by original form of the 'buffer' equation.

From Figure 3.3, it may be seen that using Equation 3.46 in the above form results in an inverse bell-shaped curve. The minimum of S = 0.5 corresponds to a potential value of E_t, and the maxima of S = 1 for E values either side of E_t. This does not correspond to the desired form of S.

3.3.1.1 Alterations to Published Form of Buffer Equation

In order for S to have a value less than 0.5, $(A(E - E_t)^p)$ must be negative. This cannot occur with the above parameters, since the term $(E - E_t)^p$ will always be positive with p = 2 (or any other even number). If the constant A is multiplied by -1 when $E > E_t$, S values of between 0 and 0.5 (as desired) will be generated.

For odd values of p, the same treatment of A yields the desired form of the curve. However, negative values of $(E - E_t)$ raised to non-integer powers results in a mathematical error being reported by the computer. This can be avoided by using the absolute value of $(E - E_t)$. Such a logic scheme will yield the desired form of S curve for all values of p. Thus the algorithm required to generate S functions differs slightly from that quoted in the literature.

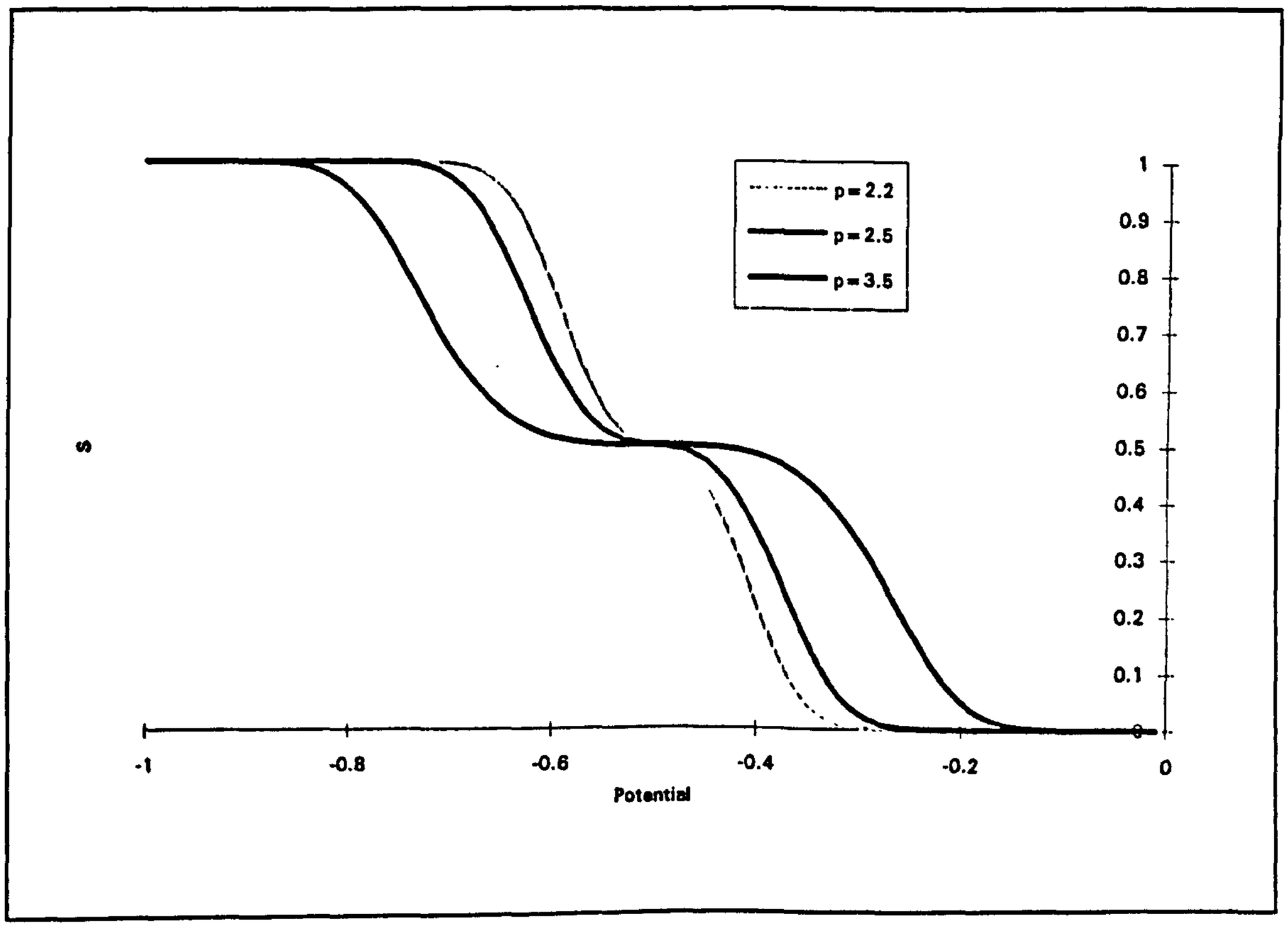

Figure 3.4 S Curves for non-integer values of p.

The effects of using this logic scheme for non-integer values of p are shown in Figure 3.4.

3.3.1.2 Incorporation of the Buffer Equation into the Modelling Software

The modified algorithm was coded into a fortran module called SBUF (listed in Appendix C) , and incorporated into the SIMPLER software. It is used in the section of the

calculation which considers the anodic activation polarization. As the potential, E, is incremented from electronegative values to more electropositive values, a check is made on the value of S. If S is less than or equal to 1, the calculated value of the current density then alters from that solely attributable to activation polarization, and instead becomes the sum of the activation polarization and passive current density components of the surface, as defined in Equation 3.44.

3.3.1.3 Floating Point Errors within The SBUF Module

Problems were found when large values of $(E - E_t)$ were input into Equation 3.45, and values of X with very small exponents were calculated. An example is shown below :

$$\text{if } (E - E_t) = 1.13 \text{ V}$$

then

$$\text{Exp}(-A(E - E_t)^p) = 7.07 \times 10^{-99}$$

where A = 200 and p = 2.

The fortran compiler could not cope with such large numbers, and a runtime error would occur. To avoid this, upper and lower limiting S value of 0.9999 and 0.0001 were used, thus :

$$0.0001 = X/(1 + X)$$

which rearranges to

$$1 + X = 10000X$$

thus

$$X = 1/9999$$

taking natural logs

$$(-A(E - E_t)^p) = -9.21$$

Similarly, an upper value of 9.21 gives an S value of 0.9999.

These new limits were coded into the SBUF routine, and such a logic sequence produces an S-curve of the desired form between 0.0001 and 0.9999, for any combination of A and p.

3.3.1.4 The Current Density Supported by the Unfilmed Metal During the Active-to-Passive Transition

The current density supported by the unfilmed metal surface is assumed to be solely under activation control. However, it is not clear whether the value of this current density should be calculated for :

(i) the value of the polarization while in the active-to-passive transition

or (ii) whether a fixed value should be taken for the value of the polarization when the transition begins.

Figure 3.5 shows the curve obtained using the current density calculated at $E = E_t$ for i_{active} in Equation 3.44 (case (ii) above). It is clear that this does not result in the correct form of the curve. For all curves modelled in sections 3.3.1.4 to 3.3.1.9 ie those modelled using the 'buffer' equation, i_o and E_o values of 1 nA cm^{-2} and -0.44 V SHE are used, together with a pH = 0 and a solution resistance of 0 ohms.

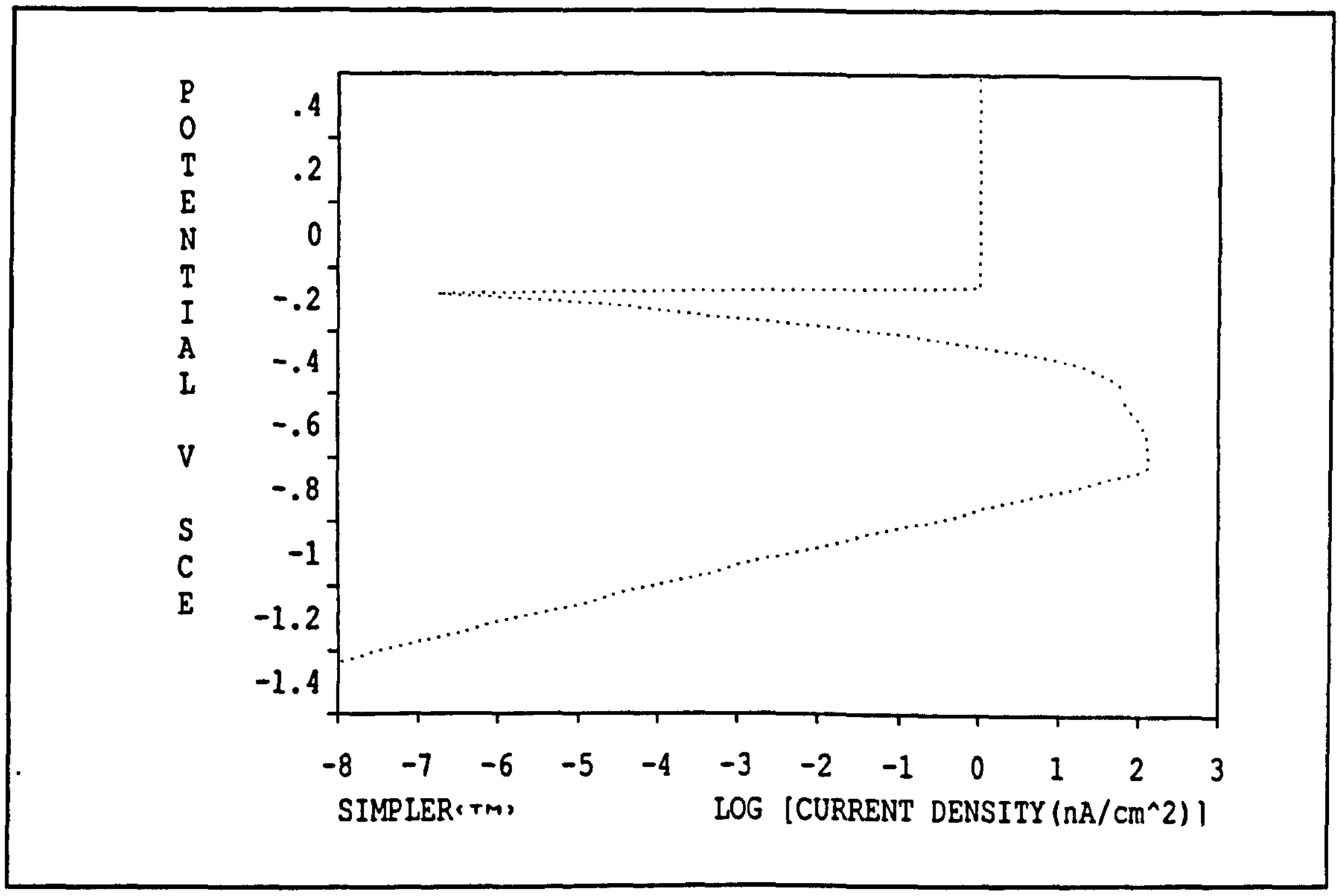

Figure 3.5 Curve generated using value of i at E_t as i_{anodic} in Equation 3.44.

Figure 3.6 is the result of using the activation-controlled current density calculated for each incremented value of E ie according to the Tafel equation.

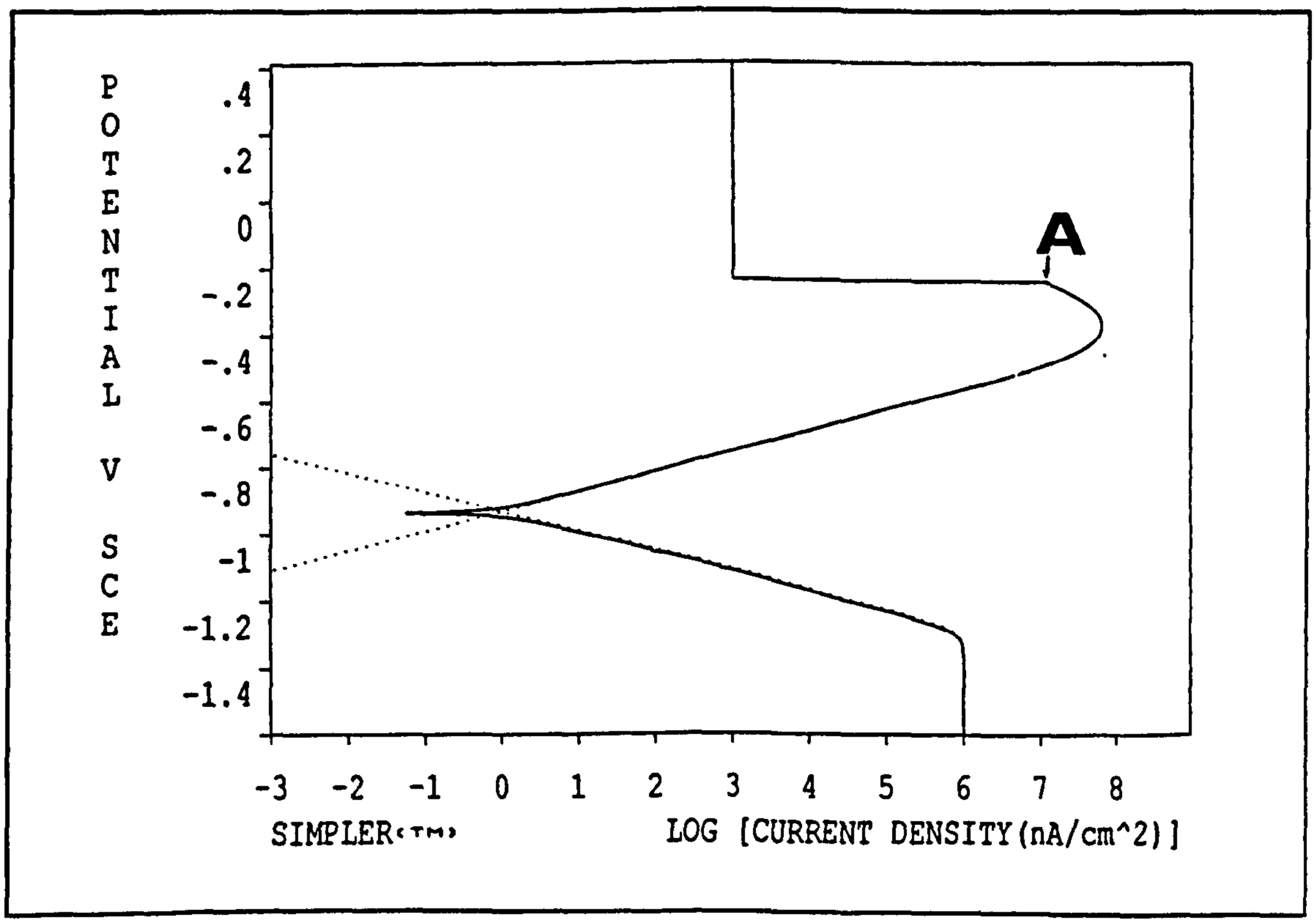

Figure 3.6 Curve generated by using Equation 3.4 for i_{active} in Equation 3.44.

This is the desired form of curve, and thus it is the varying value of *i* that is used for value of i_{active} in Equation 3.44. The parameters used to calculate Figures 3.5 and 3.6 are shown in Table 3.2.

i_{pass} (nA cm^{-2})	E_t (V SCE)	A (V^{-p})	p
1×10^3	-0.5	200	2
i_o (nA cm^{-2})	E_o (V SHE)	solution resistance (ohms)	pH
1	-0.44	0	0

Table 3.2 Passivation parameters used in Figures 3.4 and 3.5.

A further modification can be made to the logic sequence used in conjunction with the 'buffer' algorithm. The transition between the active-to-passive loop and the fully passivated surface has a discontinuity. This is marked as point A in Figure 3.6, and is due to the lower limiting value for S of 0.0001. This S value, when multiplied by a large value of i_{active}, results in a large difference between the resultant current density as calculated by Equation 3.44, and the current density solely modelled as i_{pass}. In the case of Figure 3.6, the discontinuity is almost four orders of magnitude.

As mentioned in section 3.3.1.3, upper and lower limits must be placed on S to avoid mathematical overflow errors in the fortran compiler. If the lower limiting value in the SBUF module is altered to such a value (-23) that a lowest S value of 10^{-10} is

calculated, then this discontinuity disappears. In this way, S varies between 10^{-10} and ($1 - 10^{-10}$), rather than between 0.0001 and 0.9999. Figure 3.7 shows the effect of such a lower limiting value curve generated using the parameters in Table 3.2.

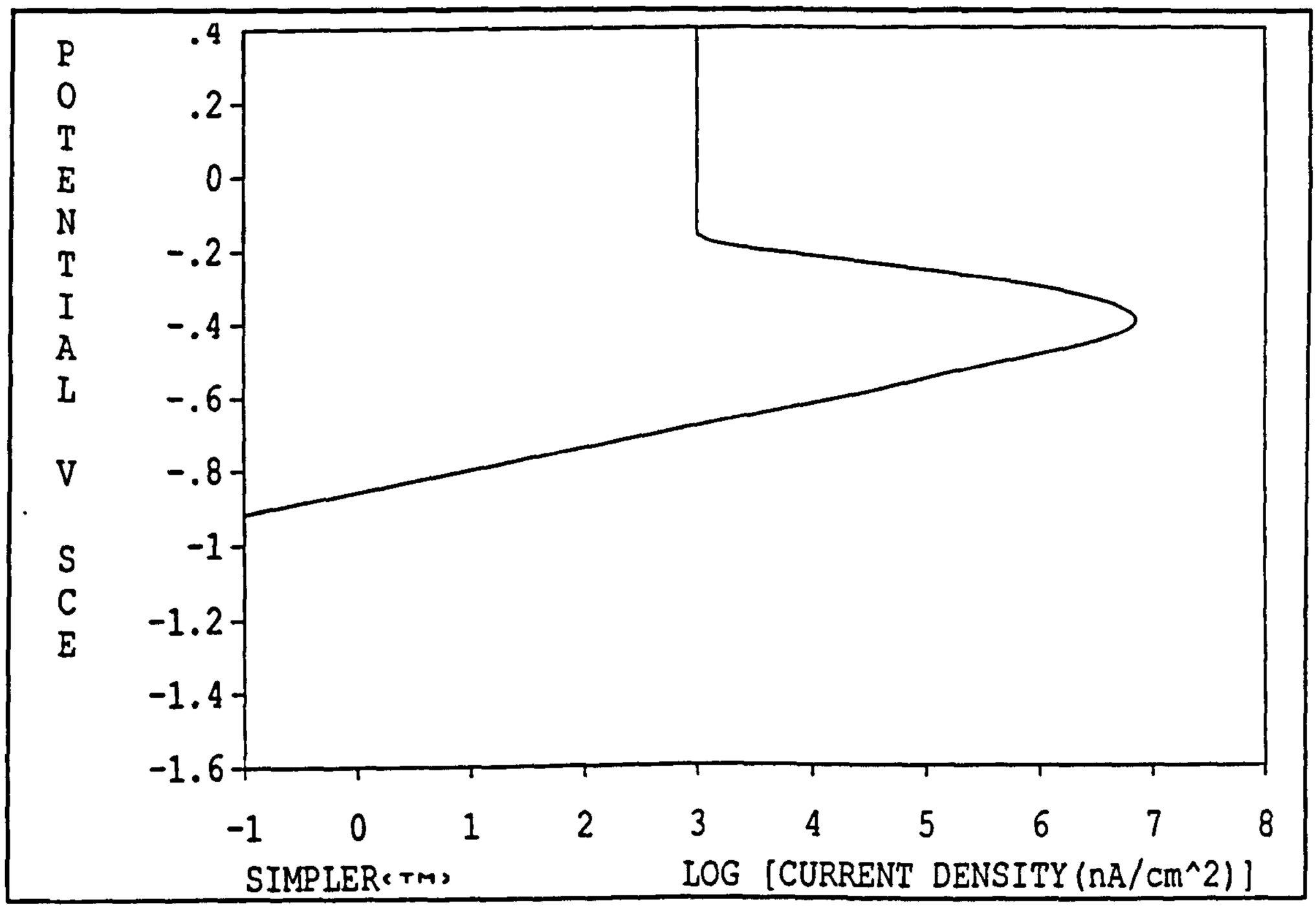

Figure 3.7 Modelled curve generated using 'buffer' equation with limiting value of log X = ± 23.

3.3.1.5 Effect of Altering the Potential at the Midpoint of the S Function

The effects of altering the potential at the midpoint of the S function are shown in Figure 3.8. The parameters used are shown in Table 3.3. Making this value more electropositive increases the width of the active-to-passive 'nose', as well as increasing i_{crit}.

i_{pass} (nA cm^{-2})	E_t (V SCE)	A (V^{-p})	p
1×10^3	-0.7 to -0.3	150	2

Table 3.3 Parameters used to generate Figure 3.8.

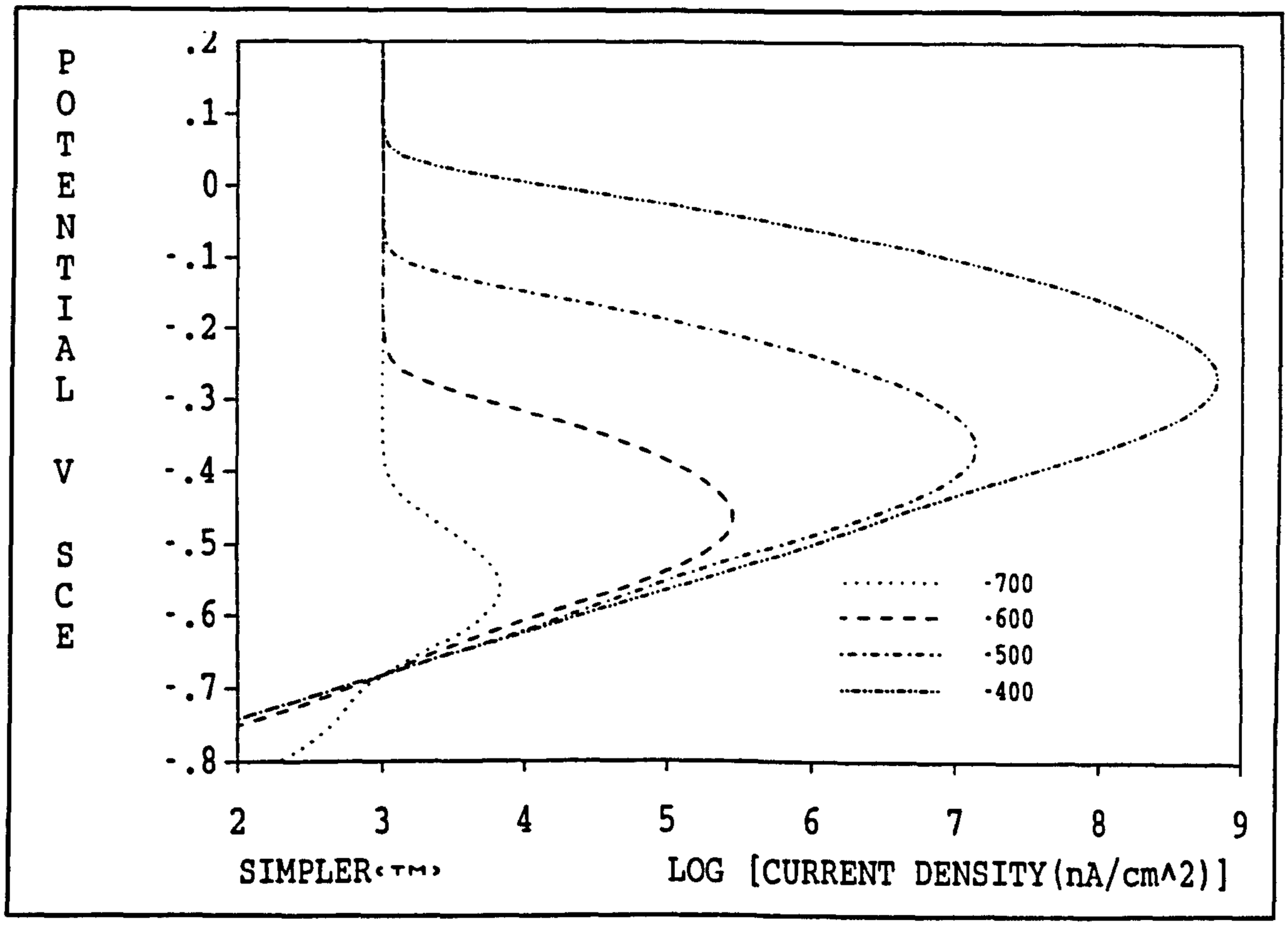

Figure 3.8 Effect of altering E_t, the potential at the midpoint of the S function on the anodic polarization curve of a passivating material using the 'buffer' equation.

3.3.1.6 Effect of Altering the Power p

The effect of altering the power p in the 'buffer' equation on the anodic polarization curve of a passivating material is shown in Figure 3.9. The parameters used are detailed in Table 3.4.

i_{pass} (nA cm^{-2})	E_t (V SCE)	A (V^{-p})	p
1×10^3	-0.5	150	1 to 3

Table 3.4 Parameters used to generate Figure 3.9.

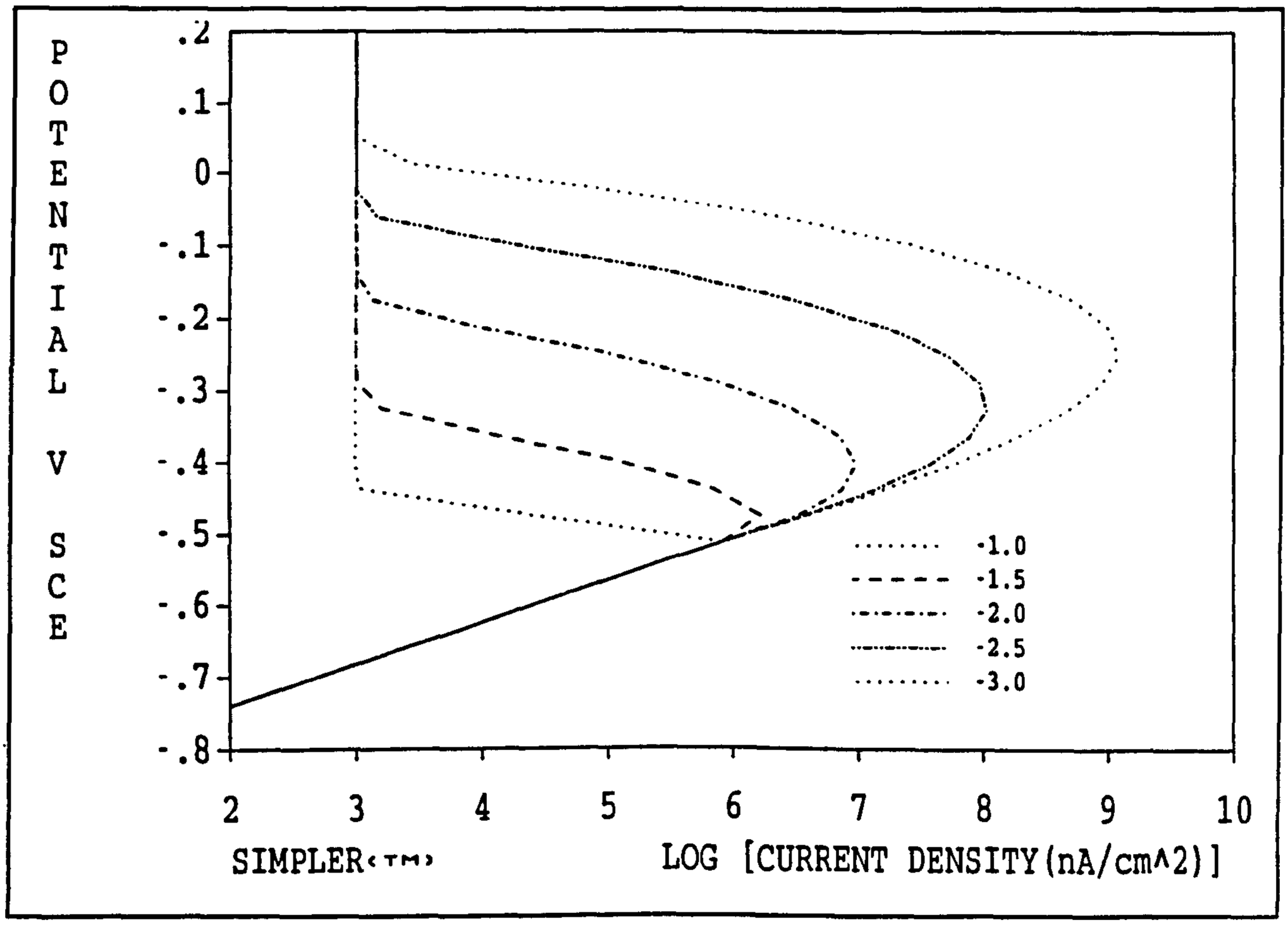

Figure 3.9 Effect of altering the power p in the 'buffer' equation on the anodic polarization curve of a passivating material.

Increasing the value of p, the power in the 'buffer' equation affects both the width of the active-to-passive nose and the value of i_{crit}, but the main effect of p is upon the shape of the nose. The curve is symmetrical around E_t when p = 1, but as may been seen from Figure 3.9, this is not true for other values of p. Rather, the gradients of the 'nose' of the curves at potentials more positive than that corresponding to i_{crit} become steeper with increasing p. Figure 3.10 shows the S functions used to generate Figure 3.9, and it may be seen that they are symmetrical around E_t, the potential at which the area of filmed and unfilmed surface are equal ie S = 0.5.

In contrast, the modelled theoretical polarization curve is symmetrical around E_t only when p = 1. The polarization curves generated using other values of p are not symmetrical around this midpoint, since the value used for i_{active} increases with increasing

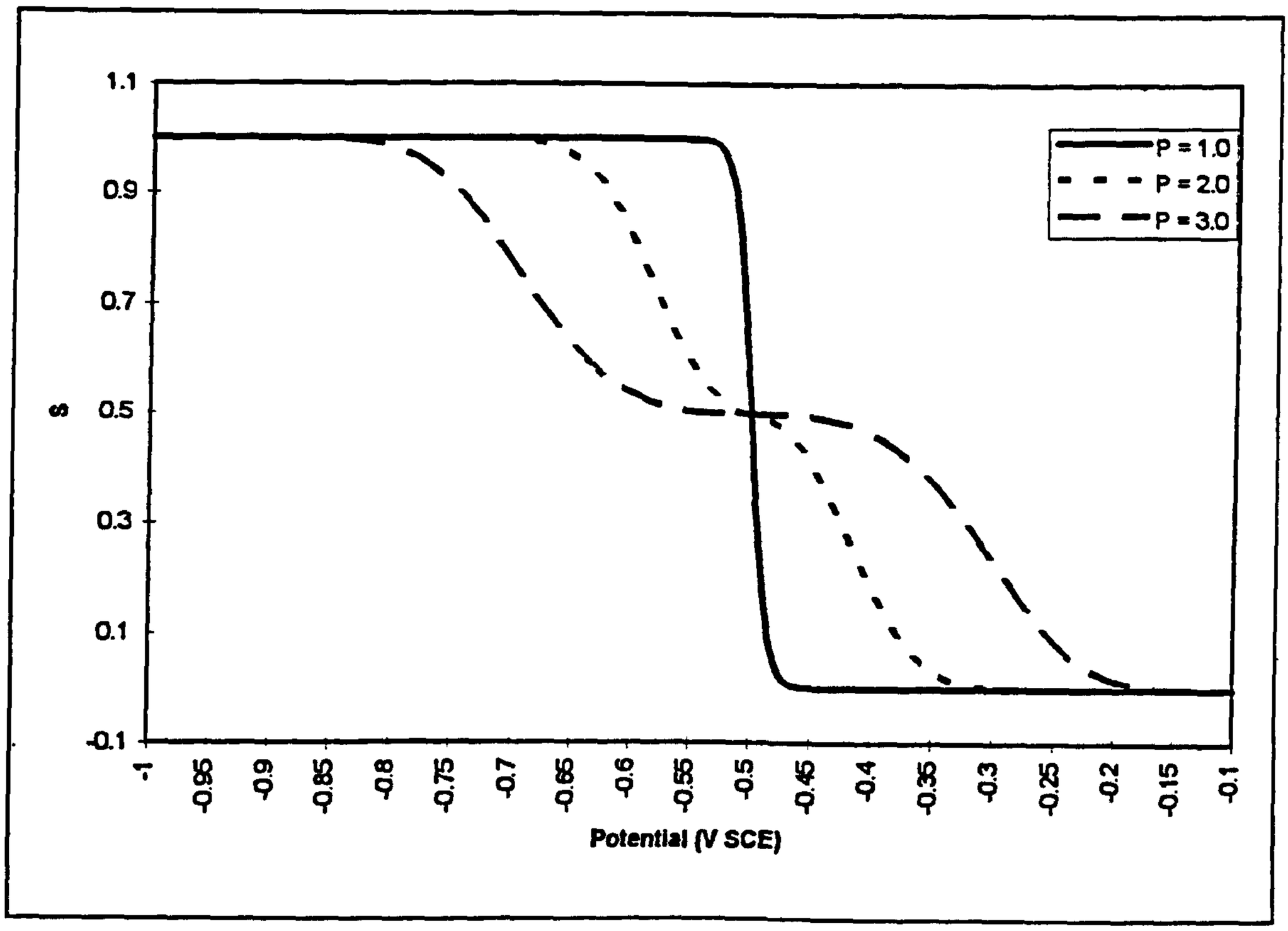

Figure 3.10 S Function used to generate Figure 3.9.

potential. If a fixed value of i_{active} was used, then the curves generated would be symmetrical around E_t. Other authors[100] have used this approach.

3.3.1.7 The Effect of Altering the Passive Current Density

The effect of altering the passive current density supported by the filmed surface on the anodic polarization curve of a passivating material is shown in Figure 3.11, with the parameters used by the 'buffer' equation shown in Table 3.5.

i_{pass} (nA cm^{-2})	E_t (V SCE)	A (V^{-p})	p
1 x 10^3 to 1 x 10^6	-0.5	150	2

Table 3.5 Parameters used by passivation algorithm to generate Figure 3.11.

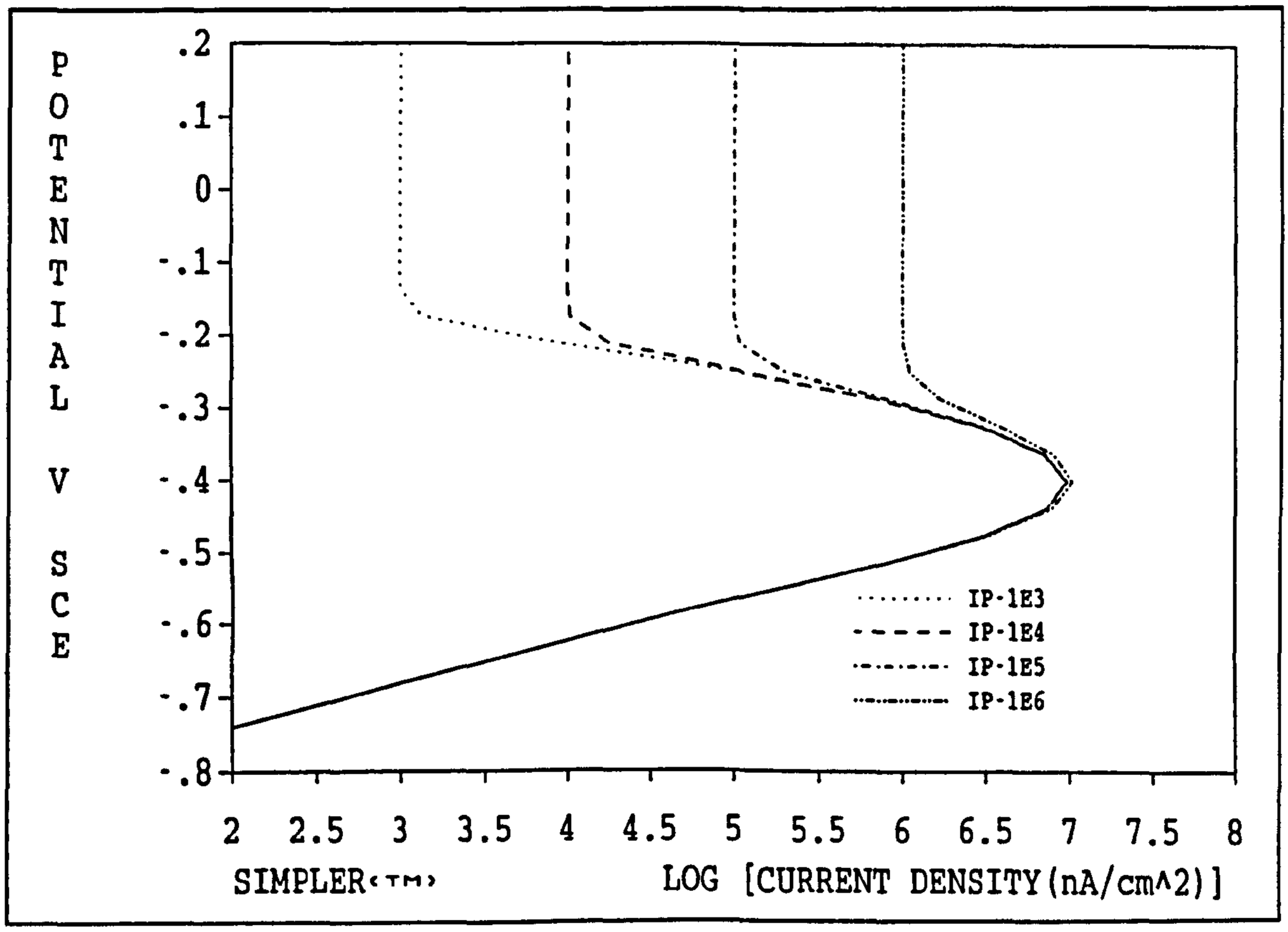

Figure 3.11 Effect of altering the passive current density supported by the unfilmed surface on the anodic polarization curve of a passivating material using the 'buffer' equation.

3.3.1.8 Effect of Altering the Constant A

The effect of altering the constant A in the 'buffer' equation on the anodic polarization curve of a passivating material is shown in Figure 3.12. The parameters used by the 'buffer' equation to model the active-to-passive transition are shown in Table 3.6.

i_{pass} (nA cm^{-2})	E_t (V SCE)	A (V^{-p})	p
1×10^3	-0.5	100 to 500	2

Table 3.6 Parameters used by passivation algorithm to generate Figure 3.12.

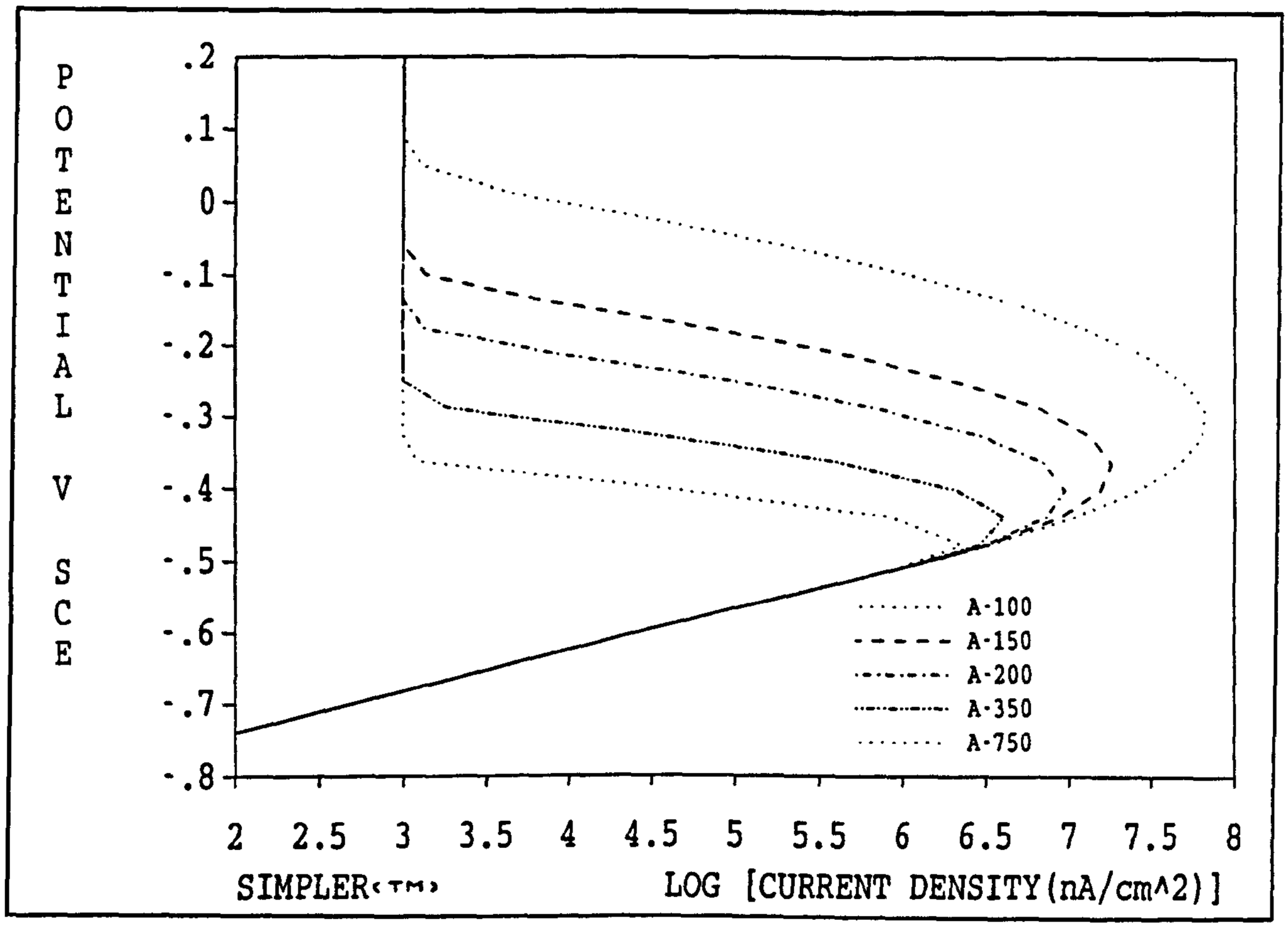

Figure 3.12 Effect of altering the constant A in the 'buffer' equation on the anodic polarization curve of a passivating material.

As noted by Otieno-Alego *et al*[100], A determines the width of the active-to-passive nose. The value of A required will depend on the units chosen for potential ie the magnitude of $(E - E_t)$, the value of p, the width of the potential range over which the transition occurs, and the magnitude of the current densities in the region of the transition. The value of A also appears to be dependent upon the system modelled. Otieno-Alego *et al* modelled mild steel in various pH sodium borate solutions and found A to be of the order 10^{-4} to 10^{-5}, while Hines[109] used A values of the order 5×10^{4} to model 304 stainless steel in sulphuric acid. Otieno-Alego *et al*[100], quote that Brook *et al*[104] found A to have a value of 4×10^{2}, although the system modelled is not mentioned.

3.3.1.9 Observations Made Regarding the Buffer Equation

The published form of the 'buffer' equation does not yield the form of S-function claimed. Using the absolute value of $(E - E_t)$ and varying the polarity of the constant A in the 'buffer' equation, yield S-curves of the desired form for all values of p.

The activation-controlled current density for each increment of potential should be used as the value of i_{filmed} in the expression for the net current density in the active-to-passive transition. Further additions to the published algorithm are required to obtain a smooth form to the desired transition; namely the use of upper and lower limiting values for S. Care must be taken in these limiting values to prevent extremely large numbers being generated by the algorithm, which cause run-time errors to occur in the program.

3.3.2 The Raindrop Equation

The 'raindrop' equation can also be used to provide the S-function in the modelling software, and the code for this is contained in a new routine called SRAIN shown in Appendix D. The routine is incorporated in exactly the same way as the SBUF module (described in Section 3.3.1.2). No modifications were needed to the published form[99] of the equation.

3.3.2.1 Effect of Altering Active-to-Passive Transition Potential

The effects of altering the potential at which the active-to-passive transition begins are shown in Figure 3.13. The relevant parameters used are listed in Table 3.7 :

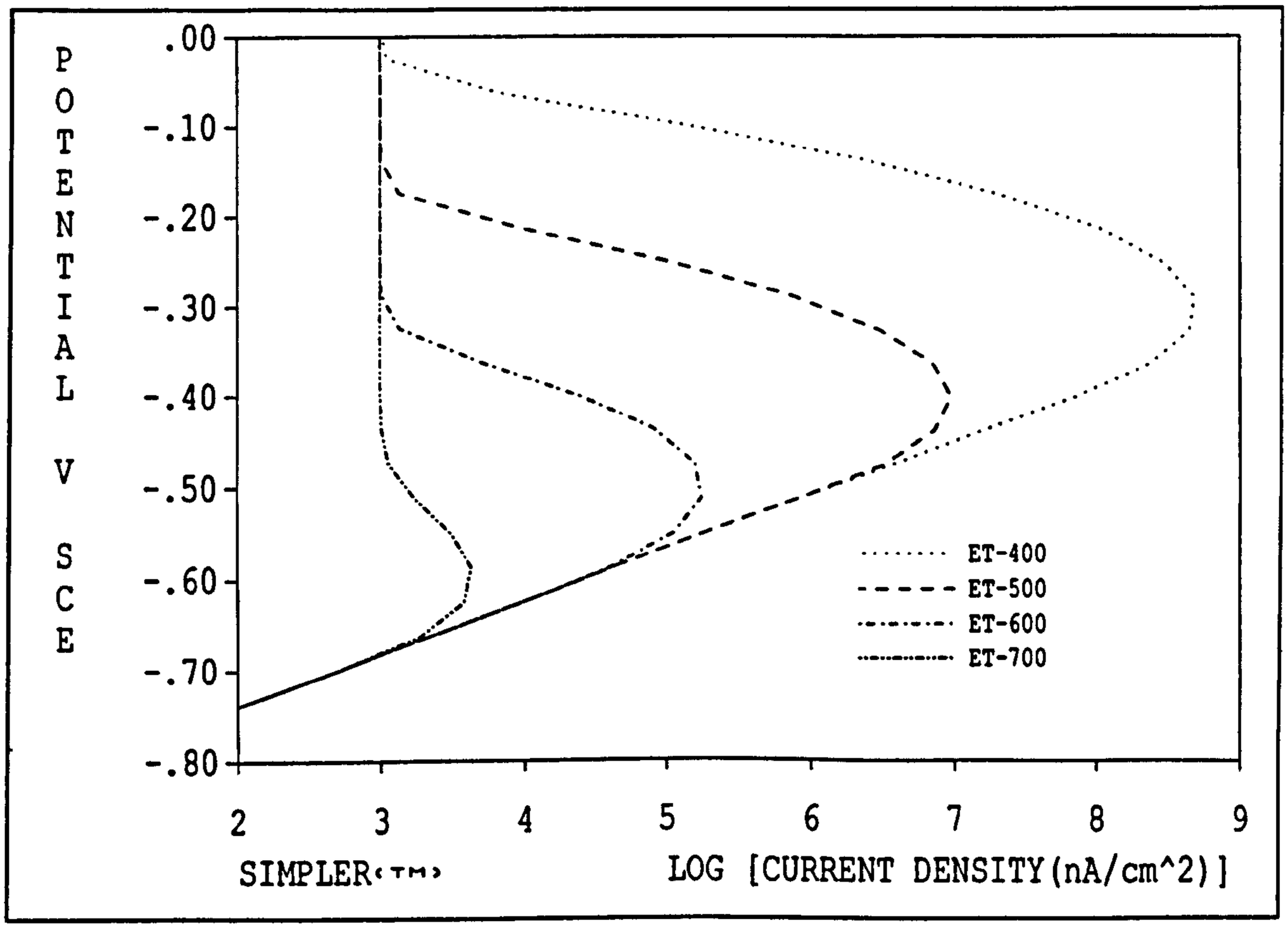

Figure 3.13 Effect of altering the active-to-passive transition potential on the anodic polarization curve of a passivating material using the 'raindrop' equation.

i_{pass} (nA cm^{-2})	E_t (V SCE)	A (V^{-p})	p
1×10^3	-0.4 to -0.7	200	2
i_o (nA cm^{-2})	E_o (V SHE)	solution resistance (ohms)	pH
1	-0.44	0	0

Table 3.7 Parameters used in Figure 3.13.

Figure 3.13 shows that as the transition potential becomes less negative, the value of i_{crit} and the potential at which it occurs increases, as does the width of the potential range over which the transition occurs.

3.3.2.2 Effect of Altering Power Used In Raindrop Equation

The effect of using p values between 1 and 3, the power in the 'raindrop' equation, is shown in Figure 3.14. The same kinetic parameters as shown in Table 3.7 were used. It can be seen that increasing the value of p results in the active-to-passive transition occurring over a wider potential range, as well as increasing the value of i_{crit}. It should also be noted that the rate at which the current falls to i_{pass}, after i_{crit} has been reached increases with increasing p.

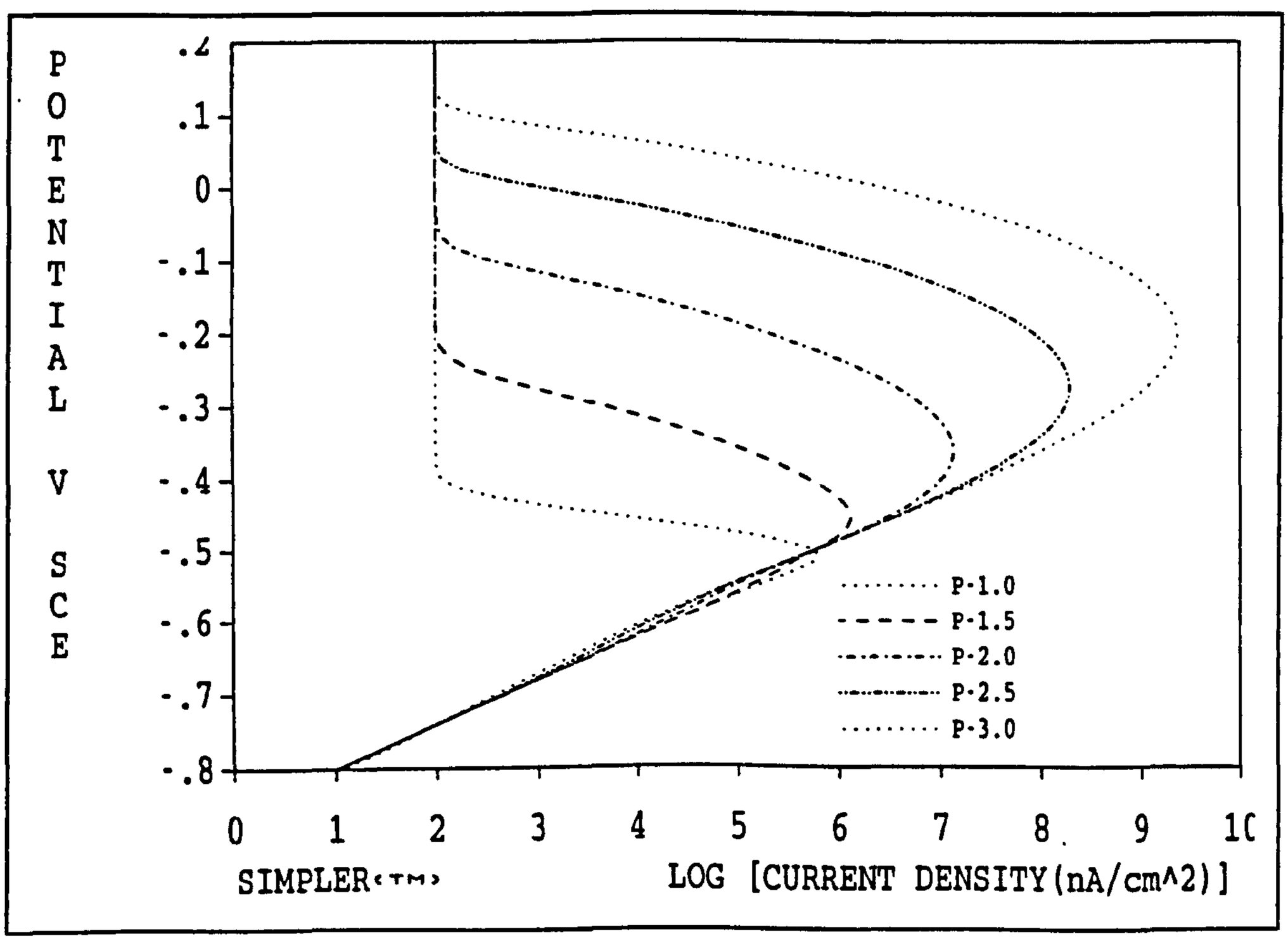

Figure 3.14 Effect of altering the power p in the 'raindrop' equation on the anodic polarization curve of a passivating system.

i_{pass} (nA cm^{-2})	E_t (V SCE)	A (V^{-p})	p
1×10^3	-0.5	200	1 to 3

Table 3.8 Parameters used in Figure 3.14.

The same set of parameters detailed in Table 3.7 were used, with the exception of the active-to-passive transition, which remained fixed at -0.55 V SCE.

3.3.2.3 Effect of Altering i_{pass}

The effects of altering i_{pass} are shown in Figure 3.15. It clearly shows the marked effect on the shape of the passivating anodic curve.

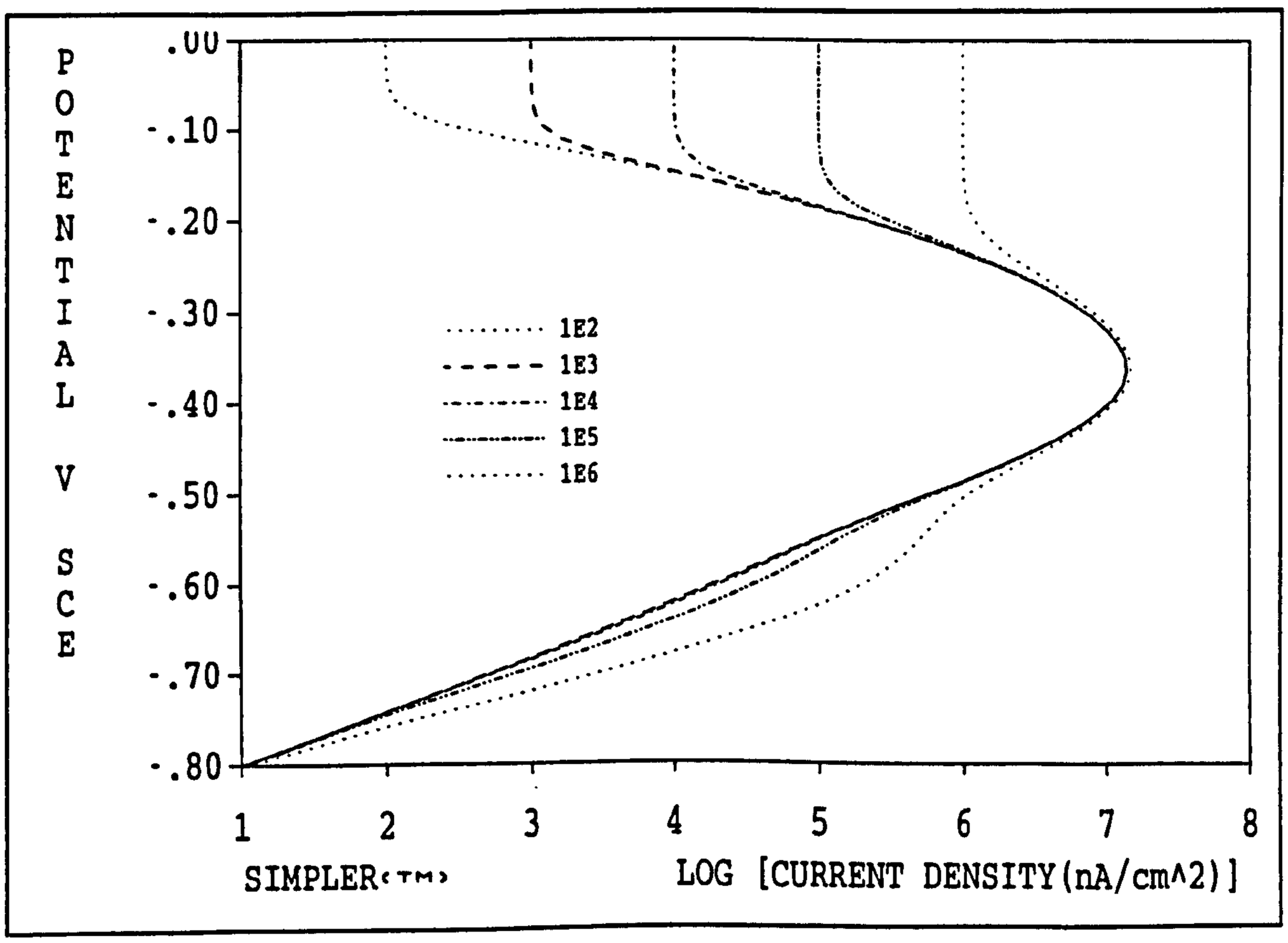

Figure 3.15 Effect of altering the passive current density on the anodic polarization curve of a passivating system using the 'raindrop' equation.

i_{pass} (nA cm^{-2})	E_t (V SCE)	A (V^{-p})	p
1×10^3 to 1×10^6	-0.5	200	2

Table 3.9 Parameters used in Figure 3.15.

3.3.2.4 Effects of Altering A in Raindrop Equation

The effect of altering the value of the constant A in the 'raindrop' equation is examined in Figure 3.16, and it can be seen that the larger the value of A, the smaller the potential range over which the active-to-passive transition occurs.

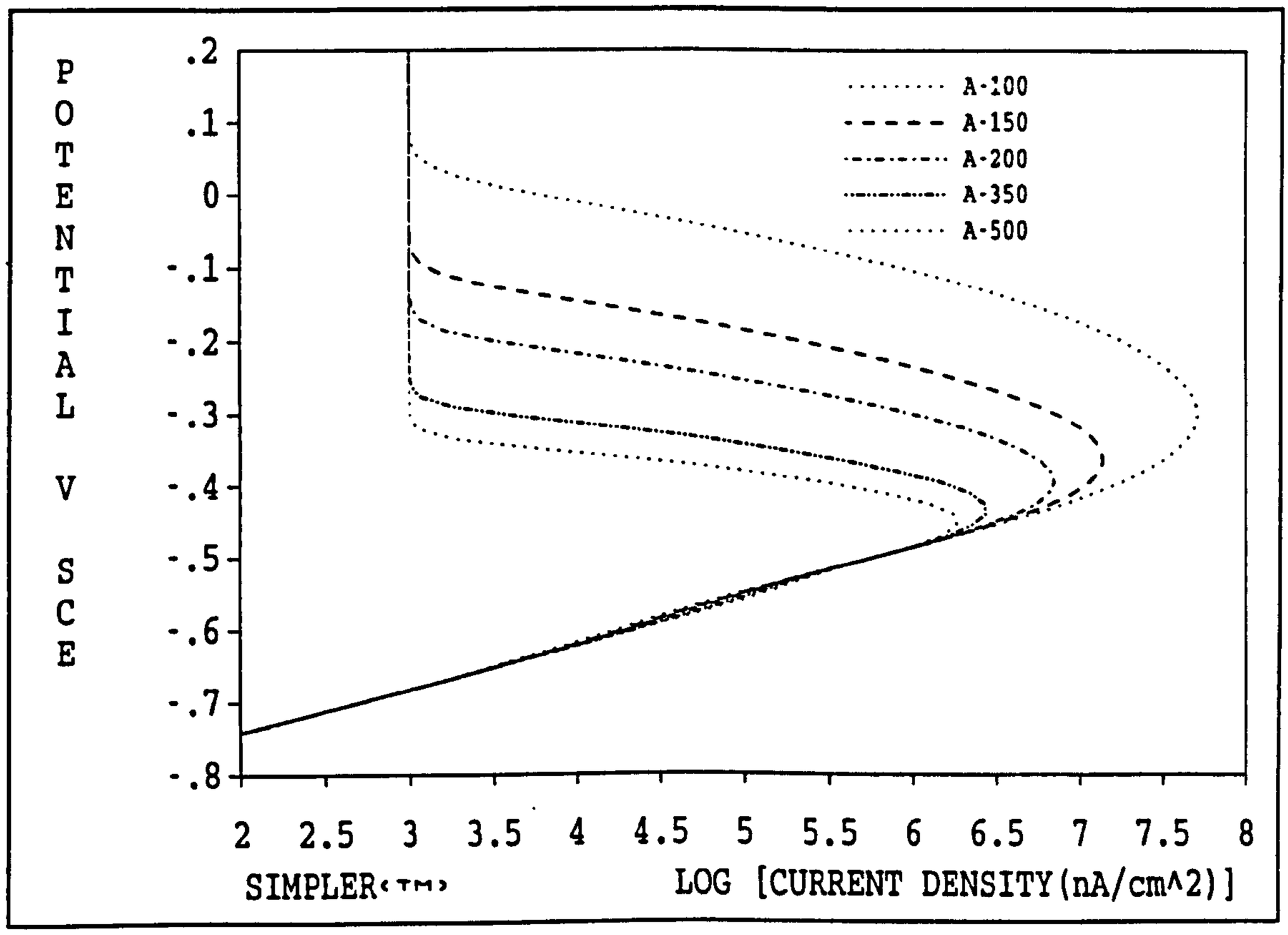

Figure 3.16 Effect of altering the constant A in the 'raindrop' equation on the anodic polarization curve of a passivating system.

Thus, it is suggested that A is related to the rate of development of the passive film.

Smaller values of A also increase the rate at which the current density decays to its final value, i_{pass} , once i_{crit} has been reached.

Parameter	Value Used
i_{pass} (nA cm^{-2})	10^2
E_{trans}(V SCE)	-0.55
i_o (nA cm^{-2})	10^2
i_{lim} cath (nA cm^{-2})	10^3
Diffusion Control	On
p	2
resistance (ohm)	0
pH	0
A	100 - 500

Table 3.9 Parameters used in Figure 3.16.

3.3.2.5 Observations Regarding the Raindrop Equation

The 'raindrop' equation does not require any modifications to the published form in order to generate S-functions of the desired form. As with the 'buffer' equation, the activation-controlled current density should be used for i_{active} in the expression for the overall current density in the region of the active-to-passive transition (Equation 3.44).

Testing has shown that experimental curves are most closely modelled using p values of 2 for both equations. However, experimental polarization curves of iron and

stainless steels in acid and marine environments are not symmetrical around a given potential (see results in Chapter 4). Thus the 'raindrop' equation is more suitable for modelling such systems, and it, rather than the 'buffer' equation, will be used in the following sections.

3.4 THE EFFECTS OF ADDING HYDROGEN AND OXYGEN REACTIONS

The effects of adding the oxygen and hydrogen redox process to the passivating iron curve are shown in Figures 3.17, 3.18 and 3.19. Figure 3.17 represents the case when the cathodic diffusion limited current density for oxygen exceeds both the value of i_{crit}, and the value of the passivation current i_{pass}. The resultant summing of the anodic and cathodic partial currents leads to the correct form of polarization curve.

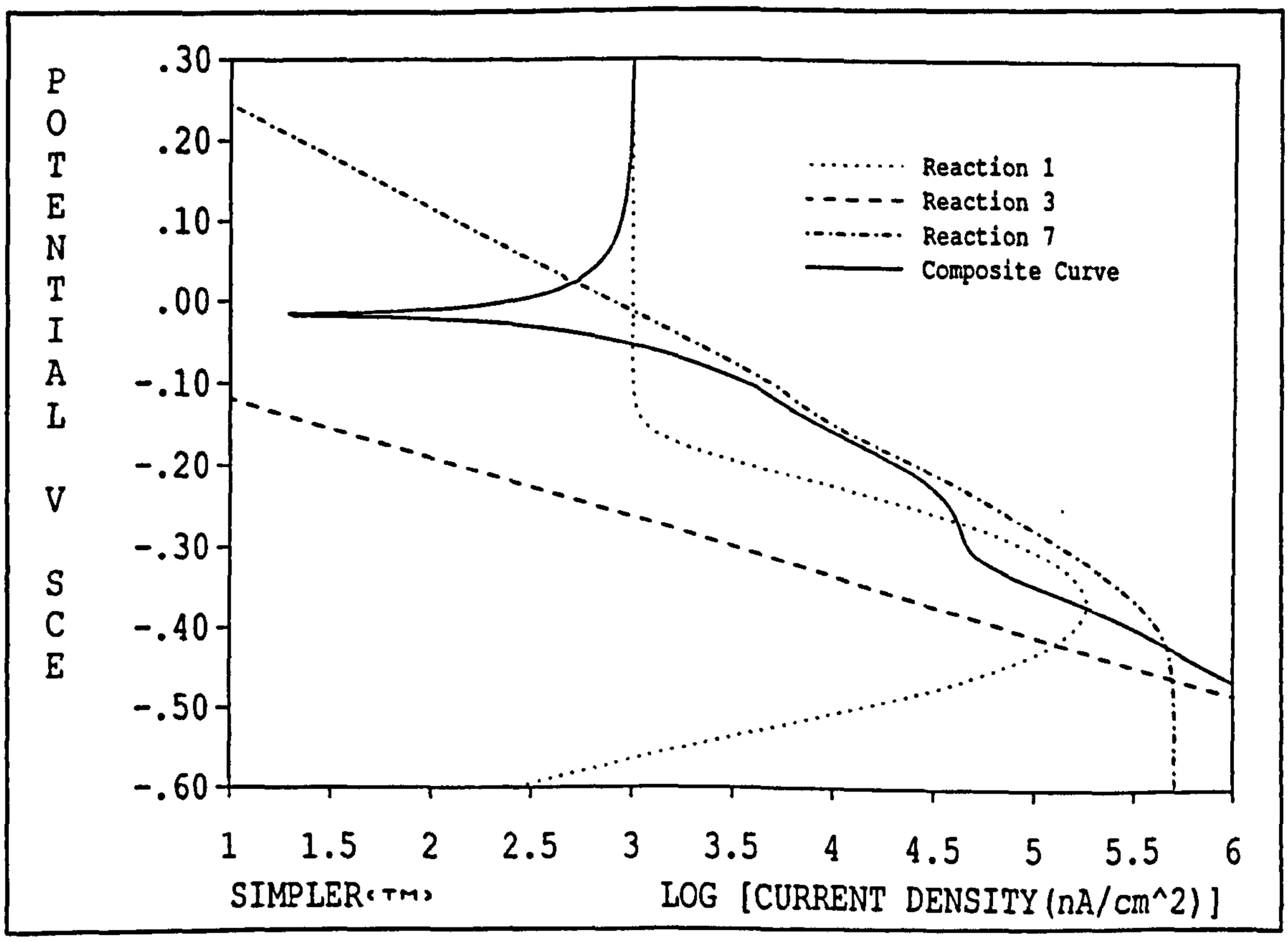

Figure 3.17 Modelled curve for a passivating material with the hydrogen and oxygen reduction processes, $i_{lim}O_2 > i_{crit}, > i_{pass}$.

However, if the value of the cathodic diffusion limited current density for oxygen does not exceed the value of i_{crit}, as in the case of a low oxygen concentration or a reducing system (Figure 3.18), then the familiar 'triple E_{corr}' plot results.

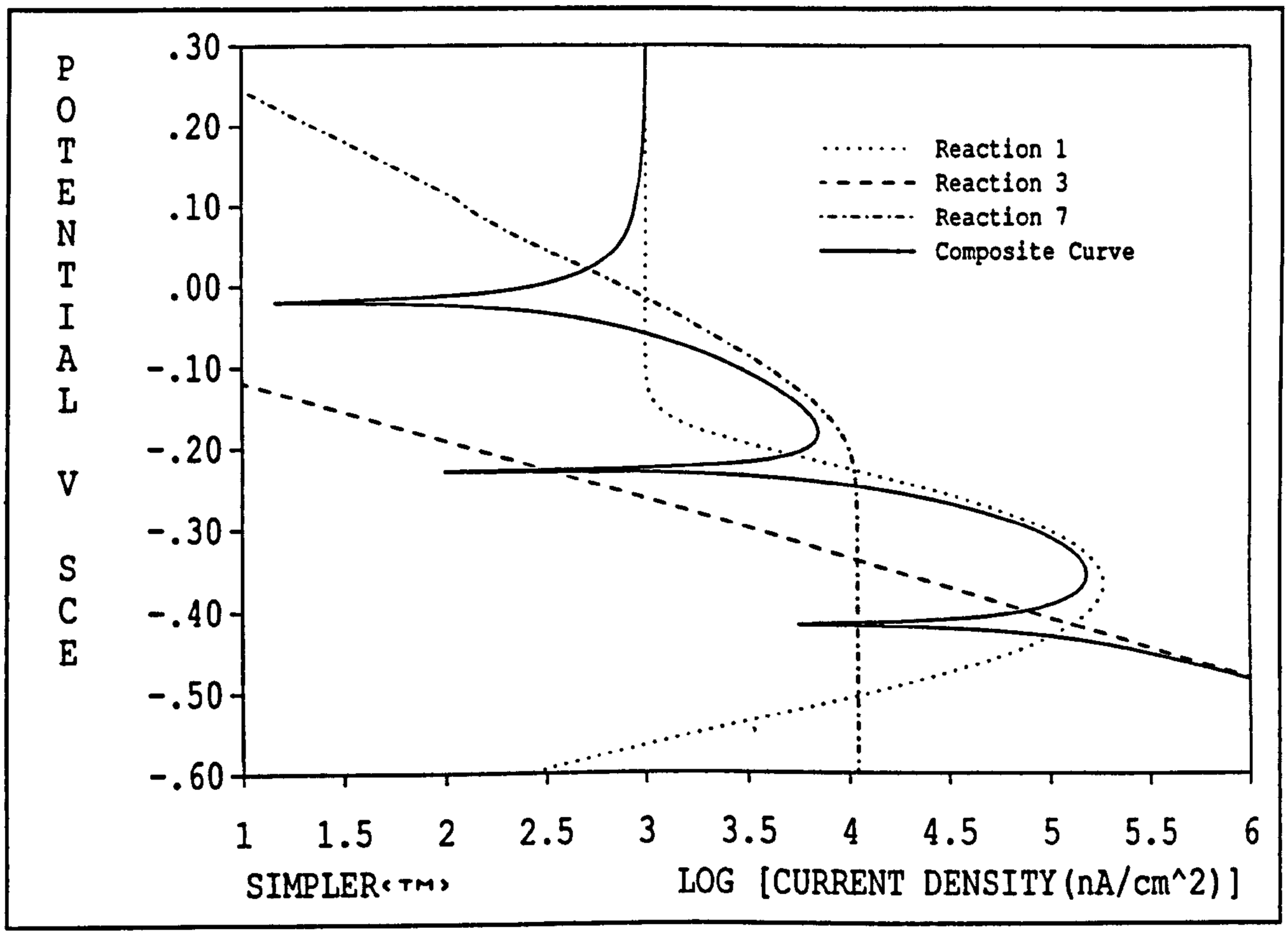

Figure 3.18 Modelled polarization curve for a passivating material, $i_{lim}O_2 < i_{crit}$.

If the oxygen reduction reaction is absent, the more traditional form of S-shaped polarization curve is generated, Figure 3.19.

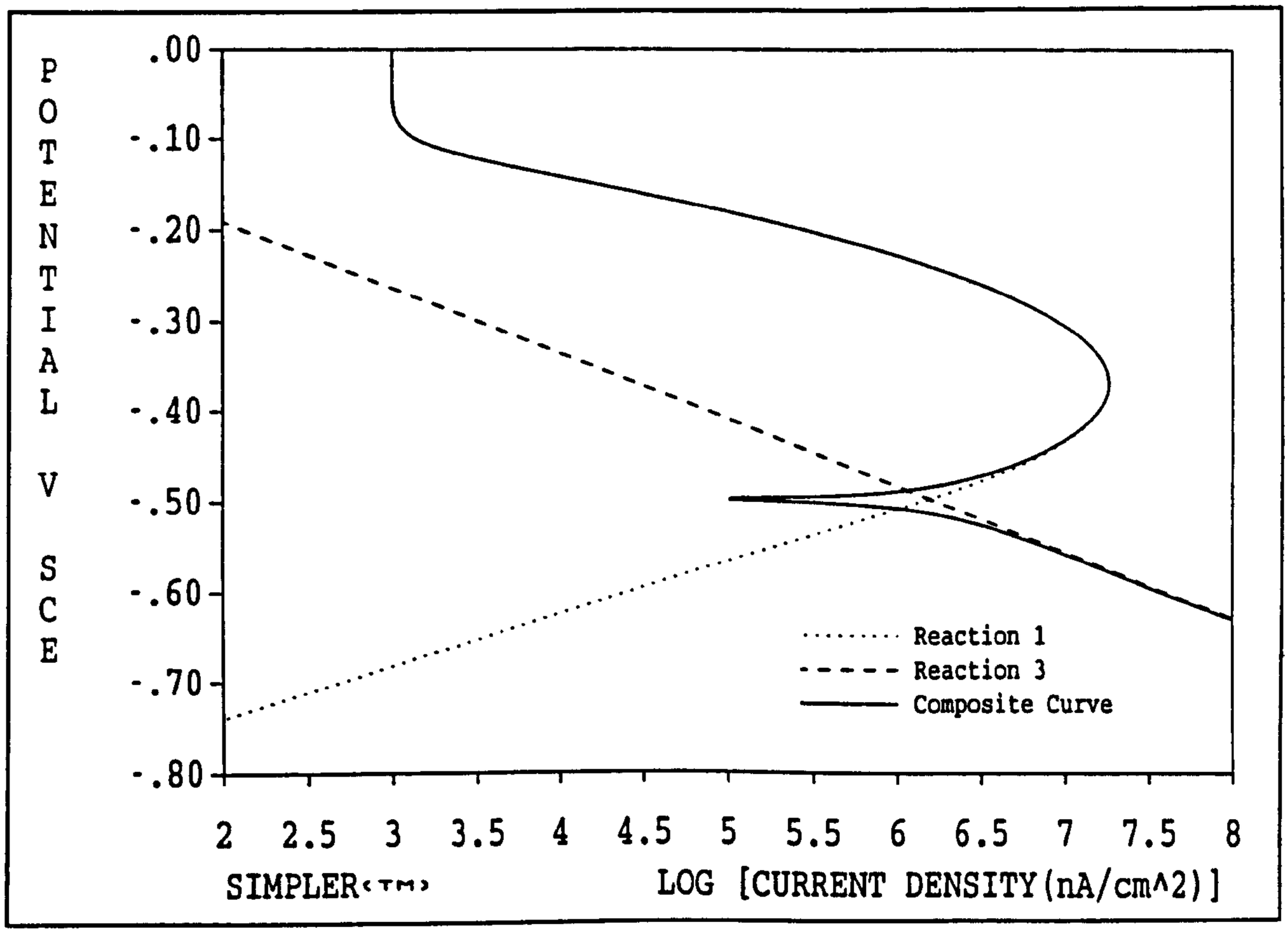

Figure 3.19 Modelled polarization curve for iron dissolution and hydrogen evolution reactions..

Chapter 4 Section 1 Modelling the Electrochemical Behaviour of Iron in Aqueous Sulphuric Acid

4.1.1 INTRODUCTION

Most texts dealing with passivity detail S curves of an ideal form, while actual curves (if shown) do not correspond to this shape.

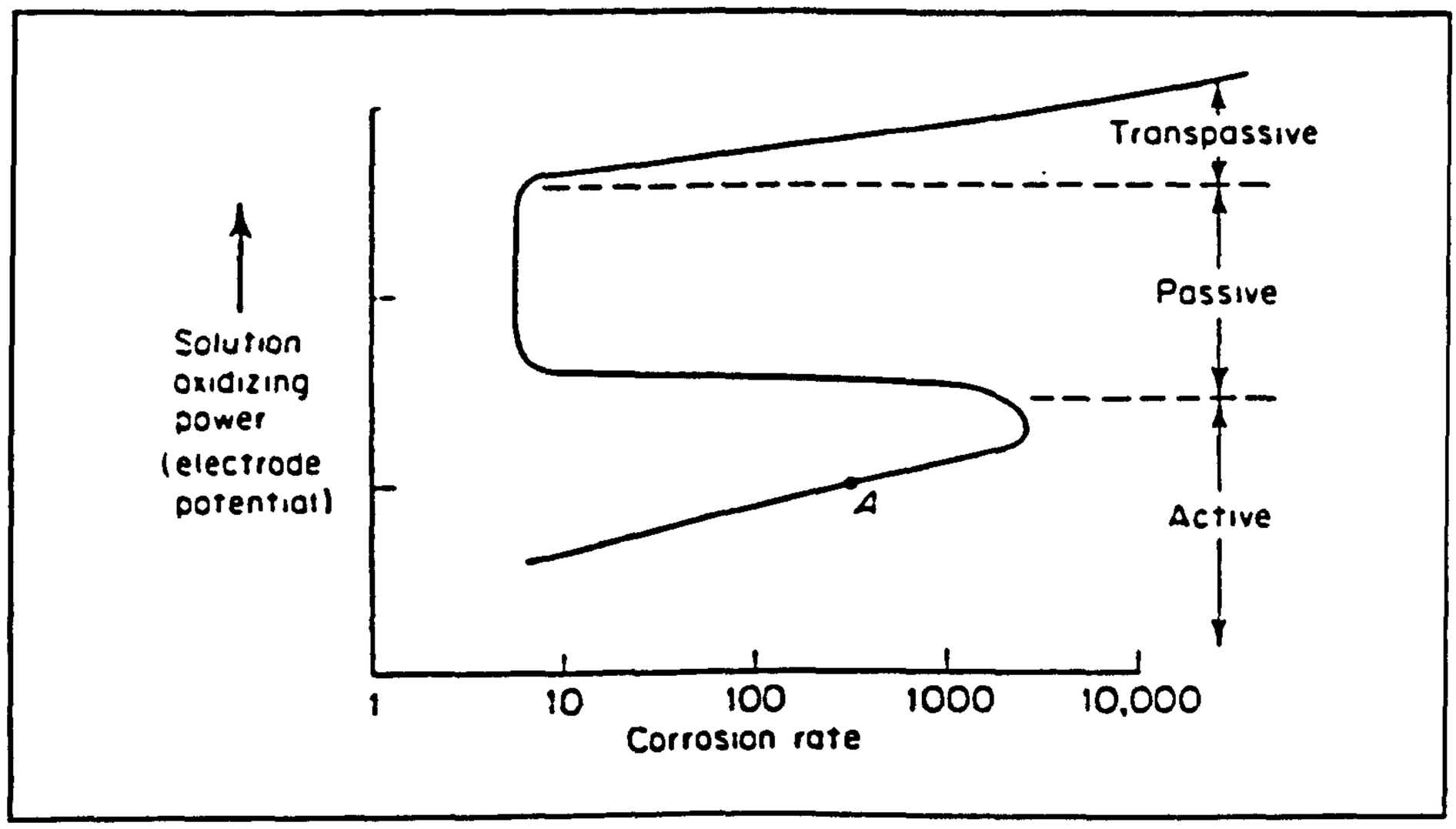

Figure 4.1.1 Ideal S Curve for a passivating metal (from Uhlig[110]).

An example is the case of iron in 5% H_2SO_4. Two such ideal curves[110,111] are shown in Figures 4.1.1 and 4.1.2.

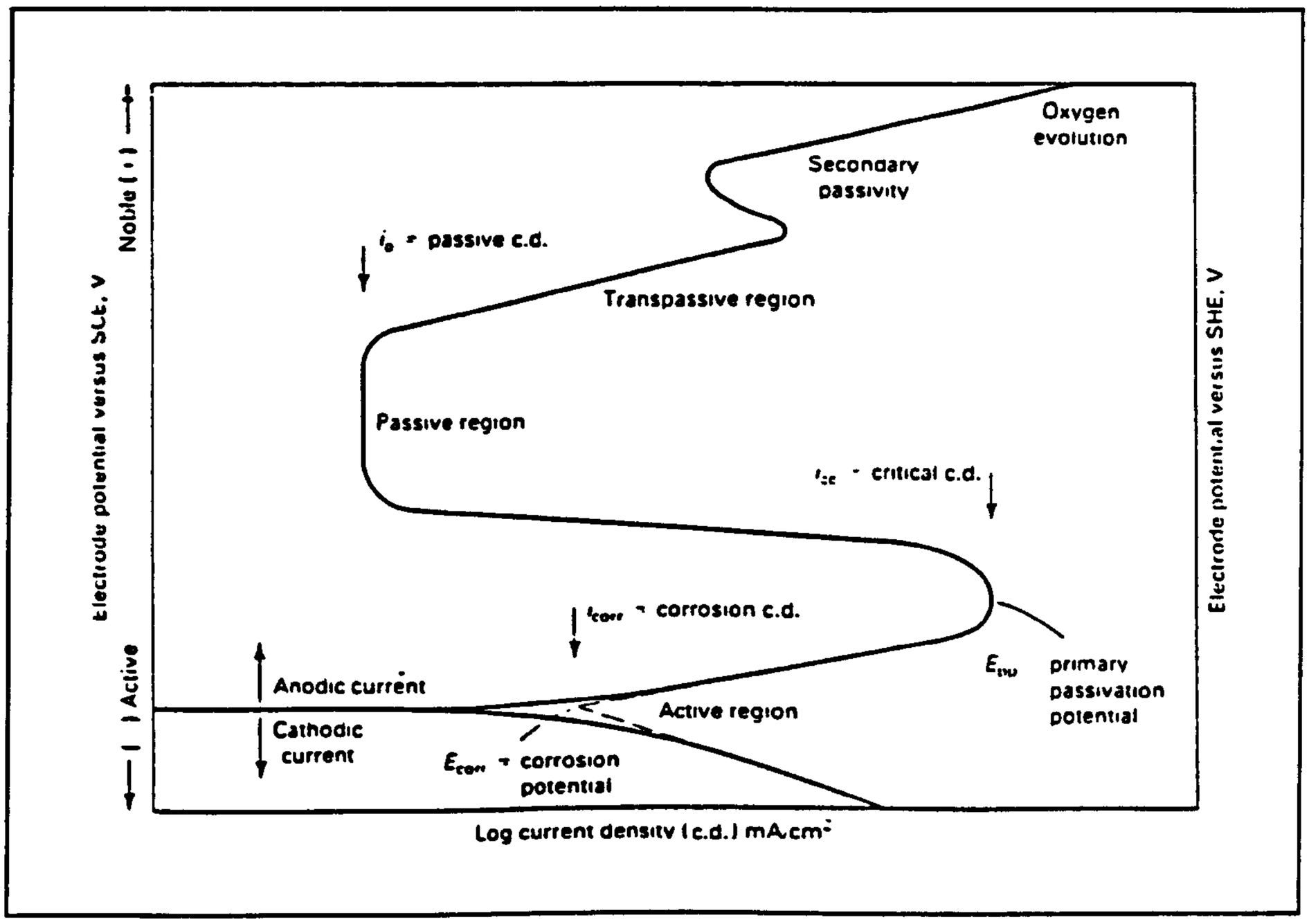

Figure 4.1.2 Ideal S Curve with Secondary Passivation (from ASTM Vol 13[111]).

Figures 4.1.3 and 4.1.4 are experimental curves for iron in deaerated H_2SO_4, while Figure 4.1.5 is the experimental curve for iron in aerated H_2SO_4.

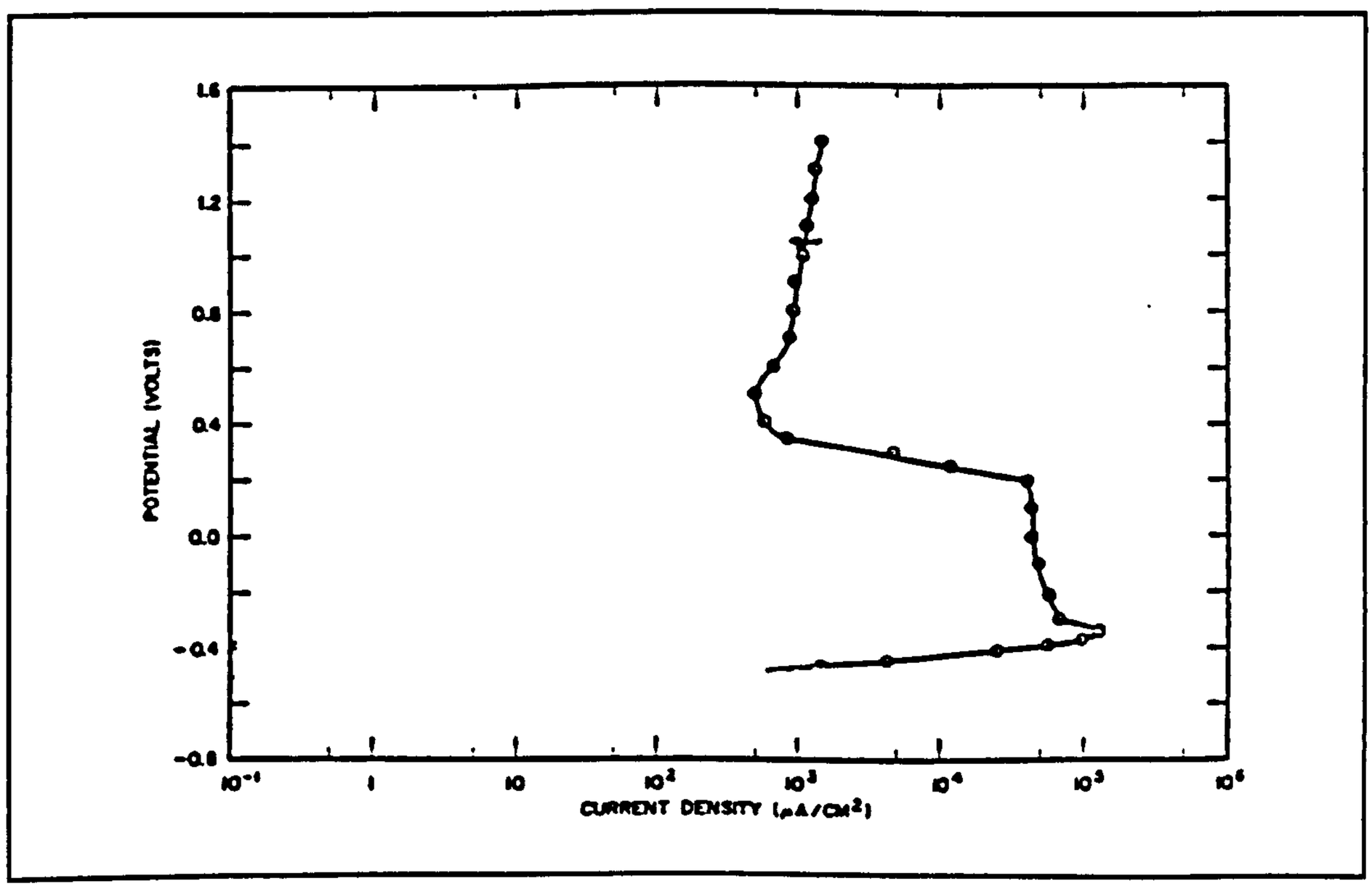

Figure 4.1.3 Experimental Curve for Iron in H_2SO_4 (from Steigerwald and Greene[160]).

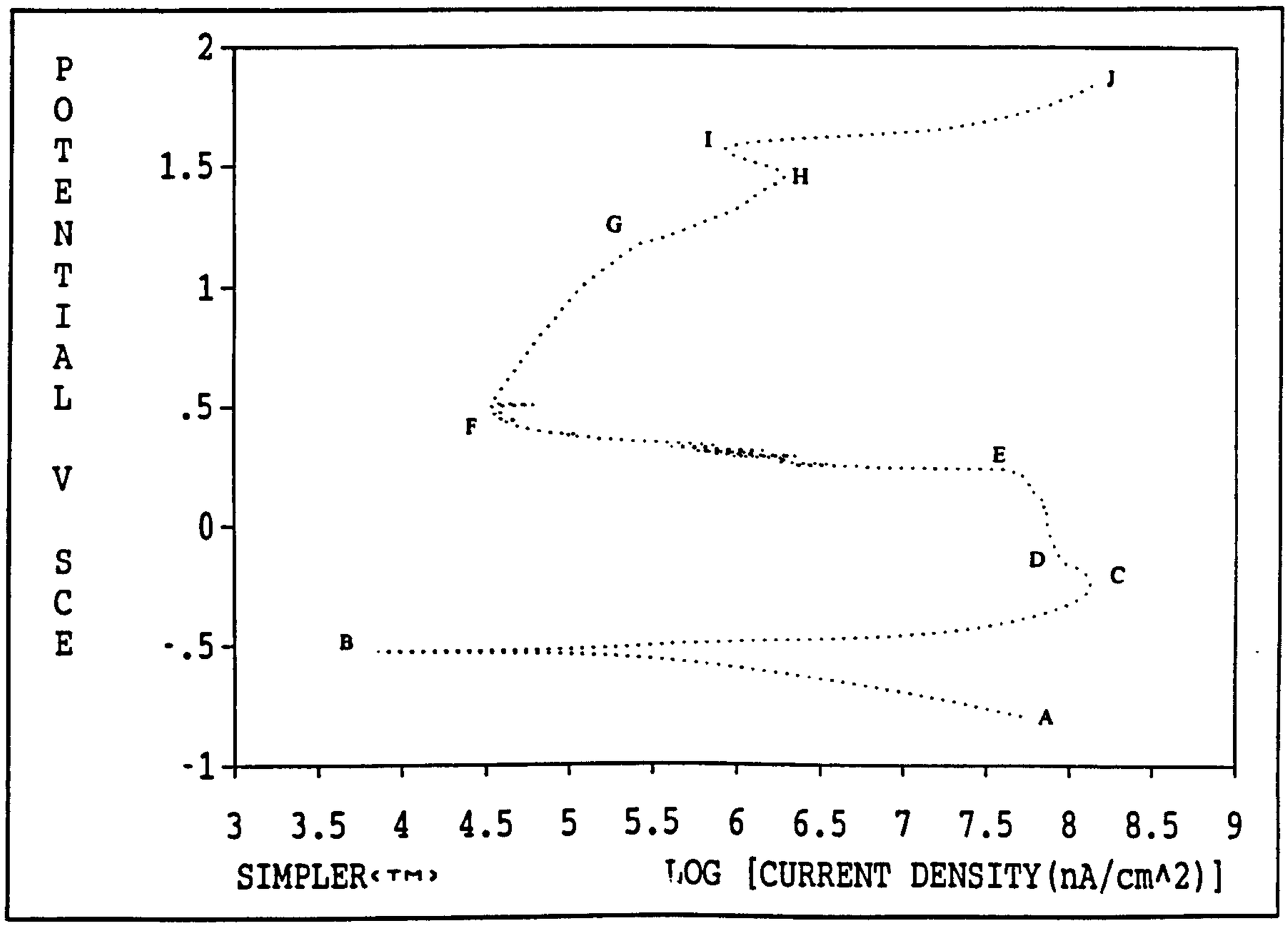

Figure 4.1.4 Experimental Curve for Iron in 5% Deaerated H_2SO_4, 0.1 mV s^{-1} scan rate, 24 °C.

The most obvious departure from ideality is in the region of the active-to-passive transition, where, after reaching i_{crit} (point C) and an initial fall in current response (region CD), there is a region of near constant current (DE), followed by another fall in current density (EF). The current supported by the passivated surface increases with potential (FG), until other processes take over at above 1 V SCE. A feature not normally shown on S curves is the secondary passivation region (GHI) in the transpassive region, which is shown in Figures 4.1.2, 4.1.4 and 4.1.5.

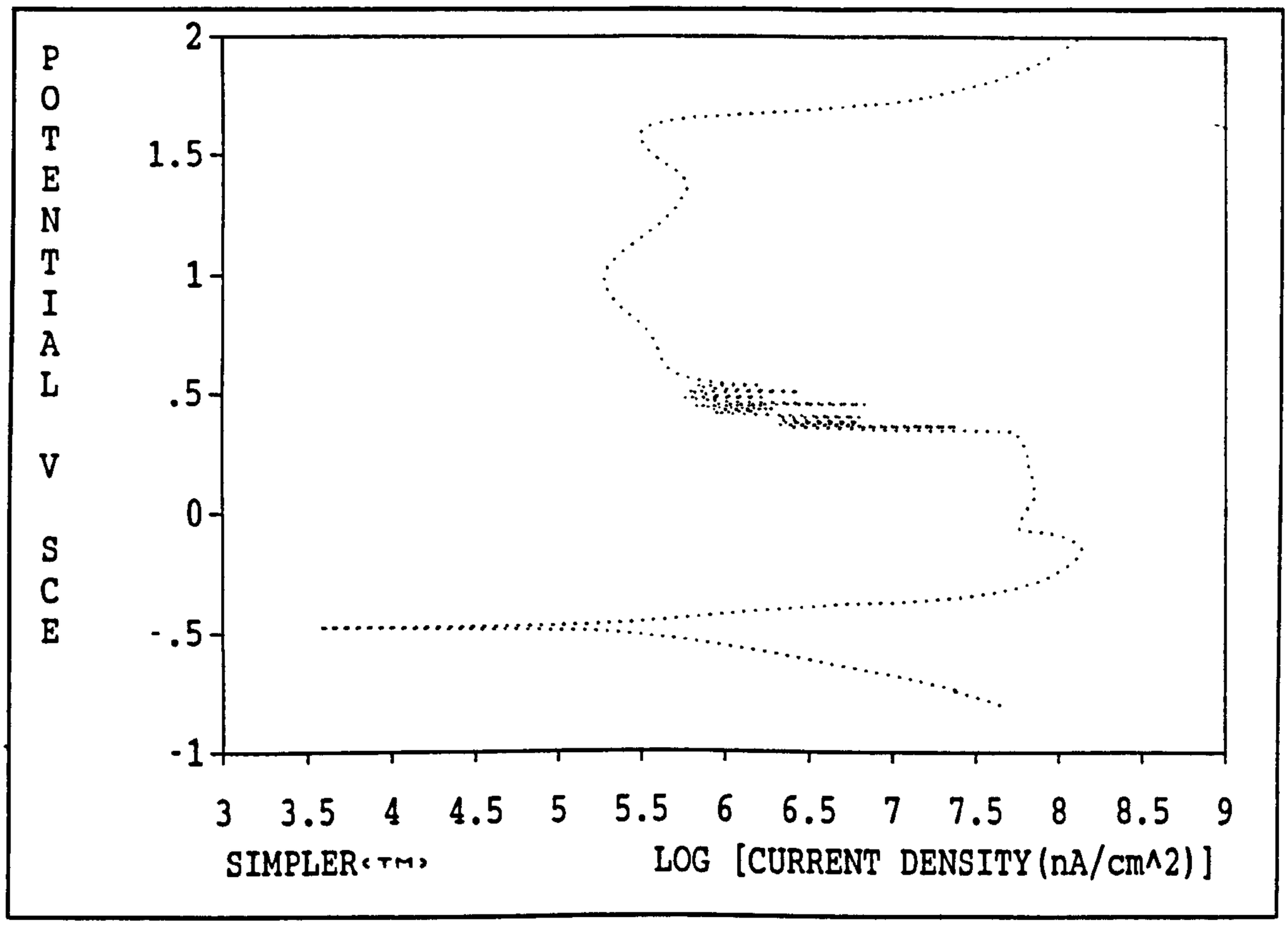

Figure 4.1.5 Experimental Curve for Iron in Aerated 5% H_2SO_4, 0.1 mV s^{-1} scan rate, 24 °C.

4.1.2 EXPERIMENTAL PROCEDURE

High purity (98%+) iron was obtained from Goodfellows, Cambridge, in bar form of diameter 19 mm. This was cut into discs of approximate 10 mm thickness before being mounted in cold-setting epoxy resin, with a wire attached to the back with silver-loaded epoxy resin, for electrical connectivity. The samples were successively ground to a 600 grit finish prior to degreasing with methylated spirit and rinsing in deionised water.

The electrolyte used in all cases was 5% (by volume) H_2SO_4, made from deionised water and Analar grade concentrated sulphuric acid. The temperature was 20 °C.

Potentiodynamic polarization scans were carried out using a EG&G PAR model 273

potentiostat with 352 software™ control. In all cases (unless stated) the samples were immersed in the electrolyte and left for 1 hour to equilibrate, before being scanned from the cathodic region (usually -250 mV with respect to the free corrosion potential attained after the initial hours' immersion) in an anodic direction. The final potential was between 1.8 and 2.4 V SCE, and scan rates of between 0.05 and 0.1 mV s^{-1} were used. The rotating disc electrode (RDE) experiments used a Uniscan SR-100 Scanning Reference Electrode Technique (SRET) instrument to rotate the samples, with the working, reference and auxiliary electrode connections appropriately wired to the potentiostat.

4.1.3 RESULTS

4.1.3.1 Electrochemical Reaction Scheme for Iron in Sulphuric Acid

In order to model the behaviour, the processes occurring on or near the surface must be understood. The following reactions were considered.

$Fe \rightarrow Fe^{2+} + 2e^-$	Reaction 1
$O_2 + 2H_2O + 4e^- \rightarrow 4OH^-$	Reaction 7
$2H^+ + 2e^- \rightarrow H_2$	Reaction 3

The cathodic behaviour of iron in both aerated and deaerated (Figures 4.1.4 and 4.1.5) solutions of 5% H_2SO_4 is very similar. The diffusion-limited current density of the oxygen reaction[112] in air-saturated, non-agitated solutions is about 10^5 nA cm^{-2}. At potentials corresponding to cathodic regions of the experimental polarization curves shown, the oxygen reduction reaction exhibits diffusion-limited behaviour. Neither Figure 4.1.4 or 4.1.5 exhibits a vertical portion characteristic of a diffusion-limited process; thus it may be

deduced that the hydrogen evolution reaction is the dominant cathodic process in both the aerated and deaerated cases.

Further evidence for this deduction is found by dissolved oxygen measurements. When the solution is deaerated, the measured value of the partial pressure of dissolved oxygen in the electrolyte falls to 0.01, compared to 0.20 for aerated solutions at ambient temperatures. It may then be considered that the solution is oxygen-free. The current density attributable to Reaction 7 is therefore negligible, and the reaction is not considered in the model for iron in deaerated 5% H_2SO_4.

4.1.3.2 Modelling the Cathodic and Anodic Activation-Controlled Reactions

This section describes the use of the Hines 'raindrop' algorithm discussed in Chapter 3 to model the polarization behaviour of a complex passivating system over a wide range of potentials. The following reactions are considered :

$$Fe \rightarrow Fe^{2+} + 2e^- \qquad \text{Reaction 1}$$

$$2H^+ + 2e^- \rightarrow H_2 \qquad \text{Reaction 3}$$

Reaction 1 is plotted as being under complete activation-control, in order to determine the transition potential at which the passivation process begins. The reverse of Reaction 1 is not modelled as it is considered that there are very few (*ie* trace amounts) of Fe^{2+} ions in the solution of H_2SO_4. In all cases, the pH of the solution was 0.2, the resistance 1 ohm, and the temperature 20 °C.

Figure 4.2.6 shows the calculated polarization curve plotted using Reactions 1 and

3 using the parameters in Table 4.1.1.

	Reaction 3	Reaction 1
E_o (V SHE)	0.00	-0.44
i_o (nA cm^{-2})	10^3	0.5
i_{lim}^{Anodic} (nA cm^{-2})	10^4	10^{20}
$i_{lim}^{cathodic}$ (nA cm^{-2})	7×10^{19}	not modelled
Activity	0	10^{-6}
α	0.5	0.5

Table 4.1.1 Parameters for Reactions 1 and 2 used in Figure 4.1.6.

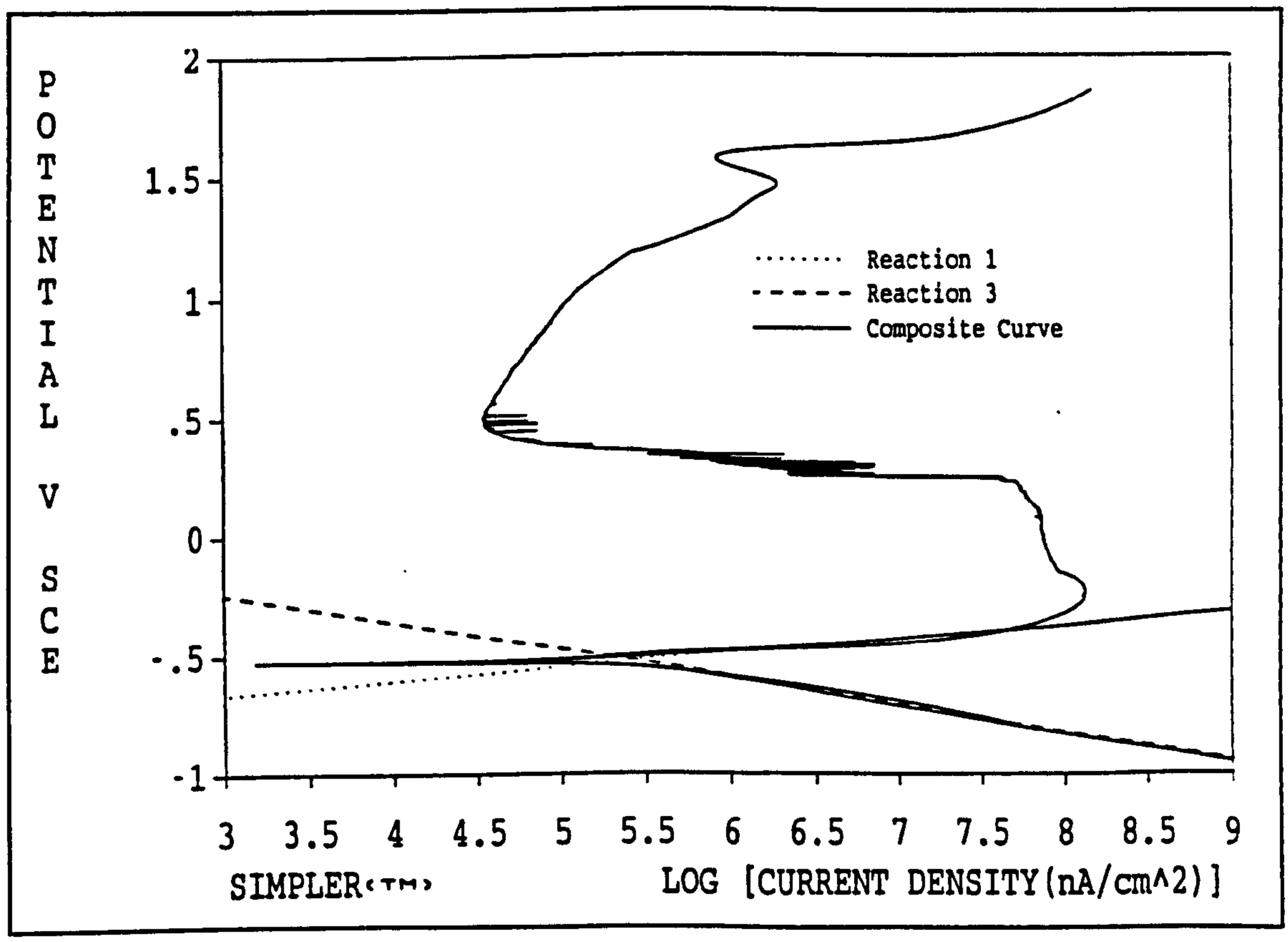

Figure 4.1.6 Model showing both Reaction 1 and 3 under activation control.

Figure 4.1.7 shows in increased detail the regions either side of the accurately modelled corrosion potential.

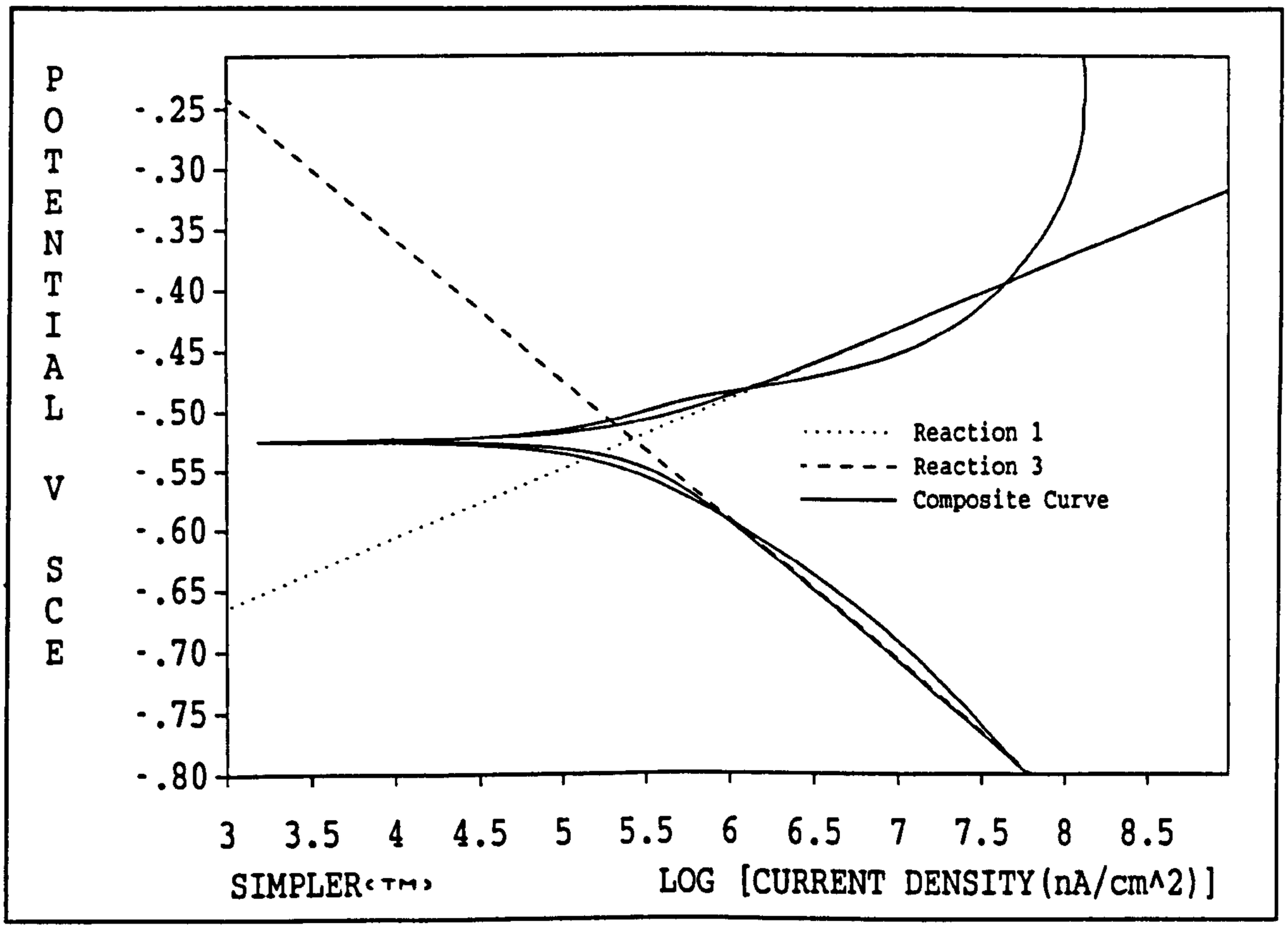

Figure 4.1.7 More Detailed View of Figure 4.1.6.

From inspection of Figure 4.1.7, a transition potential (E_t) of -0.44 V SCE was chosen for use in the raindrop equation. This was determined as the point at which the calculated activation-controlled trace for Reaction 1 crosses the experimental curve. As an approximation, the passive current is modelled as being constant, although in reality this is not the case.

4.1.3.3 Modelling the Active-to-Passive Transition

Reaction 1 is now considered to undergo a passivation process, modelled by the 'raindrop' algorithm with the parameters shown in Table 4.1.2. Figure 4.1.8 shows the result

obtained. A good correlation is obtained up to a point slightly more positive than where the maximum current density occurs. Above this point, it appears as if the passivation process is hindered, possibly by the formation of a surface film. The sample was orientated at an angle of ~ 30° to the vertical.

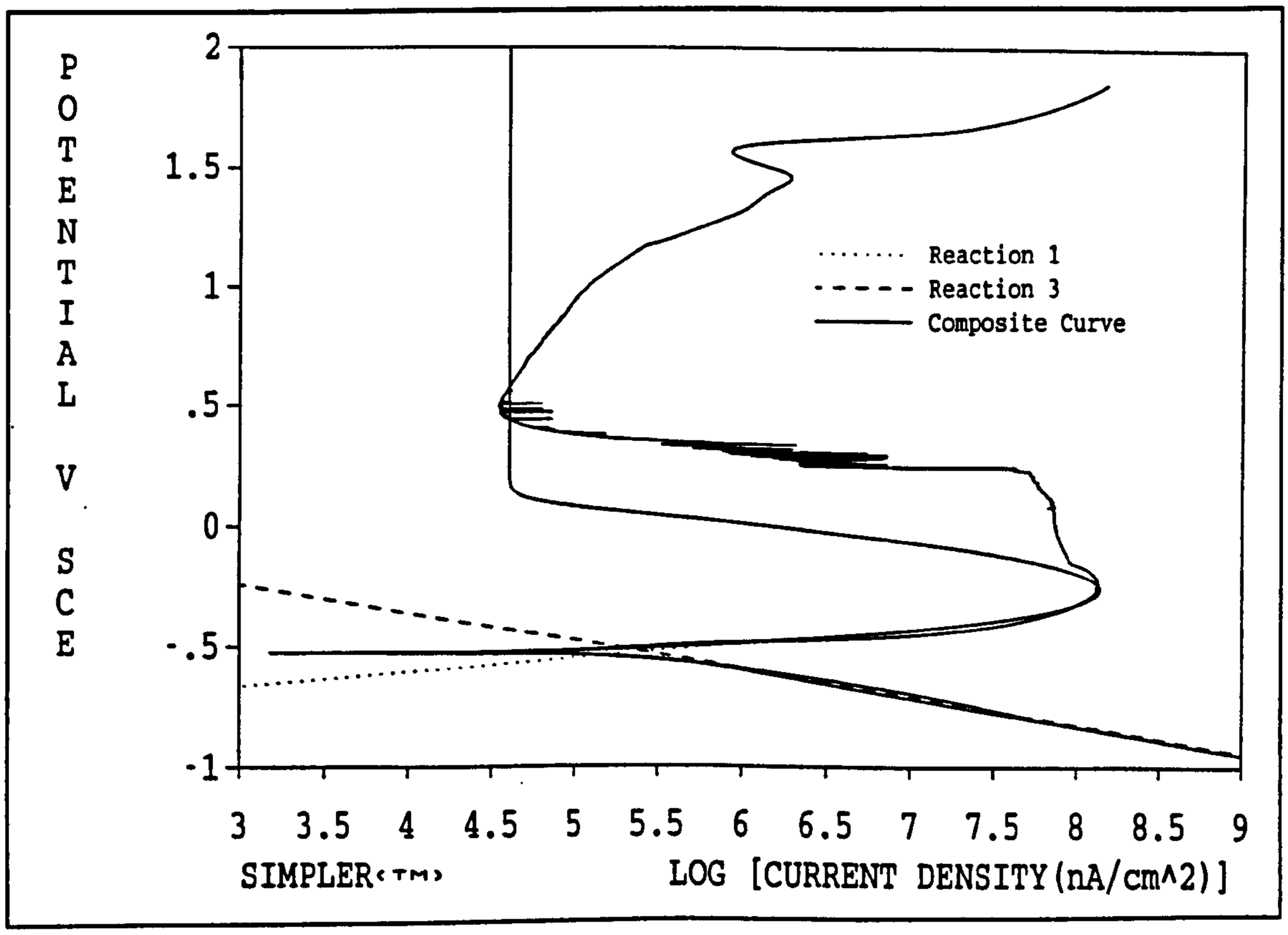

Figure 4.1.8 Introduction of 'Raindrop' Passivation Algorithm to Reaction 1.

	A (V^{-p})	p	i_{pass} (nA cm^{-2})	E_t (V SCE)
Reaction 1	77	1.7	4×10^4	-0.44

Table 4.1.2 Parameters Used in Raindrop Passivation Algorithm for Reaction 1 in Figure 4.1.8.

4.1.3.4 Addition of the Fe(II) Oxidation Process and Addition of the Oxygen Evolution Reaction

If Reaction 8, the oxidation of Fe(II) ions to Fe(III) is now considered, using the values shown in Table 4.1.3, Figure 4.1.9 is obtained.

$$Fe^{2+} \rightarrow Fe^{3+} + e^{-} \qquad \text{Reaction 8}$$

	Reaction 8
E_o (V SHE)	0.77
i_o (nA cm^{-2})	1
i_{lim}^{anodic} (nA cm^{-2})	1×10^8
$i_{lim}^{cathodic}$ (nA cm^{-2})	not modelled
activity	0
α	0.5

Table 4.1.3 Parameters for Reaction 8 used in Figure 4.1.9.

The modelling of this reaction has not previously been modelled in the literature, and is often not mentioned in the context of iron in H_2SO_4. It is modelled as being solely under activation control in Figure 4.1.9. However, from the experimental curve, it can be seen that there is a second active-to-passive 'nose' at potentials close to 1.5 V SCE, above which there is a sharp increase in current.

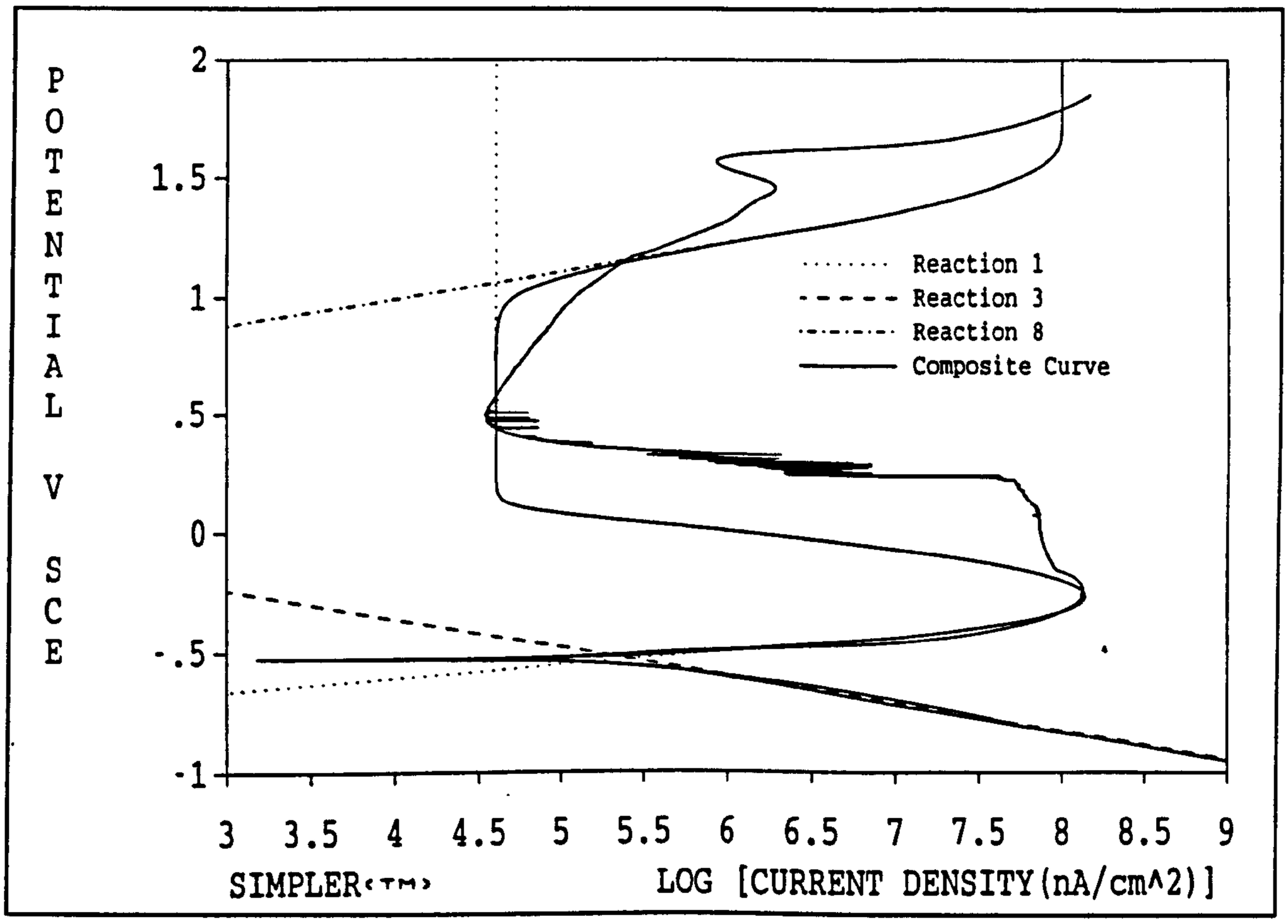

Figure 4.1.9 Model of iron in deaerated 5% H_2SO_4, introducing Reaction 8.

At potentials more positive than this nose, gas is vigorously evolved from the surface of the iron specimen. In order to model these phenomena, the passivation algorithm is applied to Reaction 8, and Reaction 2, the evolution of oxygen, is added.

$$4OH^- \rightarrow O_2 + 2H_2O + 4e^- \qquad \text{Reaction 2}$$

Figures 4.1.10 shows the effect of using the 'raindrop' passivation algorithm on Reaction 8, while Figure 4.1.11 shows the effect of adding Reaction 2. The parameters used shown in Tables 4.1.4 and 4.1.5.

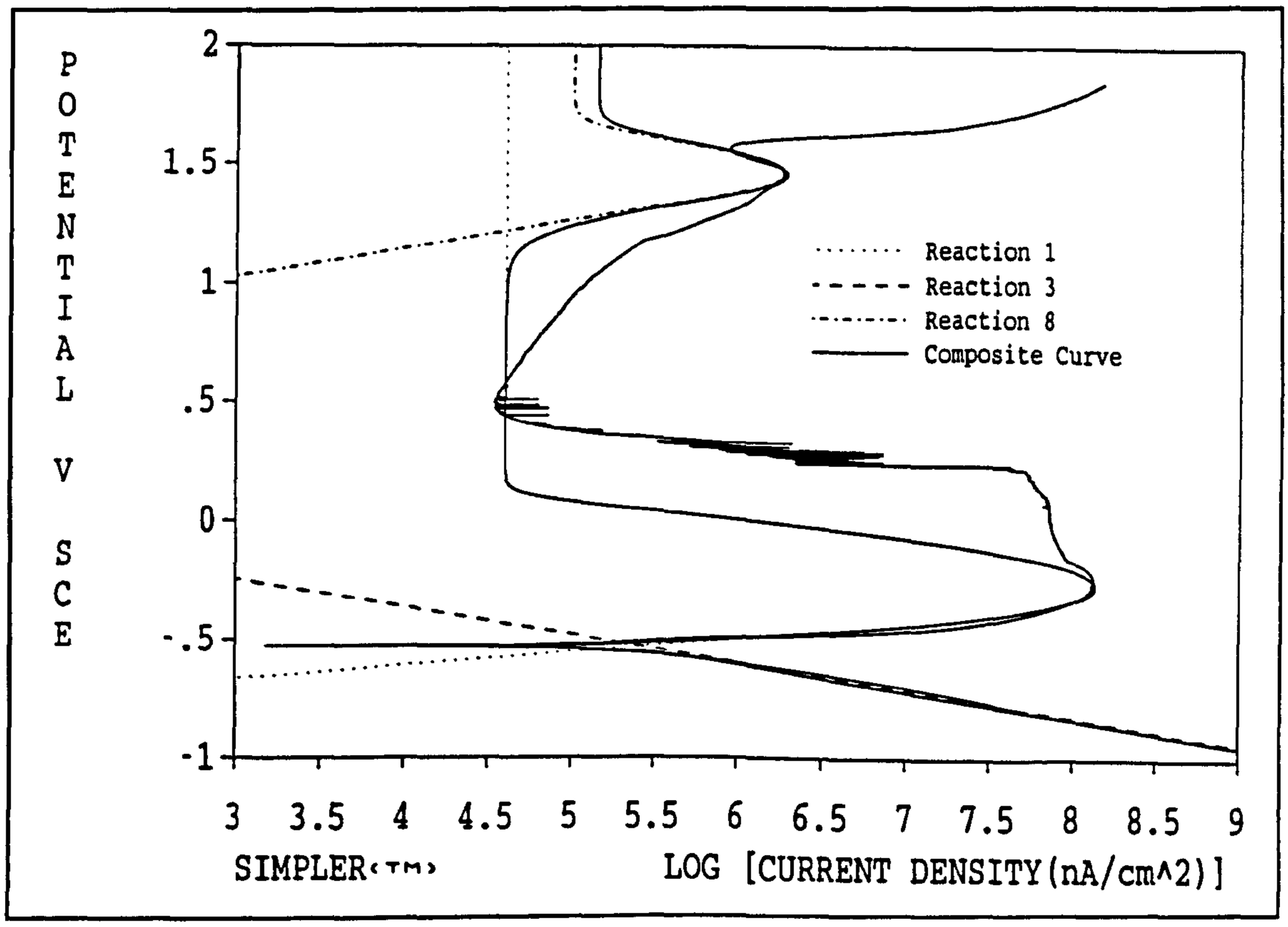

Figure 4.1.10 Model showing addition of passivation routine to Reaction 8.

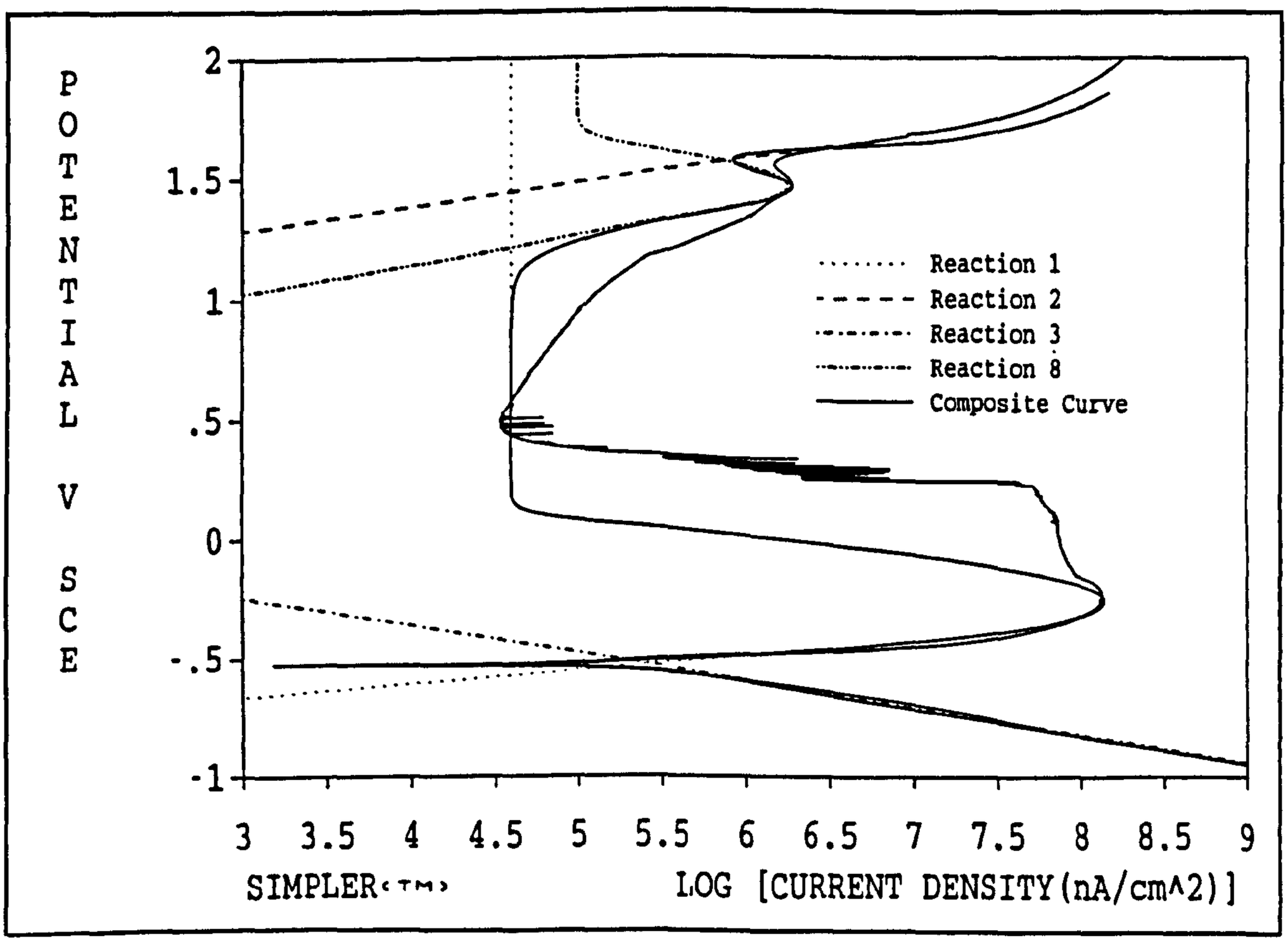

Figure 4.1.11 Final Model for Iron in Deaerated 5% H_2SO_4.

	Reaction 8	Reaction 2
E_o (V SHE)	0.77	1.228
i_o (nA cm^{-2})	0.5	0.5
i_{lim}^{anodic} (nA cm^{-2})	2×10^6	8×10^{15}
$i_{lim}^{cathodic}$ (nA cm^{-2})	1×10^4	1×10^{-3}
activity	0	0.21
α	0.5	0.6

Table 4.1.4 Kinetic Parameters for Reactions 2 and 8 used in Figures 4.1.10 and 4.1.11.

	A (V^{-p})	p	i_{pass} (nA cm^{-2})	E_t (V SCE)
Reaction 3	90	2	1×10^5	1.35

Table 4.1.5 Parameters Used in Raindrop Passivation Algorithm for Reaction 8.

4.1.4 DISCUSSION OF RESULTS

4.1.4.1 Effects of Scan Rate and Electrode Rotation

There is sometimes a marked effect of scan rate upon polarization curves generated by the use of a potentiostat, because an electrochemical system has a finite response time to any change to its equilibrium, such as a change in applied potential. Thus, if the response time of the system exceeds the time of the imposed change, an artefact is introduced and the polarization curve will show an influence due to the scan rate. Marsh has shown[108] that for mild steel in seawater, the critical scan rate is 0.2 mV s^{-1}. Thus, for the polarization curve examined here, a scan rate of 0.1 mV s^{-1} is used.

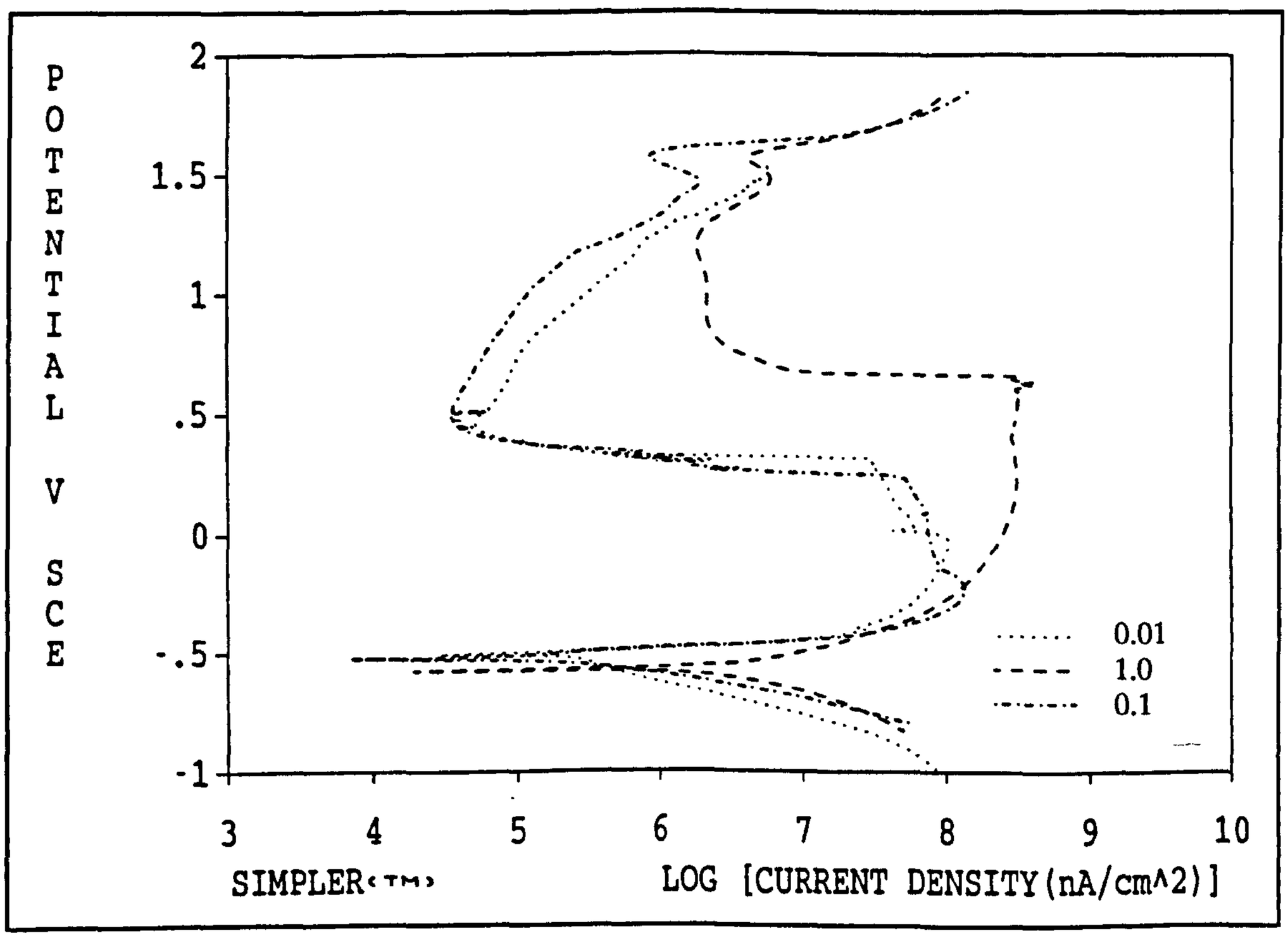

Figure 4.1.12 Effects of different scan rates on polarization curve of pure iron in deaerated 5% H_2SO_4.

Figure 4.1.12 shows the effect of different scan rates on the polarization curves of

pure iron in deaerated 5% H_2SO_4. It can be seen that the curve generated using a scan rate of 1 mV s^{-1} alters quite dramatically from those generated by scan rates of 0.1 and 0.01 mV s^{-1}, in that there is no marked active-to-passive 'nose' between -400 and 0 mV SCE.

For samples of iron in deaerated sulphuric acid which have been generated with scan rates of 0.1 mV s^{-1} and lower, there is a region within the primary passivation loop (DE in Figure 4.1.4) that cannot be explained by the model at present. It appears that the active-to-passive transition begins to take place, after which some reaction or agent prevents this transition from occurring. There then follows a region where the current density response is constant with potential, until at a potential some 200 mV more positive, passivation occurs, with the concomitant fall in current density of 3 orders of magnitude. This discrepancy between ideal and real behaviour is evident when Figures 4.1.1 to 4.1.5 are compared.

Figure 4.1.13 shows the effect of using a rotating electrode with different rotation speeds. As noted in Chapter 2, this is often used as a method[55,56,61] to determine whether the chemisorption or dissolution-precipitation mechanism is responsible for the passivation process.

There is a marked change in the form of the polarization curve between stationary and rotating electrodes, and thus it may be thought that the dissolution-precipitation mechanism is responsible for passivation.

4.1.4.2 Possible Explanations for Deviations in Behaviour of Active-to-Passive Transition

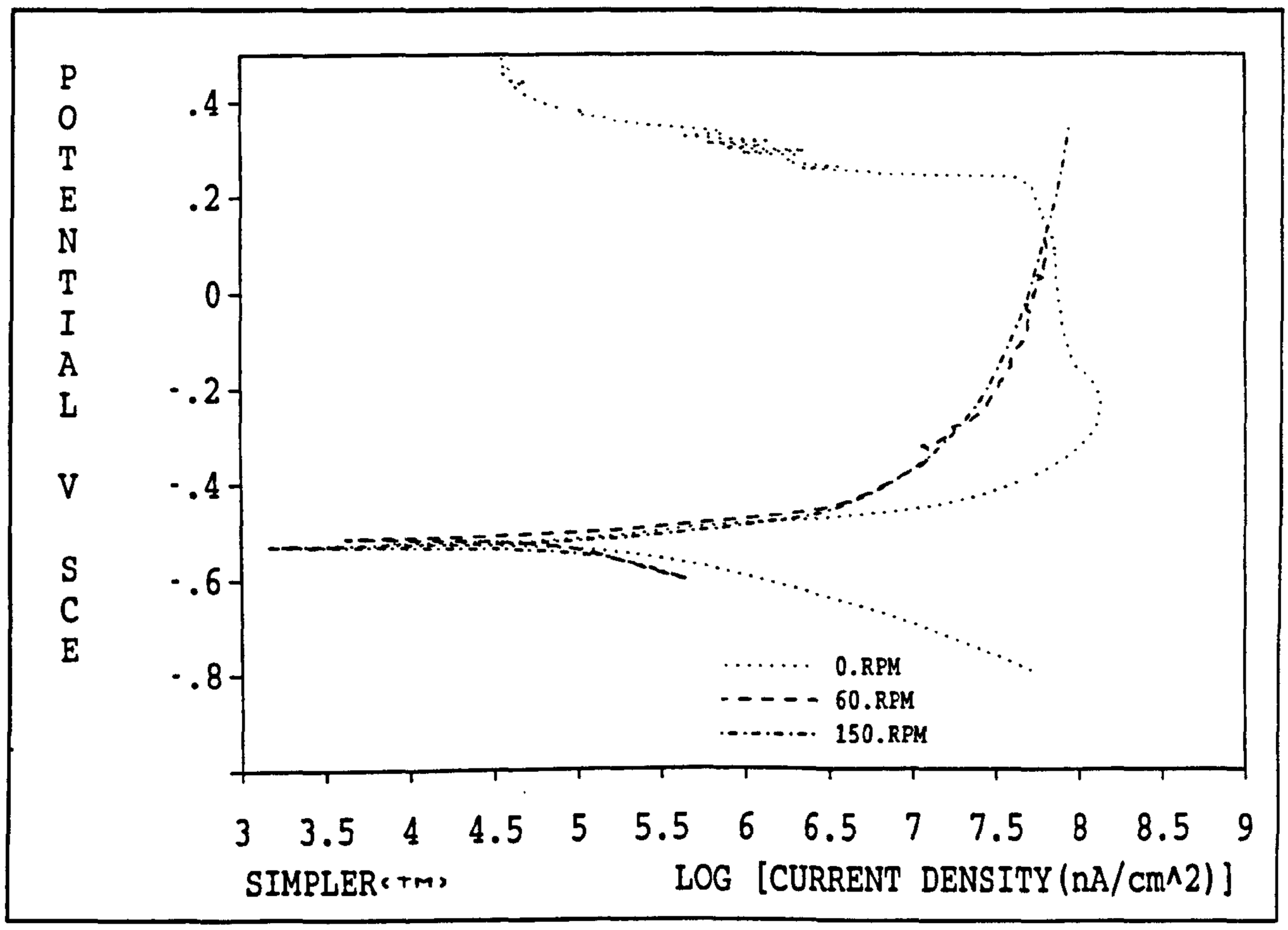

Figure 4.1.13 Effect of rotation speed on the polarization curve for pure iron in deaerated 5% H_2SO_4

At potentials more positive than the free corrosion potential, the metal loses iron atoms via the loss of two electrons, and Fe^{2+} enters solution. This portion of the curve is under activation control. These ferrous ions are formed due to the high dissolution rates, and the solution adjacent to the surface may become supersaturated, leading to the precipitation and formation of a layer of $FeSO_4$. This insulating layer is porous, thereby allowing further ferrous ion production through these pores. These pores in turn become supersaturated, at thus the pores 'move' statistically across the surface of the iron specimen, leading to the appearance of a 'swarming' specimen[113]. This $FeSO_4$ may cover much of the surface, and thus although the true current density on the uncovered surface is higher than at lower potentials, the total recorded current density is less than that predicted by the Tafel equation, due to this super-saturation and precipitation. The magnitude of this current drop depends on the nucleation and growth kinetics of the $FeSO_4$. Hence a fast scan rate will

result in less current drop than a slow scan rate, since the former allows less time for the crystals to nucleate and grow[114]. This effect may be viewed in Figure 4.1.12.

The same argument concerning $FeSO_4$ can be adapted for the rotating electrode experiments. In this case, increased mass transfer due to convection currents will lead to a lower degree of supersaturation in the locality of the electrode, hence less $FeSO_4$ will be precipitated, and there will be less current drop across the insulative layer. It could be argued that due to the similarity of the 60 and 150 rpm curves, there is a critical rotation rate (below 60 rpm) below which supersaturation is not reached. Evidence for this was found by the lack of the characteristic 'swarming' appearance of pores within a $FeSO_4$ layer on the electrode during such experiments.

An alternative explanation for the potential-independent current between -130 and 250 mV SCE was proposed by Lorenz *et al*[105]. Their mechanism for the dissolution and passivation of iron is given below :

Step 1

$$Fe \underset{-e^-}{\overset{+OH^-}{\rightleftharpoons}} \underset{a}{(FeOH)_{ads}} \underset{RDS}{\overset{e^-}{\rightleftharpoons}} \underset{b}{FeOH^+} \overset{-OH^-}{\rightleftharpoons} \underset{c}{Fe^{2+}_{aq}}$$

Step 2

$$d\updownarrow \underset{-e^-}{\overset{+OH^-}{\langle Fe(OH)_2\rangle_{ads}}} \underset{RDS}{\overset{\overset{+OH^-}{-e^-}}{\rightleftharpoons}} \underset{e}{\langle Fe(OH)_3\rangle_{ads}} \rightleftharpoons \underset{f}{\gamma\text{-}Fe_2O_3,\ Fe_3O_4}$$

step 3

$$RDS\updownarrow \begin{matrix} -OH^- \\ g \end{matrix} \quad FeOH^+ \quad \underset{h}{\overset{-OH^-}{\rightleftharpoons}} \quad Fe^{2+}_{aq}$$

Steps *a*, *b* and *c* are the steps that finish with the production of Fe^{2+} ions, which precipitate to form $FeSO_4$ on supersaturation. An alternative process may also occur, in which an adsorbed intermediate species $\langle Fe(OH)_2 \rangle_{ads}$ is produced (step *d*). Step *d* is slower than step *a*, and thus gradually the surface becomes covered with a layer of adsorbed $\langle Fe(OH)_2 \rangle_{ads}$, which then acts as a membrane inhibitor on the dissolution process[115]. This is said to retard the dissolution rate (and could therefore be responsible for the potential-independent current density viewed between -130 and 250 mV SCE) until step *e*, passivation, occurs. This involves a fall in current density of several orders of magnitude to the passive current density, i_{pass}. Further increasing the potential causes ferric (Fe^{3+}) ions to be produced from the passive film. A supersaturated solution may be built up close to the specimen surface, leading to the precipitation of an insulating, porous layer, but this is followed by oxygen evolution and ferric ion production on further anodic polarization.

Keddam *et al*[116,117] proposed a different reaction scheme to that proposed by Lorenz *et al.* They used electrochemical impedance spectroscopy techniques and found that there were three separate dissolution mechanisms. Their proposed reaction scheme is shown below :

At low current densities, Fe^{2+} is formed by the simple, direct mechanism (K_1, K_2), but at higher current densities, they found self-catalytic paths, implying intermediate ferrous species are responsible for the current density. Reaction K_7 is deemed to form a bivalent passivation species (probably adsorbed $Fe(OH)_2$), and the main current decrease is attributable to increasing coverage of this species[118]. A Fe(III) passivation species is found

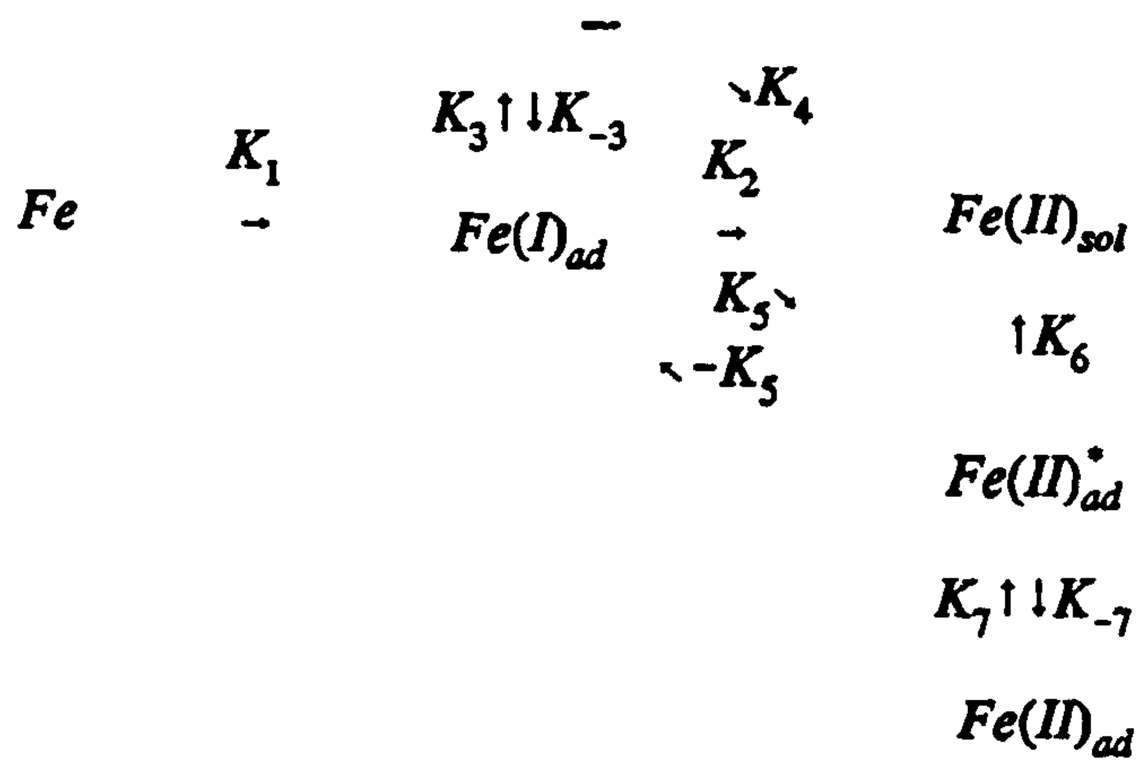

to form close to the Flade potential of ~ 0.58 V SHE (~ 0.35 V SCE). This species could be formed by the reactions (or similar to) steps *e* and *f* in the scheme proposed by Lorenz.

Whatever the actual mechanism responsible for the changes in passivation behaviour in the iron/sulphuric acid system viewed here and elsewhere, it is now accepted that there is more than one dissolution reaction occurring. The Hines 'raindrop' algorithm accurately modelled the initial active-to-passive nose, but could not predict system behaviour when a second mechanism became dominant.

Olivier[49] has proposed a mechanism for the current density oscillations viewed close to the passive region in the polarization curve for iron in 5% H_2SO_4. Full passivity is expected at the Flade potential, while dissolution can take place at potentials more negative than this. Franck[119] found that the Flade potential varies with pH:

$$E_f = E_f^{\theta} - 0.059pH \qquad 4.1.1$$

where E_f^{θ} is the Flade potential at pH 0

When $FeSO_4$ crystals are being precipitated, the current passing through the pores of the insulative $FeSO_4$ layer is carried mainly by H^+ ions moving outwards. This movement of H^+ causes a local decrease in acidity in the liquid close to the metal. Passivity

will soon be established (the Flade potential will alter according to equation 4.1.1), thereby lowering the current. H^+ can then move back close to the metal by diffusion, causing the local pH to fall, and dissolution may then occur, with the associated rise in current density. The software model does not consider local changes in pH, and thus this feature of the polarization curve is not modelled.

4.1.4.3 Comparison of Parameters Used with Published Data

The final value for i_o for the Fe/Fe^{2+} system of 1 nA cm^{-2} compares well with the value of 1 to 10 nA cm^{-2} quoted by West[112], while the corresponding value for the oxygen redox system of 10^{-6} nA cm^{-2} was obtained from the same source. It did not provide a good theoretical model when compared with experimental data. Instead a value of 0.5 nA cm^{-2} was used to model the oxygen evolution reaction. Otieno-Alego *et al*[101,102,100] also used the former value with success. This issue is addressed in section 4.2.

The value of 10^4 nA cm^{-2} for the hydrogen i_o is higher by 1-2 orders of magnitude compared to the two above sources. It should be noted that they used a solution of pH 6.8, as opposed to an acidic solution of pH ~ 0, as is the case here. Thus, in their electrolyte the oxygen reduction process has a dominant role in the shape of the overall cathodic curve, which is not the case in the acidic solution covered here.

4.1.4.4 Passive Current Density

The model assumes that the current density supported by the passivated iron surface remains constant, but it can be seen from the experimental curve that this is not the case; rather the current rises from its initial low value from such potentials that it cannot all be

due to the oxidation of Fe^{2+} to Fe^{3+} (E_o for Reaction 8 is 0.77 V SHE). While it is recognised that the processes occurring on the surface of the iron are anodic in nature, and that dissolution of the metal will take place, it is not yet recognised by which mechanism the formation of iron ions through the film occurs. The model proposed by Lorentz *et al*[105] assumes that the film consists of an mixed oxide, the limits being Fe_3O_4 and Fe_2O_3, while Keddam *et al*[116,117] consider that Fe(III) species are formed close to the Flade potential. Both agree that Fe(III) ions are produced from the electrode at potentials above the Flade potential, thus the secondary passivation viewed is modelled as being the production of Fe(III) ions.

4.1.5 CONCLUDING REMARKS.

The polarization characteristics of pure iron in 5% H_2SO_4 has been investigated. A reaction model has been advanced, and the resultant polarization curve has theoretically modelled using the SIMPLER software. The cathodic and activation controlled anodic portions of the curve have been modelled to a high degree of accuracy. The transpassive section of the curve, including secondary passivation and oxygen evolution, have also been successfully modelled.

The lower portion of the active-to-passive transition has also been modelled satisfactorily. The potential-independent portion of the curve between -130 and 250 mV SCE cannot be modelled using the Hines 'Raindrop' algorithm. Possible explanations for this behaviour are advanced, on the basis of scan rate and rotating electrodes experiments.

Values of the passive current density which are potential-dependent are not modelled at present.

Chapter 4 Section 2 Modelling the Polarisation Curve Behaviour of Type 304 Stainless Steel in Aerated and Deaerated Sulphuric Acid Solution

4.2.1 INTRODUCTION

The addition of chromium in excess of 12% to iron results in the formation of a very thin, protective oxide film, which is self-healing under a variety of oxidizing conditions. Additions of nickel are made to stabilize the austenitic microstructure. Additions of 18% chromium and 8% nickel to a low carbon steel results in a generic stainless steel alloy designated 304 by the American Iron and Steelmaking Institute. It is a general purpose grade, widely used in applications requiring a good combination of corrosion resistance and formability.

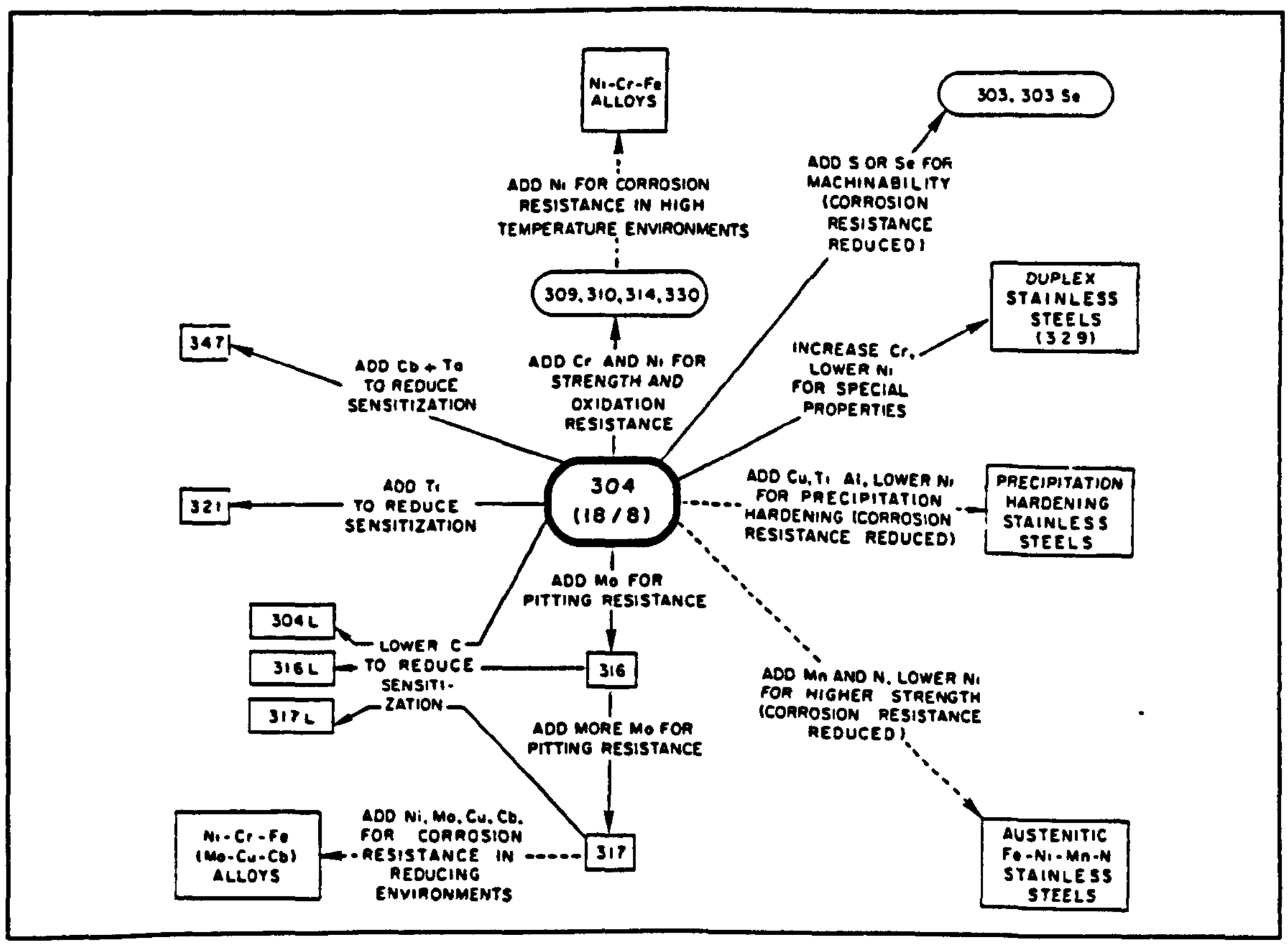

Figure 4.2.1 Link between composition of 304 stainless steels and other alloy systems.

An example of its use is in chemical plant piping carrying sulphuric acid[88]. It acts as a base composition for many other stainless steels (Figure 4.2.1).

The application of a polarization curve model to iron in 5% H_2SO_4 system has been previously described in Section 4.1. The purpose of this section is to describe the application of the model to 304 stainless steel in the same media, with three different oxygen concentrations.

4.2.2 EXPERIMENTAL

304 stainless steel in the form of bar of diameter 6.5 mm was obtained from Aalco, cut into strips, then ground flat such that rectangular samples of surface area 1.2 cm^2 were obtained. These were mounted in the manner described in Section 4.1.2. The samples were left to attain a steady potential for an hour under freely corroding conditions, prior to a potentiodynamic scan from a potential -250 mV more negative with respect to this potential, to a potential 2000 mV more positive than the free corrosion potential. A scan rate of 0.1 mV s^{-1} was used. The same equipment was used for the potentiodyanmic scans as detailed in Section 4.1.2. For deaerated solutions, argon was bubbled through the three electrode cell in which the experiment was conducted, from the time of initial immersion to completion of the experiment. Dissolved oxygen measurements were made using a Jenway POM 7 dissolved oxygen meter with a gold/saturated KCl probe, zero-calibrated with 2% sodium sulphite and to 100% with distilled water vapour.

4.2.3 MODELLING PROCEDURE

The SIMPLER modelling software[93,92] with the passivating routine described in

Chapter 3 was used to model the curve by considering the individual redox reactions that constitute the overall curve. The cathodic behaviour was studied initially, and once a good correlation had been achieved, the anodic portion of the curve was studied.

In all cases, a pH value of 0.20 and a solution temperature of 20°C were used. A resistance of 30 ohms was used to model the combined effects of solution and film resistance. The values used for the partial pressure of oxygen in the electrolyte (0.20, 0.05, 0.10 atmospheres) depended upon whether the solution was aerated, deaerated or left stagnant respectively.

4.2.3.1 304 Stainless Steel in Deaerated 5% H_2SO_4

The experimentally determined polarization scan for 304 stainless steel in deaerated 5% sulphuric acid is shown in Figure 4.2.2. The curve can be split into regions. Region AB is the cathodic portion, showing the curve to be under activation polarization control, while region BC is the corresponding anodic activation-controlled region. At the potentials denoted by CD, there is an active-to-passive transition, followed by the passive region DE, where current is largely independent of potential. Above the passive region is the transpassive section of the curve (EFGHI), where metal dissolution and/or oxygen evolution takes place.

Figure 4.2.3 shows the experimental curves for 304 and pure iron overlaid. It can be seen that the current densities supported on the surface of the pure iron are much greater than those on the 304 stainless steel surface, and, over a range of 1.5 V from -0.5 to 1.0 V, the stainless steel is between 100 and 1000 times more corrosion-resistant than pure iron.

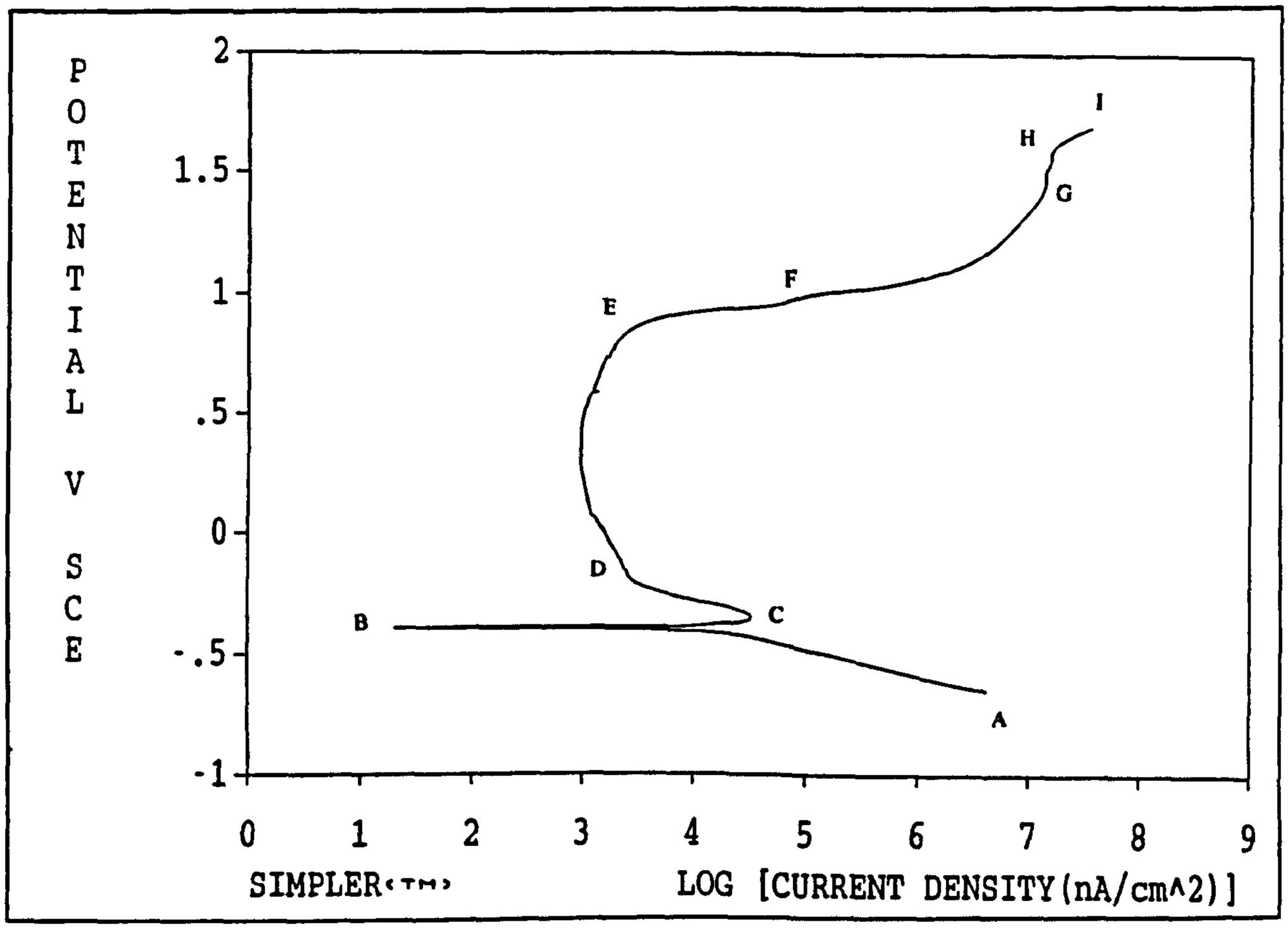

Figure 4.2.2 Experimental polarization curve for 304 stainless steel in deaerated 5% H_2SO_4.

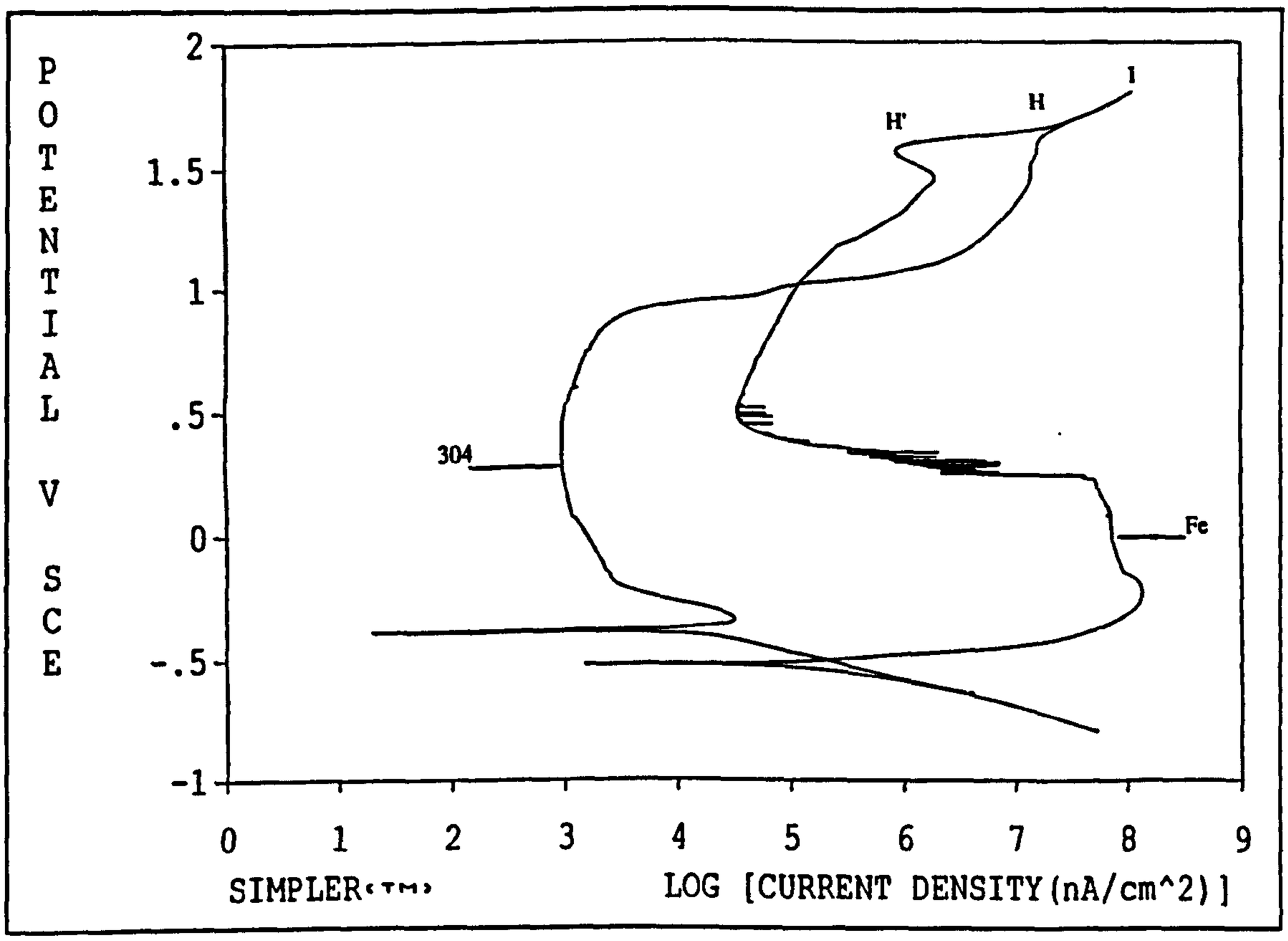

Figure 4.2.3 Experimental polarization curves for pure iron and type 304 stainless steel in deaerated 5% H_2SO_4.

4.2.3.2 Dissolution Model Proposed for 304 Stainless Steel

The passivation process of 304 stainless steel is thought to occur by a mechanism involving the selective dissolution of iron atoms from the surface, and subsequent oxidation of Cr by water to form extended -Cr-O-Cr-O-Cr-O- chains. These chains then block further iron dissolution from ledge sites. This model, based on the percolation theory advanced by Newman *et al*[62,63,64] (described in Section 2.2.5), differs from that proposed by Marcus in that Fe-Cr bonds and not Cr-Cr bonds are broken, prior to oxidation by adsorbed oxygen. It should be noted, however, that Marcus only considered pure elements, rather than alloys.

The region BC in Figure 4.2.2 thus corresponds to the dissolution of iron atoms, with the loss of 2 electrons. Since there are fewer iron atoms available to enter solution from the surface, the current associated with the dissolution process for 304 is smaller in magnitude then for pure iron. Modelling shows that the magnitude of i_o is smaller than that for pure iron.

4.2.3.3 The Devereux and Yeum Model

The iron (II), oxygen and hydrogen redox reactions (Reactions 1 to 3) were initially considered. These are the reactions used by Devereux and Yeum[96] to model the same system.

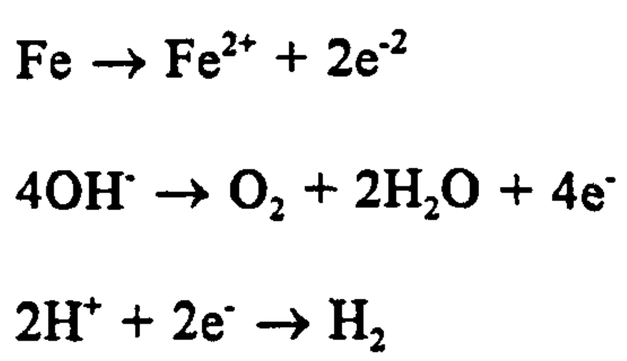

$$Fe \rightarrow Fe^{2+} + 2e^{-2} \qquad \text{Reaction 1}$$

$$4OH^{-} \rightarrow O_2 + 2H_2O + 4e^{-} \qquad \text{Reaction 2}$$

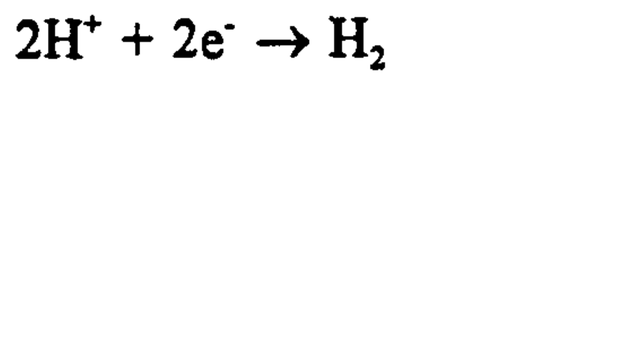

$$2H^{+} + 2e^{-} \rightarrow H_2 \qquad \text{Reaction 3}$$

Slightly modified values of the parameters used to model the behaviour of pure iron (Section 4.1) were used here, and are given in Tables 4.2.1 and 4.2.2. A negligible value in Table 4.2.1a indicates that the reaction does not occur. For example, the reduction of oxygen in deaerated acid solution (the reverse of Reaction 2) cannot occur due to the absence of oxygen in the electrolyte.

The threshold activity of iron (II) ions in solution is 10^{-6} mol litre^{-1}, while the partial pressure of oxygen was measured as 0.05 atmospheres. Both quantities are needed for the calculation of the standard redox potential for each reaction. The value of the limiting anodic current density for Reaction 1 is not required because the anodic portion of the reaction is the current density supported by the passivated metal surface. The potential-current density relationships for each of the redox reactions using the parameters in Tables 4.2.1 and 4.2.2 are shown in Figure 4.2.4, which also has both the resultant theoretical and experimental curves overlaid. The current density attributable to the oxidation of hydrogen is considered to be negligible - all the hydrogen produced by the cathodic reaction has bubbled out of the electrolyte.

	Reaction 1	Reaction 2	Reaction 3
E^o (V SHE)	0.440	1.228	0.000
i_o (nA cm^{-2})	1.5×10^{-4}	10	8×10^{2}
i_{lim}anodic (nA cm^{-2})	not required	2×10^{7}	negligible
i_{lim}cathodic (nA cm^{-2})	negligible	negligible	1×10^{20}
α	0.5	0.6	0.45

Table 4.2.1 Parameters used in Figure 4.2.4.

	i_{pass} (nA cm^{-2})	A	p	E_{trans} (V SCE)
Reaction 1	1.4 x 10^3	450	2	-0.390

Table 4.2.2 Parameters used in passivation routine for reaction 1.

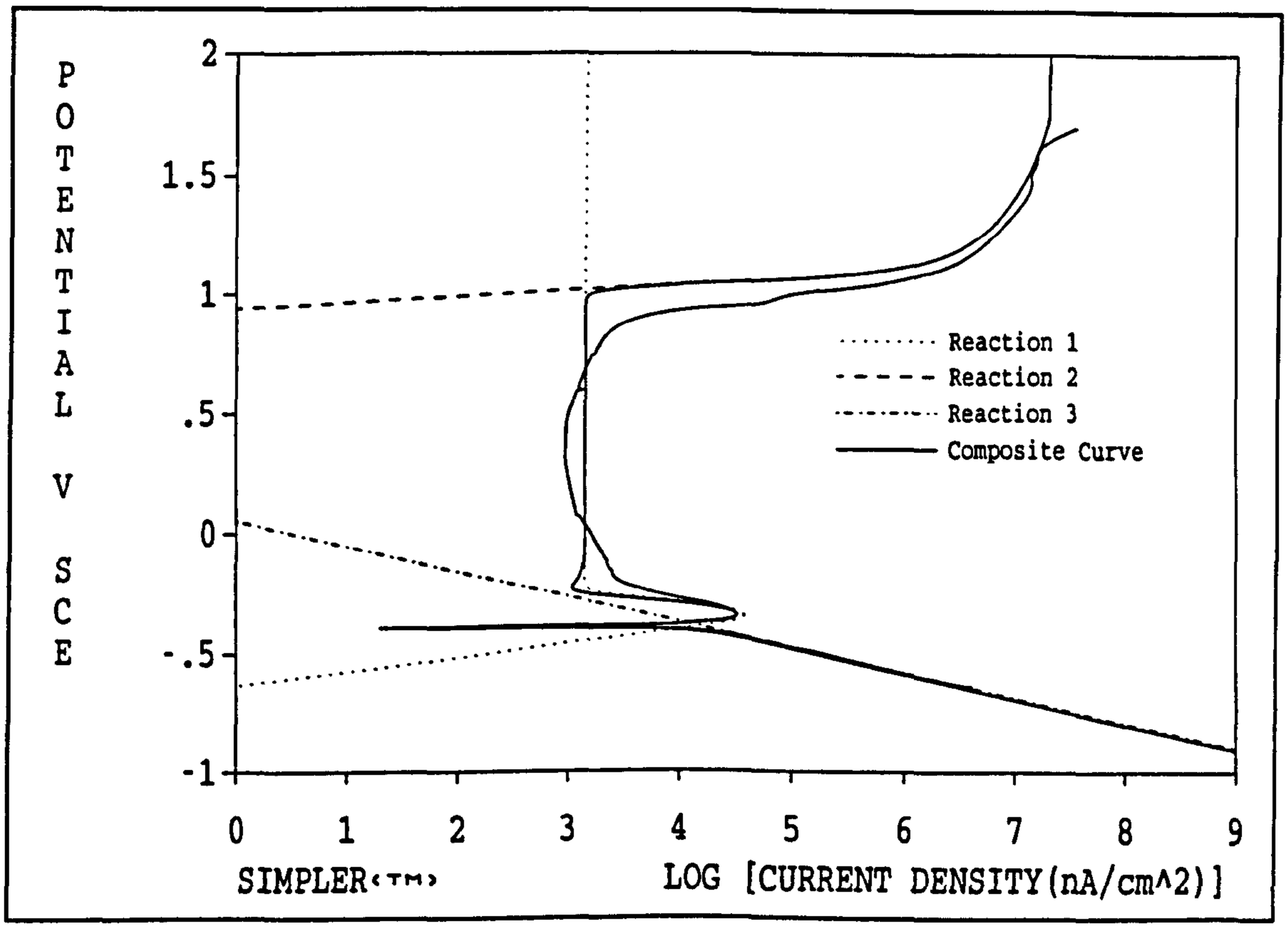

Figure 4.2.4 Modelling the behaviour of 304 stainless steel in deaerated 5% H_2SO_4 using the same reactions as Devereux and Yeum.

An excellent fit is obtained for the cathodic section of the curve, the initial activation-controlled portion of the anodic curve and the active-to-passive transition. Figure 4.2.5 shows this area in greater detail.

However, the passive region is assumed to support a constant current density by the model, which does not occur in the experimental curve. This is discussed later in Section 4.2.4.3.

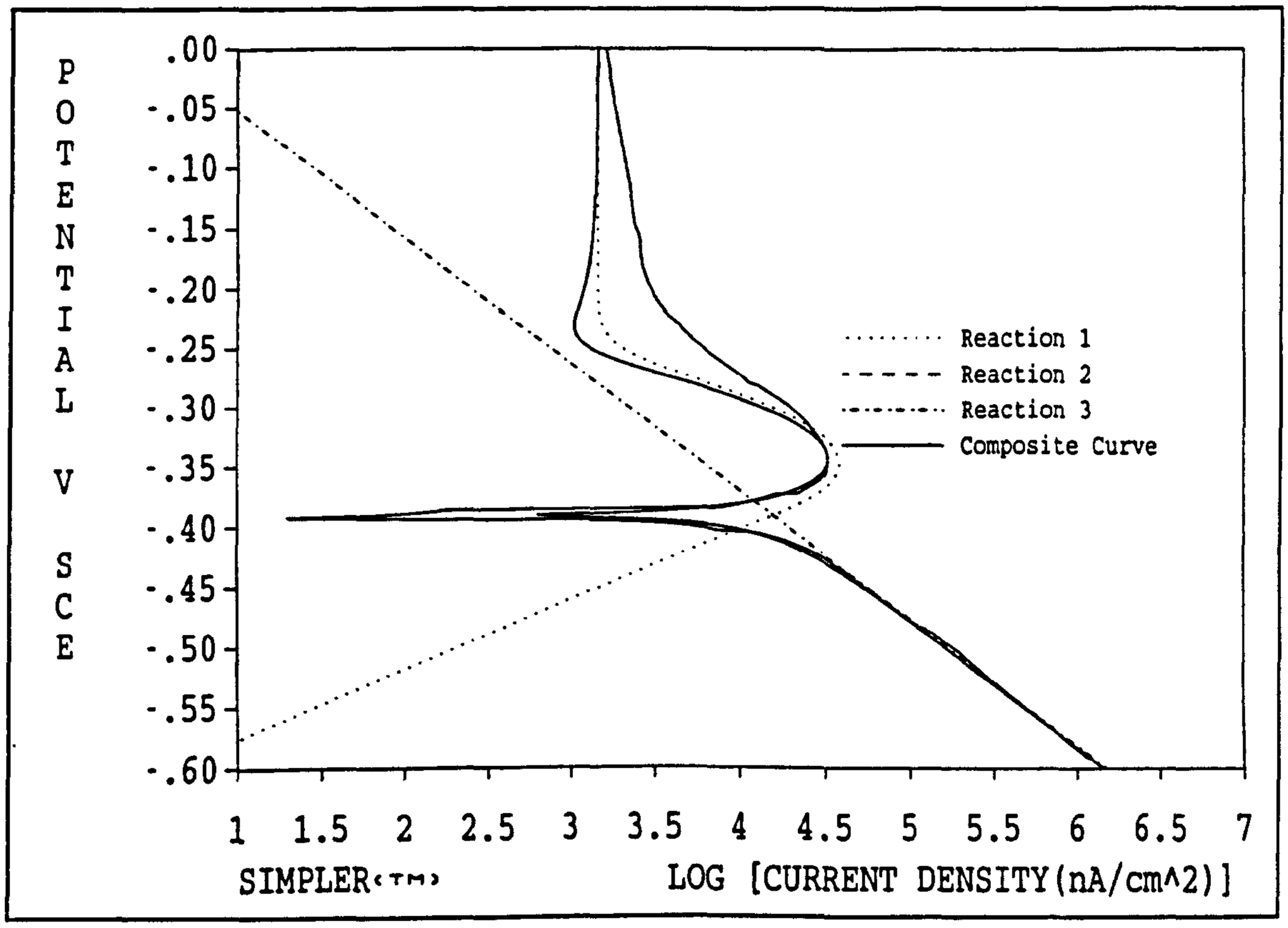

Figure 4.2.5 More Detailed View of the Curve Modelled in Figure 4.2.4.

The transpassive region is poorly modelled by the use of Reaction 2 in this form. It should be noted that the oxygen evolution reaction used in this way has a larger value of i_o (10 nA cm^{-2}) than that quoted by Bockris[58] for an iron surface of 0.1 nA cm^{-2}. Other authors have used different values for i_o, although most only model the reduction process. A value of 3×10^{-4} nA cm^{-2} was used for both a low alloy steel in a steam environment system [103] and for low carbon steel in sugar juice[101]. The same group of workers have also used i_o values of 1×10^{-5} nA cm^{-2} [100] for iron in sodium benzoate and 3×10^{-6} nA cm^{-2} for mild steel in sugar juice[102]. However, Bird[104] have modelled the oxidation process, and used a value of 1×10^{-5} nA cm^{-2} for an iron electrode in deaerated solutions of pH 10 - 14.

α is found to be 0.6. If the reaction was a simple, single electron transfer reaction, this would simply mean that the OH^- ions have to travel more than halfway across the

double layer before they release an electron and form oxygen and water molecules. This is not the case; rather the reaction proceeds in a series of intermediate steps, and thus the symmetry factor α is replaced by the transfer coefficients $\alpha^{\rightarrow}$ and $\alpha^{\leftarrow}$. This will be discussed later in Section 4.3. At this point however, α is best regarded as a measure of the efficiency of the reaction.

In the iron/sulphuric acid system, the oxygen reaction does not become appreciable until the applied potential is more positive than 1500 mV SCE. In the experimental curve for both 304 and pure iron in deaerated H_2SO_4 (Figure 4.2.3), there is another branch (H'HI) above the transpassive region at a potential of slightly above 1500 mV SCE. This is due to the current produced by the oxygen evolution reaction. Visual observation of gas evolution on the metal at these potentials supports this. Thus the reaction scheme proposed by Devereux and Yeum for 304 stainless steel in sulphuric acid appears incorrect; an improved model is proposed below.

4.2.3.4 Chromium Oxide Influence

The portion of the curve previously designated as region EFGH in Figure 4.2.2 will now be investigated. The metal surface exhibits transpassive behaviour at a potential of around 900mV SCE (point E) appearing to exhibit diffusion-limited current density at almost 1400 mV SCE (point G), whilst another reaction becomes predominant at around 1600 mV SCE (point HI). In the transpassive region between 900 and 1400 mV SCE, there is also a slight change (or shoulder) in the slope of the experimental curve (point F). This transition appears in many experimental curves and is not a result of instrumentation error.

To model the transpassive region, a redox reaction involving chromium oxide was

considered :

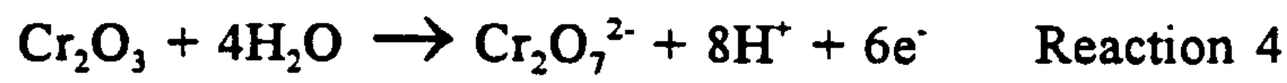

$$Cr_2O_3 + 4H_2O \rightarrow Cr_2O_7^{2-} + 8H^+ + 6e^- \qquad \text{Reaction 4}$$

This reaction accounts for the degradation of the Cr_2O_3 film, and also for any attack to the underlying solid solution of chromium in the austenitic iron matrix. The Cr_2O_3 was assumed to be in the form of $Cr(OH)_3$.

New parameter values were used for Reactions 1 to 3, and kinetic parameter values for Reactions 1 to 4 are shown in Table 4.2.3. Such values will correct the position of the modelled oxygen evolution process to the more electropositive potentials observed experimentally. However, the magnitude of i_o for the oxygen evolution process is much smaller than before. This is discussed later in Section 4.2.4.1.

	Reaction 1	Reaction 2	Reaction 3	Reaction 4
E° (V SHE)	0.440	1.228	0.000	1.242
i_o (nA cm^{-2})	2×10^{-4}	1×10^{-20}	2×10^{3}	1
i_{lim}anodic (nA cm^{-2})	not required	1×10^{22}	negligible	3×10^{7}
i_{lim}cathodic (nA cm^{-2})	negligible	negligible	1×10^{20}	negligible
α	0.5	0.6	0.45	0.5

Table 4.2.3.Modified parameters for Reactions 1,2, 3 and 4.

The result of these modifications is shown in Figure 4.2.6. As may be seen, reaction

4 describes the upper portion (FG).

The value of E° quoted for Reaction 4 was taken for Cr_2O_3 in the form of $Cr(OH)_3$. Pourbaix[10] quotes three E° values for Cr_2O_3, in the form $Cr(OH)_3$, anhydrous Cr_2O_3, or as $Cr(OH)_3.nH_2O$ respectively. The current density attributable to the reduction of chromate ions is negligible, since initially there are no $Cr_2O_7^{2-}$ ions present in the electrolyte that may be reduced to Cr_2O_3 ions.

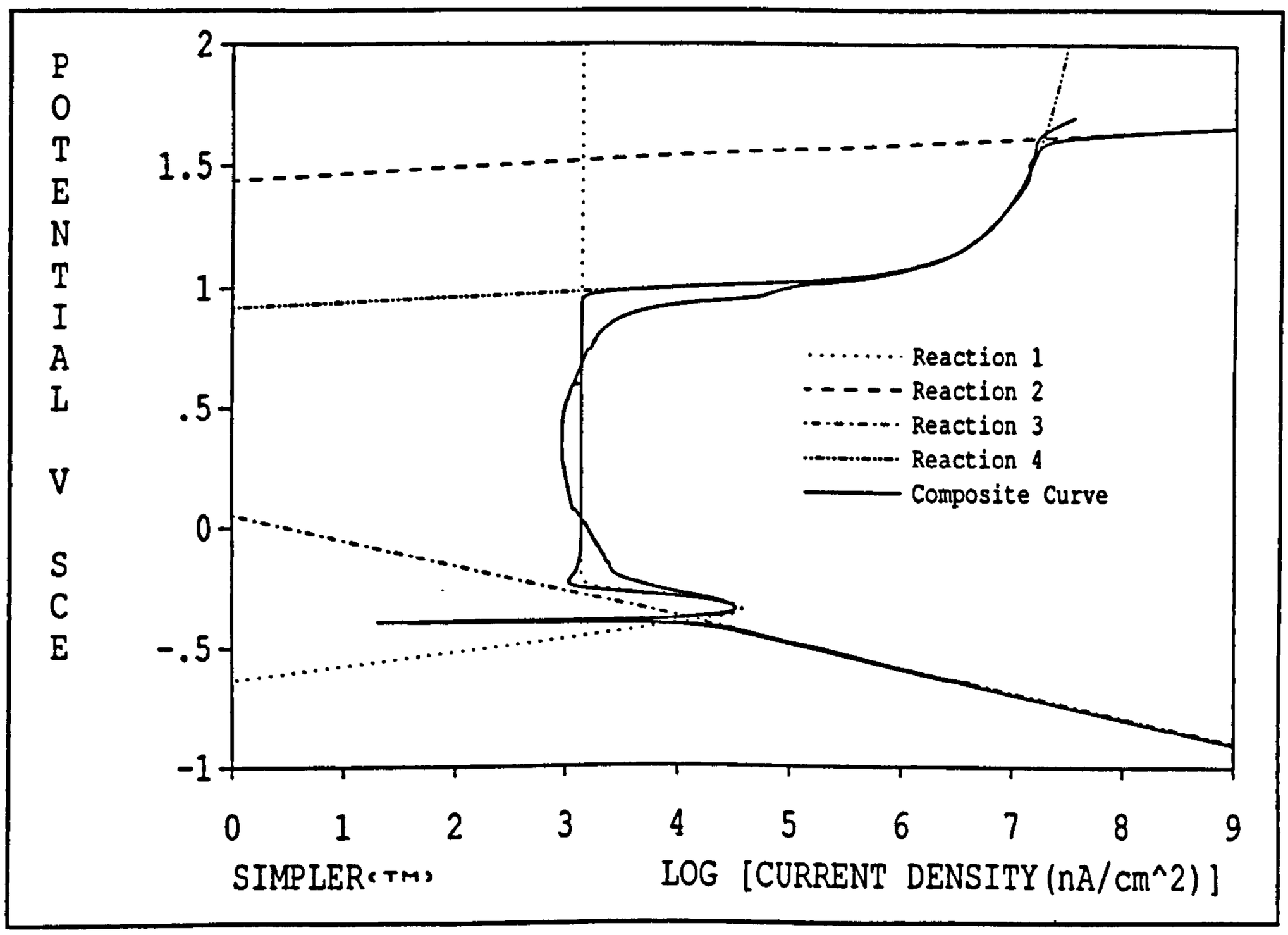

Figure 4.2.6 Model of behaviour of 304 Stainless Steel in deaerated 5% H_2SO_4, using reactions 1,2,3 and 4.

4.2.3.5 Effect of Coefficients in Nernst Equation and Symmetry Factor on Tafel Slopes for the Oxygen Evolution Reaction

As mentioned previously, it appears that the region HI in Figure 4.2.1 is due to evolution of oxygen. However, the magnitude of i_o, 1×10^{-20} nA cm^{-2}, is extremely small

compared to other values quoted by other authors[100,112] casting doubt about the model used. It was decided to investigate the calculation and its parameters further. Figures 4.2.7 to 4.2.9 generate similar curves for the oxygen evolution process in different ways. The same effect may be generated by considering the meanings of the terms used in the modified Nernst equation for the O_2/OH^- redox process.

$$4OH^- \rightarrow O_2 + 2H_2O + 4e^- \qquad \text{Reaction 2}$$

$$E_1 = E_0 \pm (\frac{c}{d})\frac{RT}{F}pH \pm (\frac{a}{b})\frac{RT}{F}\log[pO_2]$$

The algorithm then calculates the Tafel constants (β_{anodic} and $\beta_{cathodic}$) in the following way:

$$\beta = \frac{2.303RT}{zF}$$

where,

if a = 0, then z = (d/c)

otherwise

if a ≠ 0, then z = (b/a)

The ratio (a/b) can be considered in two ways:

(i) the total number of electrons transferred per oxygen molecule in Reaction 2, giving $z = 4$.

(ii) the number of electrons transferred per hydroxide ion in Reaction 2. In this case, $z = 1$ and $\beta = 0.06/\alpha$ at 20 °C.

This second case leads to lower values of the Tafel constants for a given value of

α. As mentioned previously, Bockris[58] quotes 0.1 nA cm^{-2} as the i_o value for the oxygen redox reaction, but this is for a noble metal substrate, such as platinum. Exchange current densities can vary by many orders of magnitude on different metal surfaces. West[112] quotes a value of 1 x 10^{-5} nA cm^{-2} for an iron substrate. Table 4.2.4 lists three sets of parameters used in Figures 4.2.7, 4.2.8 and 4.2.9.

Figure No	a	b	α	i_o (nA cm^{-2})
4.2.7	1	4	0.2	10^{-1}
4.2.8	1	4	0.23	10^{-5}
4.2.9	4	4	0.5	3

Table 4.2.4 Parameters used in Figures 4.2.7 to 4.2.9

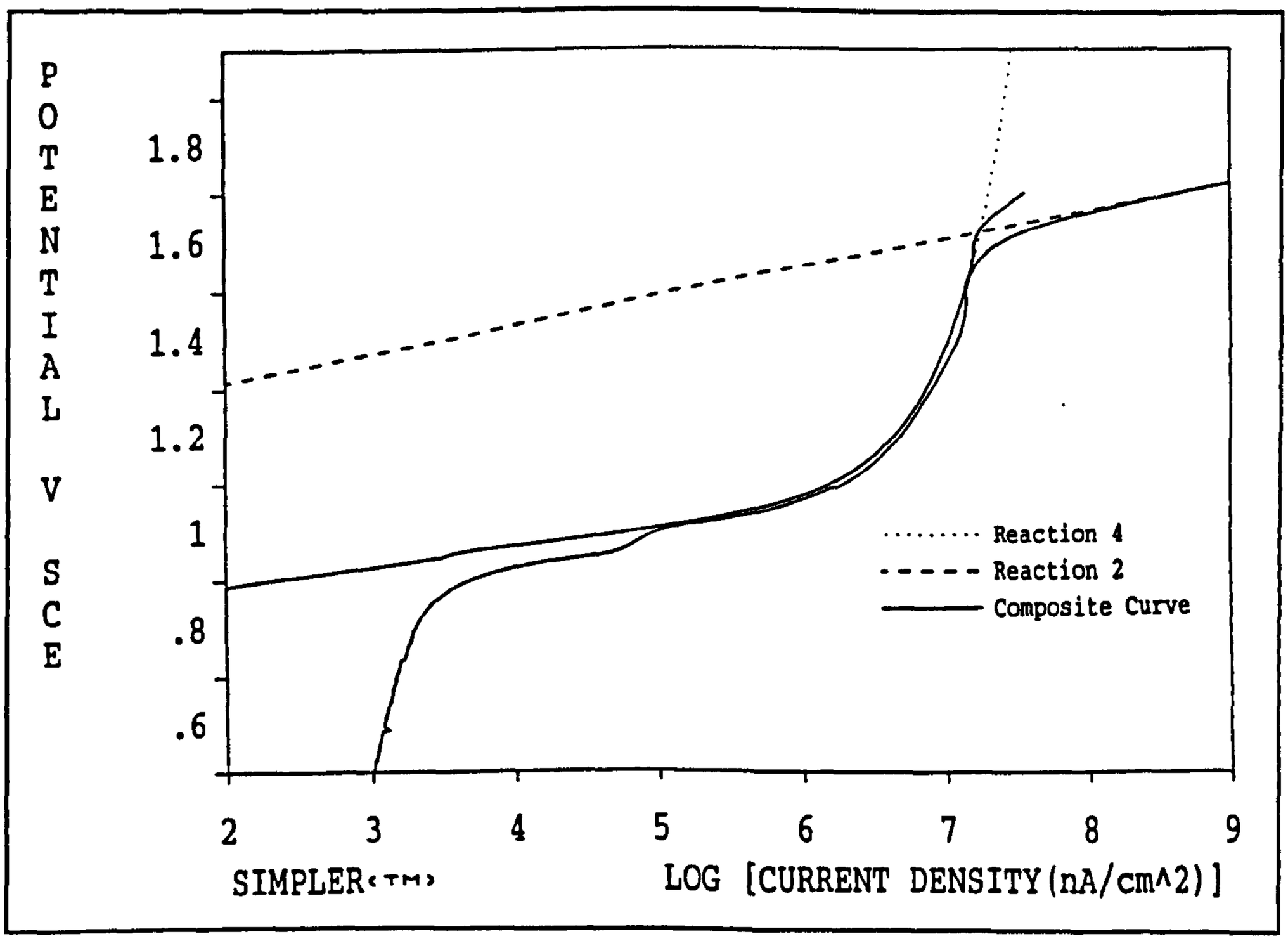

Figure 4.2.7 Model showing effect of Reaction 2 with α = 0.25, z = 4 and i_o = 0.1 nA cm^{-2}.

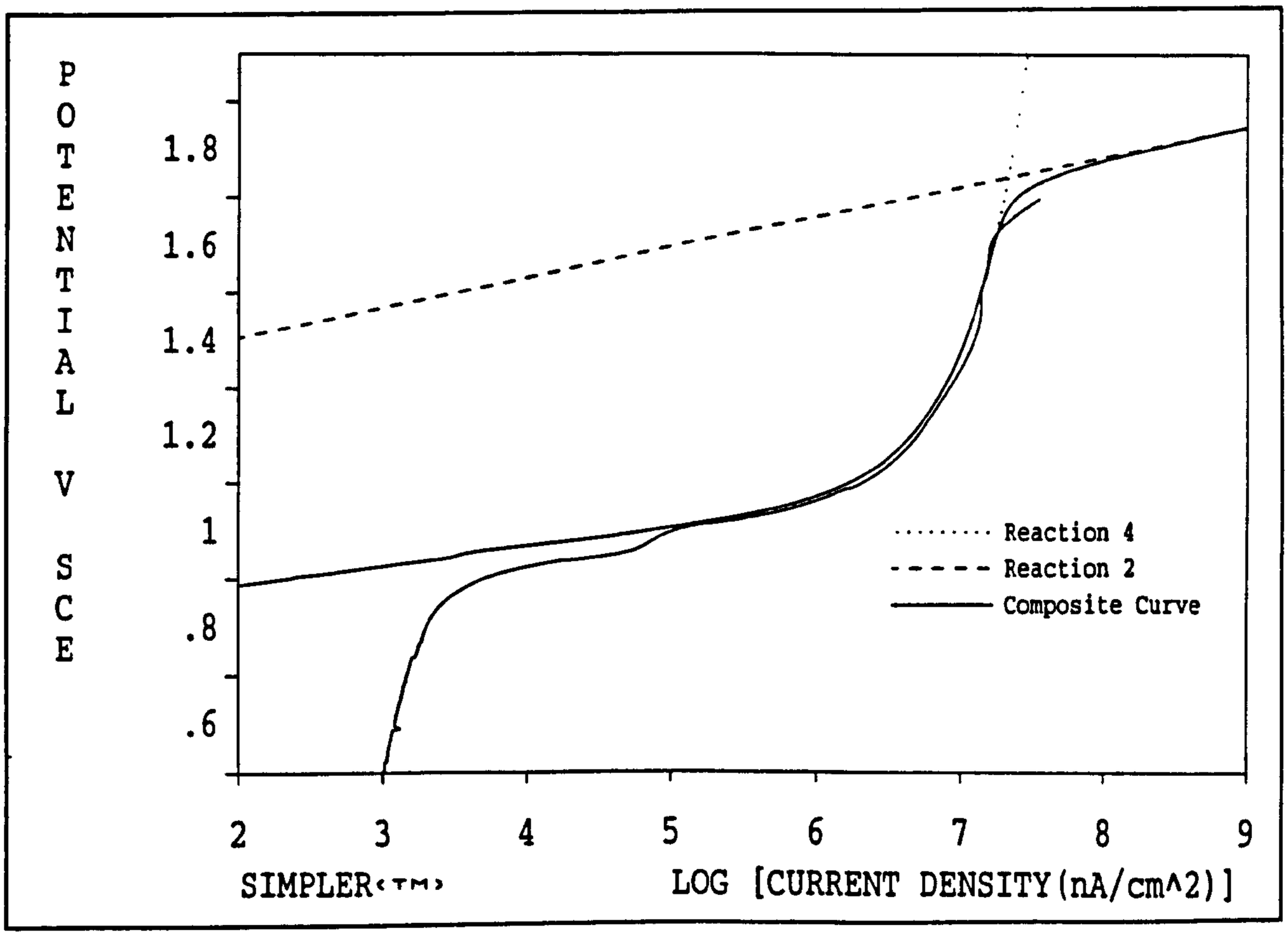

Figure 4.2.8 Model showing effect of Reaction 2 with $\alpha = 0.23$, $z = 4$ and $i_o = 10^{-5}$ nA cm^{-2}.

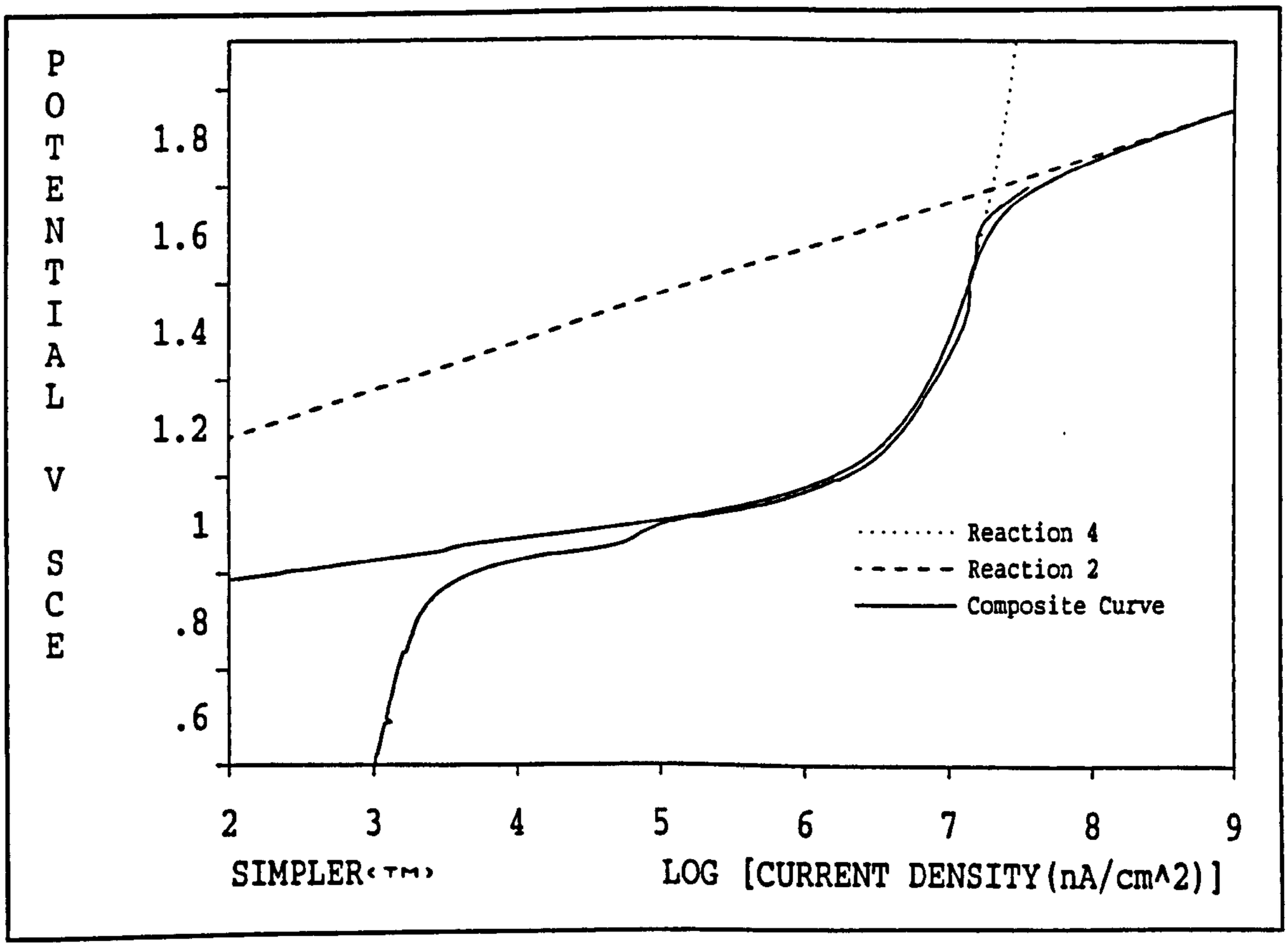

Figure 4.2.9 Model showing effect of Reaction 2 with $\alpha = 0.5$, $z = 1$ and $i_o = 3$ nA cm^{-2}.

Figure 4.2.7 and 4.2.8 yield Tafel slopes of around 0.06, while Figure 4.2.9 assumes a = b = 4, with α = 0.6, leading to a Tafel slope of 0.10. This compares well with the Tafel slope of 0.118 used by Otieno-Alego *et al*[100] for a carbon steel, while West[112] quotes values in excess of 0.12 for the same reaction.

The parameters used for Figure 4.2.9 thus lead to a Tafel slope which most closely maps the actual slope of the upper transpassive branch; hence $z = 1$ has been used to model both the oxygen evolution curve here, and the reduction of oxygen in the aerated system later. The latter case cannot be satisfactorily modelled with $z = 4$, whereas $z = 1$ does lead to a satisfactory fit to the experimental curve. Thus it is concluded that z is the ratio of electrons transferred per ion rather than the total number of electrons transferred per oxygen molecule.

The difficulties associated with accurate measurements of the exchange current density for the oxygen evolution reaction are discussed in Section 4.2.4.1.

4.2.3.6 Role of the Dichromate and Acid Chromate Ions

From close examination of the experimental polarization curve between 850 and 1100 mV, it can be seen that there is a 'shoulder' to the curve (point F in Figure 4.2.2). This 'shoulder' was seen on many experimental curves, and is not an instrumentation error.

Figure 4.2.10 shows the domains of relative predominance of ions of hexavalent chromium. Examination of this system shows that there are two hexavalent chromium ions, dichromate ($Cr_2O_7^{2-}$) and acid chromate ($HCrO_4^-$), which are thermodynamically stable in acidic solutions of pH up to 6.3[51]. The acid chromate reaction is shown below:

$$Cr_2O_3 + 5H_2O \rightarrow 2HCrO_4^- + 8H^+ + 6e^- \quad \text{Reaction 5}$$

At low concentrations of hexavalent chromium, the acid chromate ion predominates, but at higher concentrations the dichromate ion is the dominant species. It was hypothesised that the region EFG could be represented by :

(i) the chromium oxide dissolving out of the surface film, forming acid chromate ions, $HCrO_4^-$ (EF).

(ii) at a certain threshold level of hexavalent chromium in solution, the dichromate ion ($Cr_2O_7^{2-}$) forms preferentially (FG).

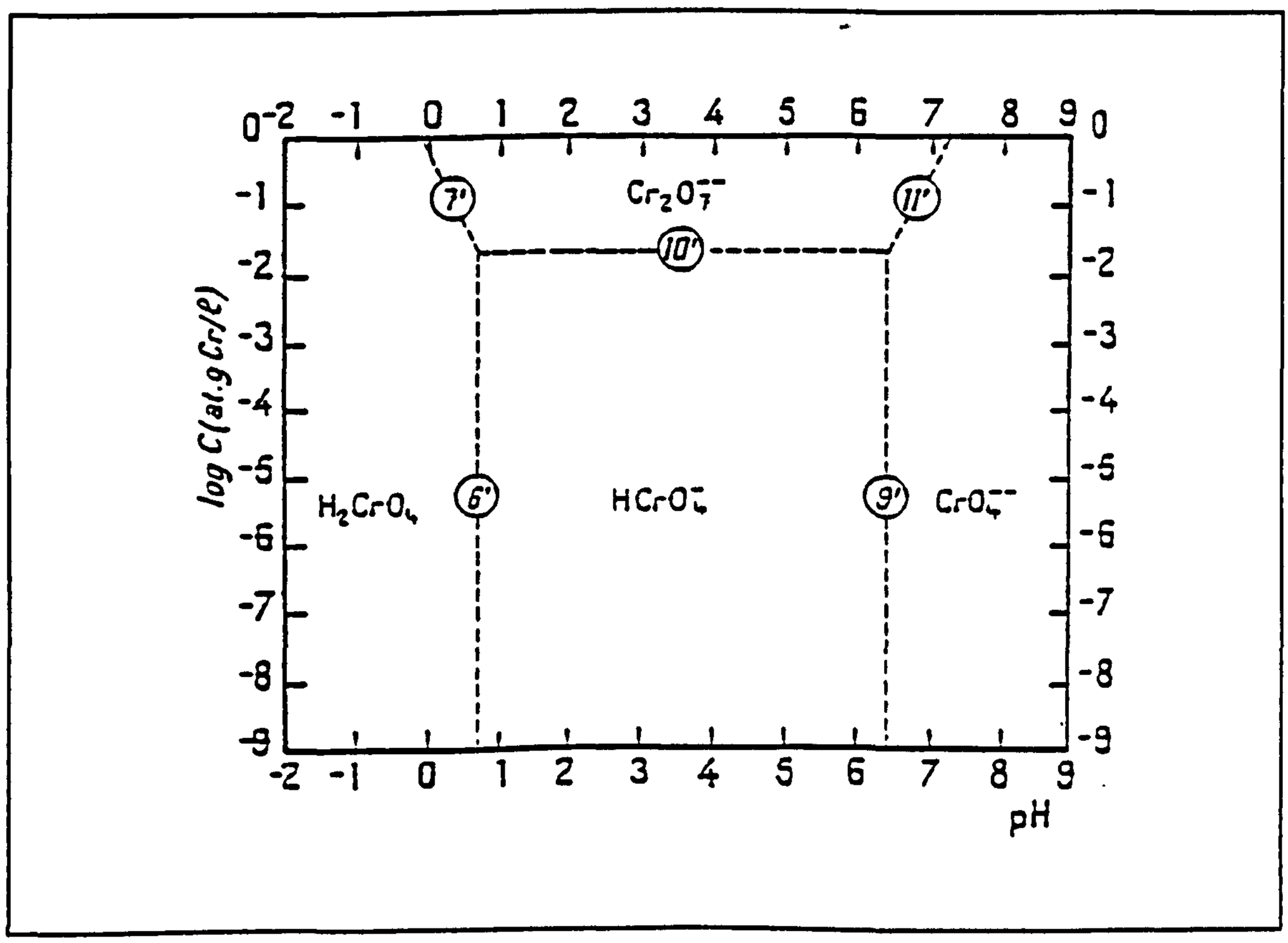

Figure 4.2.10 Stability diagram showing relative predominance of hexavalent chromium ions.

In this model, the point F could be attributed to the limiting threshold of acid chromate ion concentration in the solution. Unfortunately, the E° values quoted by Pourbaix[51] (Table 4.2.5) show that Reaction 5 occurs at more electropositive potentials than

Reaction 4, regardless of the form of Cr_2O_3.

Form of Cr_2O_3	Reaction 5	Reaction 4
$Cr(OH)_3$	1.259	1.242
anhydrous Cr_2O_3	1.184	1.168
$Cr(OH)_3.nH_2O$	1.117	1.101

Table 4.2.5 E° (V SHE) values for reactions 4 and 5 for Cr_2O_3 in differing forms[51].

Despite altering the activities of the two hexavalent chromium ions in the solution, the free corrosion current densities and the charge transfer coefficients, no correlation could be made with the experimental curve. An example of the two reactions, overlaid on the experimental curve is given in Figure 4.2.11, which uses the values given in Table 4.2.6.

Again, the cathodic current densities are negligible, due to the absence of the relevant chromate ions in the electrolyte at the potentials where the reverse of Reactions 4 and 5 are thermodynamically favourable.

Metal dissolution processes are not ordinarily considered to become diffusion-limited. The parameters used as the diffusion-limited current densities for these two reactions may better be viewed as the current densities at which other processes (such as the formation of an alternative chromium ion or oxygen evolution) become the dominant process. This is further discussed in Section 4.2.4.4.

	Reaction 5	Reaction 4
E^o (V SHE)	1.117	1.242
i_o (nA cm^{-2})	10	10
i_{lim}anodic (nA cm^{-2})	6×10^4	7×10^7
i_{lim}cathodic (nA cm^{-2})	negligible	negligible
α	0.5	0.5

Table 4.2.6 Parameters used for Reactions 4 and 5 in Figure 4.2.11.

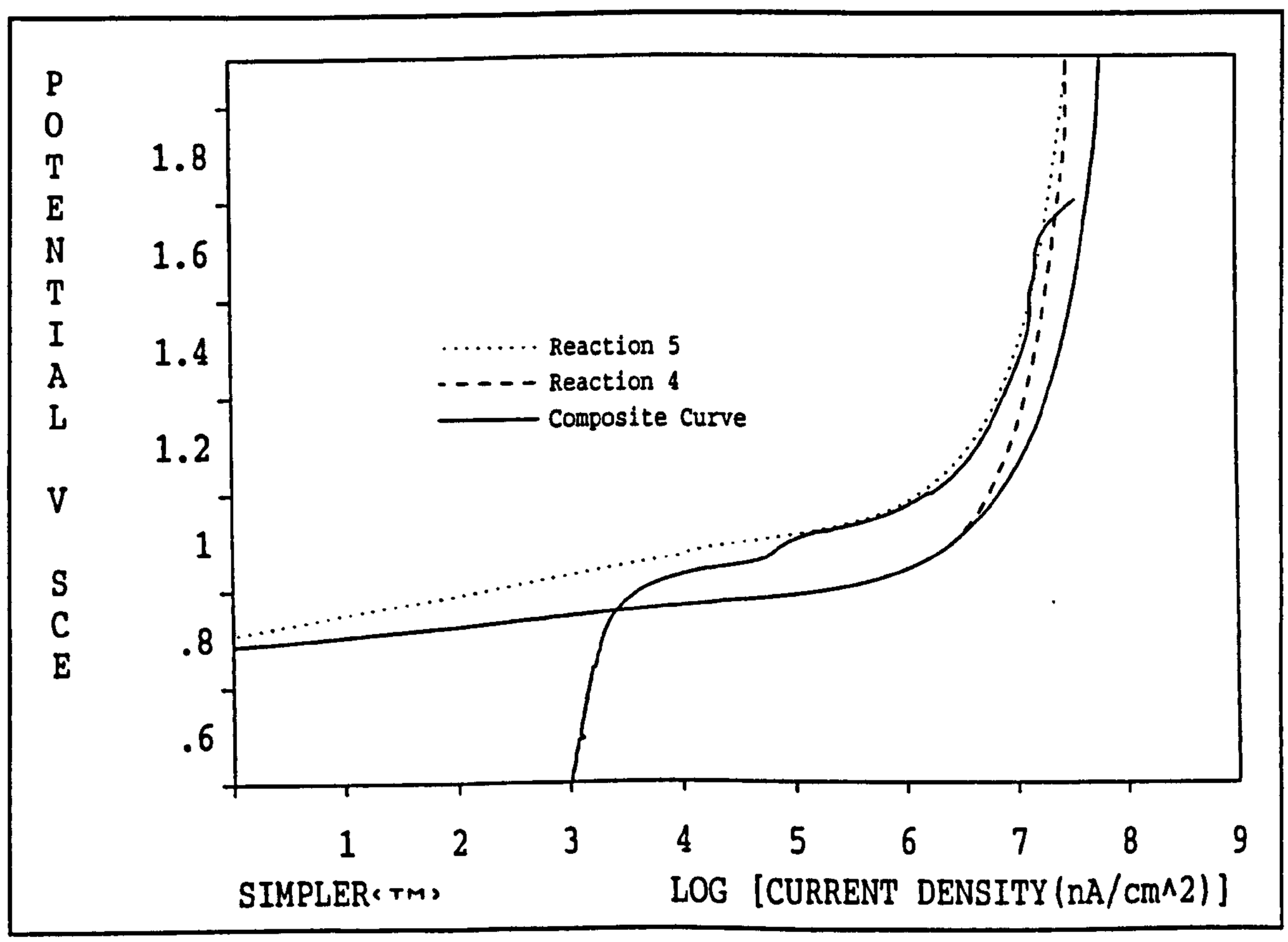

Figure 4.2.11 Acid chromate and dichromate reactions shown together.

4.2.3.7 The Form of the Cr_2O_3 Film

The form of the passive film was discussed in Section 2.8. In the model proposed here, it is considered that the inner layer consists of anhydrous Cr_2O_3, and the outer layer hydrated chromium hydroxide $Cr(OH)_3.nH_2O$. From Table 4.2.5 it may be seen that for the production of Cr(VI) salts, anhydrous Cr_2O_3 and $Cr(OH)_3.nH_2O$ have different E° values. The model used here assumes $HCrO_4^-$ is produced, and thus E° values of 1.184 and 1.117 V SHE are used for the inner and outer layers respectively.

The result of using two distinct forms is shown in Figure 4.2.12. This clearly shows that the slight shoulder in the lower transpassive branch can be modelled using these two reactions. An excellent simulation of the experimental curve is obtained using the parameters shown in Table 4.2.7.

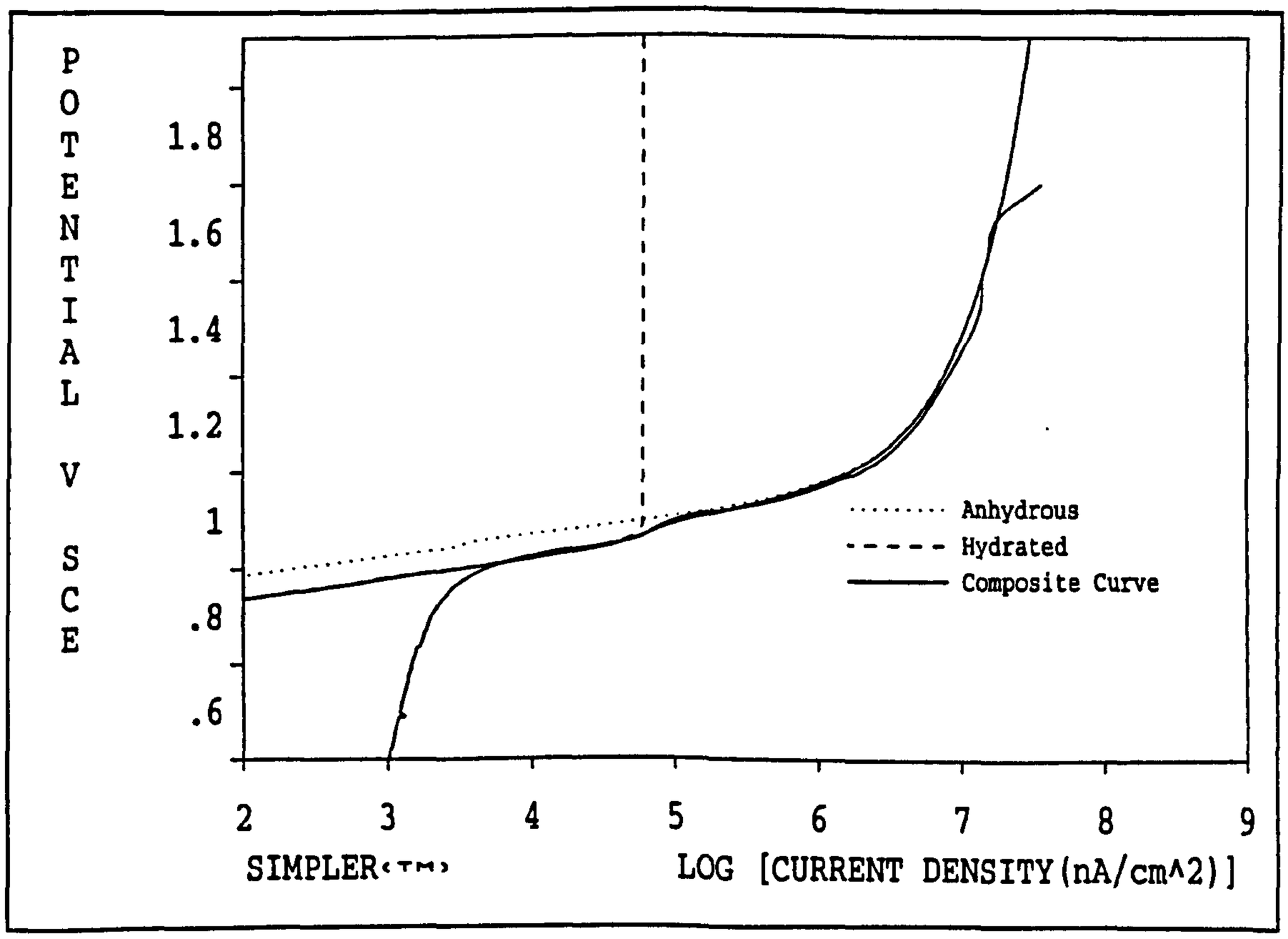

Figure 4.2.12 Modelled curve showing effect of considering Cr_2O_3 to have two forms, from which $HCrO_4^-$ ions are formed.

In both chromate reactions, the solid species is considered to have unit activity, and the threshold ionic species activity is 10^{-6} mol litre^{-1}. As before, the diffusion limited current densities in Table 4.2.7 are used to represent the point at which another reaction becomes dominant.

	Reaction 5	Reaction 5
Cr_2O_3 form	$Cr(OH)_3.nH_2O$	anhydrous
E^o (V SHE)	1.117	1.184
i_o (nA cm^{-2})	0.31	1
i_{lim}anodic (nA cm^{-2})	6×10^4	3×10^7
i_{lim}cathodic (nA cm^{-2})	negligible	negligible
α	0.5	0.5

Table 4.2.7 Kinetic parameters for the two acid chromate reactions considered.

4.2.3.8 Final Set of Parameters Used To Model 304 Stainless Steel in Deaerated Sulphuric Acid

The final set of parameters used to model the polarization curve of 304 stainless steel in deaerated 5% sulphuric acid is given in Table 4.2.8. The overall modelled curve is shown in Figure 4.2.13.

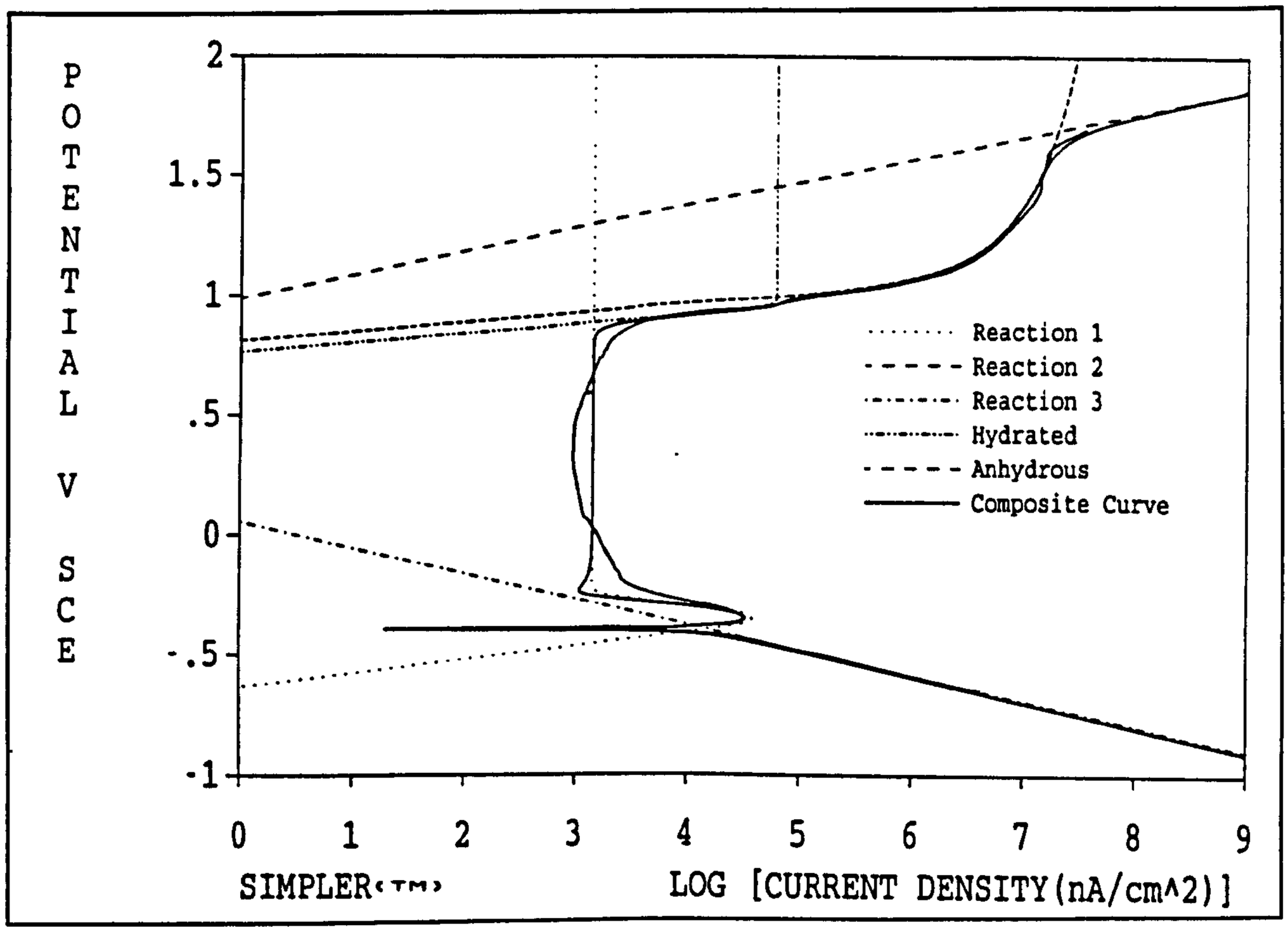

Figure 4.2.13 Modelled curve for 304 stainless steel in deaerated 5% H_2SO_4.

	Reaction 1	Reaction 2	Reaction 3	Reaction 5	Reaction 5
Cr_2O_3 form				$Cr(OH)_3.nH_2O$	anhydrous
E° (V SHE)	-0.440	1.228	0.000	1.117	1.184
i_o (nA cm^{-2})	1.5×10^{-4}	0.12	8×10^{2}	0.31	1
i_{lim}anodic (nA cm^{-2})	not required	1×10^{22}	negligible	6×10^{4}	3×10^{7}
i_{lim}cathodic (nA cm^{-2})	negligible	negligible	1×10^{20}	negligible	negligible
α	0.5	0.6	0.45	0.5	0.5

Table 4.2.8 List of parameters used to model 304 stainless steel in deaerated 5% sulphuric acid.

4.2.3.9 Modelling the Behaviour of 304 in Aerated 5% Sulphuric Acid

The behaviour of 304 in aerated and deaerated 5% sulphuric acid is shown in Figure 4.2.14.

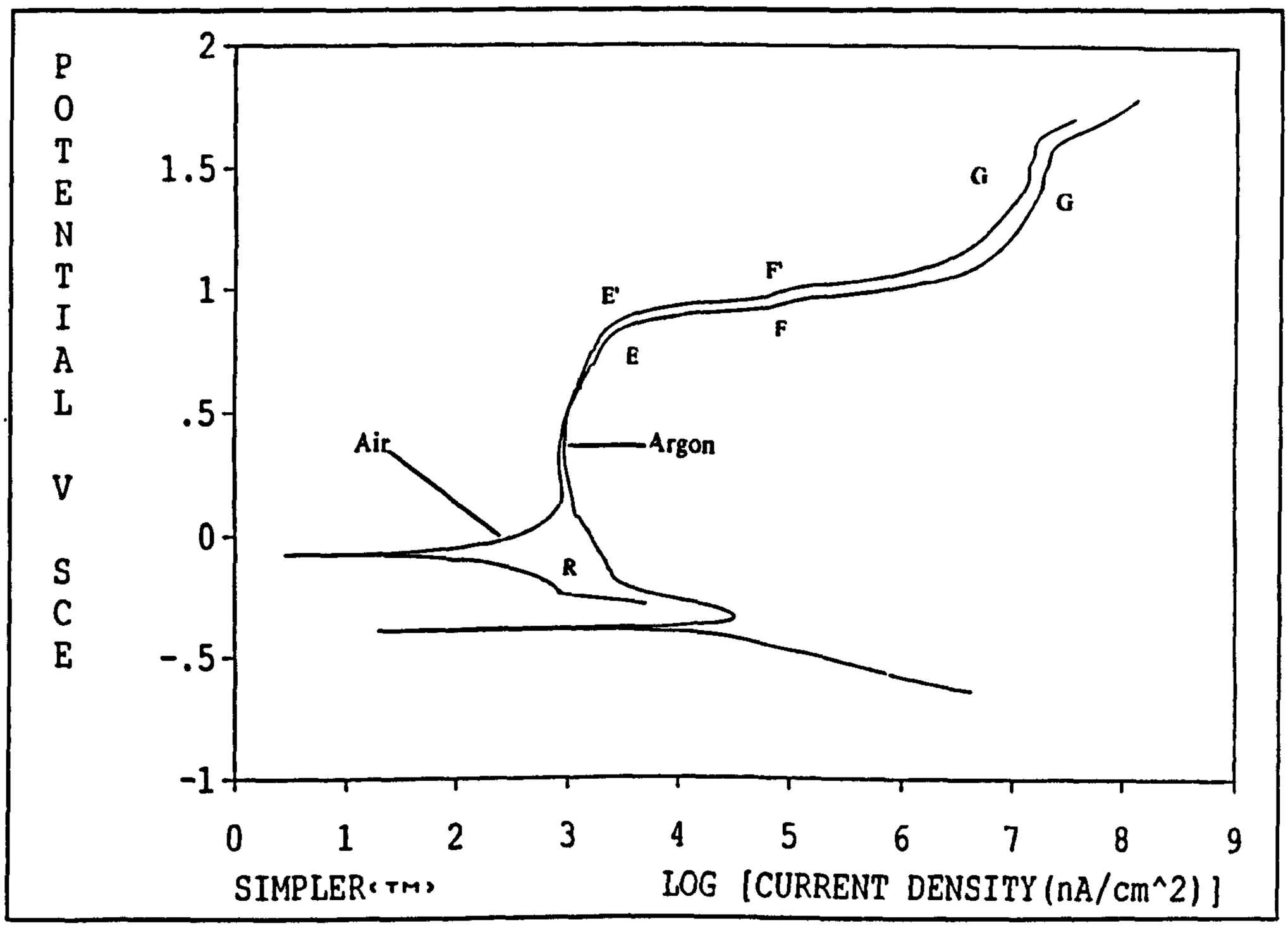

Figure 4.2.14 Experimental polarization for 304 stainless steel in aerated and deaerated 5% H_2SO_4.

The current densities supported by the passivated surfaces are similar in both cases. Since the only difference between the two systems is the level of dissolved oxygen into the electrolyte, any differences in the scan must result from the addition of reactions involving oxygen, or the effect of this addition of oxygen upon other reactions. To consider the aeration of the system, the oxygen reduction process must be considered:

$$O_2 + 2H_2O + 4e^- \rightarrow 4OH^- \qquad \text{Reaction 7}$$

It can be seen that the current densities supported by the surface below the passive region in an aerated solution are lower than in the deaerated case, and the free corrosion potential is more electropositive. The active-to-passive transition does not show a marked 'nose' (a decrease in current density) in the aerated solution. The passive current densities supported by the aerated and deaerated systems are almost equal, and once the anodic current density in the aerated system reaches this value, the surface appears to passivate. This view of the passivation process differs from that which assumes that a threshold current density of i_{crit} must be reached for passivation to occur.

For Reactions 2 and 7, a measured value of 0.20 atmospheres is used for the dissolved oxygen partial pressure in the electrolyte.

Above the passive range, there is an obvious similarity in the form of the transpassive regions of the aerated (EFG) and deaerated (E'F'G') cases ie both have an inflexion point (F and F'). Thus the oxidation of the Cr_2O_3 film to $HCrO_4^-$ is not markedly dependent upon the concentration of dissolved oxygen in the electrolyte.

Figure 4.2.15 shows the curves predicted by the model using the same values as for the deaerated case, but with Reaction 7 added.

The limiting cathodic current density for the O_2/OH^- reduction process was given the value of 5×10^4 nA cm^{-2}, which is a commonly accepted value[112] for the diffusion limited current density for the reduction of oxygen on an iron surface in well aerated electrolytes.

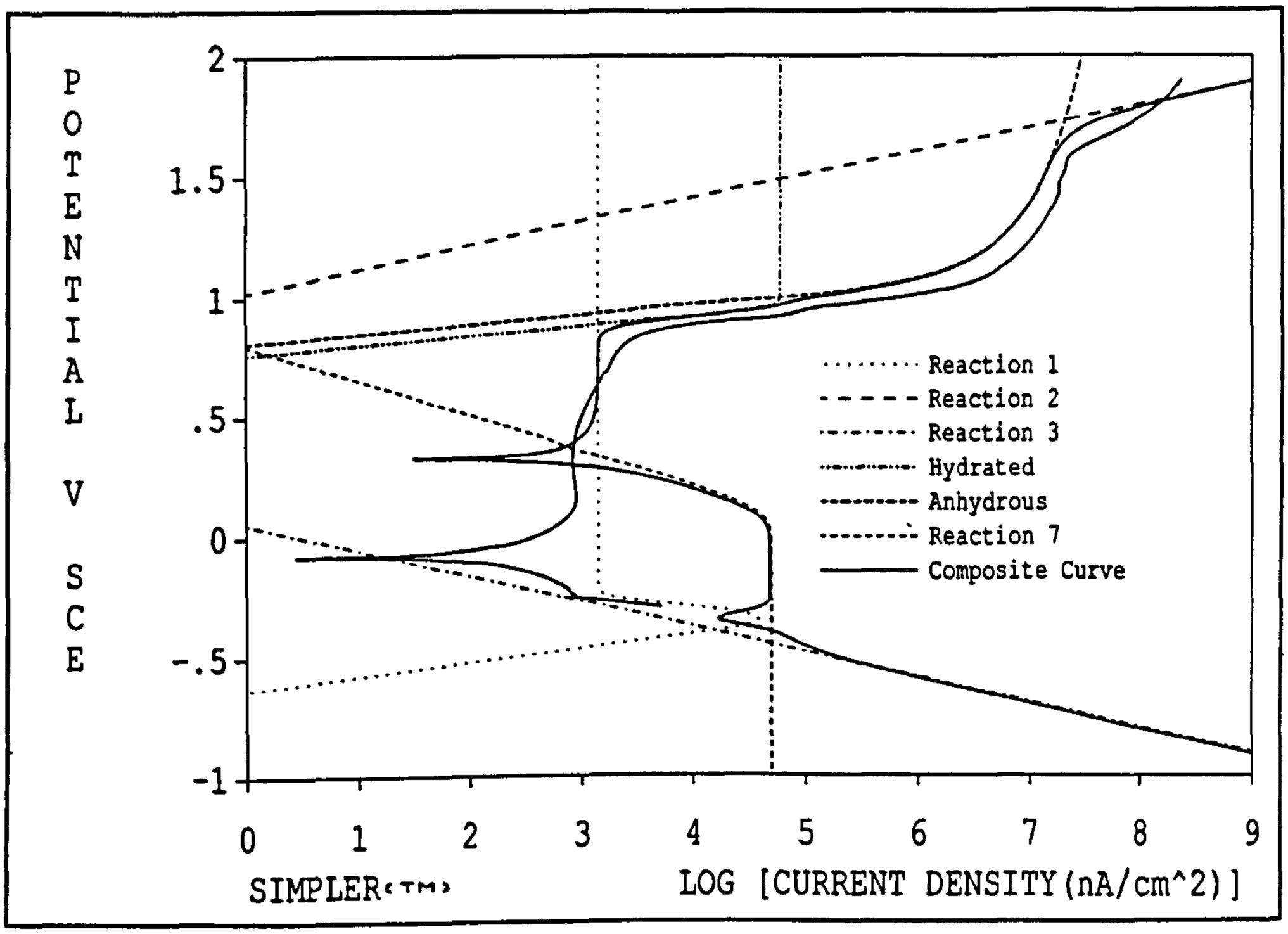

Figure 4.2.15 Modelled polarization curve for 304 stainless steel in aerated 5% H_2SO_4, using Reactions 1, 2, 3, 5 and 7.

The model in Figure 4.2.15 is a poor one at potentials more negative than the transpassive region. It is likely that the formation of OH^- ions affects the other processes occurring upon the surface of the stainless steel. Below E_{corr}, the reduction of oxygen on the surface may impede the access of hydrogen ions to the surface. This will reduce the rate of evolution of the hydrogen, and hence the kinetic parameters of the hydrogen evolution process will be different to the deaerated electrolyte.

Figure 4.2.16 shows the modelled curve for the aerated case, and the parameters used are listed in Table 4.2.9. The major differences between the aerated and deaerated cases are in the i_o value for Reaction 1, and the inclusion of the oxygen reduction reaction, Reaction 7.

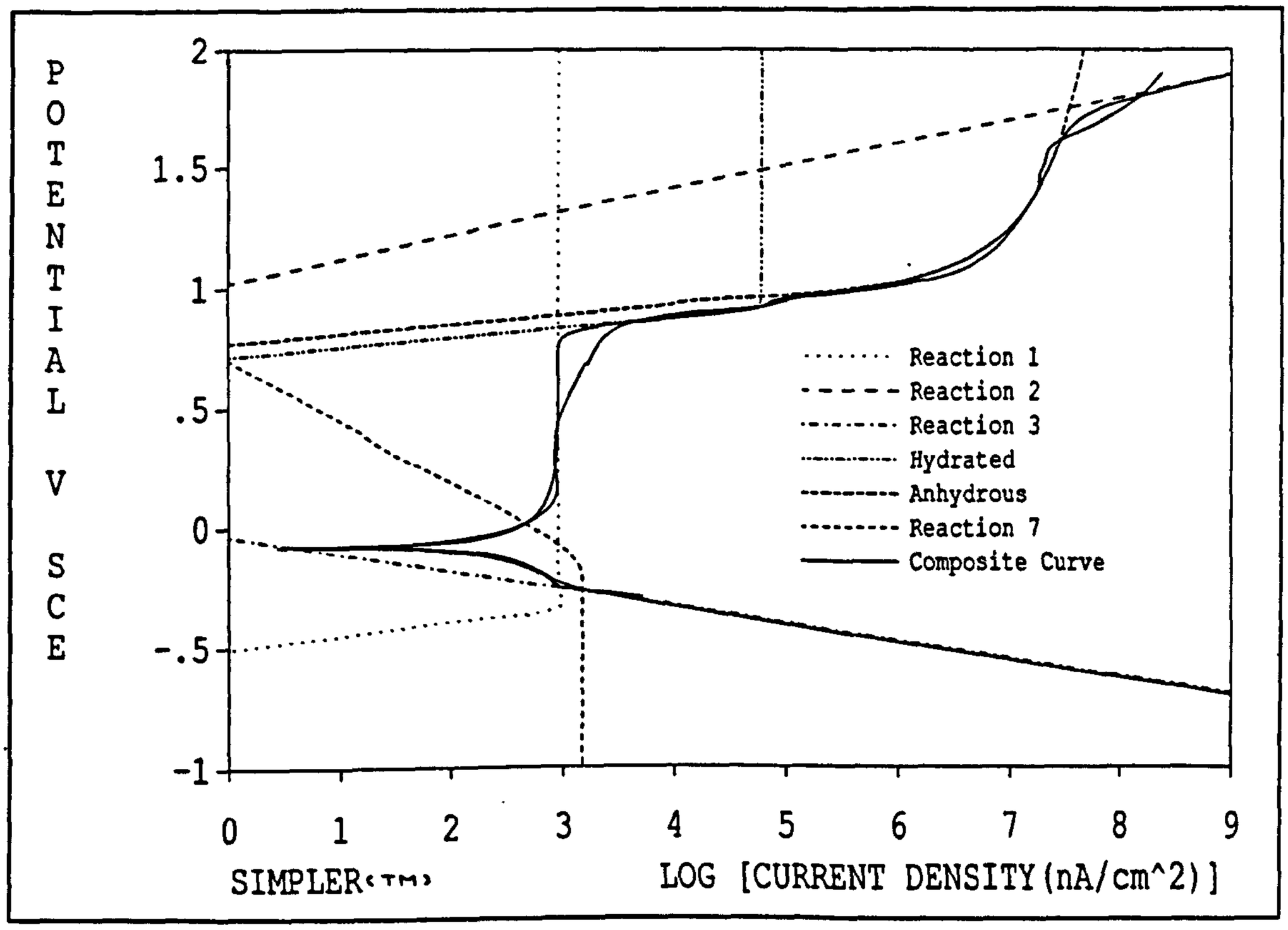

Figure 4.2.16 Modelled polarization curve for 304 stainless steel in aerated 5% H_2SO_4.

To correlate with experimental results, the magnitude of i_o for Reaction 1 must be reduced by 3 orders of magnitude. This is thought to be due to a monolayer of adsorbed O_2 or OH, aided by the ready supply of O_2 in the electrolyte. This monolayer may then block active areas, such as kink sites, which would otherwise dissolve. The free energy of the initial state of the atom in the dissolution reaction is reduced, thereby reducing the i_o for the dissolution reaction.

	Reaction 1	Reaction 2	Reaction 7	Reaction 3	Reaction 5	Reaction 5
Cr_2O_3 form					$Cr(OH)_3.nH_2O$	anhydrous
E° (V SHE)	-0.440	1.228	1.228	0.000	1.117	1.184
i_o (nA cm^{-2})	1×10^{-6}	0.12	0.12	1×10^{3}	5	10
i_{lim}anodic (nA cm^{-2})	not required	1×10^{22}	negligible	negligible	6×10^{4}	1×10^{11}
i_{lim}cathodic (nA cm^{-2})	negligible	negligible	1.5×10^{3}	1×10^{20}	negligible	negligible
α	0.5	0.6	0.77	0.2	0.5	0.5

Table 4.2.9 List of parameters used to model 304 stainless steel in aerated 5% sulphuric acid.

For Reaction 3, α is low, an effect which may be due to the concomitant O_2 cathodic reaction, ie the two reactions compete for reaction sites at the electrode. The small α value is required to model the abrupt change from hydrogen evolution to oxygen diffusion limited current densities in the experimental curve (point R in Figure 4.2.14).

The charge transfer coefficient for the reduction of O_2 is also much greater in the aerated case with respect to the oxidation of OH^- ions in the deaerated solution, in order to model the experimental curve. The values used for the software passivation routine are the same as for the deaerated case.

As noted previously in Section 4.2.3.3, other authors[100,104] have used alternative values of i_o for Reactions 2 and 7. It was decided to investigate the use of such values, and the result of using a i_o value of 5.2×10^{-4} nA cm^{-2} for Reaction 7 is shown in Figure 4.2.17. The kinetic parameters used are shown in Table 4.2.10.

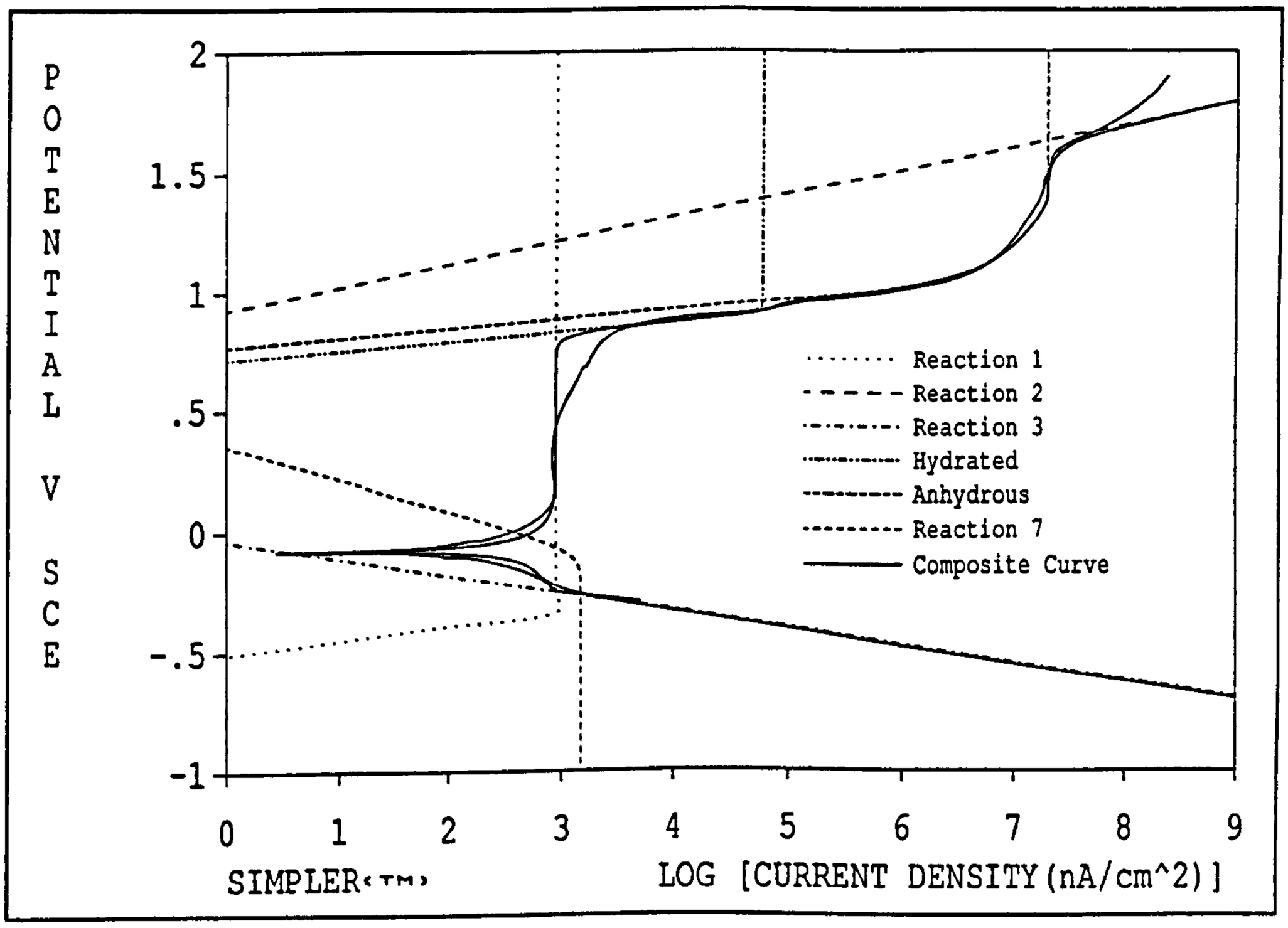

Figure 4.2.17 Model of 304 stainless steel in aerated 5% H_2SO_4 using alternative kinetic parameters for Reaction 7.

The major difference between the two methods of modelling Reaction 7 is in the slope, position of intersection and subsequent interaction of the line representing the current density with the curve representing Reaction 1.

	Reaction 1	Reaction 2	Reaction 7	Reaction 3	Reaction 5	Reaction 5
Cr_2O_3 form					$Cr(OH)_3.nH_2O$	anhydrous
E^o (V SHE)	-0.440	1.228	1.228	0.000	1.117	1.184
i_o (nA cm^{-2})	1×10^{-6}	0.12	5.2×10^{-5}	1×10^{3}	5	10
i_{lim}anodic (nA cm^{-2})	not required	5.8×10^{15}	negligible	negligible	6×10^{4}	2×10^{8}
i_{lim}cathodic (nA cm^{-2})	negligible	negligible	1.5×10^{3}	1×10^{20}	negligible	negligible
α	0.5	0.6	0.57	0.2	0.5	0.5

Table 4.2.10 List of parameters used to model 304 stainless steel in aerated 5% sulphuric acid using alternative kinetic parameters for Reaction 7.

The latter set of kinetic for Reaction 7 increases the sensitivity of the modelling process to the region of the curve between the free corrosion potential and the passive region, especially in cases of intermediate dissolved oxygen levels (Sections 4.2.10 and 4.3). The oxygen evolution process (Reaction 2) cannot be modelled using this new value of i_o, since such a value moves the reaction too far in the electropositive direction. It is thought that the difference in i_o values for Reactions 2 and 7 may be attributed to the differing mechanisms of oxygen reduction and oxidation.

4.2.3.10 Modelling the Behaviour of 304 in 5% Sulphuric Acid with Restricted Oxygen Access

The experimental polarization curve of 304 stainless steel in 5% sulphuric acid with restricted oxygen access is shown in Figure 4.2.18. This is a 'triple E_{corr} point' plot, indicative of unstable behaviour, and occurs when the total cathodic current density does not exceed the peak current in the active-to-passive transition (i_{crit})

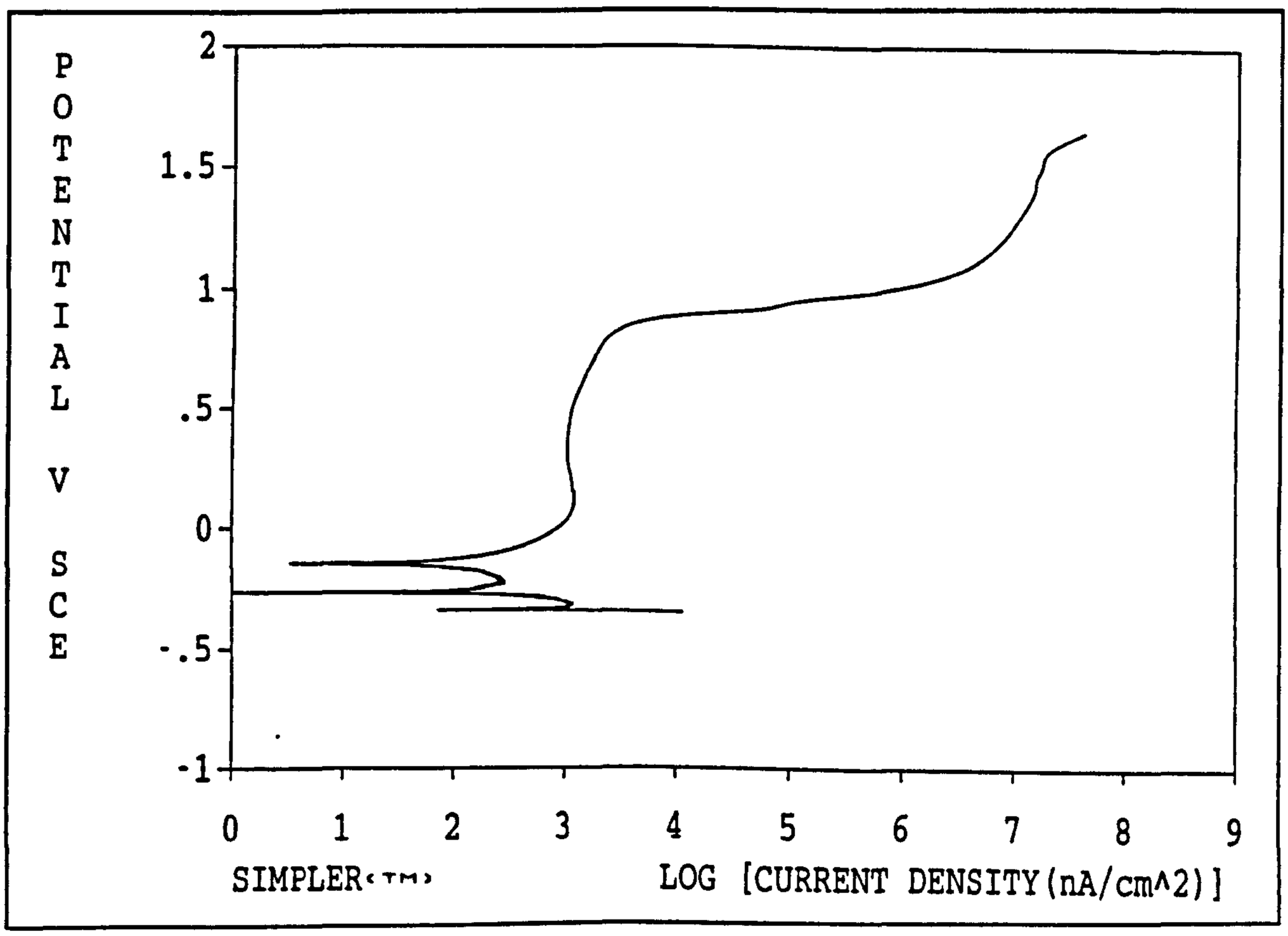

Figure 4.2.18 Experimental polarization curve for 304 stainless steel in 5% H_2SO_4 with intermediate dissolved oxygen concentration.

Instead, the cathodic current density curve intersects the anodic loop twice. Thus, there are three points at which the anodic and cathodic currents have equal magnitudes. This is shown schematically in Figure 4.2.19 by the line DHK.

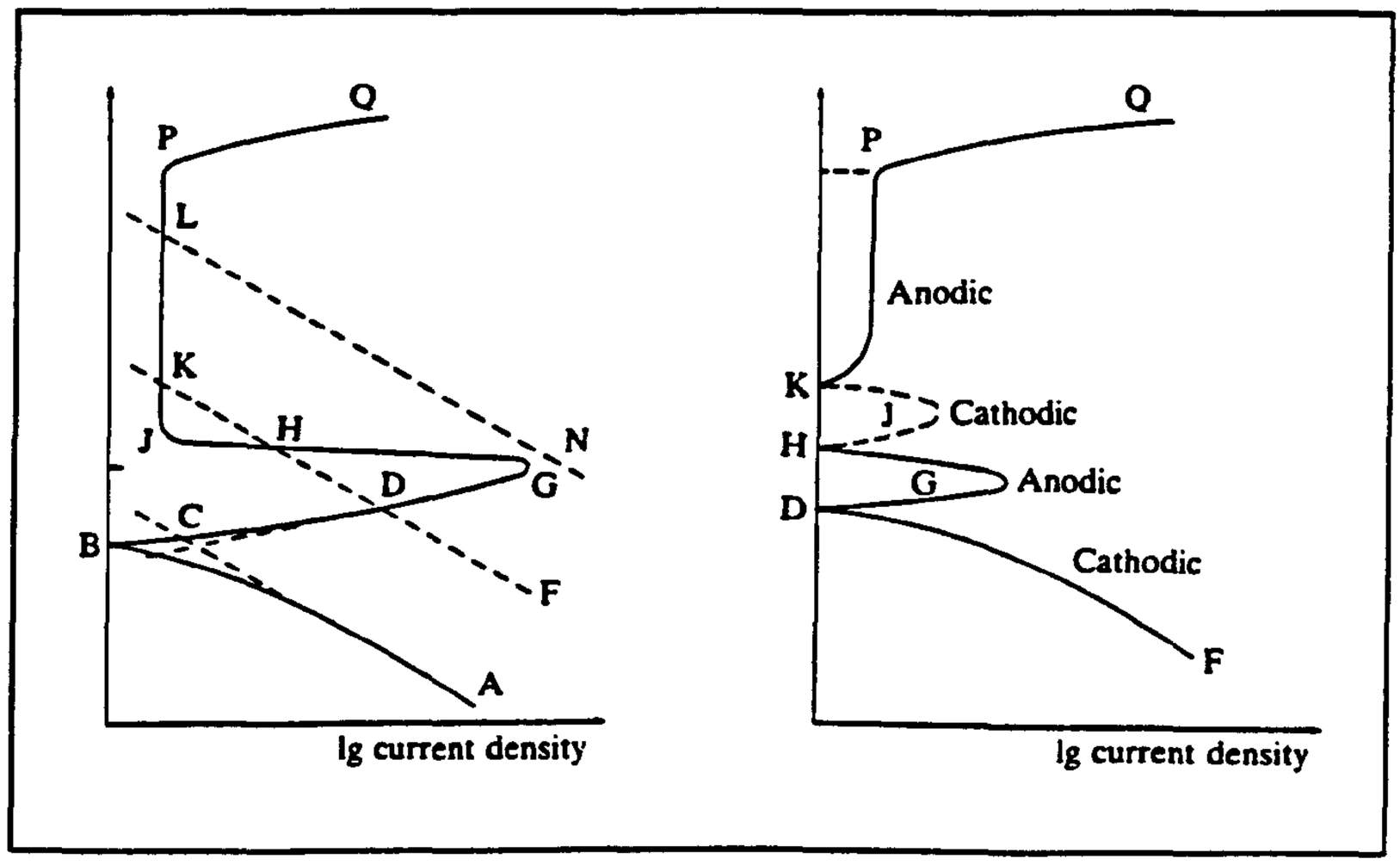

Figure 4.2.19 Schematic polarization curve showing effect of different levels of dissolved oxygen[1].

To model such a curve, parameters must be used such that the total cathodic current supplied by the reduction of hydrogen and oxygen does not exceed the peak current in the active-to-passive transition. Such an effect is mainly attributable to a decrease in the amount of oxygen being reduced. Thus, the parameter input to the algorithm for the partial pressure of dissolved oxygen in the electrolyte is reduced to 0.09 atmospheres. The cathodic limiting current density for the oxygen reduction process must also be reduced. This is shown, together with the other relevant parameters in Table 4.2.11, and the curves generated by this model is shown in Figure 4.2.20.

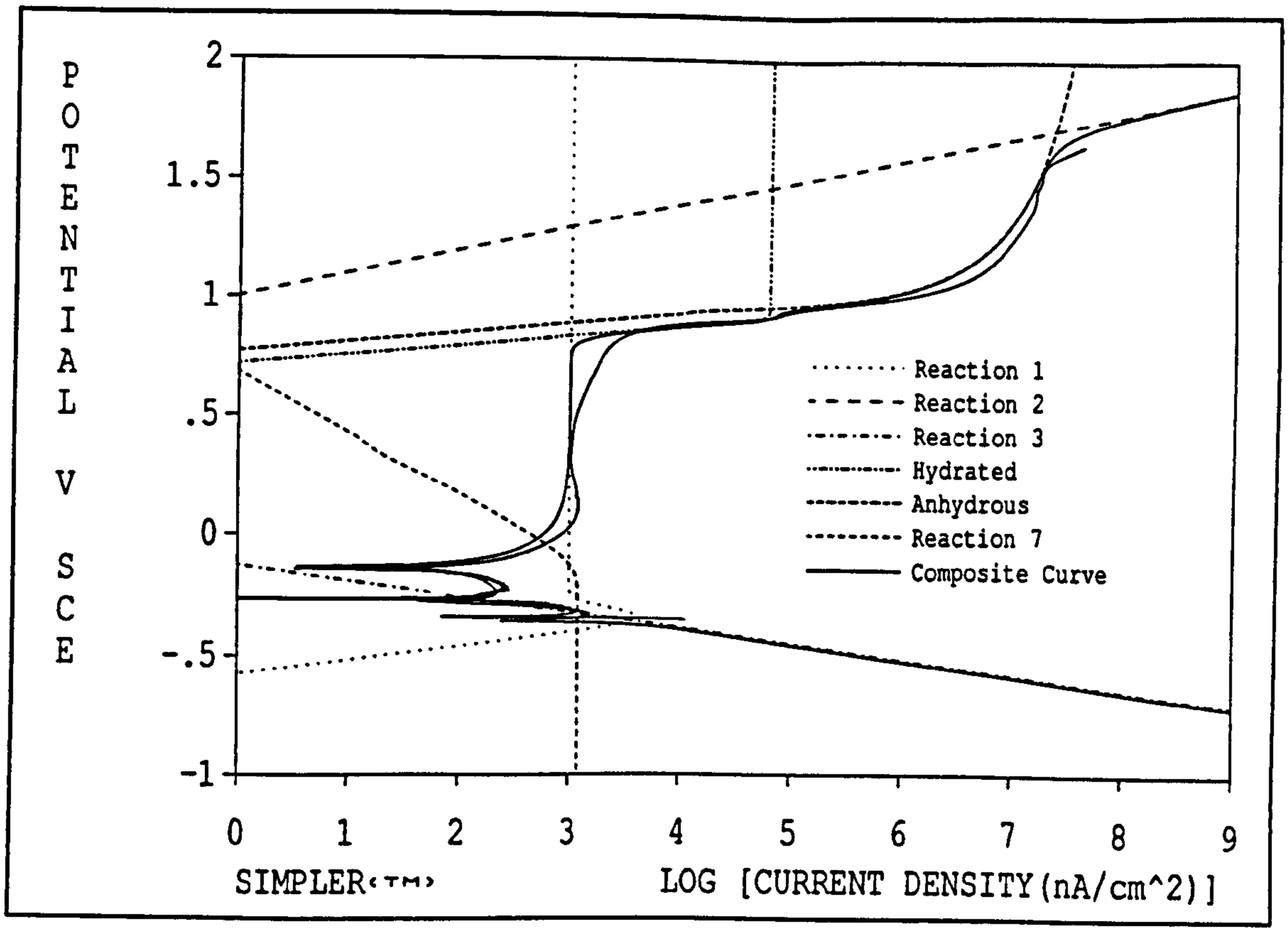

Figure 4.2.20 Modelled polarization curve for 304 stainless steel in 5% H_2SO_4 with intermediate level of dissolved oxygen.

	Reaction 1	Reaction 2	Reaction 7	Reaction 3	Reaction 5	Reaction 5
Cr_2O_3 form					$Cr(OH)_3.nH_2O$	anhydrous
E^o (V SHE)	-0.440	1.228	1.228	0.000	1.117	1.184
i_o (nA cm^{-2})	1.4×10^{-5}	0.12	0.12	1×10^{2}	5	10
i_{lim}anodic (nA cm^{-2})	not required	1×10^{22}	negligible	negligible	6×10^{4}	1×10^{11}
i_{lim}cathodic (nA cm^{-2})	negligible	negligible	1.1×10^{3}	7×10^{18}	negligible	negligible
α	0.5	0.6	0.77	0.1	0.5	0.5

Table 4.2.11 Parameters used to model behaviour of 304 stainless steel in 5% sulphuric acid with restricted oxygen access.

The curve may also be modelled by using the alternative values of i_o and α for Reaction 7. The parameters used are shown in Table 4.2.12, and the resultant curves shown in Figure 4.2.21.

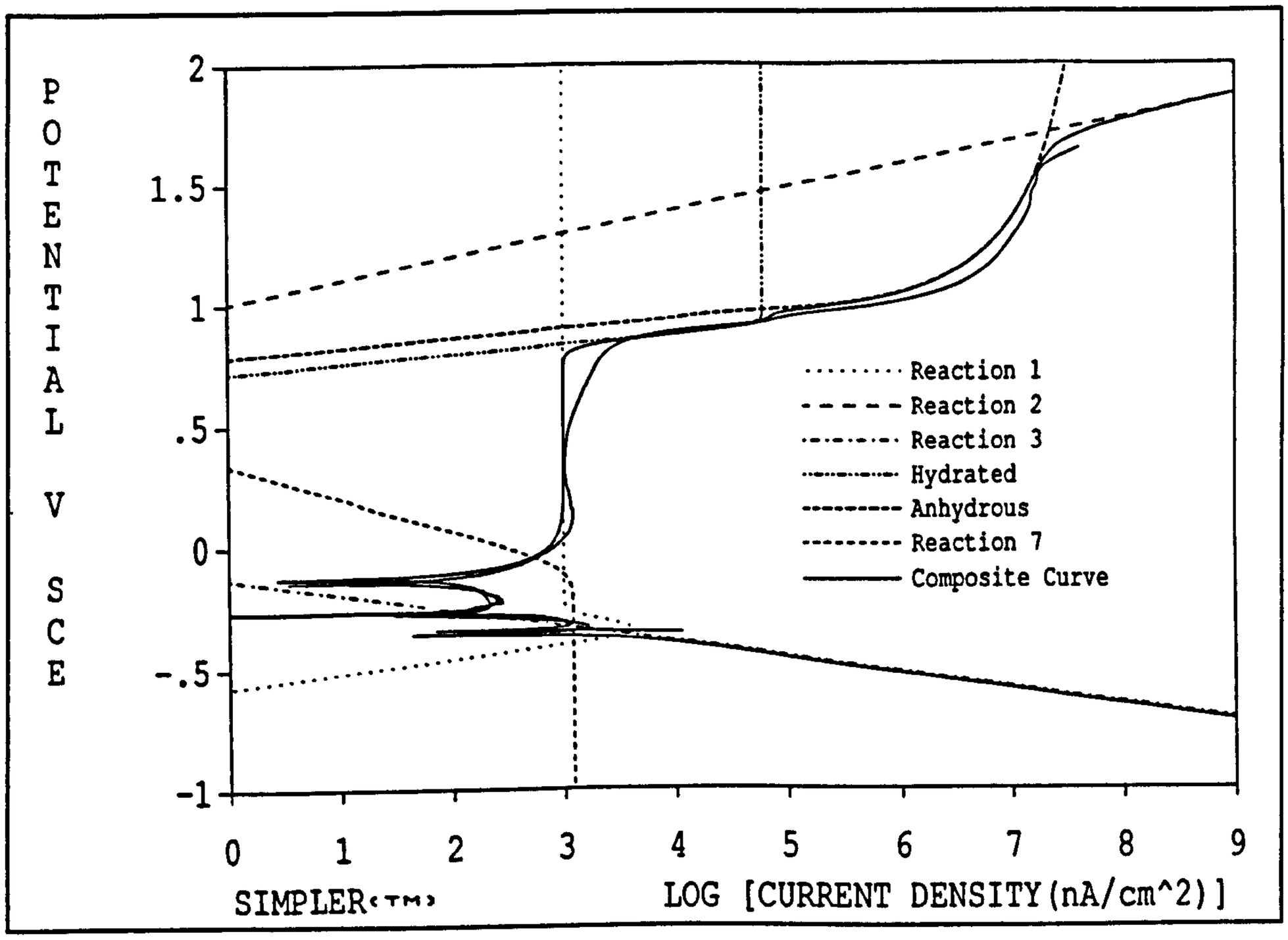

Figure 4.2.21 Model of 304 stainless steel in 5% H_2SO_4 with alternative kinetic parameters for Reaction 7.

	Reaction 1	Reaction 2	Reaction 7	Reaction 3	Reaction 5	Reaction 5
Cr_2O_3 form					$Cr(OH)_3.nH_2O$	anhydrous
E^o (V SHE)	-0.440	1.228	1.228	0.000	1.117	1.184
i_o (nA cm^{-2})	1.4×10^{-5}	0.12	5.2×10^{-5}	90	5	10
i_{lim}anodic (nA cm^{-2})	not required	1×10^{22}	negligible	negligible	6×10^{4}	1×10^{11}
i_{lim}cathodic (nA cm^{-2})	negligible	negligible	1.2×10^{3}	7×10^{18}	negligible	negligible
α	0.5	0.6	0.57	0.1	0.5	0.5

Table 4.2.12 Parameters used to model behaviour of 304 stainless steel in 5% sulphuric acid with restricted oxygen access.

4.2.4 DISCUSSION

4.2.4.1 The Oxygen Reduction Reaction and Overpotential

There are many practical difficulties associated with the experimental determination of the exchange current density, i_o, for the oxygen redox process. When studying any given reaction at a given potential, competing processes often occur at the metal-solution interface. Any electron-accepting species may be reduced if the equilibrium potential for this reaction is more positive than the potential difference across the solid/liquid interface, while any electron-donating will be oxidized if the equilibrium potential for this reaction is more negative.

For Reaction 7, $i_o \approx 0.1$ nA cm^{-2} on a platinum electrode[58]. Electron acceptors and donors present as impurities will be reduced and oxidized at the same time as the oxygen molecules. The normal impurity content of an 'ordinarily purified' solution is $\approx 10^{-6}$ mole $litre^{-1}$. At such low concentrations, the net current from the impurity electrodic processes is likely to be under diffusion control. Using appropriate values, this can be shown[58] to lead to an impurity current of $\approx 4 \times 10^2$ nA cm^{-2}, which is 2 to 3 orders of magnitude greater than the i_o of the oxygen reaction. Thus, under near-equilibrium conditions, the bulk of the current density will be associated with impurity electrode reactions, and not with oxygen reduction. Thus, the study of the oxygen reaction is very difficult. It has been shown[120] that impurity levels of 10^{-10} mole $litre^{-1}$ are required due to the very low i_o value and the need to work near the equilibrium potential where $i \approx i_o$. Only under conditions of extreme solution purity therefore will oxygen be evolved at the equilibrium potential of 1.228 V SHE.

The process is made even more complicated in the systems considered here since the metal substrate itself dissolves at the potentials involved. When considering polarization curves, the following must be borne in mind :

> When electrode kinetics are analyzed....., even with restrictive hypotheses, the results are interpreted on the basis of a model. A steady state polarization curve indicates only the overall, reaction path; which depends on the slowest reaction path, or on the fastest reaction path for a parallel process.[117]

The most energetically and kinetically favourable process must also be considered for parallel processes. For the system considered here, the production of $HCrO_4^-$ is more favourable at potentials above the passive range, and it is not until potentials close to 1500 mV SCE that oxygen evolution is considered to become the predominant process.

The i_o (0.12 nA cm^{-2}) value used to model the oxygen evolution process on 304 stainless steel compares closely to the value of 0.1 nA cm^{-2} quoted by many sources[58,112,121] for the oxygen redox reaction on a platinum substrate, and is higher than the value of 10^{-5} nA cm^{-2} quoted by West[112] for an iron substrate. This latter value has also been used by Otieno-Alego[100] to model iron in sodium benzoate. However, it is not known whether both oxidation and reduction reactions were observed by these authors, or whether only one component was studied.

This value of 0.12 nA cm^{-2} has been used to model the three different aeration regimes investigated, with α values of 0.6 and 0.77 for the oxidation and reduction processes respectively. The two components of the oxygen redox reaction (in the aerated case) are modelled separately since there is a marked difference in the Tafel slopes between the reduction and oxidation portions of the overall reaction. The α value is an intrinsic characteristic of any given combination of charge-transfer reaction and substrate on which

the reaction occurs. It can be thought of as the proportion of the distance through the double layer in which work must be done on an electron acceptor before it accepts an electron. For a large value of α, the reaction is less efficient than for a small value. The high value of α for the reduction of oxygen molecules was not expected, but may be due to the proximity of the diffusion controlled region, which is known to affect Tafel constants[112].

It was also found that using an i_o value of 0.12 nA cm^{-2} could not model certain systems (Section 4.3.3.16), whereas using a value of 5.2×10^{-5} nA cm^{-2} gave enhanced sensitivity to the modelling process, and thus a better fit to the curve. It is therefore assumed that Reactions 2 and 7 proceed by different mechanisms, and have different i_o values.

4.2.4.2 Modelling in Aerated and Deaerated Sulphuric Acid

West[112] quotes values of 0.1 to 1 nA cm^{-2} for the Fe/Fe^{2+} redox process on an iron surface, which is presumed to be for an aerated system, although no details of the experimental conditions are given. Otieno-Alego *et al*[100] successfully used the smaller of these two values.

The value of i_o for the Fe/Fe^{2+} redox process on a stainless steel surface is likely to be different due to the presence of Cr, and this has been shown confirmed here. The i_o value for Reaction 1 used in the 304 stainless steel model is 3 orders of magnitude smaller (10^{-7} nA cm^{-2}) for the aerated case compared to the deaerated (10^{-4} nA cm^{-2}). The stagnant electrolyte yielded an intermediate value of 1.4×10^{-5} nA cm^{-2}.

It is thus suggested that the presence (or otherwise) of oxygen and chromium has a marked effect on the rate of dissolution of Fe^{2+} from a stainless steel surface under equilibrium conditions, i_o. The decrease of the rate in the aerated solution is thought to be due to a monolayer of adsorbed O_2 or OH, aided by the ready supply of O_2 in the electrolyte. This monolayer may then block active areas, such as kink sites, which would otherwise dissolve, lowering the free energy of the initial state of the atoms in the dissolution reaction, and thereby lowering the i_o for the dissolution reaction.

4.2.4.3 Passive Current Density

The model used here uses a constant passive current density, but the experimental results produced here show that this is not necessarily the case. There are several factors which influence the actual response.

Chromium, nickel and iron all form films that have low ion conductivity, thus the film may spread laterally very quickly while still very thin, leading to very rapid passivation of the surface. Electron conductivity is high, allowing anodic processes (such as oxygen evolution) to occur on the surface, and electrons being passed through the film. Thus the electric field across the film cannot be raised to sufficiently high values to promote the large amounts of ion transport required for substantial thickening of the film.

At potentials less electropositive than those required to support such anodic processes as oxygen evolution, a passivated anode can still support small currents, due to small amounts of ion flow in the film. This effect may increase with increasing anodic polarization, diminish with time, or remain almost constant because of slow film dissolution.

Increasing values of i_{pass} with potential may be associated with further oxidation of the metal at the metal/oxide interface. As this oxidation proceeds, cation vacancies may be introduced into the film, to preserve electroneutrality. This will lead to an increase in the conductivity of the film, and hence, as the potential rises, i_{pass} also increases. Such behaviour may be observed in all three aeration regimes considered.

4.2.4.4 Current Density Limits in Oxidation Reactions

As mentioned in Section 4.2.3.6, metal oxidation reactions are not ordinarily considered to exhibit diffusion-limited polarization effects. For reduction processes, the rate-debarring step is the diffusion of the electron-accepting species down a concentration gradient *towards* the electrode from the bulk solution, whereas for oxidation processes, the electron-donating species diffuses *away* from the electrode into the solution.

If the curve in Figure 4.2.2 is considered, the dissolution of the oxide film appears to become current density limited at the point F and the region GH. For the purpose of the model, they are considered the current densities that an alternative process becomes dominant. A possible mechanism of current limitation is now discussed.

If it is assumed that the movement of hexavalent chromium ions away from the electrode at a given potential obeys a simple Fick's Law model of a linear activity gradient across a diffusion layer of thickness δ, the ionic flux may be defined as :

$$\frac{i}{zF} = \frac{D_{M^{z+}}(h_{M^{z+}}^{electrode} - h_{M^{z+}}^{solution})}{\delta}$$

where D is the diffusion coefficient of the species in question

h is the concentration of species in question at position denoted by superscript

δ is the thickness of the double layer

Since the experiments were carried out in sealed flasks, the electrolyte is not replenished. As the oxidation reaction proceeds, the concentration of $HCrO_4^-$ ions in the solution will increase, and the magnitude of the difference between the activities of the ions in solution and at the electrode will decrease. This will lead to a lower value of current for a given potential, and thus the current density trace deviates from the straight line (in semi-logarithmic space) predicted for the activation and solution polarization alone.

An alternative way of viewing the process is to consider the Pourbaix diagram for a metal such as chromium. As the activity of ions in solution is increased due to oxidation occurring, the E° value for the reaction increases, in accordance with Le Chatelier's principle of a system opposing any imposed perturbation. An increase in the E° for the reaction will lead to a decrease of the current at a given potential imposed by a potentiostat. As the potential increases during the potentiodynamic scan, there will be both a current increase associated with a step increase of applied polarization, and a decrease associated with an increase in ionic activity in the solution. The overall effect of these competing mechanisms could be a limiting value of current density, such as shown by region GH.

The algorithm does not take into account the changing activity of ions in solution, rather it takes 10^{-6} as the threshold above which corrosion is deemed to have occurred. It also does not take into account the dependence of E° on ionic activity. Instead, it uses an anodic current limit to model the behaviour of oxidation reactions such as Reaction 5.

4.2.5 CONCLUDING REMARKS

The polarization behaviour of 304 stainless steel in 5% H_2SO_4 with three different levels of dissolved oxygen has been investigated. A model using five redox processes has been advanced for the polarization behaviour of 304 stainless steel in deaerated sulphuric acid during polarization from -600 mV SCE to 1800 mV SCE. The reaction scheme comprising three redox processes used by Devereux and Yeum to model the behaviour of 304 in deaerated sulphuric acid has been shown to be incorrect.

New algorithms created in this study can model the active-to-passive transition of 304 stainless steel in deaerated 5% H_2SO_4. Iron dissolution was used for the anodic activation-controlled reaction, in agreement with the percolation theory advanced by Newman *et al*[62,63,64] A model for the role of two forms of Cr_2O_3 from which $HCrO_4^-$ ions are produced in the lower transpassive part of the curve has been advanced.

The oxygen evolution reaction can be modelled by using the number of charges transferred per ion in the denominator of the Tafel slope expression, together with a value of 0.6 for the charge transfer coefficient (α) for all three oxygenation levels. It can also be modelled by using the number of charges transferred per oxygen molecules in the denominator, but the i_o values required are unreasonably low. The oxygen reduction process cannot be modelled in this way.

A model for the behaviour of 304 stainless steel in aerated and stagnant 5% H_2SO_4 has also been verified by the addition of the oxygen reduction process to the five reactions used to model the deaerated system. The simple addition of an oxygen reduction component to the processes used to model the behaviour in deaerated sulphuric acid is insufficient to

model the behaviour in aerated and stagnant sulphuric acid.

The oxygen reduction process affects the kinetics of the iron dissolution and hydrogen evolution with respect to the deaerated system. The i_o value for the iron (II) dissolution process is especially dependent on the level of oxygen in the electrolyte. This is attributed to a monolayer of adsorbed O_2 or OH, which can then block active areas, such as kink sites, which would otherwise dissolve. This lowers the free energy of the initial state of the atoms in the dissolution reaction, thereby lowering the i_o for the dissolution reaction.

It was found that using a different i_o value for the oxygen reduction process (compared to the oxygen evolution process) gave a better fit to the curve. It was suggested that different mechanisms are responsible for these two process. The parameters used in this model of the passivation process can be used for both the aerated and deaerated systems.

Chapter 4 Section 3 Polarization Curve Behaviour of 304 Stainless Steel in 5% H_2SO_4 with Three Different Levels of Dissolved Oxygen at Different Temperatures

4.3.1 INTRODUCTION

Reaction models for 304 stainless steel in 5% sulphuric acid with three different levels of dissolved oxygen have been discussed in the previous section. This set of experiments investigates the effects of temperature on the behaviour of 304 stainless steel in the same media. The temperatures used were ambient, 30, 35 and 45°C. Section 4.3.3 details the rationale behind additions to the model detailed in the previous section, and shows both the theoretical figures and the parameters used by the algorithm to generate them. Section 4.3.4 discusses the trends found by the modelling process.

4.3.2 EXPERIMENTAL

304 stainless steel in the form of bar of diameter 6.5 mm was obtained from Aalco, cut into strips, approximate length 20 mm, and ground to flats such that rectangular samples of surface area 1.2 cm^2 were obtained. These were mounted and prepared as detailed in Section 4.1.2. The samples were conditioned (using the equipment detailed in Section 4.1.2) at -800 mV SCE for 300 seconds, prior to a potentiodynamic scan from this potential to 2000 mV SCE. A scan rate of 0.1 mV s^{-1} was used.

This conditioning treatment differs from the previous experimental regime, and was introduced in order to achieve a uniform surface for all samples. The high rate of hydrogen

evolution which results at such a potential has a cleaning action, both cathodically reducing oxide films and removing any residual dirt from the polishing process.

For deaerated solutions, argon was bubbled through the three electrode cell in which the experiment was conducted, from the time of initial immersion to completion of the experiment. For aerated solutions, air was bubbled through the cell, again from the time of initial immersion to completion of the experiment. The intermediate level of dissolved oxygen was achieved by sealing with glass stoppers (supplied by EG&G PARC) the unused electrode hole of the cell. Dissolved oxygen measurements were made using the equipment detailed in Section 4.2.2. Temperature control was achieved by immersing the cell in a water bath, with a Hakke DC5 heater. The accuracy with which the temperature was controlled was ± 0.1°C. The Scanning Electron Microscopy (SEM) micrograph was taken using an ISI-DS 130 scanning electron microscope.

4.3.3 RESULTS AND INITIAL DISCUSSION

4.3.3.1 Experimental Results

The results of the experiments discussed in the previous section are shown in Figures 4.3.1 to 4.3.7, both by oxygen concentration and by temperature.

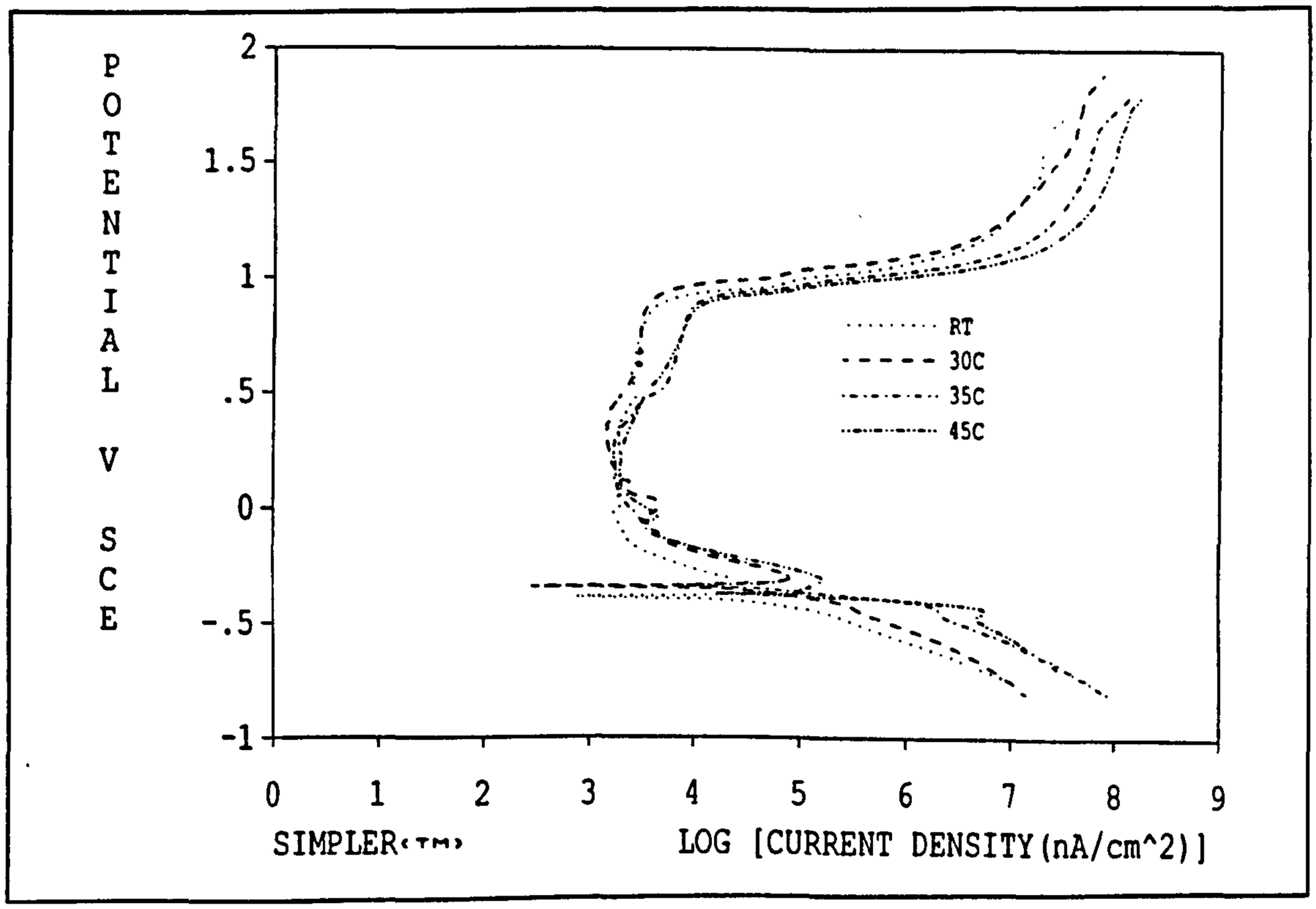

Figure 4.3.1 Polarization curves of 304 stainless steel in deaerated 5% H_2SO_4 at 4 temperatures.

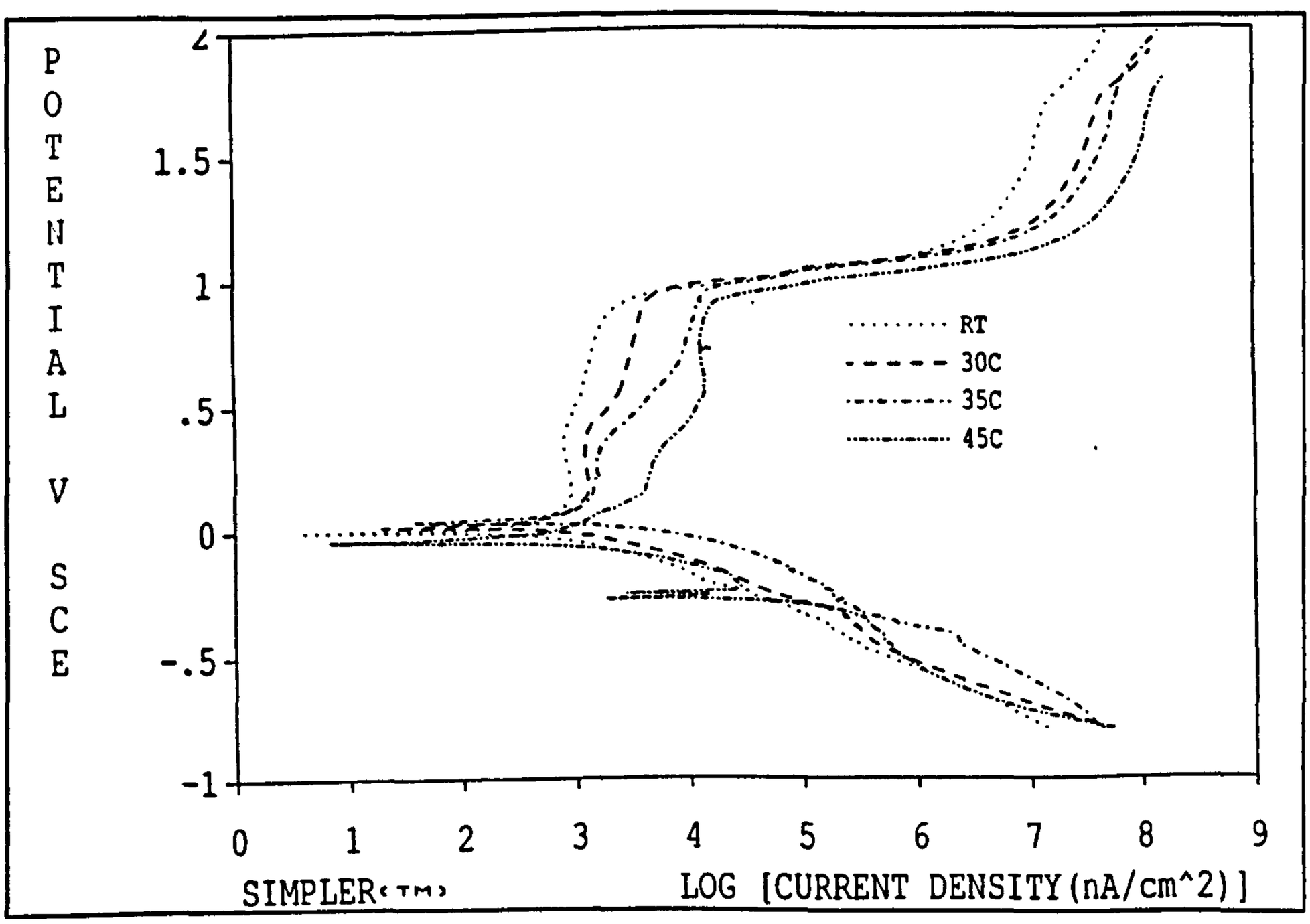

Figure 4.3.2 Polarization curves of 304 stainless steel in aerated 5% H_2SO_4 at 4 temperatures.

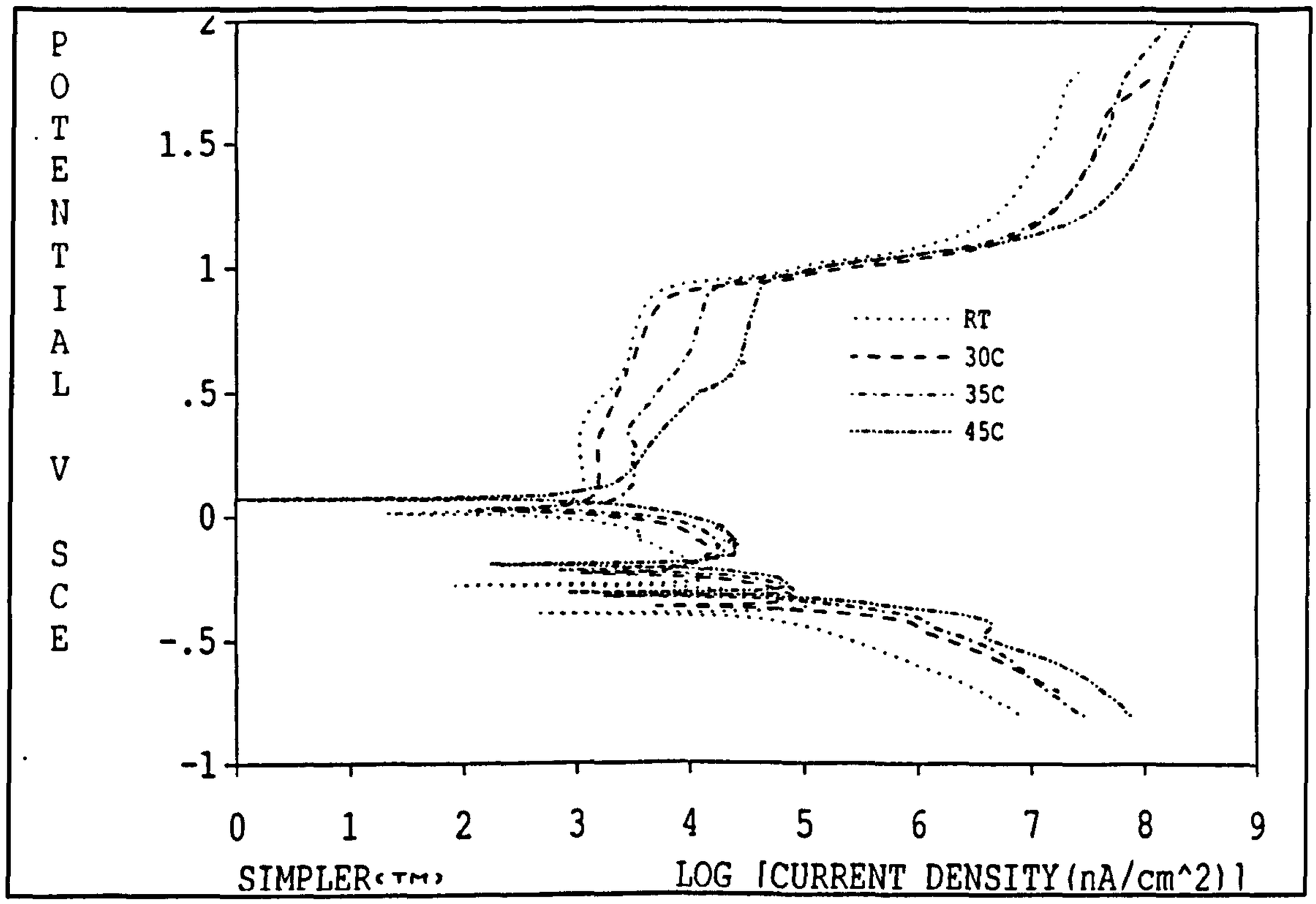

Figure 4.3.3 Polarization curves of 304 stainless steel in stagnant 5% H_2SO_4 at 4 temperatures.

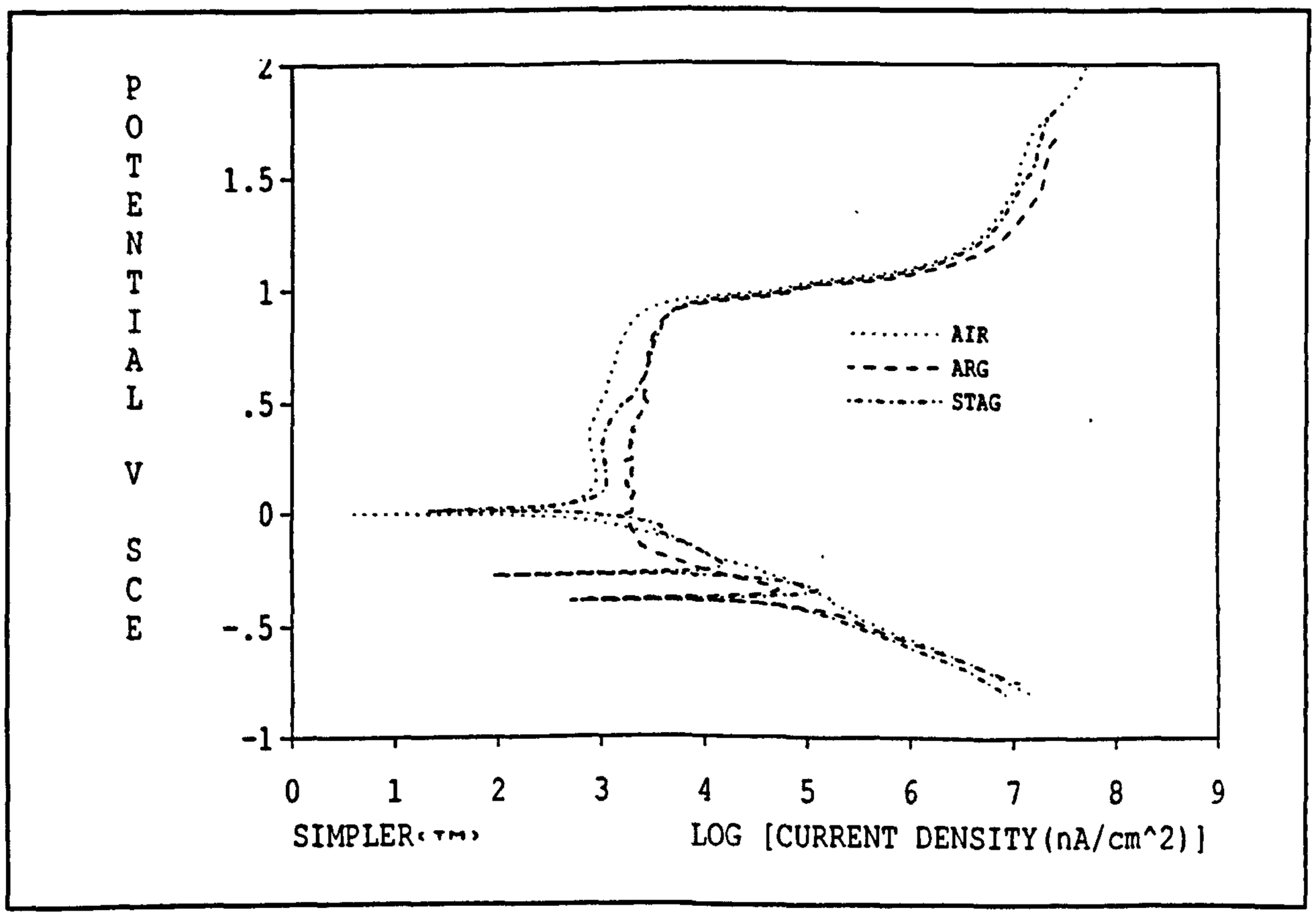

Figure 4.3.4 Polarization curves of 304 stainless steel in 5% H_2SO_4 at 24°C with three different dissolved oxygen contents.

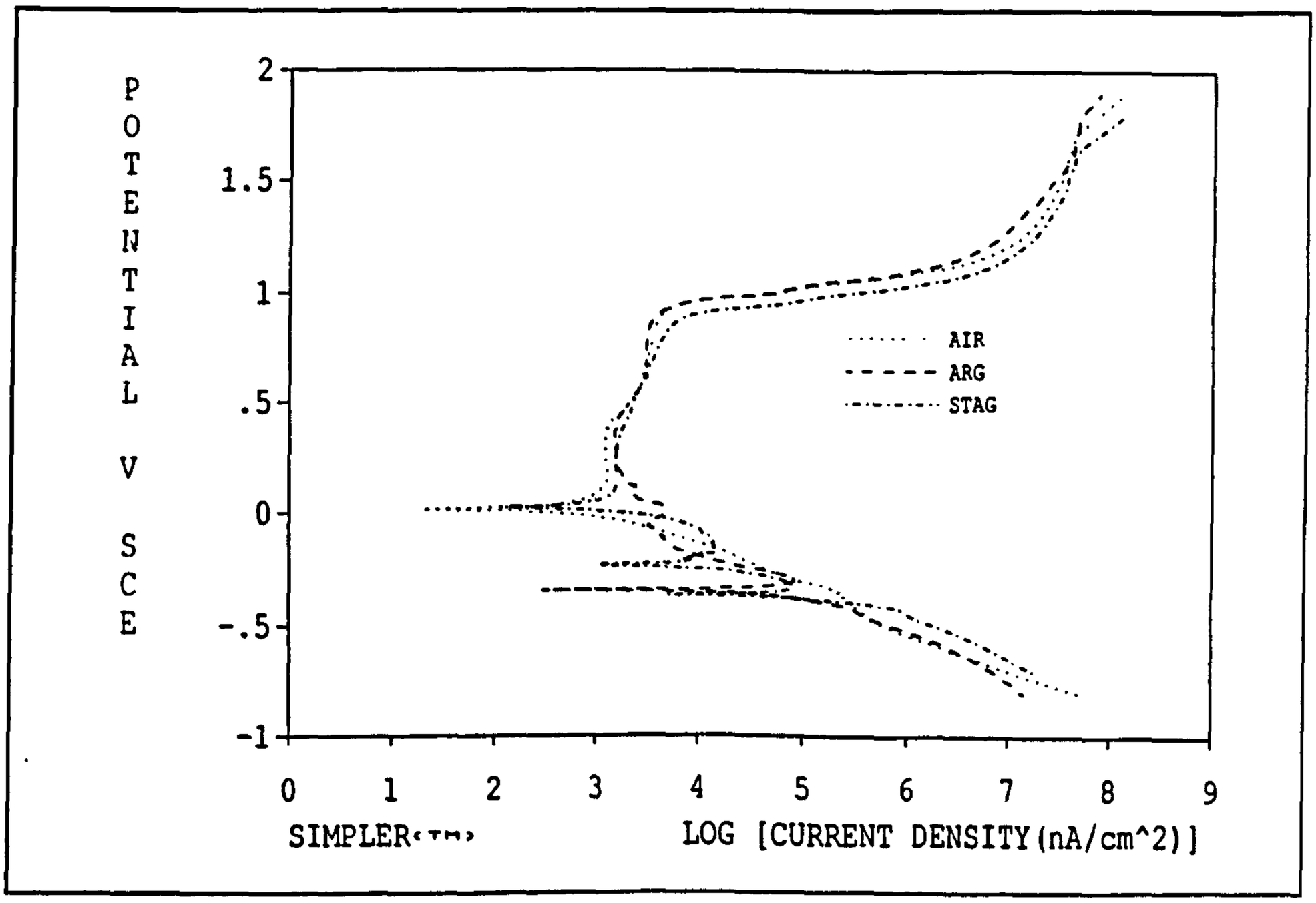

Figure 4.3.5 Polarization curves of 304 stainless steel in 5% H_2SO_4 at 30°C with three different dissolved oxygen contents.

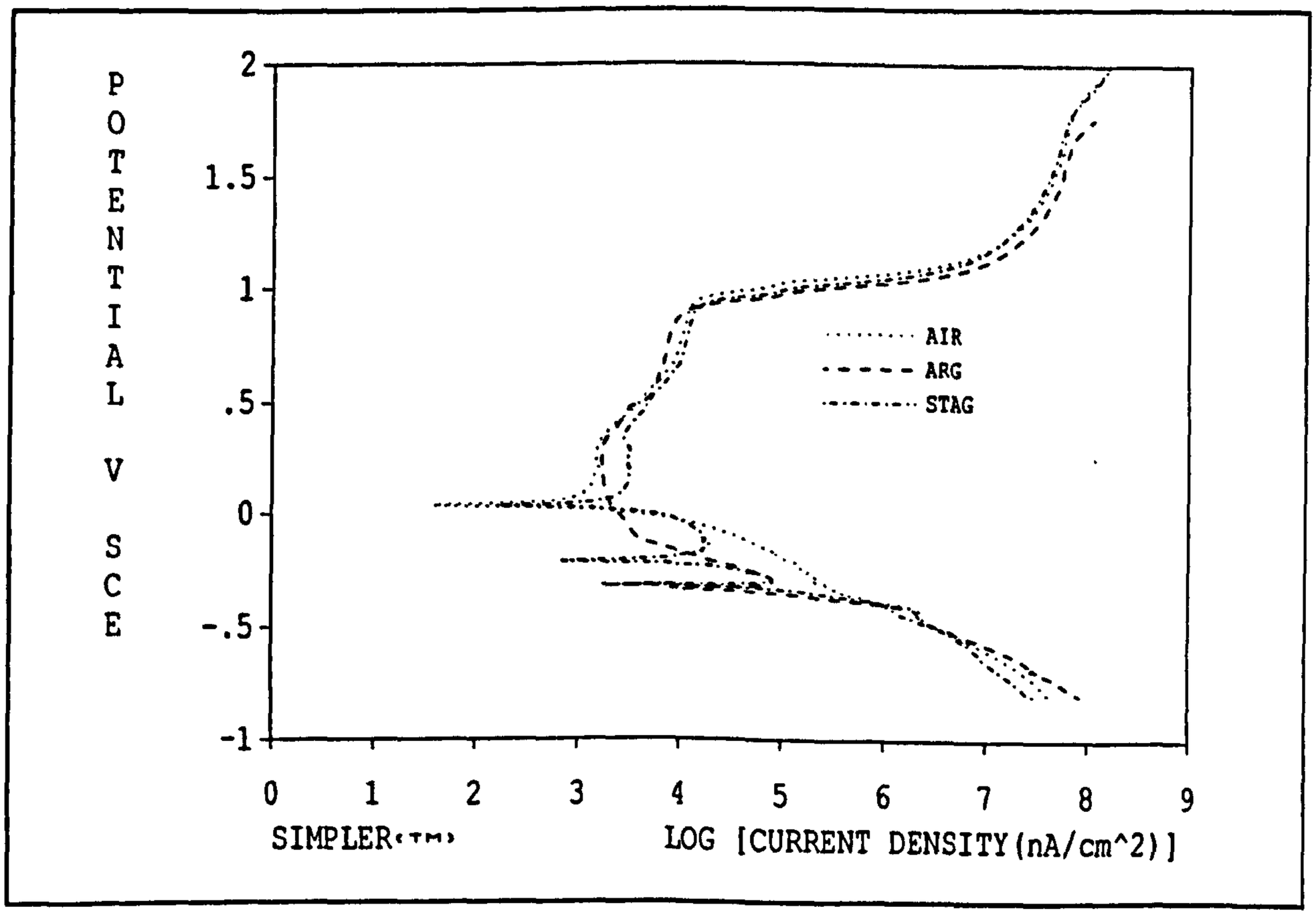

Figure 4.3.6 Polarization curves of 304 stainless steel in 5% H_2SO_4 at 35°C with three different dissolved oxygen contents.

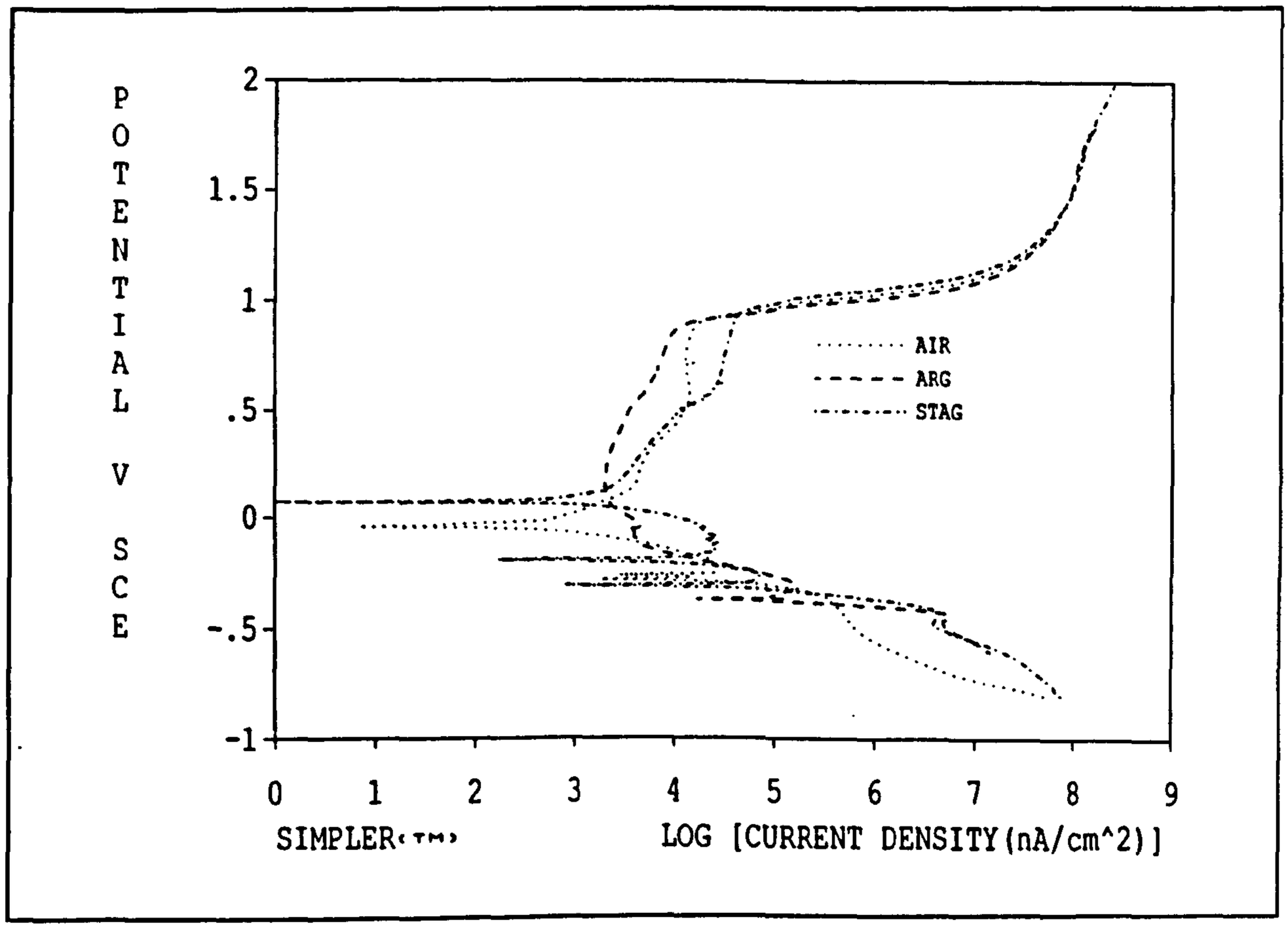

Figure 4.3.7 Polarization curves of 304 stainless steel in 5% H_2SO_4 at 45°C with three different dissolved oxygen contents.

It can be seen that 304 stainless steel exhibits unstable passivity in aerated 5% H_2SO_4 at 45°C, and in stagnant electrolyte at all temperatures studied. This is shown by characteristic 'triple point' polarization curves.

4.3.3.2 304 Stainless Steel in Deaerated 5% H_2SO_4

The polarization curve for the conditioned room temperature experiment (using the conditions described above) is shown as the dotted line in Figure 4.3.8, while the solid line is the unconditioned experimental curve described and modelled in Section 4.2.3. Figure 4.3.8a shows the cathodic and active-to-passive transition portions of the curve in greater detail.

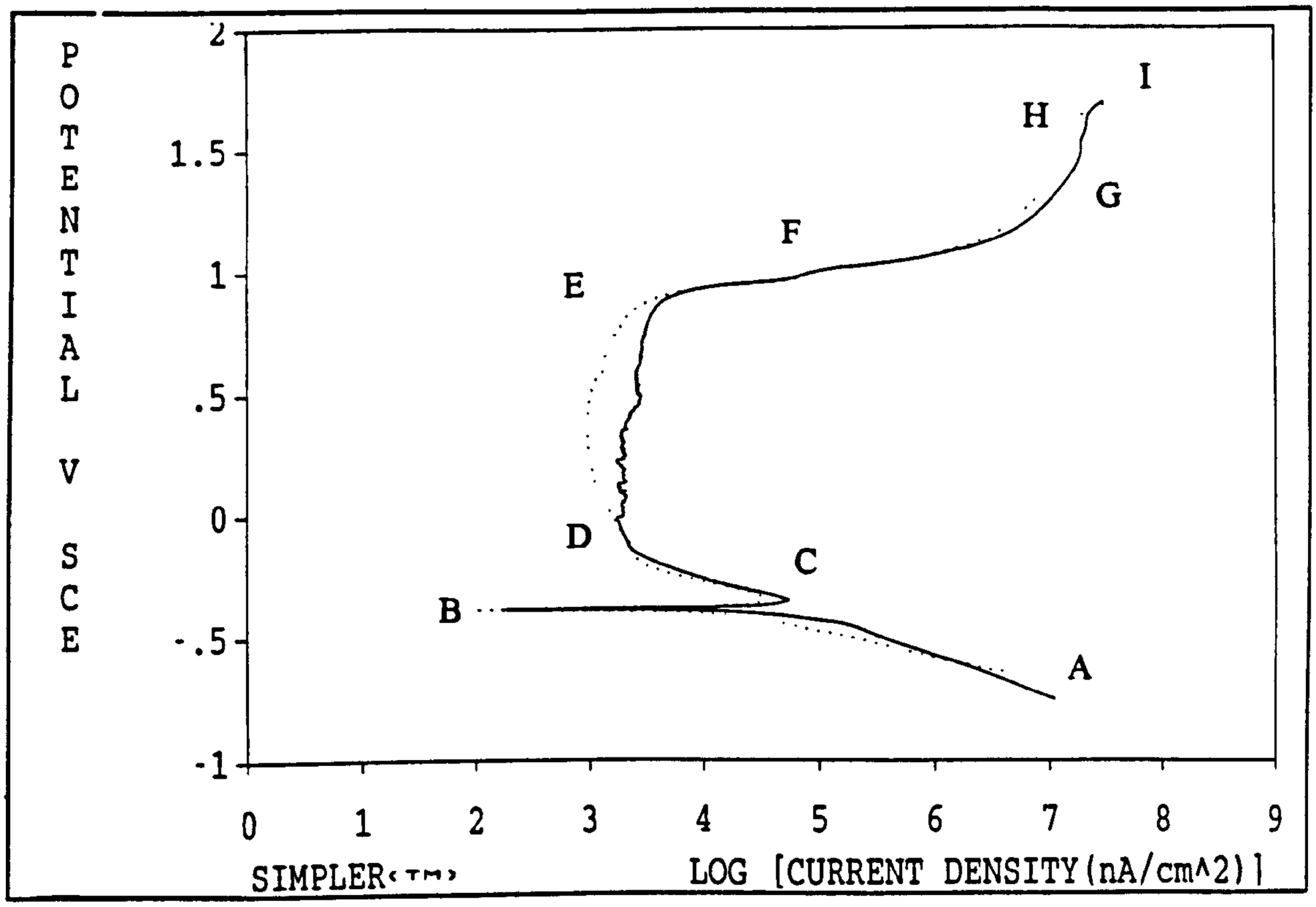

Figure 4.3.8 Experimental curves for 304 stainless steel in deaerated 5% H_2SO_4.

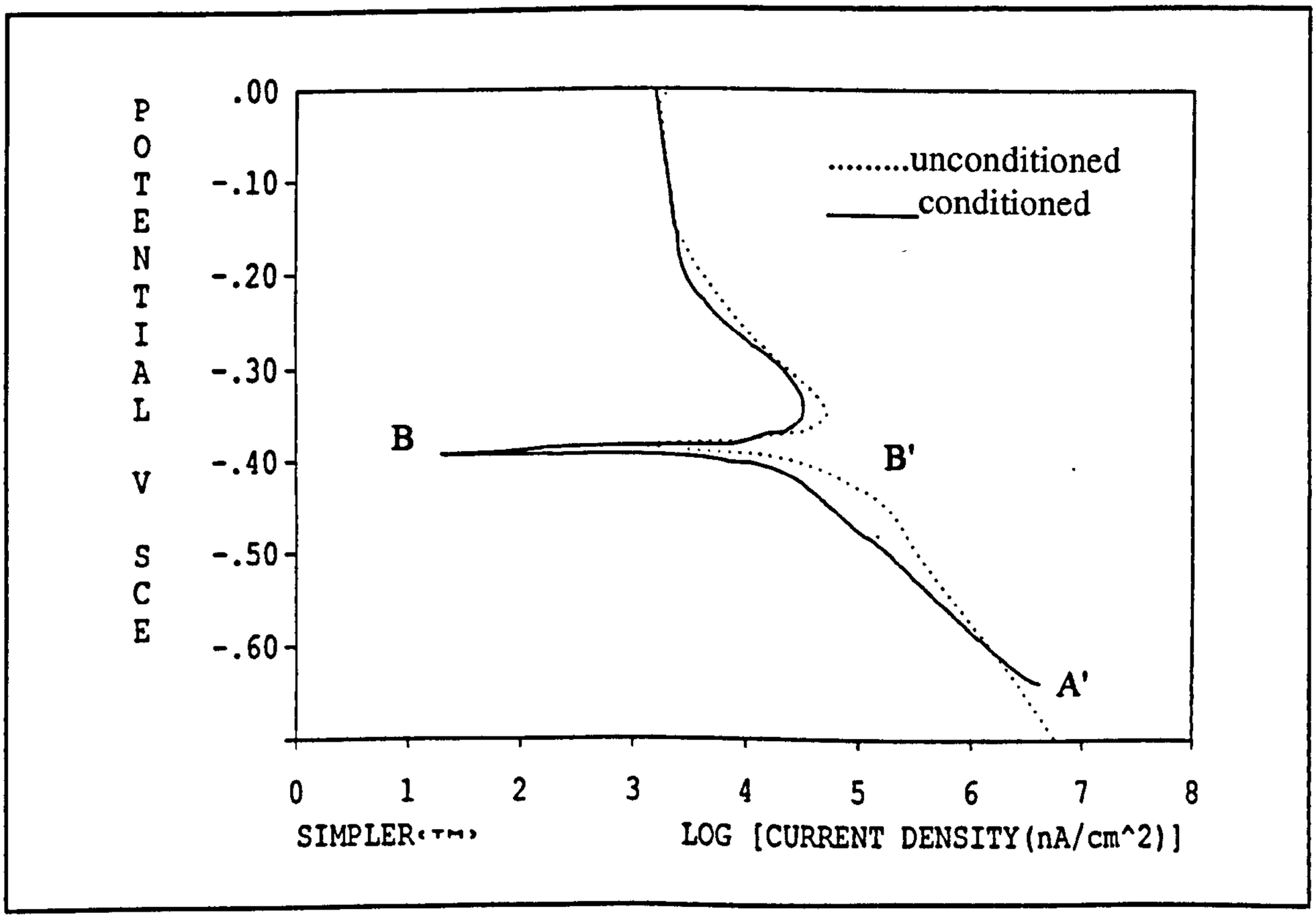

Figure 4.3.8a Cathodic and active-to-passive transition portions of the Figure 4.3.8 in greater detail.

The form of the curves is essentially similar, but with some important differences. For the unconditioned sample, the passive current density (region DE) and the critical current density (point C) are both smaller in magnitude than for the conditioned sample, as is the current density at which Reaction 5 becomes current density limited (region GH). The current density at which the form of the oxide film in Reaction 5 changes (point F) and the free corrosion potential (point B) are identical in both plots.

4.3.3.3 Reactions Used in Model

The same reactions as used in Chapter 4 Section 2 were used in the model for 304 stainless steel in deaerated 5% H_2SO_4, namely:

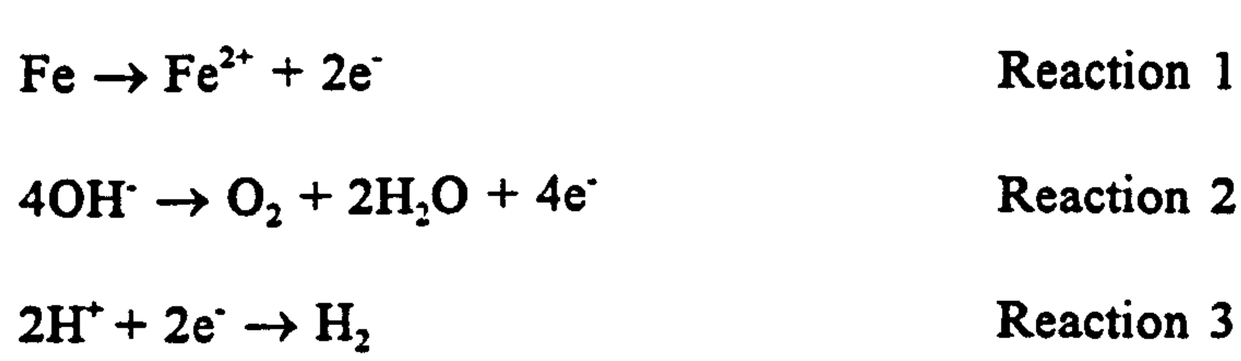

$Fe \rightarrow Fe^{2+} + 2e^-$ Reaction 1

$4OH^- \rightarrow O_2 + 2H_2O + 4e^-$ Reaction 2

$2H^+ + 2e^- \rightarrow H_2$ Reaction 3

$Cr_2O_3 + 5H_2O \rightarrow 2HCrO_4^- + 8H^+ + 6e^-$ Reaction 5

Two values of E^o are again used for Reaction 5 to model the differing compositions of the passive film. Reaction 7 is added for the models concerned with aerated and stagnant electrolyte.

$O_2 + 2H_2O + 4e^- \rightarrow 4OH^-$ Reaction 7

4.3.3.4 Change of Tafel Slope for Reaction 3

The major difference in the two experimental results is in the cathodic region (AB). For unconditioned samples, this can be represented by Reaction 3 with a single set of kinetic parameters (namely α, E^0, i_o and i_{lim}). The conditioned sample appears to exhibit two

modes of cathodic behaviour, between AB' and B'B. The portion AB' may be considered as tending towards a diffusion limited current density, but with such a high concentration of H^+ in solution, this is unlikely to occur at current densities of 10^5 nA cm^{-2}. Also, experience has shown that the transition from activation polarization to diffusion controlled polarization is very much more marked than the change in slope shown in Figure 4.3.8a.

Oxygen reduction (the reverse of Reaction 2) normally has a limiting cathodic current density of 10^4 - 10^5 nA cm^{-2}. The bubbling of argon through the electrolyte and subsequent oxygen entrainment in the argon bubbles means the concentration of dissolved oxygen in the electrolyte is very low (~0.04 partial pressure of dissolved oxygen). Thus, this reaction cannot occur to any great extent. No metal ions are present (other than trace impurities) that could be reduced, leaving Reaction 3 as the only possible cathodic reaction.

These two regions can be separately represented by Reaction 3 with two sets of kinetic parameters (α, E^0, i_o and i_{lim}). Different values of α and i_o are used in each, and the reasons for this are discussed in the next sections. The significance of α is also investigated.

4.3.3.5 Introduction of Concept of Multistep Electron Transfer Reactions

Previously, reactions have been considered as simple, single step electron transfer reactions, such as

$$M \rightarrow M^{z+} + ze^- \qquad (4.3.1)$$

with little consideration given to the overall reaction path. The Tafel constant b calculated for such a process is given by :

$$b = \frac{2.303RT}{\beta_{sym} zF} \tag{4.3.2}$$

where β_{sym} is the symmetry factor

z the overall number of electrons transferred.

R is the universal gas constant (8.314 J mol^{-1} K^{-1})

F is Faraday's constant (96484 C mol^{-1})

The likelihood of more than one electron being passed in a single step is extremely unlikely[58,122,1]. More complex reactions thus take place via a number of intermediate steps. This makes the determination of the constant β_{sym} within Equation 4.3.2 more complex. The rate of a redox process is dependent upon the slowest reaction step (or the fastest step for a parallel process), which is termed the rate determining step (RDS). Thus, it is this step which determines the Tafel constant and hence the form of the polarization curve. If the net reaction path changes, the RDS is likely to change, and thus the Tafel slope may also alter.

4.3.3.6 Calculation of Transfer Coefficients for A Multistep Reaction

The following treatment is based upon that of Bockris and Reddy[58].

$$A + e^- \rightarrow Y \tag{4.3.3}$$

Consider the overall reaction above. It has a net single electron transfer, but may have a number of intermediate steps, thus :

$$A + e^- \rightleftharpoons B \qquad \text{Step 1} \tag{4.3.4}$$

$$B + e^- \rightleftharpoons C \qquad \text{Step 2} \tag{4.3.5}$$

....	.....	
....	.....	
$Q + e^- \rightleftharpoons R$	Step $\gamma^{\rightarrow}$	(4.3.6)
$R + e^- \rightarrow S$	RDS	(4.3.7)
$S + e^- \rightleftharpoons T$	Step($\gamma^{\leftarrow} = n - \gamma^{\rightarrow} - 1$)	(4.3.8)
....	.....	
....	.....	
$X + e^- \rightleftharpoons Y$	Step n	(4.3.9)

The overall number of electrons transferred is n, $\gamma^{\rightarrow}$ electrons are transferred prior to the RDS; $\gamma^{\leftarrow}$ steps follow the RDS. Taking the reactions before and after the RDS, their respective forward and backward rates can be assumed to be at equilibrium. Thus for step 1 at equilibrium, the forward and backward rates are equal, as are the currents generated by these reactions:

$$\vec{i} = F\vec{k}_1 c_A e^{-\beta\frac{F\eta}{RT}} \rightleftharpoons \overleftarrow{i} = F\overleftarrow{k}_1 c_B e^{(1-\beta)\frac{F\eta}{RT}} \tag{4.3.10}$$

where k is the rate constant for a given reaction and c is the concentration of the species in question. Thus :

$$c_B = K_1 c_A e^{\frac{-F\eta}{RT}} \tag{4.3.11}$$

where

$$K_1 = \frac{\vec{k}_1}{\overleftarrow{k}_1} \tag{4.3.12}$$

For the steps preceding the RDS:

In the limit:

$$c_C = K_2 c_B e^{\frac{-F\eta}{RT}} = K_2 K_1 c_A e^{\frac{-2F\eta}{RT}} \tag{4.3.14}$$

$$c_D = K_3 c_C e^{\frac{-F\eta}{RT}} = K_3 K_2 K_1 c_A e^{\frac{-3F\eta}{RT}} \tag{4.3.15}$$

$$c_R = [\prod_{i=1}^{\vec{\gamma}} K_i] c_A e^{\frac{-\vec{\gamma}F\eta}{RT}} \tag{4.3.16}$$

Substituting 4.3.16 in 4.3.10, we find the current associated with the RDS :

$$i_{o,R} = F\vec{k}_R [\prod_{i=1}^{\vec{\gamma}} K_i] c_A e^{-(\vec{\gamma}+\beta)\frac{F\eta}{RT}} \tag{4.3.17}$$

The term $i_{o,R}$ denotes that the rate of the RDS is now related to the concentration of the initial reactants, and not the species actually involved in the RDS. Similarly, for the rate of the reverse RDS, the reaction can be shown to be related to the concentration of the final reaction species, Y:

$$\overleftarrow{i}_{o,R} = F\overleftarrow{k}_R \sum_{i=n-\vec{\gamma}-1}^{n} K_i c_Y e^{-(\overleftarrow{\gamma}+1-\beta)\frac{F\eta}{RT}} \tag{4.3.18}$$

Hence the new parameters to replace β_{sym} in Equation 4.3.2 are now ($\gamma^{\rightarrow} + \beta$) and ($\gamma^{\leftarrow}+1 - \beta$). Now, $\gamma^{\leftarrow} = (n - \gamma^{\rightarrow} - 1)$, thus we have the new transfer coefficients :

$$\overleftarrow{\alpha} = n - \vec{\gamma} - \beta \tag{4.3.19}$$

If the RDS does not involve electron transfer, ($n - \gamma^{\rightarrow}$) electrons are transferred after

$$\vec{\alpha} = \vec{\gamma} + \beta \tag{4.3.20}$$

the RDS, rather than $(n - \vec{\gamma} - 1)$ electrons. A new term r is introduced to compensate for this, where r = 1 for electron transfer, r = 0 for no charge transfer. The previous derivation assumes that for every occurrence of the RDS, the overall reaction path also occurs once. This need not be the case. For the chemical desorption mechanism (see Section 4.3.3.5) for the evolution of hydrogen (Reaction 3), the adsorption reaction must occur twice for every molecule of hydrogen produced, whereas it need only occur once for the electrodic desorption mechanism. The *stoichiometric number* v is the ratio of RDS occurrences to each overall reaction occurrence. If v > 1, (n - v) electrons transferred in the $(n - \vec{\gamma} - rv)$ steps after the RDS, and v electrons are transferred in v occurrences of the RDS.

If the reaction scheme for a multistep reaction with multiple overall electron transfer is considered :

$$A + ne^- \rightarrow Y \tag{4.3.21}$$

In the same way as the previous derivation, the more general expressions for the transfer coefficients are given by:

$$\overleftarrow{\alpha} = \frac{n - \vec{\gamma}}{v} - r\beta \tag{4.3.22}$$

Again, it is these coefficients which take the place of the symmetry factor in Equation 4.3.2. The transfer coefficients are associated with forward and reverse reactions,

$$\vec{\alpha} = \frac{\vec{\gamma}}{\nu} + r\beta \qquad (4.3.23)$$

and thus they have a sign associated with them. Since they have both a sign and a magnitude, they may be considered as vector quantities. This work takes the convention of considering oxidation currents as positive and reduction currents as negative, even though signs are not immediately apparent in semi-logarithmic plots. If a reaction proceeds through a number of steps, and the RDS differs for the forward and reverse reactions, the sum of the transfer coefficients will no longer be unity.

4.3.3.7 Reaction Paths for Reaction 3

It is now considered that there are two likely mechanisms for Reaction 3[58], and that they both[123] share the same first step. Under cathodic polarization, a metal surface has a surfeit of negative charge, carried by electrons. Hydrated protons, which may also be regarded as H_3O^+ ions, can accept electrons from the surface, and are said to form a layer of *adsorbed* hydrogen atoms on the surface. The process is termed discharge (D) or adsorption.

Step 1 $M(e^-) + H_3O^+ \rightarrow MH + H_2O$ Discharge

The second step is that of *desorption*, and can proceed by two different mechanisms (steps 2a and 2b). In the first case, adsorbed hydrogen atoms diffuse around the surface until they collide, at which point they combine to form gaseous hydrogen, which evolves from the surface. Since the desorption step does not involve a charge transfer step, it is called *chemical desorption* (CD). The reaction mechanism may be written as:

Step 2a $MH + MH \rightarrow 2M + H_2$ Chemical Desorption

The second step of the other hydrogen evolution reaction mechanism does involve charge transfer, and is termed *electrodic desorption* (ED). While the adsorbed hydrogen atoms are on the surface, other H_3O^+ ions above it can accept electrons from the surface, thus:

Step 2b $MH + H_3O^+ + M(e^-) \rightarrow 2M + H_2O + H_2$ Electrodic Desorption

In both cases, the net reaction is still the evolution of hydrogen. The second mechanism differs in that the surface concentration of adsorbed hydrogen must be high, otherwise the probability of an H_3O^+ ion meeting an adsorbed H atom and accepting an electron (step 2b) is very low. Thus, as the driving force for hydrogen adsorption falls (ie the cathodic polarization decreases), the fraction of the surface covered by adsorbed hydrogen becomes lower, and the rate at which hydrogen is evolved will also decreases. However, the chemical desorption reaction can still proceed at low fractions of adsorbed hydrogen, although the rate of hydrogen evolution may well be less with respect to the electrodic desorption mechanism.

For 304 stainless steel in deaerated 5% H_2SO_4, it is proposed that the mechanism of hydrogen evolution at large cathodic polarizations is electrodic desorption, but at lower polarizations, the alternative chemical desorption step is more favourable, and occurs in preference. The change in Tafel slope at point B' is thus the point at which the desorption mechanism changes. However the situation is more complicated since either the discharge or desorption step of either mechanism can be taken as the RDS and thus control the overall rate, which will alter the value of $\alpha^{\rightarrow}$. Also, the concept of a RDS is not solely

concerned with just one controlling step. If there is more than one process with similar activation energies, there may be more than one RDS ie a *dual control mechanism.*

If each of the two overall reaction paths involved is considered, using ($\rightleftharpoons$) to denote the reaction in equilibrium and ($\rightarrow$) for the RDS, for the chemical desorption step:

$$H_3O^+ \overset{D}{\rightarrow} MH \overset{CD}{\rightleftharpoons} H_2 \qquad (4.3.24)$$

$$H_3O^+ \overset{D}{\rightleftharpoons} MH \overset{CD}{\rightarrow} H_2 \qquad (4.3.25)$$

For the electrodic desorption mechanism, similarly :

$$H_3O^+ \overset{D}{\rightarrow} MH \overset{ED}{\rightleftharpoons} H_2 \qquad (4.3.26)$$

$$H_3O^+ \overset{D}{\rightleftharpoons} MH \overset{ED}{\rightarrow} H_2 \qquad (4.3.27)$$

If the rate of the backward reaction of a step is negligible with respect to the forward rate, all steps other than the RDS can no longer be considered to be in equilibrium, as before. In such a case, increasing the velocity of the step in question causes the velocity of the other step(s) to increase as well. Such reactions are said to be *coupled*[58]. Thus, for the chemical desorption mechanism: (see equations overleaf)

where v is the overall rate of reaction, $v^{\rightarrow}_1$, $v^{\leftarrow}_1$, $v^{\rightarrow}_2$, $v^{\leftarrow}_2$ are the forward and

$$M(e^-) + H_3O^+ \underset{\overset{\leftarrow}{v_1} \to 0}{\overset{\vec{v} = \overset{\rightarrow}{v_1}}{\rightarrow}} MH + H_2O \tag{4.3.28}$$

$$2MH \underset{\overset{\leftarrow}{v_2} \to 0}{\overset{\vec{v} = \overset{\rightarrow}{v_2}}{\rightarrow}} 2M + H_2 \tag{4.3.29}$$

backward steps of the discharge and chemical desorption reactions respectively.

For the electrodic discharge mechanism, the discharge and desorption reactions may also be coupled:

$$M(e^-) + H_3O^+ \underset{\overset{\leftarrow}{v_1} \to 0}{\overset{\vec{v} = \overset{\rightarrow}{v_1}}{\rightarrow}} MH + H_2O \tag{4.3.30}$$

$$MH + H_3O^+ + M(e^-) \underset{\overset{\leftarrow}{v_3} \to 0}{\overset{\vec{v} = \overset{\rightarrow}{v_3}}{\rightarrow}} 2M + +H_2O + H_2 \tag{4.3.31}$$

v, $v^{\rightarrow}_1$ and $v^{\leftarrow}_1$ have the same meanings as for the previous reaction, while $v^{\rightarrow}_3$, $v^{\leftarrow}_3$ are the forward and backward rates for the electrodic desorption reaction.

Rate Determining Step		$\gamma^{\rightarrow}$	$\gamma^{\leftarrow}$	r	v
$M(e^-) + H_3O^+ \rightleftharpoons MH + H_2O$	Discharge	0	0	1	2
$MH + MH \rightleftharpoons 2M + H_2$	Chemical Desorption	2	0	0	1
$M(e^-) + H_3O^+ \rightleftharpoons MH + H_2O$	Discharge	0	1	1	1
$MH + H_3O^+ + M(e^-) \rightleftharpoons 2M$	Electrodic Desorption	1	0	1	1

Table 4.3.1 Parameters required for calculation of cathodic transfer coefficient for Reaction 3.

Thus for the six variations of the hydrogen evolution reaction discussed, the transfer coefficients may be determined from the parameters listed in Table 4.3.1.

If a reaction path is coupled, then it will have the same parameters as the participating discharge step. It may be seen from Table 4.3.2 that four of the mechanisms considered give the same value (equal to the symmetry factor, β_{sym}, which may not be the same for each mechanism) for the cathodic transfer coefficient.

Mechanism No.	Mechanism	Cathodic transfer coefficient, $\alpha^{\rightarrow}$
1	Discharge rate-determining followed by chemical desorption	β
2	Discharge followed by rate-determining chemical desorption	2
3	Coupled discharge\chemical desorption	β
4	Discharge rate-determining followed by electrodic desorption	β
5	Discharge followed by rate-determining electrodic desorption	$1 + \beta$
6	Coupled discharge\electrodic desorption	β

Table 4.3.2 Transfer coefficients for 6 mechanisms for Reaction 3.

For conditioned 304 stainless steel in deaerated 5% H_2SO_4, the measured Tafel slopes for AB' and B'B are 0.06 and 0.15 respectively. Mechanisms 2 and 5 may be disregarded, as the theoretical Tafel slopes cannot match the measured values using transfer coefficients of 2 and $(1 + \beta)$. It is also interesting to note that diffusion polarization generates an $\alpha^{\rightarrow}$ value of 2[58]; confirming the assumption made earlier in Section 4.4.3.2 that the change in Tafel slopes for AB'B not being a move towards a diffusion limited current density.

4.3.3.8 Incorporation of Different Reaction Mechanisms and $\alpha^{\rightarrow}$ into the Tafel Constant Calculation

For a single step reaction, the cathodic Tafel constant is calculated in the following way:

$$b_c = \frac{2.303RT}{(1 - \beta_{sym})zF} \tag{4.3.32}$$

where β_{sym} is the symmetry factor for the oxidation reaction and $(1 - \beta_{sym})$ is the corresponding reduction symmetry factor.

For a more complex multistep, multi-electron transfer reaction, $\alpha^{\leftarrow}$ and $\alpha^{\rightarrow}$ replace β_{sym} and $(1 - \beta_{sym})$ respectively. The calculation uses the anodic transfer coefficient $\alpha^{\leftarrow}$ in the place of β_{sym}. For a reaction in which the oxidation and reduction processes proceed by the same mechanism and have the same RDS (if multiple steps are involved), the sum of the transfer coefficients will be unity. If the forward and reverse steps proceed by different mechanisms or have a different RDS, the sum no longer equals unity. Figure 4.3.9 shows the effect of transfer coefficients on the form of polarization curve for a material undergoing oxidation and reduction.

It is these transfer coefficients which, along with z, determine the value of the Tafel constants in the same manner that β_{sym} and $(1 - \beta_{sym})$ do in the less complex case. It has already been shown (Chapter 4 Section 2) that different α (0.60 and 0.77) values are needed for Reactions 2 and 7 (oxygen evolution and reduction reactions respectively). This corresponds to β_{sym} values of 0.4 and 0.23 for the oxygen reduction and evolution processes respectively.

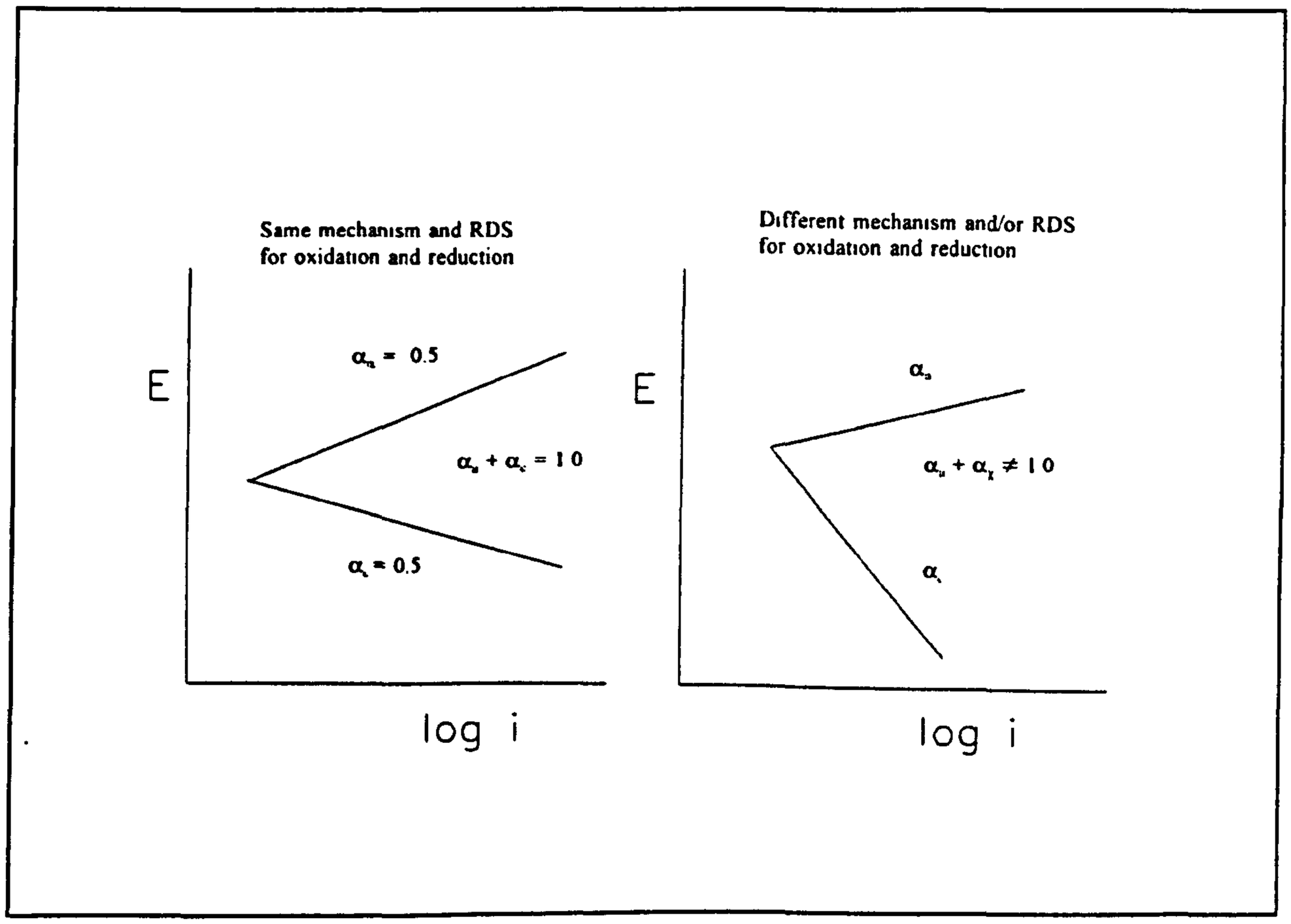

Figure 4.3.9 Schematic showing effect of transfer coefficient on form of polarization curves.

In the case of Reaction 3, the factor $\alpha = (1 - \beta_{sym})z$ in the denominator must be replaced by a factor which takes into account the stoichiometric number v. To calculate the desired cathodic Tafel slopes of 0.06 and 0.15, the value of this new factor must be 1 and 0.4 respectively (since the value of 2.303RT/F is equal to 0.06). The z parameter has been defined in Section 4.2.3.5 as the ratio of electrons transferred to ions in the overall reaction, thus for all mechanisms of reaction 3, $z = 2$.

If the mechanism at low cathodic polarizations is considered to be discharge-controlled followed by chemical desorption ie mechanism 1, $\alpha^{\rightarrow}$ = cathodic β_{sym}, together with a stoichiometric number of 2. If we take the anodic symmetry factor to be 0.5, then the cathodic factor will also be 0.5, and thus $(\alpha^{\rightarrow}z) = 1$, as required. For the reaction at higher cathodic polarizations, the mechanism is proposed to be electrodic discharge (or

possibly coupled discharge-chemical desorption) ie mechanism 3, 4, or 6; all of which have $\nu = 1$. This leads to $\alpha^{\rightarrow}$ being equal to 0.4 and $\alpha^{\leftarrow} = 1 - \alpha^{\rightarrow}(\nu/z)$. Since $z = 2$ and $\nu = 1$, $\alpha^{\leftarrow}$ equals 0.8, and it is this value that is used in the model.

Metal	i_o (nA cm^{-2})	probable mechanism
Platinum	7.94×10^5	2
Rhodium	2.51×10^5	2
Nickel	6.31×10^3	5
Tungsten	1.26×10^3	6 (5 at high η)
Cadmium	15.8×10^{-3}	4
Lead	1×10^{-3}	4

Table 4.3.3 Exchange current density for Reaction 3 in 1M H_2SO_4[58,122].

It is well known that exchange current densities for Reaction 3 are heavily dependent on the nature of the electrode[58,122]. Table 4.3.3 shows some i_o values for metals in ~ 1M H_2SO_4 and the different mechanisms by which they proceed. There is a difference of eight orders of magnitude in the i_o values. The mechanism on a tungsten surface is reported to change at high hydrogen atom coverages, while platinum and rhodium are reported to support different mechanisms depending on surface condition[122]. The two different mechanisms for Reaction 3 on 304 stainless steel are here assumed to have different i_o values, although there is no experimental proof that this occurs.

The results of considering Reaction 3 to proceed through two different mechanisms are shown in Figures 4.3.10 and 4.3.11. The parameters used are shown in Tables 4.3.4 and 4.3.5 respectively. It can be seen (Figure 4.3.11) that the parameters used in Table 4.3.5

show a better correlation with the cathodic portion of the curve at cathodic polarizations in excess of ~ 100 mV (ie at potentials of ~ -500 mV SCE).

	Reaction 1	Reaction 3
E° (V SHE)	-0.440	0.000
i_o (nA cm^{-2})	2.5×10^{-4}	6×10^{4}
$i_{lim}^{cathodic}$	negligible	1×10^{20}
i_{lim}^{anodic}	not required	negligible
α	0.5	0.8

Table 4.3.4 Kinetic parameters used in Figure 4.3.10

At potentials more electronegative, the interaction of such parameters with the anodic line representing Reaction 1 lead to a 'triple point' *ie* unstable passive behaviour. Such behaviour is not viewed in deaerated solutions of 5% H_2SO_4. The parameters detailed in Table 4.3.4 show better correlation with the cathodic portion of the curve at potentials greater than -500 mV SCE, and the interaction with the Reaction 1 line leads to the desired form of the curve.

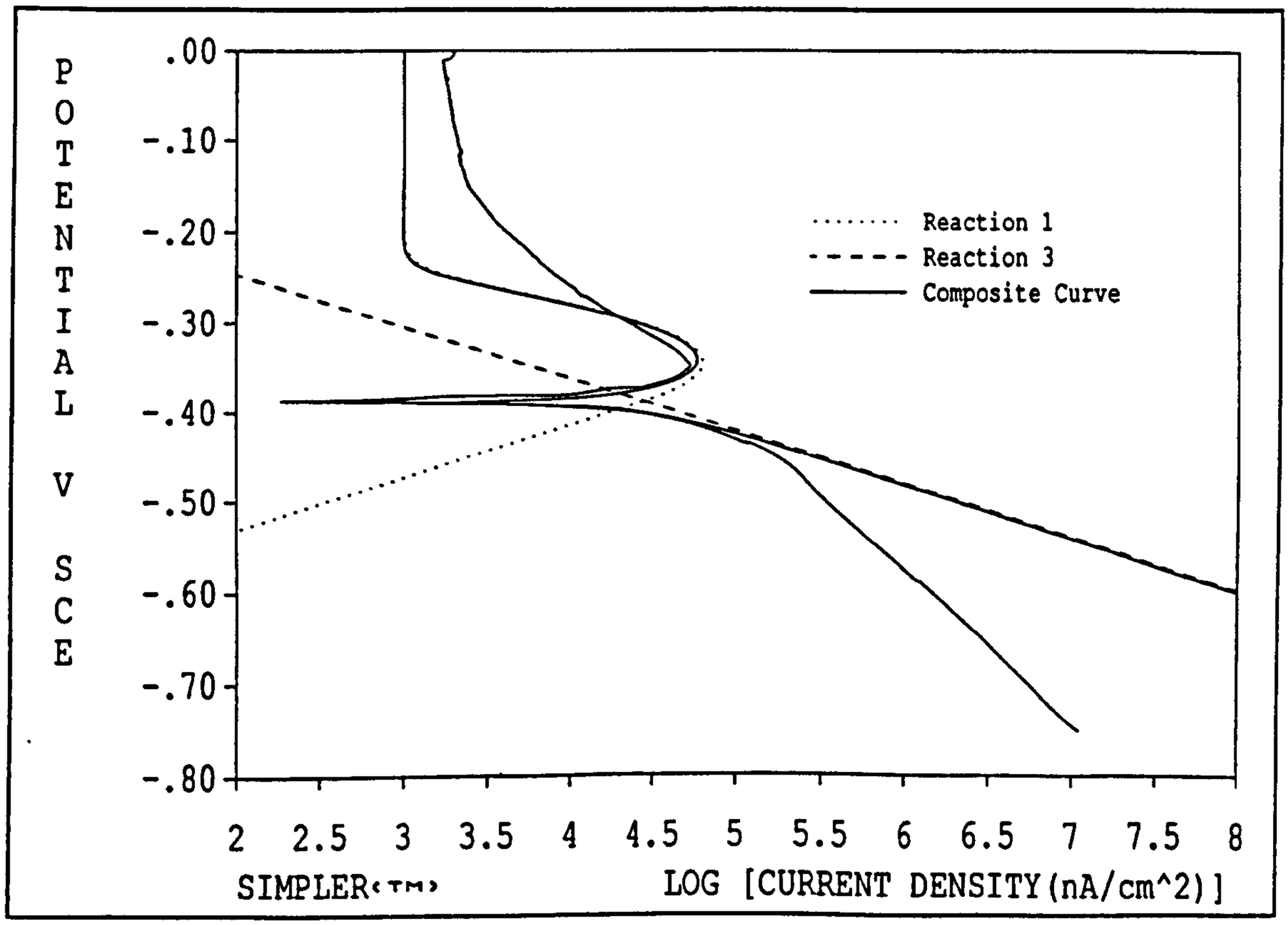

Figure 4.3.10 Model of conditioned 304 stainless steel in deaerated 5% H_2SO_4 - Reaction 3 modelling region B'B.

	Reaction 1	Reaction 3
E° (V SHE)	-0.440	0.000
i_o (nA cm^{-2})	2.5×10^{-4}	30
$i_{lim}^{cathodic}$	negligible	1×10^{20}
i_{lim}^{anodic}	not required	not required
α	0.5	0.5

Table 4.3.5 Kinetic parameters used in Figure 4.3.11.

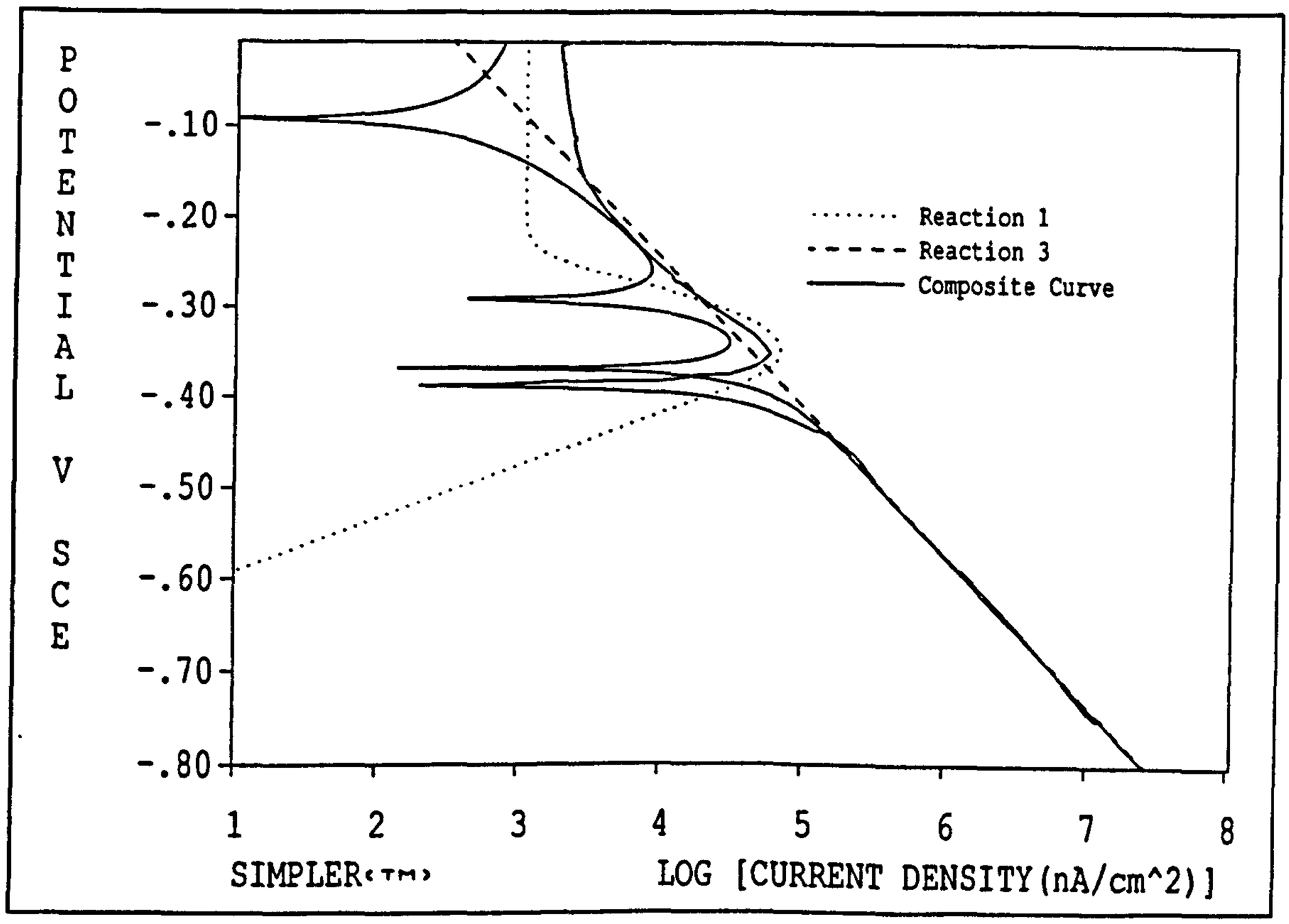

Figure 4.3.11 Model of conditioned 304 stainless steel in deaerated 5% H_2SO_4 - Reaction 3 modelling region AB'.

4.3.3.9 Dissolved Oxygen Measurements

The dependence of the concentration of dissolved oxygen in 5% H_2SO_4 on temperature using the three different aeration regimes is shown in Figure 4.3.12. The appropriate values of both oxygen partial pressure and temperature are used in the modelling of the polarization curves shown in Figures 4.3.1 to 4.3.7. Sections 4.3.3.10 to 4.3.3.13 show the resultant synthesised curves, while appendices E to G show the parameters used for individual theoretical polarization curve.

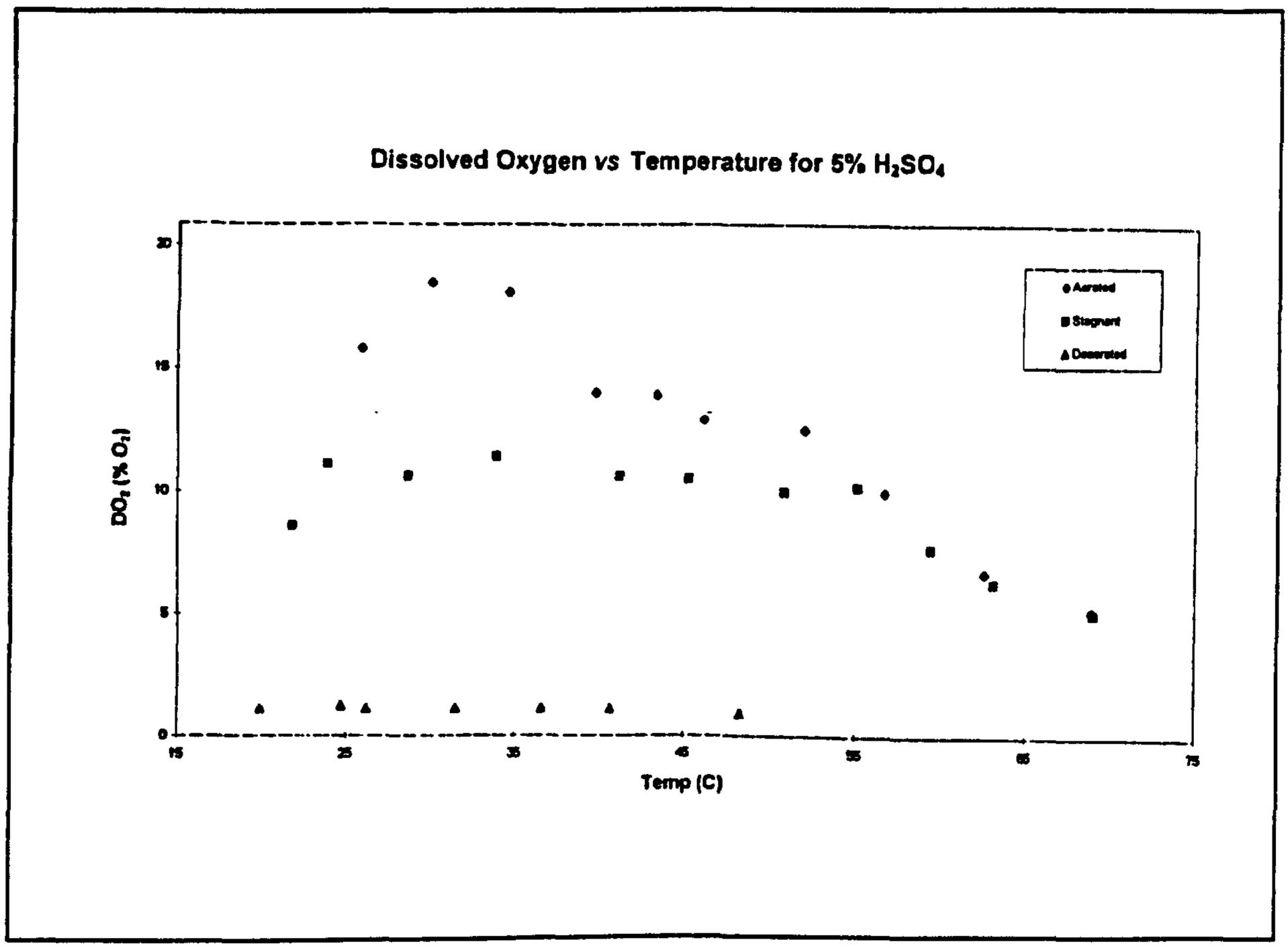

Figure 4.3.12 Dissolved oxygen *vs* temperature for 5% H_2SO_4 for three different aeration regimes.

4.3.3.10 Models of 304 Stainless Steel in Deaerated 5% H_2SO_4

Figure 4.3.13 shows an SEM micrograph of the surface of the sample polarized in deaerated 5% H_2SO_4 at 24°C , and it can be seen that general dissolution of the surface, rather than pitting, is the dominant mode of degradation.

To model the curves in deaerated solutions, Reaction 3 is fitted to the cathodic portion of the curve, and then the parameters for Reaction 1 can be deduced from the interaction of the resultant current density trace with the cathodic trace attributable to Reaction 3.

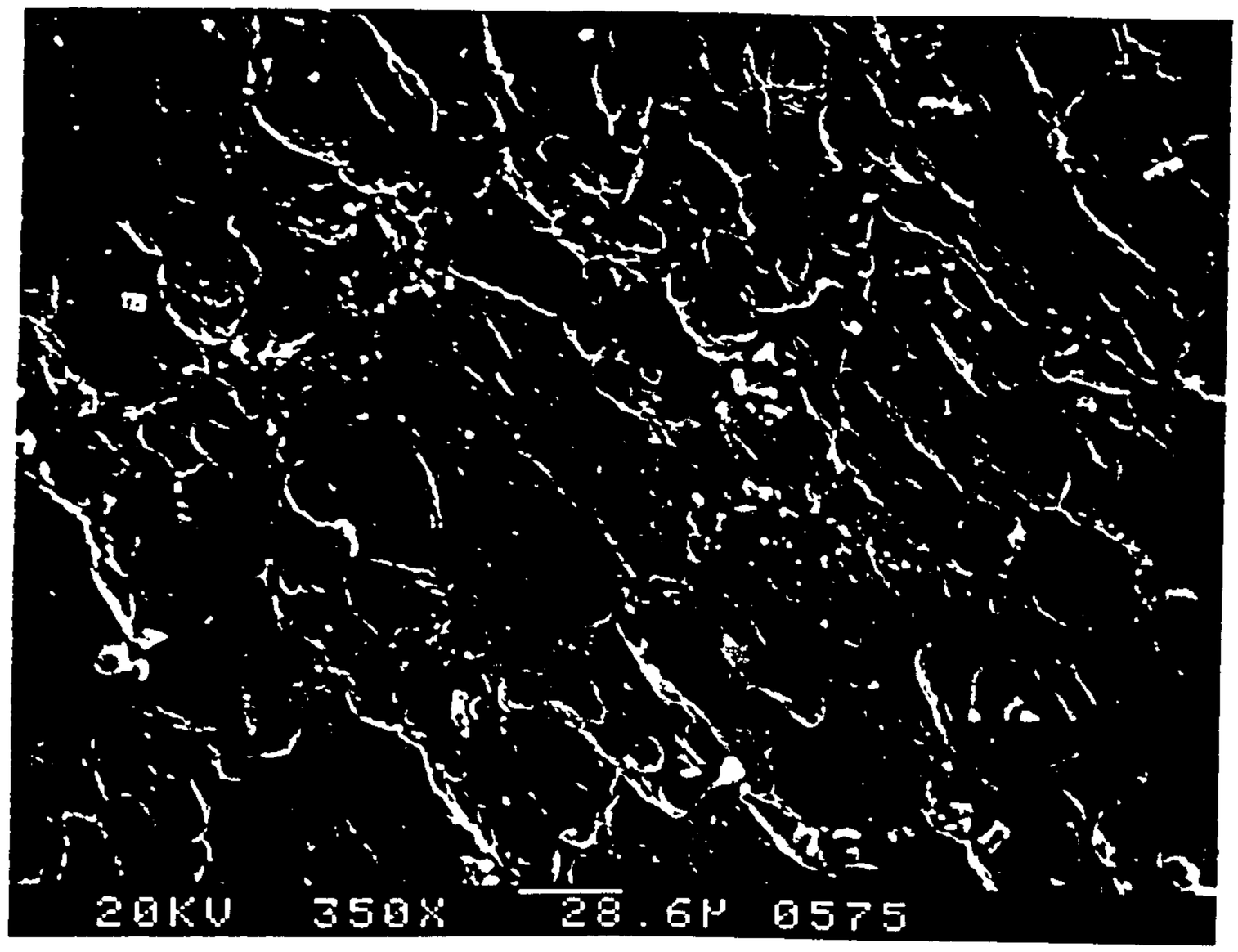

Figure 4.3.13 SEM micrograph showing surface of sample polarized in deaerated 5% H_2SO_4 at 24°C

The model for 304 stainless steel in deaerated 5% H_2SO_4 at 24°C is shown in Figure 4.3.14, using the parameters listed in Tables E-1 and E-2 in appendix E.

Tables E-5 and E-6 in appendix E show the parameters used to construct Figure 4.3.16, which models the behaviour of 304 stainless steel in deaerated 5% H_2SO_4 at 35°C.

Figure 4.3.17 shows the theoretical curve which models the behaviour of 304 stainless steel in deaerated 5% H_2SO_4 at 45°C, using the parameters detailed in Tables E-7 and E-8 in appendix E.

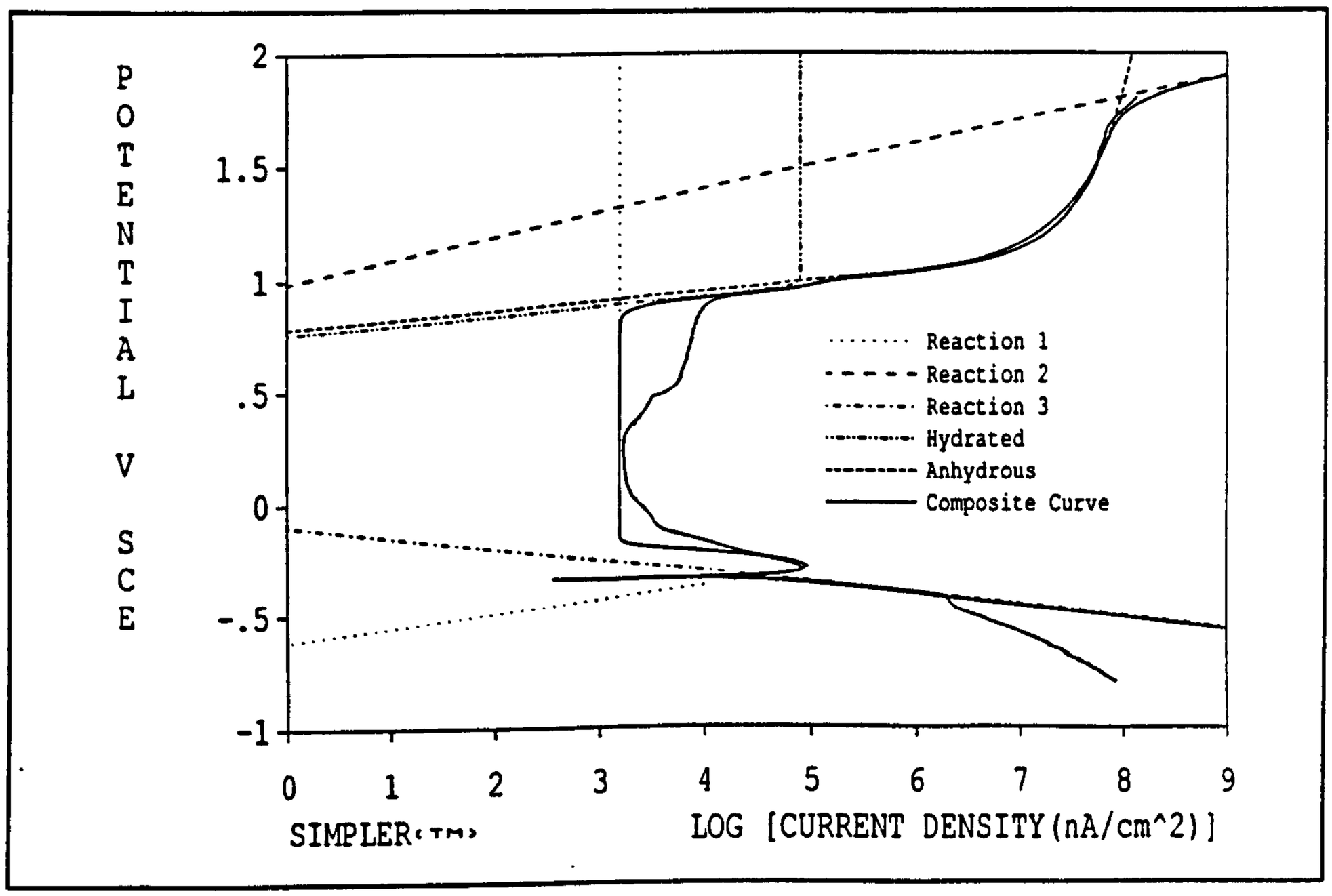

Figure 4.3.14 Model of 304 stainless steel in deaerated 5% H_2SO_4 at 24°C

The model for 304 stainless steel in deaerated 5% H_2SO_4 at 30°C is shown in Figure 4.3.15, which was constructed using the parameters shown in appendix E, Tables E-3 and E-4.

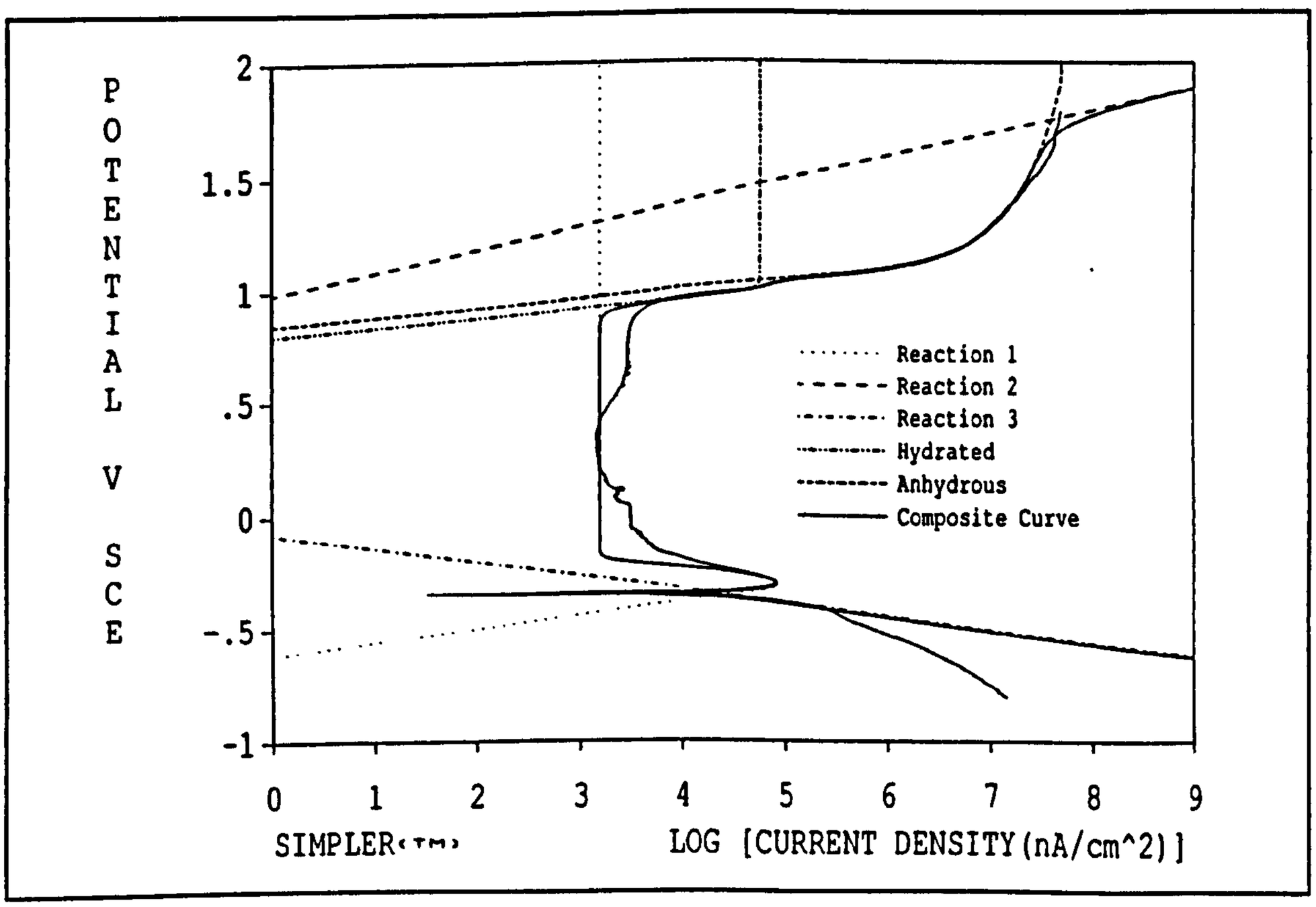

Figure 4.3.15 Model of 304 stainless steel in deaerated 5% H_2SO_4 at 30°C

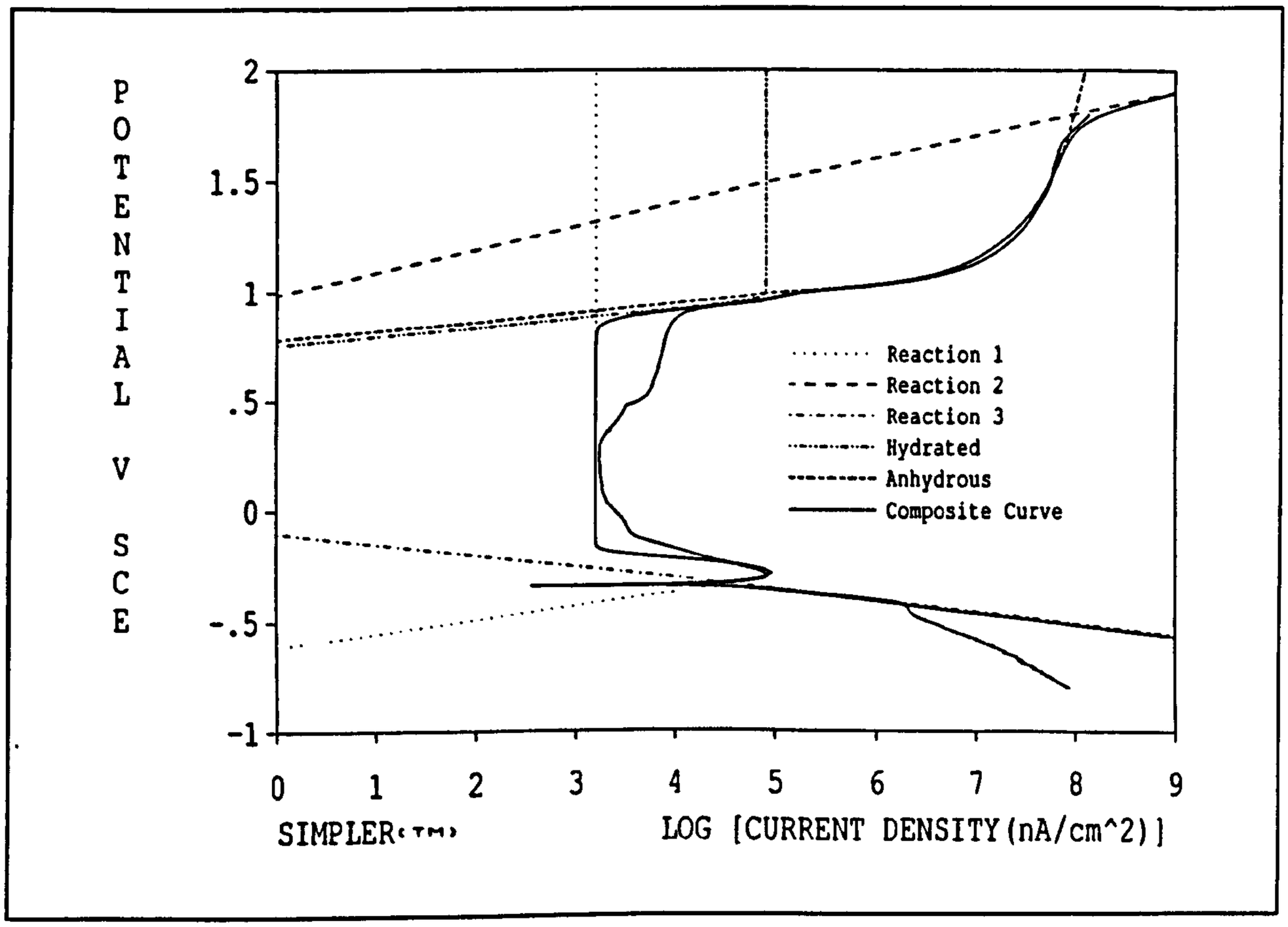

Figure 4.3.16 Model of 304 stainless steel in deaerated 5% H_2SO_4 at 35°C

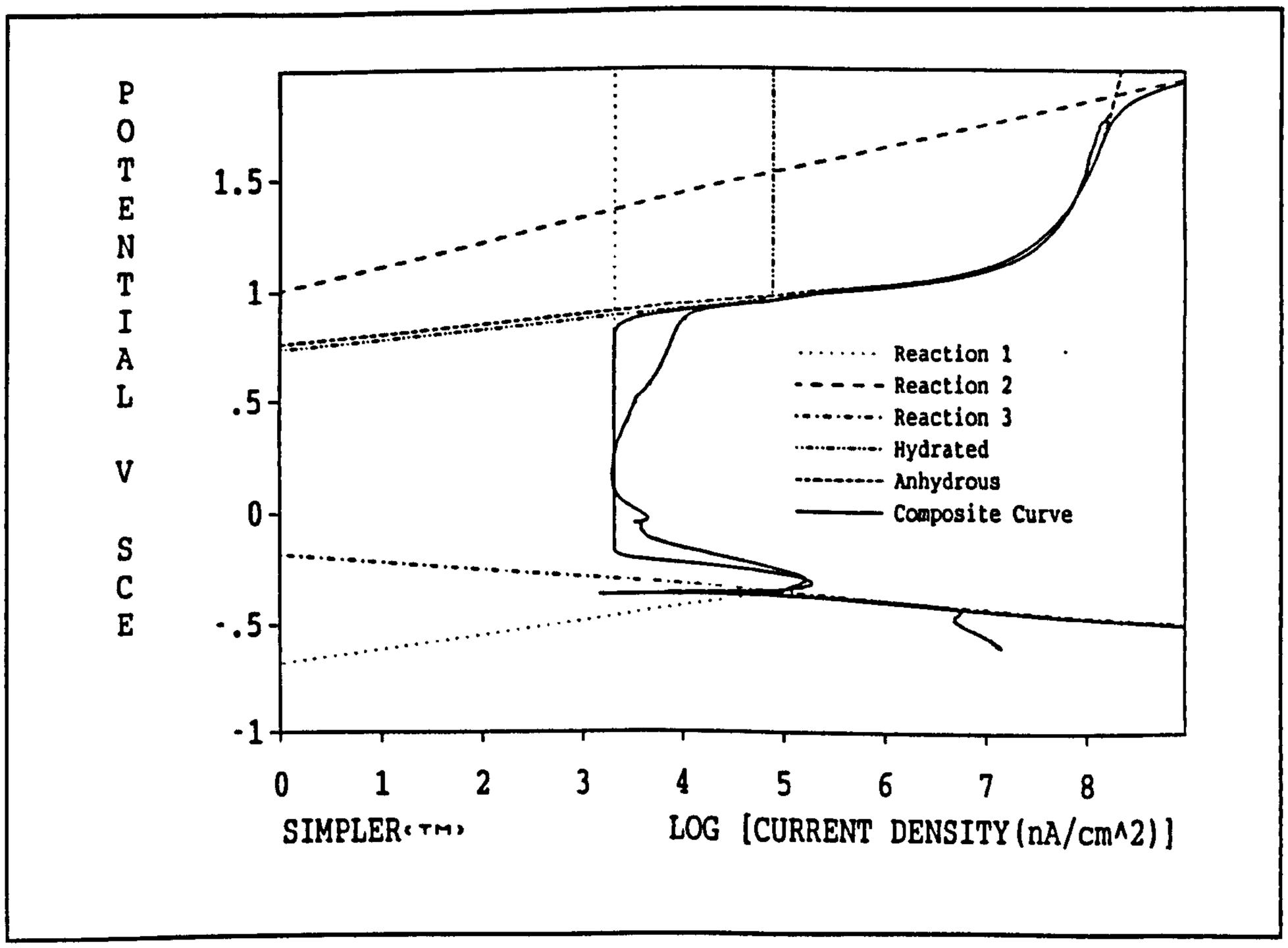

Figure 4.3.17 Model of 304 stainless steel in deaerated 5% H_2SO_4 at 45°C

Table 4.3.6 shows the range of parameters used to model behaviour of 304 stainless steel in deaerated 5% H_2SO_4.

	Reaction 1	Reaction 2	Reaction 3	Reaction 5	Reaction 5
Cr_2O_3 Form				$Cr(OH)_3.nH_2O$	anhydrous
E° (V SHE)	-0.440	1.228	0.000	1.117	1.184
i_o (nA cm^{-2})	7.5×10^{-4} to 8.0×10^{-5}	0.12	7.0 to 200	0.031 to 0.7	1.0 to 7.0
i_{lim} anodic (nA cm^{-2})	not required	1.0×10^{22}	negligible	6.0 to 8.0 x 10^4	3.0×10^7 to 1.0×10^9
i_{lim} cathodic (nA cm^{-2})	negligible	negligible	1×10^{21}	negligible	negligible
α	0.50	0.60	0.10 to 0.50	0.50	0.50

Table 4.3.6 Range of kinetic parameters used in Figures 4.3.14 to 4.3.17

	i_{pass} (nA cm^{-2})	A	p	E_{trans} (V SCE)
Reaction 1	1.6 to 2.1×10^3	450	2.0	-0.330 to -0.390

Table 4.3.7 Range of parameters used in passivation routine for Reaction 1 in Figures 4.3.14 to 4.3.17

4.3.3.11 Models of 304 Stainless Steel in Aerated 5% H_2SO_4

The presence of larger concentrations of dissolved oxygen into the electrolyte leads to a change in the shape of the polarization curve of 304 stainless steel. This is accounted for by the introduction of Reaction 7, the reduction of oxygen. The curvature in the cathodic portion of the curve below the free corrosion potential is attributed to the diffusion-limited polarization of this reaction, while the region of the curve below this is attributed to hydrogen evolution. Reactions 7 and 3 are fitted to these features, and then the parameters for Reaction 1 are deduced from the interactions of the modelled anodic and cathodic lines.

The model for 304 stainless steel in aerated 5% H_2SO_4 at 24°C is shown in Figure 4.3.18, using the parameters shown in Tables F-1 and F-2 in appendix F.

The model for 304 stainless steel in aerated 5% H_2SO_4 at 30°C is shown in Figure 4.3.19, which was constructed using the parameters shown in Tables F-3 and F-4 in appendix F.

Figure 4.3.20 uses the parameters in Tables F-5 and F-6 in appendix F to model the behaviour of 304 stainless steel in aerated 5% H_2SO_4 at 35°C.

Tables F-7 and F-8 in appendix F show the parameters used to model the behaviour of 304 stainless steel in aerated 5% H_2SO_4 at 45°C. The resultant theoretical curve is shown in Figure 4.3.21.

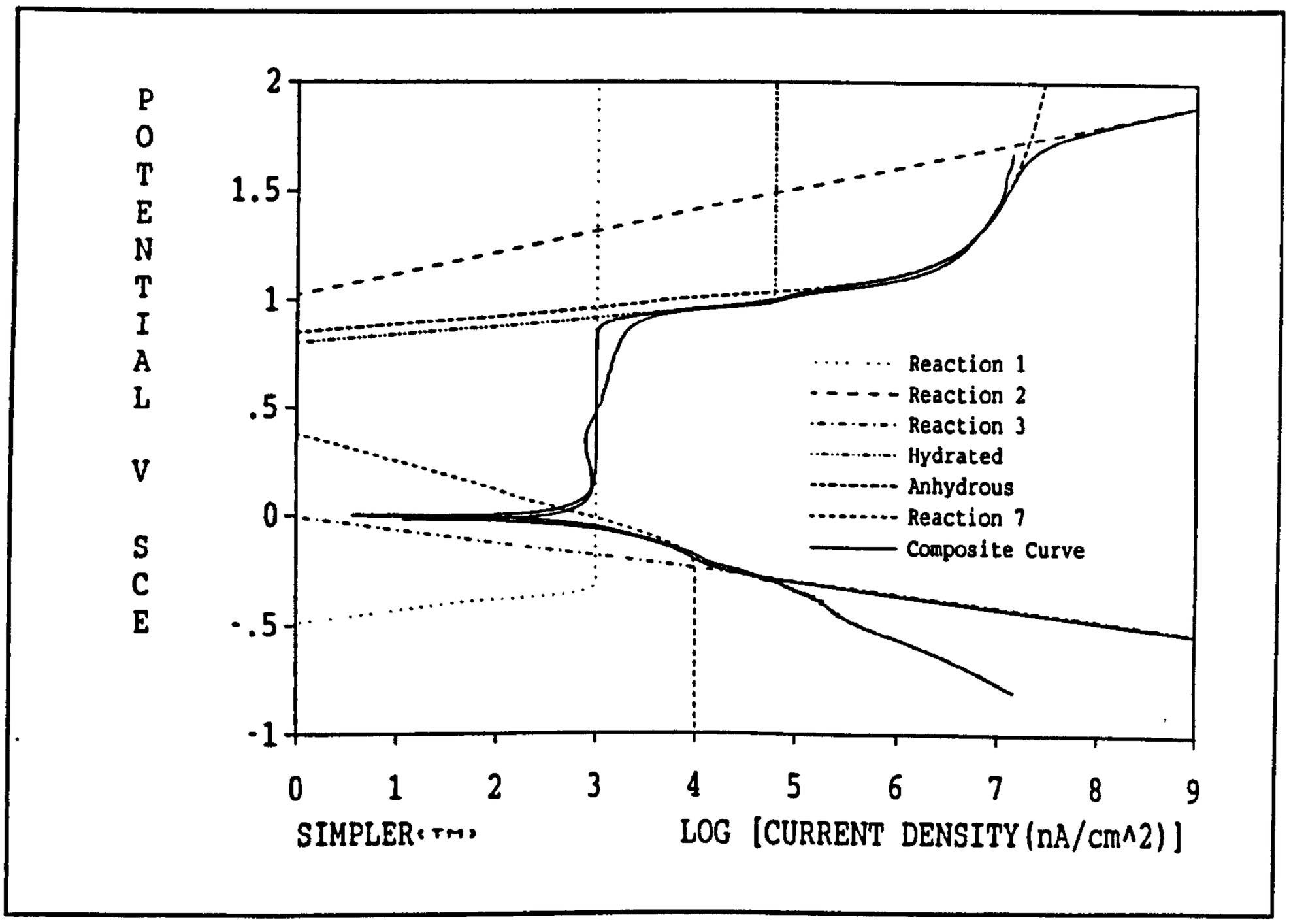

Figure 4.3.18 Model of 304 stainless steel in aerated 5% H_2SO_4 at 24°C

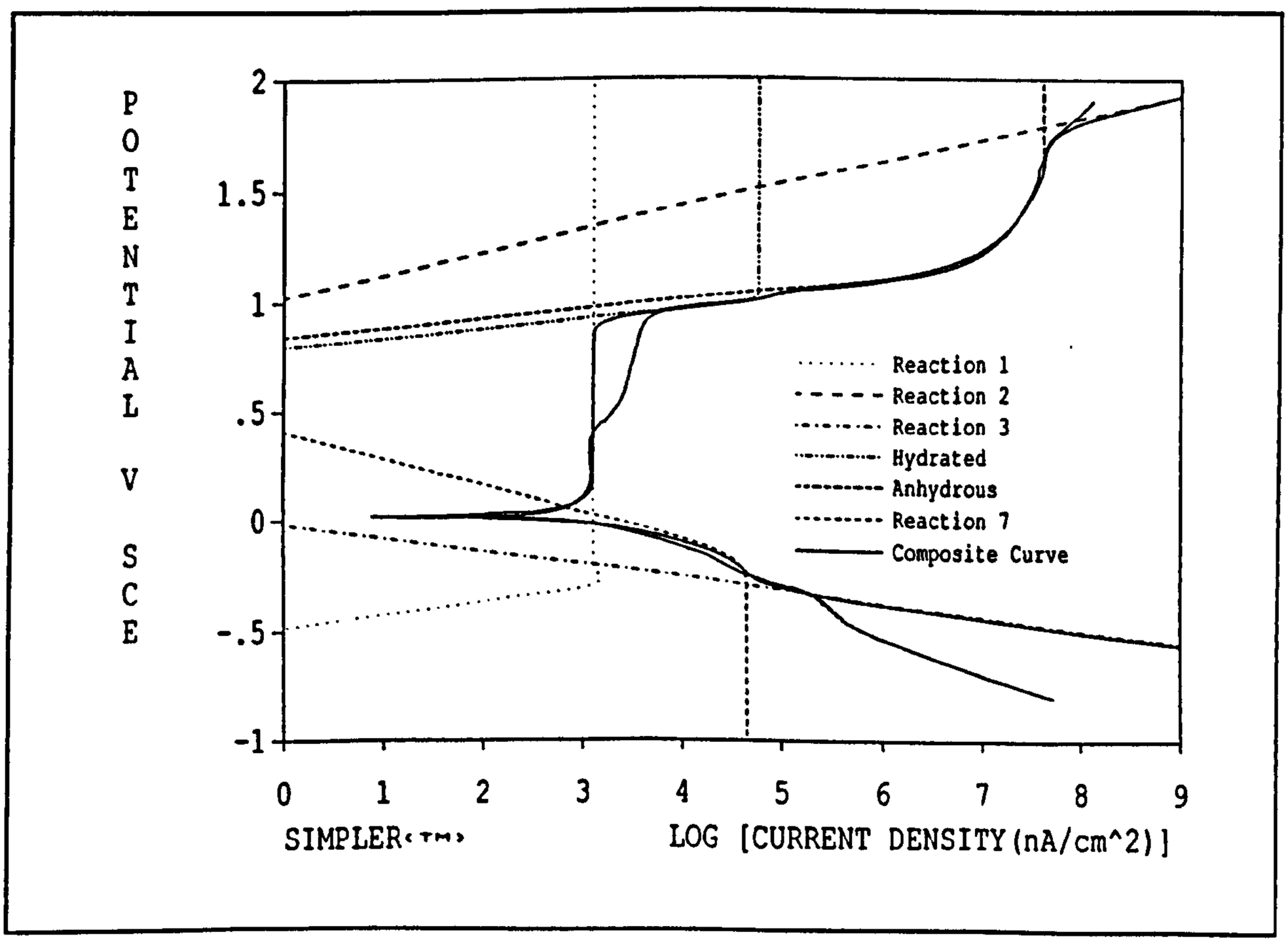

Figure 4.3.19 Model of 304 stainless steel in aerated 5% H_2SO_4 at 30°C

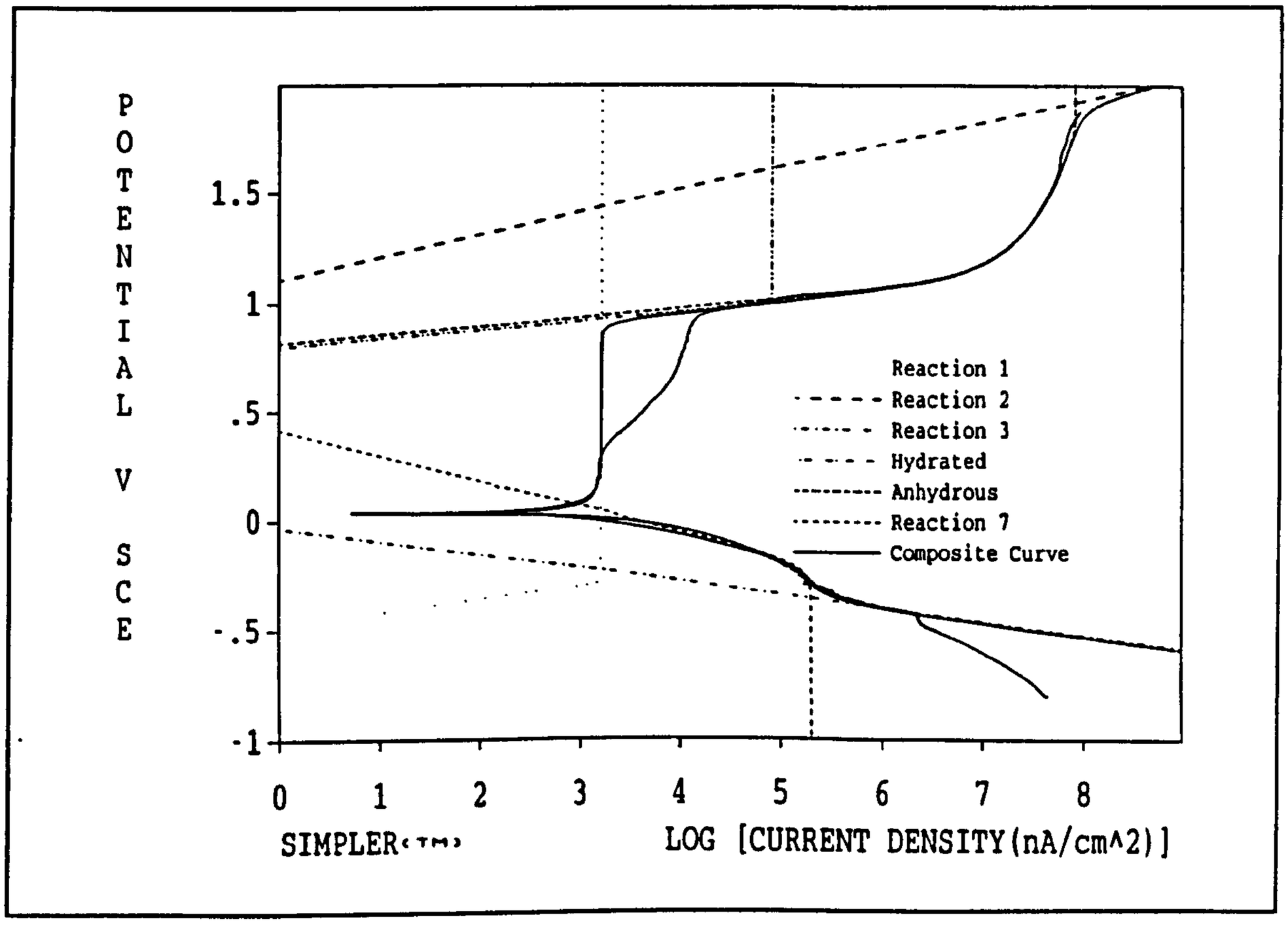

Figure 4.3.20 Model of 304 stainless steel in aerated 5% H_2SO_4 at 35°C

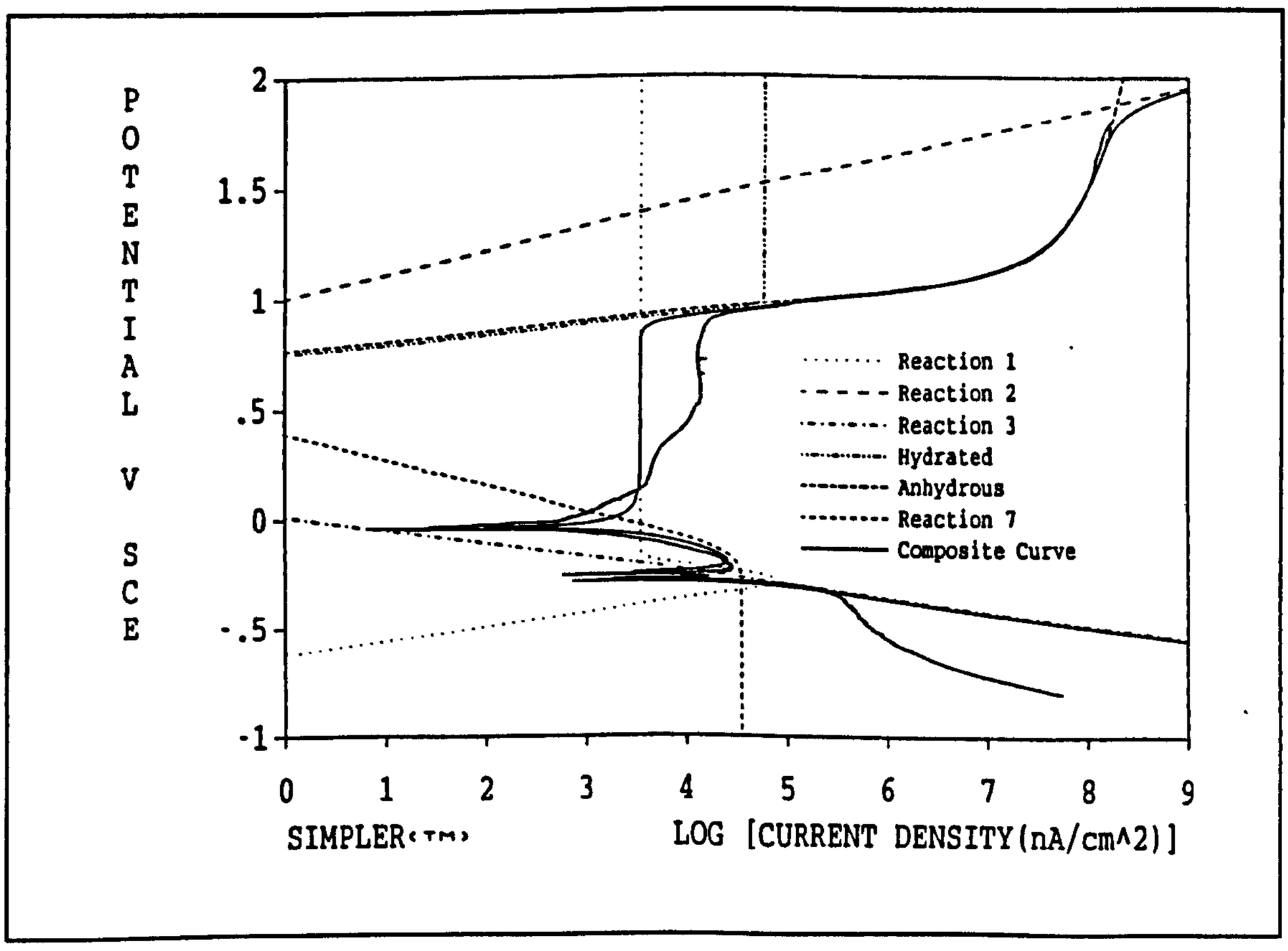

Figure 4.3.21 Model of 304 stainless steel in aerated 5% H_2SO_4 at 45°C

Tables 4.3.8 and 4.3.9 show the range of parameters used to model the behaviour of 304 stainless steel in aerated 5% H_2SO_4.

	Reaction 1	Reaction 2	Reaction 3	Reaction 5	Reaction 5	Reaction 7
Cr_2O_3 Form				$Cr(OH)_3.nH_2O$	anhydrous	
E° (V SHE)	-0.440	1.228	0.000	1.117	1.184	1.228
i_o (nA cm^{-2})	5.0×10^{-7} to 1.0×10^{-4}	0.12	1.0 to 4.0 x 10^3	0.031 to 0.31	0.1 to 5.0	5.2×10^{-5}
i_{lim} anodic (nA cm^{-2})	not required	1.0×10^{22}	negligible	6.0 to 8.0 x 10^4	3.0×10^7 to 3.0×10^9	negligible
i_{lim} cathodic (nA cm^{-2})	negligible	negligible	1×10^{21}	negligible	negligible	1.0×10^4 to 2.0×10^5
α	0.50	0.60	0.10 to 0.50	0.50	0.50	0.47 to 0.55

Table 4.3.8 Range of kinetic parameters used to model behaviour of 304 stainless steel in aerated 5% H_2SO_4

	i_{pass} (nA cm^{-2})	A	p	E_{trans} (V SCE)
Reaction 1	1.0 to 3.5×10^3	450	2.0	-0.330 to -0.390

Table 4.3.9 Range of parameters used in passivation routine for Reaction 1 to model behaviour of 304 stainless steel in aerated 5% H_2SO_4.

4.3.3.12 Models of 304 Stainless Steel in Stagnant 5% H_2SO_4

The same reaction model is used for 304 stainless steel in stagnant 5% H_2SO_4 at 24°C is shown in Figure 4.3.22, using the parameters shown in Tables G-1 and G-2 in appendix G.

The model for 304 stainless steel in stagnant 5% H_2SO_4 at 30°C is shown in Figure 4.3.23, which was constructed using the parameters shown in Tables G-3 and G-4 in appendix G.

The model for 304 stainless steel in stagnant 5% H_2SO_4 at 35°C is shown in Figure 4.3.24, which was constructed using the parameters shown in Tables G-5 and G-6 in appendix G.

The parameters used to construct the theoretical polarization curve for 304 stainless steel in stagnant 5% H_2SO_4 at 45°C are shown in Tables G-7 and G-8 in appendix G. The curve is shown in Figure 4.3.25.

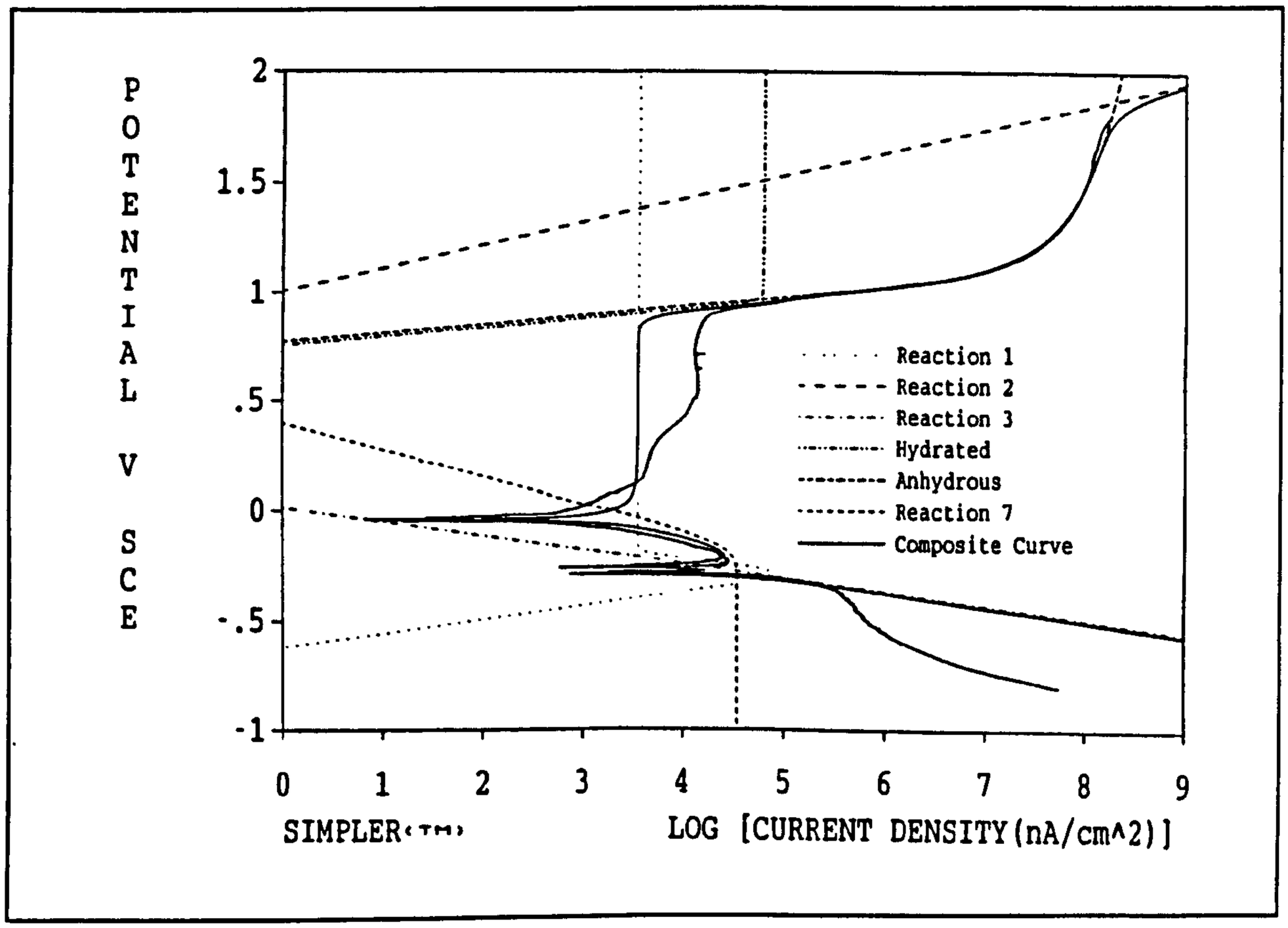

Figure 4.3.22 Model of 304 stainless steel in stagnant 5% H_2SO_4 at 24°C

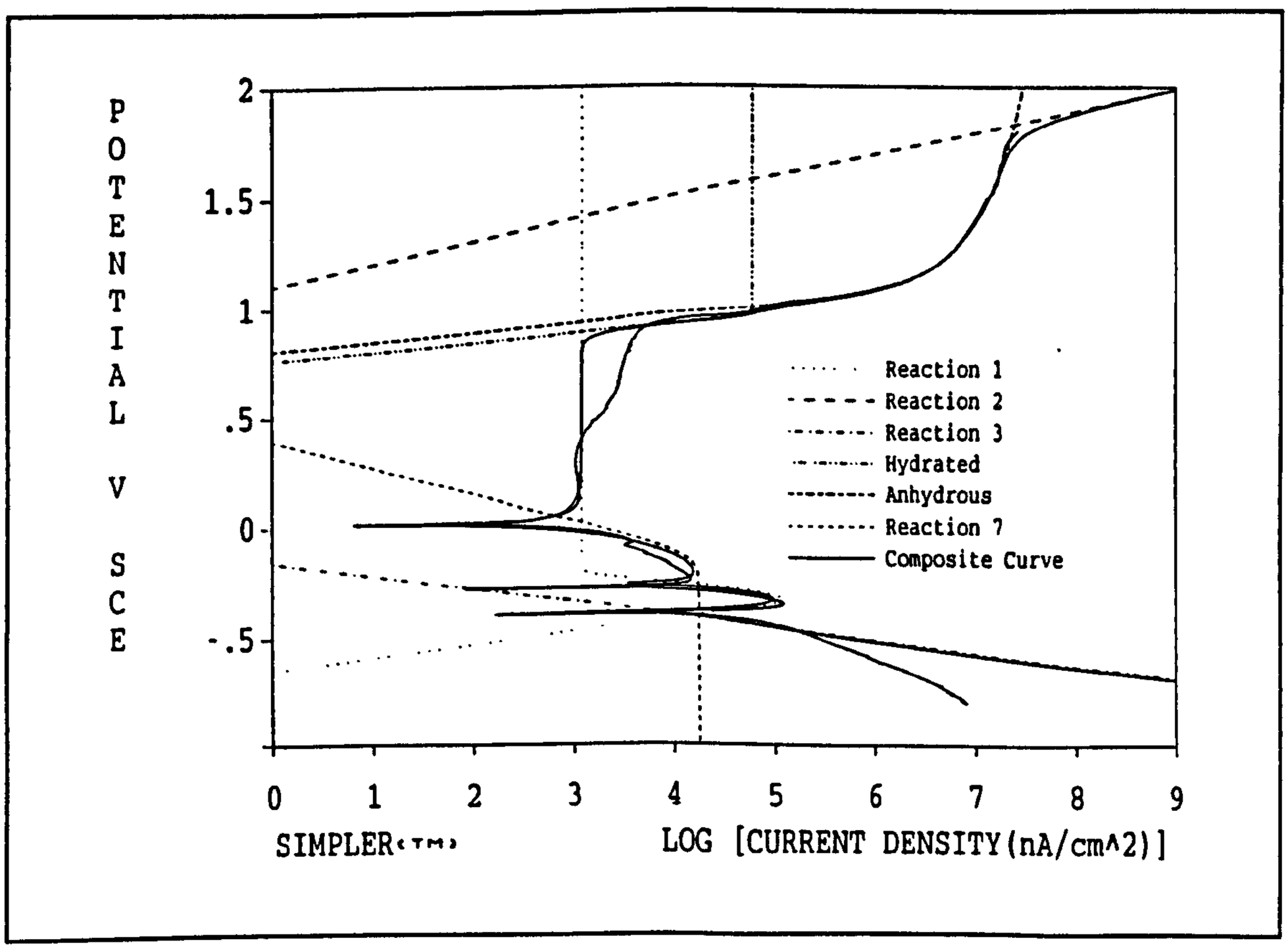

Figure 4.3.23 Model of 304 stainless steel in stagnant 5% H_2SO_4 at 30°C

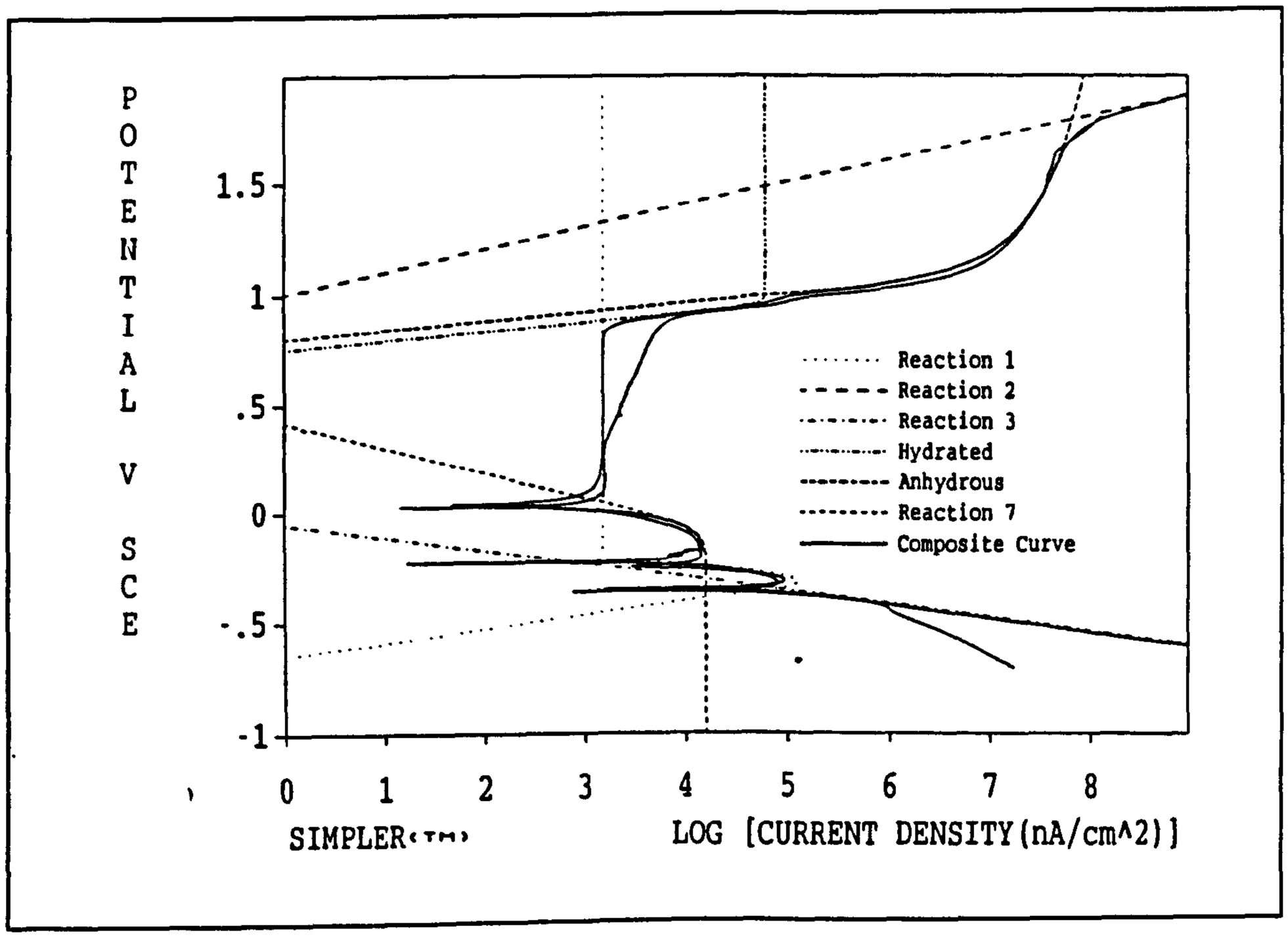

Figure 4.3.24 Model of 304 stainless steel in stagnant 5% H_2SO_4 at 35°C

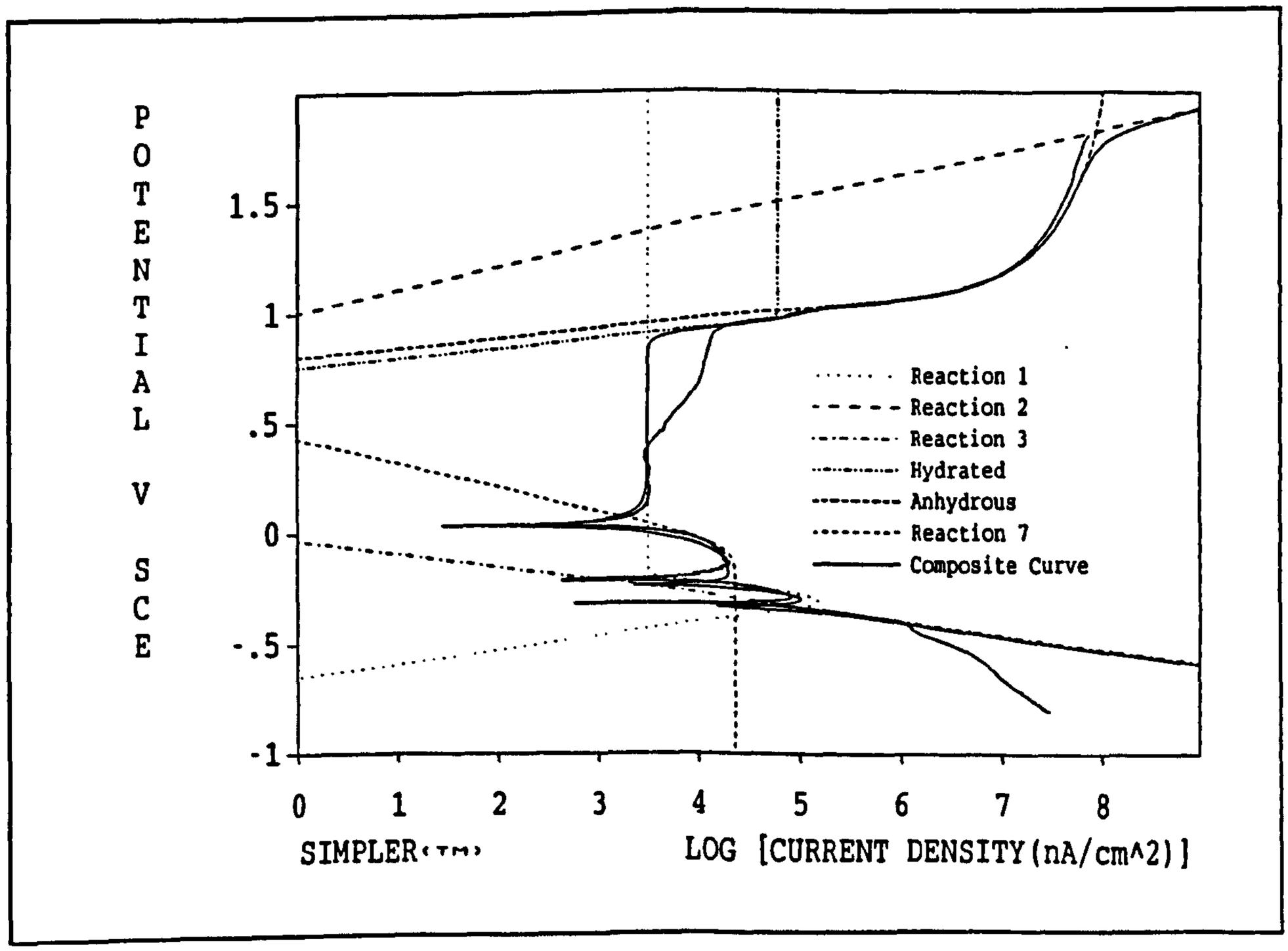

Figure 4.3.25 Model of 304 stainless steel in stagnant 5% H_2SO_4 at 45°C

The range of parameters used to model the behaviour of 304 stainless steel in stagnant 5% H_2SO_4 is shown in Tables 4.3.10 and 4.3.11.

	Reaction 1	Reaction 2	Reaction 3	Reaction 5	Reaction 5	Reaction 7
Cr_2O_3 Form				$Cr(OH)_3.nH_2O$	anhydrous	
E° (V SHE)	-0.440	1.228	0.000	1.117	1.184	1.228
i_o (nA cm^{-2})	2.5 to 7.5 x 10^{-4}	0.12	10 to 3 x 10^3	0.31 to 1.0	1.0	5.2 x 10^{-5}
i_{lim} anodic (nA cm^{-2})	not required	1.0 x 10^{22}	negligible	6.0 to 8.0 x 10^4	3.0 x 10^7 to 3.0 x 10^9	negligible
i_{lim} cathodic (nA cm^{-2})	negligible	negligible	1 x 10^{21}	negligible	negligible	1.8 to 3.0 x 10^4
α	0.50	0.60	0.50	0.50	0.50	0.40 to 0.51

Table 4.3.10 Kinetic parameters used to model the behaviour of 304 stainless steel in stagnant 5% H_2SO_4

	i_{pass} (nA cm^{-2})	A	p	E_{trans} (V SCE)
Reaction 1	1.2 to 4.0 x 10^3	450	2.0	-0.310 to -0.370

Table 4.3.11 Range of parameters used in passivation routine for Reaction 1 to model the behaviour of 304 stainless steel in stagnant 5% H_2SO_4

4.3.4 ANALYSIS OF MODELLING TRENDS

As noted in Section 4.3.3.1, the curves generated in stagnant electrolyte, as well as in aerated 45°C electrolyte, show unstable passivity. These curves possess 'triple points'; behaviour characteristic of alternating net anodic and cathodic current density on the surface of the specimens. The aerated experiments at 24, 30 and 35°C all exhibit stable passivity. The method of modelling this change in behaviour and the rationale behind it is explained in this section.

4.3.4.1 Change in Behaviour Between Stable and Unstable Passivity in 5% H_2SO_4 with Different Oxygen Contents

As noted in Section 2.3, for passivation, the cathodic current density must exceed the maximum value of the anodic current in the active-to-passive 'nose', *ie*:

$$i_{cath} > i_{crit}$$

where i_{cath} consists of the combined cathodic current from Reactions 3 and 7.

It was originally thought that the fall in oxygen concentration with temperature would affect the diffusion-limited current density to such an extent that it would account for the change from stable to unstable behaviour. However, the diffusion-limited current density does not solely depend upon the concentration of dissolved oxygen at the surface; it also depends on the diffusion coefficient of oxygen (D) and on the thickness, δ, of the double layer. Thus:

$$i_{lim} = \frac{-zFDc_s}{\delta}$$

where D is the diffusion coefficient

c_s is the concentration of oxygen at the surface

δ is the thickness of the double layer through which the oxygen must diffuse.

z is the valency of the diffusing species

F is Faraday's constant

δ will decrease with increasing degree of solution agitation, while the dependence of D is more complex, but is generally regarded to rise with temperature[121]. c_s in aerated 5% H_2SO_4, as shown in Figure 4.3.12, falls with an increase in temperature. These last two factors act in opposition to each other, and the value of i_{lim} depends on the relative dependencies of D and c_s on temperature.

The limiting current density was determined from the curvature of the curves at potentials just below 0 V SCE.

Temperature (°C)	Aerated	Stagnant
24	1.0×10^4	1.8×10^4
30	4.5×10^4	1.6×10^4
35	2.0×10^5	2.3×10^4
45	3.5×10^4	3.0×10^4

Table 4.3.12 Reaction 7 i_{lim} (in nA cm^{-2}) values for aerated and stagnant 5% H_2SO_4 .

Table 4.3.12 and Figure 4.3.26 show the limiting current density for the oxygen reduction reaction (Reaction 7) used to generate the theoretical polarization curves for both

the stagnant and aerated electrolytes.

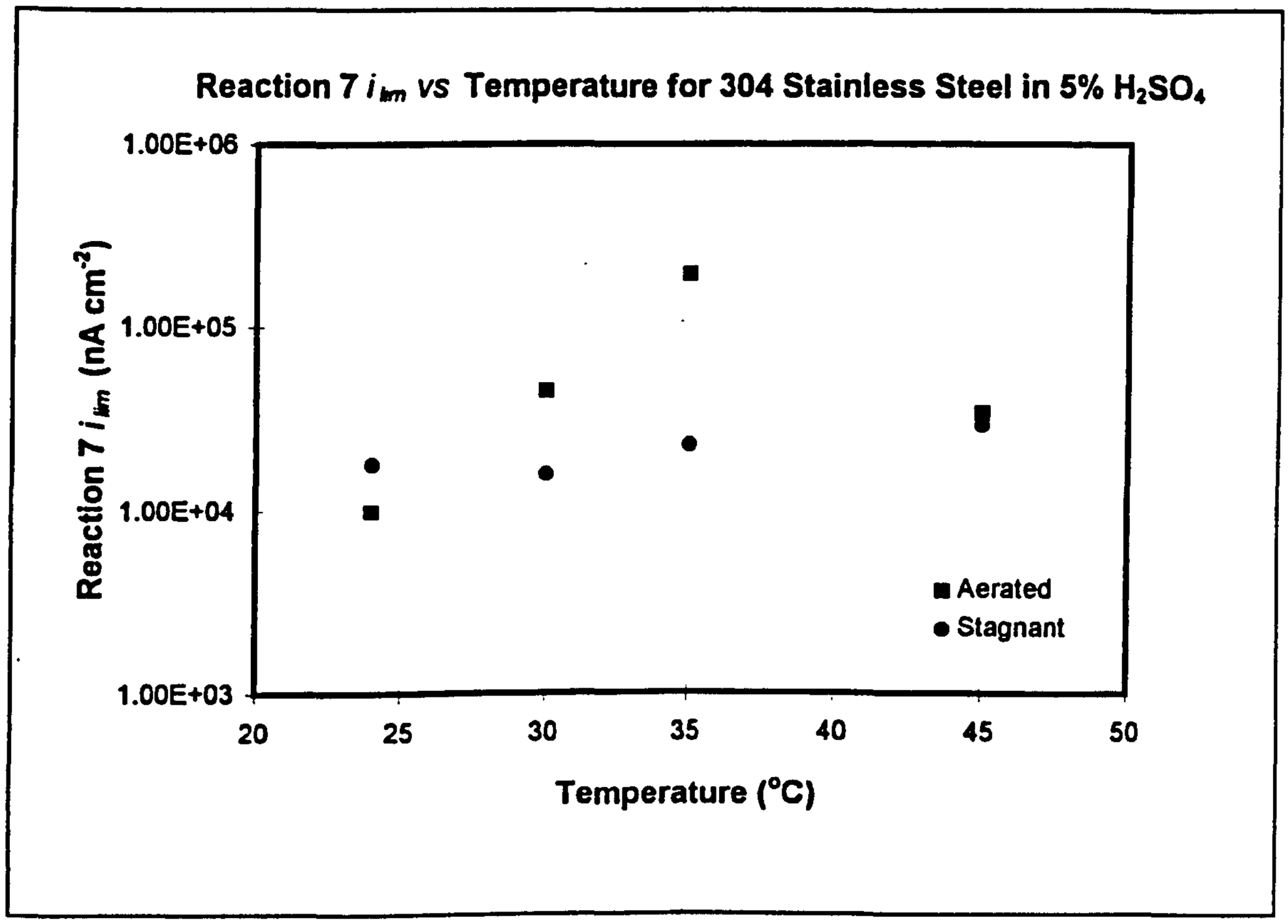

Figure 4.3.26 Diffusion-limited current density for Reaction 7 *vs* temperature

It can be seen that the limiting current densities are similar at 24°C regardless of aeration regime. They show an increase with temperature in the aerated electrolyte at 30°C and 35°C while remaining fairly constant in the stagnant electrolyte, and again are similar at 45°C. However, Figure 4.3.26 shows the same form as Figure 4.3.12, which details the variation of the partial pressure of dissolved oxygen in 5% H_2SO_4 with temperature under the three different aeration routines. Thus, it is suggested that the cathodic diffusion-limited current density for oxygen reduction exhibits a marked dependence on the partial pressure of dissolved oxygen.

The results shown in Figure 4.3.26 confirm what was found during the modelling process, namely that the variation in i_{cath} cannot solely account for the change from stable

to unstable passivity seen with the change from aerated to stagnant electrolyte at temperatures below 45°C, and with increase in temperature above 45°C in aerated electrolyte.

Different i_o values must be used to model Reaction 1, along with the potential, E_t, at which the surface is considered to start becoming covered with passivating species. Table 4.3.13 and Figure 4.3.27 shows the values of i_o used to model Reaction 1 for the three different aeration routines plotted against temperature.

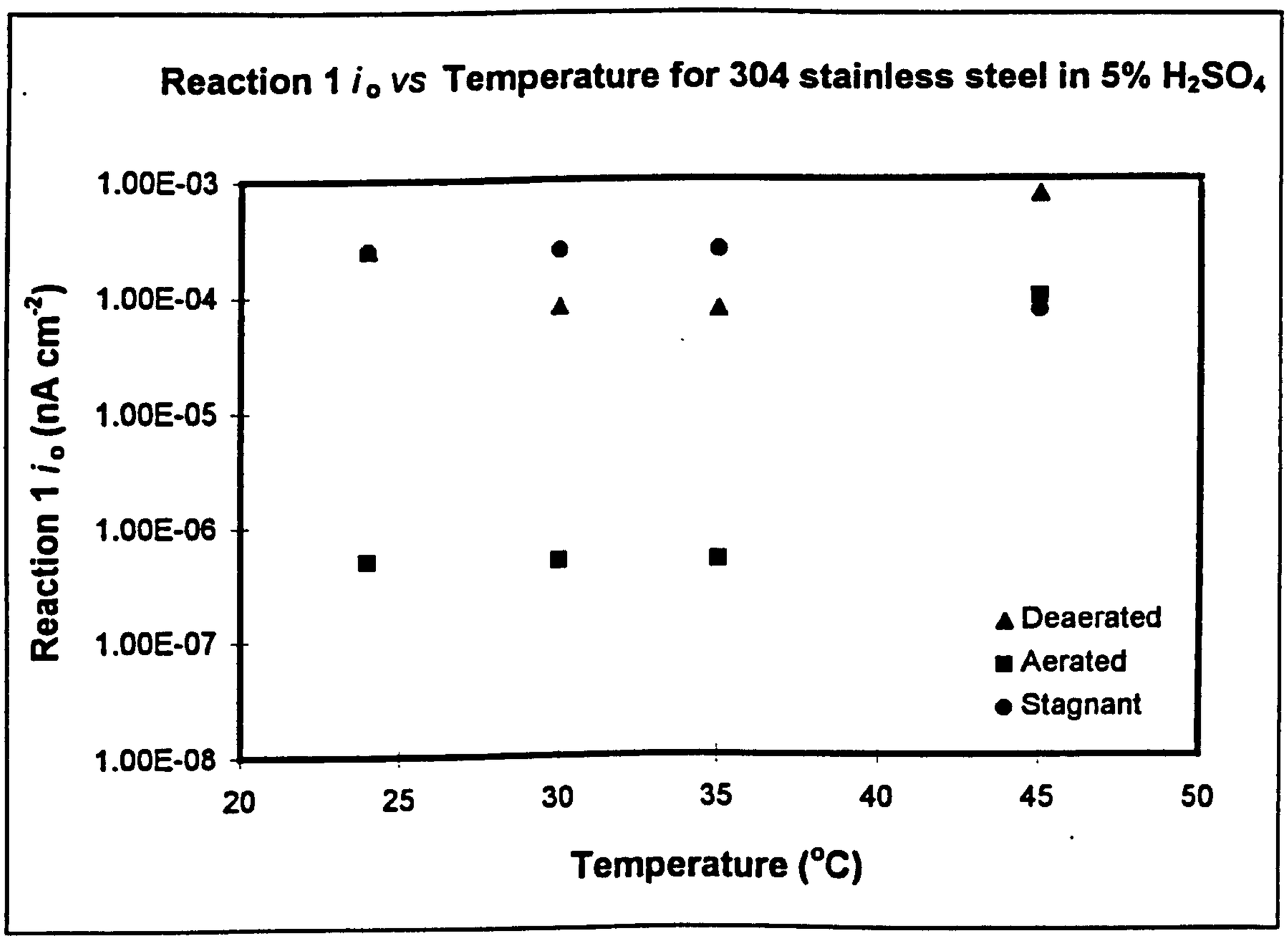

4.3.27 i_o values used for Reaction 1 *vs* temperature for 304 stainless steel in 5% H_2SO_4.

Temperature	Aerated	Stagnant	Deaerated
24	5.0×10^{-7}	2.5×10^{-4}	2.5×10^{-4}
30	5.0×10^{-7}	2.5×10^{-4}	8.0×10^{-5}
35	5.0×10^{-7}	2.5×10^{-4}	7.5×10^{-5}
45	1.0×10^{-4}	7.5×10^{-4}	7.5×10^{-4}

Table 4.3.13 Values of i_o (in nA cm^{-2}) used to model Reaction 1.

It can be seen that the values for the aerated experiments below 45°C are at least two orders of magnitude smaller than those for the stagnant and deaerated curves. The 45°C experiment uses an i_o value close to that for the stagnant case at the same temperature. It may be seen in Figure 4.3.12 that the partial pressure of dissolved oxygen falls markedly in the aerated electrolyte at ~ 40°C. It is therefore suggested that the i_o value for Reaction 1 is dependent in some manner upon the partial pressure of dissolved oxygen in the electrolyte. The absence (or low partial pressure) of dissolved oxygen causes a reduction in the i_o value for Reaction 1, as seen in Figure 4.3.27.

The actual values of i_{lim} and α used to model Reaction 7 also have a marked effect on the theoretical curve.

Figure 4.2.28 shows the effect of using the same parameters as those used in Section 4.3.3.17 to model the polarization curve of 304 stainless steel in aerated 5% H_2SO_4, with exception of an α value of 0.48 (compared to 0.47) and an i_{lim} value of 4.0 x 10 nA cm^{-2} (as opposed to 3.5 x 10 nA cm^{-2}).

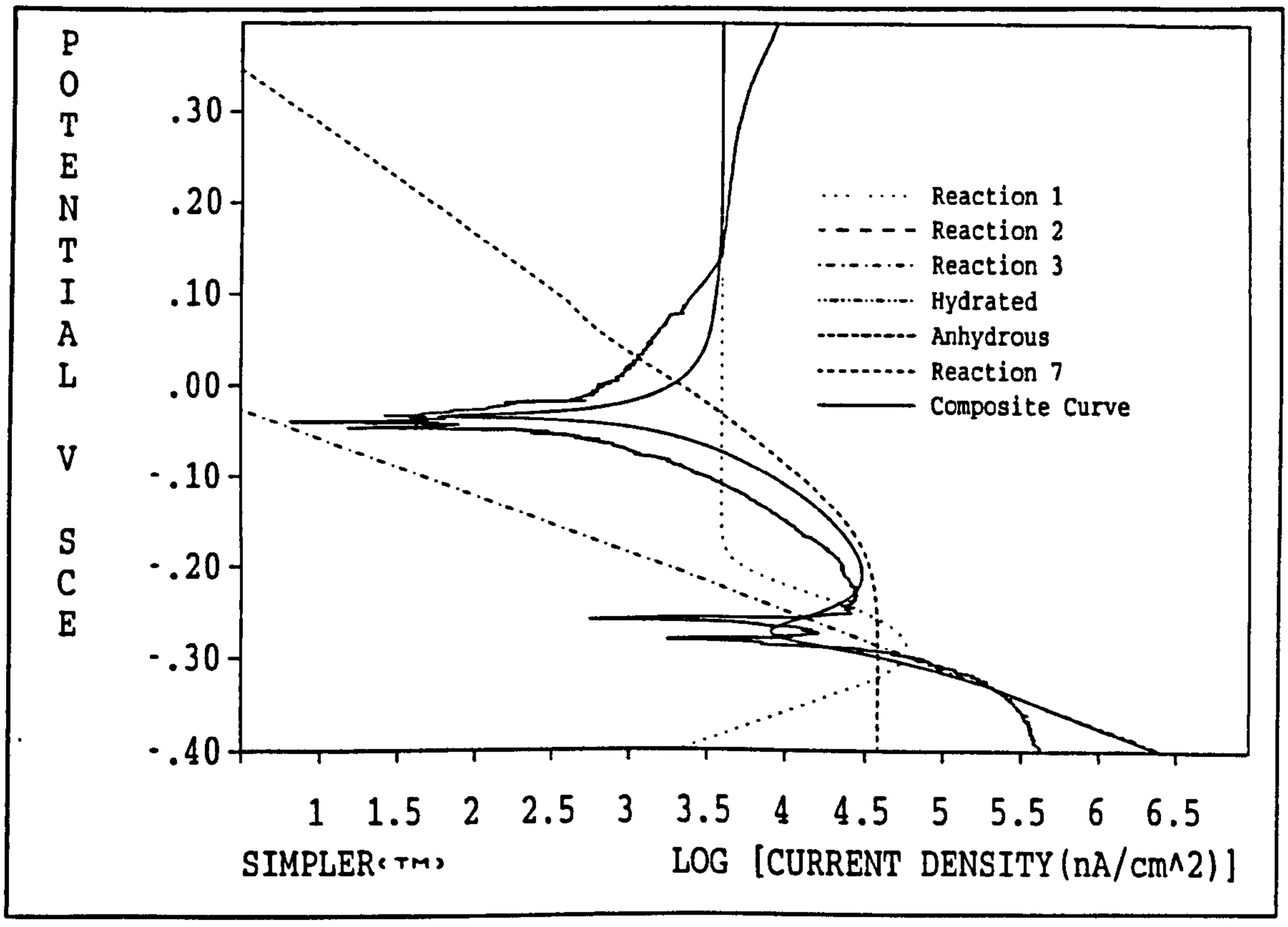

Figure 4.3.28 Theoretical curve showing effect of using i_{lim} and α values such that i_{cath} does not exceed i_{crit}.

It may be seen that there is no 'triple point', but there is a decrease in current density in the region of the lower two free corrosion potentials in the experimental curve. Such an effect was viewed only once, when a fuse blew in the temperature bath heater after being set for 45°C. This meant that the temperature of the electrolyte would have fallen during the experiment thereby allowing the level of dissolved oxygen in the electrolyte to rise, and it is thought that the value of i_{lim} and α for Reaction 7 would alter, along with i_o and E_t for Reaction 1. The experimental result is shown in Figure 4.3.29.

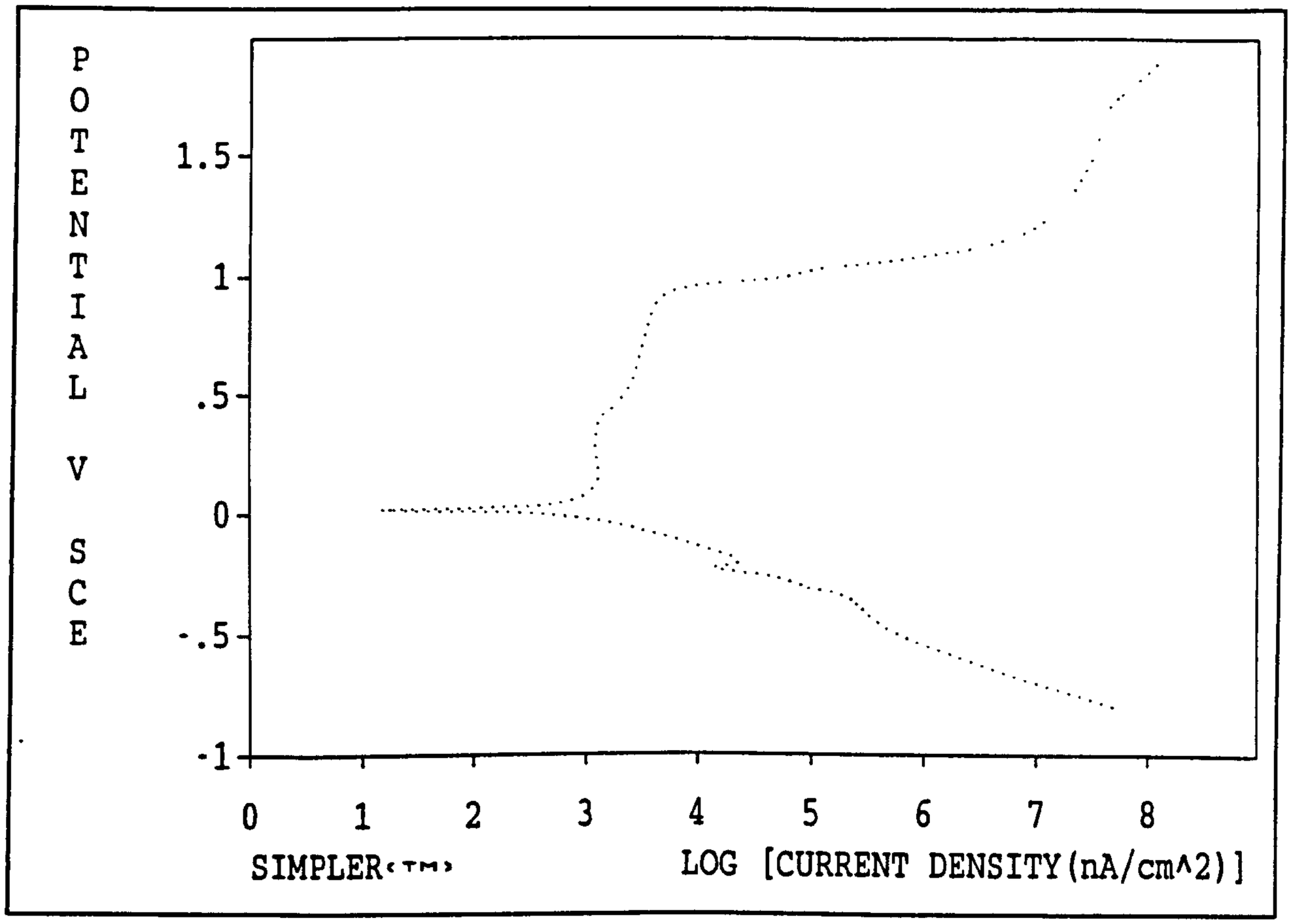

Figure 4.3.29 Experimental polarization curve for 304 stainless steel in aerated 5% H_2SO_4 starting at 45°C, and decreasing.

4.3.4.2 Variation of Transition Potential E_t with Temperature.

Temperature (°C)	Aerated	Stagnant	Deaerated
24	-.039	-0.37	-0.39
30	-0.34	-0.36	-0.34
35	-0.33	-0.35	-0.33
45	-0.36	-0.31	-0.36

Table 4.3.14 E_t values used to model passivating behaviour of 304 stainless steel in 5% H_2SO_4.

Figures 4.3.30 and Table 4.3.14 show the values of E_t used for the three different aeration routines. All show a trend of E_t becoming more electropositive with temperature up to 35°C, above which the value of E_t either remains constant or becomes more electronegative.

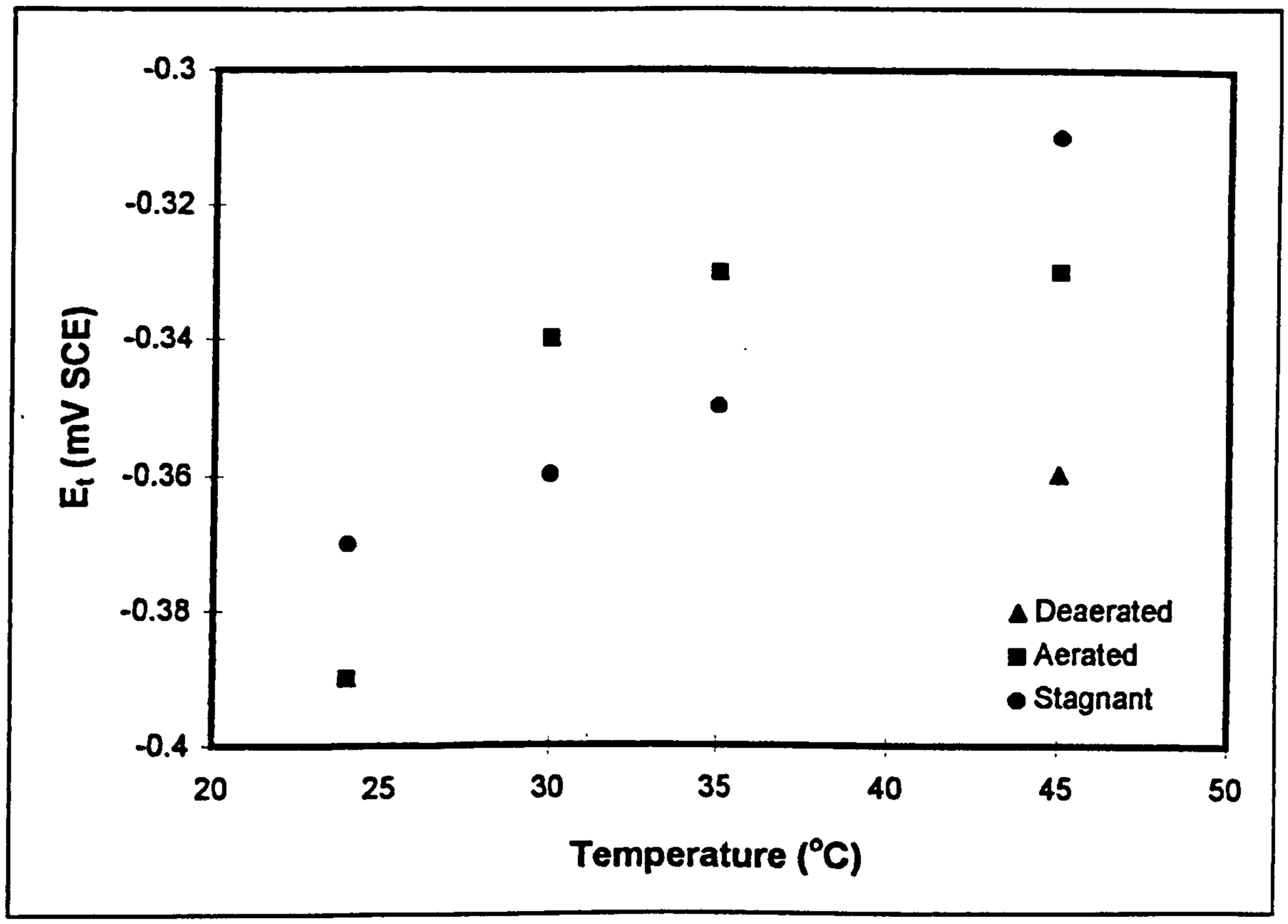

Figure 4.3.30 E_t *vs* temperature for 304 stainless steel in 5% H_2SO_4.

4.3.4.3 Variation of Reaction 7 α with Temperature

The position of the most electropositive of the three 'triple points' was found to be heavily dependent upon the Tafel slope of Reaction 7, which in turn is markedly affected by the value of α used. α is a measure of the efficiency of the electrochemical reaction[58], but may also take into consideration the mechanism of the reaction, by taking into account the stoichiometric number, *v* (see Section 4.3.3.5 and 4.3.3.6.).

A decrease in the value of α for Reaction 7 means that the sloping portion of the line representing Reaction 7 intersects the vertical line representing the passive current density supported by the specimen at more electropositive potentials, thereby causing the most electropositive of the three 'triple points' to occur at a more noble potential.

As mentioned previously, a different value of i_o is used for Reaction 7, compared to Reaction 2. This is thought to be a result of the reactions not proceeding by the same mechanism. If this is the case, the sum of the α values for the oxidation and reduction of oxygen (Reactions 2 and 7 respectively) will not be unity[124]. The use of this i_o value lends greater sensitivity to the modelling of the polarization curves of those specimens exhibiting unstable passivity. Figure 4.3.31 shows the α values used to model Reaction 7 in the aerated and stagnant electrolytes. In only one case (aerated electrolyte, 45°C) does the sum equal unity. The parameters are tabulated in Table 4.3.15.

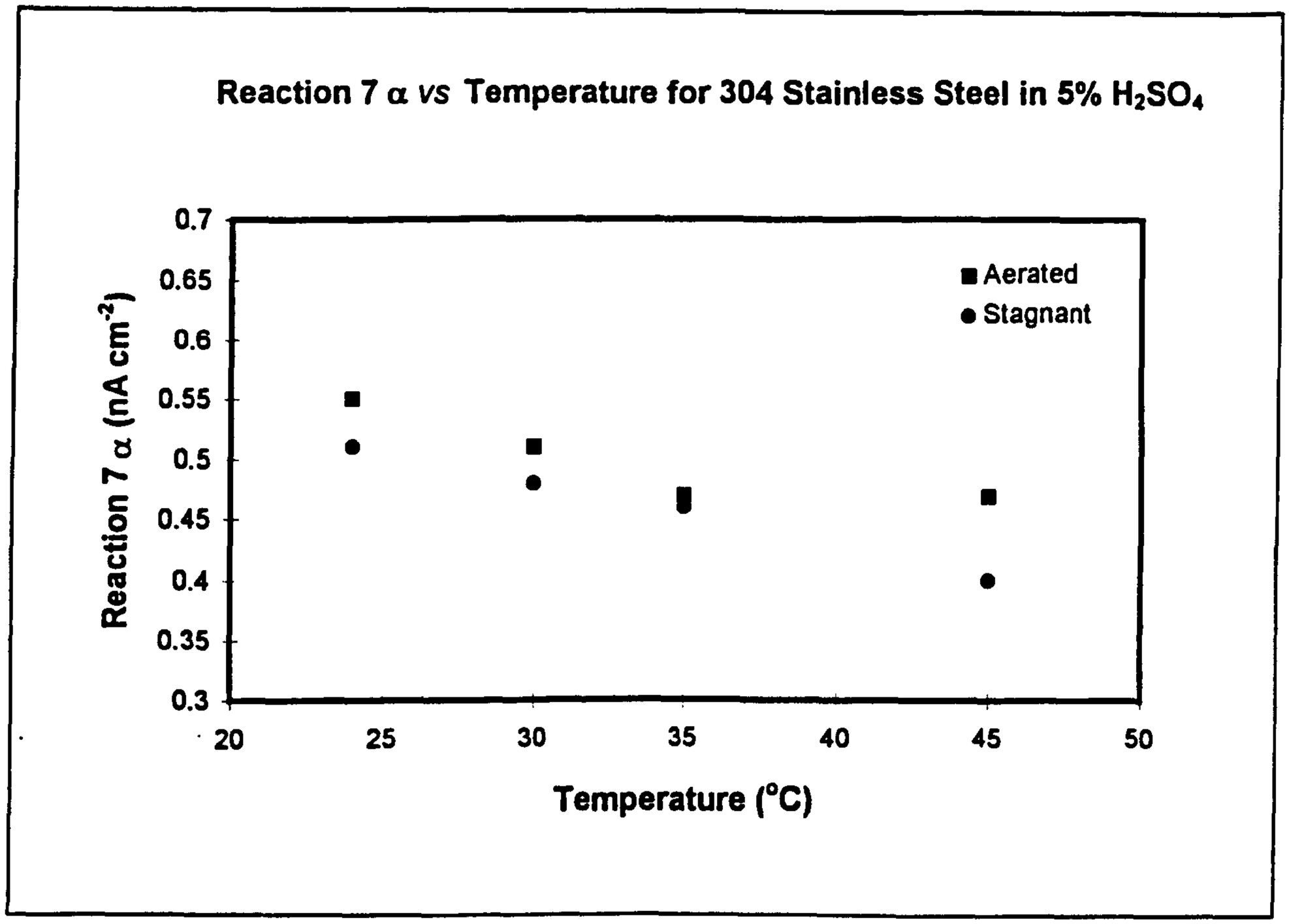

Figure 4.3.31 Variation of Reaction 7 α with temperature in 5% H_2SO_4.

Temperature (°C)	Aerated	Stagnant
24	0.55	0.51
30	0.51	0.48
35	0.47	0.46
45	0.47	0.40

Table 4.3.15 Values of α used to model passivating behaviour of 304 stainless steel in 5% H_2SO_4.

The α values for the stagnant electrolyte show an almost linear decrease with

increasing temperature, while those obtained for the aerated experiments show a similar trend of a linear decrease, but with a plateau of 0.47 at temperatures of 35°C and above.

4.3.4.4 Solution Resistance

Figure 4.3.32 and Table 4.3.16 show the values of resistance used to model the combined resistance of the solution and the metal-solution interface.

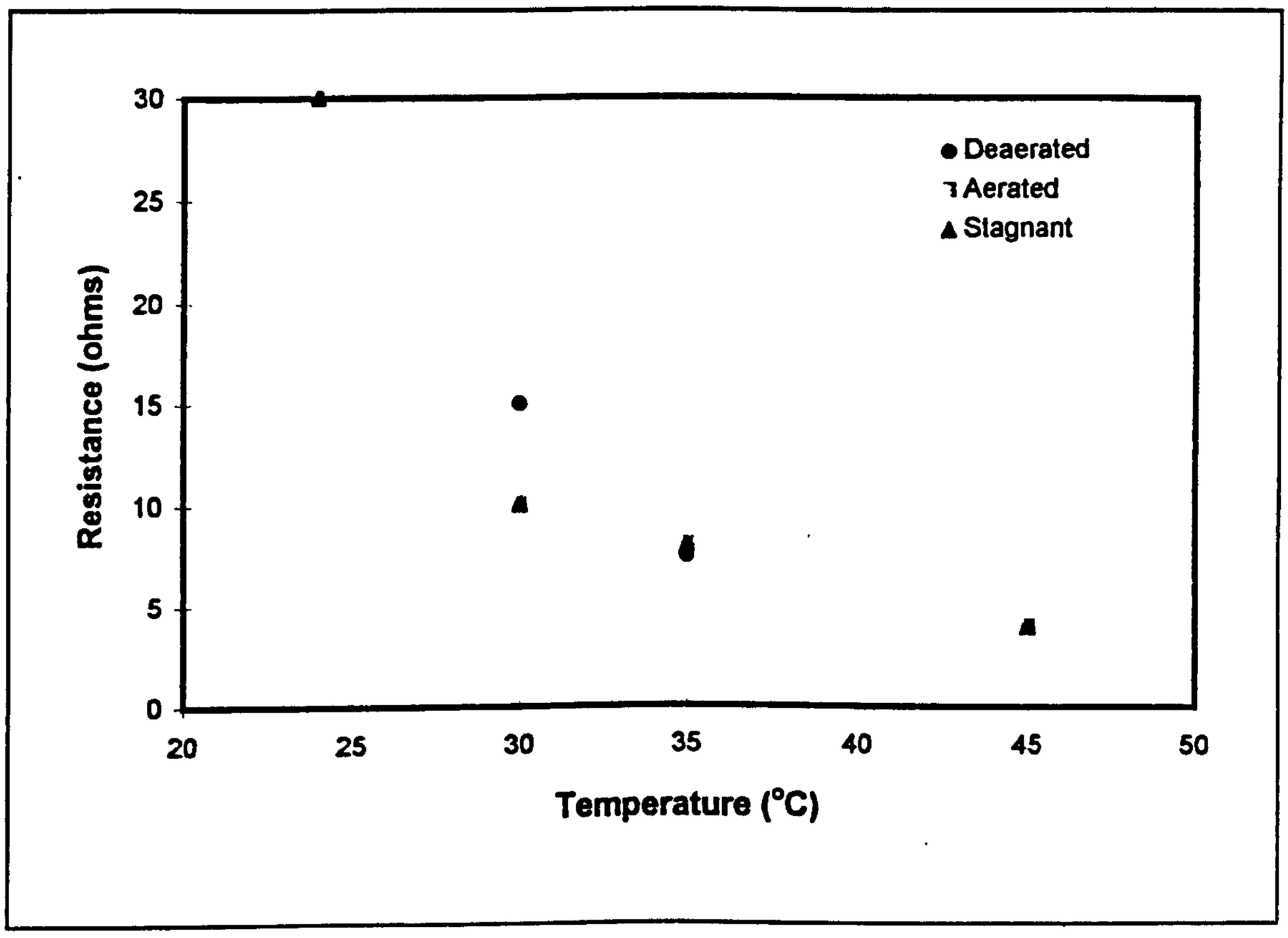

Figure 4.3.32 Variation of resistance with temperature for 304 stainless steel in 5% H_2SO_4.

Temperature (°C)	Aerated	Stagnant	Deaerated
24	30.0	30.0	30.0
30	10.0	10.0	15.0
35	8.0	8.0	7.5
45	4.0	4.0	4.0

Table 4.3.16 Values of Ω used to model passivating behaviour of 304 stainless steel in 5% H_2SO_4.

The most obvious effect of resistance on a polarization curve is to cause curvature of the current density traces - the greater the resistance, the greater the curvature. The curvature of diffusion limited current densities will also be affected by the value of resistance used. The values of resistance used were found by fitting the curvature of the portions of the experimental curves between transpassive dissolution (production of Cr(VI) species) and oxygen evolution *ie* between ~ 1 and 1.5 V SCE.. The values used show the same trend of decreasing with an increase in temperature in all three aeration regimes. This may be attributed to an increase in the diffusion coefficient for the conducting ions in solution leading to an increase in conductivity of the electrolyte[121].

4.3.5 CONCLUDING REMARKS

The polarization behaviour of 304 stainless steel in 5% H_2SO_4 with three different levels of dissolved oxygen at temperatures between 24 and 45°C has been investigated. The polarization curves have been modelled using the models described in Section 4.3. Those experiments carried out in deaerated electrolytes show clearly defined active-to-passive

'noses' in the polarization curves, while those curves obtained from stagnant electrolyte show 'triple points' characteristic of unstable passivity. The curves obtained in aerated solutions at below 45°C show stable passivity, while that obtained at 45°C shows unstable passivity. Unstable passive behaviour is often viewed in engineering applications using stainless steels where the electrolyte is stagnant or the level of dissolved oxygen is low (crevice conditions).

It was found that this change from stable to unstable passivity in aerated electrolyte at 45°C could not be solely attributed to a fall in the cathodic diffusion-limited current density (i_{lim}) from the oxygen reduction process, although there did appear to be a correlation between i_{lim} and the level of dissolved oxygen in the electrolyte.

For those curves obtained from oxygen-containing electrolytes, the value of i_o used to model the iron dissolution process (Reaction 1) showed clearly defined differences between those curves which exhibit unstable passivity (10^{-4} - 10^{-5} nA cm^{-2}) and stable passivity (5×10^{-7} nA cm^{-2}). The value of i_o needed for the iron dissolution process (to model unstable passivity) rose to a value close to that required for the 45°C experiment carried out in stagnant electrolyte.

The potential at which the most electropositive free corrosion potential in those polarization curves representing unstable passivity occurred was found to be heavily dependent upon the value of α used for Reaction 7, while the two more electronegative free corrosion potentials were found to be more dependent upon the value of i_{lim} for Reaction 7 and resultant interaction of this current density trace with the active-to-passive 'nose' representing Reaction 1.

The variation of E_t, the transition potential at which the surface starts to become covered with the passivating species with both dissolved oxygen and temperature was studied. No firm conclusions could be drawn for the 45°C experiments, but E_t became more electropositive with increasing temperature in the range 24 - 35°C, regardless of the dissolved oxygen content of the electrolyte.

The value of the joint solution and metal-solution interfacial resistance was found to decrease with increasing temperature for all three aeration regimes.

Chapter 4 Section 4 The Corrosion of Duplex Stainless Steel in Natural Seawater

4.4.1 INTRODUCTION

The duplex stainless steel Ferralium™ consists of regions of austenite (γ), in a matrix of ferrite (α), with austenite and ferrite present in approximately equal proportions. Martensite and δ ferrite are also present in the structure[125]. The presence of δ can significantly alter the physical and mechanical properties of the α matrix, and can be beneficial or deleterious depending upon the nature of the material application and its temperature regime[126]. For example, in the case of weldments, the presence of 5-10% δ has been reported to reduce the incidence of hot cracking[127] and microfissuring[128]; at high temperatures (>700°C) δ can transform to the brittle σ phase, resulting in a degradation of mechanical properties[13], and in a highly corrosive environment it can provide a path for corrosion attack[129]. The precise amounts of each phase present are varied by the introduction of stabilizers such as chromium and molybdenum for ferrite, and nickel and manganese for austenite. Duplex stainless steels have several advantages over austenitic stainless steels, such as improved mechanical strength and better corrosion resistance, especially against localised corrosion and stress corrosion cracking. They also have the advantage over fully ferritic stainless steels that they are easier to fabricate and have a higher toughness.

Duplex stainless steels are used in a variety of applications, especially where localised corrosion is a potential problem. Applications are found in the process industry as pumps, valves, bolts etc., on marine vessels for propellers, rudders, shafts and seals and

marine structures for fasteners for gauges. Its successful application relies upon the maintenance of stable passivity in variable conditions, and it is this that is the subject of this section.

4.4.2 EXPERIMENTAL

All experiments were carried out in natural seawater obtained from the Plymouth Marine Laboratory. The average conductivity of the seawater was 5.0 $\mu S\ m^{-1}$ and the pH 8.0. The material used was taken from a Royal Naval submarine shaft seal, which had been taken out of service due to pitting attack. The main constituents of the alloy were analyzed by atomic absorption spectrophotometry.

Element	Alloy Used (wt %)	Specification (wt %)
Chromium	24.12	24.0 - 27.00
Nickel	5.02	5.40 - 6.60
Copper	4.02	1.30 - 4.00
Molybdenum	2.13	2.90 - 4.00
Silicon	0.54	1.80 max
others	<1	2.16 max
Fe	balance	balance

Table 4.4.1 Composition of alloy studied and manufacturer's specification[130].

The results of this analysis are shown compared to the manufacturer's specification in Table 4.4.1.

Section 4.1.2 details the methods with which the specimens were prepared and the equipment used to perform the experiments. The seawater was aerated for 10 minutes before each experiment. For potentiodynamic scans, the scan rate used was 0.1 mV s^{-1} and for cyclic polarization scans, the scan rate was increased to 0.2 mV s^{-1} to reduce damage to the specimen at the vertex potential. Slow scan rates are required to allow sufficient time for oxygen to diffuse through the double layer[108].

For the scanning electron micrographs, an ISI D-130S Scanning Electron Microscope (SEM) was used, with a working voltage of 20 kV.

The Scanning Reference Electrode Technique (SRET) experiments used a Uniscan SR-100 rotating electrode SRET instrument. The differential platinum-wire measurement probe was calibrated using the Point-in-Space method[131,132] to give a full-scale deflection reading of 100 mA cm^{-2}. A 14 mm cylindrical electrode, rotating at 150 rpm in seawater at 30°C was used.

4.4.3 RESULTS

4.4.3.1 Potentiodynamic scans

Figure 4.4.1 shows potentiodynamic scans for Ferralium samples at temperatures of 24, 30, 35 and 45°C. In each of the potentiodynamic scans, the cathodic behaviour is similar. However, there is a marked change in the passive response of the samples. As temperature increases, the potential at which passivity is lost is greatly reduced.

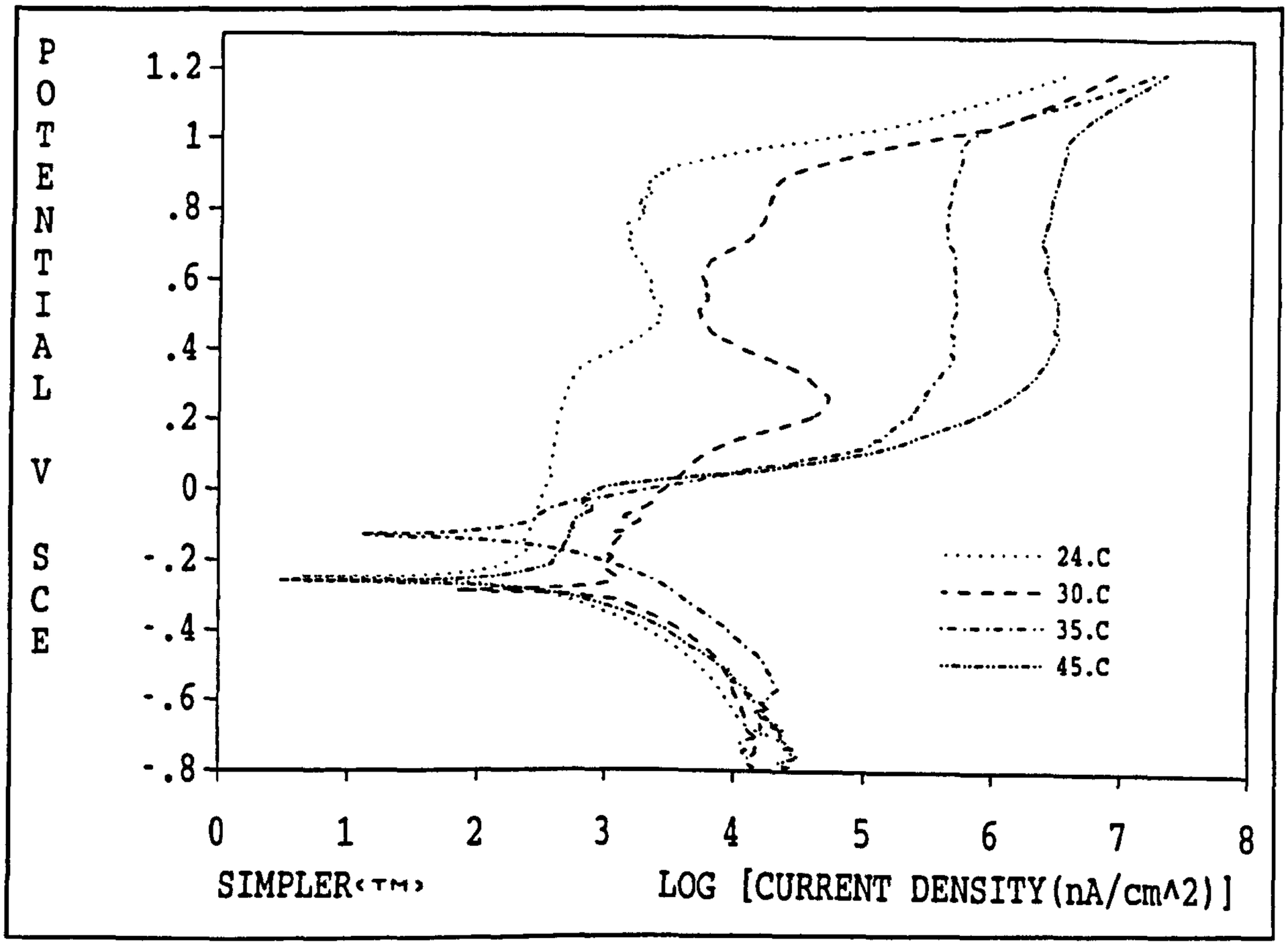

Figure 4.4.1 Potentiodynamic curves for duplex stainless steel in seawater at 24, 30, 35 and 45°C.

At very high potentials, once breakdown has been initiated, the current response (due to oxygen evolution) at each temperature is similar. This data is summarised in Table 4.4.2.

The passive current density measured for each sample at the top of the passive region was used to estimate the activation energy required for the repair of the film.

	Temperature (°C)			
	24	30	35	45
E_b (mV SCE)	+328	60	-40	-10
E_{corr} (mV SCE)	-260	-290	-120	-260
log i_{pass} (nA cm^{-2})	2.6	3.2	2.6	2.8

Table 4.4.2 Summary of electrochemical data obtained from potentiodynamic scans.

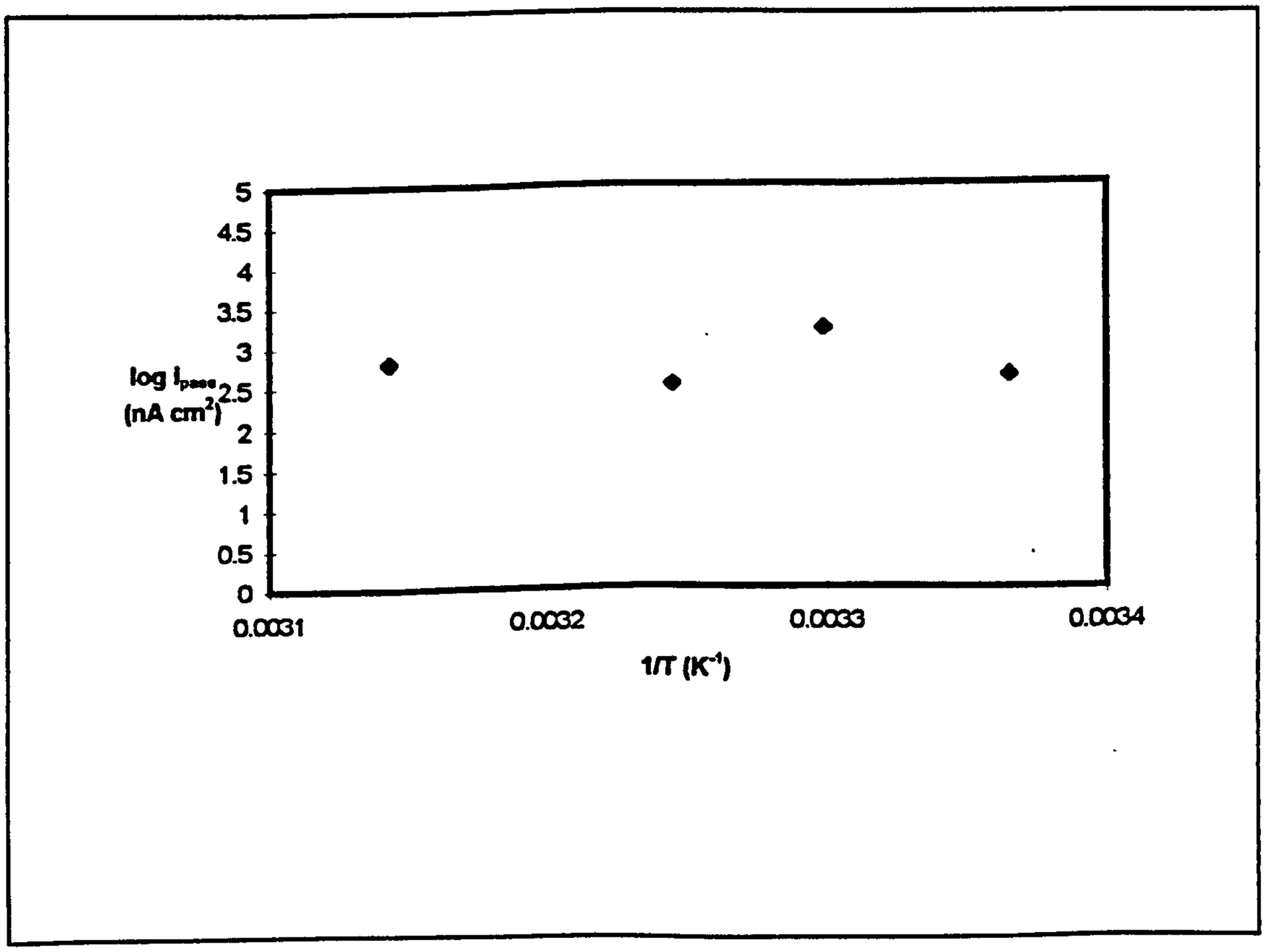

Figure 4.4.2 Relationship between log i_{pass} and 1/T for duplex stainless steel in seawater.

Figure 4.4.2 shows the linear relationship between log i_{pass} and 1/T. From the slope

of this plot, the activation energy, E_a, was estimated as 31.9 kcal mol^{-1} (133.6 KJ mol^{-1}), which compares to values of 19.8 kcal mol^{-1} (82.9 KJ mol^{-1}) quoted by Simões *et al*[133] for AISI 304 stainless steel in borate buffer solution and 18.8 kcal mol^{-1} (78.7 KJ mol^{-1}) for the same steel in sulphuric acid reported by Okamoto[134]. This comparison serves to illustrate the validity of the data.

4.4.3.2 Cyclic Polarization Scans

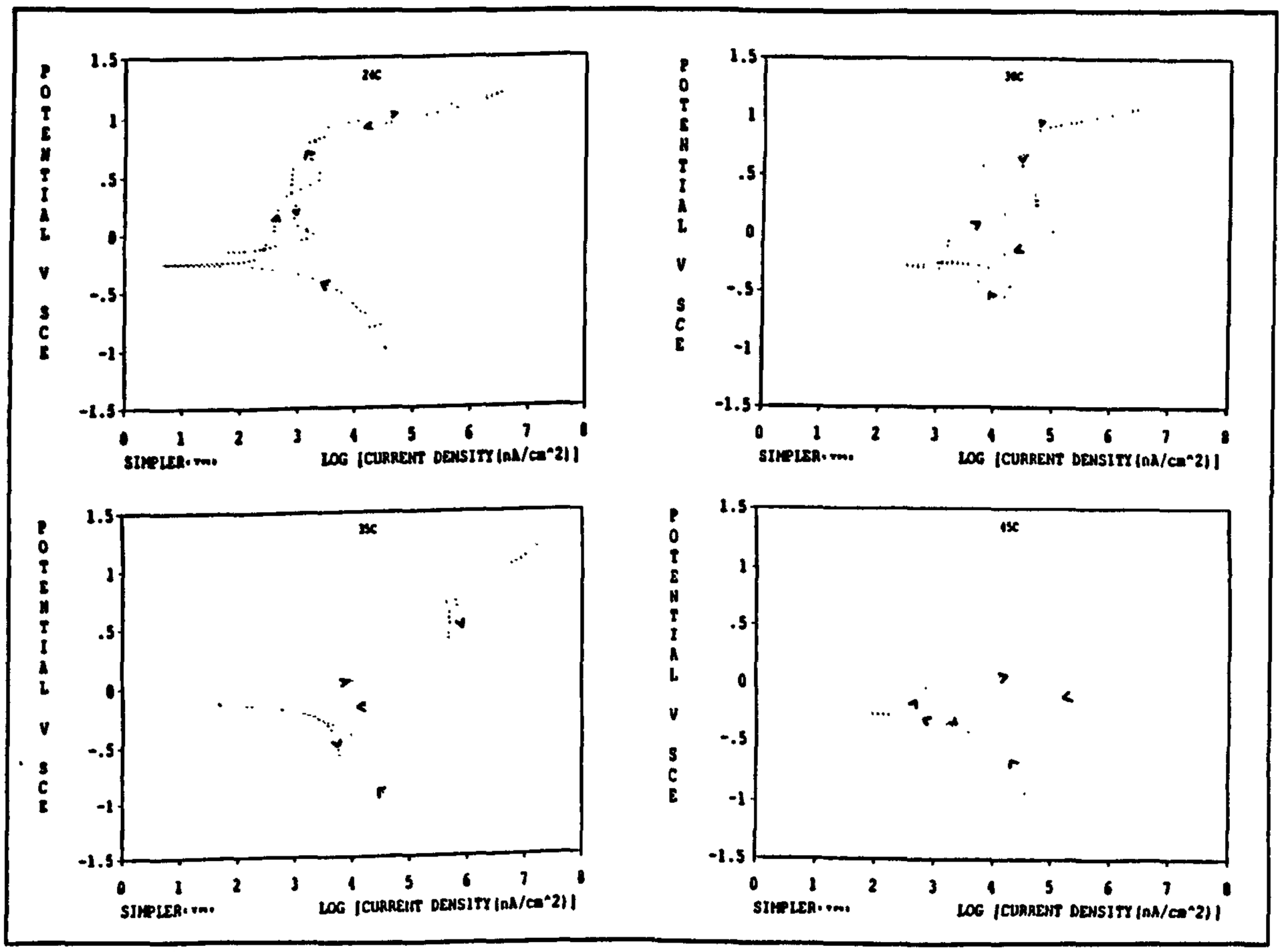

Figure 4.4.3 Cyclic polarization curves for duplex stainless steel at 24, 30, 35 and 45°C in seawater.

The cyclic polarization scans performed at temperatures of 24, 30, 35 and 45°C are shown in Figure 4.4.3. The increase in the current density supported by the surface above the passive region is obvious as the temperature increases. Interestingly, a study of the repassivation behaviour shows that only the sample at 24°C repassivates completely when

the potential scan is reversed. At 30, 35 and 45°C, the potential region between approximately 300 mV SCE and 800 mV SCE shows potential-independent current density, although the current density values are rather high for passivity (ranging from 3 nA cm^{-2} to 6.3 mA cm^{-2}). A passive region is observed on each of the anodic scans, but only the sample at 24°C shows passivity on the return loop - the other samples all show loss of passivity (breakdown) when the scan reverses. From a visual view of the specimens after polarization (Figures 4.4.4 and 4.4.5), it may be seen that the sample polarized at 45°C suffered greater pitting attack than that at 24°C - indeed, visual inspection of the 24°C sample does not appear to show any pits.

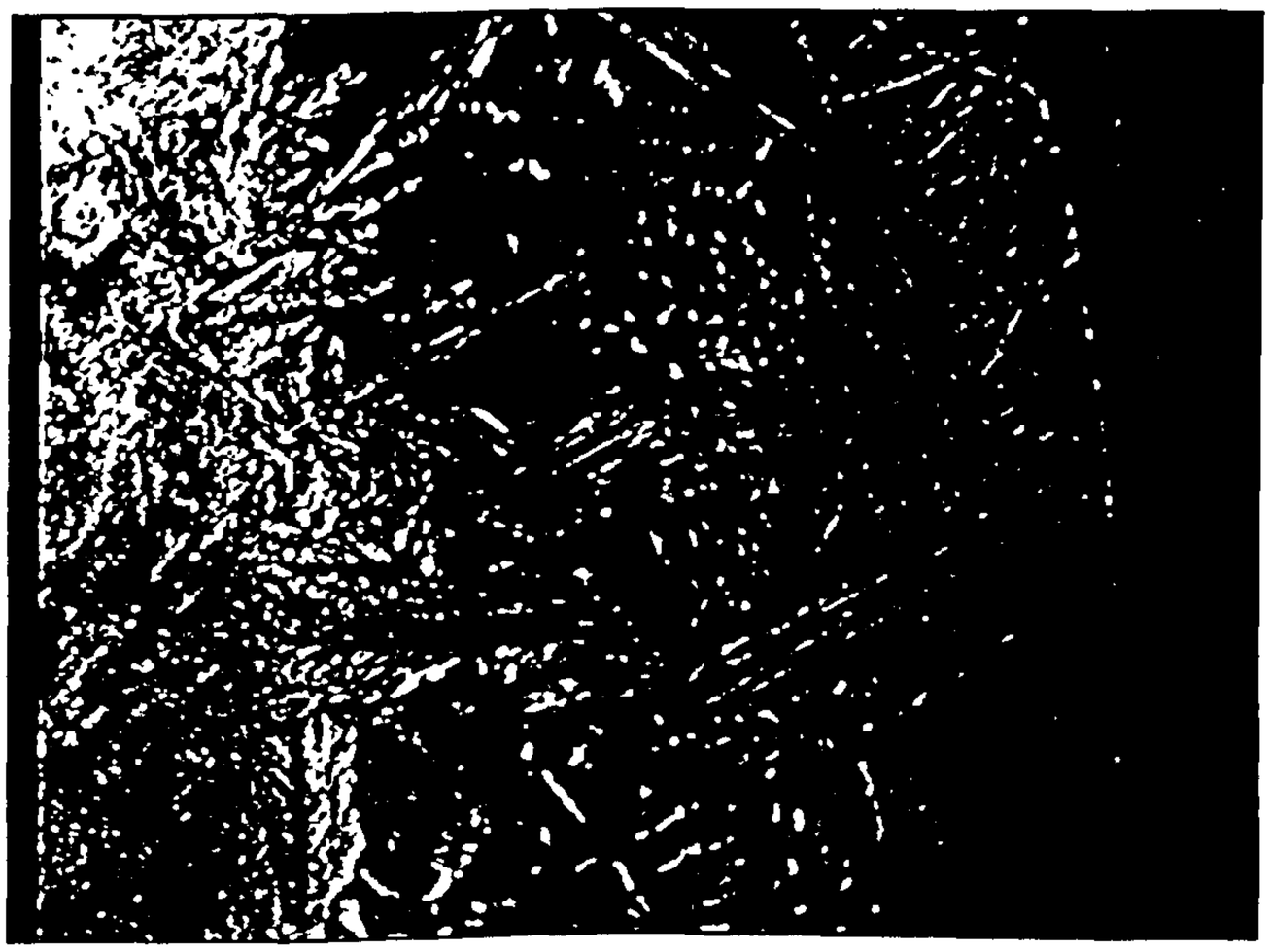

Figure 4.4.4 Ferralium duplex stainless steel sample polarized at 24°C.

Figure 4.4.5 Ferralium duplex stainless steel sample polarized at 45°C.

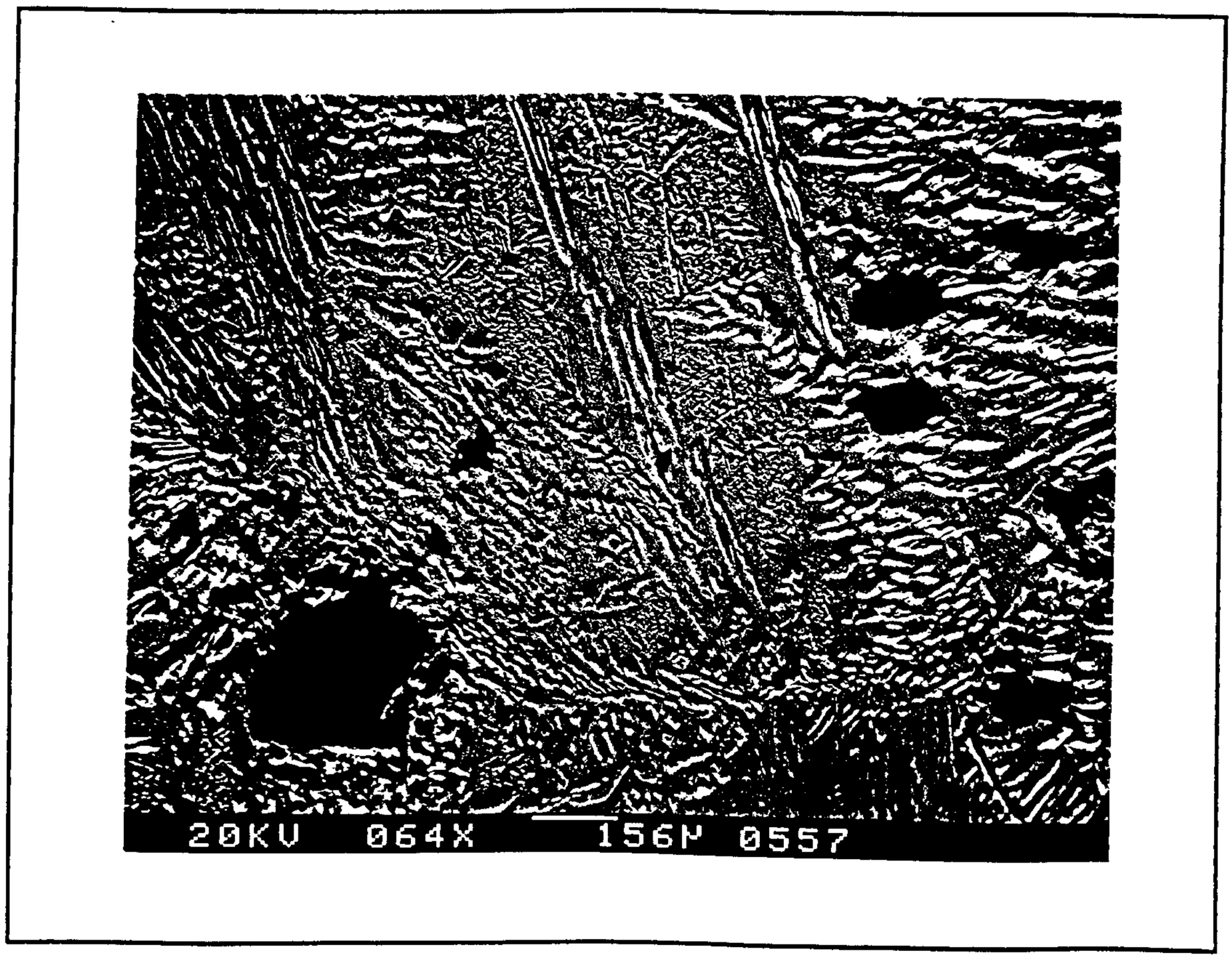

Figure 4.4.6 SEM micrograph of Ferralium duplex stainless steel after polarization at 45°C (x 64).

Samples which had been used for the cyclic polarization scans were examined under the SEM. It was established that the ferrite phase suffered general corrosion whereas the austenite phase appeared as a honeycomb of pits. This can be seen for the most severely corroded sample (45°C) in Figure 4.4.6 and more closely in Figure 4.4.7

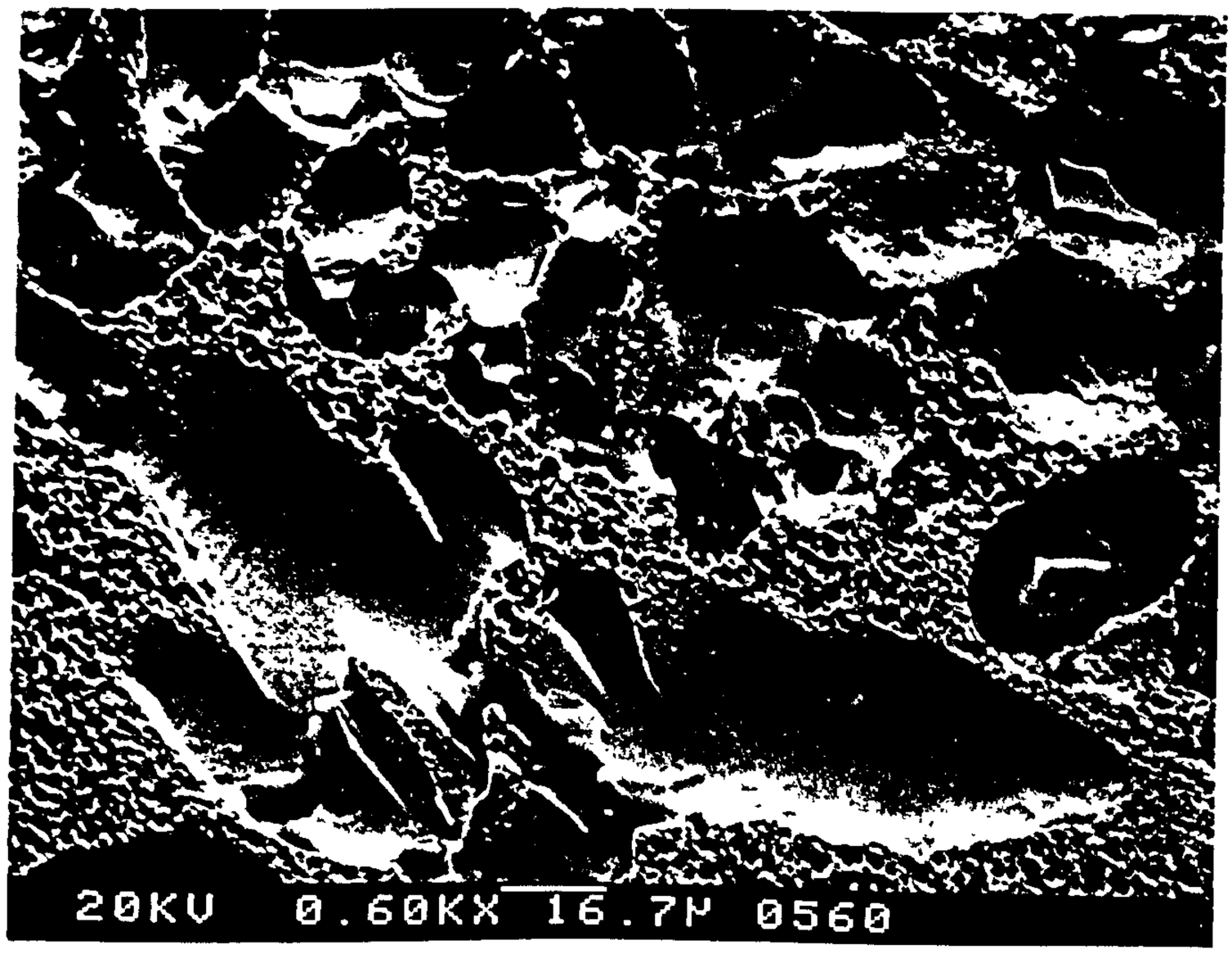

Figure 4.4.7 SEM micrograph of Ferralium duplex stainless steel after polarization at 45°C (x 600).

Figure 4.4.8 shows the sample polarized at 24°C. Most of the attack was concentrated towards the edge of the sample, leaving the interior less degraded.

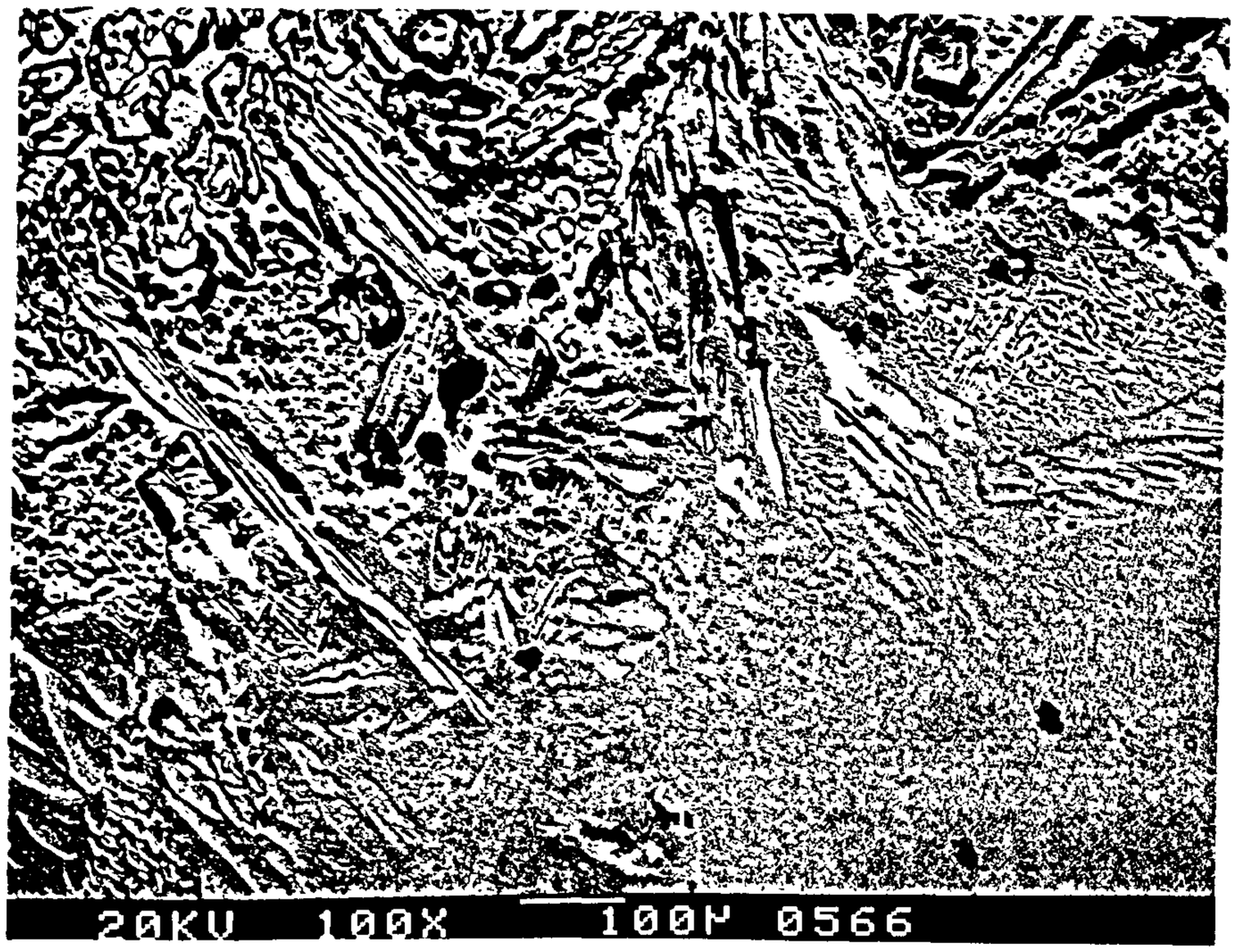

Figure 4.4.8 SEM micrograph of Ferralium duplex stainless steel after polarization at 24°C (x 100).

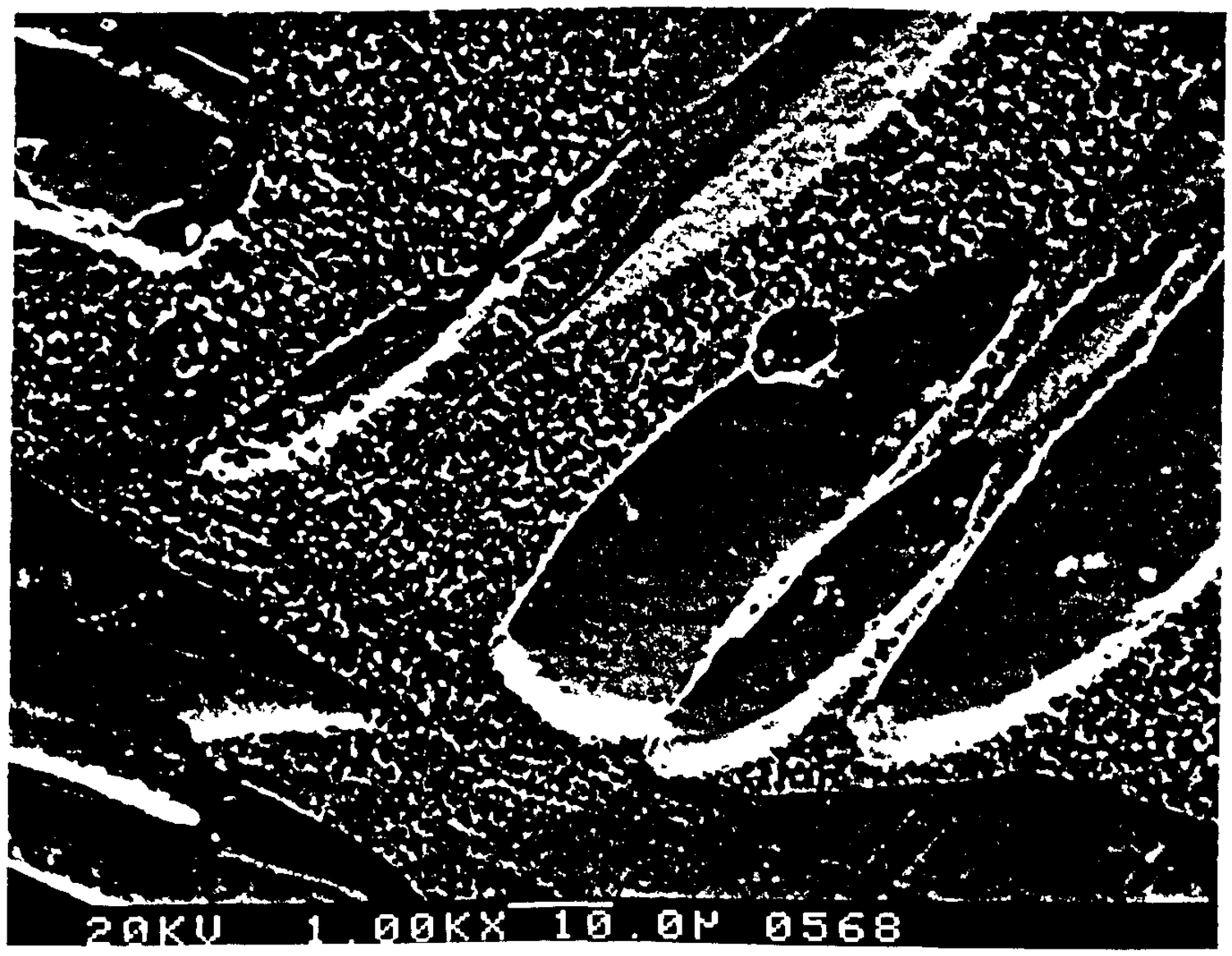

Figure 4.4.9 SEM micrograph of Ferralium duplex stainless steel after polarization at 24°C (x 1000).

Both Figures 4.4.8 and 4.4.9 show that the austenite phase does suffer pitting attack. A pit which has propagated to a greater degree can clearly be seen to have initiated at a phase boundary in Figure 4.4.9.

4.4.4.3 24°C Model

The same reactions were considered as for 304 stainless steel in 5% H_2SO_4, but with Reaction 9 in preference to Reaction 5. This is because the CrO_4^{2-} ion predominates at pH values in excess of 6.3[51] (see Figure 4.2.10).

$Fe \rightarrow Fe^{2+} + 2e^-$	Reaction 1
$4OH^- \rightarrow O_2 + 2H_2O + 4e^-$	Reaction 2
$O_2 + 2H_2O + 4e^- \rightarrow 4OH^-$	Reaction 7
$Cr_2O_3 + 5H_2O \rightarrow 2CrO_4^{2-} + 10H^+ + 6e^-$	Reaction 9

The same argument regarding two E° values for the production of Cr(VI) ions (discussed in Section 4.2.3.7 for Reaction 5) is considered here. Hence, values of 1.244 and 1.311 are used as E° values for the passive film in the form of $Cr(OH)_3.nH_2O$ and anhydrous Cr_2O_3 respectively. Figure 4.4.10 shows the potentiodynamic scan at 24°C with the model constructed using the parameters shown in Tables 4.4.3 and 4.4.4 overlaid.

It is possible that some of the nickel present in the alloy may be present in the passive film in the form of metallic nickel[83]. This could dissolve out of the film and form Ni^{2+} ions in solution (Reaction 10).

$Ni \rightarrow Ni^{2+} + 2e^-$	Reaction 10

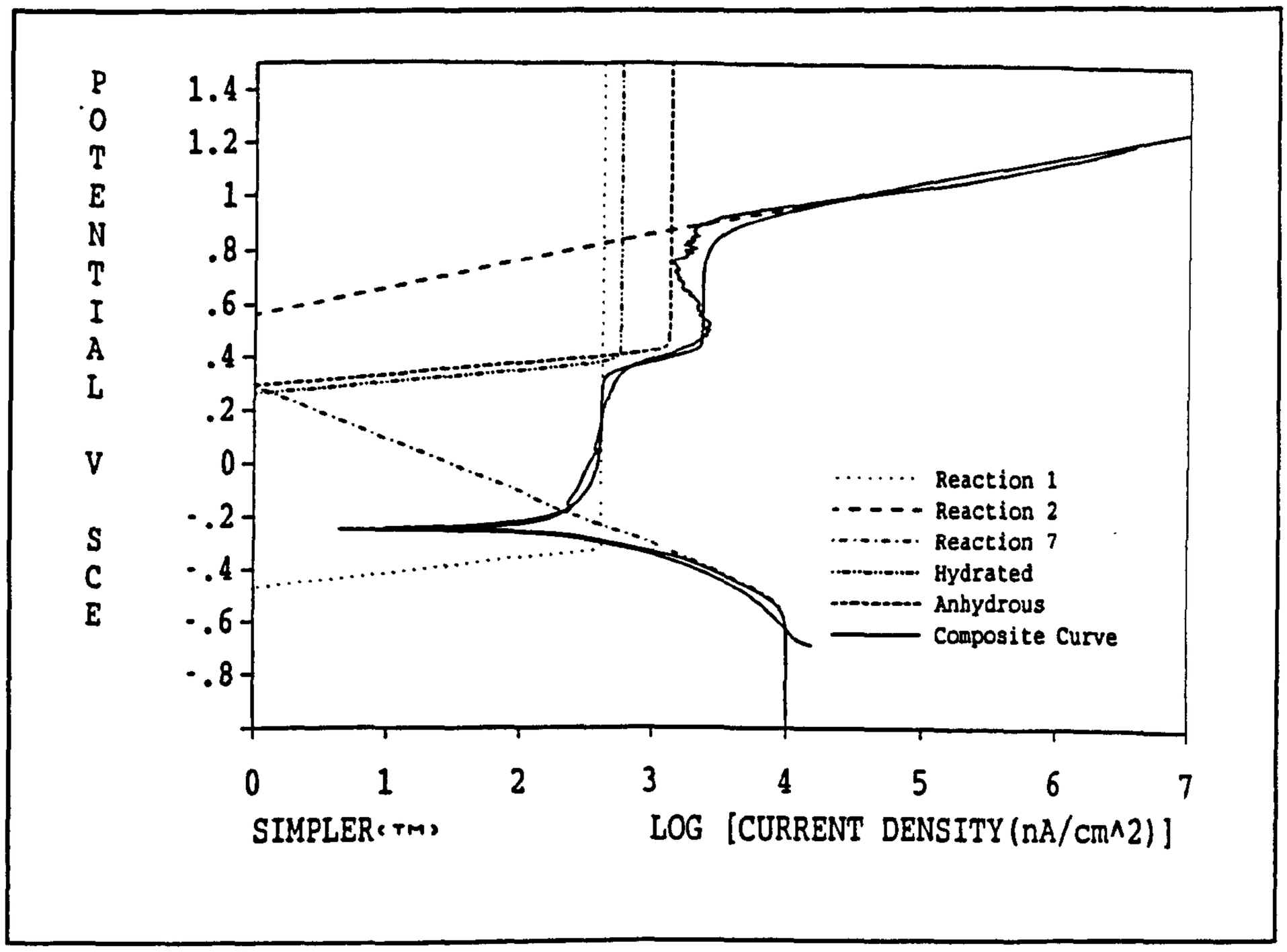

Figure 4.4.10 Model for duplex stainless steel in natural seawater at 24°C.

Reaction 10 was found to occur with an intersection of the anodic and cathodic lines at a lower potential than the free corrosion potential observed for the sample. The model lines are overshadowed by the limiting oxygen reduction line and do not contribute significantly to the total current density. Also, the amount of nickel in the film is very low[83], and thus the partial current attributable to the process would be negligible. Therefore they are not shown in the final model. The reverse of Reactions 1, 9 and 10 do not to occur due to the very low concentration of Fe^{2+}, Ni^{2+} and CrO_4^{2-} ions in the seawater; thus the cathodic limiting current densities for these reactions are assumed to be negligible in the model.

Temperature		24°C			
pH		8.0			
Solution Resistance		50 Ω			
	E° (V SHE)	i_o (nA cm^{-2})	i_{La} (nA cm^{-2})	i_{Lc} (nA cm^{-2})	α
Reaction 1	-0.44	2.5×10^{-6}	not required	negligible	0.50
Reaction 2	1.228	0.12	1.0×10^{16}	negligible	0.60
Reaction 7	1.228	0.12	negligible	1.0×10^{4}	0.70
Reaction 9 ($Cr(OH)_3.nH_2O$)	1.244	5.0×10^{-5}	1.1×10^{2}	negligible	0.50
Reaction 9 (anhydrous)	1.311	5.0×10^{-4}	3.0×10^{3}	negligible	0.50

Table 4.4.3 Parameters for the model of duplex stainless steel in natural seawater at 24°C.

	i_{pass} (nA cm^{-2})	A	p	E_{trans} (V SCE)
Reaction 1	4.1×10^{2}	975	2.0	-0.360

Table 4.4.4 Parameters used in passivation routine for the Reaction 1 for duplex stainless steel in natural seawater at 24°C.

4.4.3.4 30°C Model

Increasing the temperature to 30°C causes the potential at which the passive film breaks down to fall to ~ 100 mV SCE. The Nernst equation predicts a decrease in potential with an increase in temperature. However, this is not sufficient to fit the experimental data, and a further reduction in potential was introduced by increasing the i_o values for Reaction 9. The limiting anodic current density is also moved to a higher value. The limiting current density for the reduction of oxygen (Reaction 7) also increases slightly. The passive current density is the highest viewed for all four temperatures studied. The reason for both this and the drop in current density above ~250 mV SCE is not clear, and thus this portion of the curve is not well modelled.

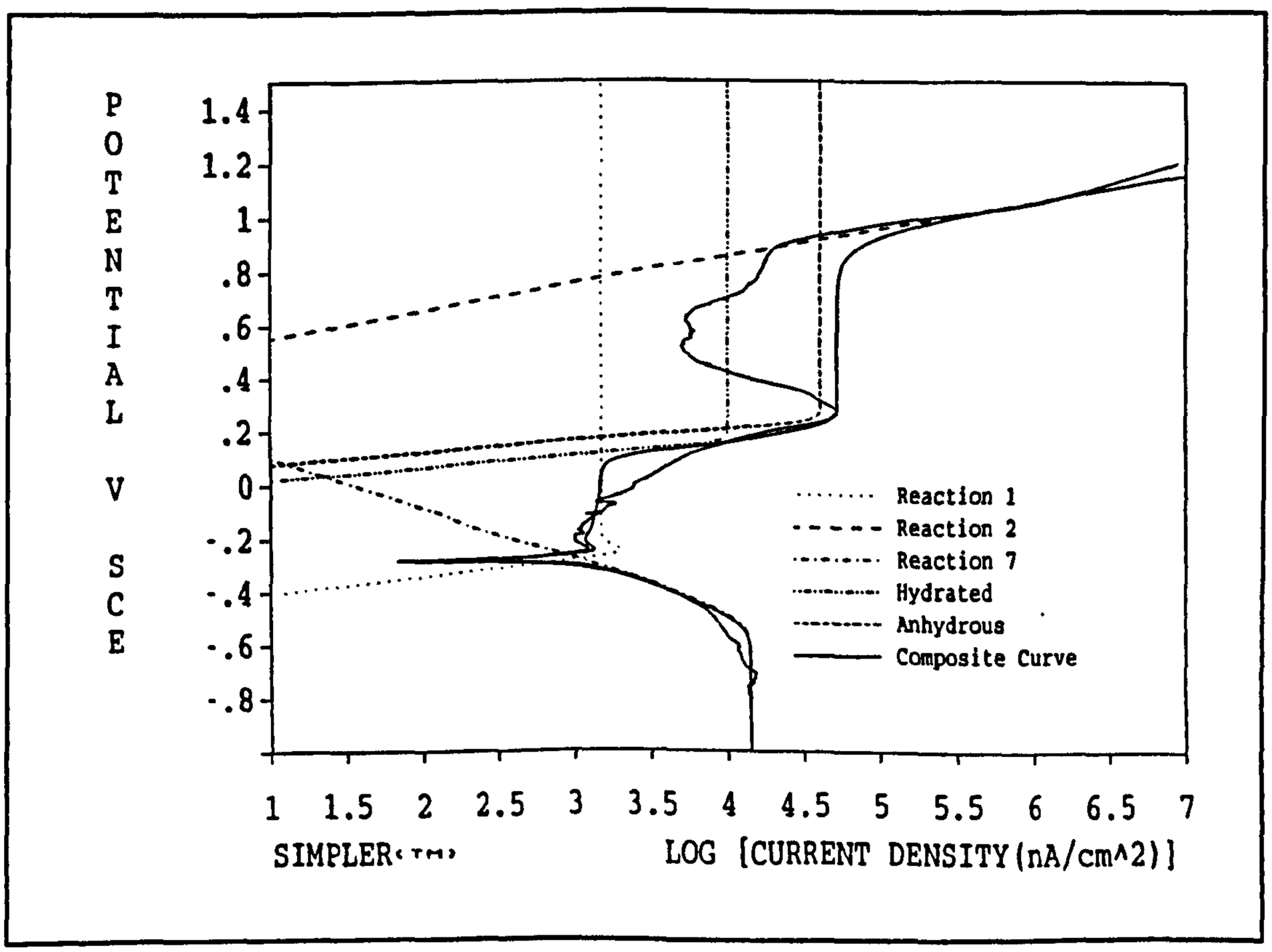

Figure 4.4.11 Model for duplex stainless steel in natural seawater at 30°C.

A different value of E_t is used in the passivation algorithm with respect to the 24°C

model (50 mV more electropositive). Figure 4.4.11 shows the model for duplex stainless steel in natural seawater at 30°C using the parameters shown in Tables 4.4.5 and 4.4.6.

Temperature		30°C			
pH		8.0			
Solution Resistance		50 Ω			
	E^o (V SHE)	i_o (nA cm^{-2})	i_{La} (nA cm^{-2})	i_{Lc} (nA cm^{-2})	α
Reaction 1	-0.44	2.5×10^{-6}	not required	negligible	0.50
Reaction 2	1.228	0.12	1.0×10^{16}	negligible	0.60
Reaction 7	1.228	0.12	negligible	1.4×10^{4}	0.68
Reaction 9 ($Cr(OH)_3.nH_2O$)	1.244	3.0×10^{2}	1.0×10^{4}	negligible	0.50
Reaction 9 (anhydrous)	1.311	5.0×10^{2}	4.0×10^{4}	negligible	0.50

Table 4.4.5 Parameters for the model of duplex stainless steel in natural seawater at 30°C.

	i_{pass} (nA cm^{-2})	A	p	E_{trans} (V SCE)
Reaction 1	1.5×10^{3}	975	2.0	-0.360

Table 4.4.6 Parameters used in passivation routine for the Reaction 1 for duplex stainless steel in natural seawater at 30°C.

4.4.3.5 35°C Model

A further increase in temperature to 35°C caused another drop in the potential at which CrO_4^{2-} ions are produced. The free corrosion potential is ~80 mV more positive than for the rest of the temperatures studied, and is modelled by using a lower α value for Reaction 7. There is no decrease in current in the portion of the curve between film breakdown and oxygen evolution (~0 and 900 mV SCE) in the curves for both the 35 and 45°C electrolytes, and thus the model shows better correlation with these experiments. Figure 4.4.12 shows the model for duplex stainless steel in natural seawater at 35°C using the parameters shown in Tables 4.4.7 and 4.4.8.

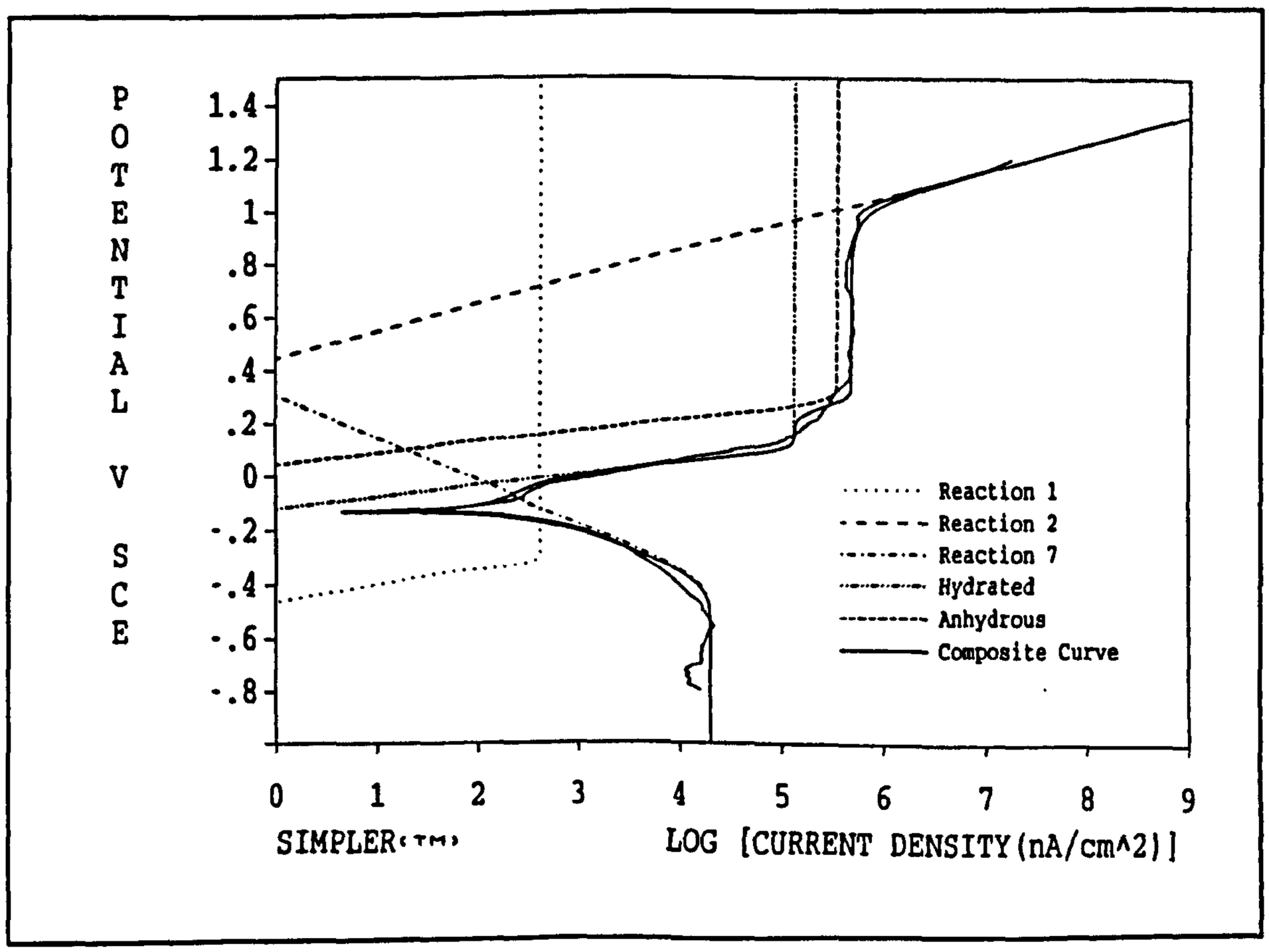

Figure 4.4.12 Model for duplex stainless steel in natural seawater at 35°C.

Temperature		35°C			
pH		8			
Solution Resistance		50 Ω			
	E° (V SHE)	i_o (nA cm^{-2})	i_{La} (nA cm^{-2})	i_{Lc} (nA cm^{-2})	α
Reaction 1	-0.44	2.5×10^{-6}	not required	negligible	0.50
Reaction 2	1.228	0.12	1.0×10^{16}	negligible	0.60
Reaction 7	1.228	0.12	negligible	2.0×10^{4}	0.62
Reaction 9 ($Cr(OH)_3.nH_2O$)	1.244	3.0×10^{4}	1.3×10^{5}	negligible	0.50
Reaction 9 (anhydrous)	1.311	1.0×10^{3}	3.4×10^{5}	negligible	0.50

Table 4.4.7 Parameters for the model of duplex stainless steel in natural seawater at 35°C.

	i_{pass} (nA cm^{-2})	A	p	E_{trans} (V SCE)
Reaction 1	4.1×10^{2}	975	2.0	-0.360

Table 4.4.8 Parameters used in passivation routine for the Reaction 1 for duplex stainless steel in natural seawater at 35°C.

4.4.3.6 45°C Model

When the temperature is increased to 45°C, the potential at which the film breaks down is close to that for the 35°C experiment. The same i_o values as for the 35°C experiment cannot be used, since the increase in temperature causes the value of E_1 calculated by the Nernst equation (Equation 3.5) for Reaction 9 to more negative potentials than desired. Thus the i_o values used are lower than for the 35°C model. The same passivation parameters are used as for the 24 and 35°C cases. Figure 4.4.13 shows the model for duplex stainless steel in natural seawater at 45°C using the parameters shown in Tables 4.4.9 and 4.4.10.

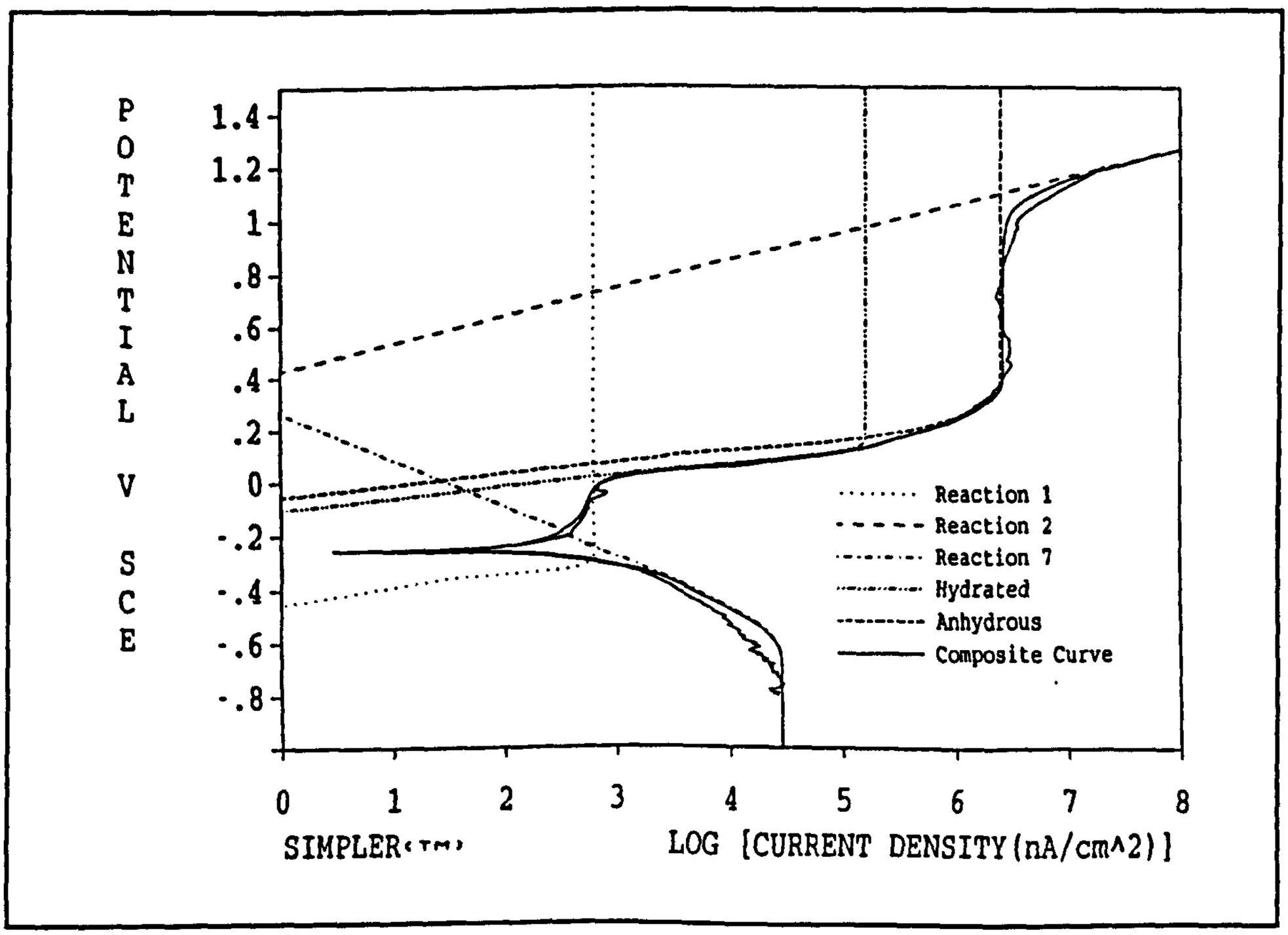

Figure 4.4.13 Model for duplex stainless steel in natural seawater at 45°C.

Temperature		45°C			
pH		8.0			
Solution Resistance		50 Ω			
	E^o (V SHE)	i_o (nA cm^{-2})	i_{La} (nA cm^{-2})	i_{Lc} (nA cm^{-2})	α
Reaction 1	-0.44	2.5×10^{-6}	not required	negligible	0.50
Reaction 2	1.228	0.12	1.0×10^{16}	negligible	0.60
Reaction 7	1.228	0.12	negligible	2.9×10^{4}	0.68
Reaction 9 ($Cr(OH)_3.nH_2O$)	1.244	2.0×10^{3}	1.6×10^{5}	negligible	0.50
Reaction 9 (anhydrous)	1.311	5.0×10^{4}	2.5×10^{6}	negligible	0.50

Table 4.4.9 Kinetic parameters for model of duplex stainless steel in natural seawater at 45°C .

	i_{pass} (nA cm^{-2})	A	p	E_{trans} (V SCE)
Reaction 1	6.2×10^{2}	975	2.0	-0.360

Table 4.4.10 Parameters used in passivation routine for the Reaction 1 for duplex stainless steel in natural seawater at 45°C.

4.4.4 DISCUSSION

4.4.4.1 Alloy Composition

From Table 4.4.1, it may be seen that the nickel and molybdenum content of the alloy studied is lower than that specified by the manufacturer, and that the copper is marginally higher. The chromium content of the alloy is just within specification, but is lower than the commercially-secret target specification of 'around 25%'[135,136] that is aimed for in the manufacturing process. When this work was presented at UKCorr 94[137], the manufacturer[138] objected to the use of the tradename 'Ferralium' in conjunction to the material used, and expressed surprise at the poor performance of the alloy. Due to security constraints imposed by the Ministry of Defence, the original quality assurance documentation and component history were not available. However, assurances[139] were given that the material supplied was indeed Ferralium, and thus the name is used here. Given that the original application for the material was such a critical component (a submarine shaft seal), it is surprising that material out of specification was used. It is possible that an unrepresentative sample was used for AAS, or that errors associated with the AAS equipments lead to an incorrect analysis. Another possibility is that the material was taken from within the main body of the component, and that the chromium and molybdenum had moved preferentially to the surface to enrich the passive film (as described in Section 2.9), thereby altering the composition of the material in the bulk of the specimen.

4.4.4.2 PRE_N Calculations

The Pitting Resistance Equivalent Number (PRE_N) is used as a measure of a

stainless steels' ability to resist localised corrosion in seawater. The larger the PRE_N, the greater the resistance of the alloy. It is a formula based upon the chemical composition of the alloy, and is shown below:

$$PRE_N = \%Cr + 3.3\%Mo + 16\%N$$

Unfortunately, nitrogen was not tested for, but the manufacturer quoted 0.18[140] as being the average for cast material. Using this value leads to PRE_N values of between 36.5 and 43.1 for the manufacturer's specification, and 34.0 for the material studied here. It is often held[141] that a PRE_N value of 40 is the critical limit for seawater applications. Thus, using PRE_N considerations, the material studied here would not be regarded as suitable for the application it was used for.

4.4.4.3 Comparison of Ferralium with Other Stainless Steels

The behaviour of four stainless steels in natural seawater at room temperature is compared in Figure 4.4.14. It may be seen that the potential at which the passive film breaks down becomes more electronegative with increasing chromium (and molybdenum) content *ie* the greater the % Cr and % Mo, the greater the resistance to breakdown of the alloy. Nominal compositions and PRE_N values for the steels are given in Table 4.4.11. The data for 316[142] and 25-6Mo[143] are from manufacturer's reference guides; 304 and Ferralium are from the studies described here.

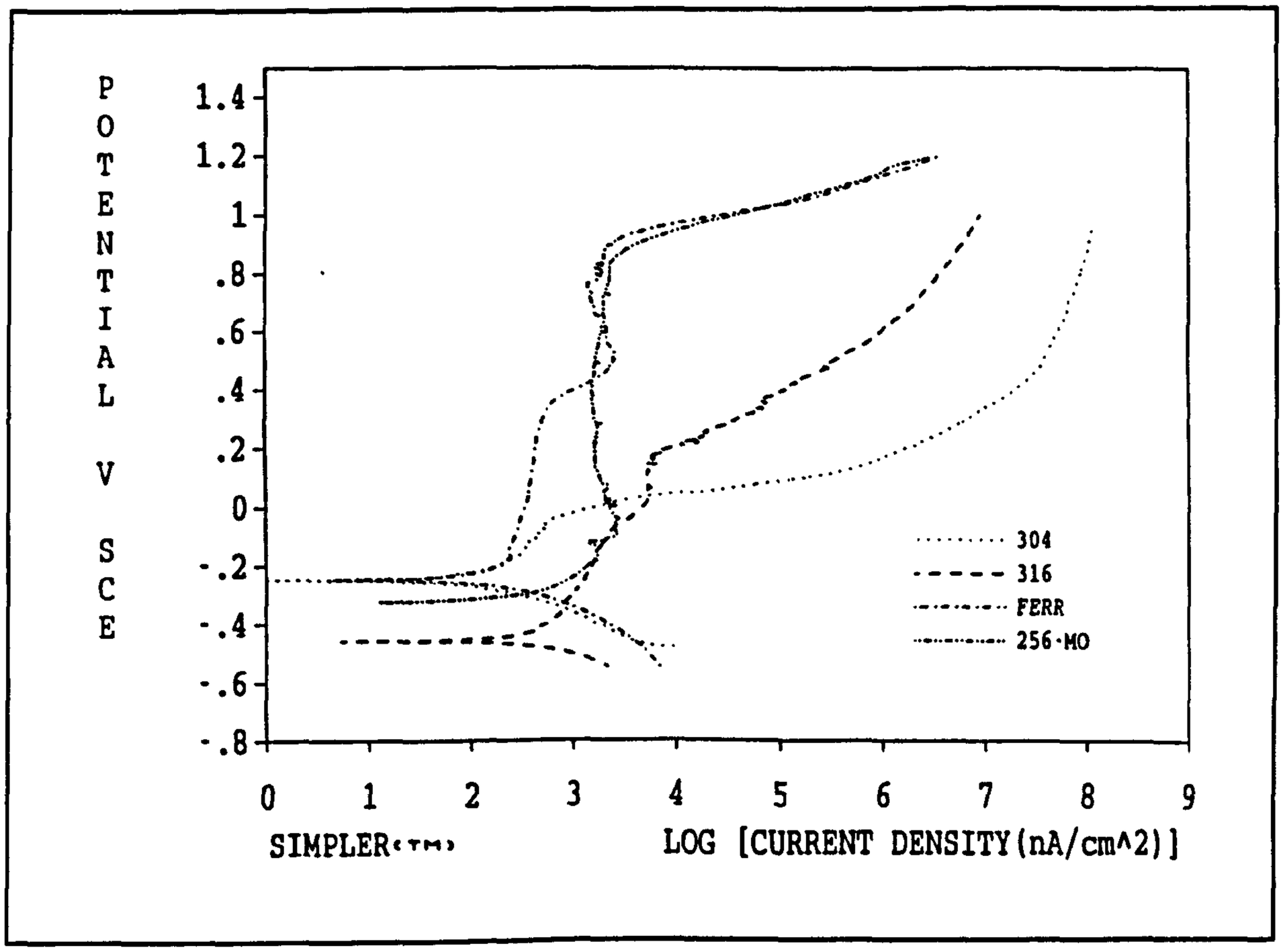

Figure 4.4.14 Polarization curves for four stainless steels in natural seawater at 24°C.

Alloy	% Cr	% Mo	PRE_N[141]	E_b (mV SCE)
304	18	-	21.7	-50
316	18	2.5	26.2	160
Ferralium	24	2.0	34.0	328
25-6Mo	21.5	6.0	47.0	848

Table 4.4.11 Table showing E_b, % Cr and % Mo for four stainless steels in natural seawater at 24°C

Threshold levels of 10, 18 and 22 - 25 %Cr have been proposed as the levels of alloying additions that produce step-changes in Fe-Cr alloy behaviour[65,62,63,64,144,145,146]. The

behaviour of the 25-6Mo and Ferralium alloys in natural seawater at 24°C is markedly superior to the 18% Cr alloys, supporting this theory. The 25-6Mo alloy may be argued to exhibit better corrosion resistance than the duplex stainless steel considered in this study, since there appears to be no breakdown prior to oxygen evolution at ~1 V SCE, despite having a lower chromium content. The nickel content is much higher (24 - 26%), and thus the alloy is fully austenitic[143]. Ferralium contains large amounts of ferrite in its microstructure, which was found to suffer general attack (as opposed to pitting attack) at potentials more electronegative than those at which pitting occurred in the austenite phase.

Bernhardsson[147] and Tuck[148] found that the PRE_Ns differ for the two phases due to different partition coefficients for different elements in the two phases, the ferrite phase having the larger PRE_N. They also found that increasing the annealing temperature causes the PRE_N of the ferrite phase to fall, while that of the austenite will increase. Thus, at a critical annealing temperature, the ferrite phase will pit in preference to the austenite. However, since pitting occurred in the austenite phase in this study, it can be deduced that the material was not annealed above this critical temperature, as was proposed by the manufacturer[138].

4.4.4.4 Dependence of Breakdown Potential on Temperature

Pallota *et al*[149] investigated the dependence of the breakdown potential of 316 stainless steel on temperature in NaCl solutions, and their results are shown in Figure 4.4.15.

Similar behaviour has been reported by other authors[150,151]. It may be seen from the polarization curves for Ferralium (Figure 4.4.1) that in some cases, there are current density

oscillations prior to film breakdown, and these are related to the two events associated with pit initiation.

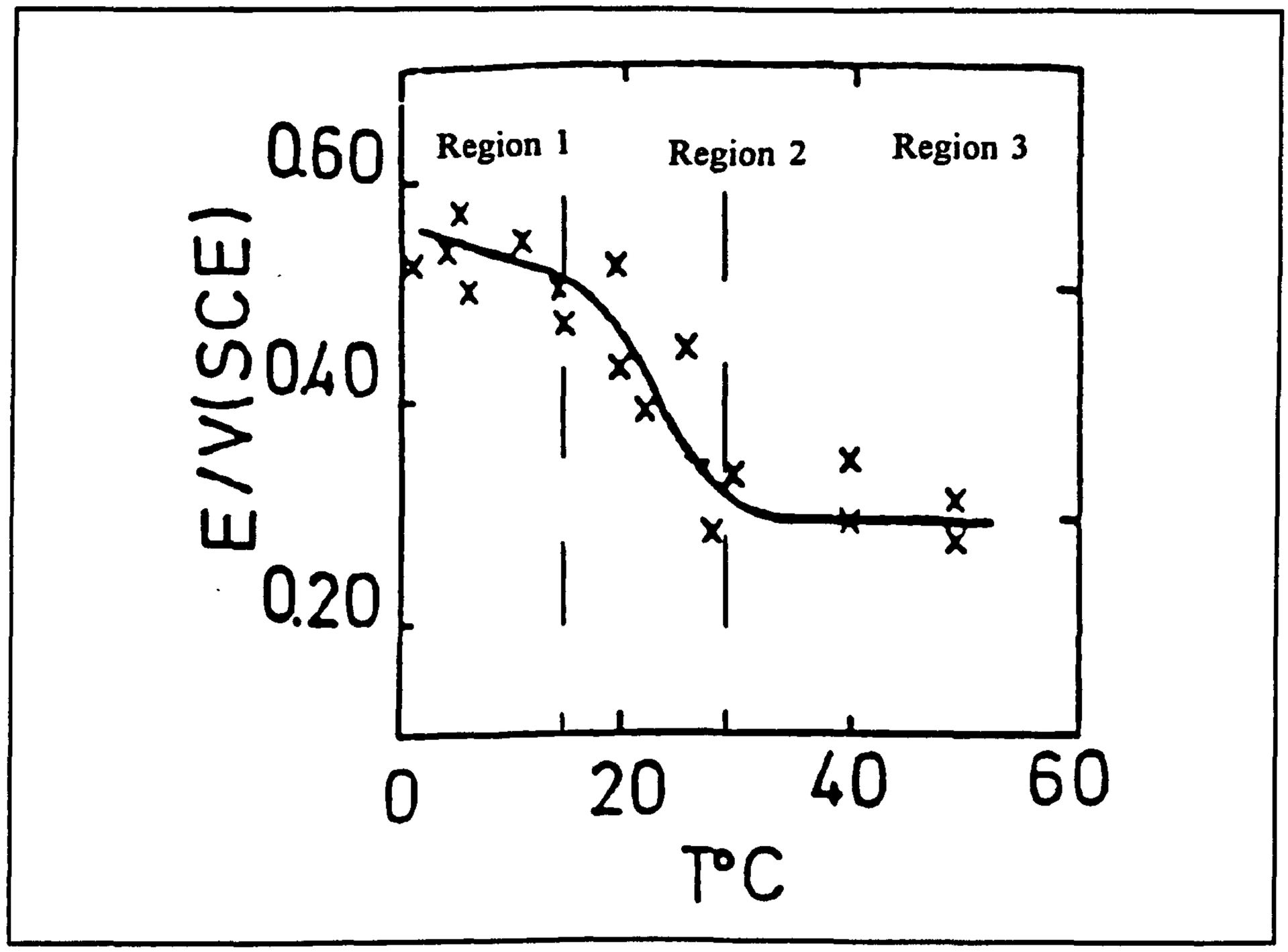

Figure 4.4.15 E_b *vs* temperature curve for 316 stainless steel in NaCl solution[149].

The first process (I) is breakdown of the passive layer, which depends on the presence of Cl^- ions in solution, and on the degree of crystallinity of the passive film[152]. When a Cl^- ion reaches the surface, a pit may nucleate, which involves a 'microscopically violent'[153] oxidation process resulting in a current transient, which may then propagate, while the second process (II) is repair of the passive film, with the associated decrease in current density. This process is associated with the presence of chromium and bound water, forming an amorphous structure[134]. Each oscillation is indicative of these two counterbalancing processes[149].

The influence of temperature on E_b in region 1 is associated with an increase in the

rate of process I, while process II remains constant. In region 2, the rate of process I still increases, but that of process II falls, since the ability of the film to repair itself is much reduced. Thus the number of oscillations prior to breakdown is increased, and E_b is more electronegative. As the film can no longer repair itself, CrO_4^{2-} ions are formed according to Reaction 9. The rate at which they form increases with temperature, and this corresponds to an increase in the rate of dissolution. Region 3 corresponds to constant rates of both processes I and II.

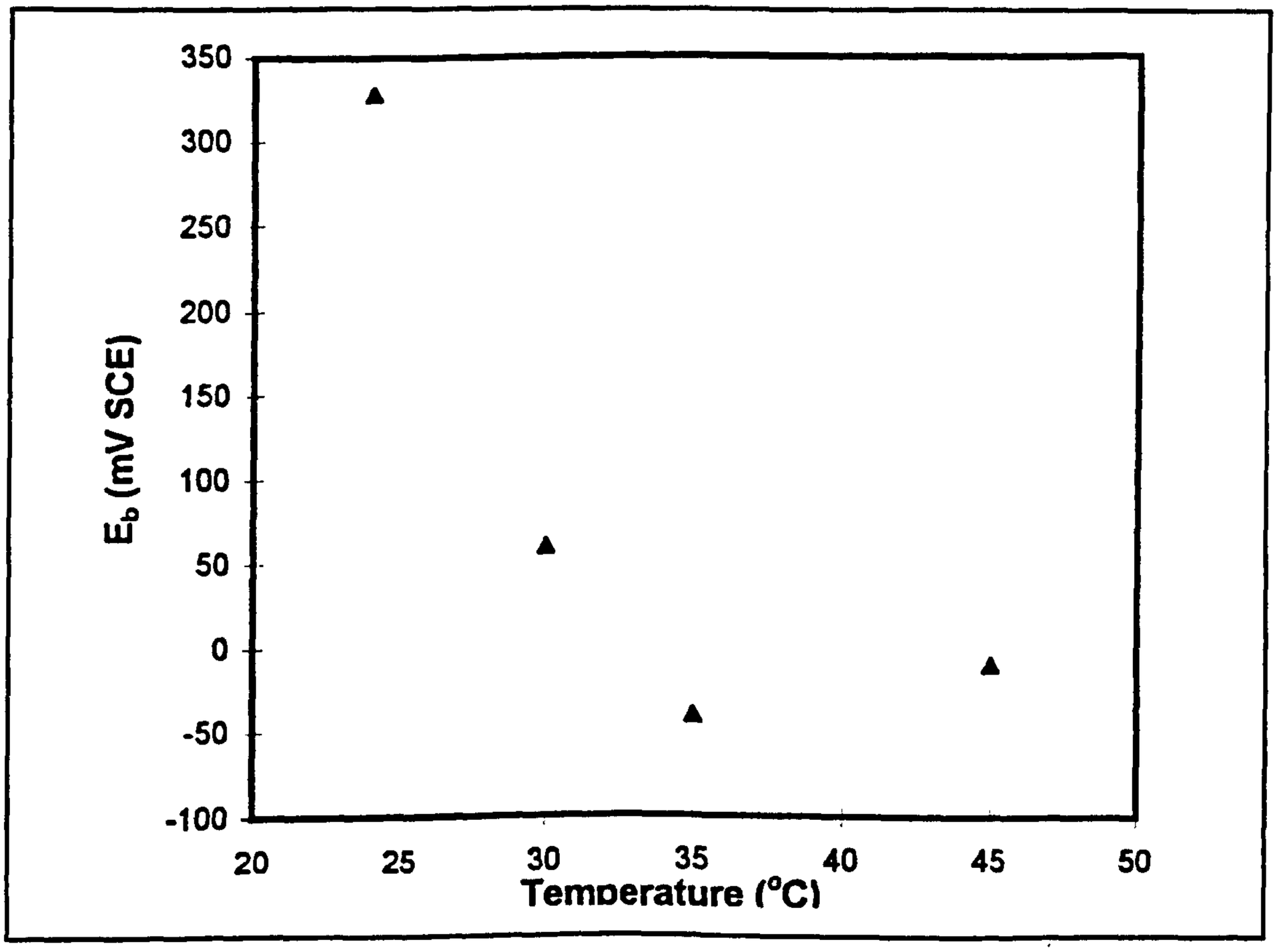

Figure 4.4.16 E_b *vs* temperature curve for duplex stainless steel in natural seawater.

Figure 4.4.16 shows the corresponding E_b *vs* temperature curve for the duplex stainless steel studied here.

Newman *et al* have shown that increasing the chromium content of an alloy causes the passive film to become more amorphous[144,145]. As mentioned above, the repair process is associated with the formation of an amorphous structure of chromium and bound water.

Thus, it is suggested that the superior performance of the higher alloyed stainless steels shown in Figure 4.4.14 is attributable to this increasing amorphous character.

4.4.4.5 Modelling the Dependence of Breakdown Potential on Temperature

The model of the polarization behaviour of Ferralium in natural *se* awater has shown that the destruction of the protective chromium oxide layer (represented by Reaction 9) is very sensitive to temperature in the presence of the chloride ion. As temperature increases, the current density increases, resulting in a significant reduction in passive behaviour. That this reaction proceeds with such ease is the reason that repassivation to the initial degree of protectiveness is not seen on the cyclic polarization scans at temperatures above 30°C. This is explained by considering the effect of temperature on the kinetics of oxidation of chromium (III) oxide to chromate ion. Figure 4.4.17 shows the i_o values used for Reaction 9 in Sections. 4.4.3.4 to 4.4.3.7.

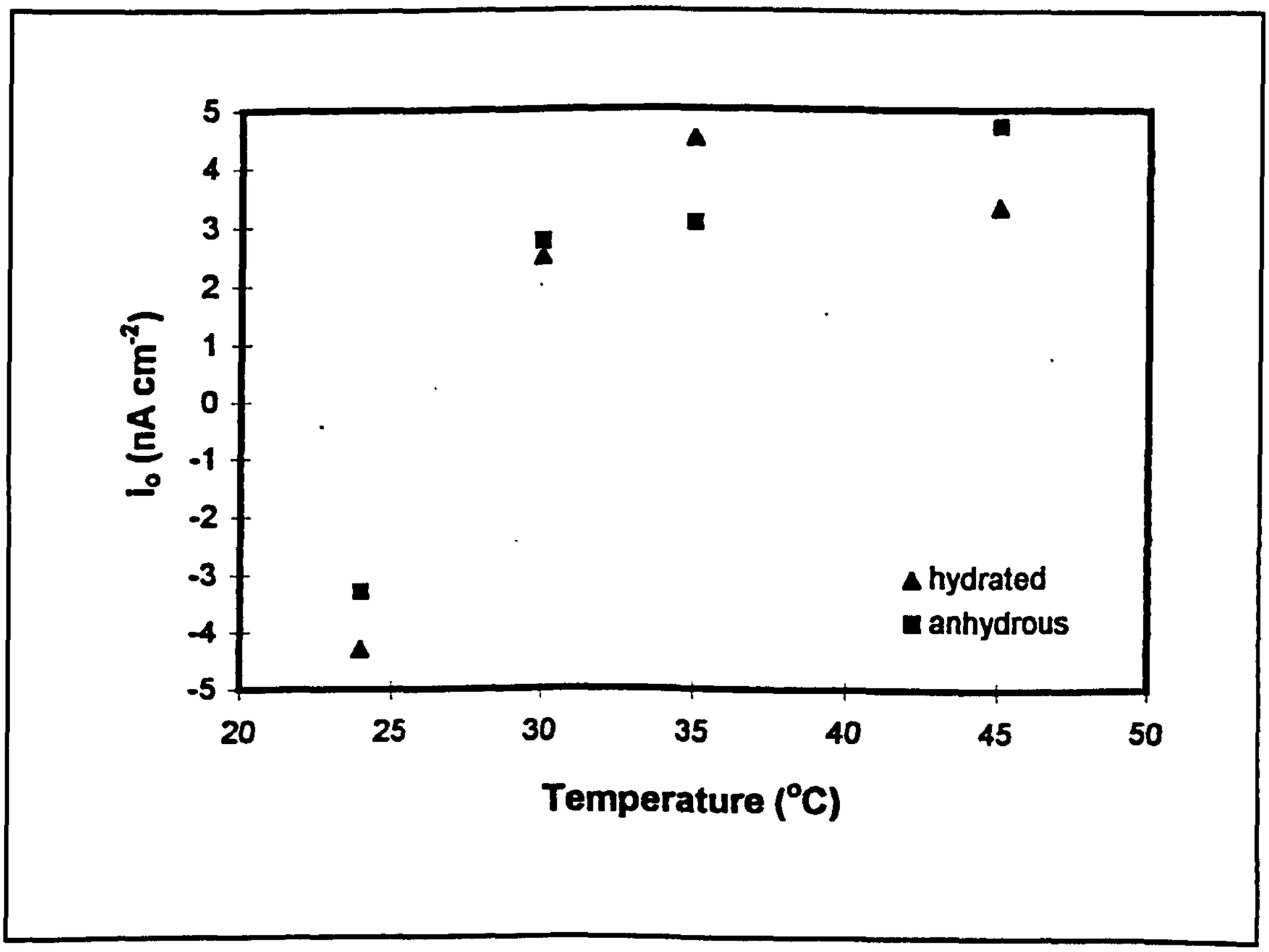

Figure 4.4.17 i_o values used to model Reaction 9 *vs* Temperature

It may be seen that there appears to be a step change between the value for the non-pitting 24°C and other (pitting) cases. This was assumed to correspond to whether the active mode of CrO_4^{2-} production is from pitting and general dissolution, or from general dissolution alone.

However, SEM studies have shown that pits are present in the 24°C sample, albeit much smaller than those viewed at higher temperatures. Thus, it is suggested that pits do initiate on the lower temperature samples, but do not propagate to the same extent as on the higher temperatures, and thus the current densities observed are lower.

The i_o values for the latter are extremely high, but this is due to the extremely high current densities supported by pits. Figure 4.4.18 show the results obtained by SRET techniques for Ferralium at 35°C.

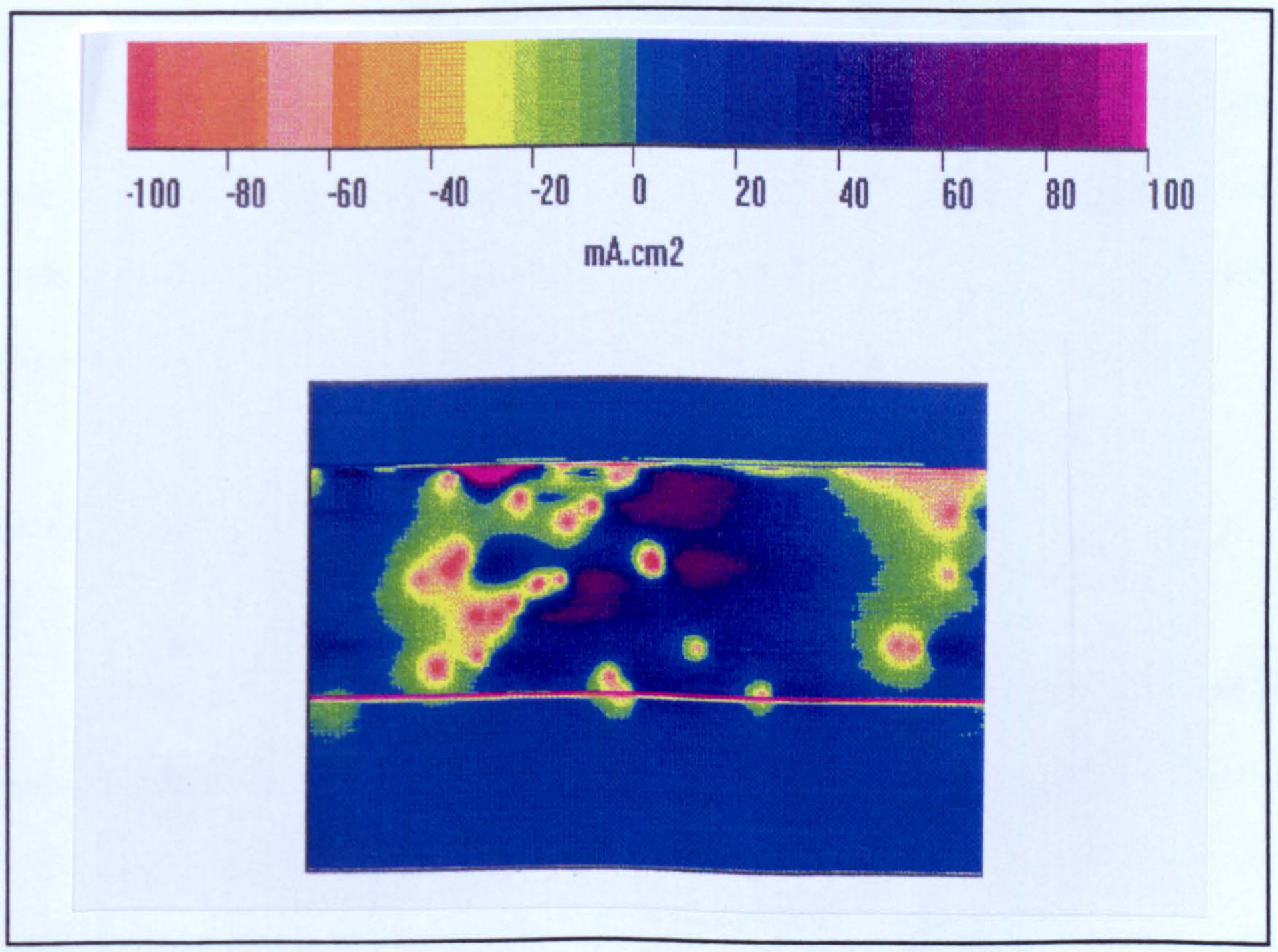

Figure 4.4.18 SRET images for Ferralium duplex stainless steel in natural seawater at 35°C; rotation speed 150 rpm.

It can be seen that current densities exceed 100 mA cm^{-2}. The true value may be greater, since the limits of the 12 bit A/D data acquisition board in the SRET instrument were exceeded (denoted by dark red colours in Figures 4.4.18). Trethewey *et al*[131] found current density values for 304 stainless steel in seawater to reach 250 mA cm^{-2}, while Newman[154] suggested values of 100 mA cm^{-2} for artificial pits during propagation, and 5 A cm^{-2} for the initiation phase. However, due to the localised nature of pits, such high current densities occur only on a small fraction of the surface, as opposed to general dissolution. Trethewey *et al* found that there was no relationship between measured current density and pit size and geometry[131], an observation which was matched here..

It may be seen that the i_o - T curve in Figure 4.4.17 shows a reciprocal relationship with the E_b - T curve shown in Figure 4.4.16. This is to be expected, since increasing the i_o of a redox process such as Reaction 9, which has the electrons on the right hand side of the equation, causes the current density line to be displaced to more electronegative potentials. Reactions such as the hydrogen evolution reaction, which have the electrons on the left hand side of the redox equation, are moved to more electropositive potentials by a lower i_o.

4.4.4.6 Modelling of Active Dissolution of Iron

Keddam[146] proposed that binary Fe-Cr alloys with Cr contents of the order of 22% lose their 'iron characteristics', due to the absence of free iron in the alloy matrix. Newman *et al* have shown that an Fe-Cr alloy is fully amorphous at 25% Cr[144]. However, in the model considered here, iron dissolution still has to occur for the enrichment of chromium in the surface film, as described in Section 2.9. Thus, the activation-controlled anodic dissolution portion of the polarization curves for the duplex steel considered here is again

modelled by the dissolution of iron, Reaction 1.

4.4.4.7 The Oxygen Reduction Reaction

To model those polarization curves generated in 5% H_2SO_4, it has been found necessary to use different i_o values for the oxygen reduction and oxidation processes (0.12 and 5.2 x 10^{-5} nA cm^{-2} respectively), and an explanation regarding different reaction mechanisms has been proposed. However, for seawater electrolytes, the oxygen reduction process (Reaction 7) is best modelled using the same value as for the oxidation process, namely 0.12 nA cm^{-2}. Figure 4.4.19 shows the poor fit to the cathodic portion of the curve obtained by using an i_o value of 5.2 x 10^{-5} nA cm^{-2}.

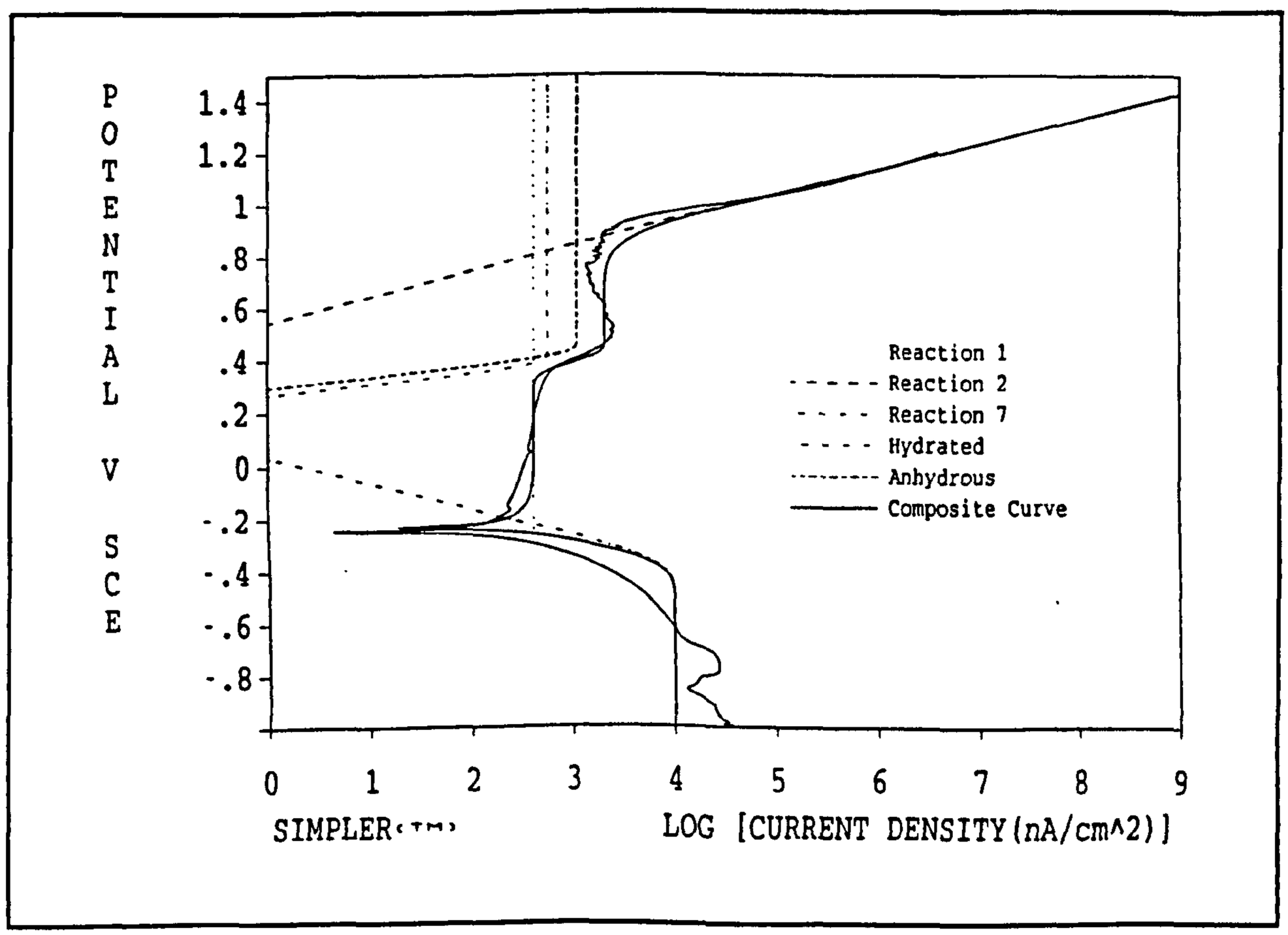

Figure 4.4.19 Model of Ferralium in seawater, 24°C, using 5.2 x 10^{-5} nA cm^{-2} as Reaction 7 i_o.

A possible explanation for these two values of Reaction 7 i_o is that the oxygen

reduction process itself proceeds by different mechanisms in seawater and 5% H_2SO_4. Different mechanisms have been proposed[58,155,156] although the substrates in these cases have been the platinum metals.

4.4.4.8 Other Efforts at Modelling Breakdown Potential

Bird *et al*[104] considered pure iron in solutions of pH 10 - 14 with NaCl concentrations of 10^{-3} to 10^{0} M and found the following relationship :

$$E_b = -0.015 - 0.31\frac{[Cl^-]}{[OH^-]_s}$$

where ⊏Cl^-⊐ is the concentration of chloride ions

⊏OH^-⊐$_s$ is the concentration of hydroxyl ions at the surface of the electrode

However, they considered the oxygen evolution reaction (Reaction 2) to be responsible for the current densities found above E_b, which has been shown here not to be the case, rather it occurs at a constant potential. They did not consider the effect of temperature.

4.4.4 CONCLUDING REMARKS

The polarization characteristics of the duplex stainless steel Ferralium, in natural seawater, have been investigated and were found to be sensitive to temperature. A model for the behaviour of Ferralium duplex stainless steel in seawater of temperature between 24 and 45°C has been advanced. The anodic activation-controlled reaction was shown to be iron dissolution, as in the case of stainless steels in 5% H_2SO_4, while in contrast, the

dominant cathodic reaction was shown to be oxygen reduction, as opposed to hydrogen evolution.

Above the passive region, pitting was found to be at least a contributing, if not the major mode of producing Cr(VI) salts from the Cr(III) species in the passive film. The potential above which pitting occurred (E_b) was found to depend markedly upon temperature, and this was modelled by altering the i_o of the reaction in question. This approach is in contrast to other published models of synthesised polarization curves of pitting systems, which assume that the oxygen evolution reaction is responsible for the current density observed above E_b, and use E_b in place of E° for this latter reaction.

Some observations are made about the behaviour of Ferralium stainless steel compared to other stainless steels. It is suggested that 22% Cr content represents a threshold above which there is a increase in the performance of the alloy in question. Differences in the dissolution behaviour of the ferrite and austenite phases of Ferralium have been observed.

An explanation for the difference in breakdown potentials between Ferralium and other stainless steels with lesser %Cr contents has been advanced. This takes 22% Cr as the threshold above which there is no free iron left in the matrix, and thus breakdown does not occur at lower potentials due to Cl^- attacking the iron matrix; rather it occurs due to breakdown of the protective chromium oxide layer.

Chapter 4 Section 5 The Corrosion of 316 Stainless Steel in 5% H_2SO_4 and Natural Seawater

4.5.1 INTRODUCTION

The addition of 1.75-3.0 %[111] molybdenum to an alloy containing 16-18% chromium and 10-14% nickel results in an austentic alloy system designated 316 by the AISI. The nickel expands the γ-loop in the phase diagram[157] and lowers the M_s temperature to below ambient temperatures, such that the austenitic microstructure is stabilized. This addition of molybdenum increases the resistance to pitting attack in marine and chemical environments by enhancing the ion-selective nature of the bipolar passive film, as described in Section 2.9. There are many different variations[88] within the generic 316 alloy system. These include a low carbon grade (316L) for welding, a nitrogen-bearing (316N) alloy for increased strength and a sulphur containing grade (316F) for increased machinability. It should be noted that the latter grade has markedly less corrosion resistance[158] than other varieties of 316, since MnS 'stringer's act as local anodes which quickly dissolve, weakening the structure.

A typical PRE_N for 316 is 26.2[141], which is below the value of 40 often taken as the threshold above which an alloy may be used for critical applications in a marine environment. However, the material used in this study was from a cast destined for yacht deck fittings. 316 is generally regarded as passive[88] in dilute H_2SO_4 in oxygenated solutions at ambient temperatures, although a decrease in oxygen concentration may lead to unstable passivity.

4.5.2 EXPERIMENTAL

The material used was obtained from AVESTA, from a cast designated 316XS. Section 4.1.2 details the methods used to prepare the samples (specimen area 4 cm^2) and the equipment used to perform the potentiodynamic scans. Section 4.2.2 details the methods used to obtain the three different dissolved oxygen concentrations. The samples were conditioned at -800 mV SCE for 300 seconds. Table 4.5.1 gives the chemical composition of the alloy used.

Element	EDAX	AAS
Chromium	16.7	15.45
Nickel	12.2	12.35
Molybdenum	2.3	2.34
Carbon	0.03*	0.06
Silicon	2.2	0.11
Manganese	1.6	0.74
Sulphur	0.52*	0.02
Iron	64.5	68.93

Table 4.5.1 Chemical composition of 316 alloy used (* from residual carbon/sulphur analyzer).

The seawater was again obtained from Plymouth Marine Laboratories.

4.5.3 RESULTS

The experimental results are shown in Section 4.5.3, and the modelled curves, along with the range of parameters used to generate them, are shown in Sections 4.5.3.2 to 4.5.3.6. Full lists of modelling parameters are given in appendices H to K.

4.5.3.1 Potentiodynamic Scans

Figures 4.5.1 to 4.5.3 show the polarization curves for 316 stainless steel in 5% H_2SO_4 with three different dissolved oxygen concentrations, while Figure 4.5.4 shows the behaviour of the same alloy in natural seawater.

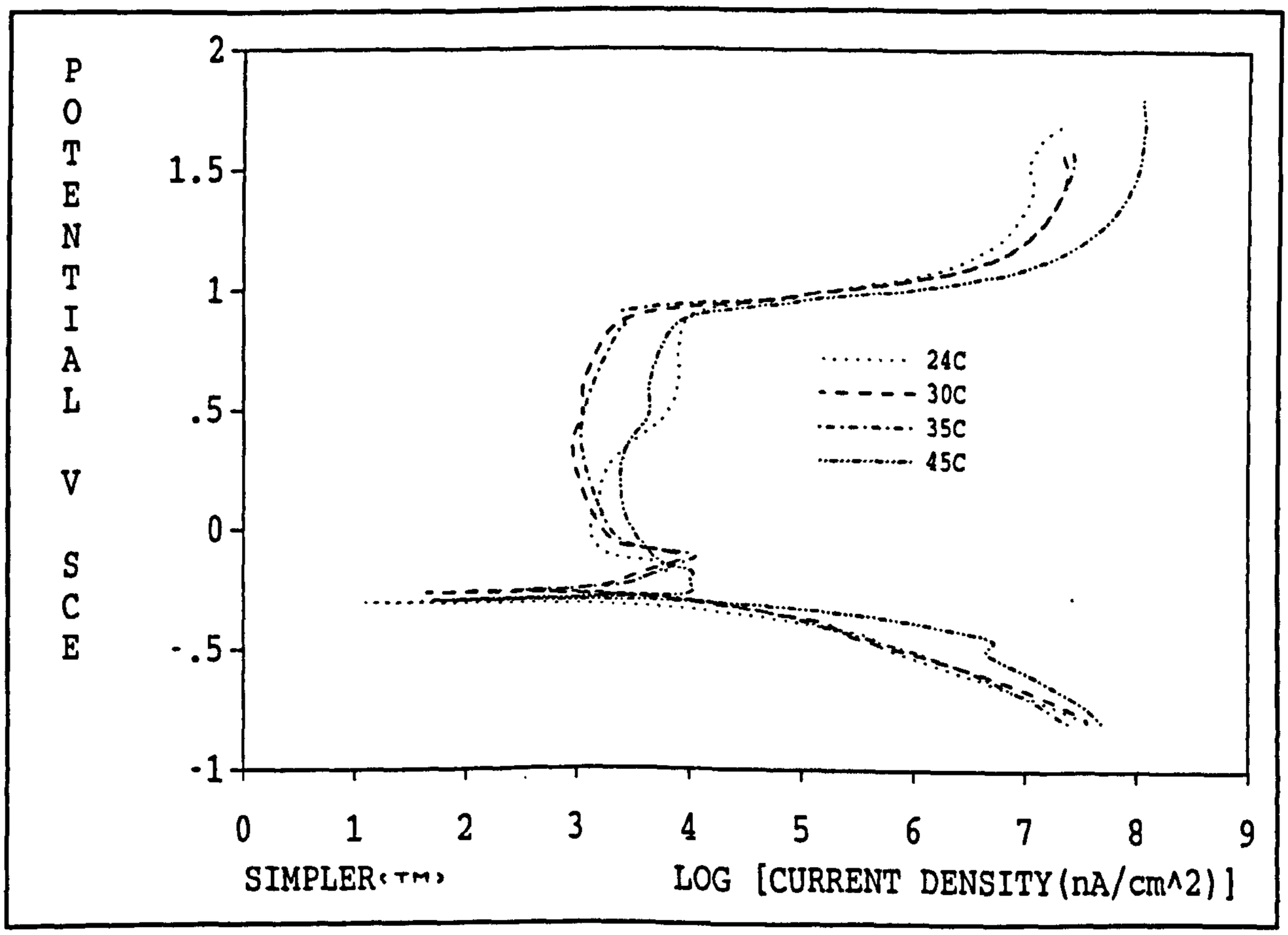

Figure 4.5.1 Potentiodynamic polarization curves for 316 stainless steel in 5% deaerated H_2SO_4.

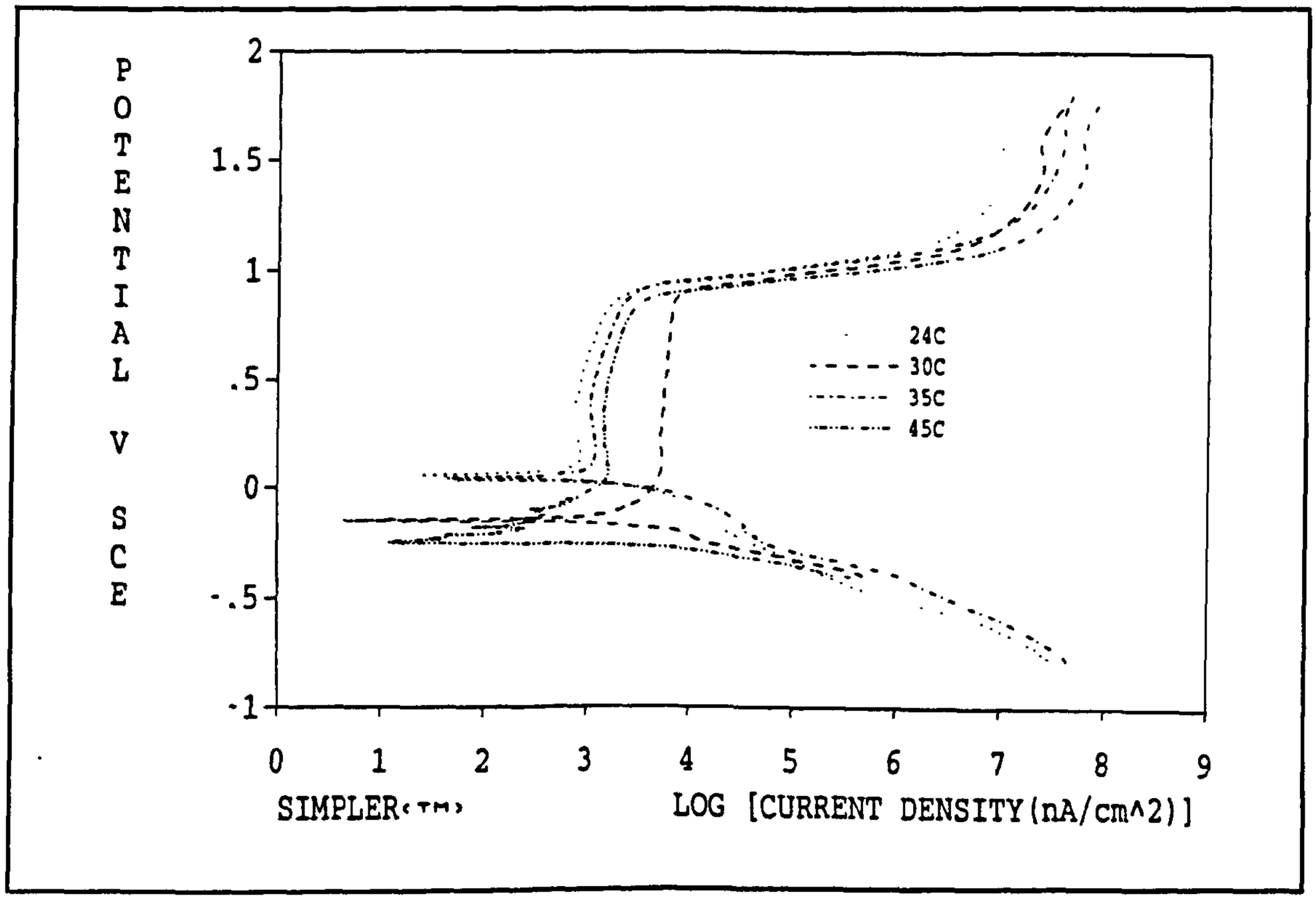

Figure 4.5.2 Potentiodynamic polarization curves for 316 stainless steel in 5% aerated H_2SO_4.

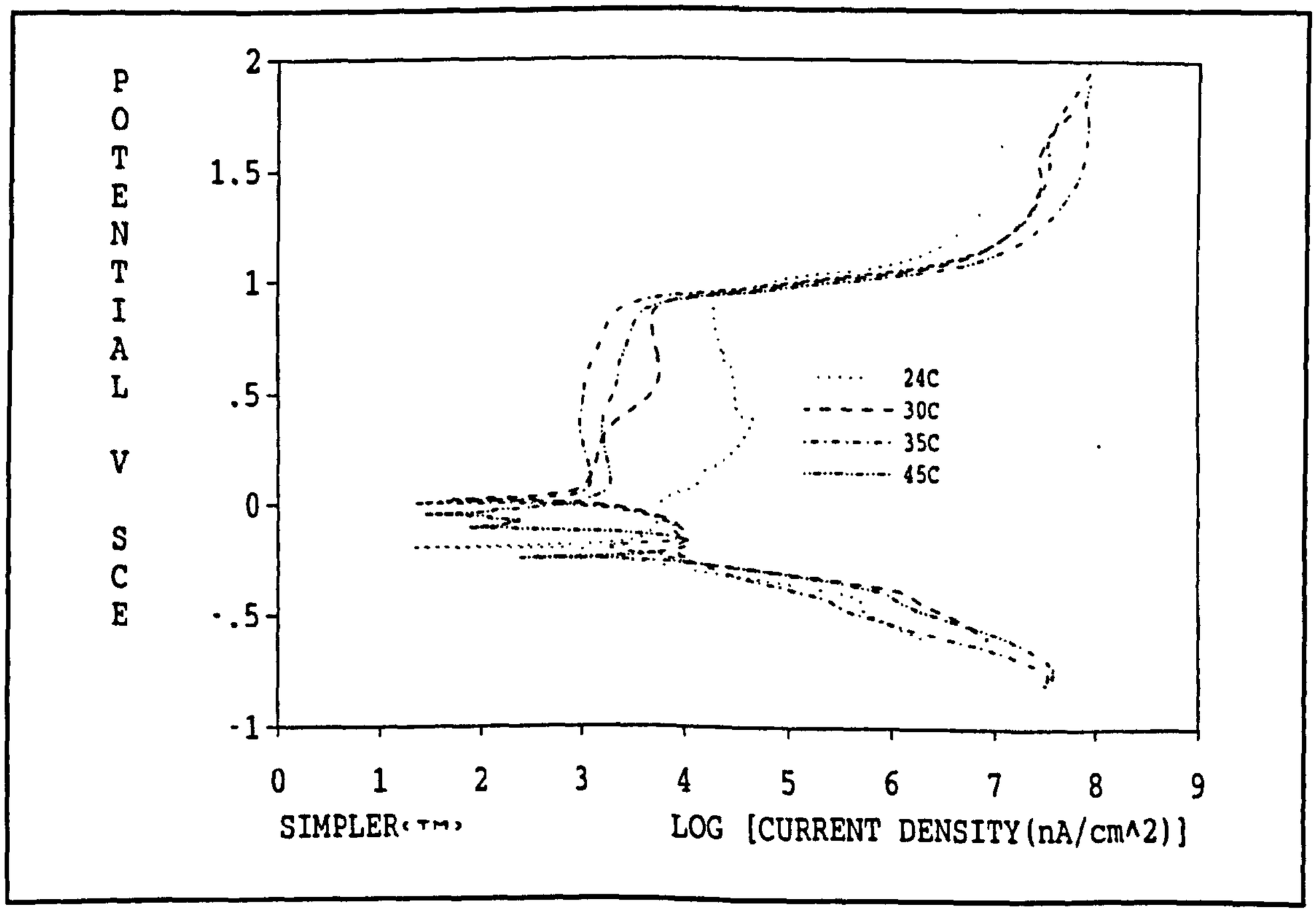

Figure 4.5.3 Potentiodynamic polarization curves for 316 stainless steel in 5% stagnant H_2SO_4.

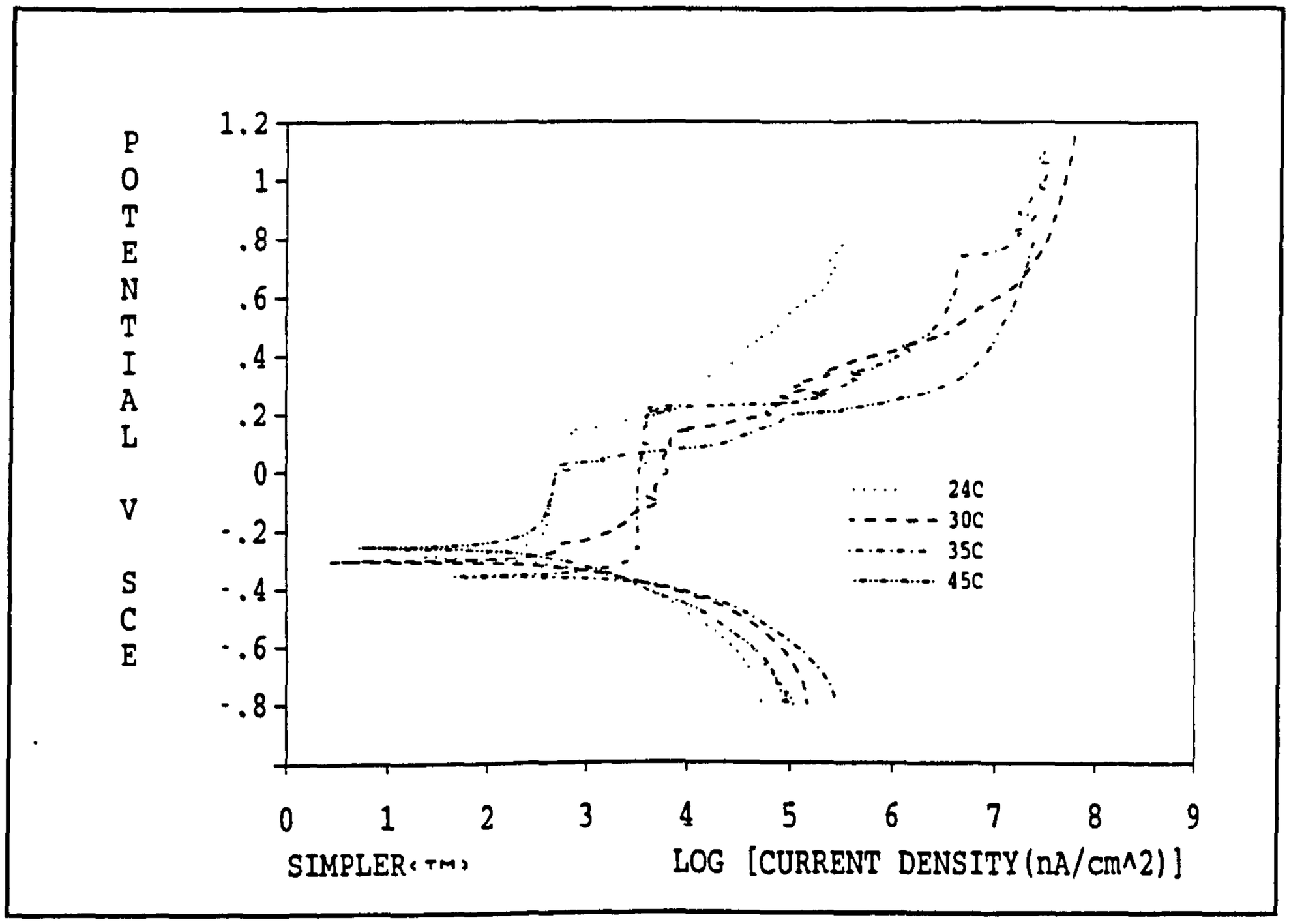

Figure 4.5.4 Potentiodynamic polarization curves for 316 stainless steel in natural seawater.

4.5.3.2 Models for 316 Stainless Steel in Deaerated 5% H_2SO_4.

The same reaction scheme as used to model 304 stainless steel in H_2SO_4 is used to model the behaviour of 316 stainless steel in the same electrolyte. The behaviour at 24°C is shown in Figure 4.5.5, which uses the parameters shown in Tables H-1 and H-2 in appendix H. Figure 4.5.6 shows the behaviour of 316 stainless steel in deaerated 5% H_2SO_4 at 30°C. The parameters used to synthesise this curve and listed in Table H-3 and H-4 in appendix H. Figure 4.5.7 uses the parameters listed in Tables H-5 and H-6 of appendix H to model the behaviour of 316 stainless steel in deaerated 5% H_2SO_4 at 35°C. Figure 4.5.8 shows the model for 316 stainless steel in deaerated 5% H_2SO_4 at 45°C, using the parameters listed in Tables H-7 and H-8 in appendix H.

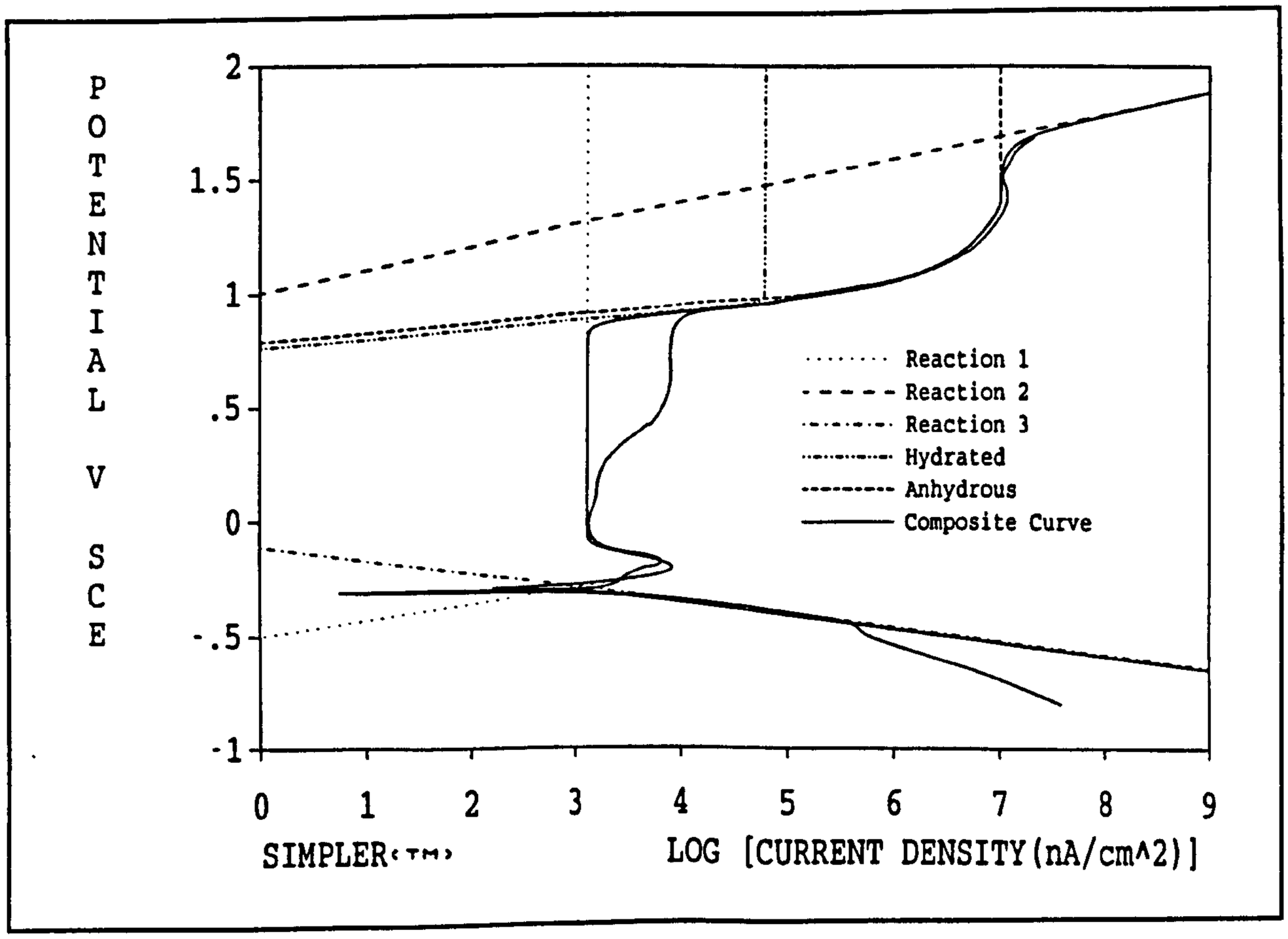

Figure 4.5.5 Model of 316 stainless steel in deaerated H_2SO_4 at 24°C.

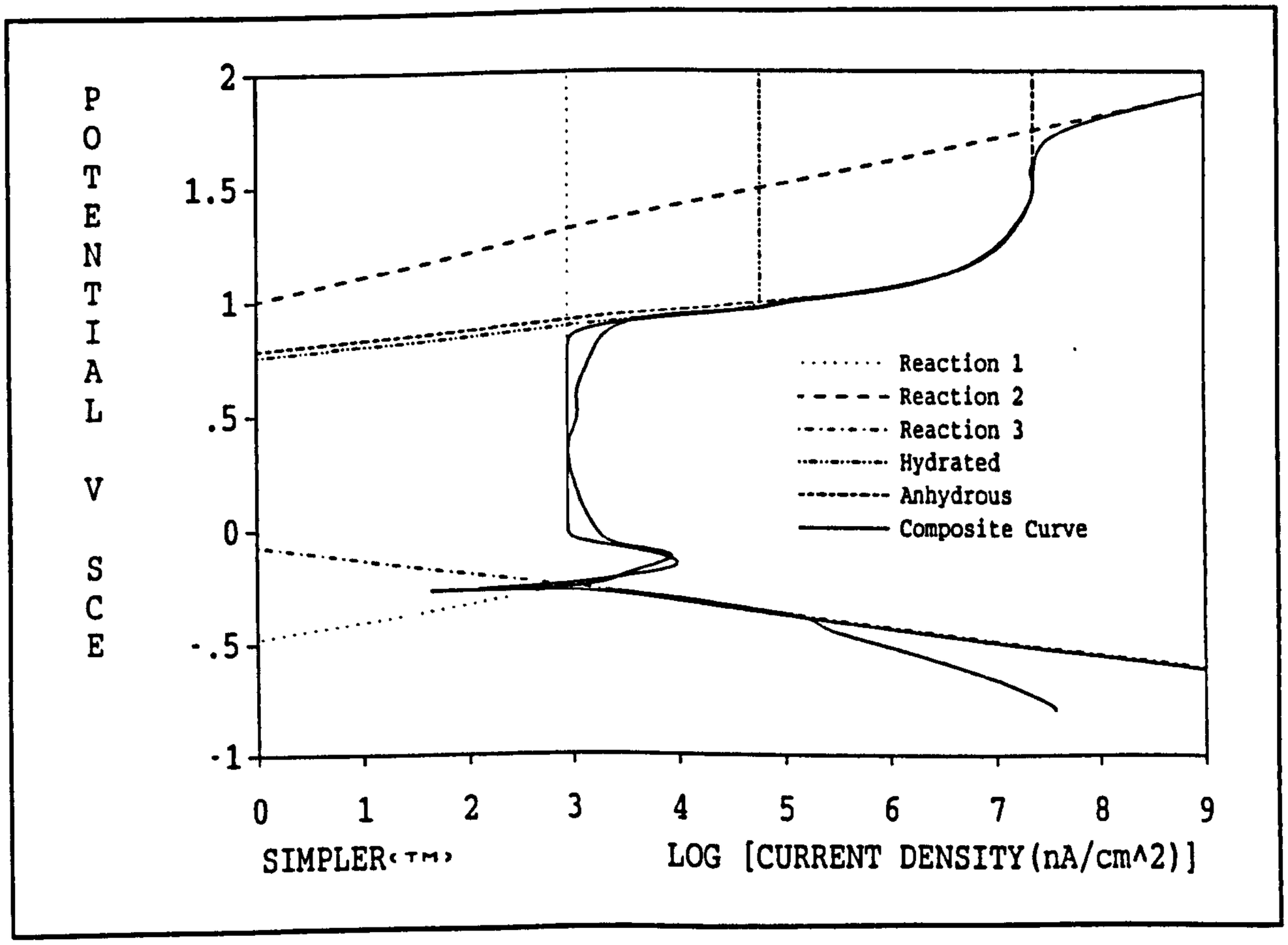

Figure 4.5.6 Model of 316 stainless steel in deaerated H_2SO_4 at 30°C.

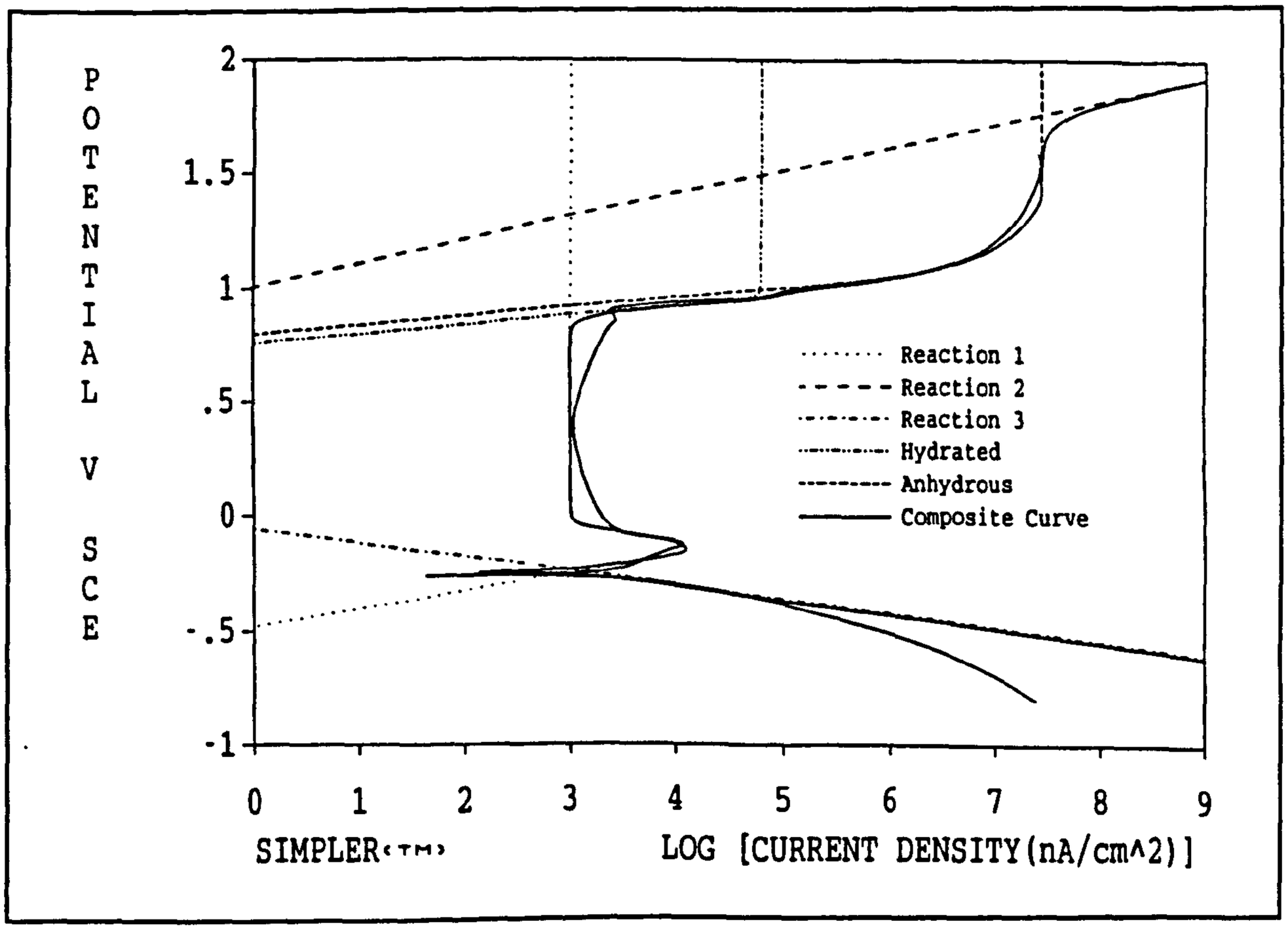

Figure 4.5.7 Model of 316 stainless steel in deaerated H_2SO_4 at 35°C.

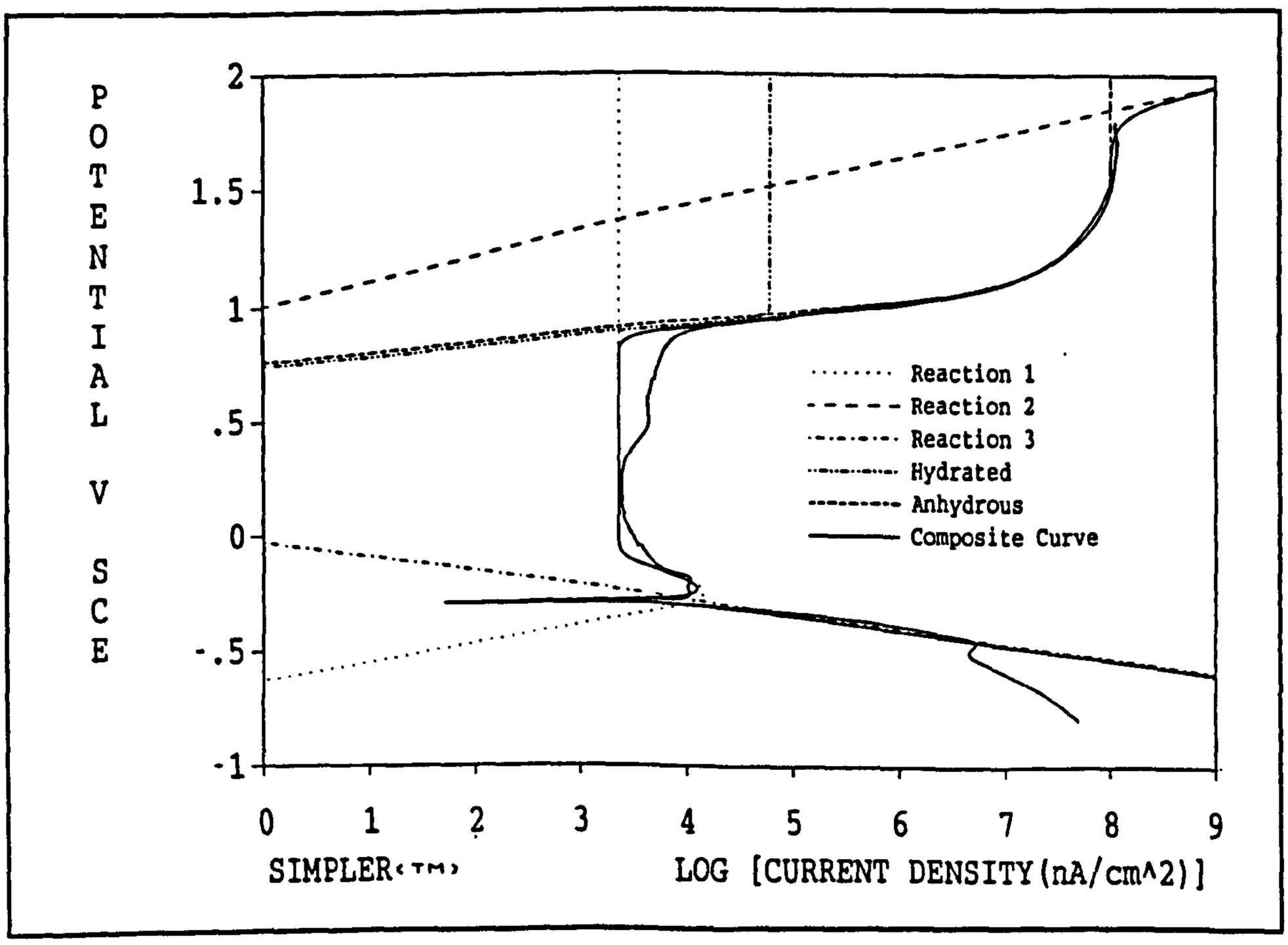

Figure 4.5.8 Model of 316 stainless steel in deaerated H_2SO_4 at 45°C.

	Reaction 1	Reaction 2	Reaction 3	Reaction 5	Reaction 5
Cr_2O_3 form				$Cr(OH)_3.nH_2O$	anhydrous
E° (V SHE)	-0.440	1.228	0.000	1.117	1.184
i_o (nA cm^{-2})	7.5×10^{-4} to 1.5×10^{-7}	0.12	70.0 to 900	0.31 to 0.5	1.5 to 7.0
i_{lim}anodic (nA cm^{-2})	not required	1.0×10^{21}	negligible	6.0×10^{4}	1.0×10^{7} to 1.0×10^{8}
i_{lim}cathodic (nA cm^{-2})	negligible	negligible	1.0×10^{21}	negligible	negligible
α	0.40 to 0.49	0.50 to 0.60	0.50	0.50	0.50
Temperature	24 - 45°C				
pH	0.2				
Resistance	4.0 - 30.0				

Table 4.5.2 Range of parameters used to model 316 stainless steel in deaerated 5% H_2SO_4.

	i_{pass} (nA cm^{-2})	A	P	E_t (V SCE)
Reaction 1	900 to 2.3×10^{3}	150 to 350	2.0	-0.190 to -0.350

Table 4.5.3 Range of passivation parameters used to model 316 stainless steel in deaerated 5% H_2SO_4.

The range of parameters used to model 316 stainless steel in deaerated 5% H_2SO_4 are listed in Tables 4.5.2 and 4.5.3.

4.5.3.3 Models for 316 Stainless Steel in Aerated 5% H_2SO_4

The parameters used to model the behaviour of 316 stainless steel in aerated 5% H_2SO_4 at 24°C are listed in Tables I-1 and I-2 of Appendix I, and the resultant theoretical curve is shown in Figure 4.5.9.

The parameters used to model the behaviour of 316 stainless steel in aerated 5% H_2SO_4 at 30°C are listed in Tables I-3 and I-4 of Appendix I, and the resultant theoretical curve is shown in Figure 4.5.10.

The parameters used to model the behaviour of 316 stainless steel in aerated 5% H_2SO_4 at 35°C are listed in Tables I-5 and I-6 of Appendix I, and the resultant theoretical curve is shown in Figure 4.5.11.

The parameters used to model the behaviour of 316 stainless steel in aerated 5% H_2SO_4 at 45°C are listed in Tables I-7 and I-8 of Appendix I, and the resultant theoretical curve is shown in Figure 4.5.12.

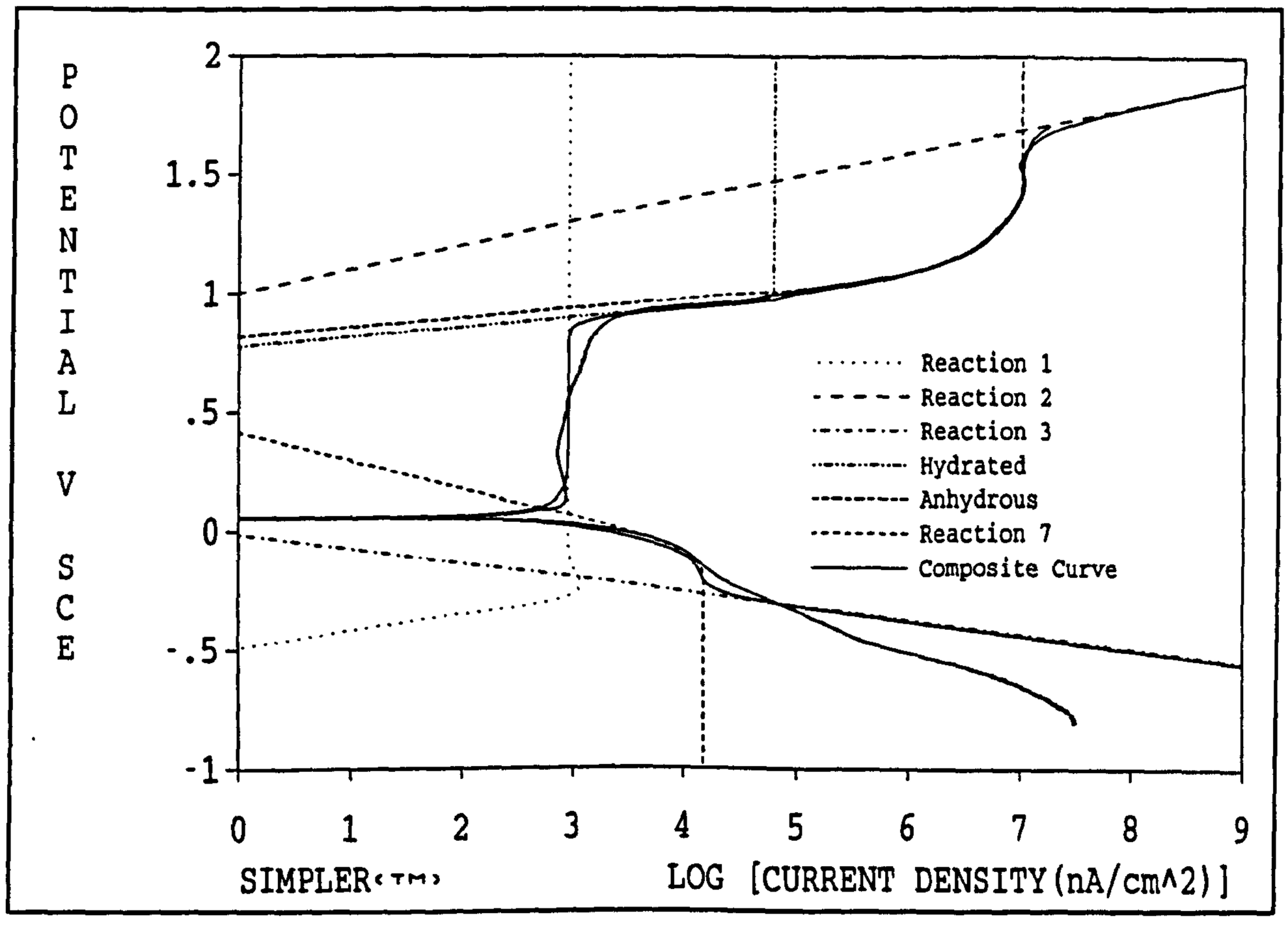

Figure 4.5.9 Model of 316 stainless steel in aerated H_2SO_4 at 24°C.

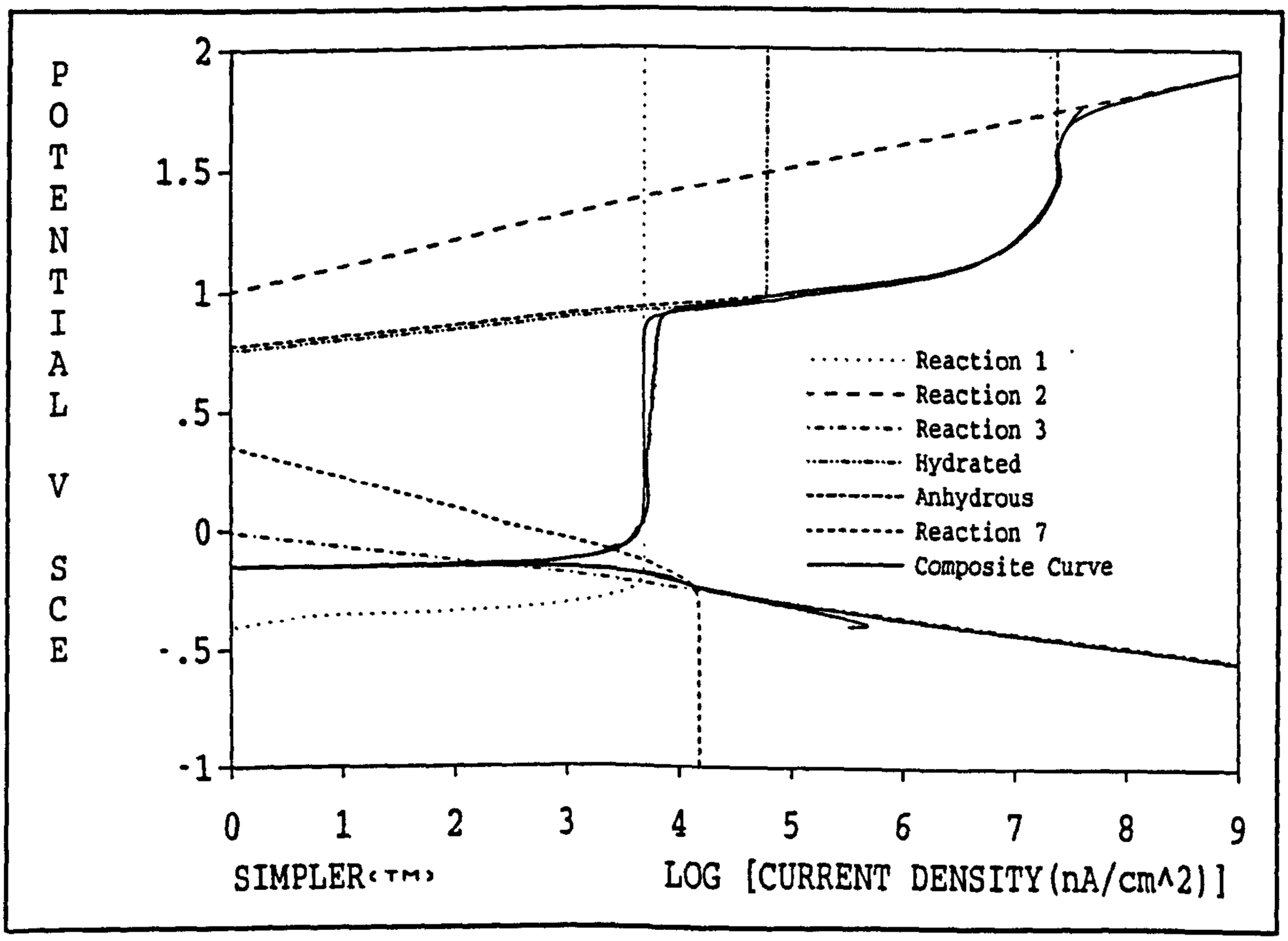

Figure 4.5.10 Model of 316 stainless steel in aerated H_2SO_4 at 30°C.

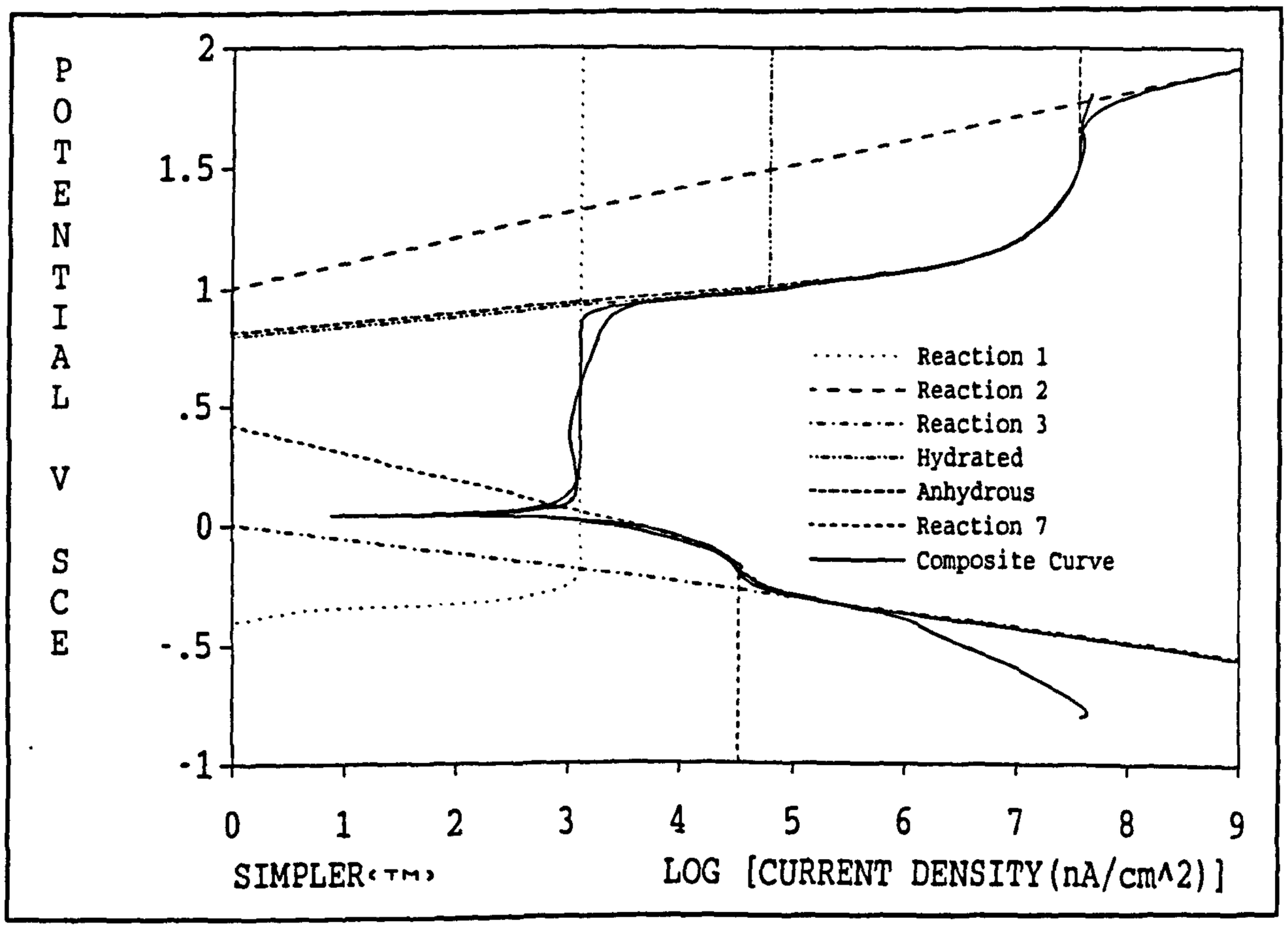

Figure 4.5.11 Model of 316 stainless steel in aerated H_2SO_4 at 35°C.

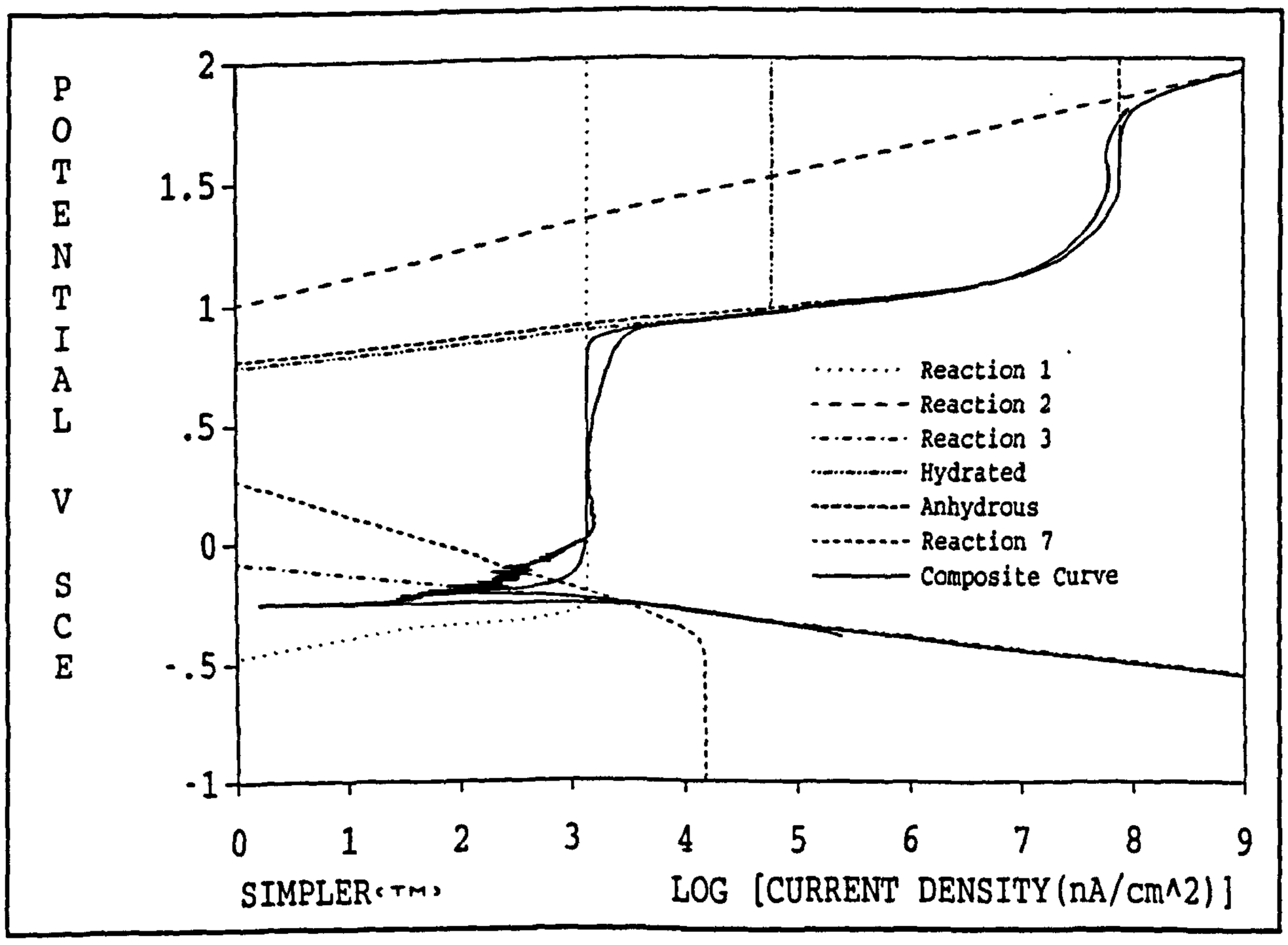

Figure 4.5.12 Model of 316 stainless steel in aerated H_2SO_4 at 45°C.

The range of parameters used to model the behaviour of 316 stainless steel in aerated 5% H_2SO_4 are shown in Tables 4.5.4 and 4.5.5.

	Reaction 1	Reaction 2	Reaction 7	Reaction 3	Reaction 5	Reaction 5
Cr_2O_3 form					$Cr(OH)_3.nH_2O$	anhydrous
E_o (V SHE)	-0.440	1.228	1.228	0.000	1.117	1.184
i_o (nA cm^{-2})	9.0×10^{-6} to 9.0×10^{-6}	0.12	5.2×10^{-5}	400 to 4.0×10^{3}	0.03 to 0.5	0.5 to 5.0
i_{lim}anodic (nA cm^{-2})	not required	1.0×10^{21}	negligible	negligible	6.0×10^{4}	1.0×10^{7} to 7.7×10^{7}
i_{lim}cathodic (nA cm^{-2})	negligible	negligible	1.5×10^{4} to 3.3×10^{4}	1.0×10^{21}	negligible	negligible
α	0.40	0.60	0.47 to 0.58	0.40 to 0.50	0.50	0.50
Temperature	24 to 45°C					
pH	0.2					
resistance	4 to 30					

Table 4.5.4 Range of passivation parameters used to model 316 stainless steel in aerated 5% H_2SO_4.

	i_{pass} (nA cm^{-2})	A	p	E_t
Reaction 1	900 to 1.4 x 10^3	150 to 350	2.0	-0.350

Table 4.5.5 Passivation parameters for model of 316 stainless steel in aerated 5% H_2SO_4.

4.5.3.4 Model for 316 Stainless Steel in Stagnant 5% H_2SO_4

The parameters used to model the behaviour of 316 stainless steel in stagnant 5% H_2SO_4 at 24°C are listed in Tables J-1 and J-2 of Appendix J, and the resultant theoretical curve is shown in Figure 4.5.13.

The parameters used to model the behaviour of 316 stainless steel in stagnant 5% H_2SO_4 at 30°C are listed in Tables J-3 and J-4 of appendix J, and the resultant theoretical curve is shown in Figure 4.5.14.

The parameters used to model the behaviour of 316 stainless steel in stagnant 5% H_2SO_4 at 35°C are listed in Tables J-5 and J-6 of appendix J, and the resultant theoretical curve is shown in Figure 4.5.15.

The parameters used to model the behaviour of 316 stainless steel in stagnant 5% H_2SO_4 at 45°C are listed in Tables J-7 and J-8 of appendix J, and the resultant theoretical curve is shown in Figure 4.5.16.

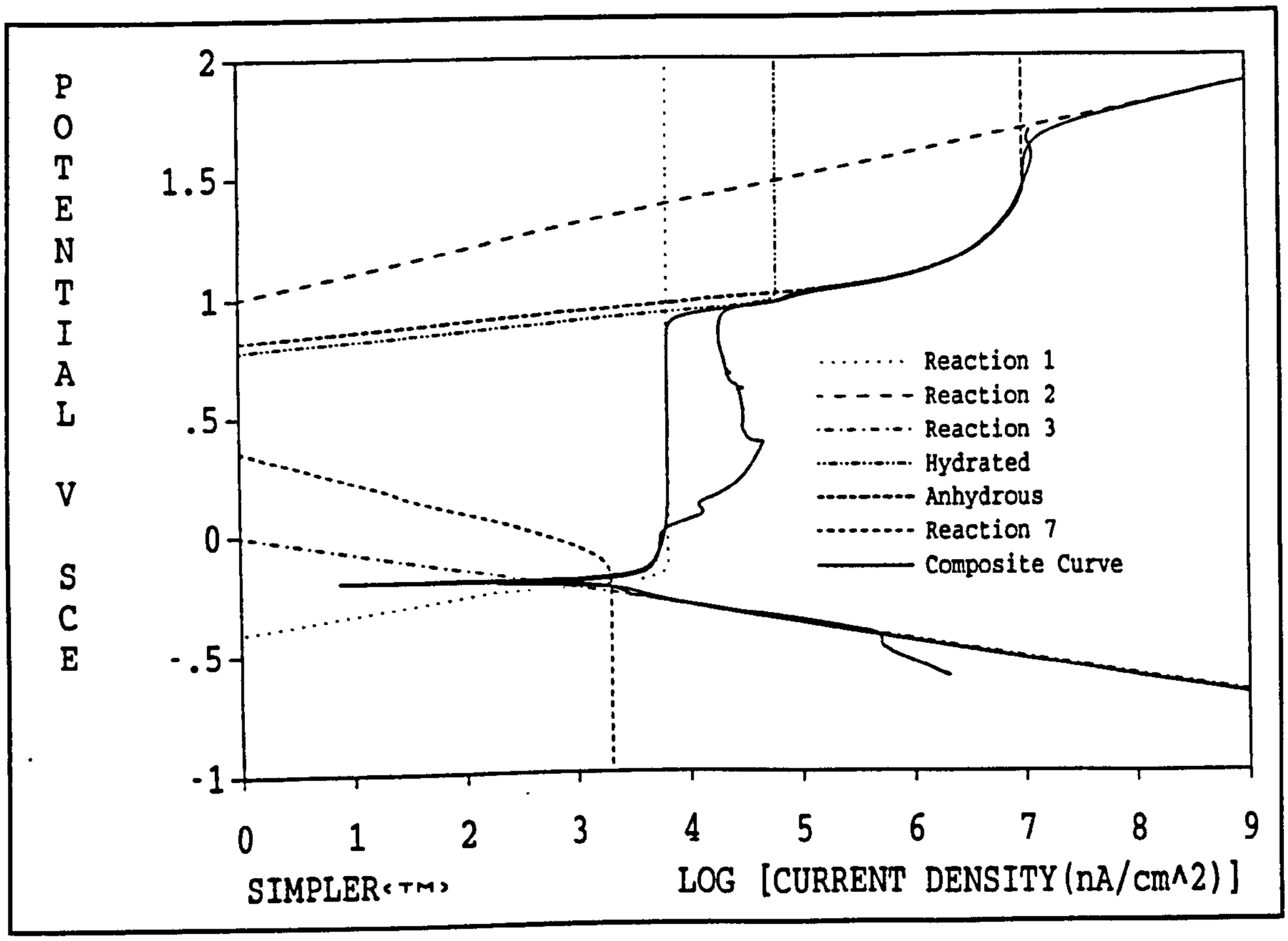

Figure 4.5.13 Model of 316 stainless steel in stagnant H_2SO_4 at 24°C.

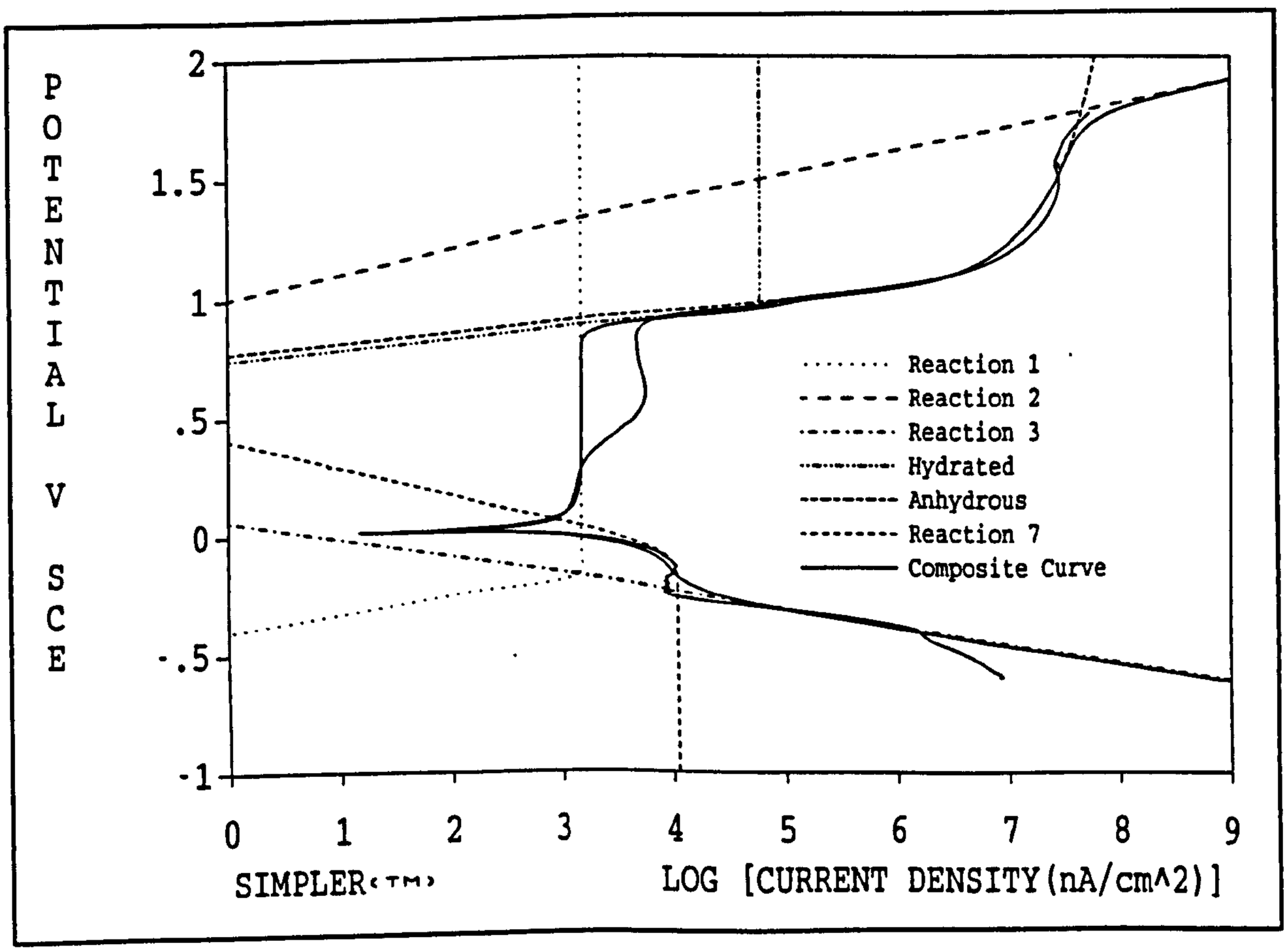

Figure 4.5.14 Model of 316 stainless steel in stagnant 5% H_2SO_4 at 30°C.

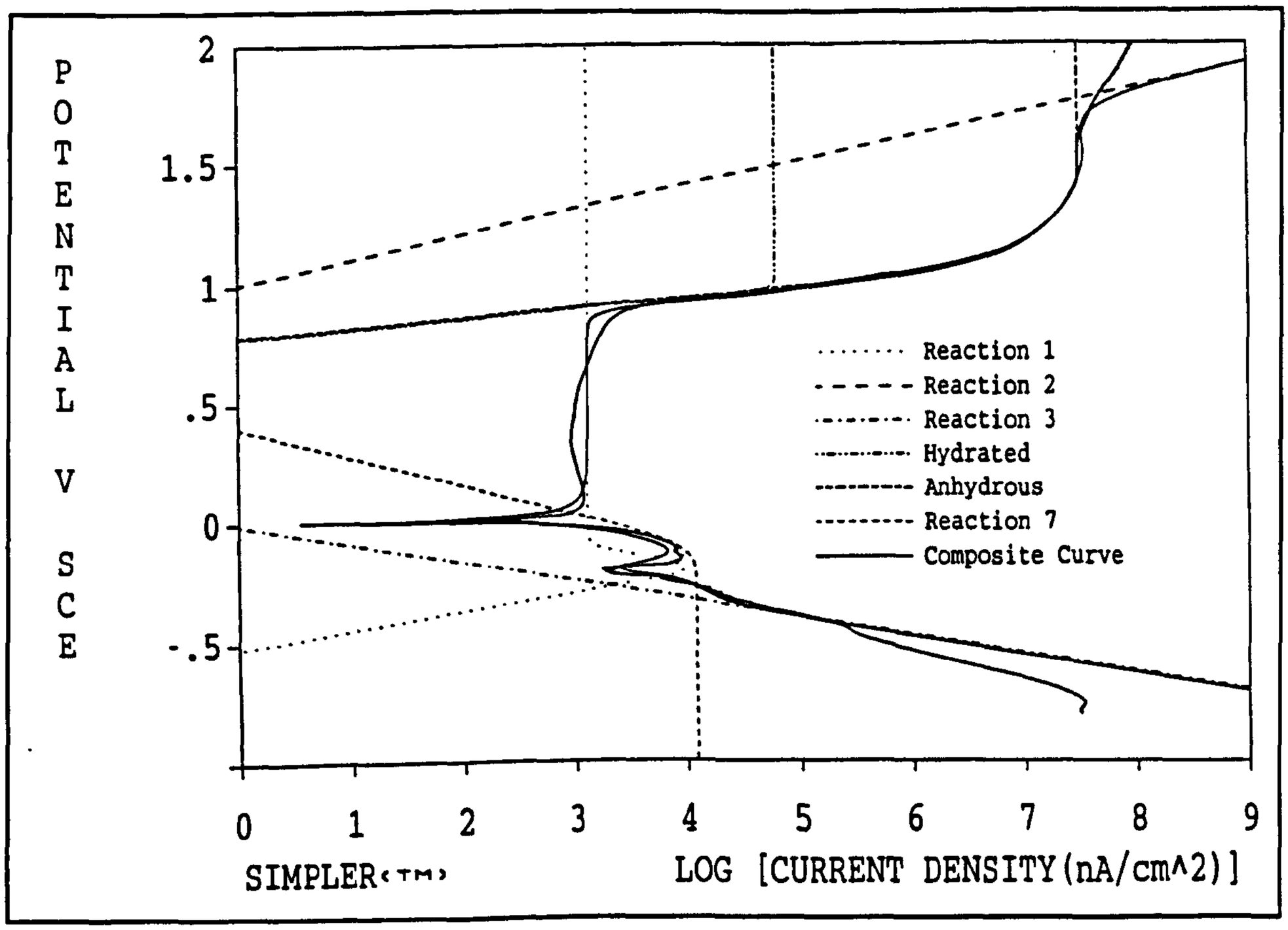

Figure 4.5.15 Model of 316 stainless steel in stagnant H_2SO_4 at 35°C.

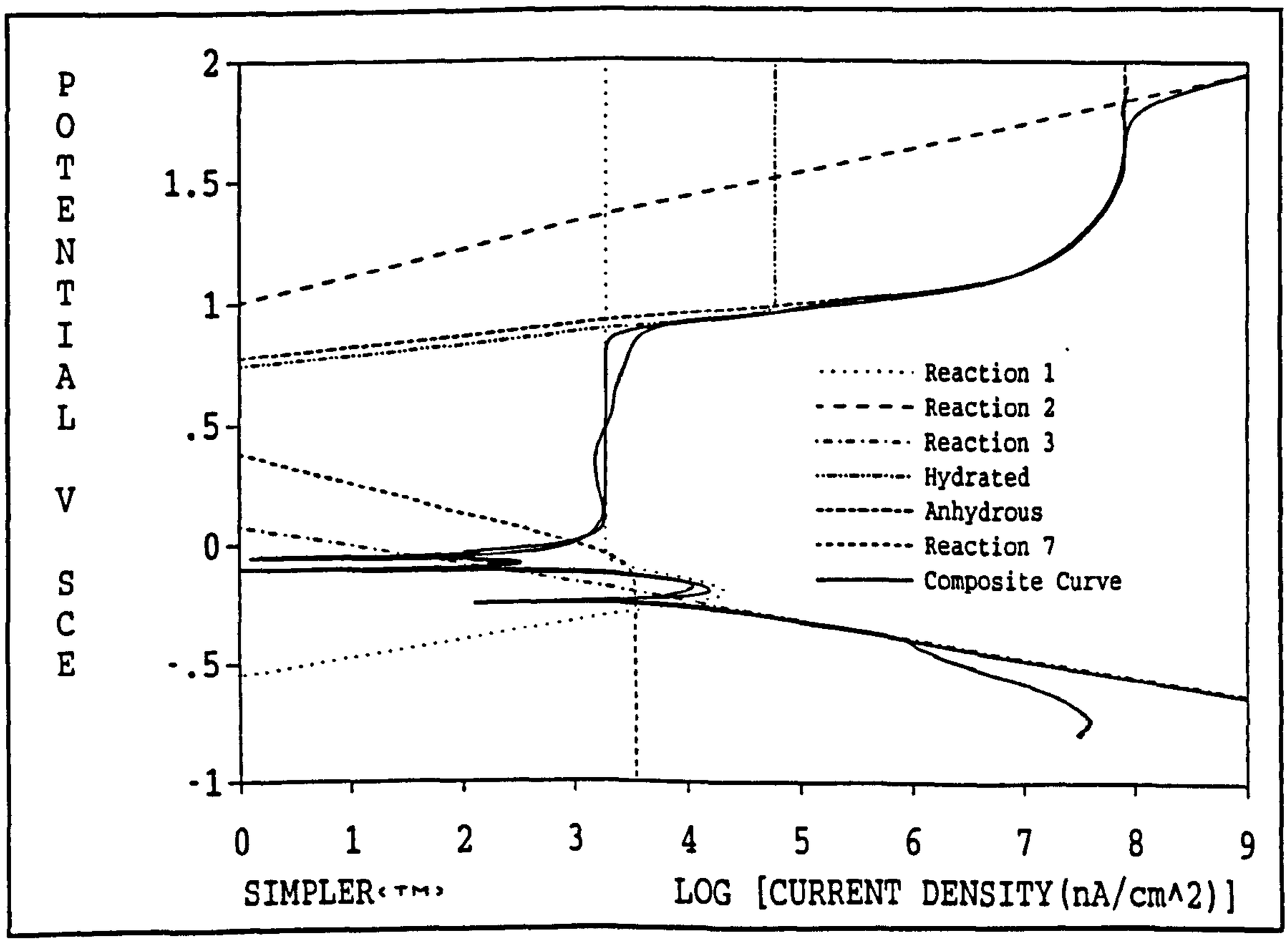

Figure 4.5.16 Model of 316 stainless steel in stagnant H_2SO_4 at 45°C.

The range of parameters used to model the behaviour of 316 stainless steel in stagnant 5% H_2SO_4 are shown in Tables 4.5.6 and 4.5.7.

	Reaction 1	Reaction 2	Reaction 7	Reaction 3	Reaction 5	Reaction 5
Cr_2O_3 form					$Cr(OH)_3.nH_2O$	anhydrous
E_o (V SHE)	-0.440	1.228	1.228	0.000	1.117	1.184
i_o (nA cm^{-2})	5.0×10^{-5} to 7.5×10^{-7}	0.12	5.2×10^{-5}	800 to 5.0×10^{3}	0.1 to 0.5	0.5 to 3.0
i_{lim}anodic (nA cm^{-2})	not required	1.0×10^{21}	negligible	negligible	6.0×10^{4}	1.0×10^{7} to 3.0×10^{8}
i_{lim}cathodic (nA cm^{-2})	negligible	negligible	3.5×10^{3}	1.0×10^{21}	negligible	negligible
α	0.40 to 0.42	0.60	0.49 to 0.55	0.60	0.50	0.50
Temperature	45°C					
pH	0.2					
Resistance	5 - 30 Ω					

Table 4.5.6 Range of parameters used to model 316 stainless steel in stagnant 5% H_2SO_4.

	i_{pass} (nA cm^{-2})	A	P	E_t
Reaction 1	1.3 x 10^3 to 6.5 x 10^3	300 to 350	2.0	-0.240 to -0.250

Table 4.5.7 Range of passivation parameters for model of 316 stainless steel in stagnant 5% H_2SO_4.

4.5.3.5 Models for 316 Stainless Steel in Natural Seawater

The parameters used to model the behaviour of 316 stainless steel in natural seawater at 24°C are listed in Tables K-1 and K-2 of appendix K, and the resultant theoretical curve is shown in Figure 4.5.17.

The parameters used to model the behaviour of 316 stainless steel in natural seawater at 30°C are listed in Tables K-3 and K-4 of appendix K, and the resultant theoretical curve is shown in Figure 4.5.18.

The parameters used to model the behaviour of 316 stainless steel in natural seawater at 35°C are listed in Tables K-5 and K-6 of appendix K, and the resultant theoretical curve is shown in Figure 4.5.19.

The parameters used to model the behaviour of 316 stainless steel in natural seawater at 45°C are listed in Tables K-7 and K-8 of appendix K, and the resultant theoretical curve is shown in Figure 4.5.20.

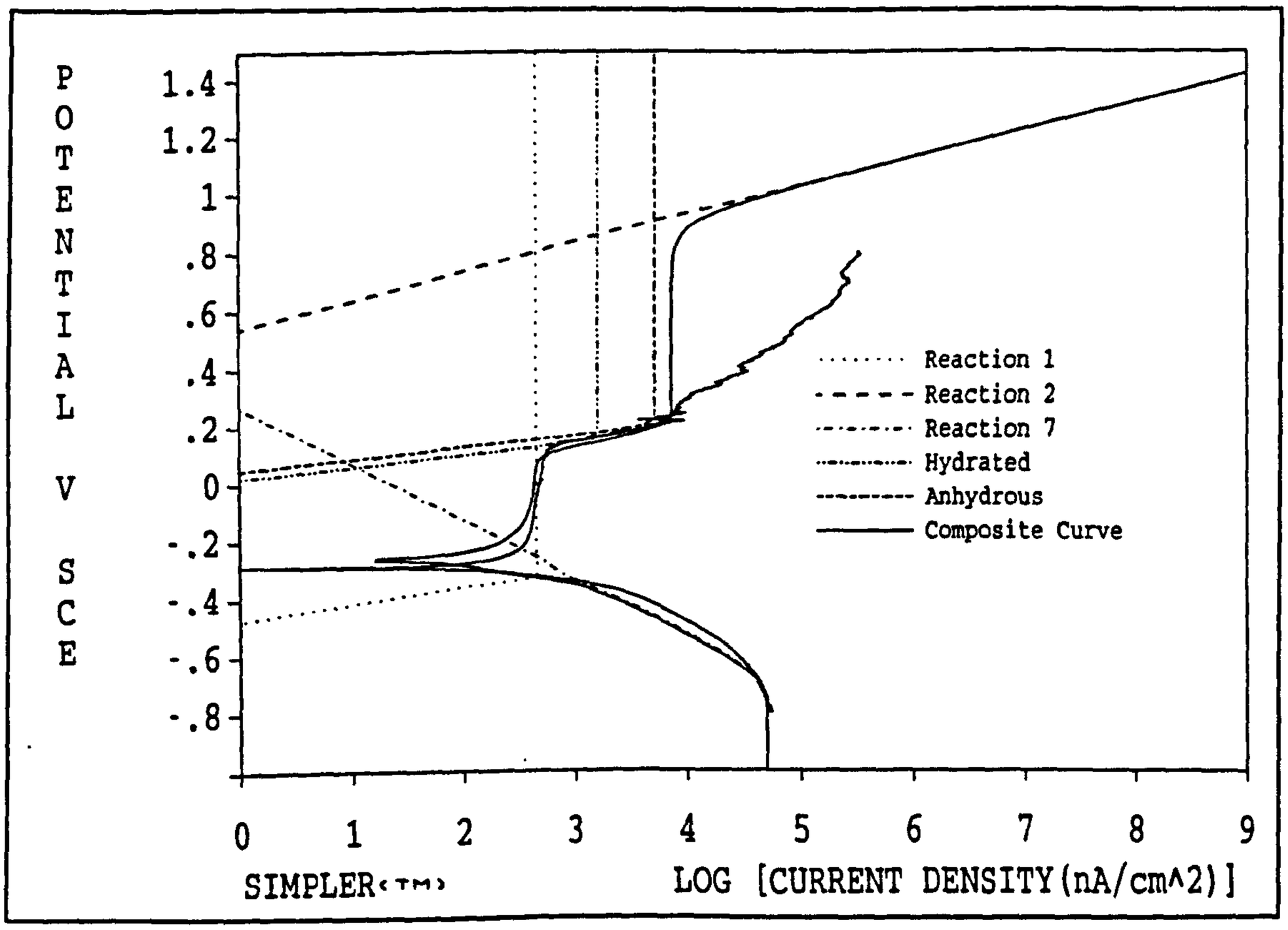

Figure 4.5.17 Model of 316 stainless steel in natural seawater at 24°C.

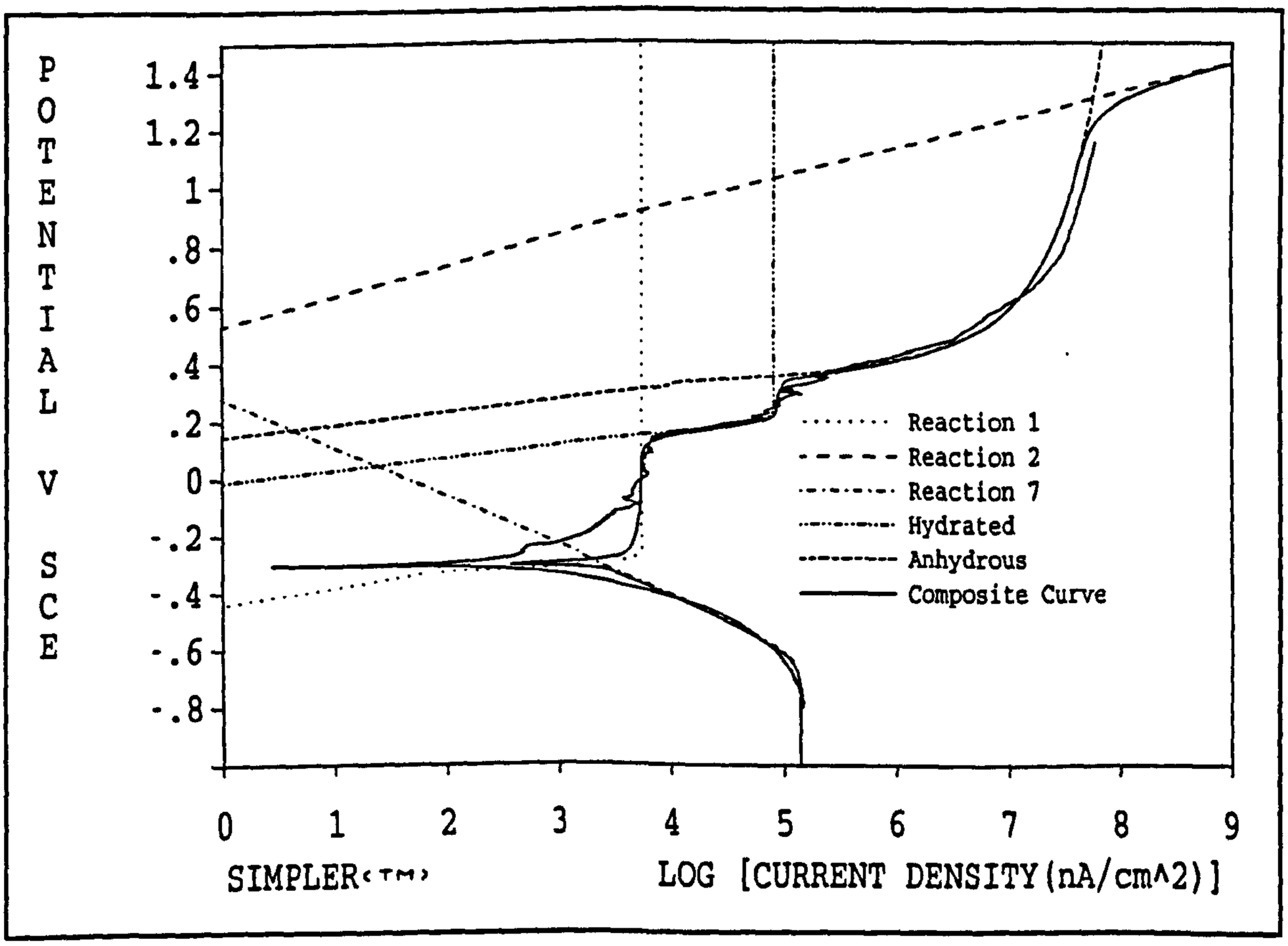

Figure 4.5.18 Model of 316 stainless steel in natural seawater at 30°C.

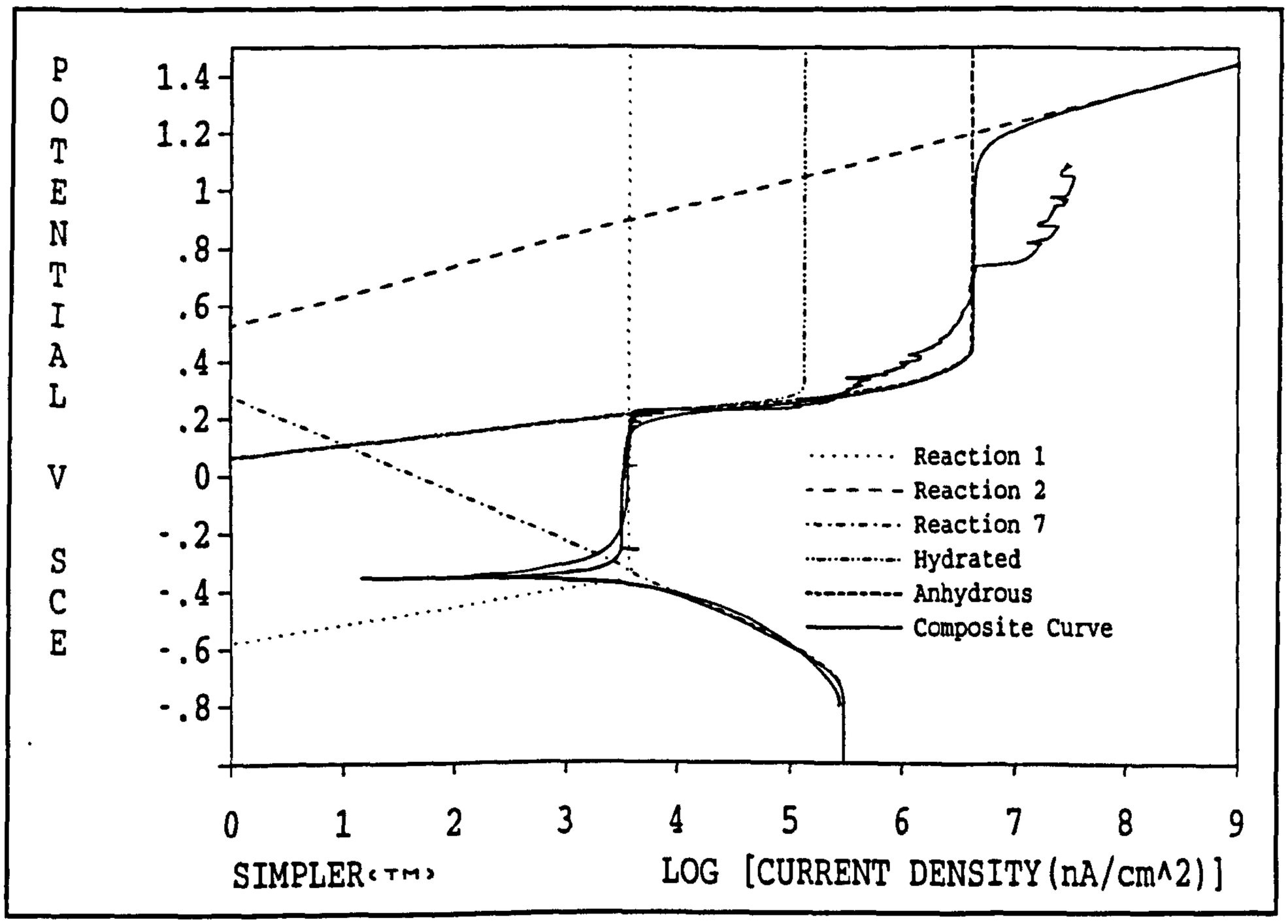

Figure 4.5.19 Model of 316 stainless steel in natural seawater at 35°C.

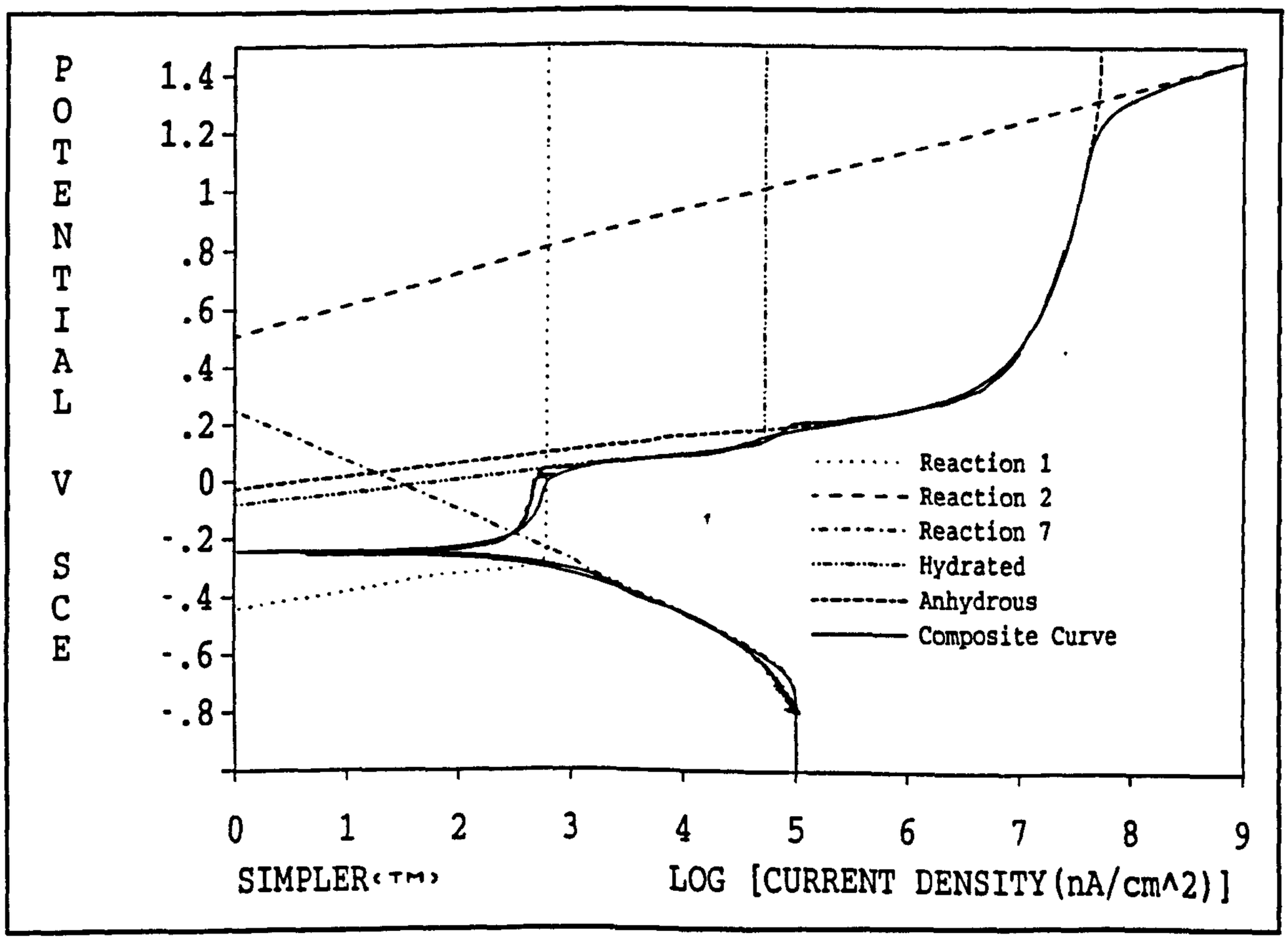

Figure 4.5.20 Model of 316 stainless steel in natural seawater at 45°C.

	Reaction 1	Reaction 2	Reaction 7	Reaction 9	Reaction 9
Cr_2O_3 form				$Cr(OH)_3.nH_2O$	anhydrous
E_o (V SHE)	-0.440	1.228	1.228	1.244	1.311
i_o (nA cm^{-2})	1.5×10^{-4} to 3.0×10^{-7}	0.12	5.2×10^{-5}	1.0 to 500	0.5 to 500
i_{lim}anodic (nA cm^{-2})	not required	1.0×10^{21}	negligible	5.6×10^{3} to 8.1×10^{4}	1.1×10^{4} to 1.0×10^{10}
i_{lim}cathodic (nA cm^{-2})	negligible	negligible	5.0×10^{4} to 2.6×10^{5}	negligible	negligible
α	0.40	0.60	0.37 to 0.44	0.50	0.50
Temperature	24 to 45°C				
pH	8.0				
Resistance	15 to 100Ω				

Table 4.5.8 Range of parameters used to model 316 stainless steel in natural seawater.

	i_{pass} (nA cm^{-2})	A	P	E_t
Reaction 1	430	975	2.0	-0.370

Table 4.5.9 Range of passivation parameters for model of 316 stainless steel in natural seawater.

4.5.4 ANALYSIS OF MODELLING TRENDS

It can be seen (Figure 4.5.1) that the shape of the active-to-passive transition 'nose' of 316 stainless steel in deaerated 5% H_2SO_4 is different to that of 304 stainless steel in the same media. In aerated electrolyte (Figure 4.5.2), the samples show stable passivity at all temperatures. The stagnant electrolyte (Figure 4.5.3) shows the enhanced resistance of the passive film on 316 compared to 304, with only the 45°C electrolyte leading to unstable passivity. The 35°C experiment (Figure 4.5.15) shows a decrease in current density below the free corrosion potential, but without a 'triple point' occurring; instead, the current density remains cathodic in nature at all potentials more electronegative than the free corrosion potential. This is modelled (Section 4.5.3.12) by making the total cathodic current (*ie* that from both Reaction 3 and Reaction 7) being just smaller than the total anodic current in the active-to-passive transition 'nose', but with added criteria that the oxygen reduction line does not intersect the active-to-passive 'nose'.

4.5.4.1 Modelling the Behaviour of 316 Stainless Steel in 5% H_2SO_4 - Variation of Reaction 7 i_{lim} and α

Figure 4.5.2.21 shows the variation of i_{lim} (listed in Table 4.5.10) for Reaction 7 for 316 stainless steel in 5% H_2SO_4. Comparison with the same graph for 304 stainless steel (Figure 4.3.26) shows that i_{lim} is not the same for the two alloys, although the general form of the variation with temperature for the two different oxygen concentrations are roughly similar (Figures 4.5.22 and Figure 4.5.23).

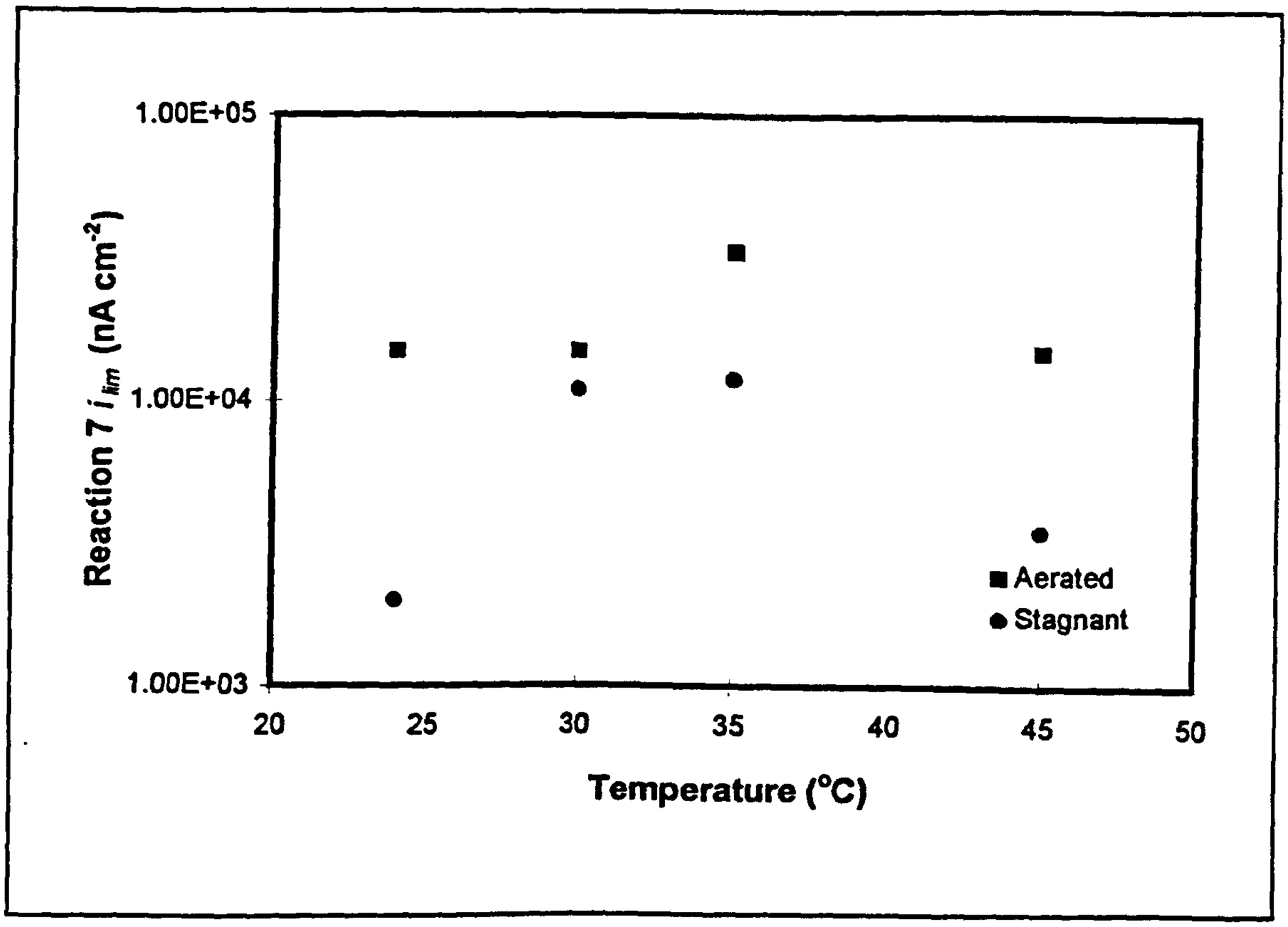

Figure 4.5.21 Variation of Reaction 7 i_{lim} with temperature for 316 stainless steel in 5% H_2SO_4.

	Aerated	Stagnant
24°C	1.5×10^4	2.0×10^3
30°C	1.5×10^4	1.1×10^4
35°C	3.3×10^4	1.2×10^4
45 °C	1.5×10^4	3.5×10^4

Table 4.5.10 Reaction 7 i_{lim} values for 316 stainless steel in 5% H_2SO_4.

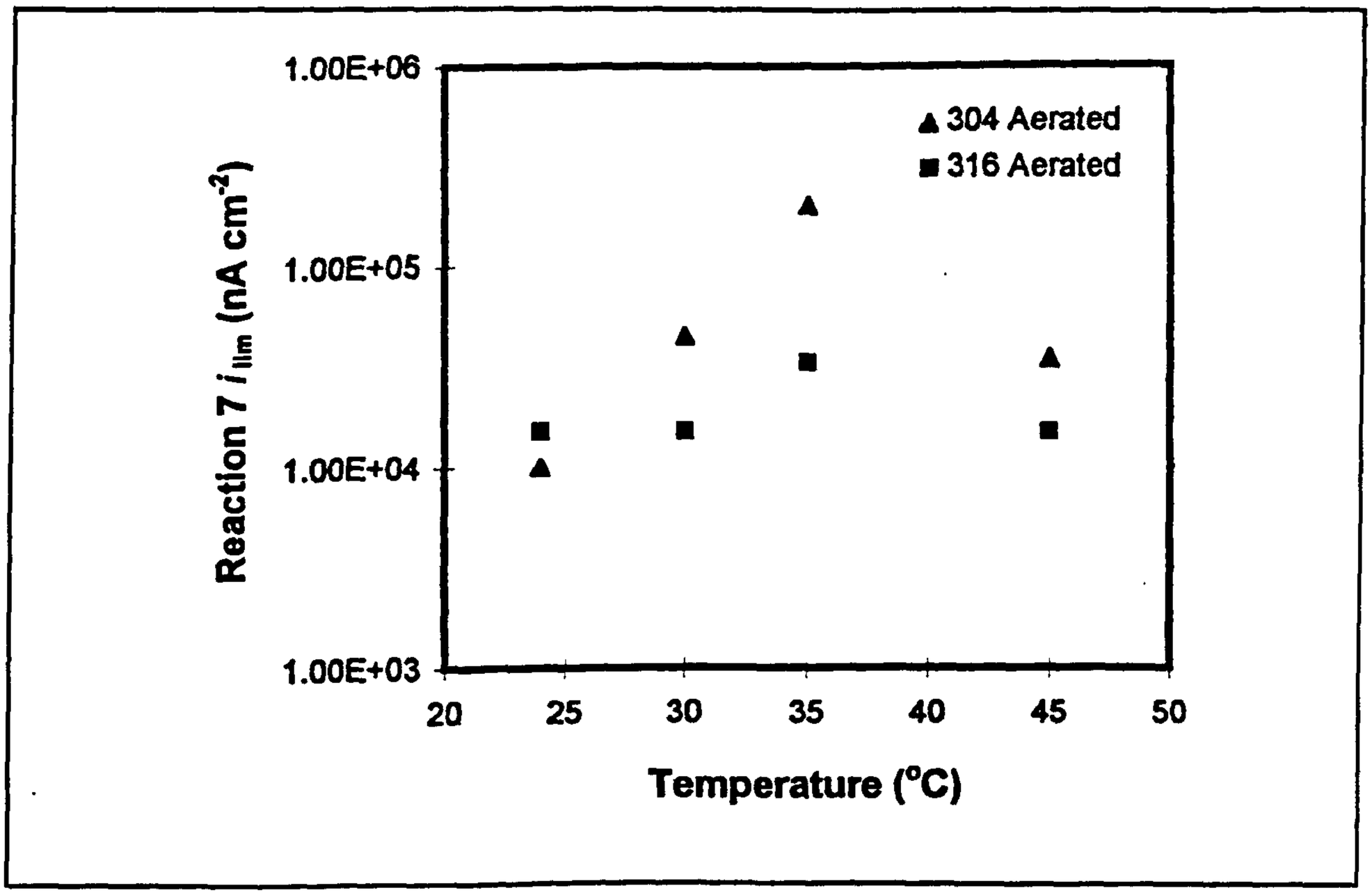

Figure 4.5.22 Variation of Reaction 7 i_{lim} for 304 and 316 stainless steels in aerated 5% H_2SO_4.

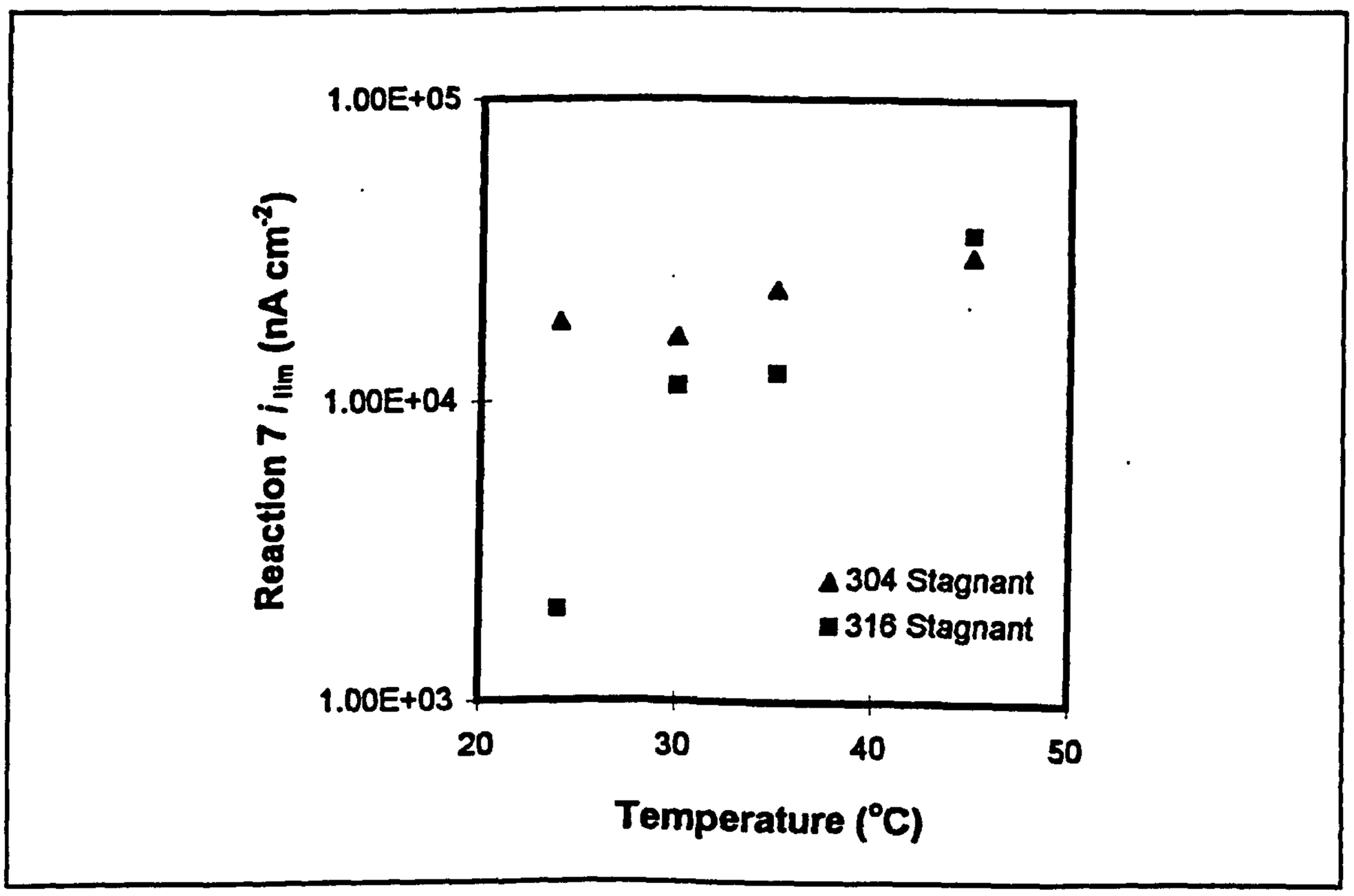

Figure 4.5.23 Variation of Reaction 7 i_{lim} for 304 and 316 stainless steels in stagnant 5% H_2SO_4.

The α values for Reaction 7 are listed in Table 4.5.11, and shown in Figure 4.5.24. Comparison with Figure 4.3.31 (Reaction 7 α values for 304) reveals no common trends.

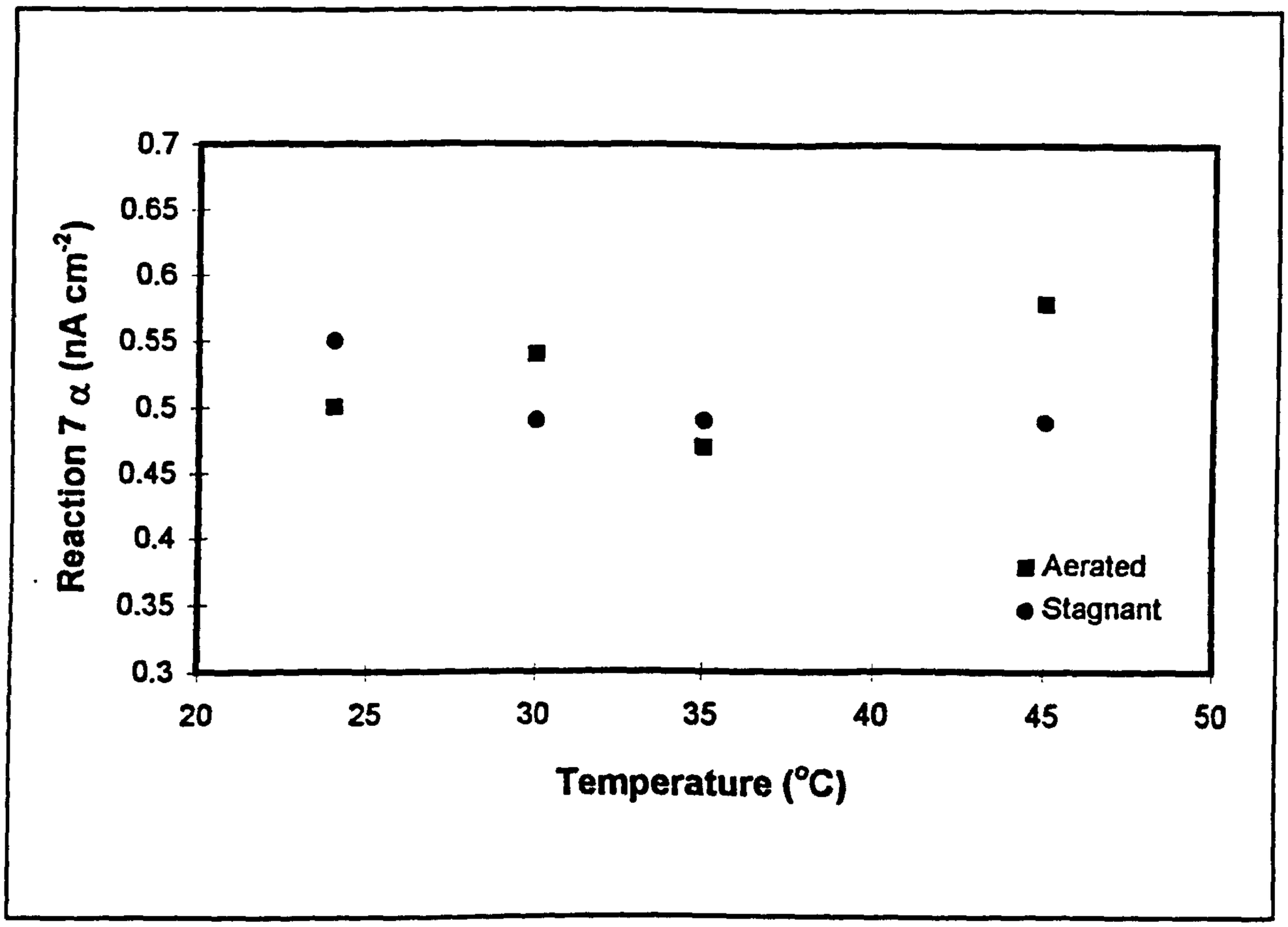

Figure 4.5.24 Variation of Reaction 7 α for 316 stainless steel in 5% H_2SO_4.

	Aerated	Stagnant
24 °C	0.50	0.55
30°C	0.54	0.49
35°C	0.47	0.49
45°C	0.58	0.49

Table 4.5.11 Variation of Reaction 7 α with temperature for 316 stainless steel in 5% H_2SO_4.

4.5.4.2 Modelling the Behaviour of 316 Stainless Steel in 5% H_2SO_4 variation of Reaction 1 i_o with Temperature and Oxygen Concentration

As was found for 304 stainless steel in 5% H_2SO_4, the polarization curve behaviour cannot be solely modelled by variation of Reaction 7 i_{lim} and α. Rather, the resultant curve also depends on the interaction on the oxygen reduction line with that representing the iron dissolution reaction. The position of this line depends upon the i_o value used for Reaction 1, which was found to be dependent on the concentration of dissolved oxygen. Figure 4.5.25 and Table 4.3.12 shows the values of i_o used to model Reaction 1 for 316 stainless steel in 5% H_2SO_4.

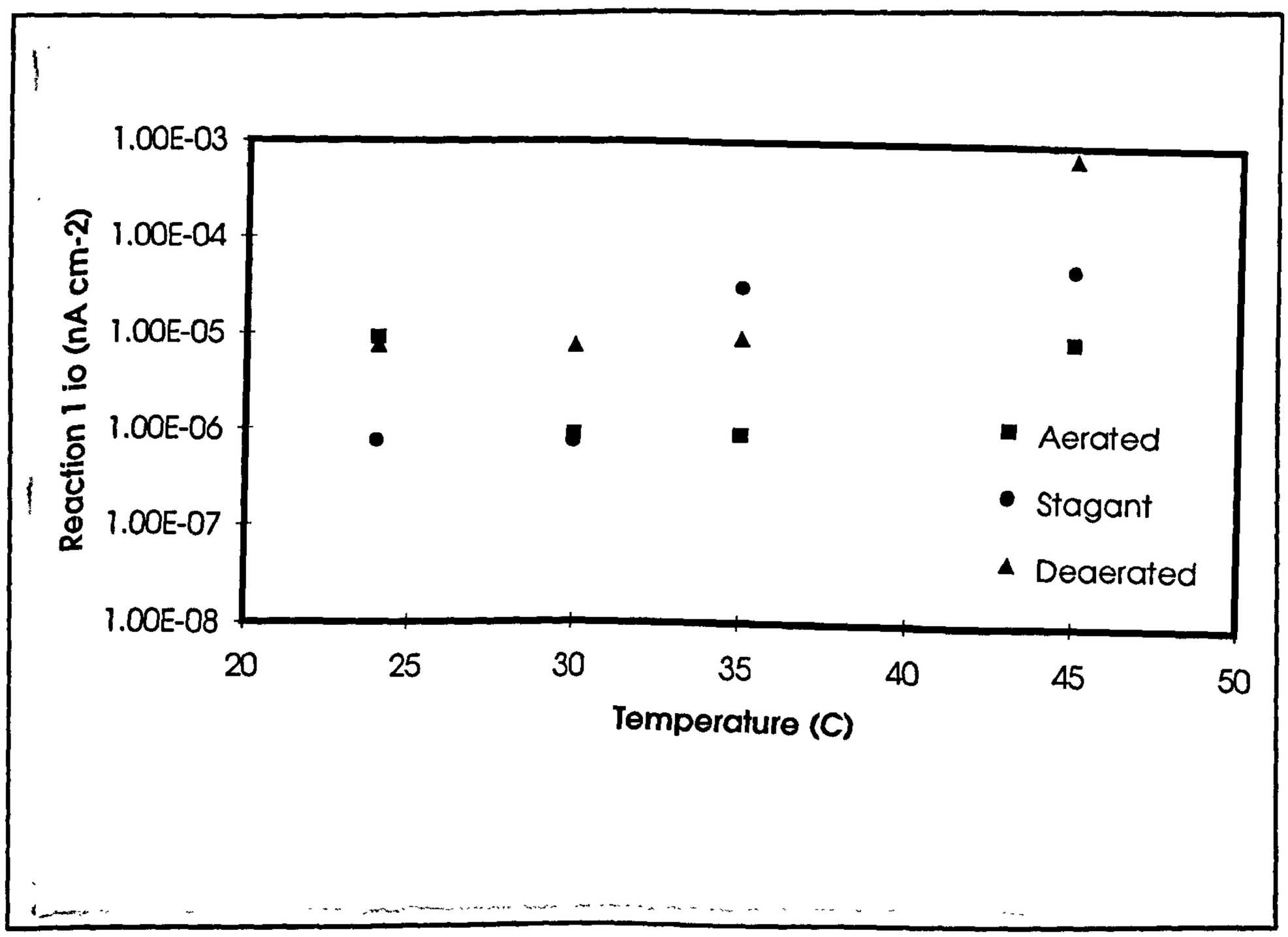

Figure 4.5.25 Variation of Reaction 1 i_o for 316 stainless steel with temperature for 316 stainless steel in 5% H_2SO_4.

	Aerated	Stagnant	Deaerated
24°C	9.0×10^{-6}	7.5×10^{-7}	7.5×10^{-6}
30°C	9.0×10^{-7}	7.5×10^{-7}	7.5×10^{-6}
35°C	9.0×10^{-7}	3.0×10^{-5}	9.0×10^{-6}
45°C	9.0×10^{-6}	5.0×10^{-5}	7.5×10^{-4}

Table 4.5.12 Variation of Reaction 1 i_o for 316 stainless steel in 5% H_2SO_4.

Comparison of Reaction 1 i_o values for 304 and 316 stainless steel in 5% H_2SO_4 (Tables 4.3.12 and 4.5.12, Figures 4.3.27 and 4.5.25 respectively) shows that deaerated solutions lead to modelled i_o values in the range 10^{-4} to 10^{-6} nA cm^{-2}. Aerated and stagnant solutions which yield curves exhibiting stable passivity have modelled i_o values of magnitude 10^{-7} nA cm^{-2}, while those curves exhibiting unstable passivity (or close to unstable behaviour *eg* 316 stainless steel in stagnant 5% H_2SO_4 at 35°C) in aerated electrolyte have modelled i_o values of magnitude in the range 10^{-4} to 10^{-5} nA cm^{-2}.

4.5.4.3 Modelling the Iron Dissolution Reaction Behaviour for 316 Stainless Steel and Ferralium in Natural Seawater

The experiments carried out in natural seawater all showed (Figure 4.5.4) behaviour indicative of stable passivity, with breakdown occurring at between 30-310 mV SCE, depending upon temperature. The variation of Reaction 1 i_o with temperature for 316 stainless steel in natural seawater is shown in Figure 4.5.26 (Table 4.5.13), with the values used for Ferralium (see Section 4.4) also shown.

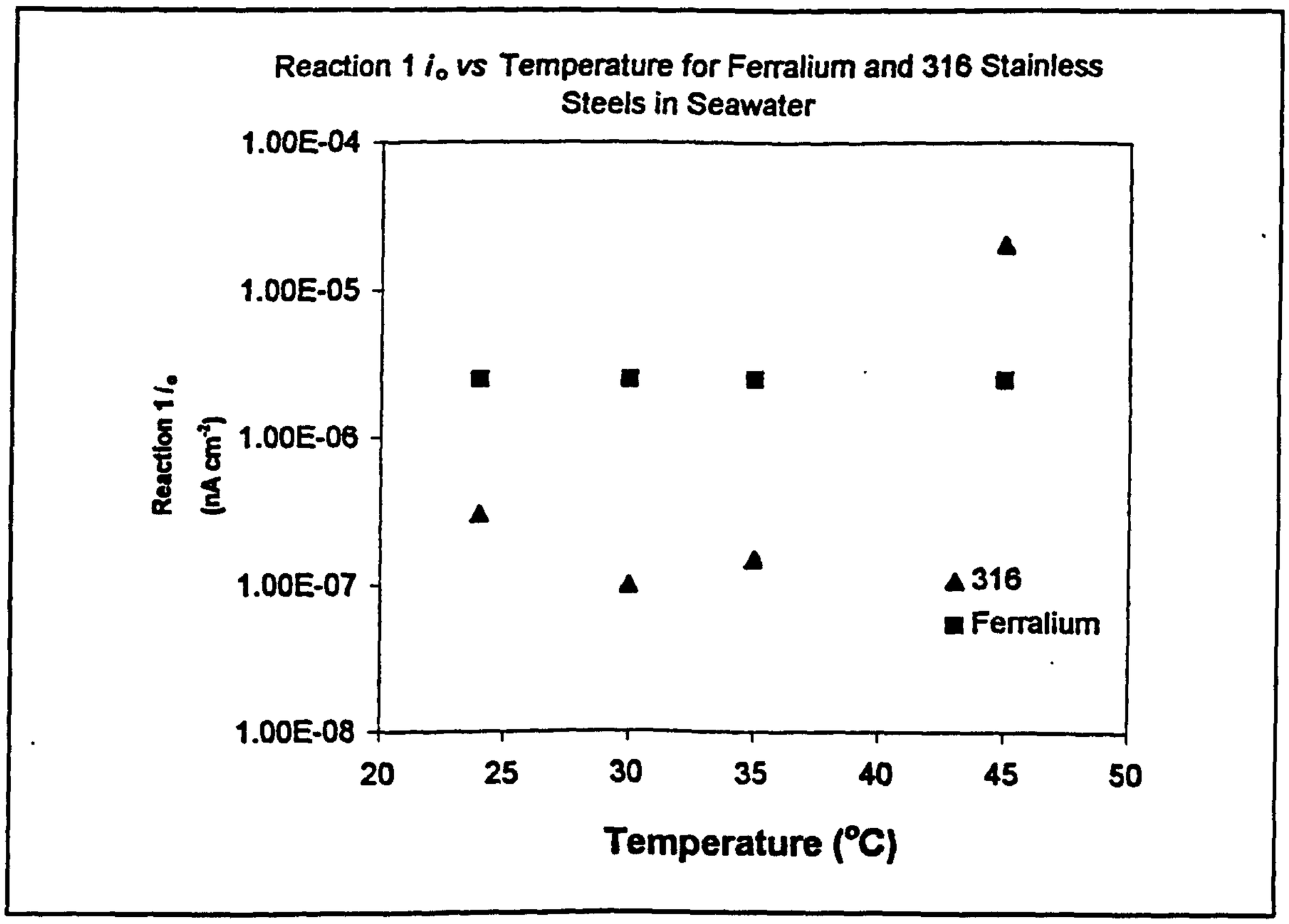

Figure 4.5.26 Variation of Reaction 1 i_o with temperature for 316 stainless steel and Ferralium in natural seawater.

	316 Reaction 1 i_o (nA cm^{-2})	Ferralium Reaction 1 i_o (nA cm^{-2})
24°C	3.0×10^{-6}	2.5×10^{-6}
30°C	1.0×10^{-7}	2.5×10^{-6}
35°C	1.5×10^{-7}	2.5×10^{-6}
45°C	2.0×10^{-5}	2.5×10^{-6}

Table 4.5.13 Reaction 1 i_o values for 316 stainless steel and Ferralium in natural seawater.

It can be seen that the values used to model the behaviour of Ferralium remain constant, while those used for 316 vary. As noted in the previous section, curves exhibiting stable passivity are modelled by using values of i_o less than 10^{-5} nA cm^{-2}, and this is also the case for all but one of the curves modelled here. The exception is 316 in 45°C electrolyte, which also has the lowest breakdown potential (~30 mV SCE) of all the 316 experiments. In this case, an i_o value of 2.0×10^{-5} nA cm^{-2} is used, which is two orders of magnitude greater than the other values used to model 316 in natural seawater. It is also close to the value of 5.0×10^{-5} nA cm^{-2} used to model the 'triple point' curve of 316 stainless steel in stagnant 5% H_2SO_4. It is suggested that the low breakdown potential is a result of incipient unstable passive behaviour, and that the increased value of i_o required to model the 45°C polarization curve is indicative of this.

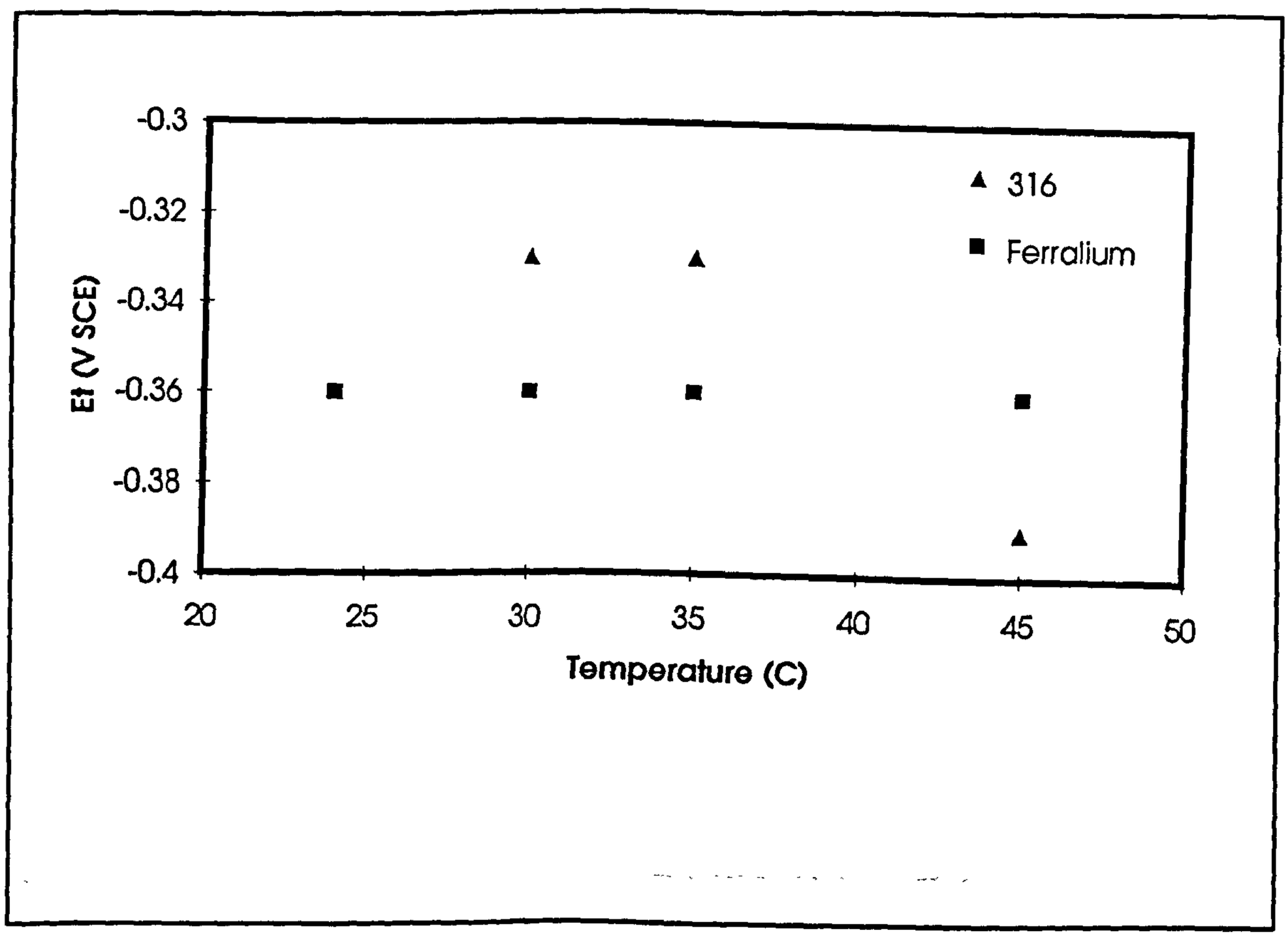

Figure 4.5.27 Variation of E_t with temperature for 316 stainless steel and Ferralium in natural seawater.

Figure 4.5.27 and Table 4.5.14 show the values of E_t used to model the behaviour

of the two alloys in natural seawater.

	316 E_t (V SCE)	Ferralium E_t (V SCE)
24°C	-0.36	-0.36
30°C	-0.33	-0.36
35°C	-0.33	-0.36
45°C	-0.39	-0.36

Table 4.5.38 E_t values used to model the behaviour of 316 stainless steel and Ferralium in natural seawater.

As for the i_0 values, the value of E_t used to model the behaviour of Ferralium remains constant with temperature, while that of 316 varies. The most electronegative value is that used for 316 in 45°C electrolyte.

4.5.4.4 Modelling Reaction 7 for 316 Stainless Steel and Ferralium in Seawater

Table 4.5.39, Figures 4.5.28 and 4.5.29 show the variation of the diffusion-limited cathodic current density and α for Reaction 7 with temperature.

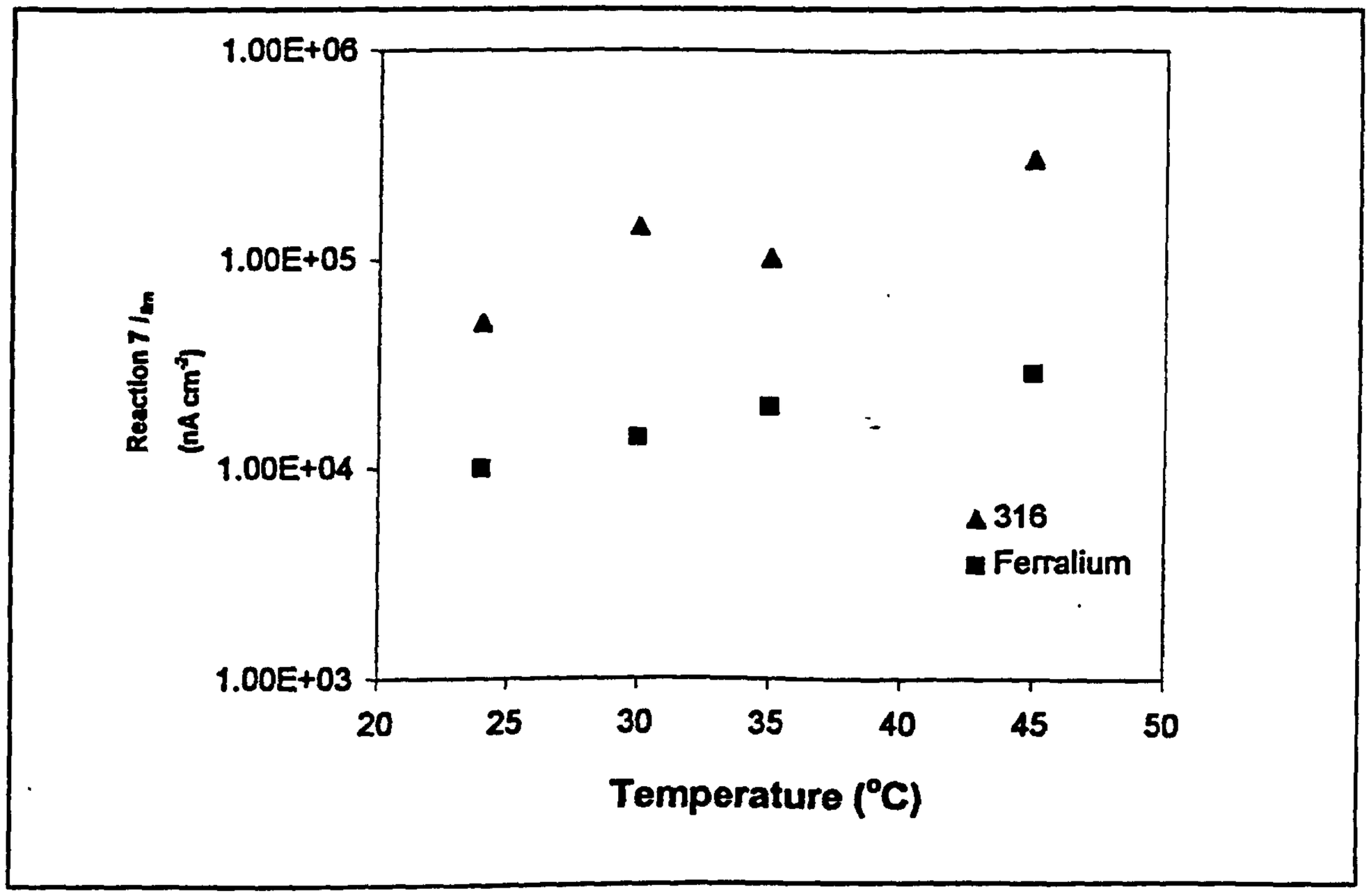

Figure 4.5.28 Variation of Reaction 7 i_{lim} with temperature for 316 stainless steel and Ferralium in natural seawater.

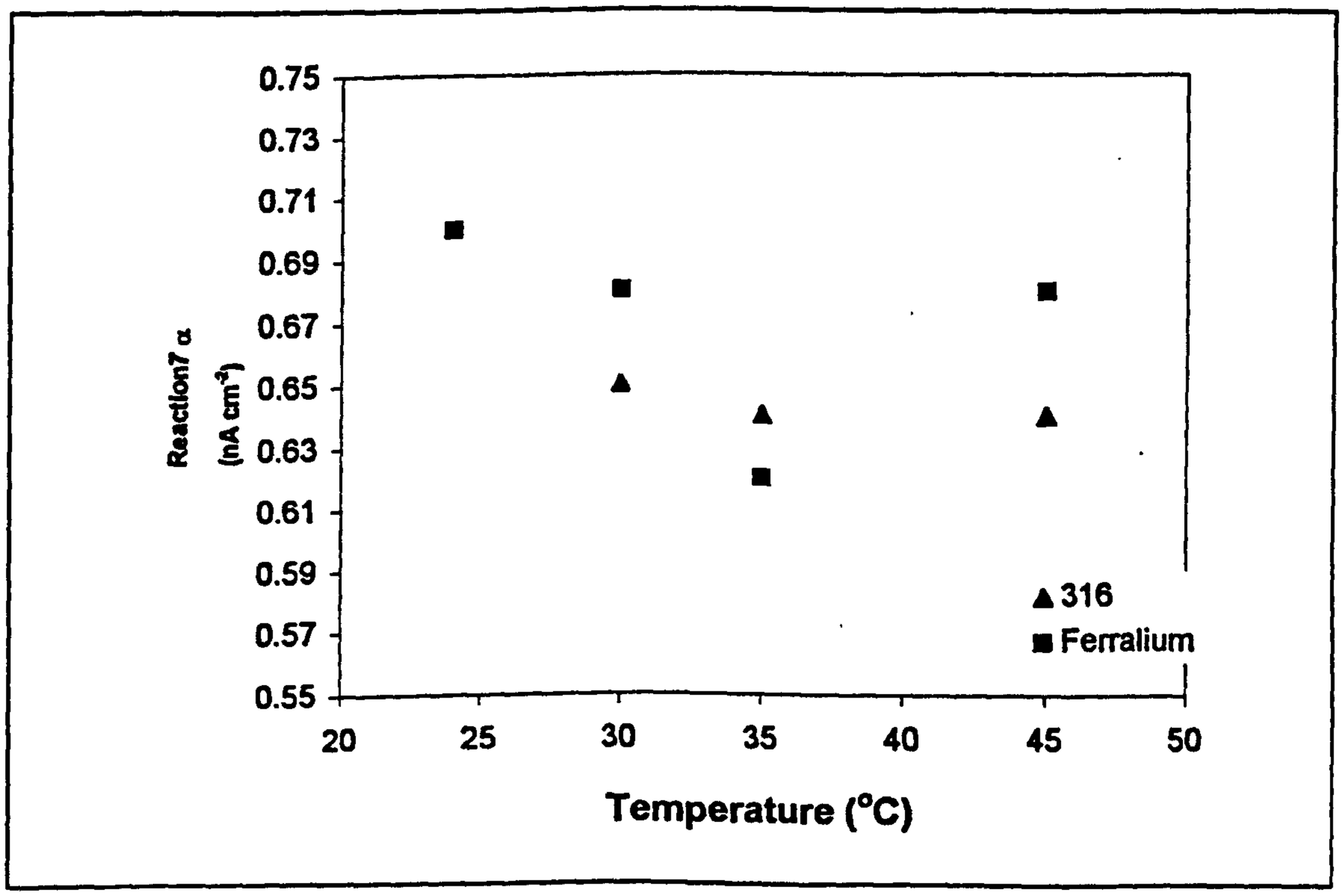

Figure 4.5.29 Variation of Reaction 7 α with temperature for 316 stainless steel and Ferralium in natural seawater.

	316 Reaction 7 i_{lim} (nA cm^{-2})	316 α	Ferralium Reaction 7 i_{lim}(nA cm^{-2})	Ferralium α
24°C	5.0×10^4	0.70	1.0×10^4	0.70
30°C	1.4×10^5	0.65	1.4×10^4	0.68
35°C	1.0×10^5	0.64	2.0×10^4	0.62
45°C	3.0×10^5	0.64	2.9×10^4	0.68

Table 4.5.39 Reaction 7 i_{lim} and α values used to model the behaviour of 316 stainless steel and Ferralium in natural seawater.

It can be seen that the α values fall with increasing temperature up to and including 35°C, a trend seen for 304 in both aerated and stagnant 5% H_2SO_4 (Figure 4.3.31). The α values for 316 and Ferralium then both increase slightly at 45°C, behaviour not repeated for 304 in 5% H_2SO_4. The values of i_{lim} for Reaction 7 on 316 and Ferralium in seawater differ, with those values for 316 being almost an order of magnitude greater than those for Ferralium. The reason for this is not clear. The values of i_{lim} show a reciprocal relationship with the concentration of dissolved oxygen in seawater, the variation of which with temperature is shown in Figure 4.5.30.

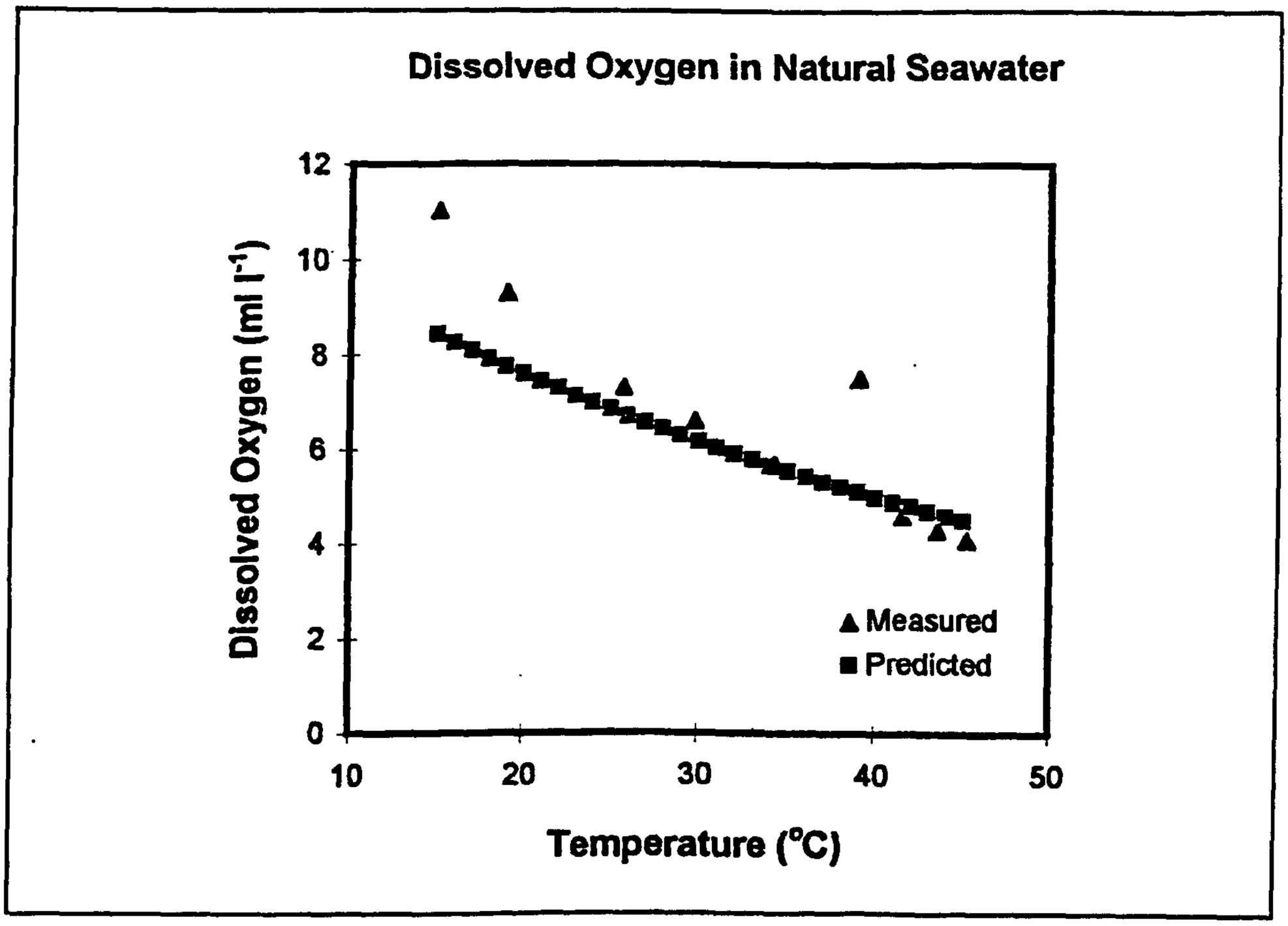

Figure 4.5.30 Variation of dissolved oxygen concentration with temperature in natural seawater.

The saturation concentration (in ml l^{-1}) of dissolved oxygen (DO_2) in seawater has been quoted as a function of temperature[159]:

$$DO_2 = 8.06Exp^{-0.021T}$$

Figure 4.5.30 shows the DO_2 values calculated by this equation plotted against the experimentally-measured values, converted into ml l^{-1}. With the exception of the 35°C experimental reading, above 20°C the correlation between theoretical and experimental values is quite close.

4.5.4.5 Modelling the Variation of E_b with Temperature for 316 Stainless Steel in Natural Seawater

The values of the i_o values used to model Reaction 9, the production of CrO_4^{2-} ions, for 316 and Ferralium in natural seawater are shown in Table 4.5.40, and plotted in Figures 4.5.31 and 4.5.32.

	316 Reaction 9 (Hydrated) i_o (nA cm^{-2})	Ferralium Reaction 9 (Hydrated) i_o (nA cm^{-2})	316 Reaction 9 (Anhydrous) i_o (nA cm^{-2})	Ferralium Reaction 9 (Anhydrous) i_o (nA cm^{-2})
24°C	50	5.0×10^{-5}	5.1×10^{3}	3.0×10^{3}
30°C	100	300	0.5	4.0×10^{4}
35°C	300	3.0×10^{4}	5.1×10^{7}	3.4×10^{5}
45°C	10	2.0×10^{3}	4.1×10^{6}	2.5×10^{6}

Table 4.5 40 Variation of Reaction 9 i_o with temperature for 316 stainless steel and Ferralium in natural seawater.

It may be seen that the Reaction 9 i_o values for Ferralium show a much greater spread than for 316, which is indicative of a much wider range of breakdown potentials.

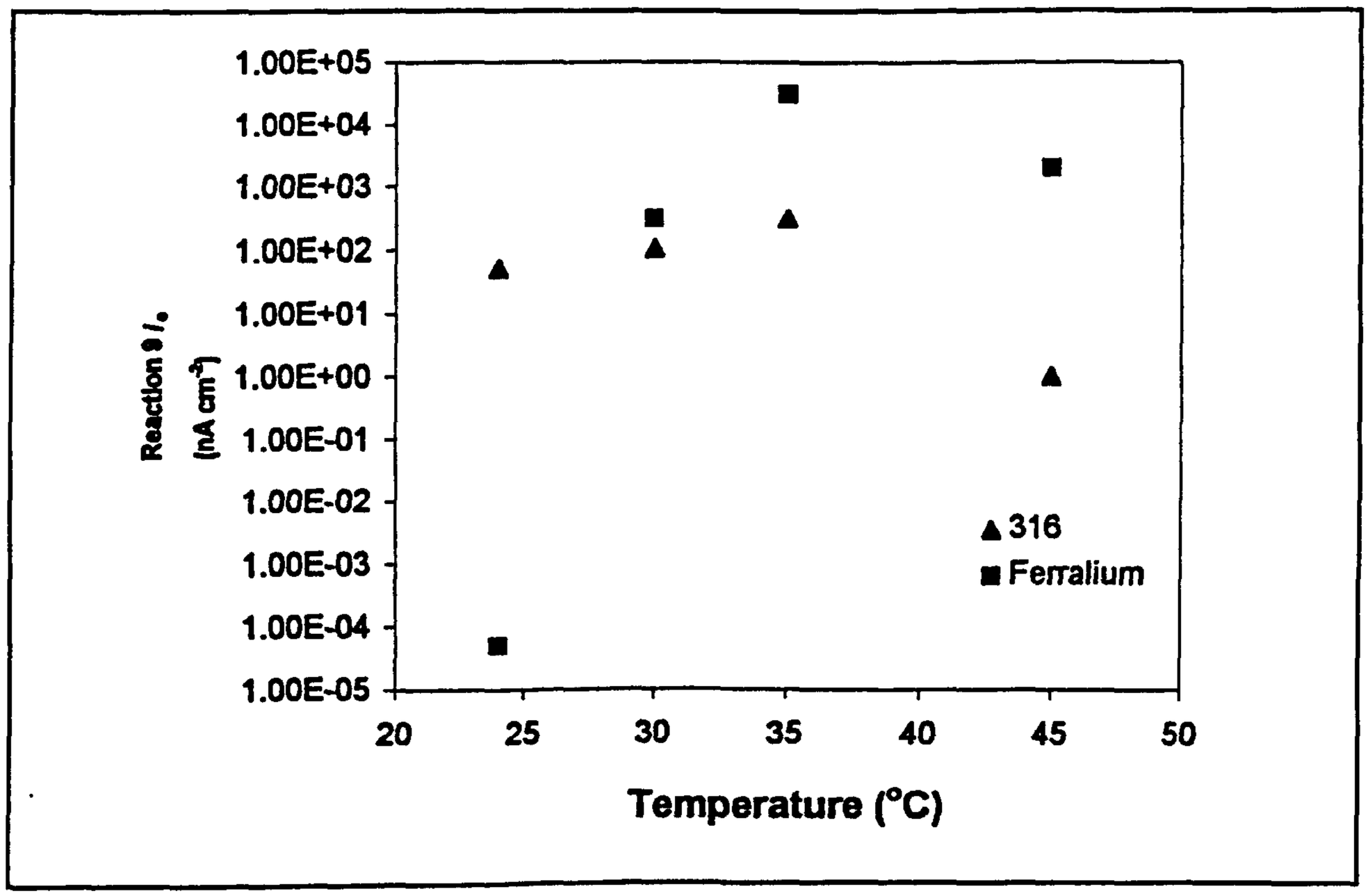

Figure 4.5.31 Variation of Reaction 9 (hydrated) i_o with temperature for 316 and Ferralium in natural seawater.

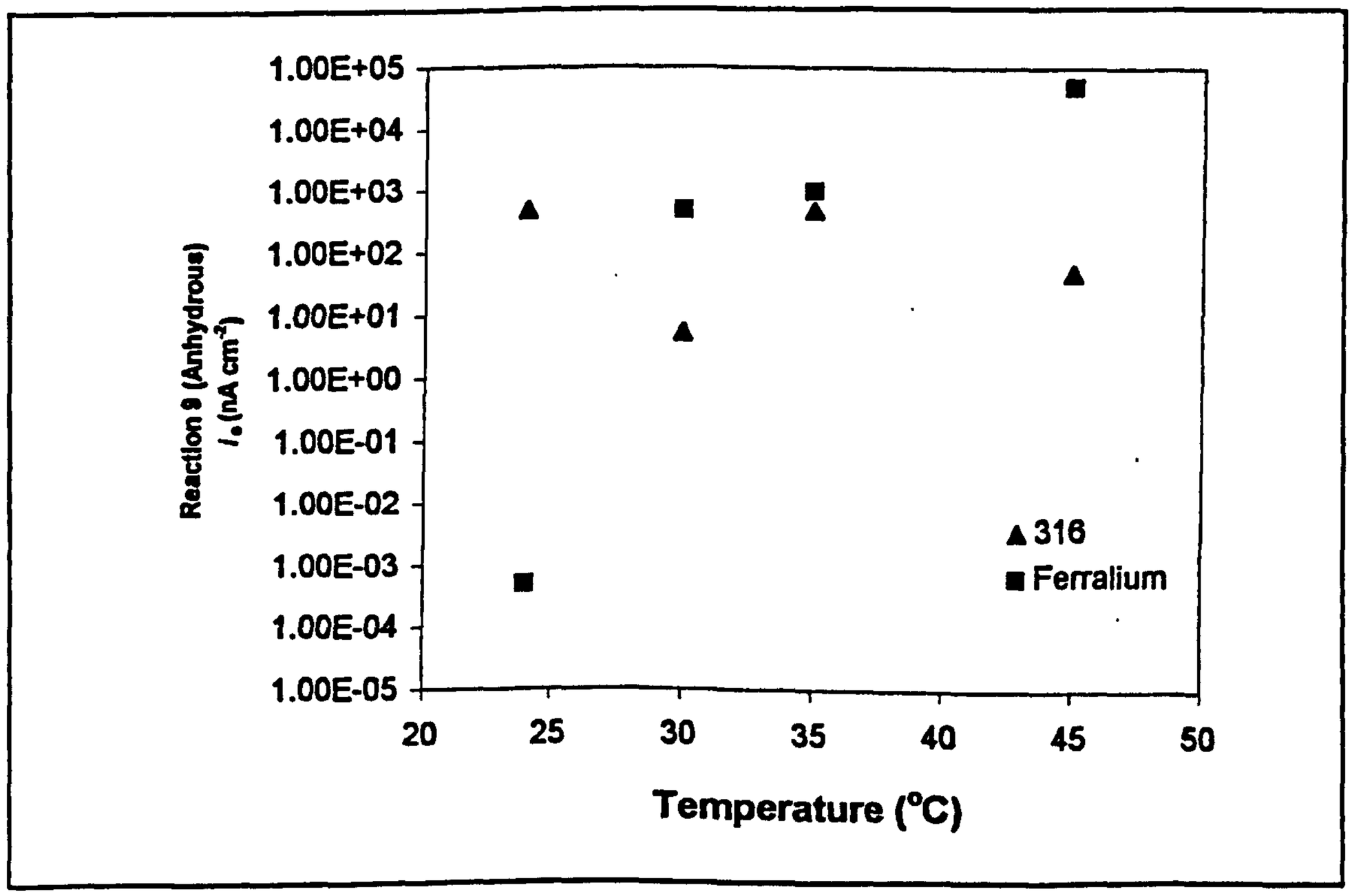

Figure 4.5.32 Variation of Reaction 9 (anhydrous) i_o with temperature for 316 and Ferralium in natural seawater.

4.5.5 CONCLUDING REMARKS

The polarization behaviour of 316 stainless steel in 5% H_2SO_4 with three different levels of dissolved oxygen at temperatures between 24 and 45°C has been investigated. The polarization curves have been modelled using the models described in Section 4.3, and comparisons made with modelling trends found for 304 stainless steel in the same media. As for 304, the deaerated solution led to curves exhibiting clearly defined active-to-passive 'noses', but in contrast to 304, of all experiments in oxygen-containing electrolyte, only the stagnant 45°C solution lead to 316 exhibiting unstable passive behaviour, the rest showing stable passivity.

The change in polarization curve behaviour for the three levels of dissolved oxygen again could not be solely attributable to the addition of, and change in, the diffusion-limited current density of the oxygen reduction reaction. The diffusion-limited current densities were found to be different for 304 and 316 stainless steel, despite using the same electrolyte and aeration regimes.

The i_o values used to model Reaction 1 showed similar trends to those used to model 304 stainless steel; namely, values of 10^{-4} to 10^{-6} nA cm^{-2} for deaerated solutions, 10^{-6} to 10^{-7} nA cm^{-2} for stable passive behaviour in aerated solutions, and 10^{-4} to 10^{-5} nA cm^{-2} for unstable passivity in oxygen-containing electrolytes.

The polarization behaviour of 316 stainless steel in natural seawater at temperatures between 24 and 45°C has also been investigated, and comparisons made with the parameters used to model Ferralium duplex stainless steel in the same media. Both alloys showed stable passivity at all temperatures. The i_o values used to model Reaction 1 are all

in the range 10^{-6} to 10^{-7} nA cm^{-2} previously found to model stable passivity in 5% H_2SO_4, with the exception of the value of 2.0 x 10^{-5} nA cm^{-2} which was used for 316 at 45°C.

The i_{lim} values for Reaction 7 were found to be different for 316 and Ferralium, again despite using the same electrolyte and aeration routines.

Ferralium exhibited a greater range of breakdown potentials than for 316 stainless steel. This was modelled by using a much wider spread of i_o values for Reaction 9, which models the production of CrO_4^{2-} ions.

4.2.6 Conclusions

The polarization curve behaviour of a number of stainless steels in marine and acid environments of differing temperature and dissolved oxygen content have been investigated. Models for such systems have been proposed, and used to provide accurate theoretical descriptions of experimental behaviour for potential range in excess of 2 V.

The raindrop equation has successfully been used to model the passivating behaviour of a number of stainless steel in acid and marine environments, using the percolation model of iron dissolution. The transition between stable and unstable passivity was found to be dependent upon the interaction between the oxygen reduction diffusion limited current density and the iron dissolution-passivation curve. This latter reaction was found to be dependent upon the iron dissolution free corrosion current density, which was shown to depend upon the temperature and dissolved oxygen concentration of the electrolyte.

A new model for the transpassive dissolution of stainless steels was proposed.

Appendices

APPENDIX A CALCULATIONS FOR CRYOGENIC FITTING OF NAB INSERT

Thermal expansion rate for NAB	$17 \times 10^{-6}\ K^{-1}$
Diameter of NAB insert	63.2 mm
Temperature of liquid nitrogen	-195.8 °C

shrinkage $= 17 \times 10^{-5} \times 63.2 \times 195.8$ mm

$= 0.210$ mm

Therefore, NAB will contract by 0.210 mm for a diameter of 63.2 mm when immersed in liquid nitrogen.

APPENDIX B POTENTIODYNAMIC CURVES FOR NAB AND TITANIUM IN 5, 50 AND 100 % CONDUCTIVITY SEAWATER AT DIFFERING FLOW RATES

NAB in Full Strength Seawater, Static Flow

```
Model 352/252 Corrosion Analysis Software, v.   2.01
Filename:  a:\JSNAB1C Pstat:  M273A[96] Ver 200
PD POTENTIODYNAMIC    File Status:  NORMAL
Date Run:  03-09-95   Time Run:  16:15:37
CP  PASS vs. R        CT  PASS
IP   -0.220 vs. R     ID  PASS
FP    0.100 vs. R     SI   1.000E-03        SR   1.000E-04
ST   1.000E+01        CR  AUTO              NP  215
IR  NONE              FL  NONE
RT  HIGH STABILITY    REF 0.24150 SCE       WRK SOLID
AR   1.140E+00        LS  NO                EW   0.000E+00
DEN  0.000E+00        OC  -0.185
Comment:  NAB in SW Static, rtp
```

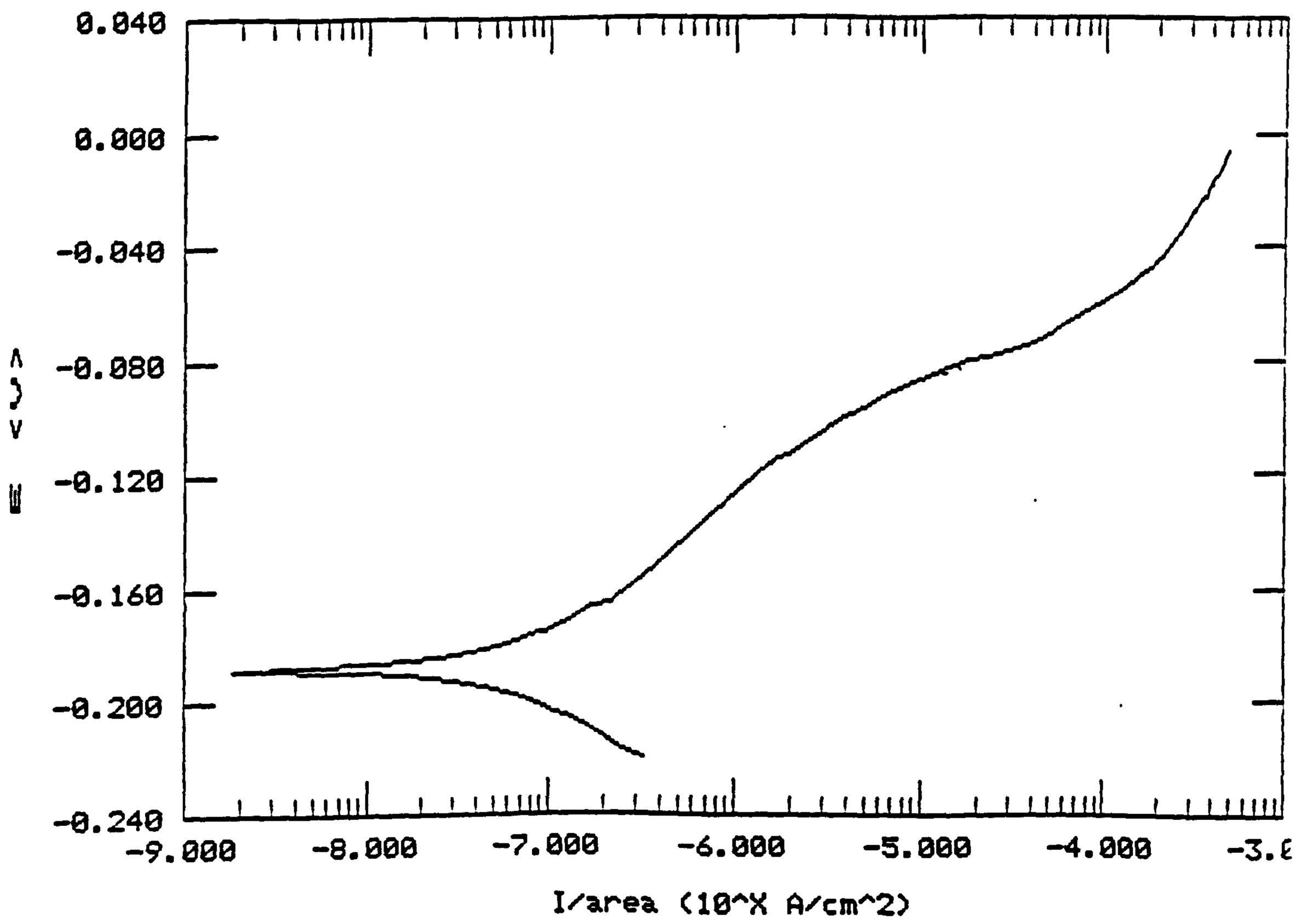

NAB in 50% Conductivity Seawater, Static Flow

Model 352/252 Corrosion Analysis Software, v. 2.01
Filename: A:\JSNAB3.DAT Pstat: M273A[96] Ver 200
PD POTENTIODYNAMIC File Status: NORMAL Date Run: 03-02-95
Time Run: 16:55:36

CP	PASS vs. R	CT	PASS	IP	-0.200 vs. R	ID	3600 S
FP	0.180 vs. R	SI	1.000E-03	SR	1.000E-04		
ST	1.000E+01	CR	AUTO	NP	381	IR	NONE
FL	NONE	RT	HIGH STABILITY	REF	0.24150 SCE	WRK	SOLID
AR	2.047E+00	LS	NO	EW	0.000E+00		
DEN	0.000E+00	OC	-0.105				

Comment: NAB in 50x SW Static

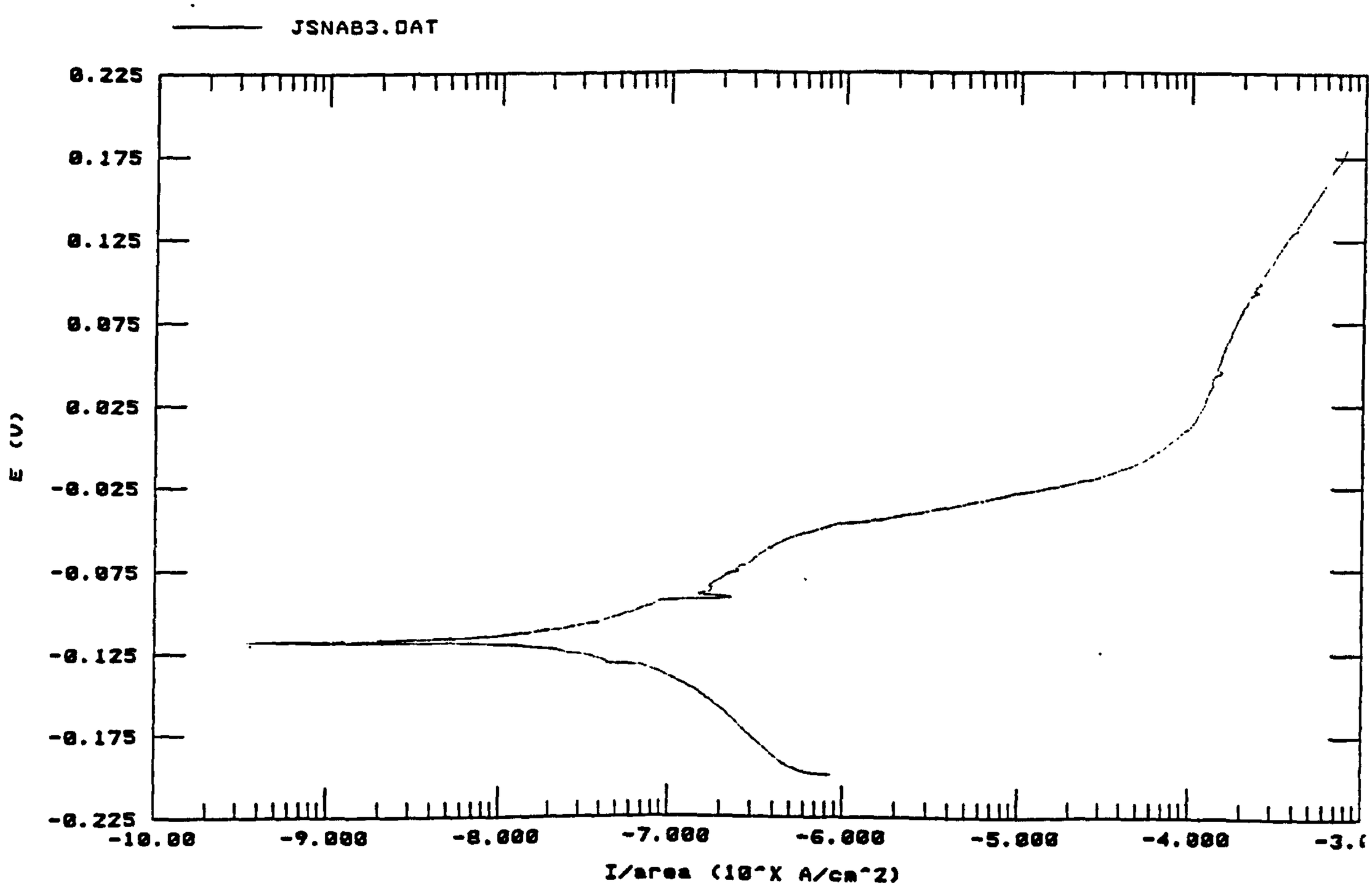

NAB in 5% Conductivity Seawater, Static Flow

```
Model 352/252 Corrosion Analysis Software, v.   2.01
Filename:  A:\JSNAB4.DAT                    Potat:  M273A[96] Ver 200
PO POTENTIODYNAMIC     File Status:  NORMAL  Date Run:  03-02-95
Time Run:  19:27:23
CP  PASS vs. R         CT  PASS              IP   -0.200 vs. R      ID  3600 S
FP    0.180 vs. R      SI   1.000E-03        SR   1.000E-04
ST    1.000E+01        CR  AUTO              NP  381                IR  NONE
FL  NONE               RT  HIGH STABILITY    REF 0.24150 SCE        WRK SOLID
AR    1.860E+00        LS  NO                EW   0.000E+00
DEN   0.000E+00        OC  -0.092
Comment:  NAB in 5x SW Static
```

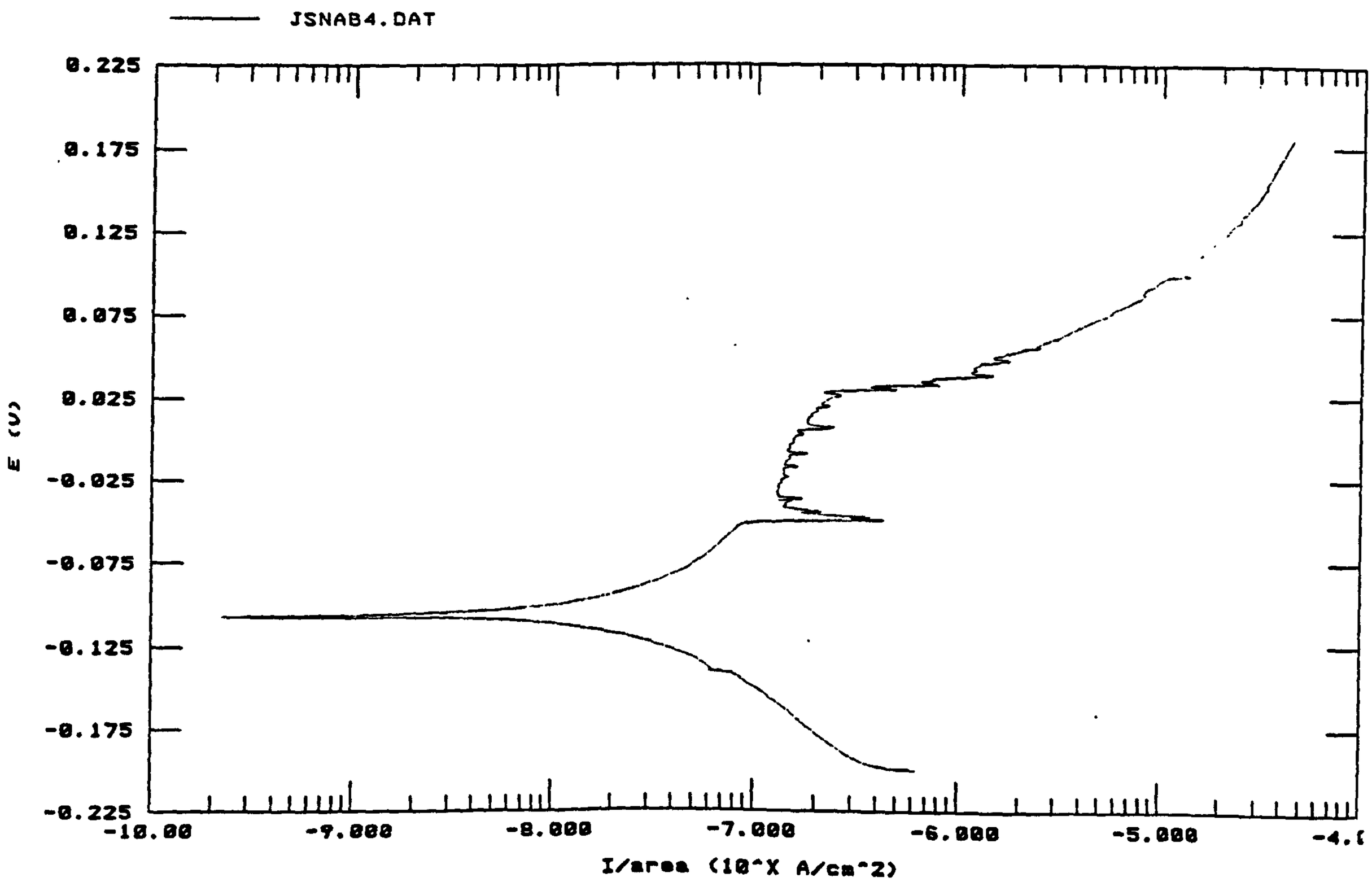

```
Model 352/252 Corrosion Analysis Software, v.   2.01
Filename:  a:\JSNAB12 Pstat:  M273A[96] Ver 200
PD POTENTIODYNAMIC    File Status:  NORMAL
Date Run:  03-06-95   Time Run:  11:36:04
CP  PASS vs. R        CT  PASS
IP   -0.230 vs. R     ID  3600 S
FP    0.100 vs. R     SI   1.000E-03          SR   1.000E-04
ST   1.000E+01        CR  AUTO                NP  197
IR  NONE              FL  NONE
RT  HIGH STABILITY    REF 0.23600 SSCE        WRK SOLID
AR   1.175E+00        LS  NO                  EW   0.000E+00
DEN  0.000E+00        OC  -0.153
Comment:  NAB in SW Flowing (1m/s)
```

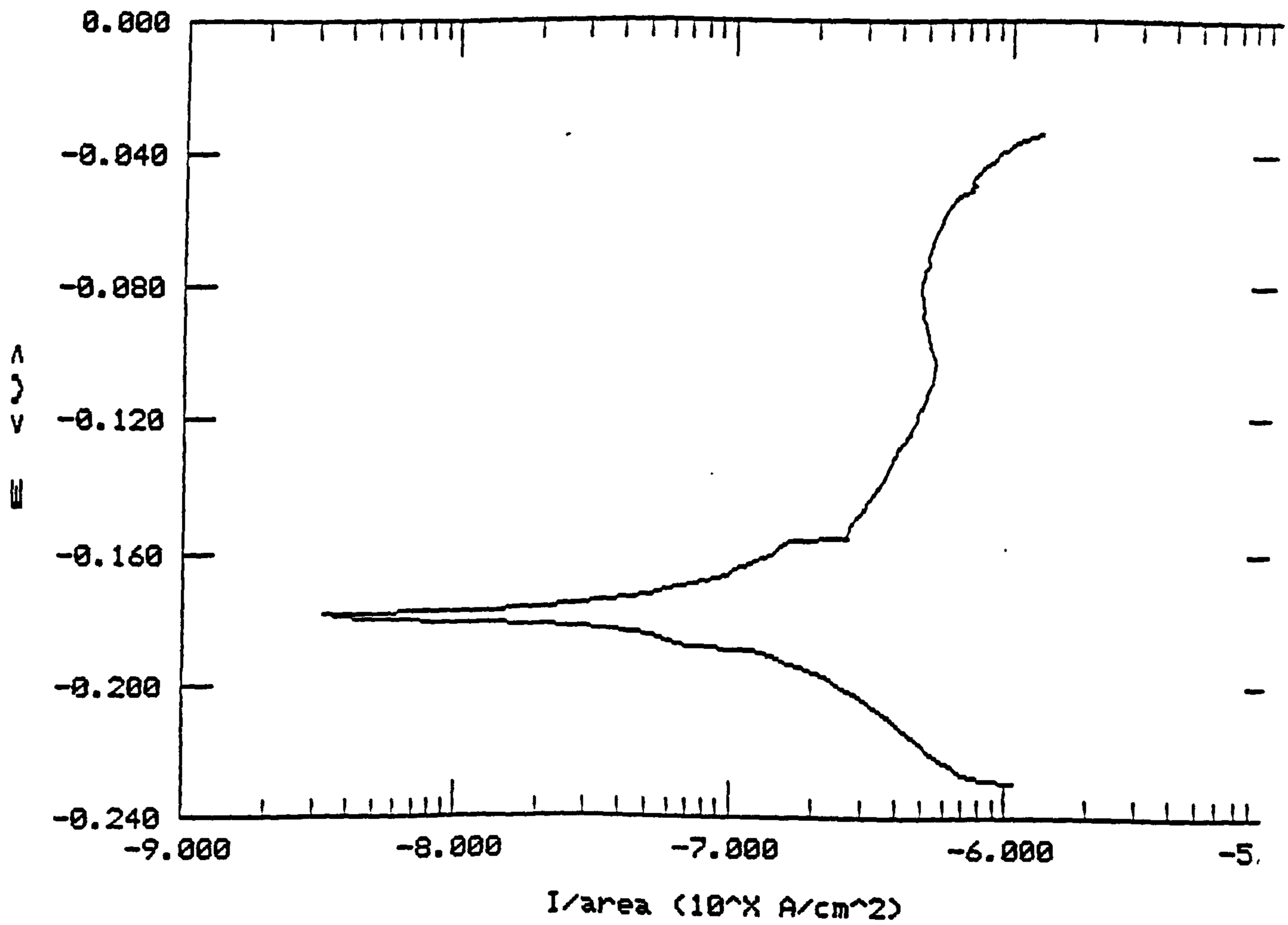

NAB in 50% Conductivity Seawater, 1 ms^{-1} Flow

```
Model 352/252 Corrosion Analysis Software, v.   2.01
Filename:  a:\JSNAB15.DAT
Pstat:  M273A[96] Ver 200
PD POTENTIODYNAMIC      File Status:  NORMAL
Date Run:  03-07-95     Time Run:  12:17:31
CP  PASS vs. R          CT  PASS
IP   -0.230 vs. R       ID  2000 S
FP    0.100 vs. R       SI   1.000E-03          SR   1.000E-04
ST   1.000E+01          CR  AUTO                NP  331
IR  NONE                FL  NONE
RT  HIGH STABILITY      REF 0.23600 SSCE        WRK SOLID
AR   1.170E+00          LS  NO                  EW   0.000E+00
DEN  0.000E+00          OC  -0.154
Comment:  NAB in 50% SW Flowing (1m/s)
```

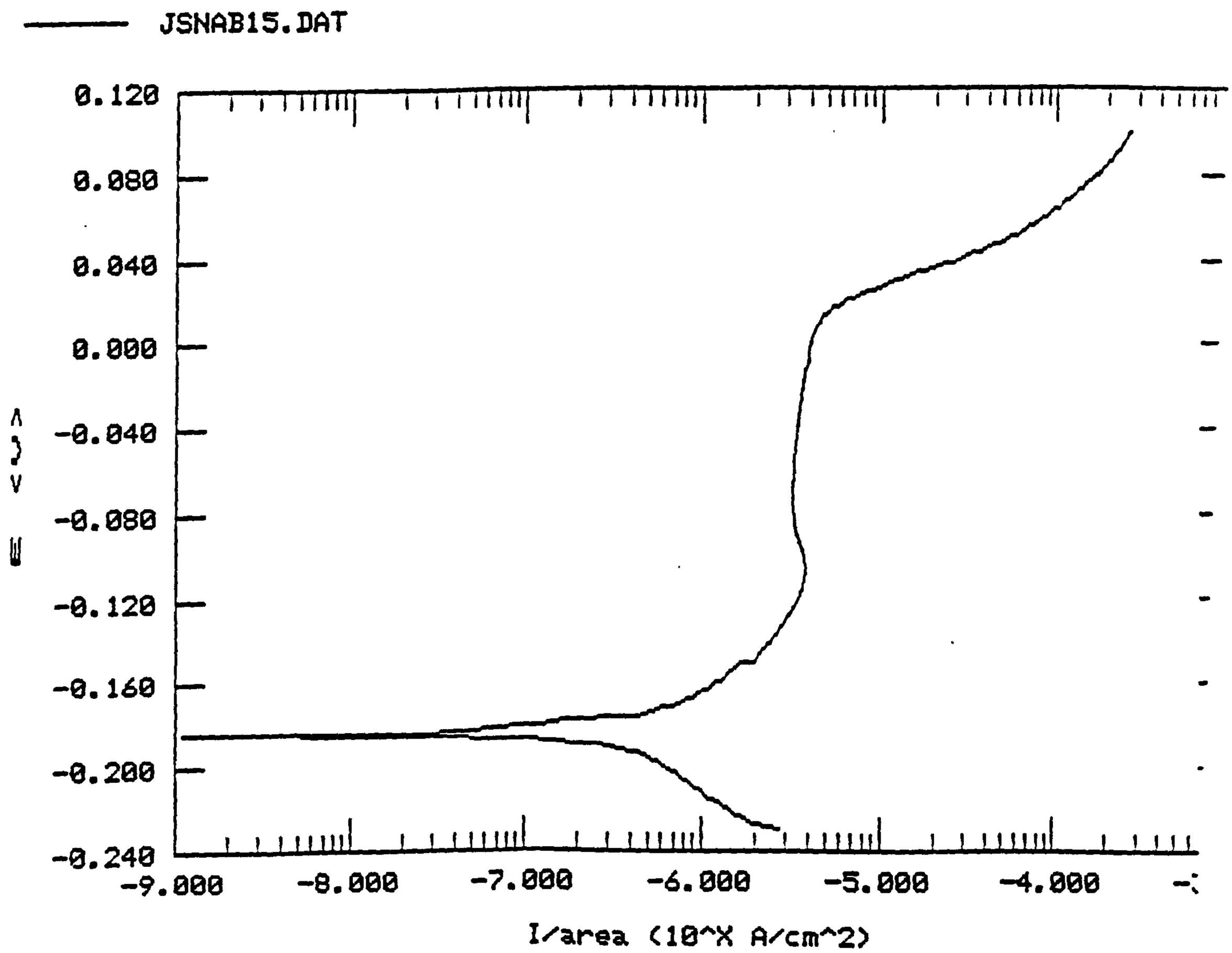

NAB in 5% Conductivity Seawater, 1 ms^{-1} Flow

```
Model 352/252 Corrosion Analysis Software, v.   2.01
Filename:  a:\jsnab6.dat
Pstat:  M273A[96] Ver 200
PD POTENTIODYNAMIC     File Status:  NORMAL
Date Run:  03-03-95    Time Run:  13:46:42
CP  PASS vs. R         CT  PASS
IP   -0.185 vs. R      ID  120 S
FP    0.160 vs. R      SI   1.000E-03          SR   1.000E-04
ST   1.000E+01         CR  AUTO                NP  346
IR  NONE               FL  NONE
RT  HIGH STABILITY     REF 0.23600 SSCE        WRK SOLID
AR   1.670E+00         LS  NO                  EW   0.000E+00
DEN  0.000E+00         OC  -0.056
Comment:  NAB in 5% SW Flowing (1m/s)
```

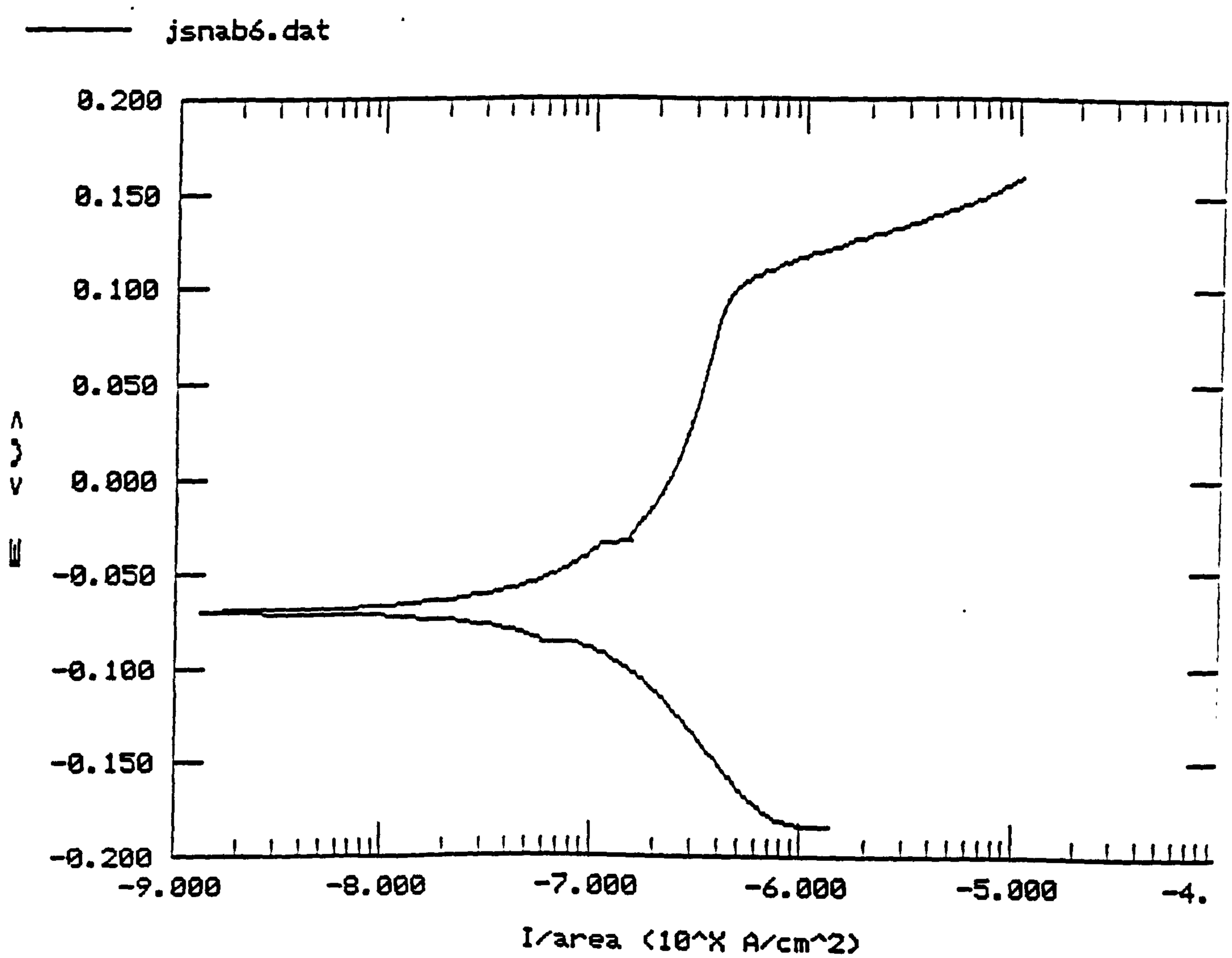

```
Model 352/252 Corrosion Analysis Software, v.   2.01
Filename:  a:\jsnab11.dat
Pstat:  M273A[96] Ver 200
PD POTENTIODYNAMIC     File Status:  NORMAL
Date Run:  03-04-95    Time Run:  15:05:04
CP  PASS vs. R         CT  PASS
IP   -0.220 vs. R      ID  PASS
FP    0.150 vs. R      SI   1.000E-03          SR   1.000E-04
ST   1.000E+01         CR  AUTO                NP  318
IR  NONE               FL  NONE
RT  HIGH STABILITY     REF 0.23600 SSCE        WRK SOLID
AR   1.758E+00         LS  NO                  EW   0.000E+00
DEN  0.000E+00         OC  -0.180
```

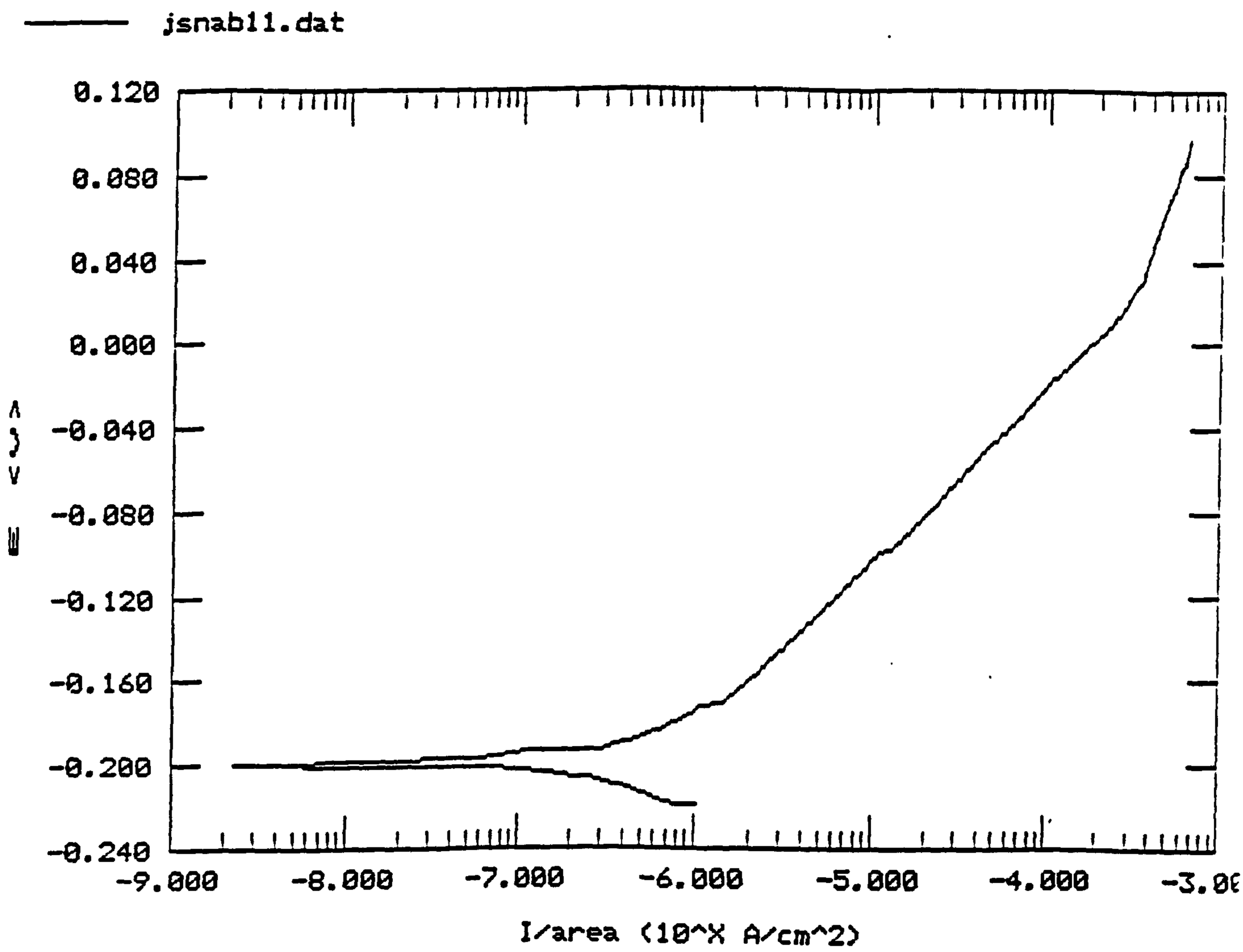

NAB in 50% Conductivity Seawater, 2 ms^{-1} Flow

```
Model 352/252 Corrosion Analysis Software, v.   2.01
Filename:  a:\jsnab16.dat
Pstat:  M273A[96] Ver 200
PD POTENTIODYNAMIC     File Status:  NORMAL
Date Run:  03-07-95    Time Run:  13:49:03
CP  PASS vs. R         CT  PASS
IP   -0.230 vs. R      ID  2000 S
FP    0.100 vs. R      SI   1.000E-03          SR   1.000E-04
ST   1.000E+01         CR  AUTO                NP  331
IR  NONE               FL  NONE
RT  HIGH STABILITY     REF 0.23600 SSCE        WRK SOLID
AR   1.170E+00         LS  NO                  EW   0.000E+00
DEN  0.000E+00         OC  -0.159
Comment:  NAB in 50% SW Flowing (2m/s)
```

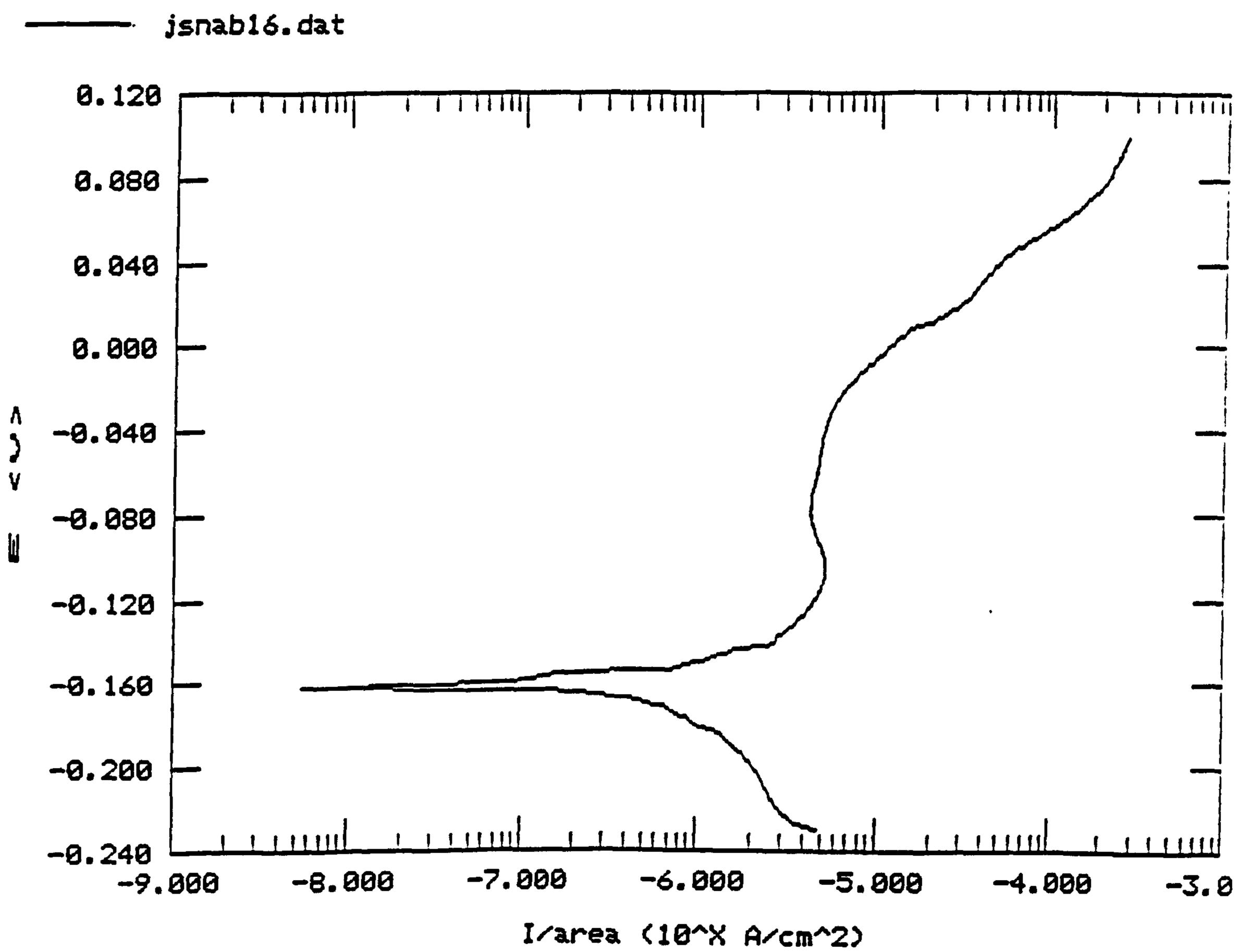

NAB in 5% Conductivity Seawater, 2 ms^{-1} Flow

```
Model 352/252 Corrosion Analysis Software, v.   2.01
Filename:  a:\jsnab8.dat
Pstat:  M273A[96] Ver 200
PD POTENTIODYNAMIC     File Status:  NORMAL
Date Run:  03-04-95    Time Run:  12:24:26
CP  PASS vs. R         CT  PASS
IP   -0.185 vs. R      ID  PASS
FP    0.150 vs. R      SI   1.000E-03          SR   1.000E-04
ST   1.000E+01         CR  AUTO                NP  336
IR  NONE               FL  NONE
RT  HIGH STABILITY     REF 0.23600 SSCE        WRK SOLID
AR   1.630E+00         LS  NO                  EW   0.000E+00
DEN  0.000E+00         OC  -0.033
Comment:  NAB in 5% SW Flowing (2m/s)
```

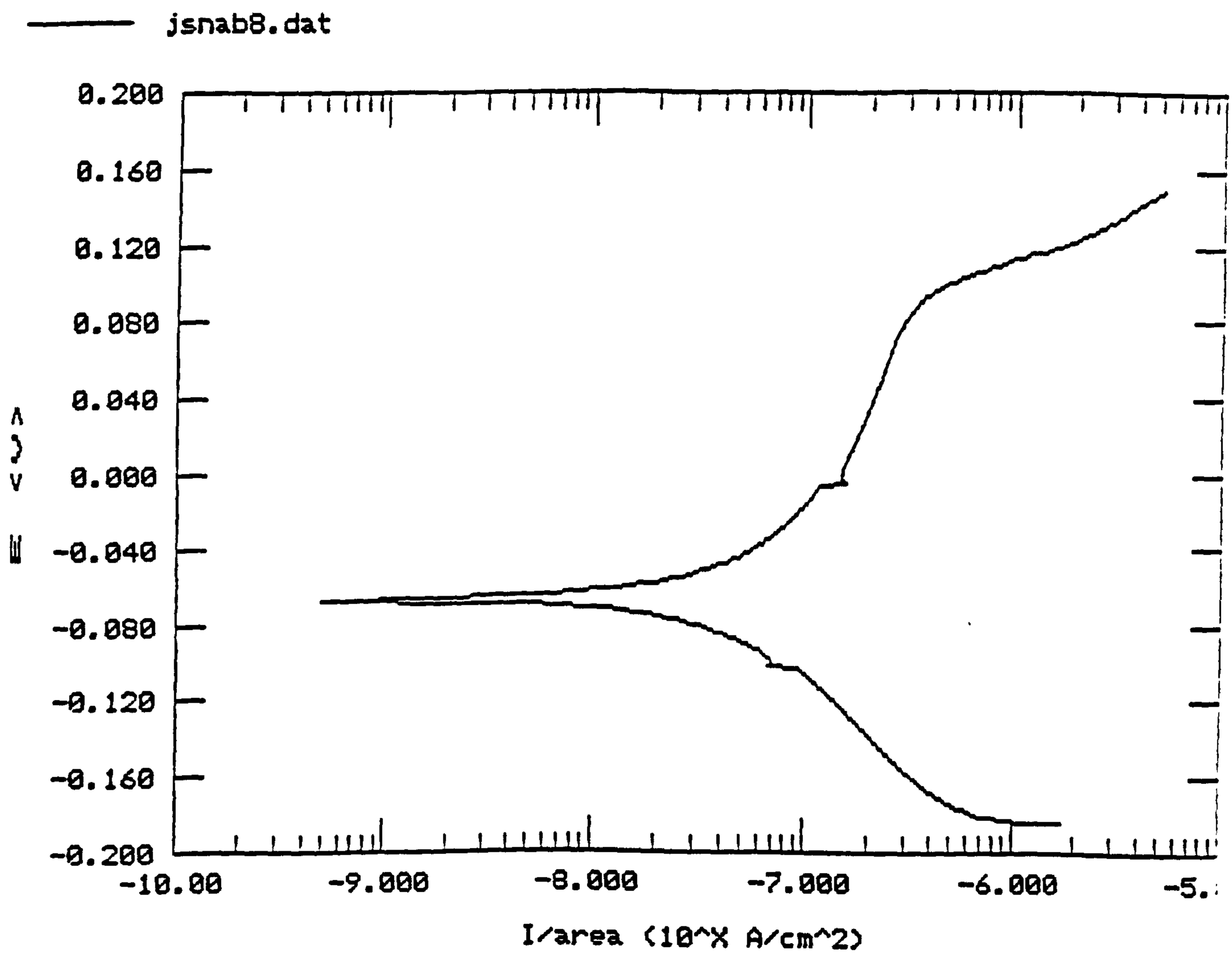

```
Model 352/252 Corrosion Analysis Software, v.   2.01
Filename:  A:\JSTIT1.DAT
Pstat:  M273 [92] Ver 19
PD POTENTIODYNAMIC     File Status:  NORMAL
Date Run:  03-08-95    Time Run:  09:14:35
CP  PASS vs. R         CT  PASS
IP   -0.100 vs. R      ID  PASS
FP    0.150 vs. R      SI   1.000E-03          SR   1.000E-04
ST   1.000E+01         CR  AUTO                NP  251
IR  NONE               FL  NONE
RT  HIGH STABILITY     REF 0.24150 SCE         WRK SOLID
AR   4.600E+01         LS  NO                  EW   0.000E+00
DEN  0.000E+00         OC   0.098
Comment:  Ti in SW Static, rtp.
```

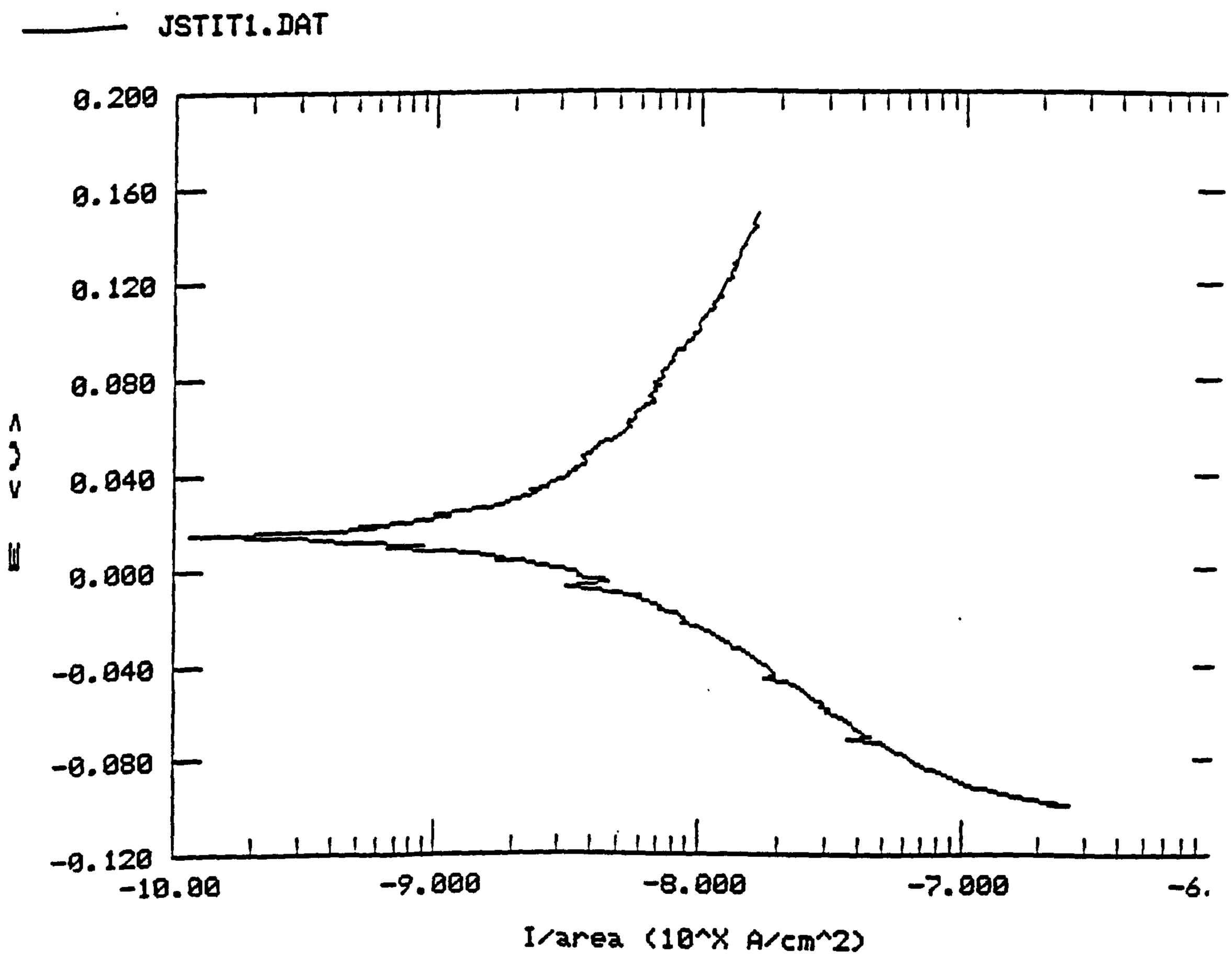

Titanium in 50% Conductivity Seawater, Static Flow

```
Model 352/252 Corrosion Analysis Software, v.   2.01
Filename:  A:\JSTIT4.DAT                    Pstat:  M273 [92] Ver 19
PD POTENTIODYNAMIC    File Status:  NORMAL  Date Run:  01-06-95
Time Run:  16:04:18
CP  PASS vs. R        CT  PASS              IP   -0.500 vs. R     ID  1800 S
FP    0.300 vs. R     SI   1.000E-03        SR   1.000E-04
ST   1.000E+01        CR  AUTO              NP  801               IR  NONE
FL  NONE              RT  HIGH STABILITY    REF 0.24150 SCE       WRK SOLID
AR   5.000E+00        LS  NO                EW   0.000E+00
DEN  0.000E+00        OC   0.050
Comment:  Titanium in 50%  seawater, room temp, area = 5
```

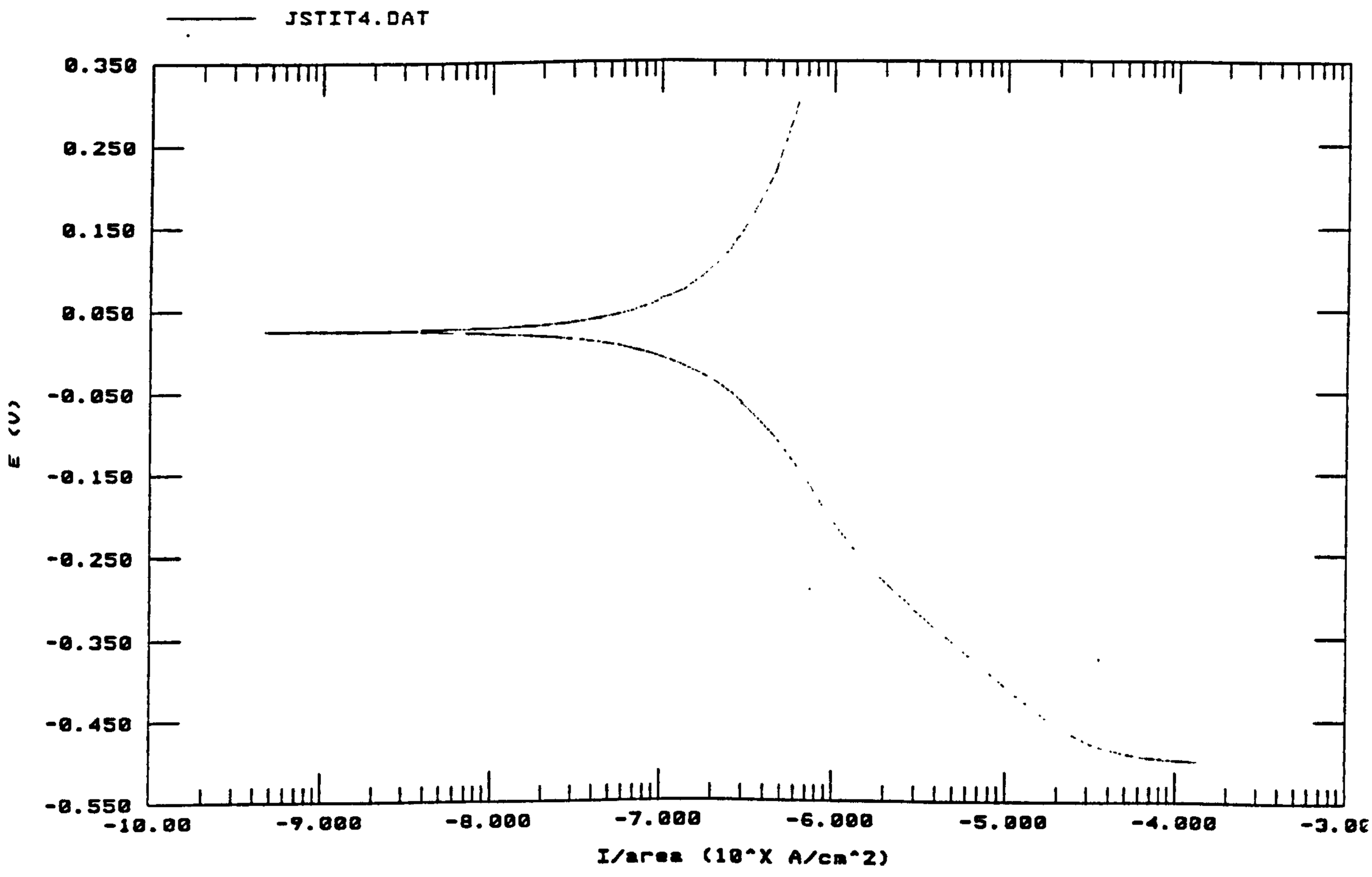

Titanium in 5% Conductivity Seawater, Static Flow

```
Model 352/252 Corrosion Analysis Software, v.   2.01
Filename:  A:\JSTIT9.DAT                          Pstat:  M273 [921 Ver 19
PD POTENTIODYNAMIC    File Status:  NORMAL  Date Run:  01-25-95
Time Run:  13:09:37
CP  PASS vs. R        CT  PASS                IP   -0.500 vs. R     ID  3600 S
FP    0.250 vs. R     SI   1.000E-03          SR   1.000E-04
ST   1.000E+01        CR  AUTO                NP  751              IR  NONE
FL  NONE              RT  HIGH STABILITY      REF 0.24150 SCE      WRK SOLID
AR   3.691E+01        LS  NO                  EW   0.000E+00
DEN  0.000E+00        OC   0.064
Comment:  Titanium in 5% SW,rtp, previously used sample
```

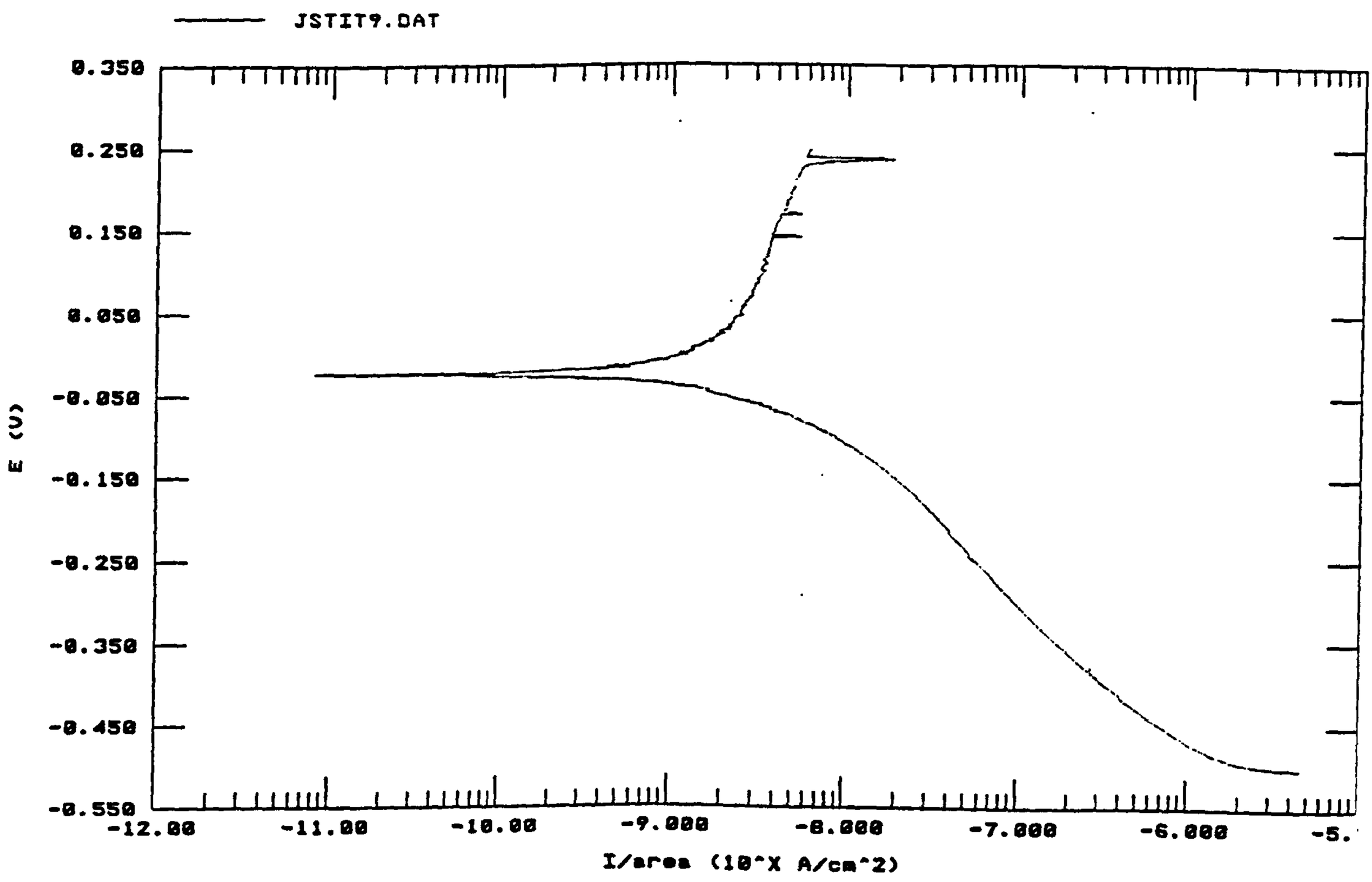

```
Model 352/252 Corrosion Analysis Software, v.   2.01
Filename:  a:\JSTIT13A.DAT
Pstat:  M273A[96] Ver 200
PD POTENTIODYNAMIC     File Status:  NORMAL
Date Run:  03-07-95    Time Run:  10:45:46
CP  PASS vs. R         CT  PASS
IP   -0.100 vs. R      ID  600 S
FP    0.160 vs. R      SI   1.000E-03          SR   1.000E-04
ST   1.000E+01         CR  AUTO                NP  261
IR  NONE               FL  NONE
RT  HIGH STABILITY     REF 0.23600 SSCE        WRK SOLID
AR   2.680E+00         LS  NO                  EW   0.000E+00
DEN  0.000E+00         OC  -0.026
Comment:  Ti in SW Flowing (1m/s)
```

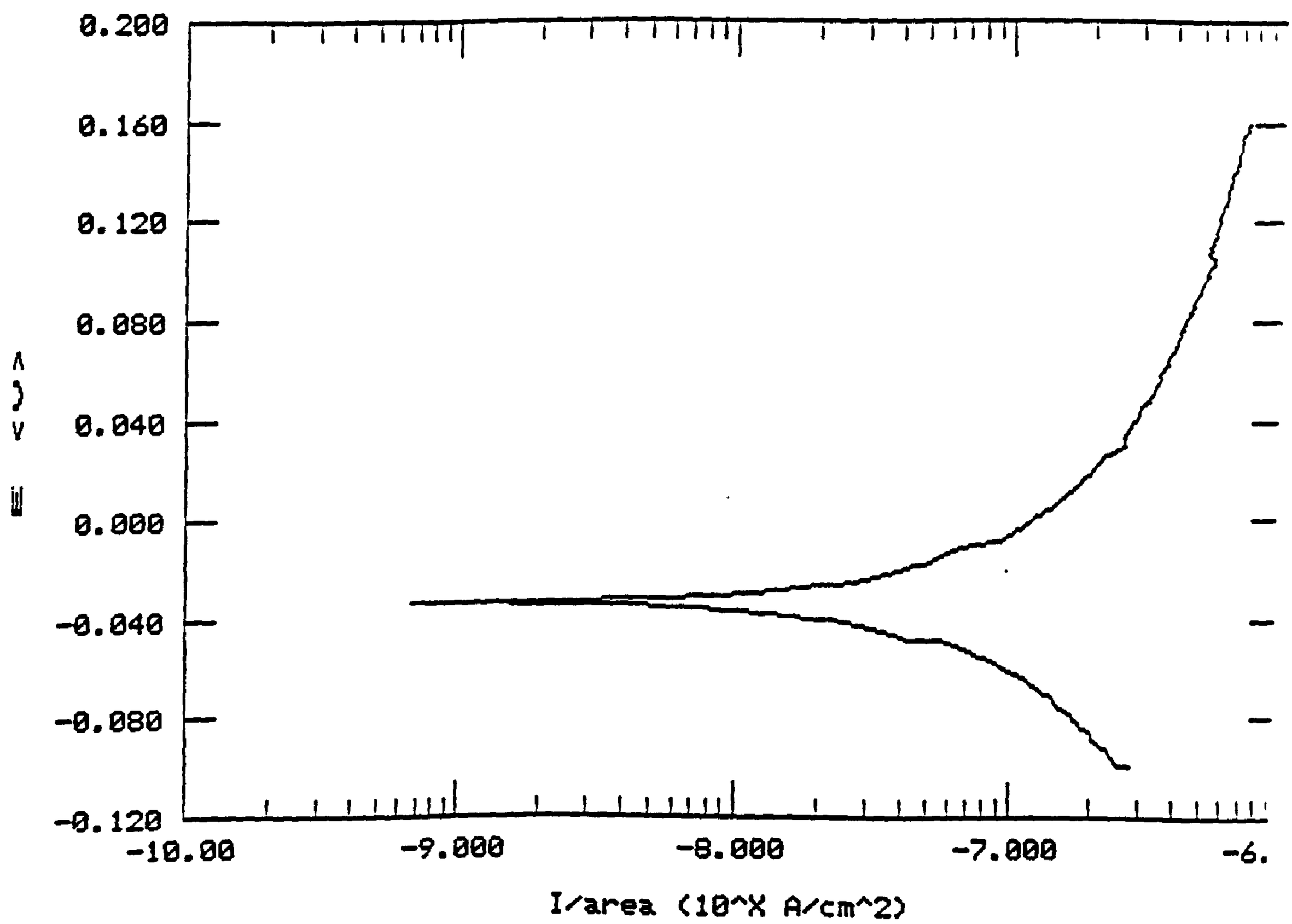

```
Model 352/252 Corrosion Analysis Software, v.   2.01
Filename:  a:\JSTIT17A.DAT
Pstat:  M273A[96] Ver 200
PD POTENTIODYNAMIC     File Status:  NORMAL
Date Run:  03-10-95    Time Run:  14:36:15
CP  PASS vs. R         CT  PASS
IP   -0.100 vs. R      ID  PASS
FP    0.250 vs. R      SI   1.000E-03          SR   1.000E-04
ST    1.000E+01        CR  AUTO                NP   351
IR  NONE               FL  NONE
RT  HIGH STABILITY     REF 0.23600 SSCE        WRK SOLID
AR    1.600E+00        LS  NO                  EW    0.000E+00
DEN   0.000E+00        OC  -0.061
```

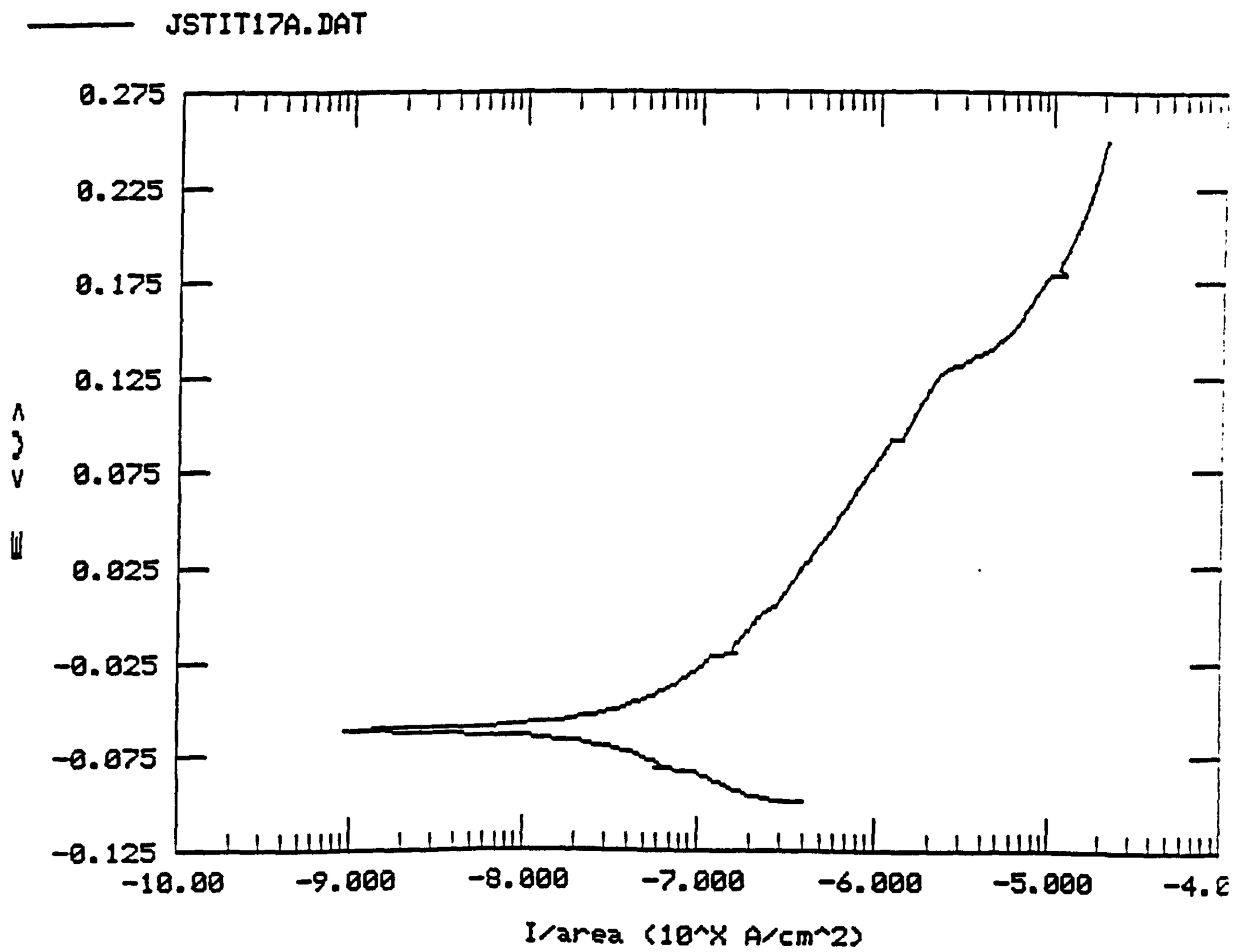

Titanium in 5% Conductivity Seawater, 1 ms^{-1} Flow

```
Model 352/252 Corrosion Analysis Software, v.   2.01
Filename:  A:\JSTIT05%
Pstat:  M273A[96] Ver 200
PD POTENTIODYNAMIC     File Status:  NORMAL
Date Run:  03-13-95    Time Run:  11:04:07
CP  PASS vs. R         CT  PASS
IP   -0.200 vs. R      ID  PASS
FP    0.150 vs. R      SI   1.000E-03          SR   1.000E-04
ST   1.000E+01         CR  AUTO                NP  351
IR  NONE               FL  NONE
RT  HIGH STABILITY     REF 0.23600 SSCE        WRK SOLID
AR   1.750E+00         LS  NO                  EW   0.000E+00
DEN  0.000E+00         OC  -0.005
Comment:  Ti in 5% SW Flowing (1m/s)
```

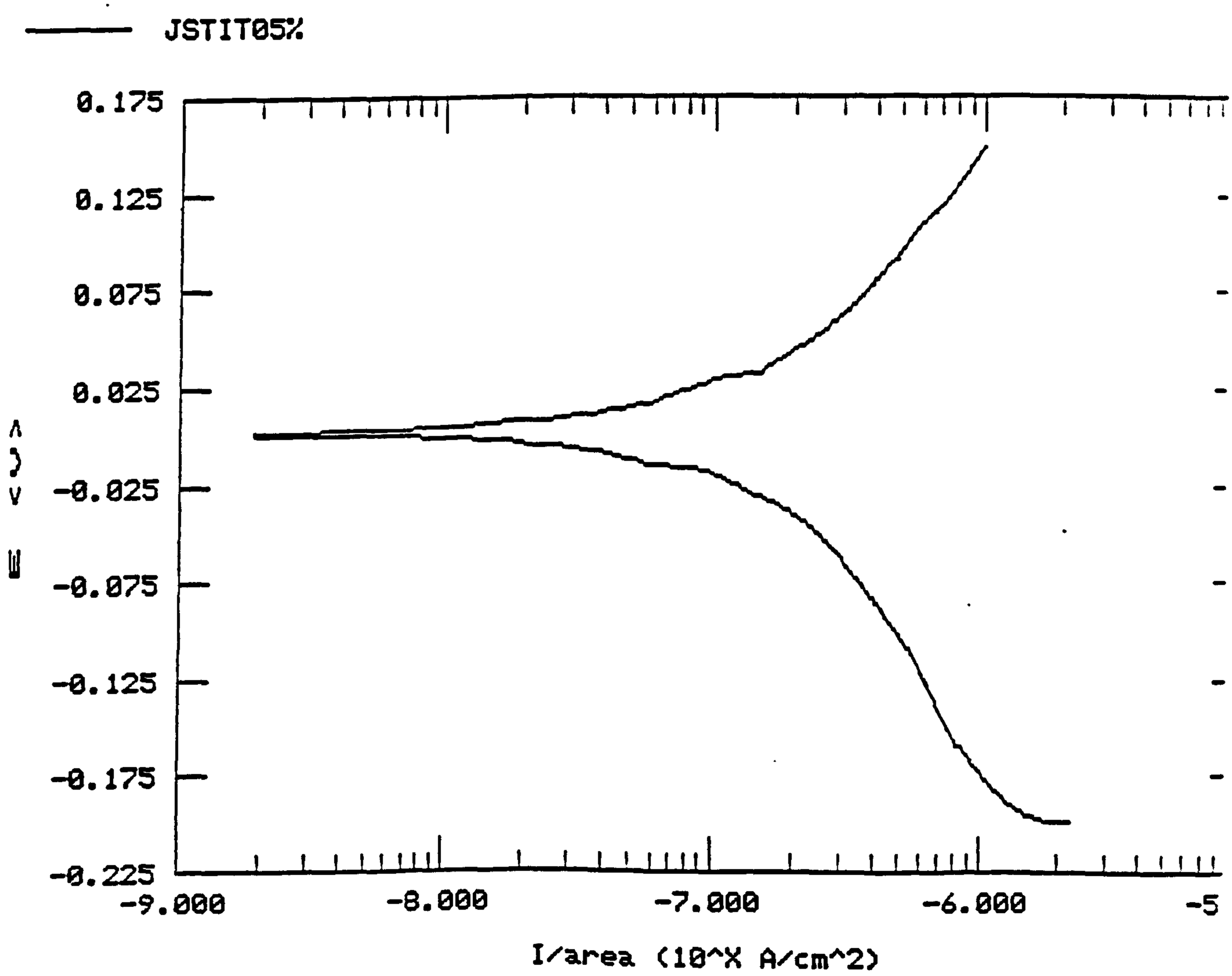

Titanium in Full Strength Seawater, 2 ms^{-1} Flow

```
Model 352/252 Corrosion Analysis Software, v.   2.01
Filename:  A:\JSTIT14.DAT                    Pstat:  M273A[96] Ver 200
PD POTENTIODYNAMIC    File Status:  NORMAL   Date Run:  03-07-95
Time Run:  09:36:13
CP  PASS vs. R          CT  PASS                IP   -0.150 vs. R     ID  200 S
FP    0.160 vs. R       SI   1.000E-03          SR   1.000E-04
ST   1.000E+01          CR  AUTO                NP  311               IR  NONE
FL  NONE                RT  HIGH STABILITY      REF 0.23600 SSCE      WRK SOLID
AR   2.680E+00          LS  NO                  EW   0.000E+00
DEN  0.000E+00          OC  -0.035
Comment:  Ti in SW Flowing (2m/s)
```

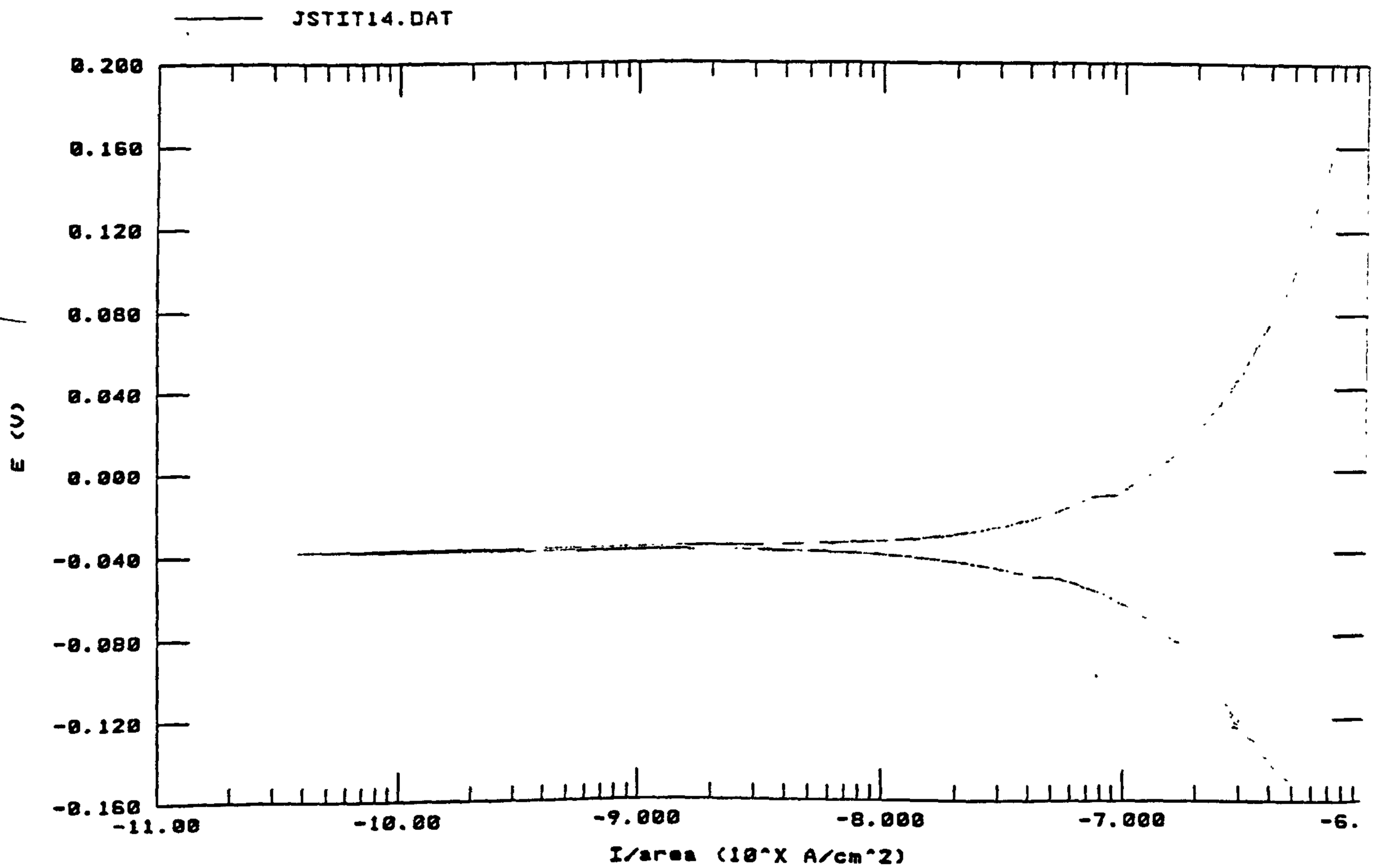

```
Model 352/252 Corrosion Analysis Software, v.   2.01
Filename:  c:\jstit18a.dat
Pstat:  M273A[96] Ver 200
PD POTENTIODYNAMIC     File Status:  EDITED
Date Run:  03-08-95    Time Run:  10:31:25
CP  PASS vs. R         CT  PASS
IP   -0.100 vs. R      ID  3000 S
FP    0.150 vs. R      SI   1.000E-03          SR   1.000E-04
ST   1.000E+01         CR  AUTO                NP  169
IR  NONE               FL  NONE
RT  HIGH STABILITY     REF 0.23600 SSCE        WRK SOLID
AR   2.760E+00         LS  NO                  EW   0.000E+00
DEN  0.000E+00         OC  -0.005
Comment:  Ti in 50% SW Flowing (2m/s)
```

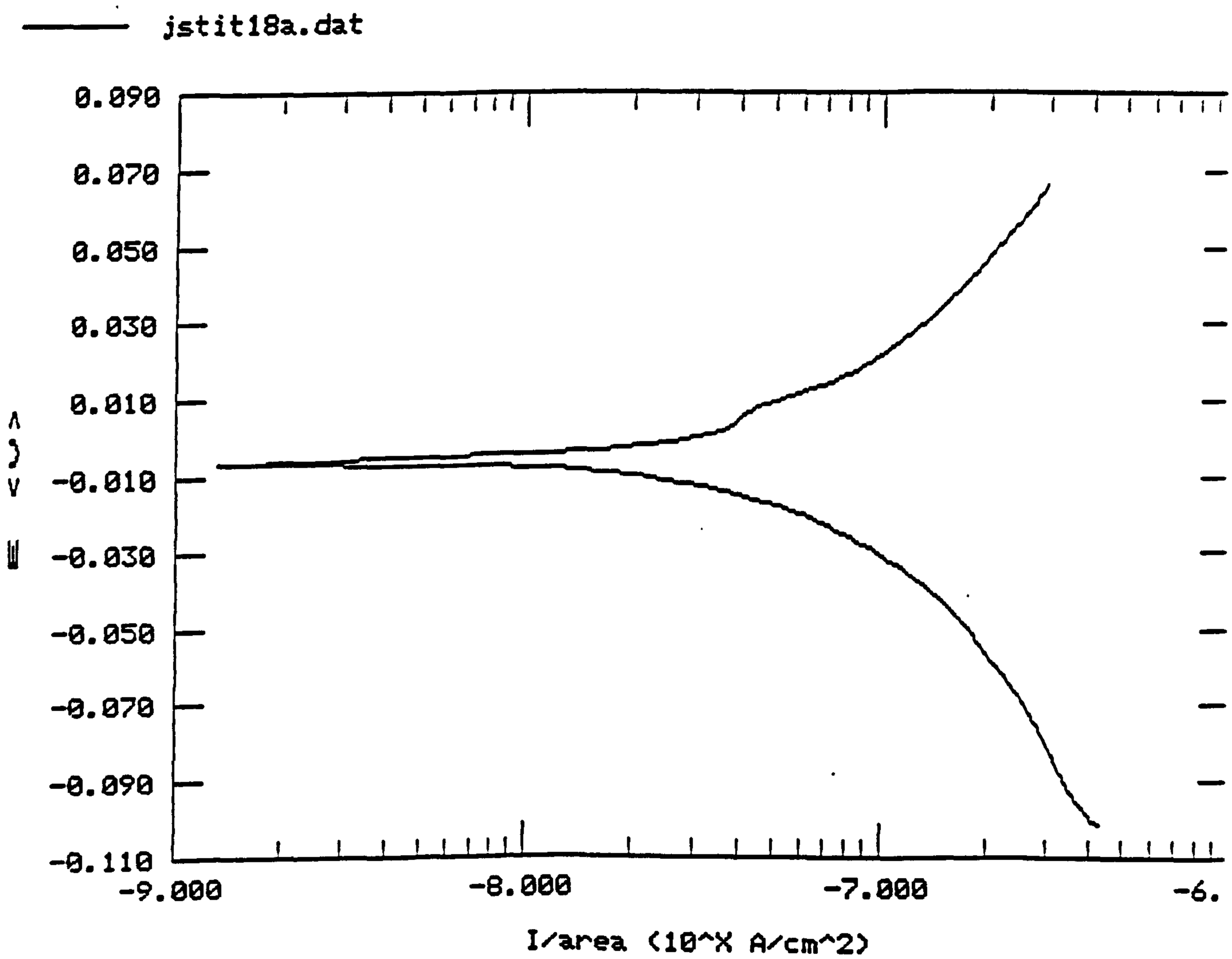

```
Model 352/252 Corrosion Analysis Software, v.   2.01
Filename:  a:\jstit10.dat
Pstat:  M273A[96] Ver 200
PD POTENTIODYNAMIC     File Status:  NORMAL
Date Run:  03-10-95    Time Run:  17:38:49
CP  PASS vs. R         CT  PASS
IP   -0.150 vs. R      ID  PASS
FP    0.250 vs. R      SI   1.000E-03          SR   1.000E-04
ST   1.000E+01         CR  AUTO                NP  358
IR  NONE               FL  NONE
RT  HIGH STABILITY     REF 0.23600 SSCE        WRK SOLID
AR   3.000E+00         LS  NO                  EW   0.000E+00
DEN  0.000E+00         OC   0.048
Comment:  Ti in 5% SW Flowing (2m/s)
```

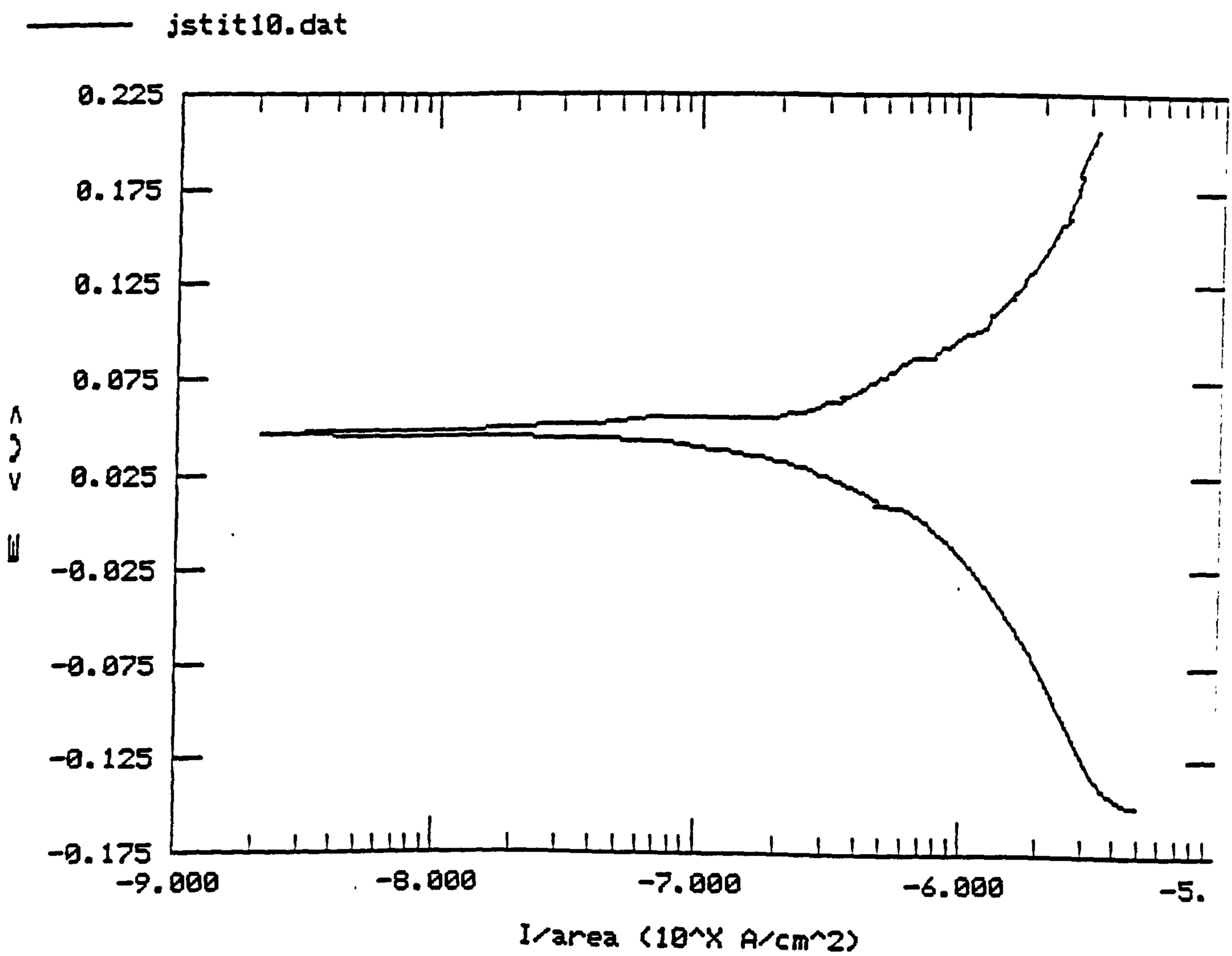

APPENDIX C FORTRAN MODULE FOR BUFFER EQUATION

```
      SUBROUTINE SBUF(EPOTL,SFUNCB,REGION,XI,LXI,ICRITPASS,OUTRAN)
C     ****************************************
C     BUFFER S FUNCTION EQ15 BCJ VOL18 NO1
C           SP 30/9/93
C     ****************************************
      REAL*8 SFUNCB,HACT,HETRANS,HPOWER,HXIPASS
      REAL TEMP,FARAD,RGAS,Z,XIDIFF
      REAL*8 LPRES,LPASS,LXI,PXI,XI
      CHARACTER REGION*1
      INTEGER ICRITPASS, OUTRAN
      FARAD=96460.0
      RGAS=8.314
111   FORMAT(1X,E7.2)
112   FORMAT(1X,F7.2)
113   FORMAT(1X,F7.2)
114   FORMAT(1X,F9.4)
      OPEN(8,FILE='HINES.DAT')
      READ(8,111)HXIPASS
      READ(8,112)HETRANS
      READ(8,113)HPOWER
      READ(8,114)HACT
      CLOSE(8)

      IF (EPOTL.GT.HETRANS) THEN
       HACT = -1 * HACT
```

```
      ENDIF
      TERM1 = ABS(EPOTL-HETRANS)
      TERM2 = TERM1**HPOWER
      TERM3 = (HACT*TERM2)
      CHECKER= 50
      XIDIFF = (ABS(LXI - HXIPASS))
C     CHECK WHETHER XFUNC TOO LARGE OR TOO SMALL
      IF(TERM3.GE.CHECKER) THEN
        REGION = '1'
        SFUNCB = 1
C       TRANSITION REGION
      ELSEIF ((TERM3.GT.(-CHECKER)).AND.(TERM3.LT.CHECKER)) THEN
        REGION = '2'
        XFUNC=EXP(TERM3)
        SFUNCB=XFUNC/(1+XFUNC)
C       PASSIVE REGION
      ELSEIF (TERM3.LE.(-CHECKER)) THEN
        REGION = '3'
        SFUNCB = 0
      ENDIF
      RETURN
      END
```

APPENDIX D FORTRAN MODULE FOR RAINDROP EQUATION

```
      SUBROUTINE SRAIN(EPOTL,ENUC,POWER,XFUNC,TEMP,ACT)
C     ***************************************
```

```
C     RAINDROP S FUNCTION EQ14 BCY VOL18 NO1
C             SP 30/9/93
C     ***************************************
      REAL XFUNC,ACT,EPOTL,ENUC,POWER,FARAD,RGAS,TEMP
      INTEGER NZ
      FARAD=96460.0
      RGAS=8.314

      XFUNC=EXP(-ACT*((ABS(EPOTL-ENUC))**POWER))
      RETURN
      END
```

APPENDIX E PARAMETERS USED FOR 304 STAINLESS STEEL IN DEAERATED 5% H_2SO_4.

Model of 304 Stainless Steel in Deaerated 5% H_2SO_4 at 24°C

The model for 304 stainless steel in deaerated 5% H_2SO_4 at 24°C is shown in Figure 4.3.14, using the parameters shown in Table E-1 and E-2.

	Reaction 1	Reaction 2	Reaction 3	Reaction 5	Reaction 5
Cr_2O_3 Form				$Cr(OH)_3.nH_2O$	anhydrous
E° (V SHE)	-0.440	1.228	0.000	1.117	1.184
i_o (nA cm^{-2})	2.5×10^{-4}	0.12	100	0.31	1
i_{lim} anodic (nA cm^{-2})	not required	1.0×10^{22}	negligible	6.0×10^{4}	3.0×10^{7}
i_{lim} cathodic (nA cm^{-2})	negligible	negligible	1.0×10^{21}	negligible	negligible
α	0.50	0.60	0.50	0.50	0.50

Table E-1 Kinetic parameters used in Figure 4.3.14

	i_{pass} (nA cm^{-2})	A	p	E_{trans} (V SCE)
Reaction 1	1.6×10^{3}	450	2.0	-0.390

Table E-2 Parameters used in passivation routine for Reaction 1 in Figure 4.3.14

Model of 304 Stainless Steel in Deaerated 5% H_2SO_4 at 30°C

The model for 304 stainless steel in deaerated 5% H_2SO_4 at 30°C is shown in Figure 4.3.15, which was constructed using the parameters shown in Tables E-3 and E-4.

	Reaction 1	Reaction 2	Reaction 3	Reaction 5	Reaction 5
Cr_2O_3 Form				$Cr(OH)_3.nH_2O$	anhydrous
E° (V SHE)	-0.440	1.228	0.000	1.117	1.184
i_o (nA cm^{-2})	8.0×10^{-5}	0.12	200	0.031	1.0
i_{lim} anodic (nA cm^{-2})	not required	1.0×10^{22}	negligible	6.0×10^{4}	5.0×10^{7}
i_{lim}cathodic (nA cm^{-2})	negligible	negligible	1.0×10^{21}	negligible	negligible
α	0.50	0.60	0.50	0.50	0.50

Table E-3 Kinetic parameters used in Figure 4.3.15

	i_{pass} (nA cm^{-2})	A	p	E_{trans} (V SCE)
Reaction 1	1.6×10^{3}	450	2.0	-0.340

Table E-4 Parameters used in passivation routine for Reaction 1 in Figure 4.3.15

Model of 304 Stainless Steel in Deaerated 5% H_2SO_4 at 35°C

Tables E-5 and E-6 show the parameters used to construct Figure 4.3.16, which models the behaviour of 304 stainless steel in deaerated 5% H_2SO_4 at 35°C.

	Reaction 1	Reaction 2	Reaction 3	Reaction 5	Reaction 5
Cr_2O_3 Form				$Cr(OH)_3.nH_2O$	anhydrous
E° (V SHE)	-0.440	1.228	0.000	1.117	1.184
i_o (nA cm^{-2})	7.5×10^{-5}	0.12	200	0.31	3.0
i_{lim} anodic (nA cm^{-2})	not required	1.0×10^{22}	negligible	8×10^{4}	5.0×10^{9}
i_{lim} cathodic (nA cm^{-2})	negligible	negligible	1.0×10^{21}	negligible	negligible
α	0.50	0.60	0.40	0.50	0.50

Table E-5 Kinetic parameters used in Figure 4.3.16

	i_{pass} (nA cm^{-2})	A	p	E_{trans} (V SCE)
Reaction 1	1.6×10^{3}	450	2.0	-0.330

Table E-6 Parameters used in passivation routine for Reaction 1 in Figure 4.3.16

Model of 304 Stainless Steel in Deaerated 5% H_2SO_4 at 45°C

Figure 4.3.17 shows the theoretical curve which models the behaviour of 304 stainless steel in deaerated 5% H_2SO_4 at 45°C, using the parameters detailed in Tables E-7 and E-8.

	Reaction 1	Reaction 2	Reaction 3	Reaction 5	Reaction 5
Cr_2O_3 Form				$Cr(OH)_3.nH_2O$	anhydrous
E° (V SHE)	-0.440	1.228	0.000	1.117	1.184
i_o (nA cm^{-2})	7.5×10^{-4}	0.12	7.0	0.7	7.0
i_{lim} anodic (nA cm^{-2})	not required	1.0×10^{22}	negligible	8.0×10^{4}	1.0×10^{9}
i_{lim} cathodic (nA cm^{-2})	negligible	negligible	1×10^{22}	negligible	negligible
α	0.50	0.60	0.10	0.50	0.50

Table E-7 Kinetic parameters used in Figure 4.3.17

	i_{pass} (nA cm^{-2})	A	p	E_{trans} (V SCE)
Reaction 1	2.1×10^{3}	450	2.0	-0.360

Table E-8 Parameters used in passivation routine for Reaction 1 in Figure 4.3.17

APPENDIX F PARAMETERS USED FOR 304 STAINLESS STEEL IN AERATED 5% H_2SO_4.

Model of 304 Stainless Steel in Aerated 5% H_2SO_4 at 24°C

The model for 304 stainless steel in aerated 5% H_2SO_4 at 24°C is shown in Figure 4.3.18, using the parameters shown in Tables F-1 and F-2.

	Reaction 1	Reaction 2	Reaction 3	Reaction 5	Reaction 5	Reaction 7
Cr_2O_3 Form				$Cr(OH)_3.nH_2O$	anhydrous	
E° (V SHE)	-0.440	1.228	0.000	1.117	1.184	1.228
i_o (nA cm^{-2})	5.0×10^{-7}	0.12	4.0×10^{3}	0.031	0.1	5.2×10^{-5}
i_{lim} anodic (nA cm^{-2})	not required	1.0×10^{22}	negligible	6.0×10^{4}	3.0×10^{7}	negligible
i_{lim} cathodic (nA cm^{-2})	negligible	negligible	1.0×10^{21}	negligible	negligible	1.0×10^{4}
α	0.50	0.60	0.50	0.50	0.50	0.55

Table F-1 Kinetic parameters used in Figure 4.3.18

	i_{pass} (nA cm^{-2})	A	p	E_{trans} (V SCE)
Reaction 1	1.0×10^{3}	450	2.0	-0.390

Table F-2 Parameters used in passivation routine for Reaction 1 in Figure 4.3.18

Model of 304 Stainless Steel in Aerated 5% H_2SO_4 at 30°C

The model for 304 stainless steel in aerated 5% H_2SO_4 at 30°C is shown in Figure 4.3.19, which was constructed using the parameters shown in Tables F-3 and F-4.

	Reaction 1	Reaction 2	Reaction 3	Reaction 5	Reaction 5	Reaction 77
Cr_2O_3 Form				$Cr(OH)_3.nH_2O$	anhydrous	
E° (V SHE)	-0.440	1.228	0.000	1.117	1.184	1.228
i_o (nA cm^{-2})	5.0×10^{-7}	0.12	2.0×10^{3}	0.031	0.1	5.2×10^{-5}
i_{lim} anodic (nA cm^{-2})	not required	1.0×10^{22}	negligible	6.0×10^{4}	4.0×10^{7}	negligible
i_{lim}cathodic (nA cm^{-2})	negligible	negligible	1.0×10^{21}	negligible	negligible	4.5×10^{4}
α	0.50	0.60	0.50	0.50	0.50	0.51

Table F-3 Kinetic parameters used in Figure 4.3.19

	i_{pass} (nA cm^{-2})	A	p	E_{trans} (V SCE)
Reaction 1	1.3×10^{3}	450	2.0	-0.340

Table F-4 Parameters used in passivation routine for Reaction 1 in Figure 4.3.19

Model of 304 Stainless Steel in Aerated 5% H_2SO_4 at 35°C

Figure 4.3.20 uses the parameters in Tables F-5 and F-6 to model the behaviour of 304 stainless steel in aerated 5% H_2SO_4 at 35°C.

	Reaction 1	Reaction 2	Reaction 3	Reaction 5	Reaction 5	Reaction 7
Cr_2O_3 Form				$Cr(OH)_3.nH_2O$	anhydrous	
E° (V SHE)	-0.440	1.228	0.000	1.117	1.184	1.228
i_o (nA cm^{-2})	5.0×10^{-7}	0.12	1.0×10^{3}	0.031	3.0	5.2×10^{-5}
i_{lim} anodic (nA cm^{-2})	not required	1.0×10^{22}	negligible	8.0×10^{4}	8.0×10^{7}	negligible
i_{lim} cathodic (nA cm^{-2})	negligible	negligible	1.0×10^{21}	negligible	negligible	2.0×10^{5}
α	0.50	0.60	0.40	0.50	0.50	0.47

Table F-5 Kinetic parameters used in Figure 4.3.20

	i_{pass} (nA cm^{-2})	A	p	E_{trans} (V SCE)
Reaction 1	1.6×10^{3}	450	2.0	-0.330

Table F-6 Parameters used in passivation routine for Reaction 1 in Figure 4.3.20

Model of 304 Stainless Steel in Aerated 5% H_2SO_4 at 45°C

Tables F-7 and F-8 show the parameters used to model the behaviour of 304 stainless steel in aerated 5% H_2SO_4 at 45°C. The resultant theoretical curve is shown in Figure 4.3.21.

	Reaction 1	Reaction 2	Reaction 3	Reaction 5	Reaction 5	Reaction 7
Cr_2O_3 Form				$Cr(OH)_3.nH_2O$	anhydrous	
E° (V SHE)	-0.440	1.228	0.000	1.117	1.184	1.228
i_o (nA cm^{-2})	1.0×10^{-4}	0.12	4.0×10^{3}	0.31	5.0	5.2×10^{-5}
i_{lim} anodic (nA cm^{-2})	not required	1.0×10^{22}	negligible	6.0×10^{4}	3.0×10^{9}	negligible
i_{lim} cathodic (nA cm^{-2})	negligible	negligible	1×10^{22}	negligible	negligible	3.5×10^{4}
α	0.50	0.60	0.10	0.50	0.50	0.47

Table F-7 Kinetic parameters used in Figure 4.3.21

	i_{pass} (nA cm^{-2})	A	p	E_{trans} (V SCE)
Reaction 1	3.5×10^{3}	450	2.0	-0.330

Table F-8 Parameters used in passivation routine for Reaction 1 in Figure 4.3.21

APPENDIX G PARAMETERS USED FOR 304 STAINLESS STEEL IN STAGNANT 5% H_2SO_4.

Model of 304 Stainless Steel in Stagnant 5% H_2SO_4 at 24°C

The model for 304 stainless steel in stagnant 5% H_2SO_4 at 24°C is shown in Figure 4.3.22, using the parameters shown in Tables G-1and G-2.

	Reaction 1	Reaction 2	Reaction 3	Reaction 5	Reaction 5	Reaction 7
Cr_2O_3 Form				$Cr(OH)_3.nH_2O$	anhydrous	
E° (V SHE)	-0.440	1.228	0.000	1.117	1.184	1.228
i_o (nA cm^{-2})	2.5×10^{-4}	0.12	10	0.31	1.0	5.2×10^{-5}
i_{lim} anodic (nA cm^{-2})	not required	1.0×10^{22}	negligible	6.0×10^{4}	3.0×10^{7}	1.8×10^{4}
i_{lim} cathodic (nA cm^{-2})	negligible	negligible	1.0×10^{21}	negligible	negligible	negligible
α	0.50	0.60	0.50	0.50	0.50	0.51

Table G-1 Kinetic parameters used in Figure 4.3.22

	i_{pass} (nA cm^{-2})	A	p	E_{trans} (V SCE)
Reaction 1	1.2×10^{3}	450	2.0	-0.370

Table G-2 Parameters used in passivation routine for Reaction 1 in Figure 4.3.22

Model of 304 Stainless Steel in Stagnant 5% H_2SO_4 at 30°C

The model for 304 stainless steel in stagnant 5% H_2SO_4 at 30°C is shown in Figure 4.3.23, which was constructed using the parameters shown in Tables G-3 and G-4.

	Reaction 1	Reaction 2	Reaction 3	Reaction 5	Reaction 5	Reaction 7
Cr_2O_3 Form				$Cr(OH)_3.nH_2O$	anhydrous	
E° (V SHE)	-0.440	1.228	0.000	1.117	1.184	1.228
i_o (nA cm^{-2})	2.5×10^{-4}	0.12	500	0.31	1	5.2×10^{-5}
i_{lim} anodic (nA cm^{-2})	not required	1.0×10^{22}	negligible	6.0×10^{4}	1.0×10^{8}	negligible
i_{lim} cathodic (nA cm^{-2})	negligible	negligible	1.0×10^{21}	negligible	negligible	1.6×10^{4}
α	0.50	0.60	0.50	0.50	0.50	0.48

Table G-3 Kinetic parameters used in Figure 4.3.23

	i_{pass} (nA cm^{-2})	A	p	E_{trans} (V SCE)
Reaction 1	1.5×10^{3}	450	2.0	-0.360

Table G-4 Parameters used in passivation routine for Reaction 1 in Figure 4.3.15

Model of 304 Stainless Steel in Stagnant 5% H_2SO_4 at 35°C

The model for 304 stainless steel in stagnant 5% H_2SO_4 at 35°C is shown in Figure 4.3.24, which was constructed using the parameters shown in Tables G-5 and G-6.

	Reaction 1	Reaction 2	Reaction 3	Reaction 5	Reaction 5	Reaction 7
Cr_2O_3 Form				$Cr(OH)_3.nH_2O$	anhydrous	
E^o (V SHE)	-0.440	1.228	0.000	1.117	1.184	1.228
i_o (nA cm^{-2})	2.5×10^{-4}	0.12	1.0×10^{3}	0.31	1.0	5.2×10^{-5}
i_{lim} anodic (nA cm^{-2})	not required	1.0×10^{22}	negligible	6.0×10^{4}	1.0×10^{8}	negligible
i_{lim} cathodic (nA cm^{-2})	negligible	negligible	1.0×10^{21}	negligible	negligible	2.3×10^{4}
α	0.50	0.60	0.50	0.50	0.50	0.46

Table G-5 Kinetic parameters used in Figure 4.3.24

	i_{pass} (nA cm^{-2})	A	p	E_{trans} (V SCE)
Reaction 1	3.1×10^{3}	450	2.0	-0.350

Table G-6 Parameters used in passivation routine for Reaction 1 in Figure 4.3.24

Model of 304 Stainless Steel in Stagnant 5% H_2SO_4 at 45 °C

The model for 304 stainless steel in stagnant 5% H_2SO_4 at 45 °C is shown in Figure 4.3.25, which was constructed using the parameters shown in Tables G-7 and G-8.

	Reaction 1	Reaction 2	Reaction 3	Reaction 5	Reaction 5	Reaction 7
Cr_2O_3 Form				$Cr(OH)_3.nH_2O$	anhydrous	
E° (V SHE)	-0.440	1.228	0.000	1.117	1.184	1.228
i_o (nA cm^{-2})	7.5×10^{-4}	0.12	3×10^{3}	1.0	1.0	5.2×10^{-5}
i_{lim} anodic (nA cm^{-2})	not required	1.0×10^{22}	negligible	8.0×10^{4}	3.0×10^{9}	negligible
i_{lim} cathodic (nA cm^{-2})	negligible	negligible	1×10^{22}	negligible	negligible	3.0×10^{4}
α	0.50	0.60	0.50	0.50	0.50	0.40

Table G-7 Kinetic parameters used in Figure 4.3.25

	i_{pass} (nA cm^{-2})	A	p	E_{trans} (V SCE)
Reaction 1	4.0×10^{3}	450	2.0	-0.310

Table G-8 Parameters used in passivation routine for Reaction 1 in Figure 4.3.25

APPENDIX H PARAMETERS USED FOR 316 STAINLESS STEEL IN DEAERATED 5% H_2SO_4.

Model for 316 in Deaerated 5% H_2SO_4 at 24°C

The parameters used to model the behaviour of 316 stainless steel in deaerated 5% H_2SO_4 are listed in Tables H-1 to H-8, and shown in Figures 4.5.4.5 to 4.5.4.8.

	Reaction 1	Reaction 2	Reaction 3	Reaction 5	Reaction 5
Cr_2O_3 form				$Cr(OH)_3.nH_2O$	anhydrous
E° (V SHE)	-0.440	1.228	0.000	1.117	1.184
i_o (nA cm^{-2})	1.5×10^{-7}	0.12	70.0	3.1	3.0
i_{lim}anodic (nA cm^{-2})	not required	1.0×10^{21}	negligible	6.0×10^{4}	1.0×10^{7}
i_{lim}cathodic (nA cm^{-2})	negligible	negligible	1.0×10^{21}	negligible	negligible
α	0.49	0.60	0.50	0.50	0.5
Temperature	24°C				
pH	0.2				
Resistance	30				

Table H-1 Parameters used to model 316 stainless steel in deaerated 5% H_2SO_4, 24°C.

	i_{pass} (nA cm^{-2})	A	p	E_t (V SCE)
Reaction 1	1.3×10^{3}	350	2.0	-0.250

Table H-2 Passivation parameters used to model 316 stainless steel in deaerated 5% H_2SO_4, 24 °C.

Model for 316 in Deaerated 5% H_2SO_4 at 30°C

	Reaction 1	Reaction 2	Reaction 3	Reaction 5	Reaction 5
Cr_2O_3 form				$Cr(OH)_3.nH_2O$	anhydrous
E° (V SHE)	-0.440	1.228	0.000	1.117	1.184
i_o (nA cm^{-2})	7.5×10^{-6}	0.12	2.5×10^{2}	3.1	3.0
i_{lim} anodic (nA cm^{-2})	not required	1.0×10^{21}	negligible	6.0×10^{4}	2.3×10^{7}
i_{lim} cathodic (nA cm^{-2})	negligible	negligible	1.0×10^{21}	negligible	negligible
α	0.40	0.50	0.50	0.50	0.50
Temperature	30°C				
pH	0.2				
Resistance	15				

Table H-3 Parameters used to model 316 stainless steel in deaerated 5% H_2SO_4, 30°C.

	i_{pass} (nA cm^{-2})	A	P	E_t (V SCE)
Reaction 1	900	350	2.0	-0.200

Table H-4 Passivation parameters used to model 316 stainless steel in deaerated 5% H_2SO_4, 30°C.

Model for 316 in Deaerated 5% H_2SO_4 at 35°C

	Reaction 1	Reaction 2	Reaction 3	Reaction 5	Reaction 5
Cr_2O_3 form				$Cr(OH)_3.nH_2O$	anhydrous
E° (V SHE)	-0.440	1.228	0.000	1.117	1.184
i_o (nA cm^{-2})	9.0 x 10^{-6}	0.12	200	0.31	1.5
i_{lim}anodic (nA cm^{-2})	not required	1.0 x 10^{21}	negligible	6.0 x 10^4	2.7 x 10^7
i_{lim}cathodic (nA cm^{-2})	negligible	negligible	1.0 x 10^{21}	negligible	negligible
α	0.40	0.60	0.50	0.50	0.50

Temperature	35°C
pH	0.2
Resistance	10

Table H-5 Parameters used to model 316 stainless steel in deaerated 5% H_2SO_4, 35°C.

	i_{pass} (nA cm^{-2})	A	P	E_t (V SCE)
Reaction 1	1.0 x 10^3	350	2.0	-0.190

Table H-6 Passivation parameters used to model 316 stainless steel in deaerated 5% H_2SO_4, 35°C.

Model for 316 in Deaerated 5% H_2SO_4 at 45°C

	Reaction 1	Reaction 2	Reaction 3	Reaction 5	Reaction 5
Cr_2O_3 form				$Cr(OH)_3.nH_2O$	anhydrous
E° (V SHE)	-0.440	1.228	0.000	1.117	1.184
i_o (nA cm^{-2})	7.5×10^{-4}	0.12	900	0.5	7.0
i_{lim} anodic (nA cm^{-2})	not required	1.0×10^{21}	negligible	6.0×10^{4}	1.0×10^{8}
i_{lim} cathodic (nA cm^{-2})	negligible	negligible	1.0×10^{21}	negligible	negligible
α	0.40	0.60	0.50	0.50	0.50

Temperature	45°C
pH	0.2
Resistance	4

Table H-7 Parameters used to model 316 stainless steel in deaerated 5% H_2SO_4, 45°C.

	i_{pass} (nA cm^{-2})	A	P	E_t (V SCE)
Reaction 1	2.3×10^{3}	150	2.0	-0.350

Table H-8 Passivation parameters used to model 316 stainless steel in deaerated 5% H_2SO_4, 45°C.

APPENDIX I PARAMETERS USED FOR 316 STAINLESS STEEL IN AERATED 5% H_2SO_4.

Model for 316 Stainless Steel in Aerated 5% H_2SO_4 at 24°C

The parameters used to model the behaviour of 316 stainless steel in aerated 5% H_2SO_4 at 24°C are listed in Tables I-1 and I-2.

	Reaction 1	Reaction 2	Reaction 7	Reaction 3	Reaction 5	Reaction 5
Cr_2O_3 form					$Cr(OH)_3.nH_2O$	anhydrous
E_o (V SHE)	-0.440	1.228	1.228	0.000	1.17	1.184
i_o (nA cm^{-2})	9.0×10^{-6}	0.12	5.2×10^{-5}	2.0×10^{3}	0.1	0.5
i_{lim}anodic (nA cm^{-2})	not required	1.0×10^{21}	negligible	negligible	6.0×10^{4}	1.0×10^{7}
i_{lim}cathodic (nA cm^{-2})	negligible	negligible	1.5×10^{4}	1.0×10^{21}	negligible	negligible
α	0.40	0.60	0.50	0.50	0.50	0.5
Temperature	24°C					
pH	0.2					
Resistance	30					

Table I-1 Parameters used to model 316 stainless steel in aerated 5% H_2SO_4, 24°C.

	i_{pass} (nA cm^{-2})	A	p	E_t
Reaction 1	900	150	2.0	-0.350

Table I-2 Passivation parameters for model of 316 stainless steel in aerated 5% H_2SO_4, 24°C.

Model for 316 in Aerated 5% H_2SO_4 at 30°C

The parameters used to model the behaviour of 316 stainless steel in aerated 5% H_2SO_4 at 30°C are listed in Tables I-3 and I-4.

	Reaction 1	Reaction 2	Reaction 7	Reaction 3	Reaction 5	Reaction 5
Cr_2O_3 form					$Cr(OH)_3.nH_2O$	anhydrous
E_o (V SHE)	-0.440	1.228	1.228	0.000	1.117	1.184
i_o (nA cm^{-2})	9.0×10^{-7}	0.12	5.2×10^{-5}	3.0×10^{3}	0.3	5.0
i_{lim}anodic (nA cm^{-2})	not required	1.0×10^{21}	negligible	negligible	6.0×10^{4}	2.3×10^{7}
i_{lim}cathodic (nA cm^{-2})	negligible	negligible	1.5×10^{4}	1.0×10^{21}	negligible	negligible
α	0.40	0.60	0.54	0.50	0.50	0.50

Temperature	30°C
pH	0.2
Resistance	15

Table I-3 Parameters used to model 316 stainless steel in aerated 5% H_2SO_4, 30°C.

	i_{pass} (nA cm^{-2})	A	p	E_t
Reaction 1	4.9×10^{3}	150	2.0	-0.350

Table I-4 Passivation parameters for model of 316 stainless steel in aerated 5% H_2SO_4, 30°C.

Model for 316 in Aerated 5% H_2SO_4 at 35°C

The parameters used to model the behaviour of 316 stainless steel in aerated 5% H_2SO_4 at 35°C are listed in Tables I-5 and I-6.

	Reaction 1	Reaction 2	Reaction 7	Reaction 3	Reaction 5	Reaction 5
Cr_2O_3 form					$Cr(OH)_3.nH_2O$	anhydrous
E_o (V SHE)	-0.440	1.228	1.228	0.000	1.117	1.184
i_o (nA cm^{-2})	9.0×10^{-7}	0.12	5.2×10^{-5}	4.0×10^{3}	0.03	0.5
i_{lim}anodic (nA cm^{-2})	not required	1.0×10^{21}	negligible	negligible	6.0×10^{4}	3.5×10^{7}
i_{lim}cathodic (nA cm^{-2})	negligible	negligible	3.3×10^{4}	1.0×10^{21}	negligible	negligible
α	0.40	0.60	0.47	0.50	0.50	0.50
Temperature	35°C					
pH	0.2					
Resistance	10					

Table I-5 Parameters used to model 316 stainless steel in aerated 5% H_2SO_4, 35°C.

	i_{pass} (nA cm^{-2})	A	P	E_t
Reaction 1	1.3×10^{3}	150	2.0	-0.350

Table I-6 Passivation parameters for model of 316 stainless steel in aerated 5% H_2SO_4, 35°C.

Model for 316 in Aerated 5% H_2SO_4 at 45°C

The parameters used to model the behaviour of 316 stainless steel in aerated 5% H_2SO_4 at 45°C are listed in Tables I-7 and I-8.

	Reaction 1	Reaction 2	Reaction 7	Reaction 3	Reaction 5	Reaction 5
Cr_2O_3 form					$Cr(OH)_3.nH_2O$	anhydrous
E_o (V SHE)	-0.440	1.228	1.228	0.000	1.117	1.184
i_o (nA cm^{-2})	9.0×10^{-6}	0.12	5.2×10^{-5}	400	0.5	5.0
i_{lim}anodic (nA cm^{-2})	not required	1.0×10^{21}	negligible	negligible	6.0×10^{4}	7.7×10^{7}
i_{lim}cathodic (nA cm^{-2})	negligible	negligible	1.5×10^{4}	1.0×10^{21}	negligible	negligible
α	0.40	0.60	0.58	0.40	0.50	0.50
Temperature	45°C					
pH	0.2					
resistance	4					

Table I-7 Parameters used to model 316 stainless steel in aerated 5% H_2SO_4, 45°C.

	i_{pass} (nA cm^{-2})	A	P	E_t
Reaction 1	1.4×10^{3}	350	2.0	-0.350

Table I-8 Passivation parameters for model of 316 stainless steel in aerated 5% H_2SO_4, 45°C.

APPENDIX J PARAMETERS USED FOR 316 STAINLESS STEEL IN STAGNANT 5% H_2SO_4.

Model for 316 Stainless Steel in Stagnant 5% H_2SO_4 at 24°C

The parameters used to model the behaviour of 316 stainless steel in stagnant 5% H_2SO_4 at 24°C are listed in Tables J-1 and J-2, and the resultant theoretical curve is shown in Figure 4.5.13.

	Reaction 1	Reaction 2	Reaction 7	Reaction 3	Reaction 5	Reaction 5
Cr_2O_3					$Cr(OH)_3.nH_2O$	anhydrous
E_o (V SHE)	-0.440	1.228	1.228	0.000	1.117	1.184
i_o (nA cm^{-2})	7.5×10^{-7}	0.12	5.2×10^{-5}	800	0.1	0.5
i_{lim}anodic (nA cm^{-2})	not required	1.0×10^{21}	negligible	negligible	6.0×10^{4}	1.0×10^{7}
i_{lim}cathodic (nA cm^{-2})	negligible	negligible	2.0×10^{3}	1.0×10^{21}	negligible	negligible
α	0.40	0.60	0.55	0.60	0.50	0.50
Temperature	24°C					
pH	0.2					
Resistance	30 Ω					

Table J-1 Parameters used to model 316 stainless steel in stagnant 5% H_2SO_4, 24°C.

	i_{pass} (nA cm^{-2})	A	p	E_t
Reaction 1	6.5×10^{3}	350	2.0	-0.240

Table J-2 Passivation parameters for model of 316 stainless steel in stagnant 5% H_2SO_4, 24°C.

Model for 316 in Stagnant 5% H_2SO_4 at 30°C

The parameters used to model the behaviour of 316 stainless steel in stagnant 5% H_2SO_4 at 30°C are listed in Tables J-3 and J-4, and the resultant theoretical curve is shown in Figure 4.5.14.

	Reaction 1	Reaction 2	Reaction 7	Reaction 3	Reaction 5	Reaction 5
Cr_2O_3					$Cr(OH)_3.nH_2O$	anhydrous
E_o (V SHE)	-0.440	1.228	1.228	0.000	1.117	1.184
i_o (nA cm^{-2})	7.5×10^{-7}	0.12	5.2×10^{-5}	5.0×10^{3}	0.5	5.0
i_{lim}anodic (nA cm^{-2})	not required	1.0×10^{21}	negligible	negligible	6.0×10^{4}	3.0×10^{8}
i_{lim}cathodic (nA cm^{-2})	negligible	negligible	1.1×10^{4}	1.0×10^{21}	negligible	negligible
α	0.40	0.60	0.49	0.60	0.50	0.50
Temperature	30°C					
pH	0.2					
Resistance	15 Ω					

Table J-3 Parameters used to model 316 stainless steel in stagnant 5% H_2SO_4, 30°C.

	i_{pass} (nA cm^{-2})	A	p	E_t
Reaction 1	1.5×10^{3}	350	2.0	-0.240

Table J-4 Passivation parameters for model of 316 stainless steel in stagnant 5% H_2SO_4, 30°C.

Model for 316 in Stagnant 5% H_2SO_4 at 35°C

The parameters used to model the behaviour of 316 stainless steel in stagnant 5% H_2SO_4 at 35°C (Figure 4.5.15) are listed in Tables J-5 and J-6.

	Reaction 1	Reaction 2	Reaction 7	Reaction 3	Reaction 5	Reaction 5
Cr_2O_3					$Cr(OH)_3.nH_2O$	anhydrous
E_o (V SHE)	-0.440	1.228	1.228	0.000	1.117	1.184
i_o (nA cm^{-2})	3.0 x 10^{-5}	0.12	5.2 x 10^{-5}	500	0.1	3.0
i_{lim}anodic (nA cm^{-2})	not required	1.0 x 10^{21}	negligible	negligible	6.0 x 10^{4}	3.0 x 10^{7}
i_{lim}cathodic (nA cm^{-2})	negligible	negligible	1.2 x 10^{4}	1.0 x 10^{21}	negligible	negligible
α	0.40	0.60	0.49	0.60	0.50	0.50
Temperature	35°C					
pH	0.2					
Resistance	10 Ω					

Table J-5 Parameters used to model 316 stainless steel in stagnant 5% H_2SO_4, 35°C.

	i_{pass} (nA cm^{-2})	A	p	E_t
Reaction 1	1.3 x 10^{3}	350	2.0	-0.240

Table J-6 Passivation parameters for model of 316 stainless steel in stagnant 5% H_2SO_4, 35°C.

Model for 316 in Stagnant 5% H_2SO_4 at 45°C

The parameters used to model the behaviour of 316 stainless steel in stagnant 5% H_2SO_4 at 45°C are listed in Tables J-7 and J-8, and the resultant theoretical curve is shown in Figure 4.5.13.

	Reaction 1	Reaction 2	Reaction 7	Reaction 3	Reaction 5	Reaction 5
Cr_2O_3					$Cr(OH)_3.nH_2O$	anhydrous
E_o (V SHE)	-0.440	1.228	1.228	0.000	1.117	1.184
i_o (nA cm^{-2})	5.0×10^{-5}	0.12	5.2×10^{-5}	5.0×10^{3}	0.5	3.0
i_{lim}anodic (nA cm^{-2})	not required	1.0×10^{21}	negligible	negligible	6.0×10^{4}	8.0×10^{7}
i_{lim}cathodic (nA cm^{-2})	negligible	negligible	3.5×10^{3}	1.0×10^{21}	negligible	negligible
α	0.42	0.60	0.49	0.60	0.50	0.50
Temperature	45°C					
pH	0.2					
Resistance	5 Ω					

Table J-7 Parameters used to model 316 stainless steel in stagnant 5% H_2SO_4, 45°C.

	i_{pass} (nA cm^{-2})	A	p	E_t
Reaction 1	1.9×10^{3}	300	2.0	-0.250

Table J-8 Passivation parameters for model of 316 stainless steel in stagnant 5% H_2SO_4, 45°C.

APPENDIX K PARAMETERS USED FOR 316 STAINLESS STEEL IN NATURAL SEAWATER

Model for 316 Stainless Steel in Natural Seawater at 24°C

The parameters used to model the behaviour of 316 stainless steel in natural seawater at 24°C are listed in Tables K-1 and K-2, and the resultant theoretical curve is shown in Figure 4.5.17.

	Reaction 1	Reaction 2	Reaction 7	Reaction 9	Reaction 9
Cr_2O_3 form				$Cr(OH)_3.nH_2O$	anhydrous
E_o (V SHE)	-0.440	1.228	1.228	1.244	1.311
i_o (nA cm^{-2})	3.0×10^{-7}	0.12	5.2×10^{-5}	50	500
i_{lim}anodic (nA cm^{-2})	not required	1.0×10^{21}	negligible	5.6×10^{3}	1.1×10^{4}
i_{lim}cathodic(nA cm^{-2})	negligible	negligible	5.0×10^{4}	negligible	negligible
α	0.40	0.60	0.44	0.5	0.5
Temperature	24°C				
pH	8.0				
Resistance	100 Ω				

Table K-1 Parameters used to model 316 stainless steel in natural seawater, 24°C.

	i_{pass} (nA cm^{-2})	A	P	E_t
Reaction 1	430	300	2.0	-0.360

Table K-2 Passivation parameters for model of 316 stainless steel in natural seawater, 24°C.

Model for 316 in Natural Seawater at 30°C

The parameters used to model the behaviour of 316 stainless steel in natural seawater at 30°C (Figure 4.5.18) are listed in Tables K-3 and K-4.

	Reaction 1	Reaction 2	Reaction 7	Reaction 9	Reaction 9
Cr_2O_3 form				$Cr(OH)_3.nH_2O$	anhydrous
E_o (V SHE)	-0.440	1.228	1.228	1.244	1.311
i_o (nA cm^{-2})	1.5×10^{-4}	0.12	5.2×10^{-5}	100	0.5
i_{lim}anodic (nA cm^{-2})	not required	1.0×10^{21}	negligible	8.1×10^{4}	1.0×10^{10}
i_{lim}cathodic(nA cm^{-2})	negligible	negligible	1.4×10^{5}	negligible	negligible
α	0.40	0.60	0.43	0.5	0.5
Temperature	30°C				
pH	8.0				
Resistance	15 Ω				

Table K-3 Parameters used to model 316 stainless steel in natural seawater, 30°C.

	i_{pass} (nA cm^{-2})	A	P	E_t
Reaction 1	650	975	2.0	-0.31

Table K-4 Passivation parameters for model of 316 stainless steel in natural seawater, 30°C.

Model for 316 in Natural Seawater at 35°C

The parameters used to model the behaviour of 316 stainless steel in natural seawater at 35°C (Figure 4.5.19) are listed in Tables K-5 and K-6.

	Reaction 1	Reaction 2	Reaction 7	Reaction 9	Reaction 9
Cr_2O_3 form				$Cr(OH)_3.nH_2O$	anhydrous
E_o (V SHE)	-0.440	1.228	1.228	1.244	1.311
i_o (nA cm^{-2})	5.5×10^{-4}	0.12	5.2×10^{-5}	1	50
i_{lim}anodic (nA cm^{-2})	not required	1.0×10^{21}	negligible	1.3×10^{5}	4.1×10^{6}
i_{lim}cathodic(n A cm^{-2})	negligible	negligible	2.6×10^{5}	negligible	negligible
α	0.40	0.60	0.40	0.50	0.50
Temperature	35°C				
pH	8.0				
Resistance	15 Ω				

Table K-5 Parameters used to model 316 stainless steel in natural seawater, 35°C.

	i_{pass} (nA cm^{-2})	A	P	E_t
Reaction 1	3.1×10^{3}	975	2.0	-0.38

Table K-6 Passivation parameters for model of 316 stainless steel in natural seawater, 35°C.

Model for 316 in Natural Seawater at 45°C

The parameters used to model the behaviour of 316 stainless steel in natural seawater at 45°C are listed in Tables K-7 and K-8, and the resultant theoretical curve is shown in Figure 4.5.20.

	Reaction 1	Reaction 2	Reaction 7	Reaction 9	Reaction 9
Cr_2O_3 form				$Cr(OH)_3.nH_2O$	anhydrous
E_o (V SHE)	-0.440	1.228	1.228	1.244	1.311
i_o (nA cm^{-2})	1.0×10^{-6}	0.12	5.2×10^{-5}	500	500
i_{lim}anodic (nA cm^{-2})	not required	1.0×10^{21}	negligible	5.2×10^{4}	1.1×10^{7}
i_{lim}cathodic (nA cm^{-2})	negligible	negligible	5.2×10^{4}	negligible	negligible
α	0.40	0.60	0.37	0.50	0.50
Temperature	45°C				
pH	8.0				
Resistance	15 Ω				

Table K-7 Parameters used to model 316 stainless steel in natural seawater, 45 °C.

	i_{pass} (nA cm^{-2})	A	P	E_t
Reaction 1	430	975	2.0	-0.370

Table K-8 Passivation parameters for model of 316 stainless steel in natural seawater, 45°C.

References

1. Trethewey, K. R. and J. Chamberlain. "Corrosion for Students for Science and Engineering." 1988 Longman Scientific and Technical. Harlow, Essex, UK.

2. Sharp, D. W. A. "Dictionary of Chemistry." 1983 Penguin Books Ltd. Harmondsworth, England.

3. Baboian, R. and S. L. Pohlman. Galvanic Corrosion. Metals Handbook. **13**: 1987.

4. Pryor, M. J. "Bimetallic Corrosion." Corrosion. Shreir ed. 1976 The Butterworth Group. London.

5. Astley, D. J. "Use of the Microcomputer for Calculation of the Distribution of Galvanic Corrosion and Cathodic Protection in Seawater Systems ." Galvanic Corrosion. Hack ed. 1986 American Society for Testing and Materials. Philadelphia.

6. Whitman, W. G. and R. P. Russel. Industr Engng Chem. **16**: 276, 1924.

7. Mansfeld, F. "Area Relationships in Galvanic Corrosion." Corr. **27**(10): 436-442, 1971.

8. Tighe-Ford, D. J. "A systematic approach to the design of warship ICCP systems." : Nato Advanced Research workshop, RNEC Manadon, Plymouth, UK, 6-8th Sep, 1993.

9. Broecker, W. S. "Chemical Oceanography." 1974 Harcourt Brace Jovanovich. New York.

10. Ijessling, F. P. "Aspects of Marine Corrosion and Testing for Seawater Applications." Marine Corrosion of Stainless Steels : Chlorination and Microbial Effects. 1993 The Institute of Materials. London.

11. Rowlands, J. R. "Seawater." Corrosion. Shreir ed. 1979 Newnes-Butterworth.

London.

12. Khambaita, P. Scale Modelling of ICCP Systems. 1995.

13. King, R. and D. Geary. "Cathodic Protection of Offshore Structures.". SINTEF/UMIST. Interim Report. 1976.

14. Riley, J. P. and R. Chester. "Introduction to Marine Chemistry." 1971 Academic Press. London.

15. Ljeon, R. "On the exchange of deep waters in the skagerak.". International Council for Exploration of the Sea, CM Hydrograph. CM No. 157. 1965.

16. Amodt, J. A. and S. E. Eliassen. Environmental conditions in the North Sea and their influence on corrosion protection systems. Corrosion Conference. 1977.

17. Rogers, T. H. "Marine Corrosion." 1969 George Newnes. London.

18. Crennel, J. T. Cathodic protection, some uncertainties. 1st International Conference on Metallic Corrosion. 1962.

19. Munn, R. S. "A review of the development of computational corrosion analysis spatial corrosion modelling through its maturity in the mid-1980s." Computer Modelling in Corrosion. Munn ed. 1992 American Society for Testing and Materials. Philadelphia.

20. Doig, P. and P. E. Flewitt. J.Electrochem.Soc. **126**(12): 2057-2063, 1979.

21. Forrest, A. W., J. W. Fu and R. T. Bicicchi. Validation of the Finite Element Technique for Modelling CP Systems. Corrosion 80. Paper 150, 1980.

22. Helle, H. P., G. H. Beek and J. Ligtelijn. Corr. **37**(9): 522-530, 1981.

23. Danson, D. J. and M. A. Warne. Current Density/Voltage Calculations using Boundary Element Techniques. Corrosion 83. Paper 221, 1983.

24. Rough, A. Boundary Element Modelling of Seawater Condensers. MPhil Thesis, University of Exeter, 1993.

25. Newman, J. "Electrochemical Systems." 1973 Prentice-Hall Inc. Englewood Cliffs, NJ.

26. Astley, D. J. "A method for calculating the extent of galvanic corrosion and cathodic protection in metal tubes assuming unidirectional current flow." Corr. Sci. **23**(8): 801-832, 1983.

27. Astley, D. J. and J. C. Rowlands. "Modelling of bimetallic corrosion in sea water systems." Br.Corros.J. **20**(2): 90-94, 1985.

28. Frumkin, A. N. Zh,.fiz. Khim. **23**(12): 1477-1482, 1949.

29. Tighe-Ford, D. T., M. J. N and L. Hodgkiss. Corr Pre and Control. **32**(5): 88-91, 1985.

30. Tighe-Ford, D. T., J. N. McGrath and L. Hodgekiss. Corr Pre and Control. **32**(2): 36-38, 1985.

31. McGrath, J. N., D. T. Tighe-Ford and L. Hodgkiss. J Nav Eng. **29**(2): 314-322, 1985.

32. Hack, H. P. "Scale modelling for corrosion studies." Corr. **45**(7): 601 - 606, 1989.

33. de Levie, R. Advances in Electrochemistry and Electrochemical Engineering. **6**: 337-340, 1967.

34. Naval Engineering Specification 747 Part 2. Requirements for nickel aluminium bronze casting and ingots part 2 nickel aluminium bronze (naval alloy) sand castings and ingots. 1987.

35. Parvin, P. S. "Polarization characteristics of ship hull materials.". RNEC Manadon. 1988.

36. Paris, W. "Identification of Warship ICCP Systems.". RNEC Manadon. 1992.

37. Brown, T. R. "An electrochemical study using natural and acidified seawater on the phases of nickel aluminium bronze.". AMTE Holton Heath. Tech Memo. AMTE(M) TM 82206. 1982.

38. Cooper, J. F. and G. Rose. AMTE Holton Heath. Laboratory Memorandum. MC 314/76. 1976.

39. Lloyd, D. M., D. M. Lorimer and N. Ridley. Metals Tech. 7: 114-119, 1980.

40. Angell, B. Personal conversation with author. 1994.

41. Lieutenant Commander Simon Mather RN, Marine Engineer (Submarine Service). Personal conversation with author. 1992.

42. Phillips, S. S. and K. R. Trethewey. "Corrosion of Cast Nickel Aluminium Bronze in a Simulated Seawater Condenser Environment." RNEC Research Report. **RNEC-RR-93003**: 1993.

43. Scully, J. R., H. P. Hack and D. G. Tipton. "Effect of exposure time on the polarization behaviour of marine alloys under flowing and quiescent conditions." Corr. **42**(8): 462-469, 1986.

44. Hack, H. P. and J. R. Scully. "Galvanic Corrosion Prediction using Long and Short Term Polarization Curves." Corr. **42**(2): 1986.

45. Trethewey, K. R. and D. J. Marsh. "Polarisation Behaviour of Titanium in Marine Systems." Proceedings of the Ninth Inter-Naval Conference. : 1992.

46. Burbridge, E. "Process Plant and Cooling Water Systems." Cathodic Protection Theory and Practice. Ashworth and Booker ed. 1986 Chichester.

47. Hoar, T. P. Corrosion. Shreir ed. 1976 Butterworths. London..

48. Bomberger, H. B. "Titanium and Titanium Alloys Source Book." 1968 ASTM. Ohio.

49. Olivier, R. 6th CITCE Meeting. 314, 1955.

50. Truman, J. E. "Stainless Steels." Corrosion. Shreir ed. 1976 Butterworths. London.

51. Pourbaix, M. "Atlas of Electrochemical Equilibria in Aqueous Solutions." 1966 Pergamon. Oxford.

52. Stephenson, L. and J. H. Bartlett. J. Electrochem. Soc. **101**: 571, 1954.

53. Reddy, A. K. N. and B. Rao. J. Elec. Soc. **113**(11): 1133, 1966.

54. Vetter, K. J. Z. Elektrochem. **62**: 642, 1958.

55. Armstrong, R. D. "Diagnostic Criteria for Distinguishing Between the Dissolution-Precipitation and the Solid-State Mechanisms of Passivation." Corr Sci. **11**(10): 693-697, 1971.

56. Armstrong, R. D. Intf. Electrochem. **35**(2): 119, 1972.

57. Okamoto, G. and M. Sato. J Electrochem Soc. **110**: 605, 1963.

58. Bockris, J. and A. Reddy. "Modern Electrochemistry." 1970 Plenum Press. London.

59. Ekerbakh, U., K. Schwabe and P. Konig. Electrochim Acta. **15**: 773, 1969.

60. Bernhardsson, S. Extended Abstracts. 25th International Society of Electrochemistry. 1974.

61. Bernhardsson, S. and R. Mellstrom. "A Method of Evaluating Polarization Curves for Stainless Steel via a Simple Passivation Model." Electrochemical Corrosion Testing, ASTM STP 727. Mansfeld and Bertocci ed. 1981 ASTM. Philadelphia.

62. Sieradzki, K. and R. C. Newman. "A Percolation Model for Passivation in Stainless Steels." J.Electrochem.Soc. **133**(9): 1979-1980, 1986.

63. Newman, R. C., F. T. Meng and K. Sieradzki. "Validation of a Percolation Model for Passivation of Fe-Cr Alloys : 1 Current Efficiency in the Incompletely Passivated State." Corr.Sci. **28**(5): 523-527, 1988.

64. Qian, S., R. C. Newman and R. A. Cottis. "Validation of a Percolation Model for Passivation of Fe-Cr Alloys : Two-Dimensional Computer Simulations." J.Electrochem.Soc. **137**(2): 435-439, 1990.

65. Steigerwald, R. F. and N. D. Greene. "Anodic Dissolution of Binary Alloys." J.Electochem.Soc. **109**(11): 1026-1034, 1962.

66. Olivier, R. "International Committee of Electrochemical Thermodynamics and Kinetics." 1954 Butterworths. London.

67. Uhlig, H. H. and S. Lord. J Electrochem Soc. **100**: 216, 1953.

68. Uhlig, H. H. and P. F. King. J phys Chem. **63**(2026): 1959.

69. Davenport, A. J., M. Sansone, J. A. Bardwell, A. J. Aldykiewicz, M. Taube and C. M. Vitus. "In Situ Multielement XANES Study on Formation and Reduction of the Oxide Film on Stainless Steel." J Electrochem Soc. **141**(1): L6, 1994.

70. Griffin, G. L. J Electrochem Soc. **131**(18): 1984.

71. Griffin, G. L. "The Cation Monolayer Model for Metal Passivation." J Electrochem Soc. **133**(7): 1315-1320, 1986.

72. Marcus, P. "On Some Fundamental Factors in the Effect of Alloying Elements on Passivation of Alloys." Corr Sci. **36**(12): 2155-2158, 1994.

73. Maurice, V., H. Talah and P. Marcus. Surface Sci. **304**: 98, 1994.

74. Maurice, V., W. Yang and P. Marcus. J Electrochem Soc. **142**: 1994.

75. Genshaw, M. A. and R. S. Sirohi. J.Electrochem.Soc. **118**: 1558, 1971.

76. Mansurov, G. N. and I. V. Boguslavskaya. Elektrokhimiya. **19**: 1252, 1983.

77. Seo, M., R. Saito and N. Sato. J.Electrochem.Soc. **127**: 1909, 1980.

78. Shlepakov, M. N., A. M. Sukhotin, P. Kostikov and E. G. Kuz'mina. Elektrokhimiya. **22**(125): 1986, 1986.

79. Oblongsky, L. J. and T. M. Devine. "A Surface Enhanced Raman Spectroscopic Study of Passive Films Formed in Borate Buffer on Iron, Nickel, Chromium and Stainless Steel." Corros.Sci. **37**(1): 17-41, 1995.

80. Lu, Y. C. and C. R. Clayton. "Evidence for a Bipolar Mechanism of Passivity in Mo Bearing Stainless Steels." J.Electrochem.Soc. **132**(10): 2517-2518, 1985.

81. Brooks, A. R., C. R. Clayton and Y. C. Lu. "On the Role of Cr in the Passivity of Stainless Steels." J.Electrochem Soc. **133**(12): 2459-2464, 1986.

82. Lumsden, J. B. and P. J. Stocker. "Effects of Exposure to Air on Passive Films on Stainless Steels." J.Electrochem.Soc. **133**(9): 1977-1978, 1986.

83. Clayton, C. R. and Y. C. Lu. "A Bipolar Model of the Passivity of Stainless Steel." J.Electrochem.Soc. **133**(2): 2465-2472, 1986.

84. Stypuka, B. and J. Stoch. "The Characterization of Passive Films on Chromium Electrodes by XPS." Corr Sci. **36**(12): 2159-2167, 1994.

85. Sunseri, C., S. Piazza and F. Di Quarto. "Photocurrent Spectroscopic Investigations of Passive Films on Chromium." J.Electrochem.Soc. **137**(8): 2411-2417, 1990.

86. Sakashita, M. and N. Sato. Passivity of Metals. 1978 The Electrochemical Society. Princeton, NJ.

87. Rozenfeld, I. L. "Corrosion Inhibitors." 1981 McGraw-Hill. New York.

88. Sedriks, A. J. "The Corrosion of Stainless Steels." The Corrosion Monograph series. 1979 John Wiley and Sons. New Jersey.

89. Clayton, C. R., Y. C. Lu and A. R. Brooks. "A Bipolar Model of the Passivity of Stainless steels II The Mechanism of MoO_4^{2-} Formation and Incorporation." Corros.Sci. **29**(7): 881-898, 1989.

90. Maximovitch, S., G. Barral, F. Le Cras and F. Claudet. "The Electrochemical Incorporation of Mo in the Passive Layer of a 17% Cr Ferritic Stainless Steel. Its Influence on Film Stability in Sulphuric Acid and on Pitting Corrosion in Chloride Media." Corros.Sci. **37**(2): 271-291, 1995.

91. Sakashita, M. and N. Sato. Corros Sci. **17**: 474, 1977.

92. Trethewey, K. R., J. S. Keenan and . "Microcomputer-Based Corrosion Modelling Applied to Polarisation Curves." ASTM STP 1154. **Computer Modelling in Corrosion, ASTM STP 1154, Ed R.S. Munn, ASTM, Philadelphia, 1992**: 113-125, 1992.

93. Trethewey, K. R. and J. S. Keenan. "The SIMPLER Computer Corrosion Modelling System." 1992 EG&G PAR. Princeton, NJ.

94. West, G. "Investigation into corrosion protection of nickel-aluminium-bronze by flame sprayed ceramic coatings. ." RNEC Project Report. : 1993.

95. Trethewey, K. R., D. J. Marsh, D. A. Sargeant, P. R. Roberge and J. Burvill. An Indicator of Crevice Corrosion Initiation Based upon Electrochemical Noise Analysis. ASTM Electrochemical Noise Symposium. **1**: 1994.

96. Devereux, O. F. and Y. K.S. "Modelling Electron Transfer, Diffusional Effects, Passivation, and Ohmic Loss in Multi-Reaction Polarization Curves." ASTM STP 1154. : pp126-142, 1992.

97. Mueller, W. A. "A Model of the Mechanism of Electrochemical Conversion from

Active to Passive States." J. electrochem Soc. **107**(3): 157-164, 1960.

98. Trethewey, K., J. Keenan and I. Wilson. "Analysis of the electrochemical corrosion behaviour of stainless steels using the SIMPLER computer model." Corr Pre and Con. **38**(5): 115-118, 1991.

99. Hines, J. G. "Analysis of complex polarisation curves." Br. Corros. J. **18**(1): 9-14, 1983.

100. Otieno-Alego, V., G. A. Hope, H. J. Flitt, G. A. Cash and D. P. Schweinsberg. "The Effects of Potential Scan Rate on the Parameters Used to Synthesize Anodic Polarization Curves." Corr Sci. **33**(11): 1719-1734, 1992.

101. Cash, G. A., D. P. Schweinsberg and G. A. Hope. "The corrosion rate of low carbon steel in stationary and stirred sugar juice : a mathematical analysis of polarisation curves." Corr. Sci. **30**(6/7): 543 - 544, 1990.

102. Cash, G. A., D. P. Schweinsberg, G. A. Hope and H. J. Flitt. "The corrosion resistance of low carbon steel in flowing sugar juice : the analysis of polarisation curves from a laboratory flow system." Corr. Sci. **33**(1): 113 - 122, 1992.

103. Otieno-Alego, V., G. A. Hope, H. J. Flitt and D. P. Schweinsberg. "The corrosion of a low alloy steel in a steam turbine environment : the effect of oxygen concentration and potential scan rate on input parameters used to computer match the experimental polarization curves." Corr Sci. **37**(3): 509-525, 1995.

104. Bird, H. E. H., B. R. Pearson and P. A. Brook. "The breakdown of passive film on iron." Corr. Sci. **28**(1): 81-86, 1988.

105. Miligy, A. A., D. Geana and W. I. Lorenz. Electrochimica Acta. **20**(2): 273, 1975.

106. Evans, U. R. "The Corrosion and Oxidation of Metals." 1960 Arnold. London.

107. Pearson, B. R. and P. A. Brook. "The synthesis of electrode polarisation curves." Corr. Sci. **32**(4): 387-398, 1991.

108. Marsh, D. J. and K. R. Trethewey. "The Effect of Scan Rate on the Polarization of Mild Steel in Seawater.". RNEC Manadon. RNEC-RP-93013. 1993.

109. Edeleanu, C. and J. G. Hines. "Modelling Approach to Corrosion Prediction." Bri Corros J. **18**(1): 6-9, 1983.

110. Uhlig, H. H. "Corrosion and Corrosion Control." 1971 J Wiley and Sons. New York.

111. Davis, J. R. Corrosion. Metals Handbook. **13**: 1987.

112. West, J. M. "Basic Corrosion and Oxidation." 1980 Ellis Horwood Ltd. Chichester.

113. Bartlett, J. H. and L. Stephenson. J. Electrochem. Soc. **99**: 504, 1952.

114. Evans, U. R. "An Introduction to Metallic Corrosion." 1981 Edward Arnold. London.

115. Geana, D., A. A. El Miligy and W. J. Lorenz. "Galvanostatic and potentiostatic measurements on iron dissolution in the range between active and passive states ." Corr Sci. **14**(11/12): 657-664, 1974.

116. Keddam, M., O. R. Mattos and H. Takenouti. "Reaction Model for Iron Dissolution I." J. Electrochem. Soc. **128**(2): 257-266, 1981.

117. Keddam, M., O. R. Mattos and H. Takenouti. "Reaction Model for Iron Dissolution Studied by Electrode Impedance II." J. Electrochem. Soc. **128**(2): 266-274, 1981.

118. Baddi, M., C. Gabrielli, M. Keddam and H. Takenouti. Passivity of Metals. The Electrochemical Society Softbound Proceedings Series. p625, 1978.

119. Franck, U. F. Z. Naturforschung. **4A**(378): 1949.

120. Huq, A. K. M. S. Proc. Roy. Soc. . **a237**(1733): 1956.

121. Parsons. "Handbook of Electrochemical Constants." 1959 Butterworths. London.

122. Shreir, L. "Corrosion." 1979 Butterworths & Co Ltd. London.

123. Riegler, P. "Electrochemistry."

124. Sato, N. and M. Seo. Boshoku Gijutsu. **24**: 399, 1975.

125. Sridhar, N., J. Kolts, S. K. Srivastava and A. I. Asphahani. Physical Metallurgy, Properties and Industrial Applications of Ferralium Alloy 255. Duplex Stainless Steels. 481, 1982.

126. Soloman, H. D. and T. M. Devine Jr. Duplex Stainless Steel - A Tale of Two Phases. Duplex Stainless Steel. 693, 1982.

127. Reid, H. F. and W. T. Delong. Met Prog. **84**: 73, 1973.

128. Lundin, C. D. and D. F. Spond. Weld. J. Res.Suppl. **55**: 356, 1976.

129. Pinnow, K. E. and A. Moskowits. J. Weld. Res. Suppl. **49**: 278, 1970.

130. Langley Alloys. "FERRALIUM alloy 255-3SC/43V Data Form.". 1993.

131. Trethewey, K. R., D. A. Sargeant, D. J. Marsh and A. A. Tamimi. "Applications of the Scanning Reference Technique to Localised Corrosion." Corr Sci. **35**(1-4): 127-134, 1993.

132. Trethewey, K. R., D. A. Sargeant, D. J. Marsh and S. Haines. New Methods of Quantitative Analysis of Localized Corrosion Scanning Electrochemical Probes. Modelling Aqueous Corrosion. 417-442, 1994.

133. Simoes, A. M. P., M. G. S. Ferreira, G. Lorang and M. Da Cunha Belo. "Influence of temperature on the properties of passive films formed on AISI 304 stainless steel ." Electrochim Acta. **36**(2): 315-320, 1991.

134. Okamoto, G. "Passive film of 18-8 stainless steel, structure and its function." Corr Sci. **13**: 471-489, 1973.

135. Bendall, K. Langley Alloys Ltd, Telephone conversation with author, 1995.

136. Bendall, K. Langley Alloys Ltd, Facsimile. 1995.

137. Phillips, S. S., D. J. Marsh and K. R. Trethewey. The Corrosion of Duplex Stainless Steel in Natural Seawater. UKCorr 94. **2**: 170 - 177, 1994.

138. Bendall, K. Langley Alloys Ltd, Conversation with author at UKCorr 94, Bournemouth, 1994.

139. Marsh, D. J. Personal communication with author. 1995.

140. Finn, M. Langley Alloys Ltd, Telephone conversation with author, 1995.

141. Johnsen, R. "North Sea Experience with the Use of Stainless Steels in Seawater Applications." Marine Corrosion of Stainless Steels : Chlorination and Microbial Effects . 1993 Institute of Materials. London.

142. Avesta Sheffield, L. "Stainless Steels Reference.". Avesta Sheffield, Ltd. 1994.

143. Inco Alloys, L. "Inco Alloy 25-6Mo.". Inco Alloys, Ltd. 1993.

144. Newman, R. C. Atomistics of Alloy Corrosion and Passivation. 45TH Annual Meeting of the International Society of Electrochemistry. 1994.

145. Ryan, M. P., M. C. Simmonds, G. E. Thompson and R. C. Newman. In-Situ STM Studies of Structural Transformations of Passive Oxide Films on Fe-Cr Alloys. UKCorr 94. 1994.

146. Keddam, M., O. R. Mattos and H. Takenouti. "Mechanism of Anodic Dissolution of Iron-Chromium Alloys Investigated by Electrode Impedances I. Experimental Results and Reaction Model." Electrochima Acta. **31**(9): 1147-1158, 1986.

147. Bernhardsson, S. The Corrosion Resistance of Duplex Stainless Steels. Duplex Stainless Steel. p185, 1991.

148. Garfias-Mesias, L. F., J. M. Sykes and C. D. S. Tuck. Effect of Constitution on the Pitting Resistance of Duplex Stainless Steels in Chloride Solutions. 35th Corrosion Science Seminar. 1994.

149. Pallotta, C., N. De Cristofano, R. C. Salvarezza and A. J. Arvia. "The Influence of Temperature and the Role of Chromium in the Passive Layer in Relation to Pitting Corrosion of 316 Stainless Steel in NaCl Solution." Electrochim Acta. **31**(10): 1265-1270, 1986.

150. Leckie, H. P. and H. H. Uhlig. J Electrochem Soc. **113**: 1261, 1966.

151. Forchhammer, P. and H. L. Engell. Werks. und Korr. **20**(1): 1969.

152. Saito, H., T. Shibata and G. Okamoto. Corr Sci. : 693, 1979.

153. Burstein, G. T., P. C. Pictorius and S. P. Mattin. "The Nucleation and Growth of Corrosion Pits on Stainless Steel." Corr Sci. **35**(1): 57-62, 1993.

154. Newman, R. C. and M. A. A. Ajjawi. "A Micro-electrode Study of the Nitrate Effect on Pitting Stainless Steels." Corr Sci. **26**: 1057, 1986.

155. Hoare, J. P. "The Electrochemistry of Oxygen." 1962 Interscience. New York.

156. Damjanovic, A. "The Kinetics of the Mechanism of the Oxygen Reduction Reaction." Modern Aspects of Electrochemistry. Bockris and Conway ed. 1969 Plenum Press. New York.

157. Higgins, R. A. "Engineering Metallurgy." 1983 Edward Arnold. London.

158. Perryman, I. Vosper Thorneycroft Ltd, Personal conversation with author, 1992.

159. Inter Ocean Systems. "Inter-Ocean catalog." 1975 Inter-Ocean Systems. San Diego,

California.

160. Steigerwald, R. F. and N. D. Greene. "Anodic Dissolution of Binary Alloys." J.Electochem.Soc. **109**(11): 1026-1034, 1962.